

DOT/FAA/TC-15/4

Federal Aviation Administration
William J. Hughes Technical Center
Aviation Research Division
Atlantic City International Airport
New Jersey 08405

A Quantitative Assessment of Advanced Nondestructive Inspection Techniques for Detecting Flaws in Composite Laminate Aircraft Structures

March 2016

Final Report

This document is available to the U.S. public through the National Technical Information Services (NTIS), Springfield, Virginia 22161.

This document is also available from the Federal Aviation Administration William J. Hughes Technical Center at actlibrary.tc.faa.gov.



U.S. Department of Transportation
Federal Aviation Administration

NOTICE

This document is disseminated under the sponsorship of the U.S. Department of Transportation in the interest of information exchange. The U.S. Government assumes no liability for the contents or use thereof. The U.S. Government does not endorse products or manufacturers. Trade or manufacturers' names appear herein solely because they are considered essential to the objective of this report. The findings and conclusions in this report are those of the author(s) and do not necessarily represent the views of the funding agency. This document does not constitute FAA policy. Consult the FAA sponsoring organization listed on the Technical Documentation page as to its use.

This report is available at the Federal Aviation Administration William J. Hughes Technical Center's Full-Text Technical Reports page: actlibrary.tc.faa.gov in Adobe Acrobat portable document format (PDF).

1. Report No. DOT/FAA/TC-15/4		2. Government Accession No.		3. Recipient's Catalog No.	
4. Title and Subtitle A QUANTITATIVE ASSESSMENT OF ADVANCED NONDESTRUCTIVE INSPECTION TECHNIQUES FOR DETECTING FLAWS IN COMPOSITE LAMINATE AIRCRAFT STRUCTURES				5. Report Date March 2016	
				6. Performing Organization Code	
7. Author(s) Dennis P. Roach and Thomas M. Rice				8. Performing Organization Report No.	
9. Performing Organization Name and Address Sandia National Laboratories FAA Airworthiness Assurance Center Box 5800 MS-0615 Albuquerque, NM 87185				10. Work Unit No. (TRAIS)	
				11. Contract or Grant No. DTFA03-95-X-900002	
12. Sponsoring Agency Name and Address Federal Aviation Administration William J. Hughes Technical Center Atlantic City International Airport, NJ 08405				13. Type of Report and Period Covered Final Report	
				14. Sponsoring Agency Code ANE-10	
15. Supplementary Notes The Federal Aviation Administration William J. Hughes Technical Center Aviation Research Division CORs were Dave Galella and David Westlund.					
16. Abstract The aircraft industry continues to increase its use of composite materials for principle structural elements. This increased use and the difficulties associated with damage tolerance analysis of composites has placed greater emphasis on the application of accurate nondestructive inspection (NDI) methods. Traditionally, a few ultrasonic (UT)-based inspection methods have been used to inspect solid laminate structures. Recent developments in more advanced NDI techniques have produced a number of new inspection options. Many of these methods can be categorized as wide-area techniques that produce 2D flaw maps of the structure. An experiment has been developed to assess the ability of both conventional and advanced NDI techniques to detect voids, disbonds, delaminations, and impact damage in adhesively bonded composite aircraft structures. A series of solid laminate, carbon composite specimens with statistically relevant flaw profiles are being inspected using conventional, handheld pulse-echo ultrasonic and resonance and new NDI methods that have recently been introduced to improve sensitivity and repeatability of inspections. The primary factors affecting flaw detection in laminates are included in this study: material type; flaw profiles; presence of complex geometries like taper and substructure elements; presence of fasteners; secondarily bonded joints; and environmental conditions. One phase of this study utilized airline personnel to study probability of detection (POD) in the field and to formulate improvements to existing inspection techniques. In addition, advanced NDI methods for laminate inspections (e.g., thermography, shearography, laser UTs, microwave, phased array UT, and linear array UT) were applied to quantify the improvements achievable through the use of more sophisticated NDI. This report presents the composite laminate experiment design and the POD results for advanced NDI with comparisons to results achieved by airline inspectors using conventional UT methods. A companion report available at the Federal Aviation's online report database (actlibrary.tc.faa.gov) provides the full set of results from the conventional NDI testing.					
17. Key Words Nondestructive inspection, Honeycomb composites, Solid laminate composites, Probability of detection, Disbonds, Delaminations, Impact, Aircraft, Ultrasonic			18. Distribution Statement This document is available to the U.S. public through the National Technical Information Service (NTIS), Springfield, Virginia 22161. This document is also available from the Federal Aviation Administration William J. Hughes Technical Center at actlibrary.tc.faa.gov.		
19. Security Classif. (of this report) Unclassified		20. Security Classif. (of this page) Unclassified		21. No. of Pages 348	22. Price

ACKNOWLEDGEMENTS

This program is sponsored by the Federal Aviation Administration (FAA) William J. Hughes Technical Center under the direction of its technical monitors, Dave Galella and David Westlund. The approach used in this study was formulated in collaboration with the Commercial Aircraft Composite Repair Committee Inspection Task Group (CACRC-ITG), which consisted of the team members listed below. The contributions of this team are gratefully acknowledged.

The CACRC-ITG (at the time of experiment planning):

Gerry Doetkott, Northwest Airlines
Alex Melton, Delta Air Lines
Richard Watkins, Delta Air Lines
Tom Dreher, Rolls Royce
Robert Stevens, United Airlines
Bruce Garbett, Airbus Industries
John Hewitt, Airbus Industries
Jim Hofer, The Boeing Company
Jeff Kollgaard, The Boeing Company
Glæe McDonald, US Airways
Eric Bartoletti, American Airlines
Kirk Rackow, Sandia Labs Airworthiness Assurance NDI Validation Center (AANC)
Dennis Roach, Sandia Labs AANC

The authors would like to recognize the data acquisition support provided by others at the Sandia Labs AANC, including Stephen Neidigk and Randy Duvall. We would like to thank those who provided FAA oversight and extensive guidance on this effort: Dave Galella and David Westlund, FAA Project Managers; and Rusty Jones, FAA Senior Technical Specialist in Nondestructive Inspection and Composites. Thanks also to Eric Chesmar and his United Airlines colleagues for their assistance in test specimen production.

Finally, the authors would like to thank the following companies for participating in this experiment: Olympus NDT, Toshiba, All Nippon Airways, RCON NDT in conjunction with Sonatest, NDT Solutions Inc., General Electric Inspection Technologies, iPhoton, Imperium, DolphiTech, Laser Technology Inc., Dantec Dynamics, Thermal Wave Imaging, MISTRAS, MoviTHERM, and Evisive.

Sandia National Laboratories is a multi-program laboratory managed and operated by Sandia Corporation (a wholly owned subsidiary of Lockheed Martin Corporation) for the U.S. Department of Energy's National Nuclear Security Administration under contract DE-AC04-94AL85000.

TABLE OF CONTENTS

	Page
EXECUTIVE SUMMARY	xxvii
1. INTRODUCTION AND BACKGROUND	1
1.1 Overview of The Composite Laminate Flaw Detection Experiment	1
1.2 Increasing Use of Composites in Aircraft Structures	3
1.3 Background on In-Service Inspection Needs for Composite Structures	7
1.4 Damage Tolerance Approach to Establish Inspection Intervals	7
1.4.1 Inspection Intervals	9
2. PURPOSE OF COMPOSITE LAMINATE FLAW DETECTION EXPERIMENT	11
3. DESCRIPTION OF CONVENTIONAL AND ADVANCED INSPECTION METHODS APPLIED TO COMPOSITE LAMINATE FLAW DETECTION EXPERIMENT	18
3.1 The PE-UTs with C-Scan Imaging	18
3.1.1 A-Scan Mode	19
3.1.2 C-Scan Mode: Use of UT Scanning Technology	20
3.2 Phased Array and Linear Array UTs	24
3.2.1 Olympus OmniScan PA-UT System	26
3.2.2 Toshiba Matrixeye PA-UT System	28
3.2.3 Boeing MAUS FlawInspecta Linear Array UT System and the Diagnostic Sonar FlawInspecta PA-UT System	31
3.2.4 General Electric RotoArray PA-UT System	35
3.2.5 Sonatest RapidScan 2 Linear Array UT System	36
3.3 Laser-Ultrasonics	39
3.3.1 The LUS Deployment	39
3.4 Acoustography—Video-Based UTs	47
3.4.1 Imperium AcustoCam Digital Acoustic Video Device	49
3.4.2 DolphiTech DolphiCam Ultrasound Video Camera Device	51
3.5 Microwave Inspection	53
3.6 Shearography	56

3.6.1	Laser Technology, Inc. LTI-5200 System	58
3.6.2	Dantec Dynamics Q-810 Laser Shearography System	61
3.7	Pulsed Thermography	63
3.7.1	Thermal Wave Imaging's EchoTherm Thermography Inspection System	65
3.8	Line Scanning Thermography	71
3.8.1	MISTRAS Line Scan Thermography Inspection System	73
3.9	Lock-In Thermography	75
3.9.1	MoviTHERM Lock-In Thermography System	77
4.	COMPOSITE SLE DESIGN	78
4.1	Experiment Design Guidelines	81
4.2	Specimen Design and Experiment Implementation Approach	84
4.3	Flaw Manufacture Options	96
4.3.1	Flaw Characterization	99
4.4	Experiment Timing	100
4.5	The RDCE	102
5.	COMPOSITE LAMINATE FLAW DETECTION EXPERIMENT IMPLEMENTATION	106
6.	RESULTS FROM COMPOSITE LAMINATE FLAW DETECTION EXPERIMENT	111
6.1	Summary of Main Inspection Results from Conventional UT Inspections	114
6.1.1	Summary Inspection Results for the 12–20 Ply Thin Laminate Experiment	115
6.1.2	Summary of Inspection Results for the 20–32 Ply Thick Laminate Experiment	124
6.1.3	Summary of Inspection Results for the Overall Combined Solid Laminate Inspection Experiment—Combined 12–20 Ply Thin Laminate Experiment and 20–32 Ply Thick Laminate Experiment	135
6.1.4	Summary of Inspection Results for the RDCE	140
6.2	Inspection Performance Results for Phased Array and Linear Array UTs	144
6.2.1	Results for the Test Specimens Inspected by Olympus OmniScan	144
6.2.2	Results for the Test Specimens Inspected by Toshiba Matrixeye	154

6.2.3	Results for the Test Specimens Inspected by Boeing MAUS V with FlawInspecta	162
6.2.4	Results for the Test Specimens Inspected by the GE RotoArray	170
6.2.5	Results for the Test Specimens Inspected by Sonatest Linear Array WheelProbe	174
6.3	Inspection Performance Results for IUS	179
6.3.1	Results for Test Specimens Inspected by iPhoton iPLUS LUS System	179
6.4	Inspection Performance Results for Video-Based UTS	187
6.4.1	Results for the Test Specimens Inspected by Imperium AcoustoCam	187
6.4.2	Results for the Test Specimens Inspected by DolphiTech DolphiCam	196
6.5	Inspection Performance Results for MW	199
6.5.1	Results for the Test Specimens Inspected by Evisive MW	199
6.6	Inspection Performance Results for Shearography	201
6.6.1	Results for the Test Specimens Inspected by LTI Shearography	201
6.6.2	Results for the Test Specimens Inspected by Dantec Dynamics Shearography	206
6.7	Inspection Performance Results for Pulsed Thermography	213
6.7.1	Results for the Test Specimens Inspected by TWI Pulsed IR	213
6.8	Inspection Performance Results for LST	221
6.8.1	Results for the Test Specimens Inspected by MISTRAS LST	221
6.9	Inspection Performance Results for Lock-In Thermography	229
6.9.1	Results for the Test Specimens Inspected by MoviTHERM Lock-In Thermography	229
6.10	Comparison of Advanced NDI Methods	236
7.	CONCLUSIONS AND RECOMMENDATIONS	254
7.1	Overview Thoughts on nondestructive inspection for Solid Laminate Composite Structures	254
7.2	Results from Conventional PE-UT POD Tests	255
7.3	Results from POD Tests Using Advanced NDI Methods	259
7.4	Summary of Key Points and Best NDI Practices	267

APPENDICES

A—COMPOSITE LAMINATE FLAW DETECTION EXPERIMENT:
EXPERIMENTER INFORMATION PACKET

B—COMPOSITE LAMINATE FLAW DETECTION EXPERIMENT: EXPERIMENT
BRIEFING

C—COMPOSITE SOLID LAMINATE FLAW DETECTION EXPERIMENT:
EXPERIMENT MONITOR DATA ACQUISITION SHEETS

D—COMPOSITE LAMINATE FLAW DETECTION EXPERIMENT: SUMMARY OF
TEST SPECIMENS

E—DISTRIBUTION LIST FOR REPORT

LIST OF FIGURES

Figure		Page
1	Subset of the 15 painted solid laminate test specimens and 5 feedback specimens	2
2	Use of composite structures on Airbus 320 series aircraft	4
3	Major composite structures on A380 aircraft	4
4	Summary of composite structures on Boeing 787 aircraft	5
5	Summary of composite structures on Cessna Citation III aircraft and conventional NDI methods used to inspect them	5
6	Production of an all-composite fuselage section	6
7	Summary of advanced composite applications on A380 primary structures	6
8	Residual strength curve	8
9	Crack growth curve showing time available for damage control	9
10	The POD vs. flaw size	10
11	Effect of circumstances on POD	11
12	Expansion in the use of composite materials in aircraft construction	12
13	Sample sources of damage to composite structures	13
14	Sample damage from ground service vehicle impact	14
15	Sample damage from ground operations	14
16	Sample damage from impacts during flight	15
17	Sample damage from lightning strike	15
18	Sources of in-service damage to composite structures	16
19	Probability of impact energy as a function of take-off speed (based on runway debris collected from 4 UK military air bases)	16
20	Effects of impact on composite structures	17
21	Example of external impact creating minor surface demarcation but significant internal damage	18
22	Comparison of visible and backside damage (crushed core and backside fiber fracture) in honeycomb structures	18
23	Schematic of PE-UT inspection and A-scan signal showing reflection of UT waves at assorted interfaces	20
24	Schematic of C-scan setup for PE-UT inspection	21
25	The MAUS automated UT scanning system	22
26	Sample UT signals generated from a (a) structure without damage and (b) structure with damage	23
27	Sample C-scan produced by an automated UT scanning device	23

28	C-scan image produced by selective gating on the amplitude of all signals received by the transducer	24
29	The PA-UT (a) deployed in a rolling wheel mechanism and (b) contained in a single probe housing	25
30	Schematic showing the operation of a UT array which allows for the generation and acquisition of multiple UT signals	26
31	Olympus OmniScan device with a 16:128 phased array transducer	27
32	Amplitude (left) and time of flight (right) data produced by OmniScan inspection of a composite laminate aircraft panel with flaw profile as shown	27
33	C-scan images produced by OmniScan PA-UT inspection of 20-ply composite laminate feedback panel with the flaw profile as shown	28
34	Matrixeye equipment deployed with an X-Y scanner and phased array probe incorporated into a soft wedge scanning shoe	29
35	C-scan image of the 32-ply NDI feedback panel showing Matrixeye use of multiple gates to detect flaws at various depths	30
36	Matrixeye C-scan image of carbon solid laminate calibration panel with interply flaws	31
37	Diagnostic sonar FlawInspecta PA-UT inspection system	32
38	FlawInspecta linear array UT system deployed on MAUS V scanner platform (linear array UT probe includes a delay line shoe)	33
39	Composite honeycomb reference standard and sample FlawInspecta results (3-ply carbon skin with 1" thick core)	33
40	Sample result from FlawInspecta PA-UT system on 6-ply carbon specimen (dashed lines represent missed flaws)	34
41	C-scan images produced by FlawInspecta MAUS V linear array UT system on a 32-ply composite laminate feedback panel with the flaw profile as shown	34
42	The GE Phasor XS RotoArray wheel probe containing a 5 MHz, 64-element linear array	35
43	Deployment of the RotoArray wheel probe on a composite laminate test specimen in the AANC flaw detection experiment	36
44	Results produced by RotoArray wheel probe on a 32-ply panel with substructure elements	36
45	The RapidScan UT array device	37
46	Carbon composite panel with stringers, ribs, and engineered flaws: three stringer-to-skin disbonds (yellow) and two rib-to-skin partial disbonds (blue)	38
47	Inspection scans of composite panel produced by the RapidScan UT array device	38
48	Scan of composite horizontal stabilizer with UT RapidScan array probe	38

49	C-scan images produced by RapidScan rolling wheel array probe on a 20-ply composite laminate feedback panel with the flaw profile as shown	39
50	Schematic of LUS system operation	40
51	Comparison of conventional and LUS interrogation of components	41
52	Schematic of LUS method and deployment in a gantry system and rail system	41
53	Inspection of a part using the iPLUS scan head and articulating robot	42
54	An iPLUS LUS scan of a 16-ply composite laminate with impact damage	43
55	An (a) iPLUS LUS inspection of 0.111" thick composite laminate test specimen and (b) photograph of the layout of the engineered flaws	43
56	An iPLUS LUS image of a composite part containing an inclusion, as highlighted	44
57	Sample results from iPLUS LUS inspection of a 3-ply fiberglass honeycomb panel	44
58	Robot camera photographs matched with associated LUS C-scans for the inspection of a BN-shaped composite component	45
59	Acoustography through-transmission mode allows instant full-field inspection of an area	47
60	Through-transmission (a) C-scan and (b) acoustography inspection of impact damage in a graphite/epoxy composite specimen	48
61	Reflection mode acoustography allows for single-sided UT inspection	48
62	Preliminary results with reflection mode acoustography (a) image of disbond at aluminum skin/honeycomb interface, and (b) image of impact damage in graphite/epoxy composite laminate AcoustoCam (Imperium)	48
63	Imperium acoustography equipment and flaw image	50
64	A 2D stitched image produced from individual AcoustoCam results on a composite panel	51
65	DolphiCam handheld portable ultrasound video camera	52
66	Dolphicam A-scan, B-scan, C-scan (time-of-flight or amplitude image) and 3D visualizer display showing interactive flaw sizing and depth measurements	52
67	DolphiCam inspection results showing (a) amplitude images of impact damage, (b) interply delamination, and (c) impact damage in composite laminate structures	53
68	DolphiCam 3D image and sample global image formed from various flaw images superimposed on the flaw layout drawing of a composite panel	53
69	Configuration of MW inspection system on a laboratory scan table	54
70	Basic equipment setup for MW inspection	54
71	Sample MW inspection results for 3-ply fiberglass honeycomb panel with engineered flaws (fiberglass skin bonded to Nomex honeycomb)	55
72	Sample MW inspection results for 3-ply and 12-ply fiberglass panels with delamination, disbonds, potted core, and core splice	55

73	The LTI-5200 portable shearography system with camera on a test specimen	57
74	Basic principles of shearography	58
75	Composite rudder inspection using LTI-5200 portable vacuum shearography system	59
76	Schematic of shearography inspection for near-side and far-side disbond detection	59
77	Near-side and far-side disbonds in an A310 composite rudder detected by the LTI-5200 shearography system	60
78	Close-up view of LTI-5200 shearography images showing (a) flaws in a composite honeycomb structure and (b) a sample shearography result for a 6-ply fiberglass panel showing near-side and far-side flaw imaging	60
79	An LTI-5200 shearographic inspection image of a scarfed repair to a honeycomb structure with anomaly indications in the repair plies	61
80	Shearography image produced from inspection of composite laminate panel (0.11" thick skin; the flaw profile is shown in the middle drawing)	61
81	The Q-810 laser shearography system	62
82	The (a) test specimen and (b) Q-810 shearography image of wrinkles in a composite laminate	62
83	Principle of active pulsed thermography	63
84	Laboratory (a) Thermal Wave Imaging system inspecting composite flaw detection panels and (b) portable field system inspecting an aircraft fuselage	64
85	Comparison of IR cameras for thermography inspection	65
86	The TWI system equipment and inspection of an aircraft	66
87	Sample thermography image showing a disbond in an aluminum fuselage-tear strap structure	67
88	A (a) Flir A40 uncooled camera inspecting the honeycomb test panels and a (b) sample IR image from a fiberglass panel	67
89	A (a) thermography image produced from inspection of composite laminate panel with flaw profile and (b) a drawing of the flaw profile	68
90	Sample thermography images showing damage in composite structures	68
91	Sequence of thermal wave images from DC-9 composite doubler inspection (frame time [f] = 1/60 of a second)	70
92	Examples of thermal images generated after scanning a composite structure using the LST technique	71
93	Setup of LST in which IR camera and heat source move in tandem over the surface to be inspected	72
94	Panel showing the observation gate selection with respect to the heat deposition location	73
95	MISTRAS Line Scan Thermography System crawler used on composites	74
96	MISTRAS Line Scan Thermography System small area scanner	74

97	Results produced by the MISTRAS Line Scan Thermography System on a 32-ply panel with substructure elements	75
98	Equipment setup used for typical lock-in thermography inspection	76
99	MoviTHERM lock-in thermography with halogen heat lamp being used as the excitation source	78
100	Results produced by lock-in thermography on a 32-ply panel with substructure elements	78
101	Subset of the 15 solid laminate test specimens and five NDI feedback specimens	79
102	The POD study breakdown to produce separate POD values related to specific inspection variables	83
103	Simulated impact damage (laminate cross-section)	85
104	Final design of the 12-ply training/feedback specimen	87
105	Final design of the 20-ply training/feedback specimen with taper	88
106	Final design of the 32-ply training/feedback specimen with taper	89
107	The 20- and 32-ply NDI feedback specimens (backside view) used by inspectors prior to starting the blind POD inspections	89
108	Final design of the second 20-ply training/feedback specimen without taper and different substructure and smaller flaws	90
109	Final design of the third 20-ply training/feedback specimen	90
110	Solid composite laminate specimens with substructure and single (type 1) or dual (type 2) ply tapers on the back side	91
111	The BN test specimen drawing	92
112	The CT “A” test specimen drawing	93
113	The CT “B” test specimen drawing	93
114	Simple taper upper test specimen drawing (12–20 plies)	94
115	Simple taper lower test specimen drawing (12–20 plies)	94
116	Simple taper 32-ply test specimen drawing (20–32 plies)	95
117	Trial S/N solid laminate specimen for preliminary testing of methods for producing engineered flaws	97
118	A UT scan of trial solid laminate specimen showing attenuation levels to establish viability of flaw engineering methods	98
119	Solid composite laminate flaw detection experiment – test specimen fabrication	98
120	Layup of composite laminates with simple taper and CT, and bonding of substructure elements	99
121	Vertical stabilizer large composite laminate test specimen used to obtain preliminary timing information for handheld PE-UT inspections	101

122	Inspection results showing detection of all stabilizer flaws by PA-UT, resonance scans, and handheld PE-UT	102
123	Test panel from the SLE	104
124	Use of template to mark the series of small inspection regions and the appropriate calibration point for the BT or RDC equipment	105
125	Drawings provided to inspectors that show the inspection regions to be covered, appropriate calibration points (note color coding), and panel design features	105
126	Test panel showing an inspector's flaw markings within the directed inspection regions	106
127	Experiment instructions being provided to supplement the written experimenter briefing and information packet	107
128	Typical experiment setup with separate inspector workstations	108
129	Inspector completing inspection using specimen drawing for reference of structural details	109
130	Inspector completing inspection and marking flaw detection on the test specimen	109
131	Airline participants in the SLE	110
132	Advanced NDI methods that participated in the SLE	111
133	Individual and cumulative POD curve comparison for the 12–20 ply specimen set for all flaws in constant thickness and CG regions for all inspectors (27) (PE-UT method)	116
134	Cumulative POD curve for the 12–20 ply specimen set for all flaws in constant thickness and CG regions for all inspectors (27) (PE-UT method)	117
135	Cumulative POD curve comparison of the performance brackets for the 12–20 ply specimen set for all flaws in constant thickness and CG regions (PE-UT method)	117
136	Cumulative POD curve for the 12–20 ply specimen set for flaws in the constant thickness region only (all inspectors; PE-UT method)	118
137	Cumulative POD curve for the 12–20 ply specimen set for flaws in the CG regions only (all inspectors; PE-UT method)	119
138	Cumulative POD curve comparison of different surface coverage techniques for the 12–20 ply specimen set for all flaws in constant thickness and CG regions (all inspectors (27); PE-UT method)	120
139	Individual and cumulative POD curve comparison for the 20–32 ply specimen set for all flaws in constant thickness and CG regions (all inspectors; PE-UT method)	125
140	Cumulative POD curve for the 20–32 ply specimen set for all flaws in constant thickness and CG regions (all inspectors (30); PE-UT method)	126
141	Cumulative POD curve performance brackets for the 20–32 ply specimen set for all flaws in constant thickness and CG regions (PE-UT method)	127
142	Cumulative POD curve for the 20–32 ply specimen set for flaws in the constant thickness regions only (32-ply; all inspectors; PE-UT method)	128

143	Cumulative POD curve for the 20–32 ply specimen set for flaws in the CG regions only (all inspectors; PE-UT method)	128
144	Cumulative POD curve comparison of different surface coverage techniques for the 20–32 ply specimen set for all flaws in constant thickness and CG regions (all inspectors (30); PE-UT method)	129
145	Cumulative POD curve for the 12–20 and 20–32 ply combined specimen sets for all flaws in constant thickness and CG regions (all inspectors [57]; PE-UT method)	136
146	Cumulative POD curve comparison for the 12–20 and 20–32 ply specimen sets for all flaws in constant thickness and CG regions (all inspectors [57]; PE-UT method)	137
147	Cumulative POD curve comparison for the 12–20 and 20–32 ply specimen sets for all flaws in constant thickness regions only (all inspectors [57]; PE-UT method)	137
148	Cumulative POD curve comparison for the 12–20 and 20–32 ply specimen sets for all flaws in CG regions only (all inspectors [57]; PE-UT method)	138
149	Cumulative POD curve comparison of different surface coverage techniques for the 12–20 and 20–32 ply specimen sets for all flaws in constant thickness and CG regions (all inspectors [57] PE-UT method)	139
150	Individual and cumulative POD curve comparison for the RDCE specimen set for all flaws	141
151	Cumulative POD curve comparison of all NDI inspectors and A&P mechanics for all flaws for the RDCE specimen set	141
152	OmniScan PA-UT device and 64 element probe	145
153	Deployment of OmniScan PA-UT system on solid laminate POD experiment	145
154	Use of different PA-UT array probes and encoders to inspect various test specimen geometries	145
155	C-scan images produced by OmniScan PA-UT system inspection of SLE 12-ply reference panel	146
156	C-scan images produced by OmniScan PA-UT system inspection of SLE 20-ply reference panel	147
157	C-scan images produced by OmniScan PA-UT system inspection of SLE 32-ply reference panel	148
158	The POD results for OmniScan PA-UT system flaw detection in solid laminate composite structure	149
159	Matrixeye PA-UT device and 64 element probe	154
160	Deployment of the Matrixeye PA-UT system on solid laminate POD experiment	154
161	Use of different PA-UT array probes and encoders to inspect various test specimen geometries	155
162	C-scan images produced by Matrixeye PA-UT system inspection of SLE 12-ply reference panel	155

163	C-scan images produced by Matrixeye PA-UT system inspection of SLE 20-ply reference panel	156
164	C-scan images produced by Matrixeye PA-UT system inspection of SLE 32-ply reference panel	156
165	The POD results for Matrixeye PA-UT system flaw detection in solid laminate composite structure	157
166	The MAUS FlawInspecta linear array UT device and 64 element probe	162
167	Deployment of the MAUS FlawInspecta linear array UT system on SLE	163
168	Use of different linear array probes and encoders to inspect various test specimen geometries	163
169	C-scan images produced by the MAUS FlawInspecta linear array UT system inspection of SLE 32-ply reference panel	164
170	The POD results for MAUS FlawInspecta linear array UT system flaw detection in solid laminate composite structure	165
171	The GE Phasor XS with RotoArray PA-UT device	170
172	Deployment of the GE Phasor XS with RotoArray PA-UT system on SLE	171
173	C-scan images produced by Phasor XS with RotoArray PA-UT system inspection of SLE 32-ply reference panel	171
174	The POD results for the RotoArray PA-UT system flaw detection in solid laminate composite structure (20–32 ply specimen set)	172
175	Sonatest RapidScan 2 and linear Array WheelProbe	175
176	Deployment of Sonatest UT linear array probe with OmniScan unit on the SLE	175
177	C-scan images produced by RapidScan 2 linear array UT system inspection of SLE 20-ply reference panel	176
178	C-scan images produced by the inspection of the SLE 32-ply reference panel using the Sonatest linear Array WheelProbe connected to the OmniScan device	176
179	The iPhoton LUS gantry-based inspection system	180
180	Deployment of the iPhoton LUS system on SLE	180
181	Use of scan pattern teaching to automate the scans of parts with the iPLUS LUS robot	180
182	C-scan images produced by iPLUS LUS inspection of SLE 20-ply reference panel	181
183	The POD results for the iPLUS LUS system flaw detection in solid laminate composite structure	182
184	The POD improvements stemming from a second analysis of iPLUS LUS data	187
185	Imperium AcoustoCam video-based UT device	188
186	Deployment of the AcoustoCam video-based UT system on solid laminate POD experiment	188

187	Photographs showing some restriction in AcoustoCam movement within the confined spaces present on BN specimens (spar cap channel region)	188
188	Typical UT image and A-scan display produced by AcoustoCam showing an individual flaw (small images can be placed into a full 2D C-scan using FirstMap software)	189
189	Image display options in AcoustoCam UT system	190
190	C-scan images produced by AcoustoCam video-based UT system inspection of SLE 20-ply reference panel (a series of individual images are placed into full 2D C-scan using FirstMap software)	190
191	The POD results for AcoustoCam video-based UT system flaw detection in solid laminate composite structure	191
192	DolphiTech DolphiCam video-based UT device	196
193	Deployment of DolphiCam video-based UT system on full-scale composite panel (image of impact damage on screen)	197
194	Typical UT image and A-scan display produced by DolphiCam showing an individual flaw	197
195	Image displays produced by DolphiCam UT system for different flaw types	198
196	Image displays produced by DolphiCam UT system for delamination and impact damage	198
197	Flaw images produced by DolphiCam video-based UT system inspection of SLE 20-ply reference panel	199
198	Evisive MW device	200
199	Deployment of Evisive MW system on SLE	200
200	Typical A-scan display image produced by Evisive MW system in SLE	201
201	Deployment of LTI Shearography System (5100 HD) on SLE	202
202	Shearography images produced by LTI Shearography System inspection of SLE 32-ply laminate test panel	202
203	Shearography images produced by LTI Shearography System showing flaw detection and missed flaws	203
204	The POD results for LTI shearography system flaw detection in solid laminate composite structure (20–32 ply specimen set)	204
205	Dantec Dynamics shearography devices: the (a) Q800 and (b) Q810	207
206	Deployment of the Dantec Dynamics Q800 shearography systems on SLE	207
207	Deployment of the Dantec Dynamics Q810 shearography systems on SLE	208
208	Shearography images produced by Dantec Dynamics shearography inspection of composite test specimens	208
209	The POD results for Dantec Dynamics shearography system flaw detection in solid laminate composite structure	209

210	The TWI EchoTherm flash thermography system	214
211	Deployment of the EchoTherm flash thermography system on SLE	214
212	An IR image produced by EchoTherm flash thermography system inspection of SLE 32-ply test specimen	215
213	The POD results for EchoTherm flash thermography system flaw detection in solid laminate composite structure	216
214	MISTRAS LST THELIS-P device	221
215	Deployment of the MISTRAS LST system on SLE	222
216	MISTRAS LST – use of heat lamps to provide thermal gradient to test specimens and rolling encoder to provide position data for IR image correlation	222
217	An IR image produced by THELIS-P LST system inspection of SLE 32-ply test specimen	223
218	The POD results for THELIS-P LST system flaw detection in solid laminate composite structure	224
219	The MoviTHERM lock-in thermography device	229
220	Deployment of the MoviTHERM lock-in thermography system on SLE	230
221	Thermography images produced by MoviTHERM lock-in thermography system inspection of (a) SLE 12–24 ply and (b) 32-ply test specimens	230
222	The POD results for MoviTHERM lock-in thermography system (flaw detection in solid laminate composite structure)	231
223	The POD results comparing performance of all advanced NDI methods (flaw detection in solid laminate composite structure)	236
224	Images showing accessibility challenge associated with inspection of spar channel; channel results removed for additional POD analysis (see tables 108 and 109)	242
225	Deployment of Matrixeye PA-UT system by All Nippon Airways on SLE	250
226	The POD results for Matrixeye PA-UT system (All Nippon Airways deployment; flaw detection in solid laminate composite structure)	251
227	Inspection impediment in which signal harmonics occur in the same time frame as the signals of interest	258

LIST OF TABLES

Table	Page
1 Test specimen matrix with design variables for solid composite laminate flaw detection experiment	82
2 Thin 12–20 ply total inspection area	96
3 Thick 20–32 ply total inspection area	96
4 Combined 12–20 ply and 20–32 ply total inspection area	96
5 Sample S/N calculations for flaws in the BN and CT test specimens	100
6 List of advanced inspection methods applied to the solid composite laminate POD experiment and the type of specimens inspected by each method	113
7 Summary of test specimen coverage by participants in SLE	114
8 Inspection false call table for the 12–20 ply specimen set (all inspectors; pulse echo method)	121
9 Inspection false call table with false calls that are below 0.25 in ² in size removed for the 12–20 ply specimen set (all inspectors; pulse echo method)	122
10 Experiment timing summary table for the 12–20 ply specimen set (all inspectors; PE-UT method)	123
11 Tabulated results showing overall flaw detection percentage and accuracy in determining flaw size for the 12–20 ply specimen set for all flaws in constant thickness and CG regions (all inspectors; PE-UT method)	124
12 Inspection false call table for the 20–32 ply specimen set (all inspectors; pulse echo method)	131
13 Inspection false call table with false calls that are below 0.25 in. ² in size removed for the 20–32 ply specimen set (all inspectors; pulse echo method)	132
14 Experiment timing summary table for the 20–32 ply specimen set (all inspectors; PE-UT method)	134
15 Tabulated results showing overall flaw detection percentage and accuracy in determining flaw size for the 20–32 ply specimen set for all flaws in constant thickness and CG regions (all inspectors; PE-UT method)	135
16 Cumulative POD results table for the 12–20 and 20–32 ply combined specimen sets	139
17 Cumulative POD results table for the RDCE specimen set	142
18 Inspection false call table for the RDCE specimen set (all participants; GE BT and Olympus NDT 35RDC)	143
19 Tabulated results showing overall flaw detection percentage and accuracy in determining flaw size for the RDCE specimen set for all flaws (all participants; GE BT and Olympus NDT 35RDC)	144

20	Flaw detection performance for OmniScan PA-UT system separated into thin laminate and thick laminate results	149
21	Flaw detection performance for OmniScan PA-UT system for the overall solid laminate POD experiment	150
22	Tabulated results showing overall flaw detection percentage and accuracy in determining flaw size for the 12–20 ply specimen set for all flaws in constant thickness regions (OmniScan PA-UT system)	151
23	Tabulated results showing overall flaw detection percentage and accuracy in determining flaw size for the 12–20 ply specimen set for all flaws in CG regions (OmniScan PA-UT system)	151
24	Tabulated results showing overall flaw detection percentage and accuracy in determining flaw size for the 12–20 ply specimen set for all flaws in constant thickness and CG regions (OmniScan PA-UT system)	152
25	Tabulated results showing overall flaw detection percentage and accuracy in determining flaw size for the 20–32 ply specimen set for all flaws in constant thickness regions (OmniScan PA-UT system)	152
26	Tabulated results showing overall flaw detection percentage and accuracy in determining flaw size for the 20–32 ply specimen set for all flaws in CG regions (OmniScan PA-UT system)	153
27	Tabulated results showing overall flaw detection percentage and accuracy in determining flaw size for the 20–32 ply specimen set for all flaws in constant thickness and CG regions (OmniScan PA-UT system)	153
28	Flaw detection performance for Matrixeye PA-UT system separated into thin laminate and thick laminate results	158
29	Flaw detection performance for Matrixeye PA-UT system for the overall SLE	158
30	Tabulated results showing overall flaw detection percentage and accuracy in determining flaw size for the 12–20 ply specimen set for all flaws in constant thickness regions (Matrixeye PA-UT system)	159
31	Tabulated results showing overall flaw detection percentage and accuracy in determining flaw size for the 12–20 ply specimen set for all flaws in CG regions (Matrixeye PA-UT system)	159
32	Tabulated results showing overall flaw detection percentage and accuracy in determining flaw size for the 12–20 ply specimen set for all flaws in constant thickness and CG regions (Matrixeye PA-UT system)	160
33	Tabulated results showing overall flaw detection percentage and accuracy in determining flaw size for the 20–32 ply specimen set for all flaws in constant thickness regions (Matrixeye PA-UT system)	160
34	Tabulated results showing overall flaw detection percentage and accuracy in determining flaw size for the 20–32 ply specimen set for all flaws in CG regions (Matrixeye PA-UT system)	161

35	Tabulated results showing overall flaw detection percentage and accuracy in determining flaw size for the 20–32 ply specimen set for all flaws in constant thickness and CG regions (Matrixeye PA-UT system)	161
36	Flaw detection performance for MAUS FlawInspecta linear array UT system separated into thin laminate and thick laminate results	165
37	Flaw detection performance for MAUS FlawInspecta linear array UT system for the overall SLE	166
38	Tabulated results showing overall flaw detection percentage and accuracy in determining flaw size for the 12–20 ply specimen set for all flaws in constant thickness regions (MAUS FlawInspecta linear array UT system)	167
39	Tabulated results showing overall flaw detection percentage and accuracy in determining flaw size for the 12–20 ply specimen set for all flaws in CG regions (MAUS FlawInspecta linear array UT system)	167
40	Tabulated results showing overall flaw detection percentage and accuracy in determining flaw size for the 12–20 ply specimen set for all flaws in constant thickness and CG regions (MAUS FlawInspecta linear array UT system)	168
41	Tabulated Results Showing Overall Flaw Detection Percentage and Accuracy in Determining Flaw Size for the 20–32 Ply Specimen Set for All Flaws in Constant Thickness Regions (MAUS FlawInspecta Linear Array UT System)	168
42	Tabulated results showing overall flaw detection percentage and accuracy in determining flaw size for the 20–32 ply specimen set for all flaws in CG regions (MAUS FlawInspecta linear array UT system)	169
43	Tabulated results showing overall flaw detection percentage and accuracy in determining flaw size for the 20–32 ply specimen set for all flaws in constant thickness and CG regions (MAUS FlawInspecta linear array UT system)	169
44	Flaw detection performance for the RotoArray PA-UT system separated into thick laminate results	172
45	Tabulated results showing overall flaw detection percentage and accuracy in determining flaw size for the 20–32 ply specimen set for all flaws in constant thickness regions (RotoArray PA-UT system)	173
46	Tabulated results showing overall flaw detection percentage and accuracy in determining flaw size for the 20–32 ply specimen set for all flaws in CG regions (RotoArray PA-UT system)	174
47	Tabulated results showing overall flaw detection percentage and accuracy in determining flaw size for the 20–32 ply specimen set for all flaws in constant thickness and CG regions (RotoArray PA-UT system)	174
48	Flaw detection performance for Sonatest linear Array WheelProbe separated into thick laminate results	177
49	Tabulated results showing overall flaw detection percentage and accuracy in determining flaw size for the 20–32 ply specimen set for all flaws in constant thickness regions (Sonatest linear Array WheelProbe)	178

50	Tabulated results showing overall flaw detection percentage and accuracy in determining flaw size for the 20–32 ply specimen set for all flaws in CG regions (Sonatest linear Array WheelProbe)	178
51	Tabulated results showing overall flaw detection percentage and accuracy in determining flaw size for the 20–32 ply specimen set for all flaws in constant thickness and CG regions (Sonatest linear Array WheelProbe)	179
52	Flaw detection performance for the iPLUS LUS system separated into thin laminate and thick laminate results	182
53	Flaw detection performance for the iPLUS LUS system for the overall SLE	183
54	Tabulated results showing overall flaw detection percentage and accuracy in determining flaw size for the 12–20 ply specimen set for all flaws in constant thickness regions (iPLUS LUS system)	183
55	Tabulated results showing overall flaw detection percentage and accuracy in determining flaw size for the 12–20 ply specimen set for all flaws in CG regions (iPLUS LUS system)	184
56	Tabulated results showing overall flaw detection percentage and accuracy in determining flaw size for the 12–20 ply specimen set for all flaws in constant thickness and CG regions (iPLUS LUS system)	184
57	Tabulated results showing overall flaw detection percentage and accuracy in determining flaw size for the 20–32 ply specimen set for all flaws in constant thickness regions (iPLUS LUS system)	185
58	Tabulated results showing overall flaw detection percentage and accuracy in determining flaw size for the 20–32 ply specimen set for all flaws in CG regions (iPLUS LUS system)	185
59	Tabulated results showing overall flaw detection percentage and accuracy in determining flaw size for the 20–32 ply specimen set for all flaws in constant thickness and CG regions (iPLUS LUS system)	186
60	Flaw detection performance for AcoustoCam video-based UT system separated into thin laminate and thick laminate results	192
61	Flaw detection performance for AcoustoCam video-based UT system for the overall SLE	192
62	Tabulated results showing overall flaw detection percentage and accuracy in determining flaw size for the 12–20 ply specimen set for all flaws in constant thickness regions (AcoustoCam video-based UT system)	193
63	Tabulated results showing overall flaw detection percentage and accuracy in determining flaw size for the 12–20 ply specimen set for all flaws in CG regions (AcoustoCam video-based UT system)	193
64	Tabulated results showing overall flaw detection percentage and accuracy in determining flaw size for the 12–20 ply specimen set for all flaws in constant thickness and CG regions (AcoustoCam video-based UT system)	194

65	Tabulated results showing overall flaw detection percentage and accuracy in determining flaw size for the 20–32 ply specimen set for all flaws in constant thickness regions (AcoustoCam video-based UT system)	194
66	Tabulated results showing overall flaw detection percentage and accuracy in determining flaw size for the 20–32 ply specimen set for all flaws in CG regions (AcoustoCam video-based UT system)	195
67	Tabulated results showing overall flaw detection percentage and accuracy in determining flaw size for the 20–32 ply specimen set for all flaws in constant thickness and CG regions (AcoustoCam video-based UT system)	195
68	Flaw detection performance for LTI shearography system separated into thick laminate results	204
69	Tabulated results showing overall flaw detection percentage and accuracy in determining flaw size for the 20–32 ply specimen set for all flaws in constant thickness regions (LTI shearography system)	205
70	Tabulated results showing overall flaw detection percentage and accuracy in determining flaw size for the 20–32 ply specimen set for all flaws in CG regions (LTI shearography system)	205
71	Tabulated results showing overall flaw detection percentage and accuracy in determining flaw size for the 20–32 ply specimen set for all flaws in constant thickness and CG regions (LTI shearography system)	206
72	Flaw detection performance for Dantec Dynamics shearography system separated into thin laminate and thick laminate results	209
73	Flaw detection performance for Dantec Dynamics shearography system for the overall SLE	210
74	Tabulated results showing overall flaw detection percentage and accuracy in determining flaw size for the 12–20 ply specimen set for all flaws in constant thickness regions (Dantec Dynamics shearography system)	211
75	Tabulated results showing overall flaw detection percentage and accuracy in determining flaw size for the 12–20 ply specimen set for all flaws in CG regions (Dantec Dynamics shearography system)	211
76	Tabulated results showing overall flaw detection percentage and accuracy in determining flaw size for the 12–20 ply specimen set for all flaws in constant thickness and CG regions (Dantec Dynamics shearography system)	212
77	Tabulated results showing overall flaw detection percentage and accuracy in determining flaw size for the 20–32 ply specimen set for all flaws in constant thickness regions (Dantec Dynamics shearography system)	212
78	Tabulated results showing overall flaw detection percentage and accuracy in determining flaw size for the 20–32 ply specimen set for all flaws in CG regions (Dantec Dynamics shearography system)	213

79	Tabulated results showing overall flaw detection percentage and accuracy in determining flaw size for the 20–32 ply specimen set for all flaws in constant thickness and CG regions (Dantec Dynamics shearography system)	213
80	Flaw detection performance for EchoTherm flash thermography system separated into thin laminate and thick laminate results	216
81	Flaw detection performance for EchoTherm flash thermography system for the overall SLE	217
82	Tabulated results showing overall flaw detection percentage and accuracy in determining flaw size for the 12–20 ply specimen set for all flaws in constant thickness regions (EchoTherm flash thermography system)	218
83	Tabulated results showing overall flaw detection percentage and accuracy in determining flaw size for the 12–20 ply specimen set for all flaws in CG regions (EchoTherm flash thermography system)	218
84	Tabulated results showing overall flaw detection percentage and accuracy in determining flaw size for the 12–20 ply specimen set for all flaws in constant thickness and CG regions (EchoTherm flash thermography system)	219
85	Tabulated results showing overall flaw detection percentage and accuracy in determining flaw size for the 20–32 ply specimen set for all flaws in constant thickness regions (EchoTherm flash thermography system)	219
86	Tabulated results showing overall flaw detection percentage and accuracy in determining flaw size for the 20–32 ply specimen set for all flaws in CG regions (EchoTherm flash thermography system)	220
87	Tabulated results showing overall flaw detection percentage and accuracy in determining flaw size for the 20–32 ply specimen set for all flaws in constant thickness and CG regions (EchoTherm flash thermography system)	220
88	Flaw detection performance for THELIS-P LST system separated into thin laminate and thick laminate results	224
89	Flaw detection performance for THELIS-P LST system for the overall SLE	225
90	Tabulated results showing overall flaw detection percentage and accuracy in determining flaw size for the 12–20 ply specimen set for all flaws in constant thickness regions (THELIS-P LST system)	226
91	Tabulated results showing overall flaw detection percentage and accuracy in determining flaw size for the 12–20 ply specimen set for all flaws in CG regions (THELIS-P LST system)	226
92	Tabulated results showing overall flaw detection percentage and accuracy in determining flaw size for the 12–20 ply specimen set for all flaws in constant thickness and CG regions (THELIS-P LST system)	227
93	Tabulated results showing overall flaw detection percentage and accuracy in determining flaw size for the 20–32 ply specimen set for all flaws in constant thickness regions (THELIS-P LST system)	227

94	Tabulated results showing overall flaw detection percentage and accuracy in determining flaw size for the 20–32 ply specimen set for all flaws in CG regions (THELIS-P LST system)	228
95	Tabulated results showing overall flaw detection percentage and accuracy in determining flaw size for the 20–32 ply specimen set for all flaws in constant thickness and CG regions (THELIS-P LST system)	228
96	Flaw detection performance for MoviTHERM lock-in thermography system separated into thin laminate and thick laminate results	231
97	Flaw detection performance for MoviTHERM lock-in thermography system for the overall SLE	232
98	Tabulated results showing overall flaw detection percentage and accuracy in determining flaw size for the 12–20 ply specimen set for all flaws in constant thickness regions (MoviTHERM lock-in thermography system)	233
99	Tabulated results showing overall flaw detection percentage and accuracy in determining flaw size for the 12–20 ply specimen set for all flaws in CG regions (MoviTHERM lock-in thermography system)	233
100	Tabulated results showing overall flaw detection percentage and accuracy in determining flaw size for the 12–20 ply specimen set for all flaws in constant thickness and CG regions (MoviTHERM lock-in thermography system)	234
101	Tabulated results showing overall flaw detection percentage and accuracy in determining flaw size for the 20–32 ply specimen set for all flaws in constant thickness regions (MoviTHERM lock-in thermography system)	234
102	Tabulated results showing overall flaw detection percentage and accuracy in determining flaw size for the 20–32 ply specimen set for all flaws in CG regions (MoviTHERM lock-in thermography system)	235
103	Tabulated results showing overall flaw detection percentage and accuracy in determining flaw size for the 20–32 ply specimen set for all flaws in constant thickness and CG regions (MoviTHERM lock-in thermography system)	235
104	Comparison of POD flaw detection performance for all advanced NDI methods separated into thin laminate results (breakout by constant thickness regions, CG regions, and all flaws)	238
105	Comparison of percent flaw detection performance for all advanced NDI methods separated into thin laminate results (breakout by constant thickness regions, CG regions and all flaws)	239
106	Comparison of POD flaw detection performance for all advanced NDI methods separated into thick laminate results (breakout by constant thickness regions, CG regions, and all flaws)	240
107	Comparison of percent flaw detection performance for all advanced NDI methods separated into thick laminate results (breakout by constant thickness regions, CG regions, and all flaws)	241

108	Comparison of POD and flaw detection values for all advanced NDI methods including adjustments in POD calculations to show effects of various inspection impediments (category set A)	243
109	Comparison of POD and flaw detection values for all advanced NDI methods including adjustments in POD calculations to show effects of various inspection impediments (category set B)	244
110	Comparison of inspection times and area coverage rate for all advanced NDI methods (thin laminate 12–20 ply specimen set)	246
111	Comparison of inspection times and area coverage rate for all advanced NDI methods (thick laminate 20–32 ply specimen set)	247
112	Descriptions of TRLs	248
113	The TRL ratings for the advanced NDI methods as pertains to maturity for aircraft inspections in a maintenance hangar environment	249
114	Flaw detection performance for Matrixeye PA-UT system (All Nippon Airways deployment) separated into thick laminate results	251
115	Tabulated results showing overall flaw detection percentage and accuracy in determining flaw size for the 20–32 ply specimen set for all flaws in constant thickness regions (Matrixeye PA-UT system; All Nippon Airways deployment)	252
116	Tabulated results showing overall flaw detection percentage and accuracy in determining flaw size for the 20–32 ply specimen set for all flaws in CG regions (Matrixeye PA-UT system; All Nippon Airways deployment)	253
117	Tabulated results showing overall flaw detection percentage and accuracy in determining flaw size for the 20–32 ply specimen set for all flaws in constant thickness and CG regions (Matrixeye PA-UT system; All Nippon Airways deployment)	253

LIST OF ACRONYMS

A&P	Airframe and power plant mechanic
AANC	Airworthiness Assurance NDI Validation Center
AO	Acousto-Optic
BN	Bullnose
BT	Bondtracer
CACRC-ITG	Commercial Aircraft Composite Repair Committee Inspection Task Group
CCD	Charge-coupled device
CG	Complex geometry
CT	Complex taper
DOT	Department of Transportation
DTA	Damage Tolerance Analyses
EM	Electromagnetic
FAA	Federal Aviation Administration
FIRE	Flaw Imaging and Reconstruction Engine
FWC	Full waveform capture
GE	General Electric
iPLUS	iPhoton LUS concept
IR	Infrared
LST	Line Scanning Thermography
LTI	Laser Technology, Inc.
LUS	Laser- ultrasonics
MAUS	Mobile Automated Scanner
MRO	Maintenance and repair organization
MW	Microwave
NASA	National Aeronautics and Space Administration
NDI	Nondestructive inspection
NDT	Nondestructive testing
OEM	Original equipment manufacturer
PA-UT	Phased array ultrasonics
PE-UT	Pulse-echo ultrasonic
POD	Probability of detection
RDC	Ramp Damage Checker
RDCE	Ramp Damage Check Experiment
SLE	Solid laminate flaw detection experiment
S/N	Signal-to-noise
ST	Simple taper
TRL	Technology readiness level
TWI	Thermal Wave Imaging
UT	Ultrasonic

EXECUTIVE SUMMARY

The aircraft industry continues to increase its use of composite materials for principle structural elements. This expanded use and the difficulties associated with damage tolerance analysis of composites have placed greater emphasis on the use of accurate nondestructive inspection (NDI) methods. Traditionally, a few ultrasonic (UT)-based inspection methods have been used to inspect solid laminate structures. Recent developments in more advanced NDI techniques have produced a number of new inspection options. Many of these methods can be categorized as wide-area techniques that produce 2D flaw maps of the structure. An experiment has been developed to assess the ability of both conventional and advanced NDI techniques to detect voids, disbonds, delaminations, and impact damage in adhesively bonded composite aircraft structures. In this experiment, Advanced NDI techniques for laminate inspections (e.g., thermography, shearography, laser UT, microwave, phased array UT, and linear array UT) were used on composite aircraft structures to quantify the improvements achievable through the use of more sophisticated NDI. This report presents the composite laminate experiment design and probability of detection results for advanced NDI, with comparisons to results achieved by airline inspectors using conventional UT methods.

1. INTRODUCTION AND BACKGROUND

1.1 OVERVIEW OF THE COMPOSITE LAMINATE FLAW DETECTION EXPERIMENT

In 1991, the Federal Aviation Administration (FAA) established the Airworthiness Assurance Nondestructive Inspection (NDI) Validation Center (AANC) at Sandia National Laboratories. Its primary mission is to support technology development, validation, and knowledge transfer to industry to enhance airworthiness and improve the aircraft maintenance practices of the commercial aviation industry. The rapidly increasing use of composite materials on commercial airplanes and the potential for economic savings associated with their use means that the demand for composite materials technology will continue to increase. Inspecting these composite structures is a critical element in ensuring their continued airworthiness. The AANC, in conjunction with the Commercial Aircraft Composite Repair Committee Inspection Task Group (CACRC-ITG), completed a study to assess conventional and advanced inspection methods of flaw detection in solid composite laminates.

The aircraft industry continues to increase its use of composite materials for principle structural elements. The extreme damage tolerance and high strength-to-weight ratio of composites have motivated designers to expand the role of fiberglass and carbon graphite in aircraft structures. The expanded use of composite materials has placed greater emphasis on the optimization of current inspection practices and the development of improved NDI techniques that are more reliable and sensitive than conventional NDI. The AANC has been pursuing this goal through studies addressing the inspection of composite structures. The goal of this study was to investigate the performance of advanced inspection methods and determine the need for improved inspections of composite structures.

The ANNC conducted the solid laminate flaw detection experiment (SLE) to assess flaw detection in composite laminate aircraft structures. The SLE involves the use of a set of composite laminate test specimens containing engineered flaws (see figure 1). The specimens were taken to airlines and third party maintenance depots to acquire flaw detection data from aviation industry inspectors. Inspectors were asked to locate and size hidden flaws in the test specimens; the experiment required approximately 2–3 days of each inspector's time. After a sufficient number of inspectors completed the experiment, industry-wide performance curves were established to determine how well current inspection techniques are able to reliably find flaws in composite laminate structures. In total, over 70 inspectors from 14 airlines and 2 maintenance and repair organizations (MROs) participated in this experiment. The test program was intended to evaluate the technical capability of the inspection procedures and the equipment (the NDI method). Evaluation of inspector-specific or environment-specific factors associated with performing this inspection were not the primary objective of this experiment; however, key insights regarding measures to improve inspection performance were obtained. The inspections emphasized flaw detection methods applicable to solid laminate structures ranging from 12–64 plies thick. The results are published in this report as industry-wide performance measures and all links to specific aircraft maintenance depots have been permanently removed.



Figure 1. Subset of the 15 painted solid laminate test specimens and 5 feedback specimens

The CACRC-ITG developed solid laminate and honeycomb NDI reference standards [1] to aid the uniform and optimum application of aircraft NDI techniques. As a follow-on activity, the CACRC-ITG completed a multiyear study to assess flaw detection capabilities in composite honeycomb structure. A natural extension of those efforts is to assess flaw detection capabilities in composite laminate structures. This document summarizes the experiment purpose, the test variables included in the study, the experiment planning issues, the set of test specimen designs, and a comprehensive set of results from the advanced NDI methods evaluated in this experiment.

This experiment used a series of solid laminate composite specimens with statistically relevant flaw profiles to evaluate flaw detection using pulse-echo ultrasonic (PE-UT) and other advanced NDI methods. These tests were conducted using nondestructive testing (NDT) equipment that the inspectors were experienced in using for this type of inspection. The effort focused on understanding the factors influencing the performance of NDI methods (device and inspector) when applied to the inspection of solid laminate composites. Some portions of the testing took the form of blind probability of detection (POD) studies, whereas other portions of the testing determined signal-to-noise (S/N) ratios from which flaw detection could be inferred.

The primary factors affecting NDI included in this study are composite materials, flaw profiles, thickness of structure, geometry of structure, presence of substructure elements, presence of bond lines, presence of fasteners, sealed joints, skin over honeycomb substructure, and environmental conditions. This phase of the study investigated advanced NDI methods to quantify performance and assess possible POD improvements over conventional PE-UT inspections that were evaluated in the first phase of this SLE.

Overall, the primary reasons for this experiment were to optimize composite laminate inspection procedures; determine in-service flaw detection capabilities of conventional NDI methods and measure potential for improvements through the application of advanced NDI methods and

equipment; and compare results from handheld devices with results from scanning systems (with a focus on A-scan versus C-scan and human factor issues in large-area coverage).

The assessment of advanced NDI methods was achieved by extending this study beyond conventional PE-UT to include new NDI equipment and methods that are in development or being proposed for use in aircraft inspections. Results from this testing will quantify the degree of improvements possible through the integration of more advanced NDI techniques and improved procedures. This report includes the results from the application of conventional PE-UT inspection methods.

1.2 INCREASING USE OF COMPOSITES IN AIRCRAFT STRUCTURES

Composite materials are increasingly becoming the material of choice for aircraft designers because of their global benefits. Engineers estimate that building comparable fuselages with aluminum would require thousands of components and fasteners, extensive tooling, and dozens of technicians; an aircraft would weigh approximately 20% more and consume more fuel. Through the use of composite technology construction, engineers can eliminate half the number of parts in an assembly, resulting in significant cost savings. Other benefits of composite technology include lower acquisition costs, lower operating costs, and improved maintainability, reliability, and durability.

New transport and commuter category aircraft, such as The Boeing Company 787 and Airbus A380, are being produced with a majority of their structure composed of composite materials. Typical damage found in composite structures includes disbonds and delaminations stemming from normal flight loads; fluid ingress; impact damage; lightning strikes; deterioration from contact with fluids such as paint strippers or hydraulic fluids; and extreme heat and ultraviolet exposure. These types of damage may be difficult to visually detect yet could be detrimental to the strength of the structure.

An industry-wide set of composite reference standards have been developed [1–3]. The standards are being used in NDI equipment calibration for damage assessment and post-repair inspection of commercial aircraft composites. A final review of the honeycomb and solid laminate standards was completed and several aircraft manufacturers have already incorporated these standards in their maintenance manuals. This study complements the composite reference standard development effort. The purpose of this experiment was to assess the ability of conventional and emerging NDI techniques to inspect for flaws in representative composite structures. The experiment established the sensitivities and limitations of applicable NDI methods. Other observations accumulated during the test program will allow for inspection improvements through optimized procedures and practices.

Figures 2–5 show the increasing use of composite materials in aircraft manufacture and highlight some of the principal structural elements that are now being fabricated from composite laminate materials. The photographs in figures 6 and 7 show several finished composite aircraft components. They underscore the degree of complexity associated with these structures and the size of components that are being fabricated from composites.



A320/A319 composite structures

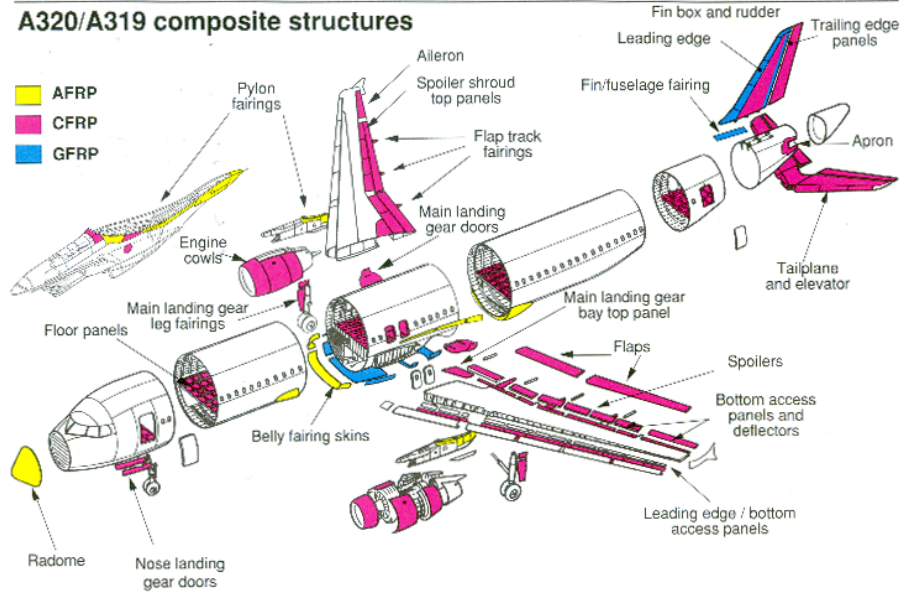


Figure 2. Use of composite structures on Airbus 320 series aircraft

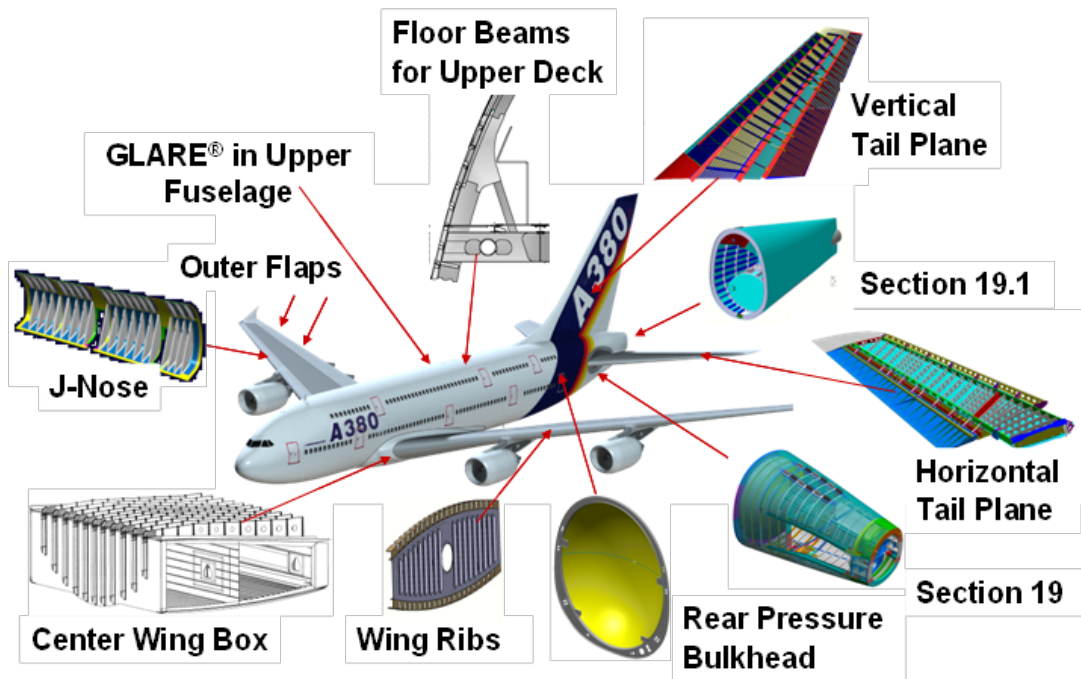


Figure 3. Major composite structures on A380 aircraft

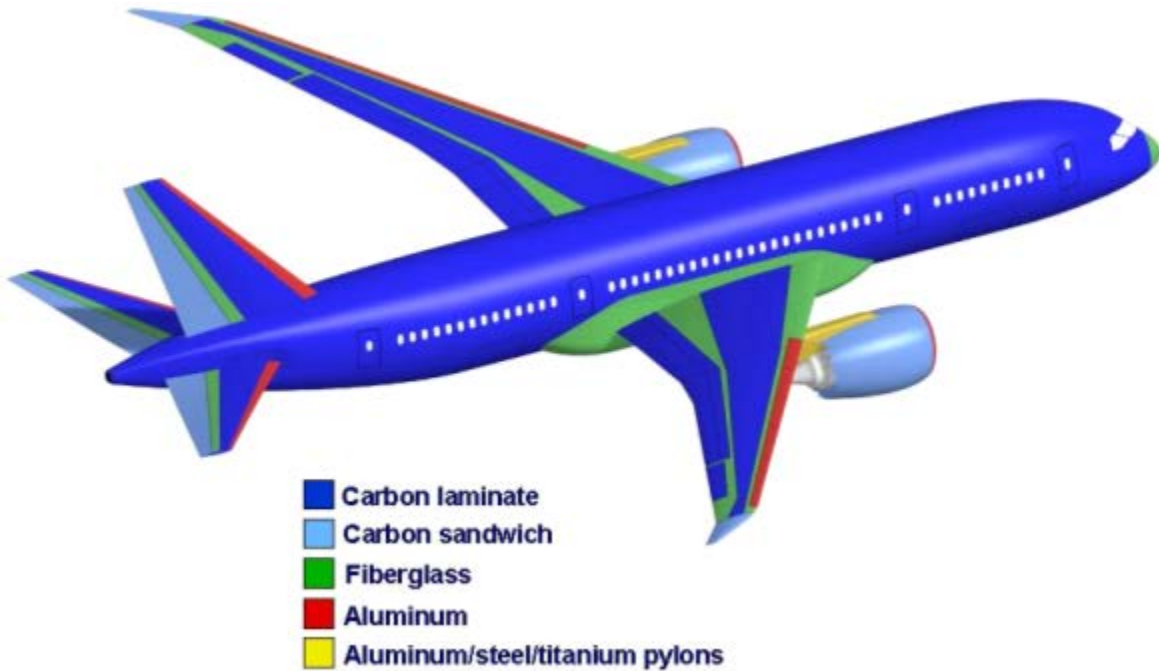


Figure 4. Summary of composite structures on Boeing 787 aircraft

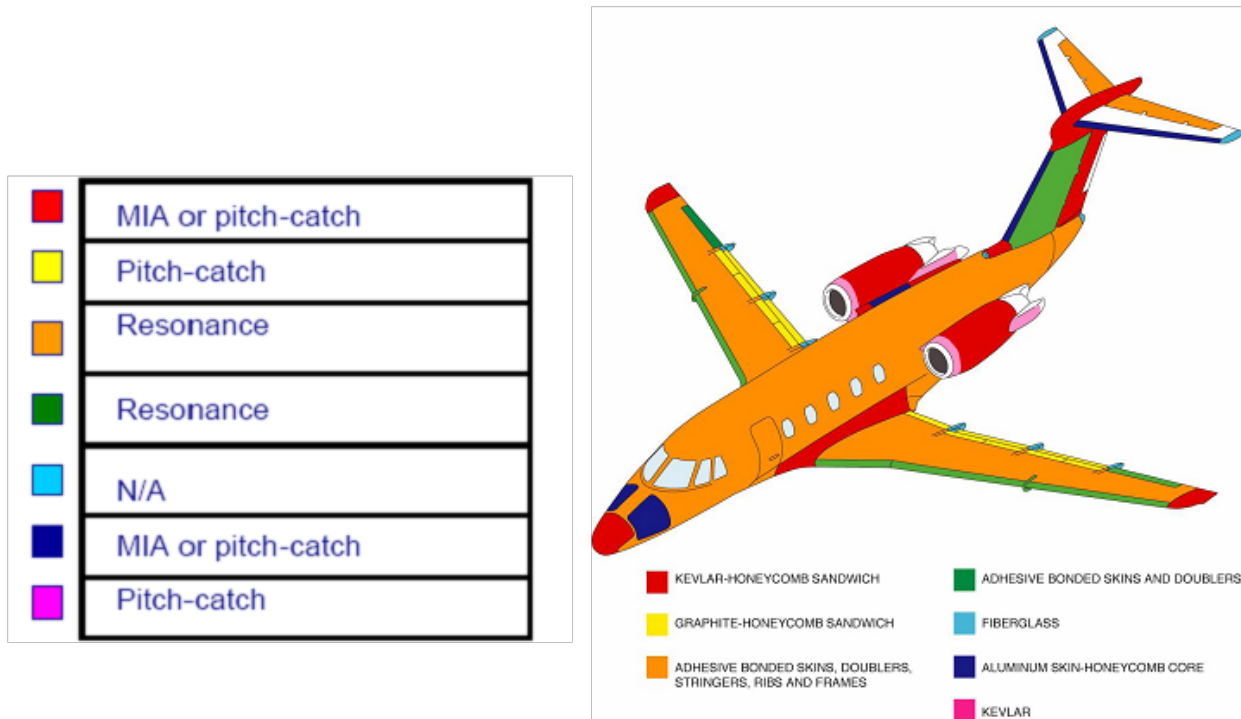


Figure 5. Summary of composite structures on Cessna Citation III aircraft and conventional NDI methods used to inspect them



Figure 6. Production of an all-composite fuselage section



Figure 7. Summary of advanced composite applications on A380 primary structures

1.3 BACKGROUND ON IN-SERVICE INSPECTION NEEDS FOR COMPOSITE STRUCTURES

Composite materials have many advantages when used for aircraft structural materials, including their high specific strength and stiffness; resistance to damage by fatigue loading; and resistance to corrosion. However, new analyses, operational experience, and aircraft safe-life extension programs may produce additional NDI requirements. The expanded use of composite structures and the difficulties associated with damage tolerance analysis of composites create a greater need for simple, low-cost NDI methods that can effectively identify degradation and damage in composite structures. Recent developments in advanced NDI techniques have produced a number of new inspection options. Many of these methods can be categorized as wide-area techniques that produce 2D flaw maps of the structure. New and future inspection techniques hold promise for reducing the direct maintenance costs while improving the capacity for detecting damage. Improved NDI techniques could also help detect damage in its early stages, thereby improving safety and reducing the costs associated with the restoration of a larger affected area.

The reliability, safety, and availability of aircraft can be improved, if deemed necessary, through the application of more sophisticated NDI methods and/or with enhanced procedures and improved training of maintenance personnel. This study compared the results from a wide array of NDI methods and identified limitations and optimum applications for specific inspection methods. Roach et al. previously addressed the application of conventional PE-UT NDI methods to establish an aviation industry performance baseline for flaw detection capability [4].

1.4 DAMAGE TOLERANCE APPROACH TO ESTABLISH INSPECTION INTERVALS

Current transport category aircraft were designed using the damage tolerance approach; they can meet continuing structural airworthiness requirements for an indefinite period. This approach is predicated on the use of an effective inspection and corrective maintenance program that ensures structural integrity over the life of the aircraft. Damage tolerance is the attribute of the structure that allows for it to retain its required residual strength without detrimental structural deformation for a period of use after the structure has sustained a given level of fatigue, corrosion, and accidental or discrete source damage. The maintenance program may be adjusted to reflect real-time operational experience and analytical findings through the use of modern analysis tools, testing, and trends assessment of historical operations. Effective maintenance programs can ensure that airplane structures continue to meet the required ultimate strength, fatigue, and damage tolerance requirements.

Inspection requirements (sensitivity and inspection intervals) are driven by damage tolerance analyses (DTA). However, the multiple plies of composite material, composite lamina (anisotropic) response characteristics, and adhesive layers make the analysis complex and hinder the calculation of an exact DTA. It is difficult to determine the effects of flaw size and the point at which a flaw size/location becomes critical. This is especially true of disbond, delamination, and porosity flaws. Therefore, an increased emphasis is placed on quantifying the probability that a flaw of a particular size and location will be detected by a piece of NDI equipment. In any surveillance of aircraft structure, there are three primary aspects to the inspection requirements:

1. The DTA, which determines the flaw onset and growth data (especially critical flaw size information).
2. The sensitivity, accuracy, and repeatability of NDI techniques which, in conjunction with the DTA, establishes the minimum inspection intervals.
3. The impediments that the NDI techniques must contend with while achieving the required level of sensitivity. In addition to this report, detailed discussions on damage tolerance assessments for composite materials are presented in reference materials [5–9].

Damage tolerance is the ability of an aircraft structure to sustain damage without catastrophic failure until the component can be repaired or replaced. The Title 14 Code of Federal Regulations Part 25 specifies that the residual strength shall not fall below limit load, P_L , which is the load anticipated to occur once in the life of an aircraft. This establishes the minimum permissible residual strength $\sigma_p = \sigma_L$. To varying degrees, the strength of composite structures is affected by crack, disbond, and delamination flaws. The residual strength as a function of flaw size can be calculated. Figure 8 shows a sample residual strength diagram. The residual strength curve is used to relate this minimum permissible residual strength, σ_p , to a maximum permissible flaw size, a_p .

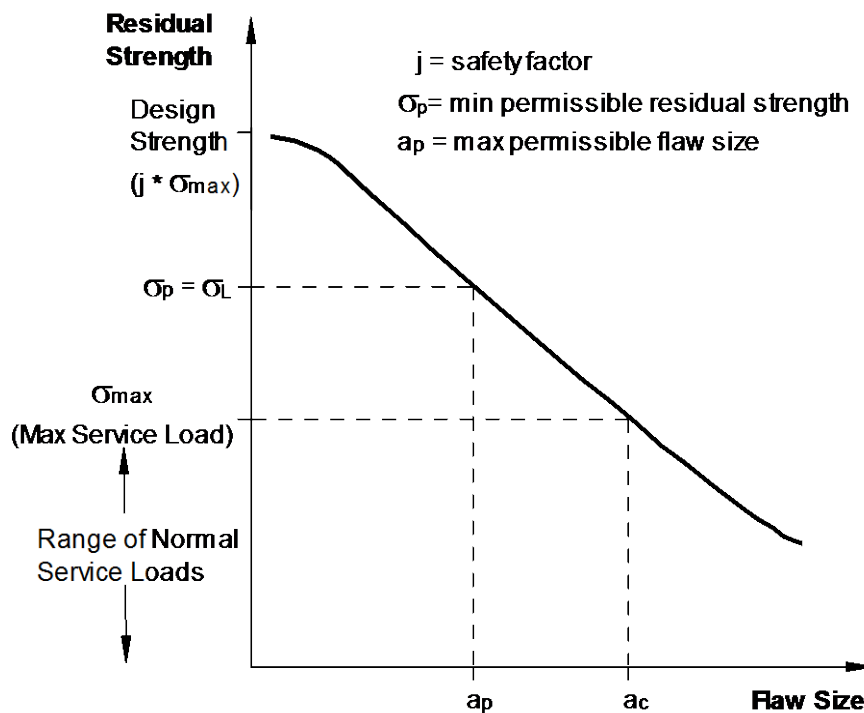


Figure 8. Residual strength curve

A damage control plan is needed to address any possible flaws which may develop in a structure. The NDI is the tool used to implement the damage control plan. Once the maximum permissible flaw size is determined, the additional information needed to properly apply NDI is the flaw

growth versus time or the number of cycles. Figure 9 contains a flaw growth curve. The first item of note is the total time, or cycles, required to reach a_p . Another item of note is a_d , which is the minimum detectable flaw size. A flaw smaller than a_d would likely be undetected, and inspections performed in the timeframe prior to n_d would be of little value. The time (i.e., number of cycles) associated with the bounding parameters a_d and a_p is set forth by the flaw growth curve and establishes $H(\text{inspection})$. Safety is maintained by providing at least two inspections during $H(\text{inspection})$ to ensure flaw detection between a_d and a_p .

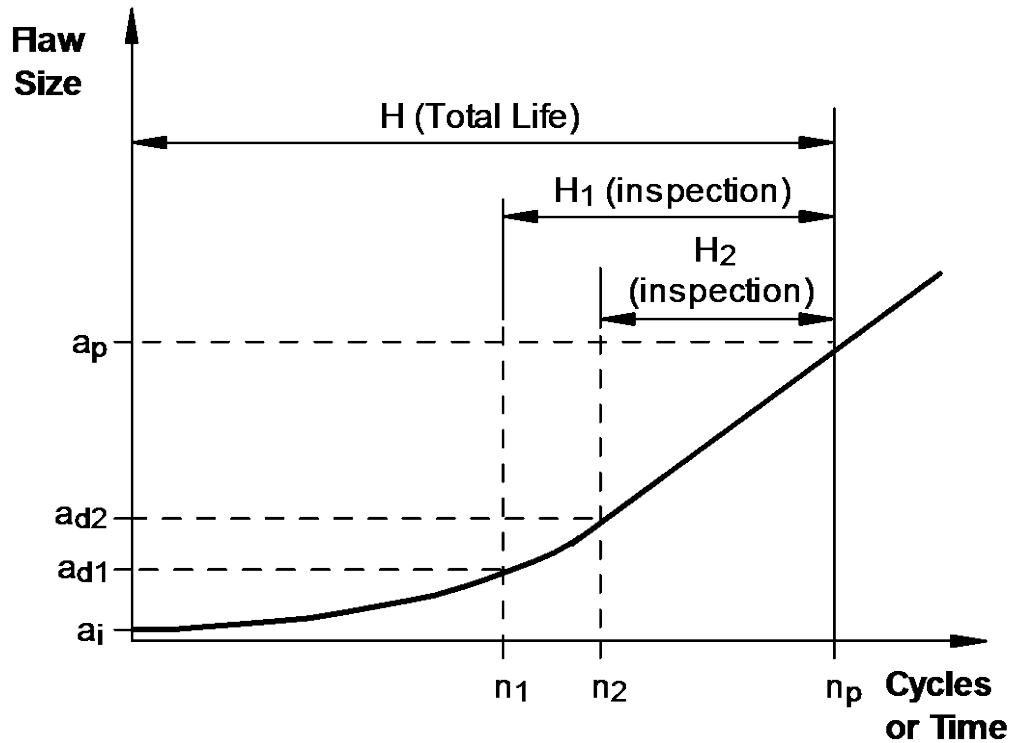


Figure 9. Crack growth curve showing time available for damage control

1.4.1 Inspection Intervals

An important NDI feature highlighted by figure 9 is the large effect that NDI sensitivity has on the required inspection interval. Two sample flaw detection levels— $a_d(1)$ and $a_d(2)$ —are shown along with their corresponding intervals n_1 and n_2 . Because of the gradual slope of the flaw growth curve in this region, the inspection interval $H_1(\text{inspection})$ can be much larger than $H_2(\text{inspection})$ if NDI can produce just a slightly better flaw detection capability. Because the detectable flaw size provides the basis for the inspection interval, it is essential that quantitative measures of flaw detection are performed for each NDI technique applied to the structure of interest. This quantitative measure is represented by a POD curve such as the one shown in figure 10. Regardless of the flaw size, the POD never quite reaches 1 (i.e., 100% possibility of detection). Inspection sensitivity requirements normally require a 90–95% POD at a_p .

For any given inspection task, the POD is affected by many factors such as:

- The skill and experience of the inspector
- Accessibility to the structure
- Exposure of the inspection surface
- Confounding attributes such as underlying structure or the presence of fasteners

The effects of circumstances on POD must be accounted for in any NDI application and associated damage control plan. Figure 11 shows how increasingly difficult circumstances can degrade the POD of an NDI technique.

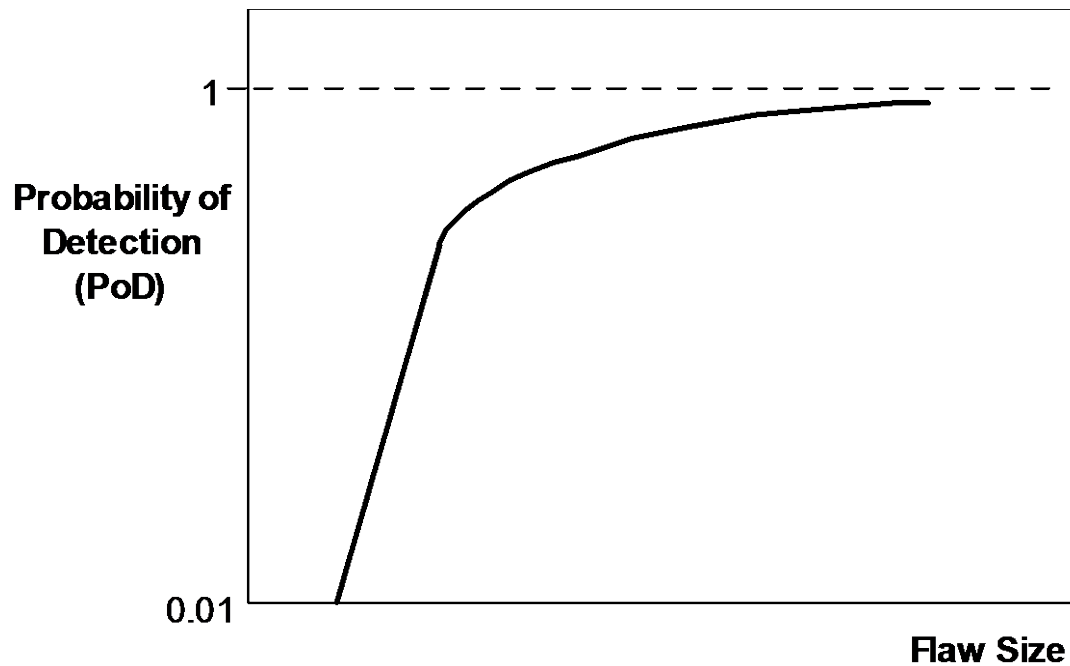


Figure 10. The POD vs. flaw size

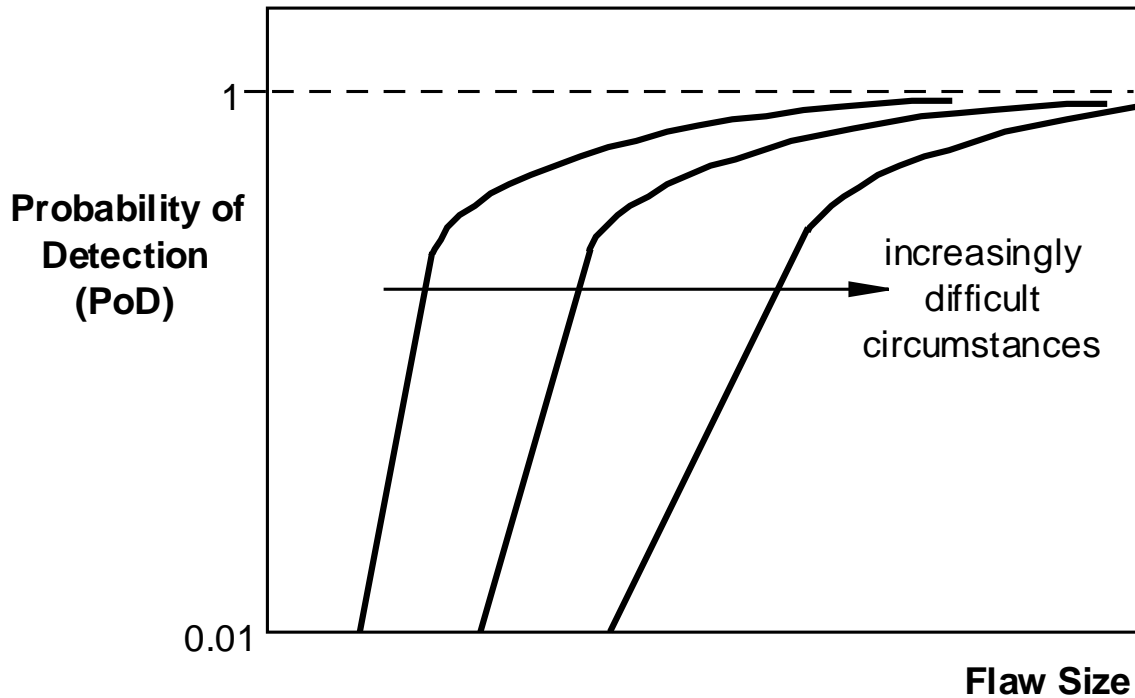


Figure 11. Effect of circumstances on POD

2. PURPOSE OF COMPOSITE LAMINATE FLAW DETECTION EXPERIMENT

Composites have many advantages for use as aircraft structural materials including their high specific strength and stiffness; resistance to damage by fatigue loading; light weight; and resistance to corrosion. The primary motivation for this program is to address the extensive and increasing use of composites on commercial aircraft and the associated increase in the array of NDI techniques used to inspect them. Figure 12 shows how the use of composite materials has increased dramatically over the last decade. The end result of this experiment is an assessment of NDI flaw detection capabilities in composite laminate structures, along with insights that can be used to improve the performance of composite inspection methods.

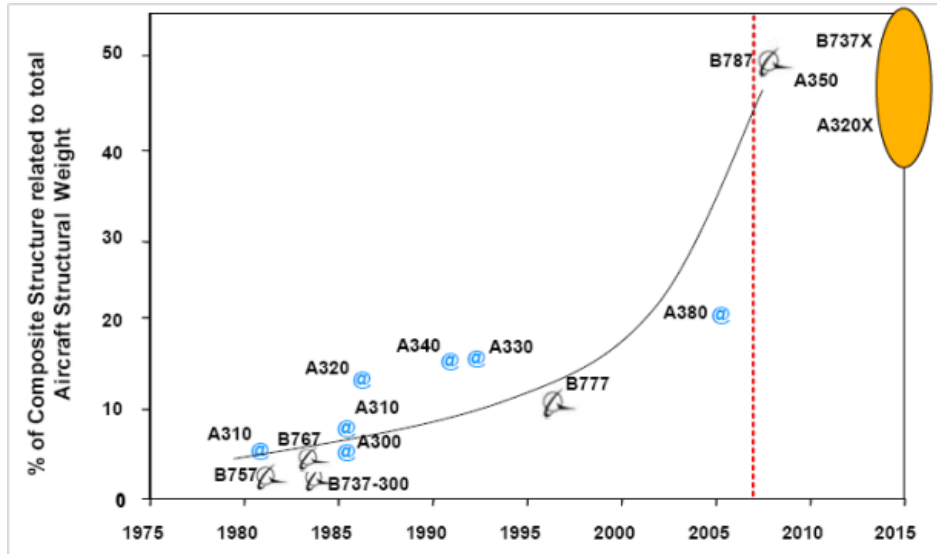


Figure 12. Expansion in the use of composite materials in aircraft construction

The goal is to utilize airline inspectors to establish industry-wide NDI performance curves that quantify:

- The ability of current inspection techniques to reliably find flaws in composite laminate structure.
- The degree of possible improvements through the integration of more advanced NDI techniques and procedures.

The related goals include improving composite laminate inspection procedures and performance and developing structured comparisons between results from handheld inspection equipment and automated scanning systems. The latter goal focuses on A-scan vs. C-scan data presentation and the human factor issues associated with inspections that cover large areas. Overall, the results from this study will provide input and recommendations to the FAA regarding guidance (e.g., advisory circulars) that can enhance the composite inspection process. This study is driven by a desire to improve aircraft safety. Airlines and original equipment manufacturers (OEMs) can use these results to guide NDI deployment and training to define what flaws/damage can be reliably found by inspectors and to reduce the human factor issues to produce improved NDI performance in the field.

The primary sources of damage to composite structures are:

- Normal and abnormal flight loads
- Fluid contamination and ingress
- Surface coating removal; erosion
- Impact (in-flight and on the ground)
 - Hail, birds, tools, runway debris, tire separation, ground handling equipment
- Lightning strikes
- Heat and ultraviolet light exposure
- Corrosion effects from adjacent metals in conductive joints (carbon materials)
- Maintenance errors

Sample damage found in composite structures is shown in figures 13–18. Figure 19 shows data on the probability of an aircraft being impacted by runway debris alone. This data indicates probability of impact that reaches the 25%–30% range. The costs associated with the repair of such impact damage averages \$200,000 per aircraft. Another report indicates that fuselage damage is incurred every 1000 flights in wide-body aircraft and every 4600 flights in narrow-body aircraft.

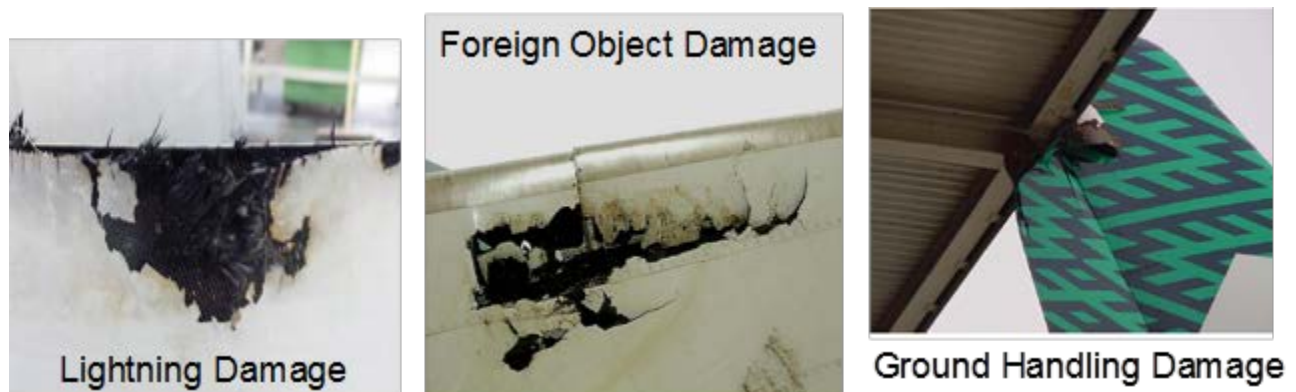


Figure 13. Sample sources of damage to composite structures



Ground Service Vehicles



Figure 14. Sample damage from ground service vehicle impact



Towing and Docking Damage

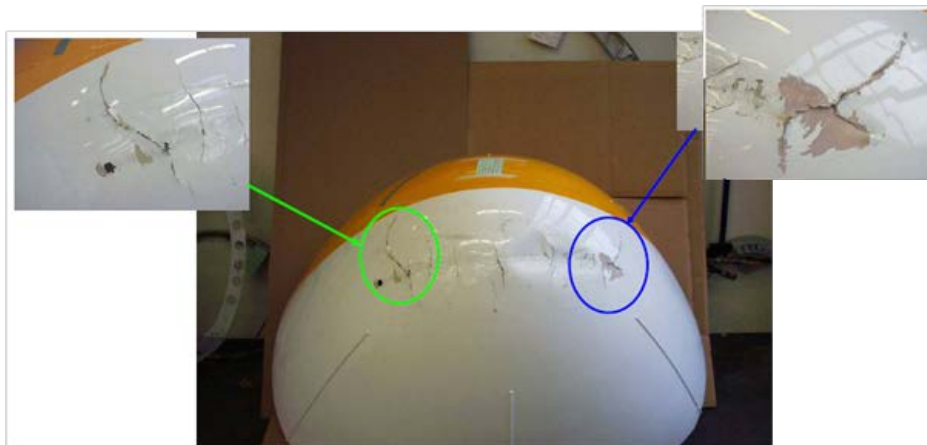
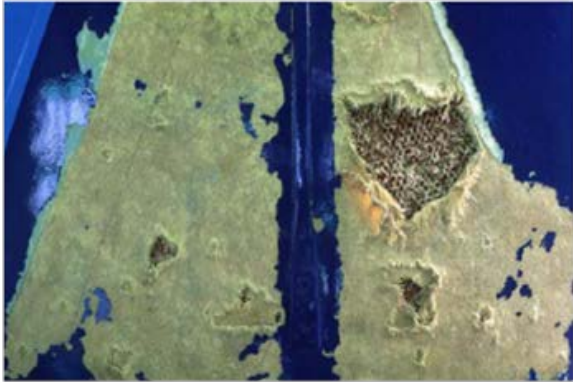


Figure 15. Sample damage from ground operations



Hailstorm Damage



Bird Strike



Figure 16. Sample damage from impacts during flight

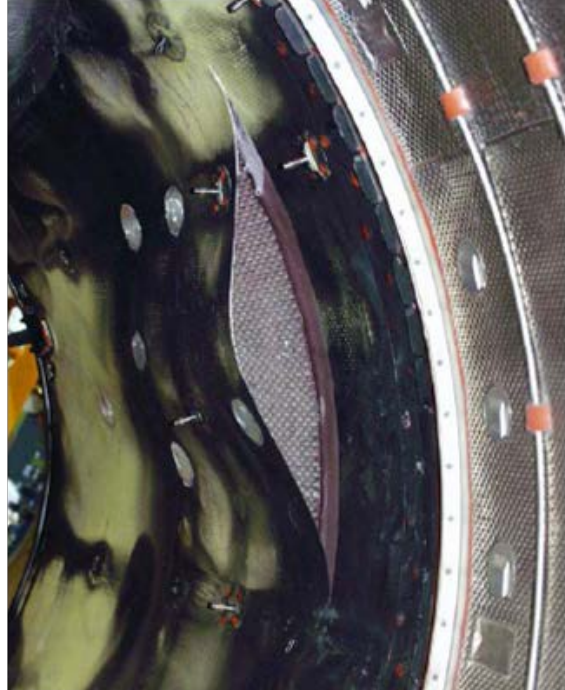


Lightning Strike on Thrust Reverser

Figure 17. Sample damage from lightning strike

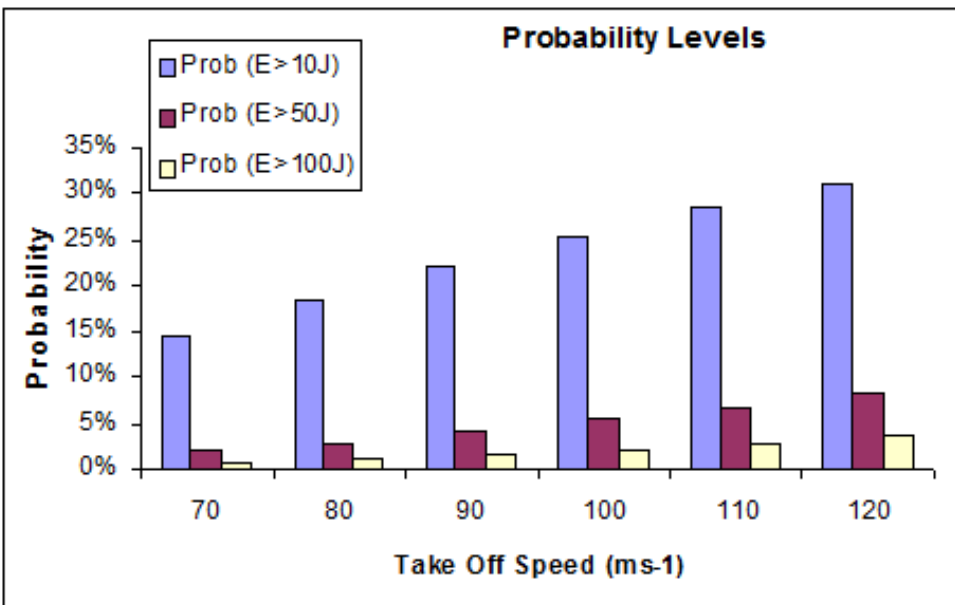


Water Ingress in Elevator



Disbonding at Skin-to-Honeycomb Interface

Figure 18. Sources of in-service damage to composite structures



Typical Runway Debris

Source: Prof Paul Curtis, DERA/MSMA2/TR000702

Figure 19. Probability of impact energy as a function of take-off speed (based on runway debris collected from 4 UK military air bases)

The inspection challenges associated with the composite damage previously described include:

- Subsurface delaminations and disbonds
- Hidden subsurface damage
- Small amounts of moisture
- Cluster of damage in which each individual damage point is quite small
- Heat damage that affects resin matrix
- Weak bonds (manufacturing or environmentally induced)

Impact damage can be especially hard to detect because this damage mode often produces subsurface damage while leaving no external surface demarcations or visual clues. Figures 20–22 describe the physics behind this impact damage scenario and include photographs of this type of “blind” damage in both solid laminate and honeycomb structures. For example, hailstorm damage can produce subsurface interply delaminations, whereas low-velocity, high-mass impacts (e.g., ground handling equipment) can produce substructure damage (e.g., stringer-to-skin disbonds, frame fracture), both of which can be challenging to detect.

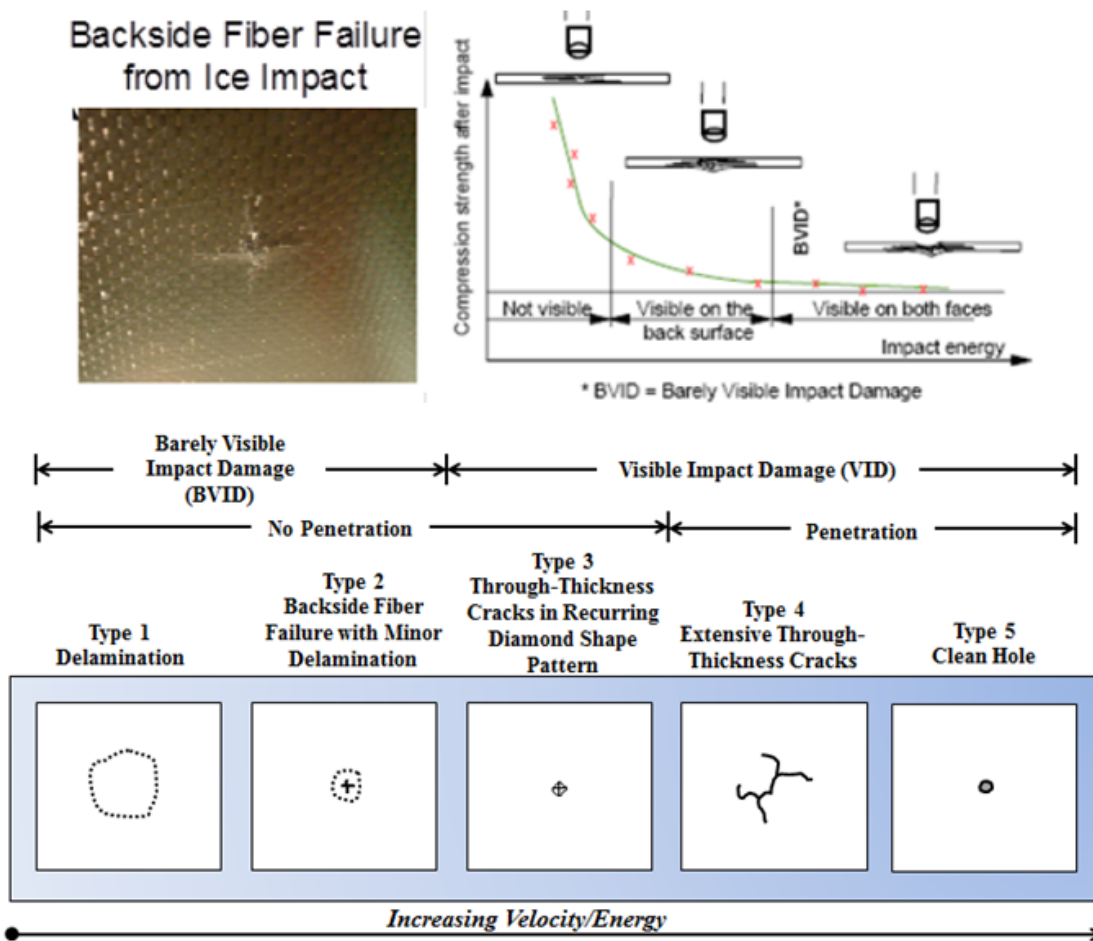
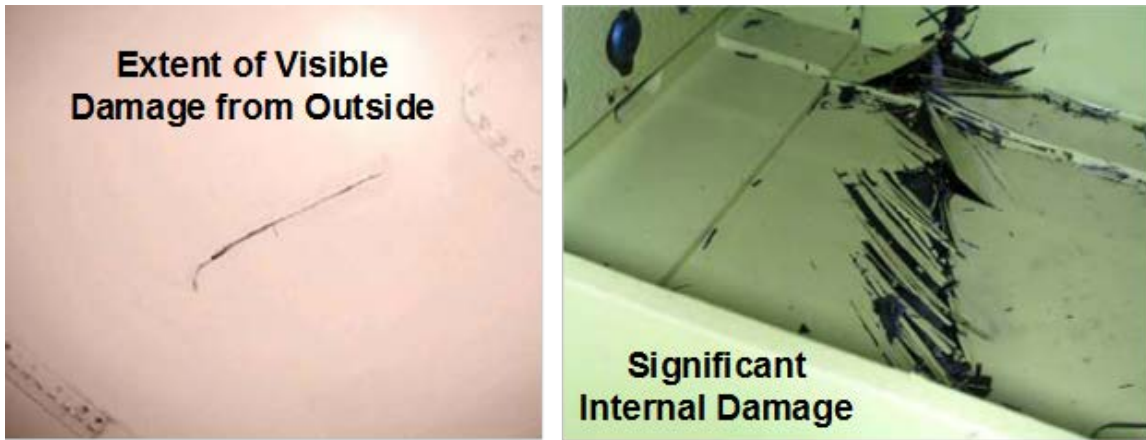


Figure 20. Effects of impact on composite structures



Source: Carlos Bloom (Lufthansa) & S. Waite (EASA)

Figure 21. Example of external impact creating minor surface demarcation but significant internal damage

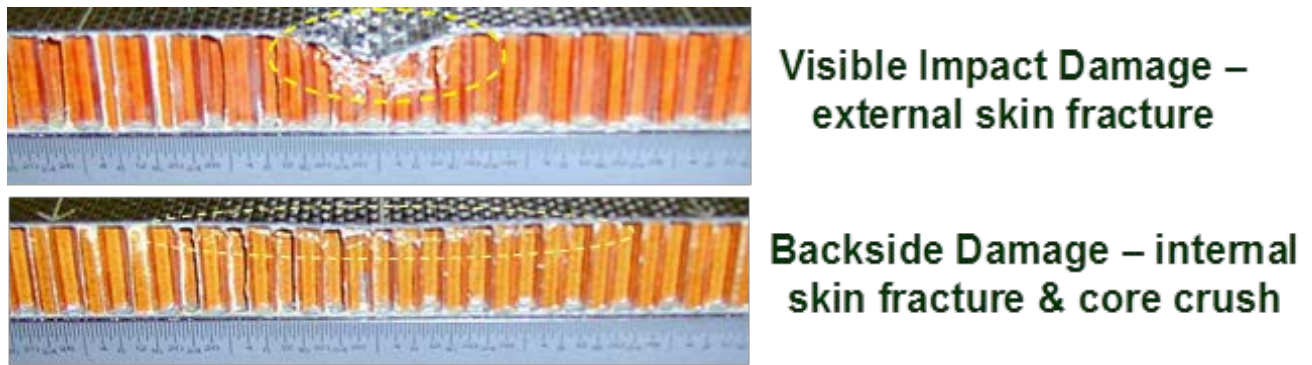


Figure 22. Comparison of visible and backside damage (crushed core and backside fiber fracture) in honeycomb structures

3. DESCRIPTION OF CONVENTIONAL AND ADVANCED INSPECTION METHODS APPLIED TO COMPOSITE LAMINATE FLAW DETECTION EXPERIMENT

3.1 THE PE-UTs WITH C-SCAN IMAGING

Ultrasonic (UT) inspection uses high-frequency sound waves as a means of detecting anomalies in materials. The UT test equipment usually operates in the range of 200 KHz to 25 MHz. The speed with which the sound waves travel through a material is dependent on the composition and density of the material. The speed of sound in carbon graphite composite material is approximately 0.117 in/ μ s. Therefore, the time it takes for a UT pulse to travel from the front surface to the back surface and back to the front surface of a 0.1" thick composite laminate (0.2" total distance) is approximately 1.7 μ s. In PE-UT inspections, short bursts of high-frequency sound waves are transmitted into materials for the detection of surface and subsurface flaws. The sound waves travel through the material with some attendant loss of energy (attenuation) and are reflected at interfaces. The reflected beam is displayed and then analyzed to define the presence and location of flaws. Sound is transmitted into the test item by

means of a transducer. The reflected waves are then received by a transducer—in PE-UT it is often the same transducer that transmits the sound—and converted back into electrical signals for display.

3.1.1 A-Scan Mode

The UT testing involves one or more of the following measurements: time of wave transit (or delay), path length, frequency, phase angle, amplitude, impedance, and angle of wave deflection (reflection and refraction). In conventional PE-UT, pulses of high-frequency sound waves are transmitted into a structure being inspected. A-Scan signals represent the response of the stress waves, in amplitude and time, as they travel through the material. As the waves interact with defects or flaw interfaces within the solid and portions of the pulse's energy are reflected back to the transducer, the flaws are detected, amplified, and displayed on a cathode ray tube (CRT) screen. The interaction of the UT waves with defects and the resulting time vs. amplitude signal produced on the CRT screen depends on the wave mode, its frequency, and the material properties of the structure. Flaw size can be estimated by comparing the amplitude of a discontinuity signal with that of a signal from a discontinuity of known size and shape. Flaw location (depth) is determined from the position of the flaw echo along a calibrated time base. In the pitch-catch UT method, one transducer transmits a pressure wave into the specimen and a second transducer detects the wave. A complex wave front is generated in the material as a result of velocity characteristics, acoustical impedance, and thickness. The time and amount of energy is affected by the changes in material properties, such as thickness, disbonds, and discontinuities. The mechanical vibration (ultrasound) is introduced into the specimen through a couplant and travels by wave motion at the velocity of sound. If the pulses encounter a reflecting surface, some or all of the energy is reflected and monitored by the transducer. The reflected beam, or echo, can be created by any normal or abnormal (flaw) interface. Complete reflection, partial reflection, scattering, or other detectable effects on the UT waves can be used as the basis of flaw detection.

In most pulse-echo systems, a single transducer acts alternately as the sending and receiving transducer. If the pulses encounter a reflecting surface, some or all of the energy is reflected and monitored by the transducer. The reflected beam, or echo, can be created by any normal (e.g., in multilayered structures) or abnormal (flaw) interface. Figure 23 is a schematic of the pulse-echo technique. It shows the interaction of UT waves with various interfaces within a structure and the corresponding A-scan waveforms that are displayed on a UT inspection instrument. Complete reflection, partial reflection, scattering, or other detectable effects on the UT waves can be used as the basis of flaw detection. In addition to wave reflection, other variations in the wave that can be monitored include time of transit through the test piece, attenuation, and features of the spectral response [10 and 11]. Sometimes it is advantageous to use separate sending and receiving transducers for pulse-echo inspection. The term pitch-catch is often used in connection with separate sending and receiving transducers. The degree of reflection depends largely on the physical state of the materials forming the interface. Cracks, delaminations, shrinkage cavities, pores, disbonds, and other discontinuities that produce reflective interfaces can be detected.

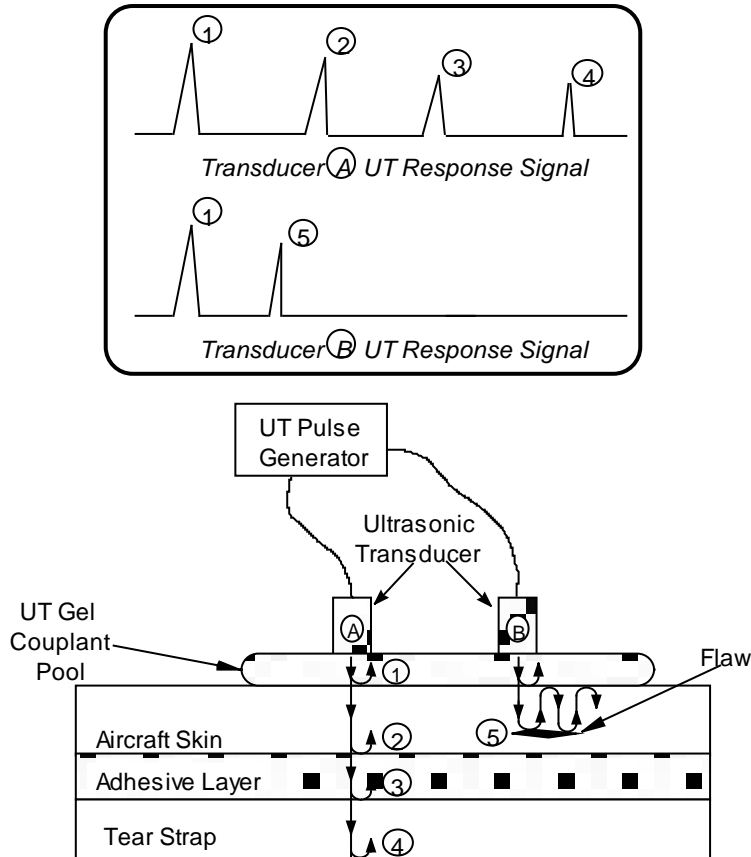


Figure 23. Schematic of PE-UT inspection and A-scan signal showing reflection of UT waves at assorted interfaces

3.1.2 C-Scan Mode: Use of UT Scanning Technology

It is sometimes difficult to clearly identify flaws using UT A-scan signals alone. Small porosity pockets commonly found in composites, coupled with signal fluctuations caused by material nonuniformities, can create signal interpretation difficulties. Significant improvements in disbond and delamination detection can be achieved by taking the A-scan signals and transforming them into a single C-scan image of the part being inspected. C-Scans are 2D images (area maps) produced by digitizing the point-by-point signal variations of an interrogating sensor while it is scanned over a surface. A computer converts the point-by-point data into a color representation and displays it at the appropriate point in an image. Specific “gates” can be set within the data acquisition software to focus on response signals from particular regions within the structure. C-Scan area views provide the inspector with easier to use and more reliable data with which to recognize flaw patterns. This format provides a quantitative display of signal amplitudes or time-of-flight data obtained over an area. The X-Y position of flaws can be mapped and time-of-flight data can be converted and displayed by image processing equipment to provide an indication of flaw depth. A variety of PC-based manual and automated scanning devices can provide position information with digitized UT signals [12].

The basic C-scan system is shown schematically in figure 24. The scanning unit containing the transducer is moved over the surface of the test piece using a search pattern of closely spaced parallel lines. A mechanical linkage connects the scanning unit to X-axis and Y-axis position indicators which feed position data to the computer. The echo signal is recorded versus its X-Y position on the test piece, and a color-coded image is produced from the relative characteristics of the sum total of signals received.

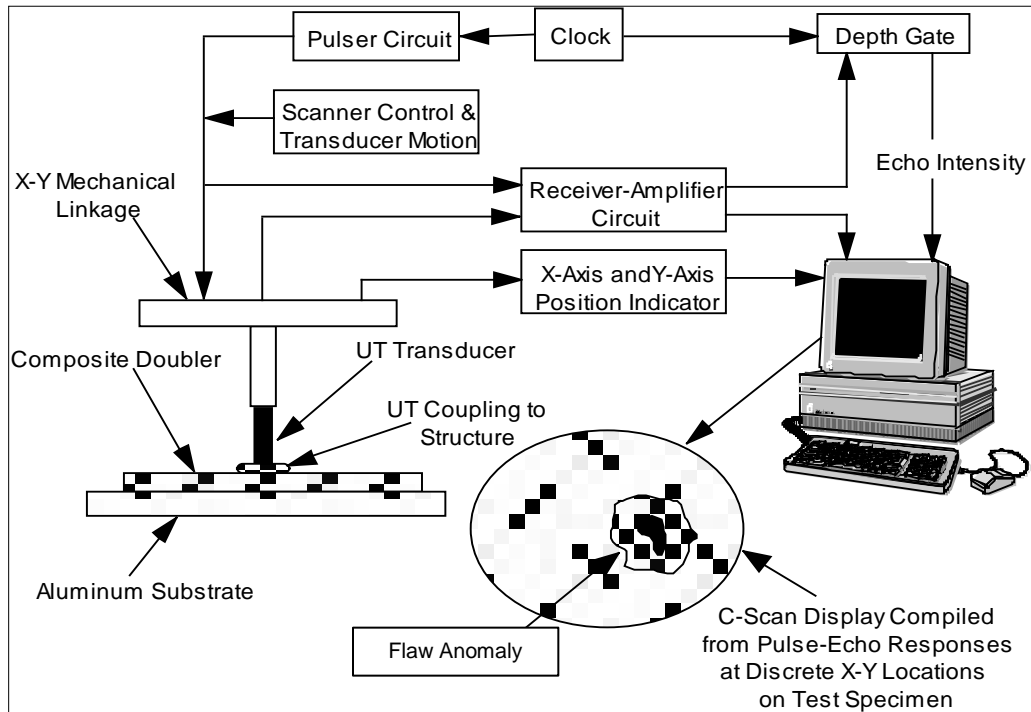


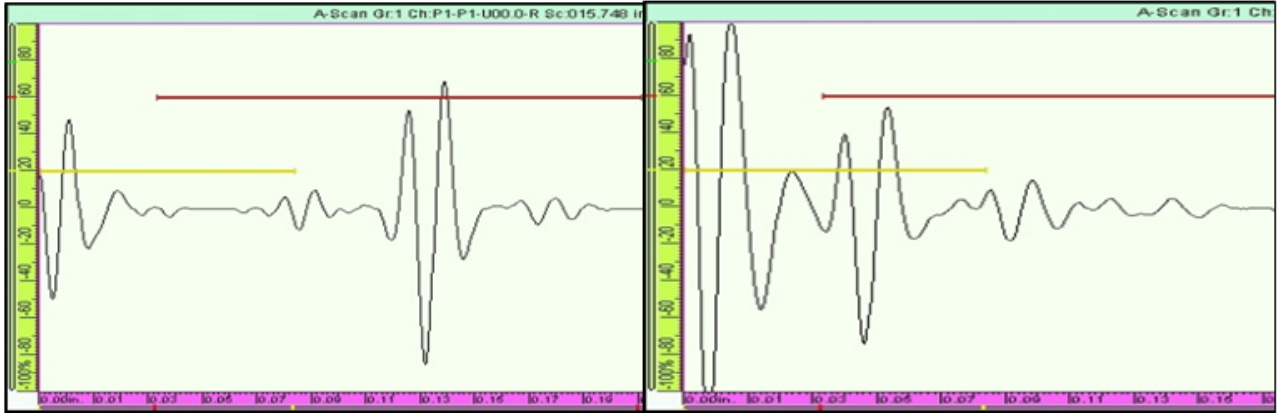
Figure 24. Schematic of C-scan setup for PE-UT inspection

A photograph of an automated (motorized) scanner, the Boeing Mobile Automated Scanner (MAUS) system, inspecting an aircraft fuselage section is shown in figure 25. The MAUS is a portable, multimodal large-area scanning system that integrates several inspection techniques into a single package. Although the unit is capable of multiple modalities of NDI, PE-UT inspection is the unit's primary method used for composite laminate parts. Unique features of the MAUS V system include equipment portability, ease of setup, inspection versatility, and rapid inspection rates. It incorporates an X-Y scanner to match the transducer position with its corresponding signal so that real-time C-scans can be constructed for the surface being inspected. The probe is held in place using a gimbal arrangement on a spring-loaded mount that allows the probe to accurately follow and maintain proper orientation over curved surfaces. Several scanner designs are available with the MAUS system. The scanners are interchangeable, allowing for the selection of an appropriate configuration for different inspection tasks. A motorized scanner is used to move the UT probe forward or backward and a strip of data is collected by the sensor. The MAUS flexible track provides fully automated, hands-free scanning. The entire UT C-scan device is attached to the structure using suction cups connected to a vacuum pump. The unit is tethered to a remotely located computer for control and data acquisition.



Figure 25. The MAUS automated UT scanning system

Figure 26 shows a comparison of A-scan signals from undamaged and damaged portions of a composite structure that were produced by the PE-UT inspection method. Note the clear reflection peak produced by uninterrupted signal travel to the back wall in the undamaged portion of the composite structure. Compare this to the A-scan signal from the damaged portion of the structure, in which the amplitude of the back wall signal is decreased and a new intermediate peak (reflection) is observed. Both of these A-scan changes indicate the presence of damage or another anomaly. Additional sample A-scan signals from PE-UT inspections can be found in appendix A. Figure 27 shows a sample C-scan image (based on amplitude) from a MAUS PE-UT inspection of a composite fuselage structure containing stringers and frame shear ties (see figure 25). Dark spots and irregularly shaped regions of nonuniform color indicate the presence of impact damage in this panel. The value of using 2D color coding, stemming from the sum total of the A-scan signals, to identify and size composite flaws is evident in this C-scan image.



(a)

(b)

Figure 26. Sample UT signals generated from a (a) structure without damage and (b) structure with damage

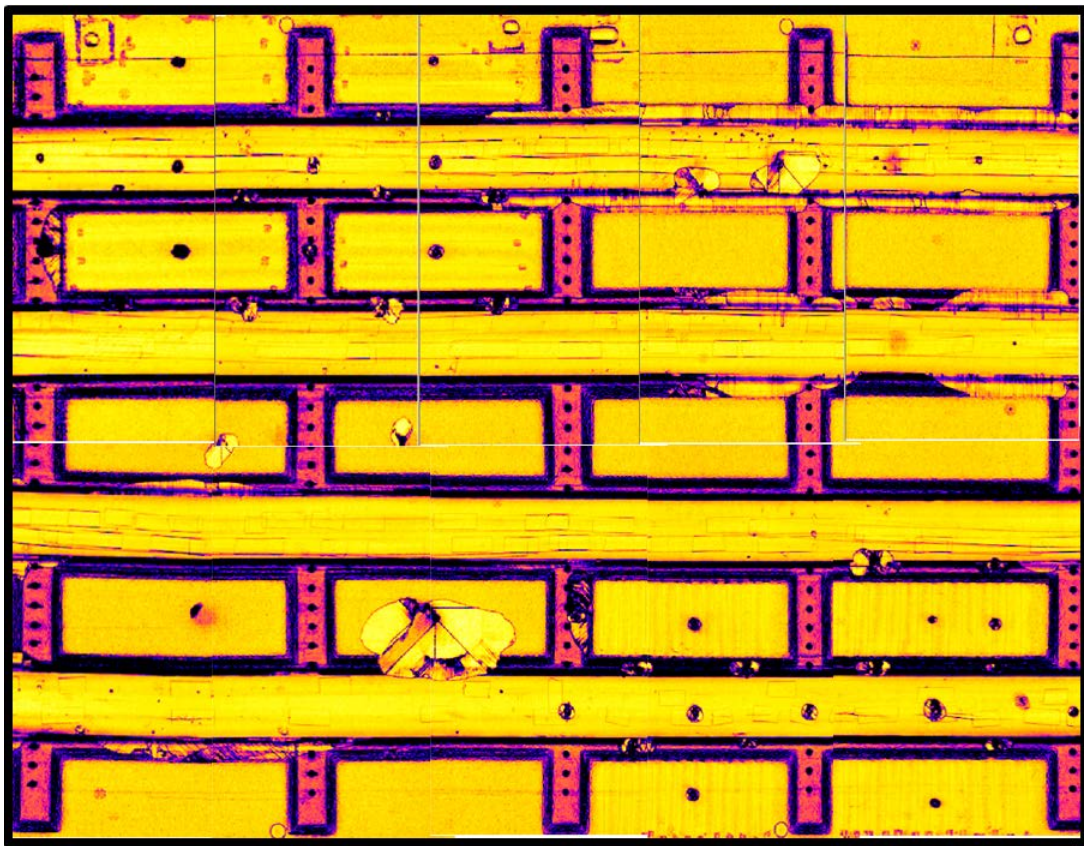


Figure 27. Sample C-scan produced by an automated UT scanning device

Figure 28 shows a C-scan image (based on amplitude) from a PE-UT inspection of a 32-ply carbon laminate test specimen with substructure. The specimen is representative of aircraft construction. The test specimen schematic is also shown on the left side of figure 28 to provide

test specimen information and the embedded flaw profile. Disbond and delamination flaws are revealed by continuous and distinct signal loss areas which, depending on the color palette chosen, are either relatively bright or dark compared to the surrounding colors. Figure 28 shows that all of the flaws are not detected in this C-scan image. This could be because the inspection method was not able to detect the presence of these types of flaws. Alternatively, for this NDI method, it could indicate that the flaws are at a depth level that requires another gate setting (separate C-scan image) to detect the presence of the deeper flaws. Normally, PE-UT testing uses multiple gate settings to optimize flaw detection.

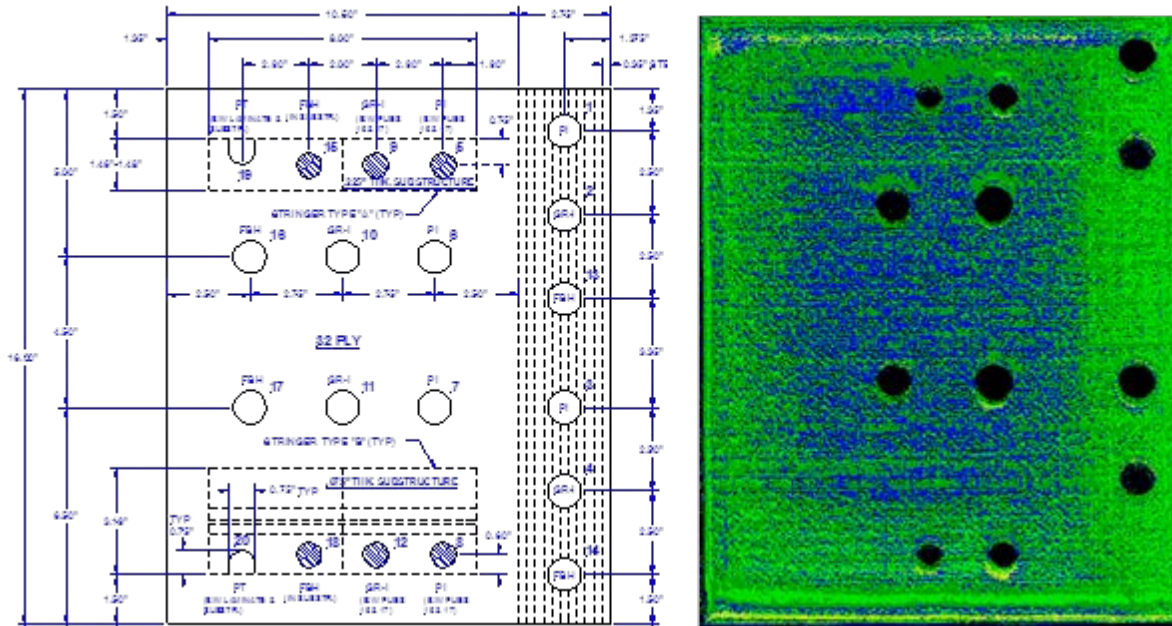


Figure 28. C-scan image produced by selective gating on the amplitude of all signals received by the transducer

3.2 PHASED ARRAY AND LINEAR ARRAY UTs

Conventional UT transducers for NDI commonly consist of either a single active element that both generates and receives high-frequency sound waves or two paired elements—one for transmitting and one for receiving. However, phased array probes typically consist of a transducer assembly with 16–256 small individual elements that can each be pulsed separately. A phased array system will also include a sophisticated computer-based instrument that is capable of driving the multi-element probe, receiving and digitizing the returning echoes, and plotting that echo information in various standard formats. Unlike conventional flaw detectors, phased array systems can sweep a sound beam through a range of refracted angles or along a linear path, or dynamically focus at a number of different depths, thereby increasing both flexibility and capability in inspection setups. The primary difference between a phased array and a linear array is that linear arrays are not capable of steering the sound beam at different angles or focusing the beam. The sound waves stay parallel to each other regardless of the depth.

Phased array ultrasonic (PA-UT) uses multiple signals from a contained series of transducers (phased arrays) to produce diagnostic images in the form of UT C-scans. The operation is similar to handheld UT; however, the simultaneous use of multiple sensors allows for rapid coverage resulting in 2D images from which to assess structural integrity. A linear array of UT sensors is placed within a single scanning probe. The width of the linear probe array determines the swath of the inspection scan as the probe is moved along the surface. A compression wave beam is electronically scanned along the array at pulse repetition frequencies in excess of 10 KHz. The response of each individual sensor is monitored and assessed using the UT wave analysis approaches described above. High-speed pulsing combined with rapid data capture enables the linear array to be quickly moved over the structure. The individual responses from each UT sensor are integrated to produce a real-time C-scan image of the covered area. Figure 29 shows an example of a PA-UT inspection device deployed by Sonascan in a rolling wheel arrangement. The physics of how the UT array works is shown in figure 30. By carefully controlling the generation of UT signals and data acquisition from select elements in the array, it is possible to produce customized focusing of the array to improve the sensitivity of the inspection. Electronic focusing allows for optimizing the beam shape and size at the expected defect location, further optimizing the POD. The ability to focus at multiple depths also improves flaw sizing of critical defects in volumetric inspections. Focusing can significantly improve S/N ratio in challenging applications, and electronic scanning across many groups of elements allows for C-scan images to be produced very rapidly.



(a)



(b)

Figure 29. The PA-UT (a) deployed in a rolling wheel mechanism and (b) contained in a single probe housing

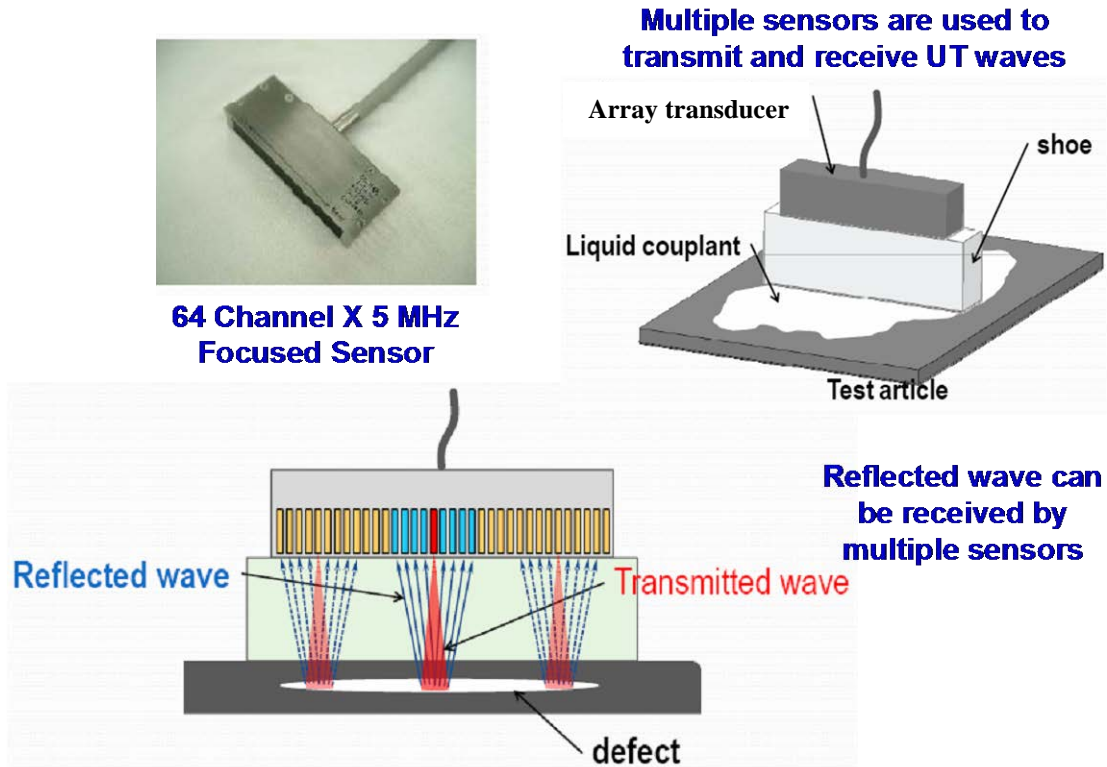


Figure 30. Schematic showing the operation of a UT array which allows for the generation and acquisition of multiple UT signals

3.2.1 Olympus OmniScan PA-UT System

The OmniScan device, shown in Figure 31, is manufactured by Olympus. The one-line scan capability of the OmniScan allows inspectors to collect data in one axis and visualize it using the top view. This feature is easy to set up and allows the data to be played back after the acquisition for offline analysis and reporting. Data can be encoder- or time-based, and phased array images can be displayed in real time. Transducers are available with up to 128 elements. The OmniScan device can be operated in manual mode or can be connected to an X-Y scanner to automate the inspection of large areas. Figures 32 and 33 show sample results produced by the OmniScan from the inspection of carbon laminate test specimens that contain engineered flaws. Damage in the parts is shown in the photographs and schematics, whereas the accompanying C-scan images show the ability of the inspection method and equipment to detect the flaws.

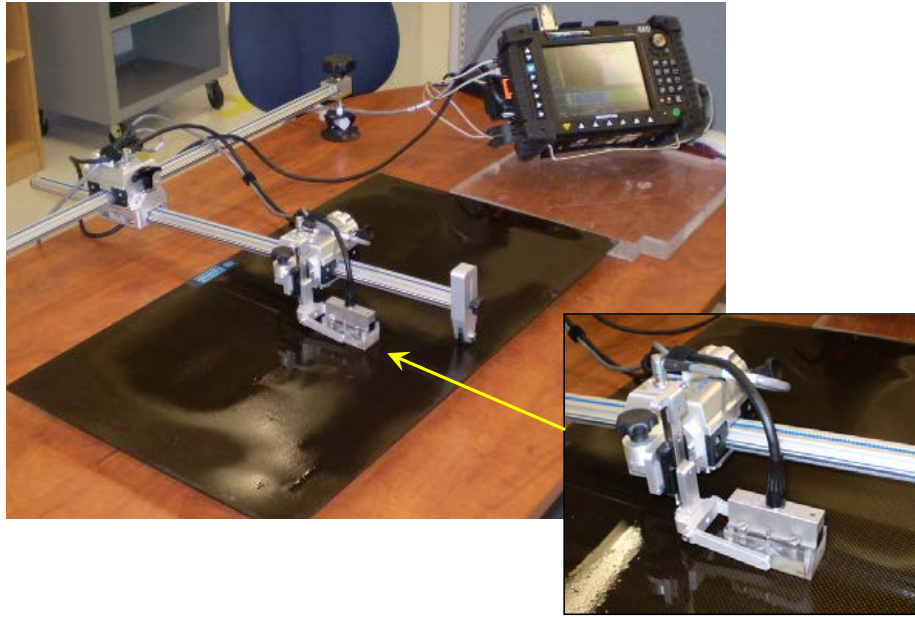


Figure 31. Olympus OmniScan device with a 16:128 phased array transducer

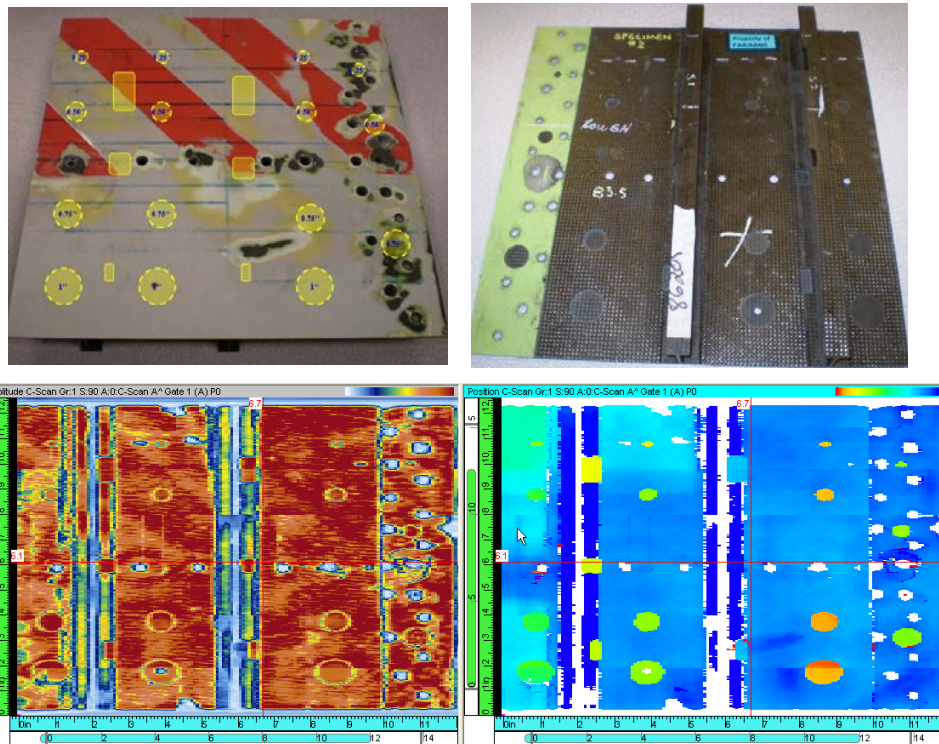


Figure 32. Amplitude (left) and time of flight (right) data produced by OmniScan inspection of a composite laminate aircraft panel with flaw profile as shown

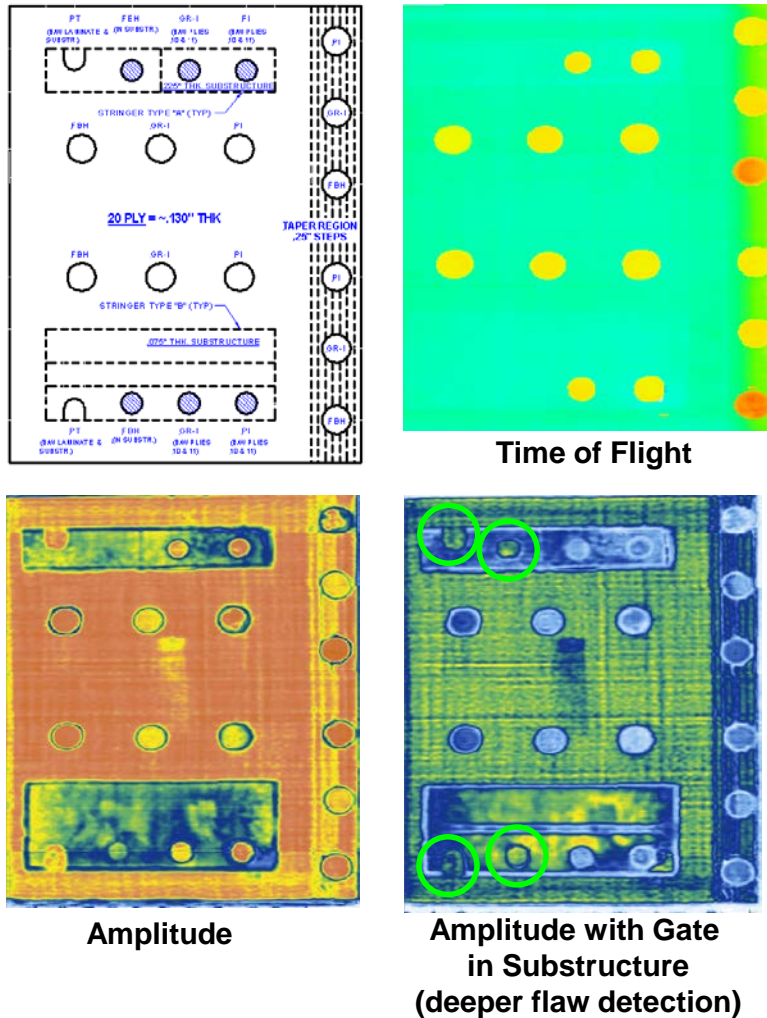


Figure 33. C-scan images produced by OmniScan PA-UT inspection of 20-ply composite laminate feedback panel with the flaw profile as shown

3.2.2 Toshiba Matrixeye PA-UT System

The Matrixeye is a portable 3D UT inspection system produced by Toshiba. Figure 34 shows the portable Matrixeye device and UT array transducer connected to an X-Y scanner. The device uses a synthetic aperture focusing technique to visualize defects, delaminations, and foreign matter three-dimensionally within materials. One of the key components of the system is a UT transducer, which contains a large number of small piezoelectric elements that have UT transmission and reception capability. The Matrixeye synthesizes a 3D image of defects by high-speed processing of UT echo data collected by electronic scanning. The 3D image is produced from a large number of UT echo data signals that have propagated through many different paths within the part being inspected. The system is designed for portability and provides rapid setup and inspection coverage through parallel processing of the UT signals. The Matrixeye system is already in use in the aviation field and shows promise for applications in many industrial fields. Figures 35 and 36 shows sample C-scans from Matrixeye inspections of

composite laminate panels containing different types of structural disbonds and interply delamination flaws.

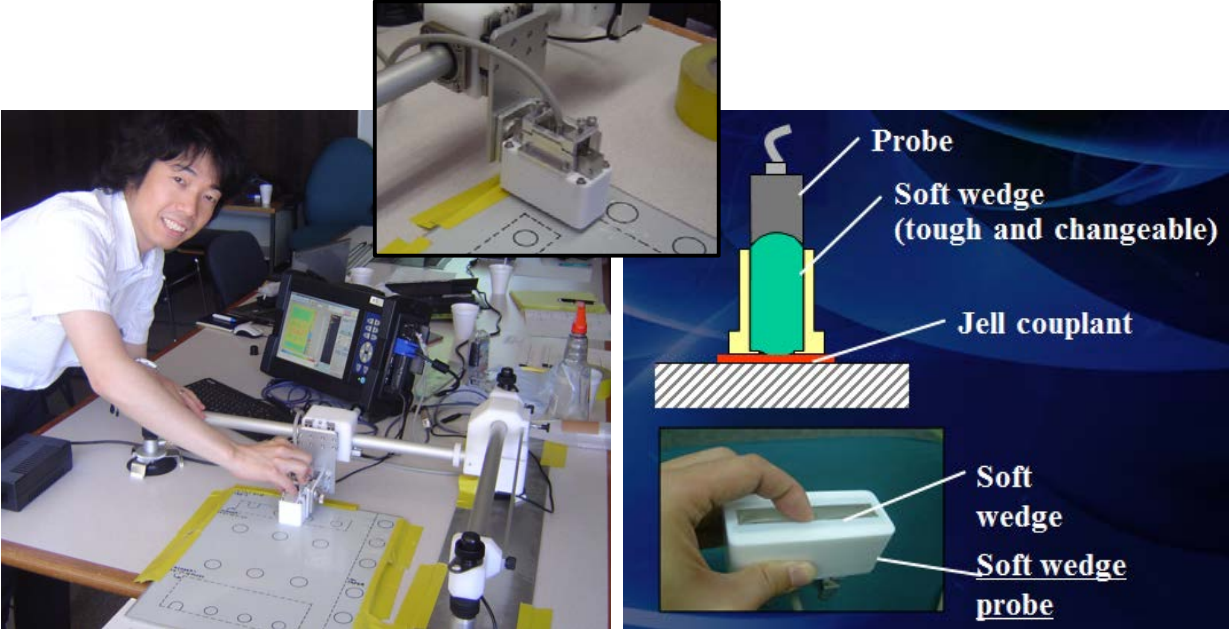
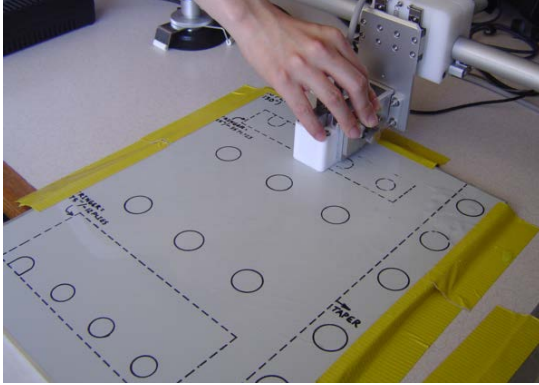
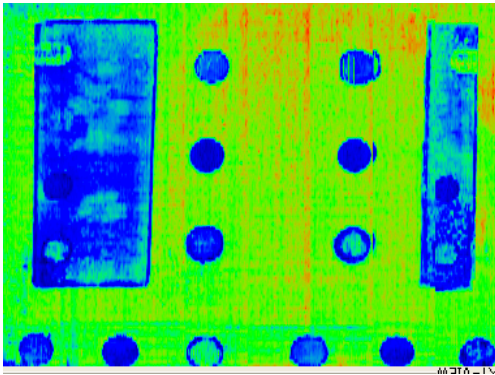


Figure 34. Matrixeye equipment deployed with an X-Y scanner and phased array probe incorporated into a soft wedge scanning shoe



**32 Ply NDI
Feedback
Specimen**

F1-gate captures most of the flaws



**F3-gate captures deepest flaws in
thicker substructure (upper right)**

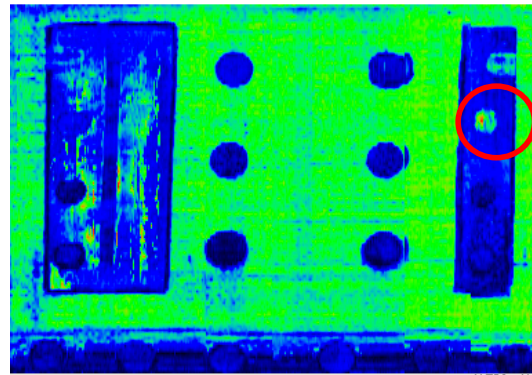


Figure 35. C-scan image of the 32-ply NDI feedback panel showing Matrixeye use of multiple gates to detect flaws at various depths

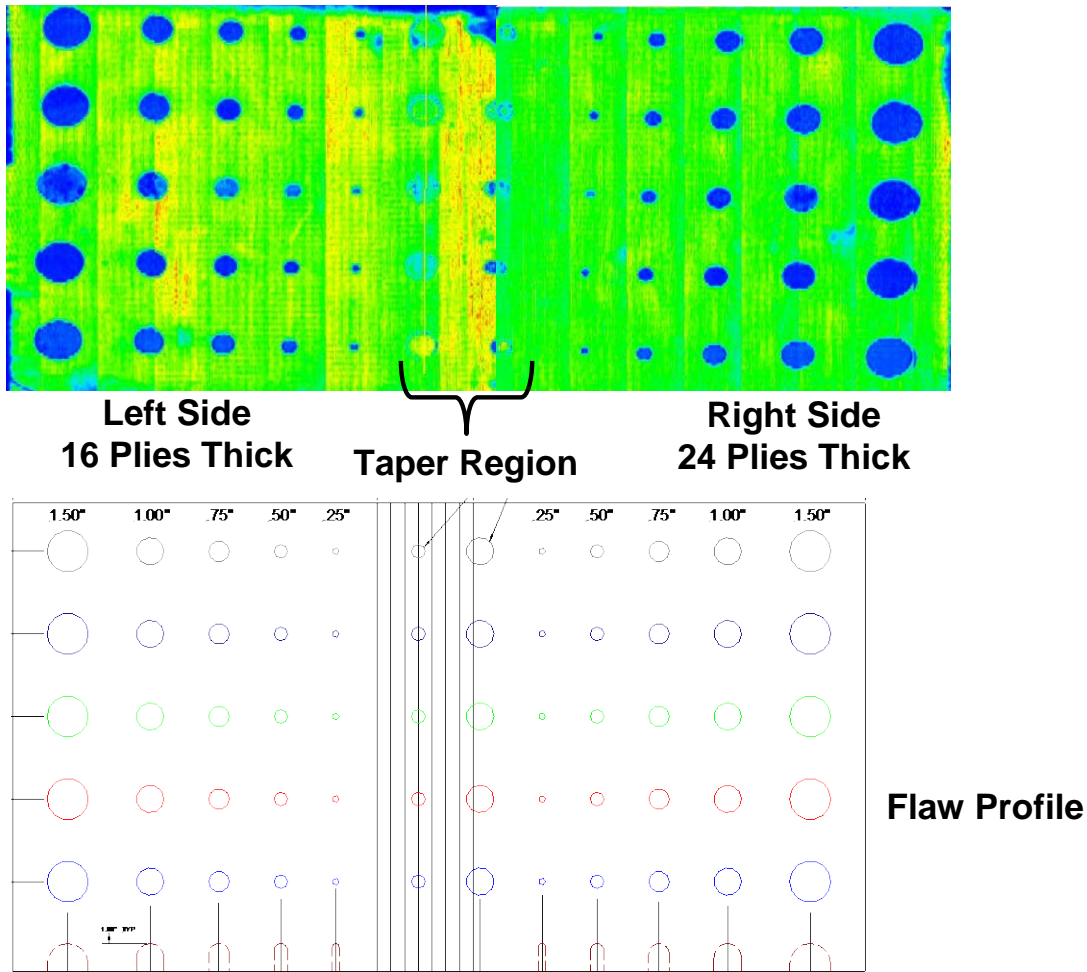


Figure 36. Matrixeye C-scan image of carbon solid laminate calibration panel with interply flaws

3.2.3 Boeing MAUS FlawInspecta Linear Array UT System and the Diagnostic Sonar FlawInspecta PA-UT System

The FlawInspecta system, shown in figures 37 and 38, was designed to address the need for a rapid, low-cost UT phased/linear array inspection system. The imager is a laptop-based device which allows for easy transfer of images to other applications, or through the Internet to remote locations. It works with a wide range of integrated arrays and is suited for applications ranging from rapid large-area flaw detection to high-speed, low-cost corrosion mapping with 100% coverage. The data acquisition is fast enough to allow for interactive B-scan imaging or rapid C-scanning—typically $40,000\text{mm}^2/\text{s}$ ($64\text{in.}^2/\text{s}$) for 1mm pixels—for manual coverage of large areas. The system is also able to perform full waveform capture (FWC) in which the full A-scan (radio frequency or rectified) is acquired and stored for every point on the inspection surface. This volumetric representation offers the ultimate in data acquisition for archiving and offline review and is achieved at similar data rates to manual methods. The FlawInspecta system is capable of a pulse rate of 30 kHz , corresponding to a scan rate of 10 in./s or $19.3\text{ ft}^2/\text{min}$ with a 128-element array. Smart arrays can be used with a wide range of conventional equipment, such

as flaw detectors, but their full capability is not realized unless used with a real-time imaging system such as the FlawInspecta. At the heart of the system is Diagnostic Sonar's Flaw Imaging and Reconstruction Engine (FIRE) technology for real-time, full-waveform acquisition and B-scan imaging. A position sensor attachment to the array extends this capability to C-scans for mapping of inspection areas. The latest FlawInspecta uses proprietary FIRE technology to provide fast, manual imaging and mapping with FWC typically over 1 m²/min for 1 mm pixels. This FIRE technology has now been integrated into other proprietary UT mapping systems and provides an easy upgrade path to high performance acquisition for users of these systems.

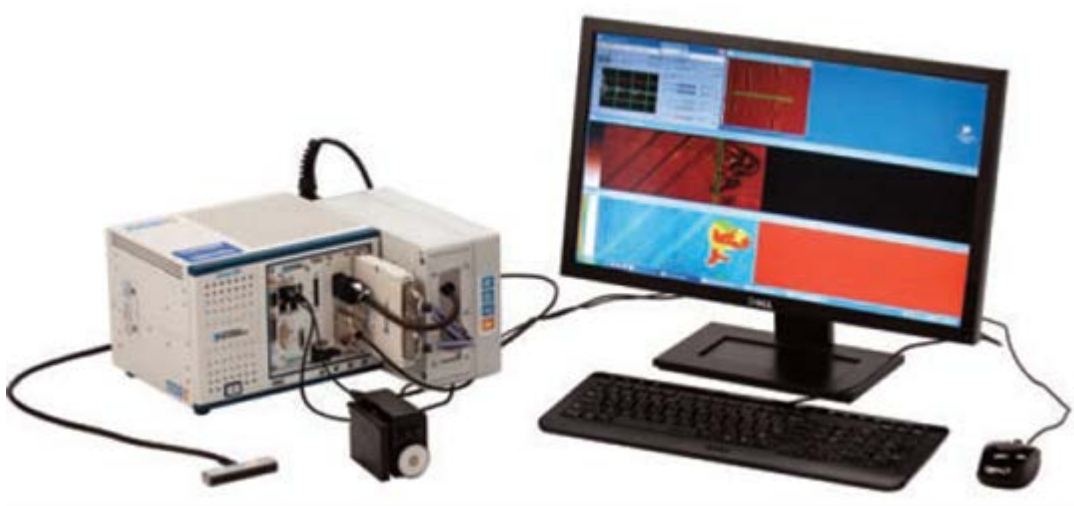


Figure 37. Diagnostic sonar FlawInspecta PA-UT inspection system



Figure 38. FlawInspecta linear array UT system deployed on MAUS V scanner platform (linear array UT probe includes a delay line shoe)

In trial tests on composite honeycomb test specimens, such as the tests shown in figures 39 and 40, the FlawInspecta system was able to detect nearly all of the engineered defects. Some of the indications are best detected when observing the B-scan display. The majority of the defects in the composite solid laminate test specimen can be seen on the C-scan images shown in figure 41. The FlawInspecta is a high-speed UT array system with dynamic real-time B-scan, FWC, and C-scan capabilities.

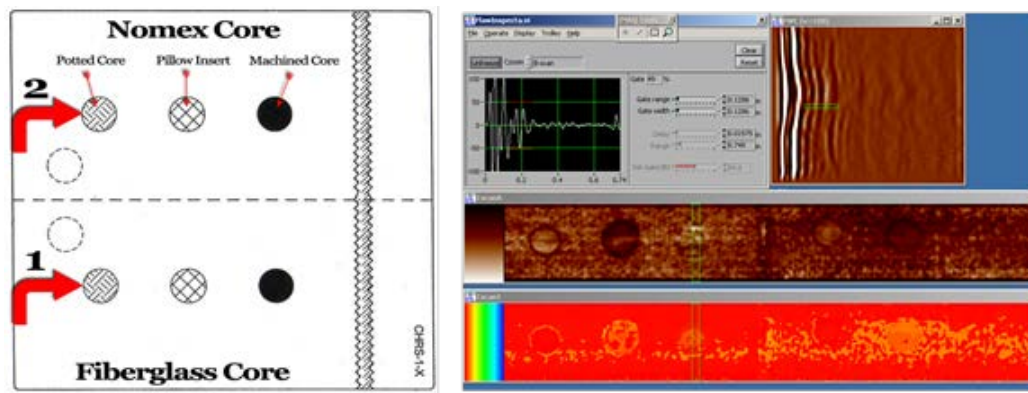


Figure 39. Composite honeycomb reference standard and sample FlawInspecta results (3-ply carbon skin with 1" thick core)

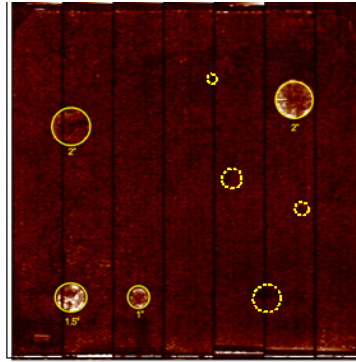


Figure 40. Sample result from FlawInspecta PA-UT system on 6-ply carbon specimen (dashed lines represent missed flaws)

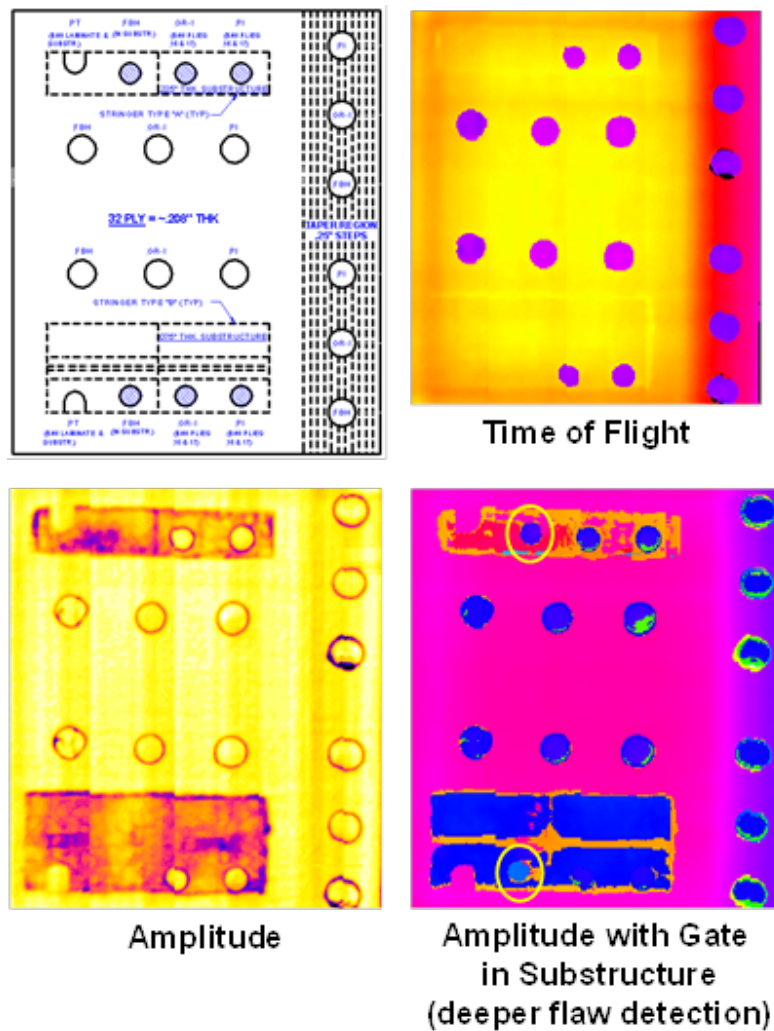


Figure 41. C-scan images produced by FlawInspecta MAUS V linear array UT system on a 32-ply composite laminate feedback panel with the flaw profile as shown

The MAUS V C-scan system uses an OEM version of the FlawInspecta UT array system that is controlled by the MAUS software. The combination of the MAUS V system with the FlawInspecta system allows for the rapid inspection of large areas of composite structures in a seamless, easy-to-use package. One of the differences between the Diagnostic Sonar FlawInspecta and the FlawInspecta add-on to the MAUS V is the phased array capability. The MAUS V FlawInspecta does not have phased array capability and is deployed in a linear array. The addition of NDT Solutions' vacuum-assisted couplant delivery and recovery system provides for excellent coupling of large arrays to those parts that possess the ability to recover and recycle the couplant, nearly eliminating the mess caused by the copious amounts of water required to couple large transducers to the inspection area.

3.2.4 General Electric RotoArray PA-UT System

Figures 42 and 43 show the RotoArray, a manually operated PA-UT scanning device. This rolling wheel array can be connected to any suitable phased array flaw detection instrument to allow for rapid scanning of a wide variety of materials and components. The RotoArray can be cabled to the General Electric (GE) Phasor XS or Olympus OmniScan control and readout devices. Results presented in this report were obtained with the RotoArray connected to the Phasor XS device. The RotoArray can provide A-, B-, and C-scan images that are achieved by rolling the handheld array probe over the inspection surface. Because of its portability, the RotoArray is well-suited for field inspections. The RotoArray consists of a linear, 64-element UT array contained within a tube that is filled with a fluid to create a flexible coupling chamber between the array and the test piece. This also produces a delay line distance between the PA-UT probe and the inspection surface, which can be advantageous in obtaining clear signals for flaw interpretation. Signal coupling between the outer wheel and the inspection surface can be achieved using a spray of water or a water-UT couplant mixture. An encoder contained within the rolling wheel arrangement provides positional data and is connected to a phased array flaw detector to display and store the results. The entire assembly fits within a scanning cart and can be rolled in a linear manner along the surface of the material to scan for flaws, delaminations, or other discontinuities. The RotoArray was designed for post-manufacturing inspections and for the inspection of aircraft in service.



Figure 42. The GE Phasor XS RotoArray wheel probe containing a 5 MHz, 64-element linear array



Figure 43. Deployment of the RotoArray wheel probe on a composite laminate test specimen in the AANC flaw detection experiment

Figure 44 shows inspection results from a 32-ply (0.23" thick skin) solid laminate composite panel with a 58-ply (0.192" thick) upper stringer and a 50-ply (0.125" thick) lower stringer. Several different C-scans, corresponding to different gates set for specific flaw depths and time-of-flight information, can be used to image these flaws. Note that several strips, generated by the linear motion of the RotoArray across the part, can be connected together to form a single image of the inspection over the entire part.

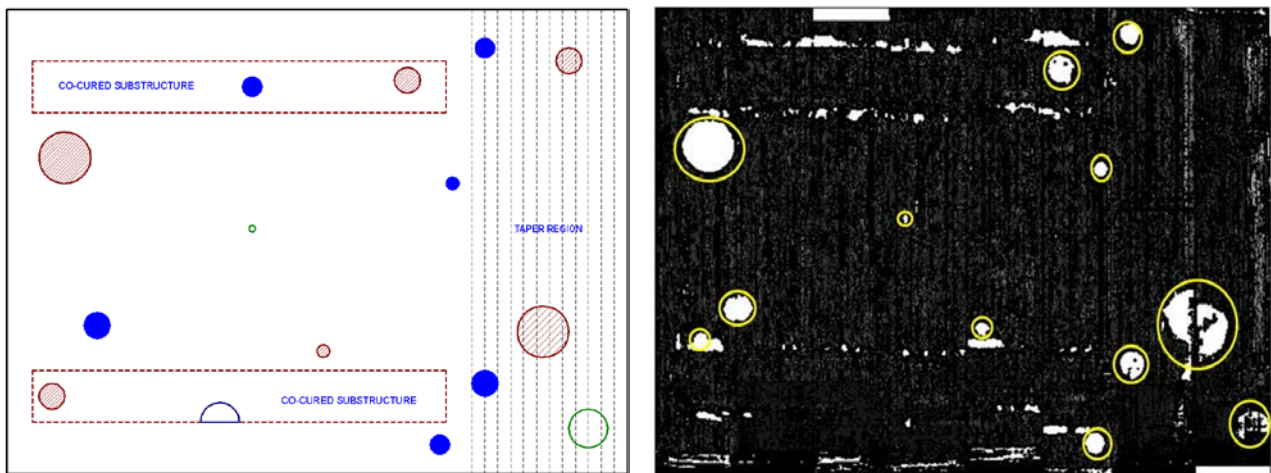


Figure 44. Results produced by RotoArray wheel probe on a 32-ply panel with substructure elements

3.2.5 Sonatest RapidScan 2 Linear Array UT System

The RapidScan 2 with the rolling Array WheelProbe, developed by Sonatest, can perform A-, B-, and C-scan inspections. It uses a novel, rubber-coupled sensor array that provides rapid, wide-area C-scan data in the field. Data acquisition, UT gating, and evaluation tools are used to

ensure proper analysis of the UT signals. The RapidScan 2 and WheelProbe, shown in figure 45, operate in a pulse-echo mode suitable for inspecting medium to large areas. A water film coupling that can be sprayed onto the inspection surface is used to transmit the UT pulse and return signals from the rolling wheel and back to the PA transducer housed within the wheel. The resultant C-scans, such as those shown in figures 46–49, show time-of-flight and amplitude data. Multiple scan strips can be assembled to produce images of entire structures (e.g., the horizontal stabilizer image shown in figure 48). Both A- and B-scans can be simultaneously displayed. The system includes a 128-channel multiplexing pulser/receiver module, data capture electronics, and standard PC laptop housed in a low-profile plastic enclosure for portability. The array WheelProbes incorporate a 64-element phased array (50 mm) and 128-element phased array (100 mm) with 0.8 mm resolution and high-resolution position encoder. Current array probes are available in 1, 2, 5, and 10 MHz to provide a range of resolutions and depth of penetration in thick and highly attenuative structures. Sonatest has cabled their 5 MHz WheelProbe to operate with an Olympus OmniScan unit; this was the setup used in this experiment.



Figure 45. The RapidScan UT array device

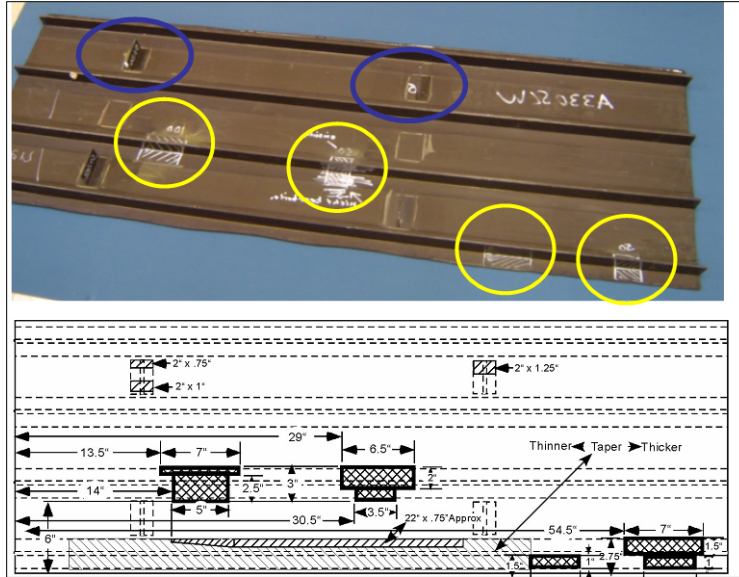


Figure 46. Carbon composite panel with stringers, ribs, and engineered flaws: three stringer-to-skin disbonds (yellow) and two rib-to-skin partial disbonds (blue)

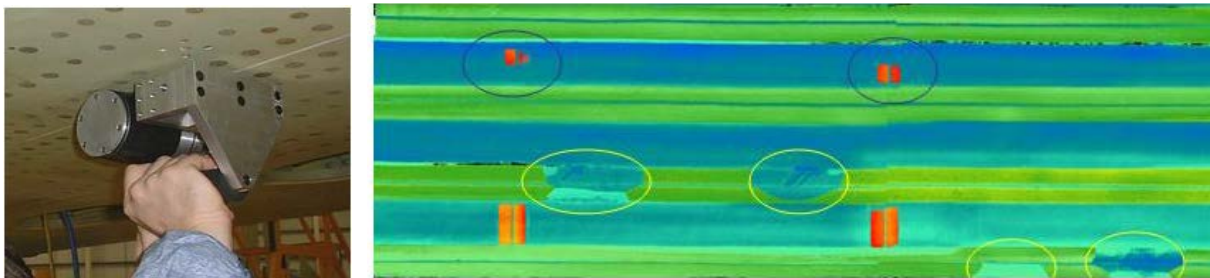


Figure 47. Inspection scans of composite panel produced by the RapidScan UT array device

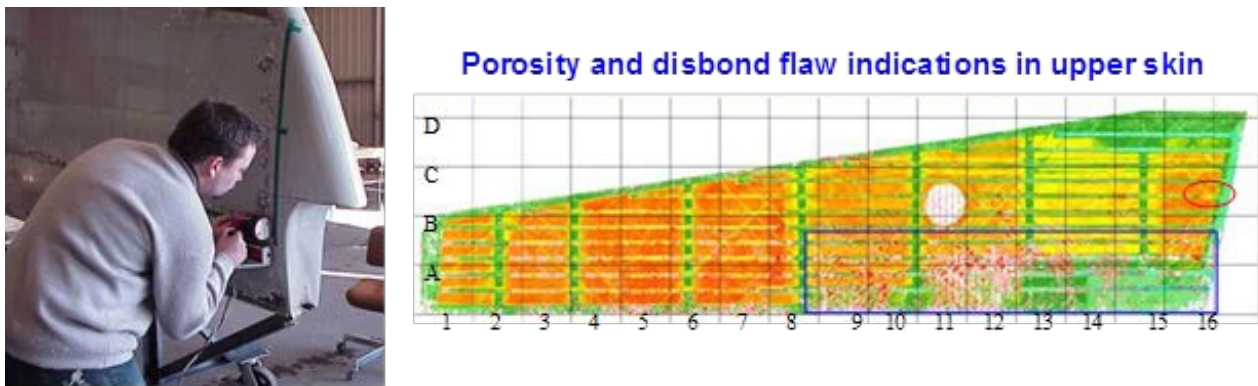


Figure 48. Scan of composite horizontal stabilizer with UT RapidScan array probe

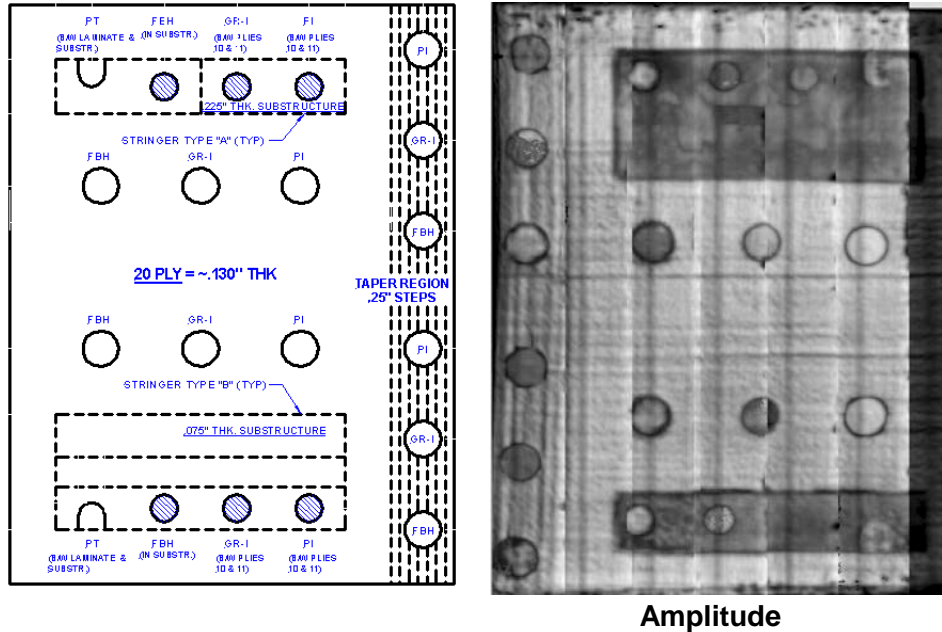


Figure 49. C-scan images produced by RapidScan rolling wheel array probe on a 20-ply composite laminate feedback panel with the flaw profile as shown

3.3 LASER-ULTRASONICS

Laser-ultrasonics (LUS) is generally defined as a technology in which one laser generates UT waves and another laser, coupled to a detection system, detects the associated UT displacements [13–15]. There are four primary issues that have limited the adoption of LUS for the inspection of composites:

1. The lack of reliability of various prototypes used to validate the technology for production
2. The acquisition cost of the LUS equipment
3. The small but significant differences between conventional and LUS signals
4. Though gantry-based LUS systems for production environments have demonstrated excellent results, a fieldable (i.e., portable) system is not available for use in hangar environments

3.3.1 The LUS Deployment

The LUS is a noncontact technique that uses a scanning laser beam to quickly move across the part in a uniform coverage pattern (see figure 50). The UT wave is generated by pulsing the laser beam, causing the surface layer to rapidly expand and contract through thermal expansion. The absorbed laser energy is converted into heat in the top 10–100µm of the surface. The resultant temperature rise creates a local expansion of the material in the UT frequency (1–10 MHz).

Therefore, a longitudinal UT wave is introduced into the part. When the echoes from this wave reach the surface they are sensed by a coaxial detection laser and converted to images proportional to the echo strength. Laser light scattered off of the surface is analyzed by an interferometer to extract the UT signals that are “imprinted” on the laser as phase and frequency modulations caused by the moving surface. The extracted UT signals are basically the same as those obtained with conventional UT systems. The two laser beams can be indexed over the material with a scanner to produce standard C-scan images [12].

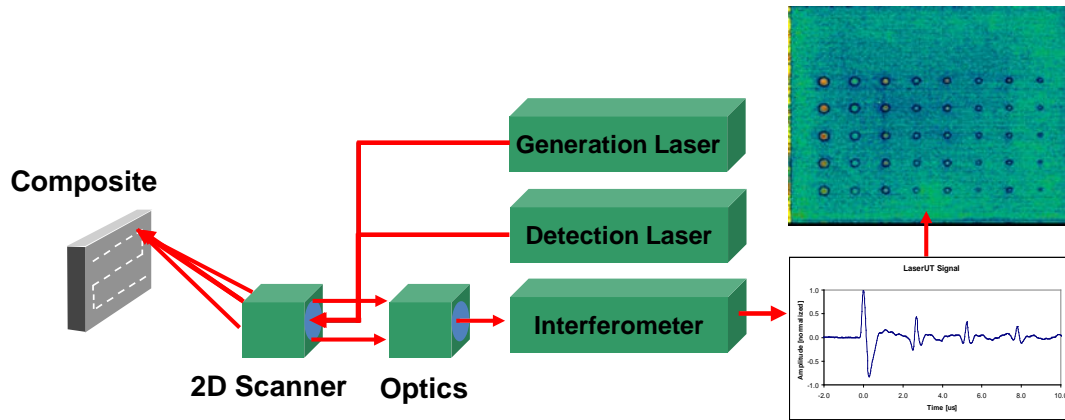
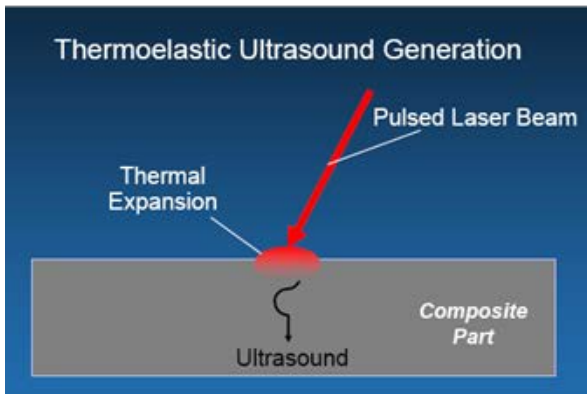


Figure 50. Schematic of LUS system operation

This data transmission and acquisition does not require the laser beam to be deployed perpendicular to the structure as in other UT methods. Therefore, it is possible to scan complex parts without detailed contour following. The UT wave propagates perpendicular to the surface regardless of the laser incident angle (up to $\pm 45^\circ$). Currently, the LUS systems are deployed using a gantry system which provides a high-speed 2D optical scanner to index the beams over the part. This allows for rapid inspection and generation of the C-scan images. Hand scanning using UT can be slow and tedious, leading to human factor concerns with respect to coverage and vigilance. In addition, water-coupled UT can be difficult and time-consuming to implement on complex shaped parts. Figure 51 compares traditional UT inspections to a LUS interrogation. The first LUS systems mounted on robots [12] used gantry-type robots. Optical alignment of the CO₂ laser beam in the optical scanner must be precisely maintained to obtain valid UT results. The CO₂ laser cannot be efficiently transmitted by optical fibers. Therefore, the most obvious solution is to move the CO₂ laser along with the optical scanner. This approach requires gantry robots because it is the only type of robot that can move equipment as large and heavy as an industrial CO₂ laser. Gantry robots present several disadvantages, the most significant being the cost. The gantry robot is typically the most expensive element of a LUS system that includes such a robot. Figure 52 shows several different deployments of the LUS inspection technique and a schematic showing the ability to inspect parts without maintaining a perpendicular inspection orientation.

Thermoelastic mechanism can efficiently generate ultrasound in composite materials (less efficient on bare metal)



Conventional coupled UT must maintain the transducer normal to the surface

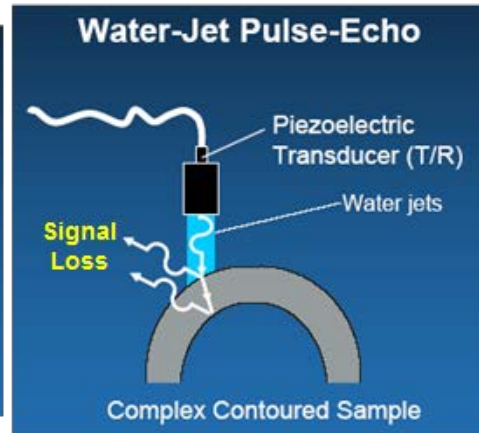
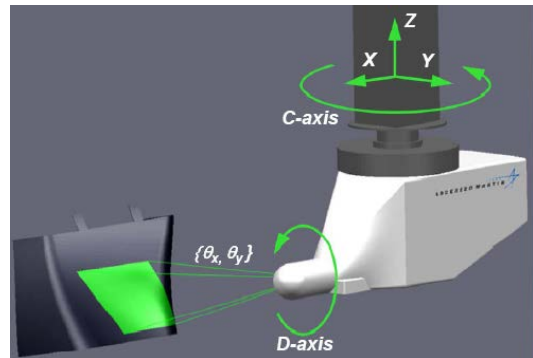


Figure 51. Comparison of conventional and LUS interrogation of components

Ultrasound propagates perpendicular to surface regardless of the laser incident angle (up to $\pm 45^\circ$)



Articulated robot system on a linear rail
Freq. Range = 0.5 MHz – 20 MHz



Figure 52. Schematic of LUS method and deployment in a gantry system and rail system

The iPhoton LUS concept (iPLUS) was used to conduct the LUS inspections listed in this report. An iPLUS III system is shown in figures 52 and 53. It uses a beam delivery system mounted on an articulated robot. To increase the working envelope, the robot, beam delivery system, and CO₂ laser are mounted on a linear rail. The linear rail provides an almost unlimited working

envelope to the iPLUS system in one direction. Articulated robots provide flexibility not possible with gantry-based approaches. Some applications require the inspection of composite substructures inside larger structures, such as stringers inside a fuselage. The iPLUS configuration was developed as a response to these applications. In the iPLUS III systems, the beam delivery system is composed of two standard beam delivery systems joined together on axis 3 of the robot. This approach, combined with a cantilevered linear rail, provides over 6 m of penetration inside a structure (e.g., a fuselage). For the inspection of parts, the iPLUS scan head is positioned using the articulating robot. Once the scan head is in position, the scanning is completed by moving the laser beams along the surface of the sample using only the two mirrors of the scanner. The scan area is defined by the angular movement θ_x and θ_y of the scanner's two mirrors. This process is shown in figures 52 and 53. When the scanning of one area is completed, the robot moves the scan head to the next pose to scan the next area.

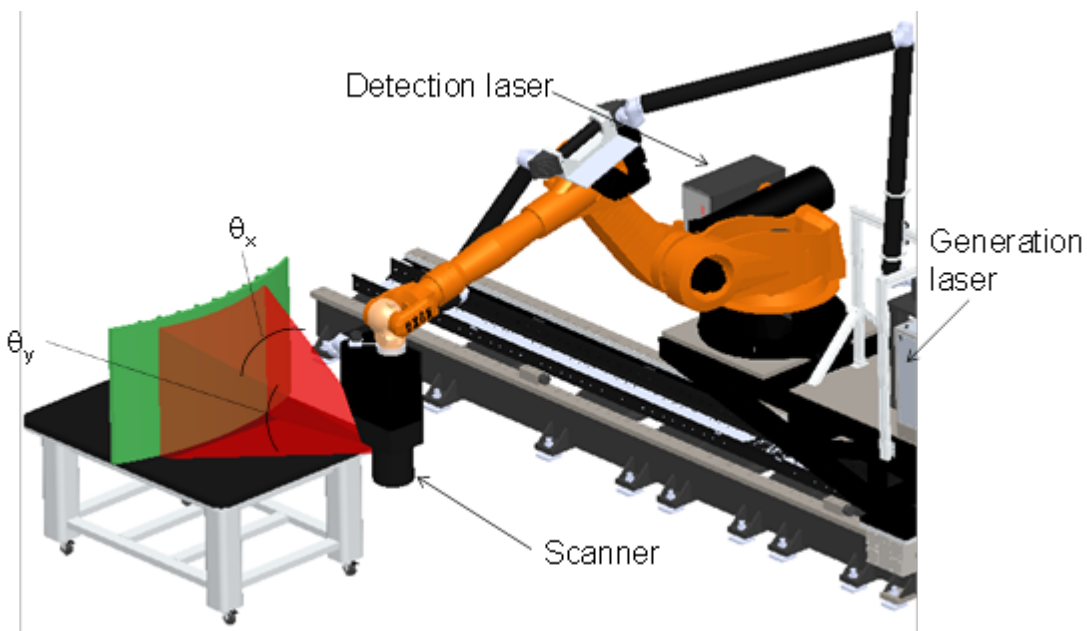


Figure 53. Inspection of a part using the iPLUS scan head and articulating robot

Figures 54–58 are sample images produced by LUS inspections on various composite parts, some of which contain substructure elements. Note that surface and subsurface structural details are imaged in the scan. The clarity of the flaws and sensitivity for flaw detection down to 0.25" diameter are depicted in the C-scan images. Figure 54 shows the iPLUS LUS results from a 16-ply, 12" x 12" composite laminate panel that was damaged by simulated hail impact. The top left and right images are the amplitude and time-of-flight C-scan images, respectively. The bottom graphics show an A-scan and B-scan corresponding to the line in the top C-scans.

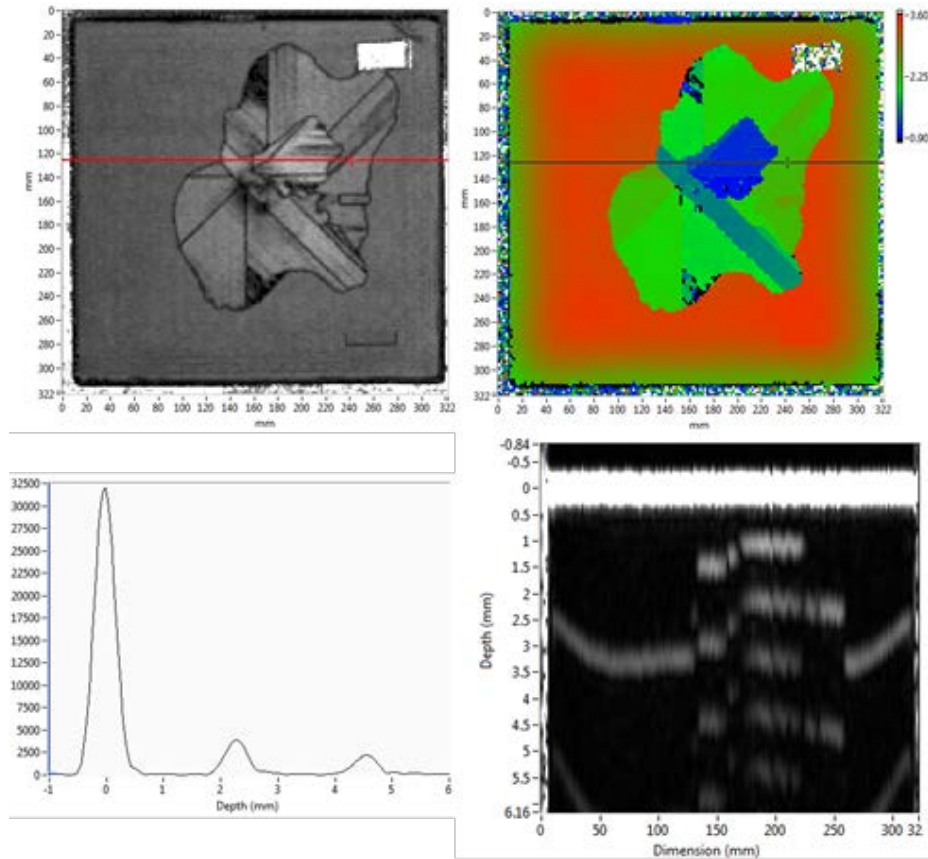


Figure 54. An iPLUS LUS scan of a 16-ply composite laminate with impact damage

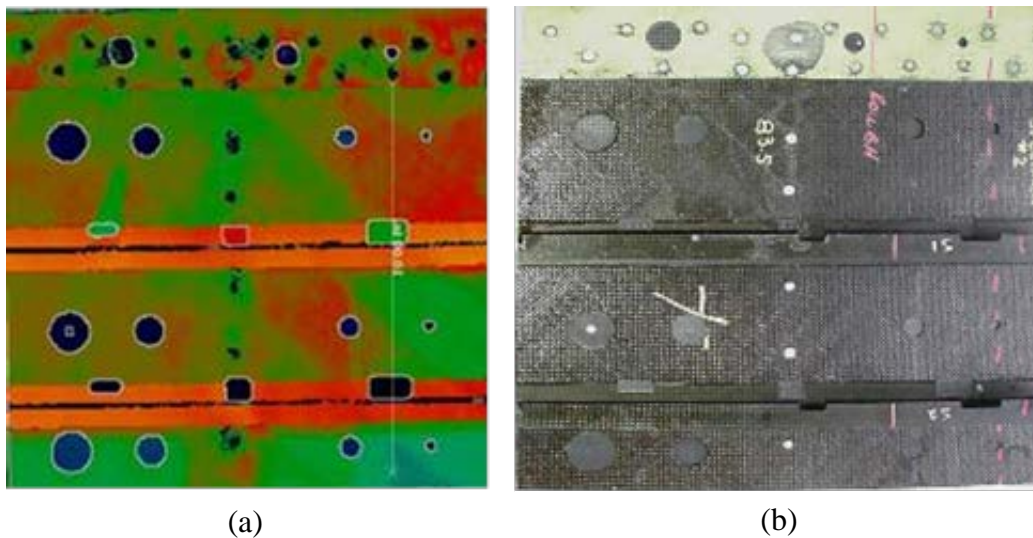


Figure 55. An (a) iPLUS LUS inspection of 0.111" thick composite laminate test specimen and (b) photograph of the layout of the engineered flaws

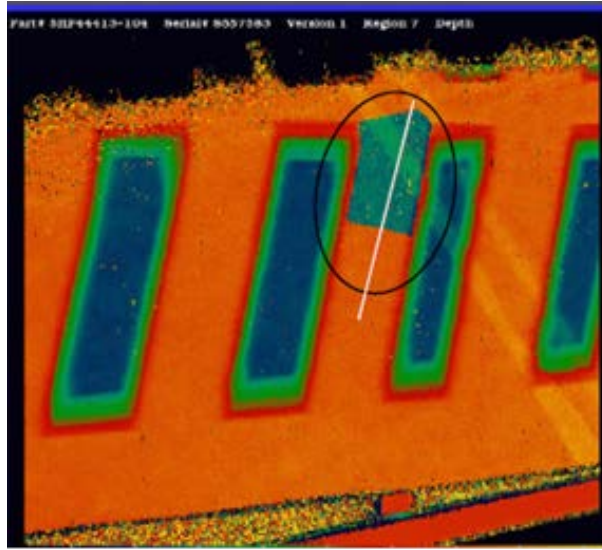


Figure 56. An iPLUS LUS image of a composite part containing an inclusion, as highlighted

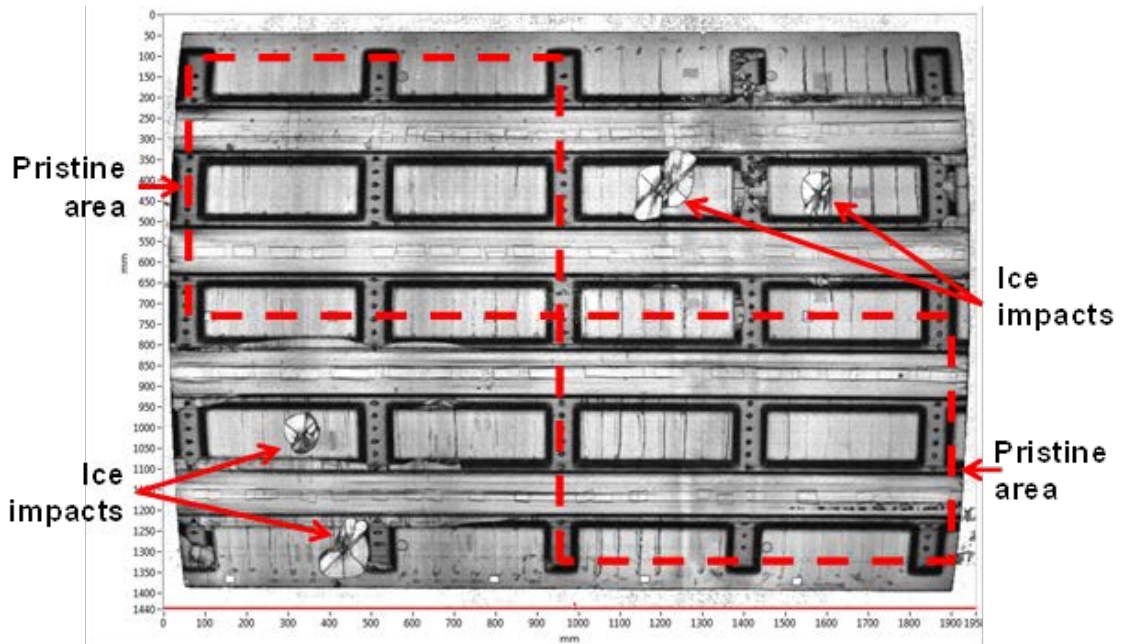


Figure 57. Sample results from iPLUS LUS inspection of a 3-ply fiberglass honeycomb panel

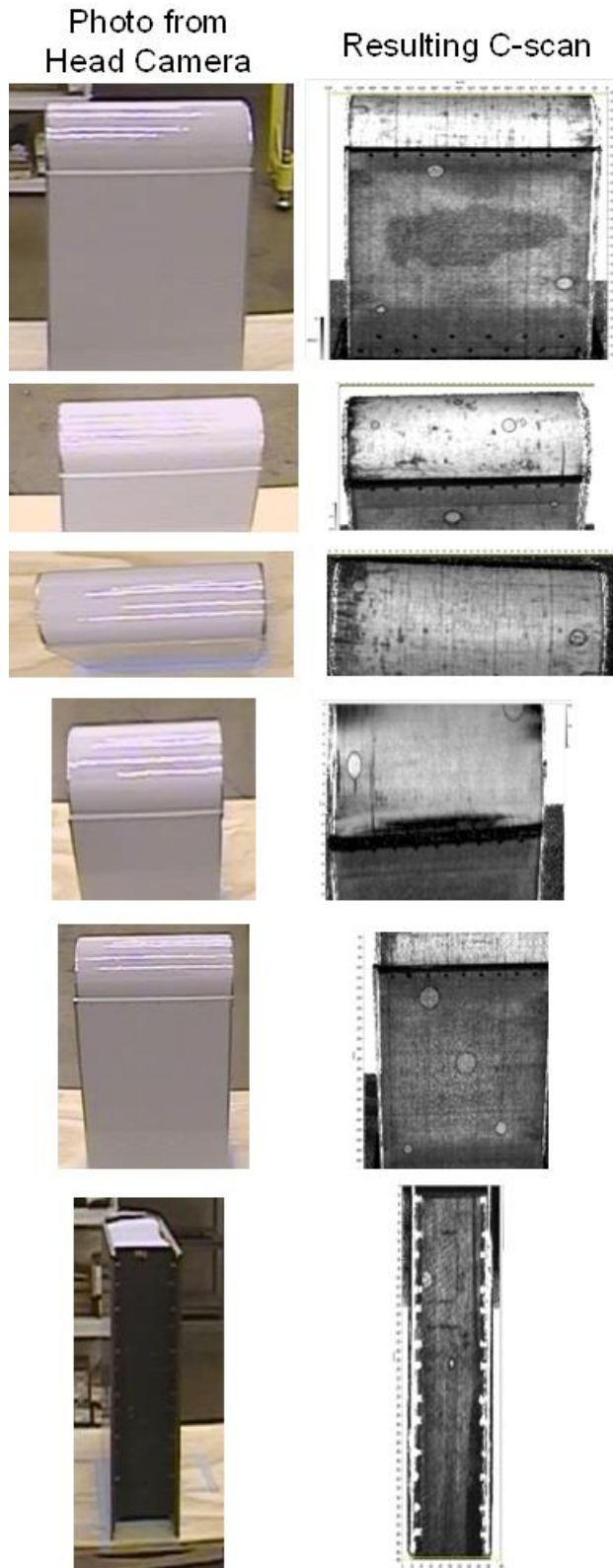


Figure 58. Robot camera photographs matched with associated LUS C-scans for the inspection of a BN-shaped composite component

Figure 57 shows UT results obtained on a curved, full-scale fuselage composite panel measuring 5' x 7' and containing stringers and skins (20 bays). The fuselage curvature is very gradual; for the purpose of LUS, it is considered flat. This panel was also impacted in the laboratory with ice/hail projectiles. A BN-shaped part approximately 2' high by 1.5' wide by 0.7' deep, with a curvature radius of approximately 0.35 ft, was inspected using an iPLUS system. Figure 58 shows the pictures from the scan head camera and the corresponding UT amplitude C-scans. The engineered flaws are clearly imaged in the LUS scans. The two flat areas of the BN part required one robot pose each, whereas the curved end of the part required three poses to limit the angles of incidence. Those five poses were recorded in a teach mode that was used for the automated UT inspection. In addition to those five poses, the part was manually moved to access the channel underneath that simulated the wing spar.

The LUS technology offers flexibility and faster inspection cycle time. However, even though LUS signals are UT signals, there are some differences with UT signals obtained with conventional UT transducers. Those differences must be understood when trying to adapt processing and analysis techniques coming from decades of experience using piezoelectric transducers.

The key advantages of LUS are:

- the ability to scan quickly in a noncontact mode, all the way to the edge of a part.
- the ability to launch a through-thickness longitudinal wave even when the laser beam impinges on the surface at an angle.

This means that the laser beam can be directed at the surface of complex shapes and scan them efficiently without the need for contour following, complicated scan shoes, or angled water jet arrangements. A laser beam can also be directed through apertures to scan the interior of a structure.

The disadvantages of LUS include:

- sensitivity to surface coatings (variations in coatings can affect the strength of the UT signal).
- maximum sensitivity requires tuning for each structure type.
- system expertise/training is needed to ensure alignment to produce uniform signal.
- safety concerns necessitating personnel exclusion zones.
- the potential for the laser to damage the part surface if not used with caution.

3.4 ACOUSTOGRAPHY—VIDEO-BASED UTs

Acoustography is a full-field UT imaging process in which an exceptionally high-resolution, 2D Acousto-Optic (AO) sensor is used to directly convert the UT wave into a visual image in real time. Acoustography uses a detector array sensitive to UT energy, much like detector arrays sensitive to light are used in digital cameras. The device produces a real-time image or “instant C-scan” of defects in the part. Acoustography is a potential field inspection technique that could be useful for rapid identification of damage from impact, lightning strikes, and other composite damage. Results from acoustography inspections are best viewed as motion pictures so that delaminations can be distinguished amid their surrounding structure.

Acoustic images can be formed in through-transmission mode, as shown in figures 59 and 60, or reflection mode, as shown in figures 61 and 62. Acoustic images can be formed using an acoustic lens that is analogous to cameras or camcorders. In the through-transmission shadow mode of acoustography, which is usually suited for NDT of components during manufacturing, a UT wave is passed through the test component where it is absorbed, reflected, and scattered by the structural material and any anomalies therein. The projection image of the material structure and anomalies is created by the UT wave as it exits the test component. This projection image is directly converted into a corresponding visual image (see figure 60) by the AO sensor in real time.

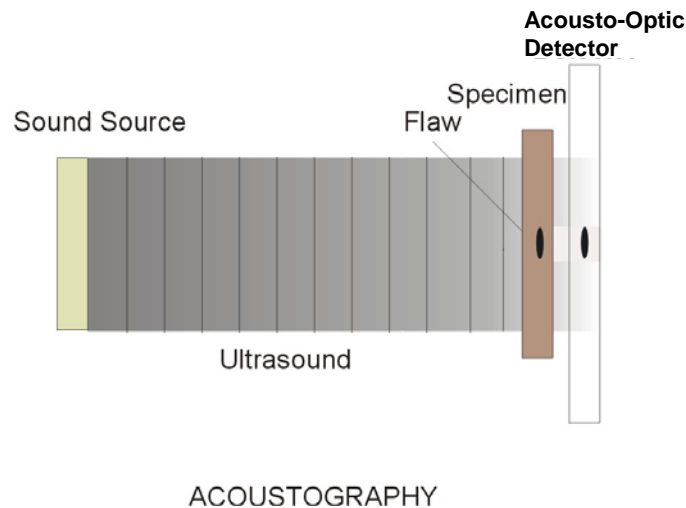


Figure 59. Acoustography through-transmission mode allows instant full-field inspection of an area

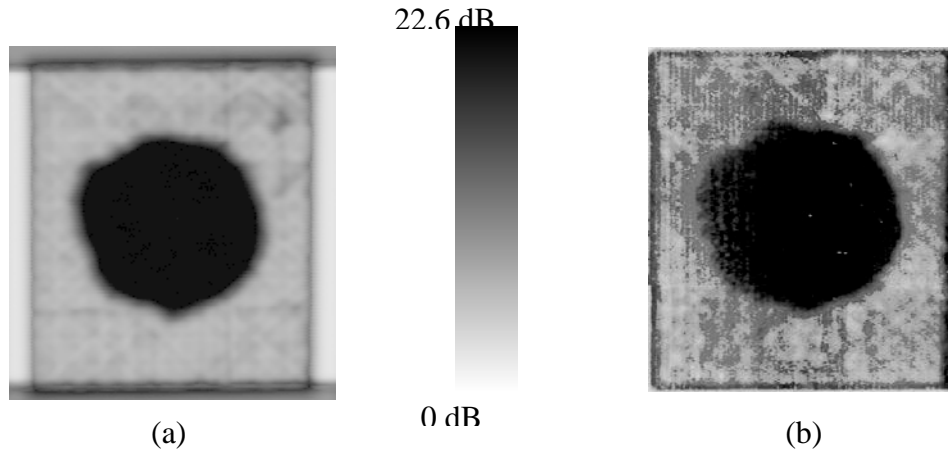


Figure 60. Through-transmission (a) C-scan and (b) acoustography inspection of impact damage in a graphite/epoxy composite specimen

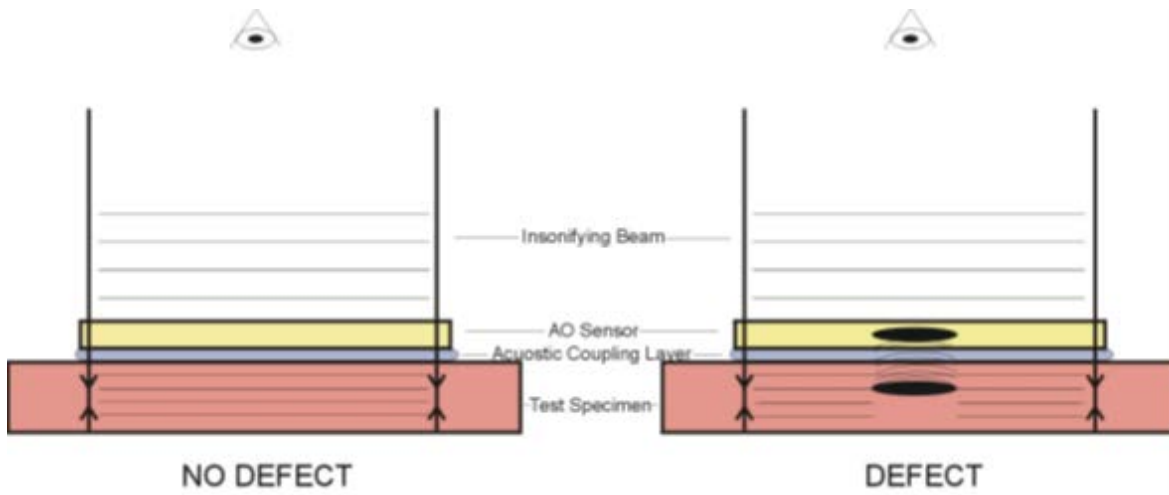


Figure 61. Reflection mode acoustography allows for single-sided UT inspection

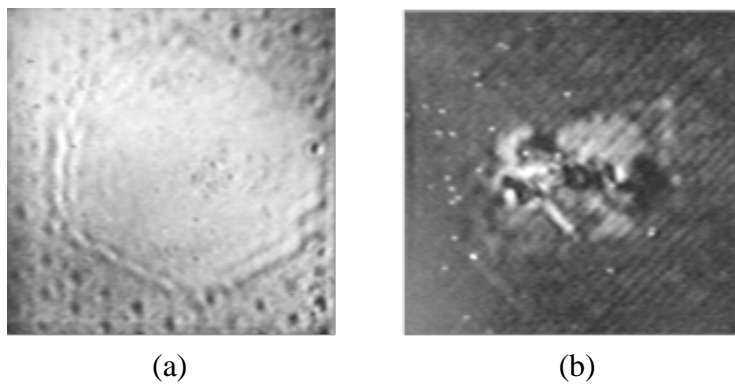


Figure 62. Preliminary results with reflection mode acoustography (a) image of disbond at aluminum skin/honeycomb interface, and (b) image of impact damage in graphite/epoxy composite laminate AcoustoCam (Imperium)

The potential advantages of acoustography include:

- full-field area inspection, not point-by-point inspection.
- near real-time, rapid screening of components.
- high lateral resolution—the UT wave is converted into visual image by minute molecules.
- simplicity—the visual images are intuitive and easy to interpret compared with electronic signals.
- low cost—a lower-skill operator is needed, which results in significant cost savings.
- hand portability—no need for bulky mechanical scanning equipment.
- easy setup—no need for an elaborate setup of a cumbersome scanning apparatus.

3.4.1 Imperium AcoustoCam Digital Acoustic Video Device

A portable (i.e., fieldable) version of acoustography is Imperium's AcoustoCam, which is slightly different in that normally the detector array is placed on the opposite surface of the part so that sound is captured in through-transmission mode, as shown figure 59. However, recent developments have produced single-sided equipment that can be used from the exterior of a structure in pulse-echo mode. To generate C-scan images, a UT wave is transferred into the target through a large, unfocused transducer. The pressure wave strikes the target and is scattered. This scattered energy is collected by an acoustic lens and focused onto the array, identical to infrared (IR). The array is in intimate contact with a water column that allows for the UT wave to propagate. The use of a lens provides a simple, inexpensive alternative to complex beam forming often used in UT imaging. The user focuses by adjusting a lens while looking at the image. Furthermore, it provides a means to trade off resolution and area coverage or zoom in and out. The device produces a real-time image, an "instant C-scan" of defects in the part.

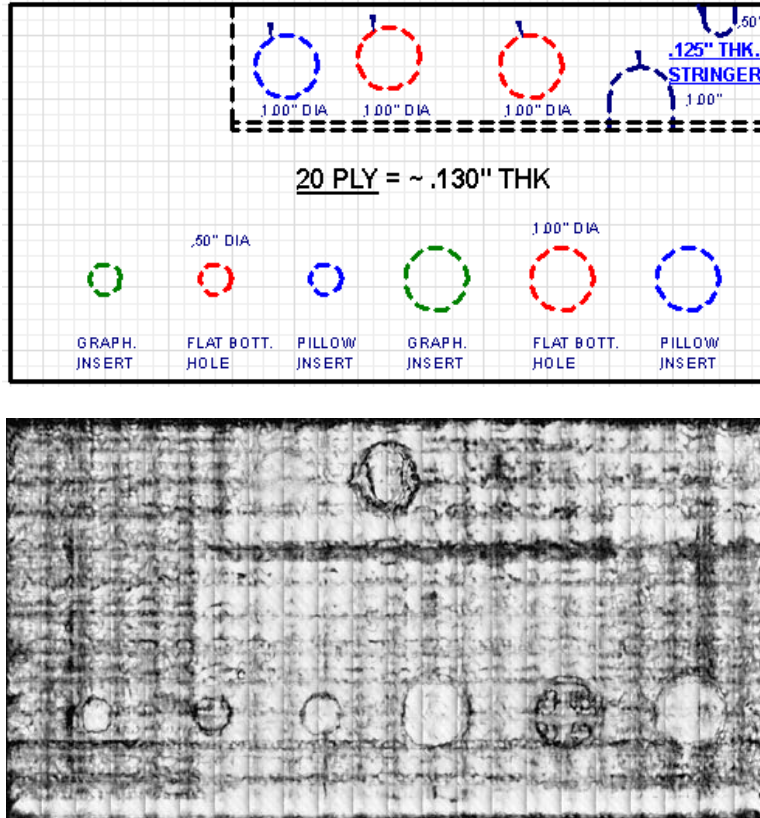
Figure 63 shows the Imperium AcoustoCam equipment and a digital image of a flaw within the structure (inset). The Imperium camera is a liquid-filled point-and-shoot UT imaging device that is placed directly on (i.e., makes contact with) the object under test. It contains a transducer and lens system that focuses the incoming UT wavefront onto the face of an internal detector and operates in the 5 KHz to 7.5 MHz range. The focus grip mechanism is located on the camera head for image focusing. The grip has indented numbering to identify the position of the lens. The lens assembly contains a 3-set aspherical F1 set of lenses. A cable connection at the base of the camera connects communication and power from the control unit to the camera head. The i600 AcoustoCam controller shown in figure 63 is a portable device that controls the camera head and displays UT imagery and values. The controller is an integrated, single-board computer with an LCD and touch screen interface. The testing output is shown on the LCD of the control unit using Imperium's AcoustoVision graphical user interface software. The controller contains a pulser board subassembly that generates a square-wave pulse train that excites the transducer in

the camera head. A knob on the upper-left front of the control unit adjusts the amplitude of this pulser signal. The controller operates on 110/240 VAC, 50/60 Hz power or rechargeable internal battery power. The controller is not serviceable by the user. There is no need to fill the gap between the membrane that contacts the inspection surface and the sensor with signal-coupling material. The camera is assembled and filled at the factory; if the front membrane rips, the user would need to fill only the 1/2" section at the front with a small syringe. However, it is best to eliminate the need to fill the camera because the fill process can introduce air bubbles into the system that can interfere with the UT signal.



Figure 63. Imperium acoustography equipment and flaw image

The Imperium AcoustoCam has an automatic C-scan gate setting that is based on the A-scan and can establish the front wall location. This feature automatically sets the C-scan gates to look just past the front surface. Even though the individual images cover small regions, the AcoustoCam system has the capability to produce 2D, wide-area images of the inspection region. Using Imperium's AcoustoVision software, the data acquisition system automatically splices a series of individual inspection images into a larger, 2D map of the component. Thickness readings from anywhere on the wide-area image can still be acquired. Figure 64 shows a 2D AcoustoCam image produced by using the AcoustoVision software on a composite panel containing engineered flaws.



Acoustcam Amplitude Results

Figure 64. A 2D stitched image produced from individual AcoustoCam results on a composite panel

3.4.2 DolphiTech DolphiCam Ultrasound Video Camera Device

The DolphiTech DolphiCam is a mobile UT camera system designed for NDT of carbon fiber reinforced plastics (see figure 65). Unique dry and wet transducer technology combined with data acquisition electronics are used to create 2D and 3D images of suspected damage areas to verify the status of the material for manufacturing quality assurance or in-service inspection applications. DolphiCam connects to a standard Windows PC or tablet through a USB port, making the system portable and adaptable. Camera settings can be stored and retrieved for quick camera configuration. The silicone-based transducer mat allows for dry coupling on painted or shiny surfaces, but the system can also be used with water or contact gel. The DolphiCam software creates A-, B-, and C-scan and 3D visualization images using amplitude or time-of-flight data. By adjusting pulse and gate settings, color thresholds, and other camera settings, material defects can more easily be identified. The transducer area (i.e., image capture size) is 32 x 32 mm consisting of approximately 16,000 elements (124 x 124). The transducer frequency ranges from 2–6 MHz, focusing at approximately 4 MHz. Therefore, the system is ideal for carbon part thicknesses that are less than 8 mm. This system can be used in a manufacturing environment for quality inspections such as borehole flaking or other manufacturing anomalies. Within the aircraft maintenance environment, this system is ideal for inspections related to impact damage, delaminations, and substructure disbonds.



Figure 65. DolphiCam handheld portable ultrasound video camera

Figures 66 and 67 show sample amplitude images from inspections on various composite laminate structures containing different ply thicknesses and damage types. The display of A-, B-, and C-scan information is shown in figure 66, whereas figure 67 shows clear DolphiCam images of delamination, disbond, and impact damage in composite laminates. Figure 67 also shows several other features of the DolphiCam image display options. The DolphiCam 3D visualizer creates images of the material defects to perform a defect analysis and allow for an optimal repair strategy. The 3D image can be zoomed, panned, and rotated. Currently, the DolphiCam is not considered a large-area scanning system, but DolphiTech has “image stitching” listed as one of its future development goals. Manual stitching support makes it easy to cover larger areas. Figure 68 shows the assembly of multiple individual images to assemble an overall image of a composite structure.

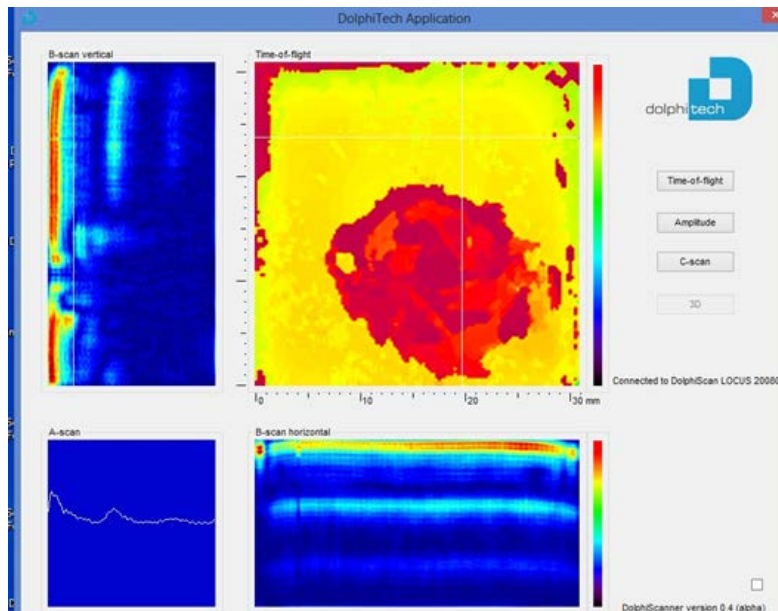
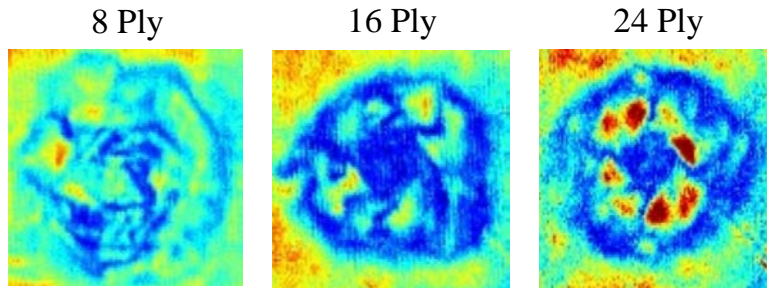
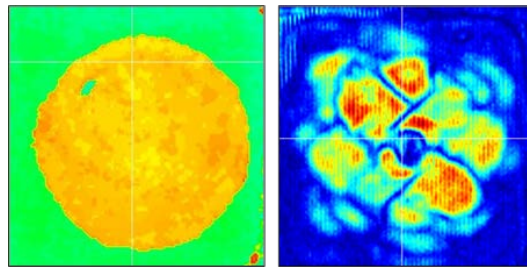


Figure 66. Dolphicam A-scan, B-scan, C-scan (time-of-flight or amplitude image) and 3D visualizer display showing interactive flaw sizing and depth measurements



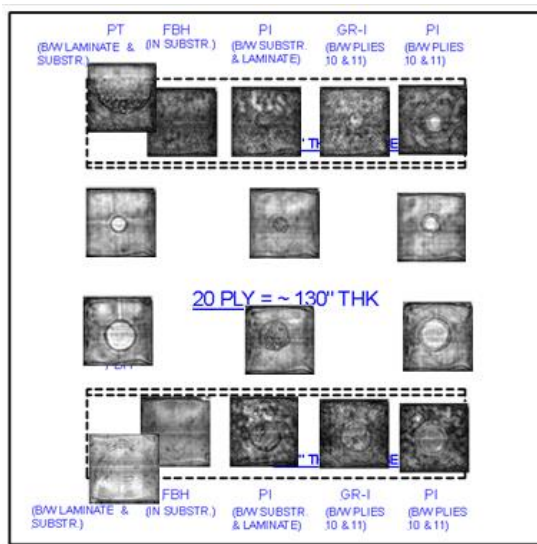
(a)



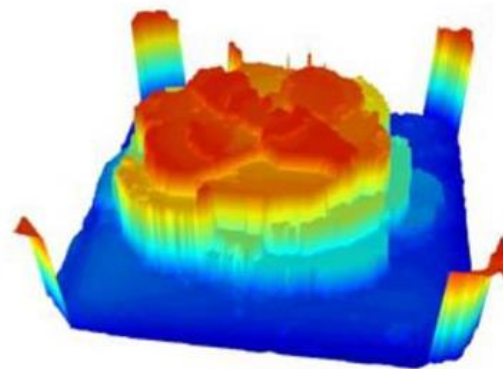
(b)

(c)

Figure 67. DolphiCam inspection results showing (a) amplitude images of impact damage, (b) interply delamination, and (c) impact damage in composite laminate structures



Amplitude



3-Dimensional Flaw Mapping

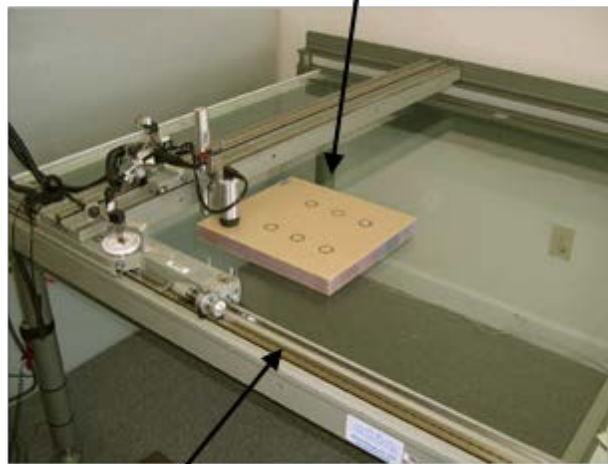
Figure 68. DolphiCam 3D image and sample global image formed from various flaw images superimposed on the flaw layout drawing of a composite panel

3.5 MICROWAVE INSPECTION

Microwave (MW) inspection works by using a specialized transducer to bathe the material of interest in MW energy of an essentially constant frequency. Several different system setups for

MW inspection are shown in figures 69 and 70. The energy is reflected from each interface between materials possessing differing dielectric constants within the specimen. The reflected energy is superimposed, creating a signal that is acquired as an analog voltage which is then digitized. This signal is sampled at numerous discrete locations across the sample to create a 2D image of the surface, as shown in figures 71 and 72.

Fiberglass Honeycomb Test Specimen



Automated scan table

Figure 69. Configuration of MW inspection system on a laboratory scan table



Figure 70. Basic equipment setup for MW inspection

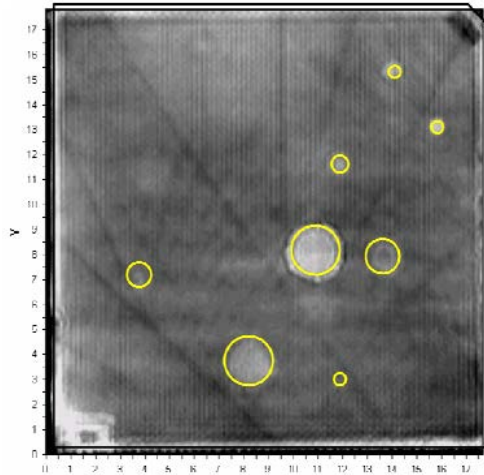


Figure 71. Sample MW inspection results for 3-ply fiberglass honeycomb panel with engineered flaws (fiberglass skin bonded to Nomex honeycomb)

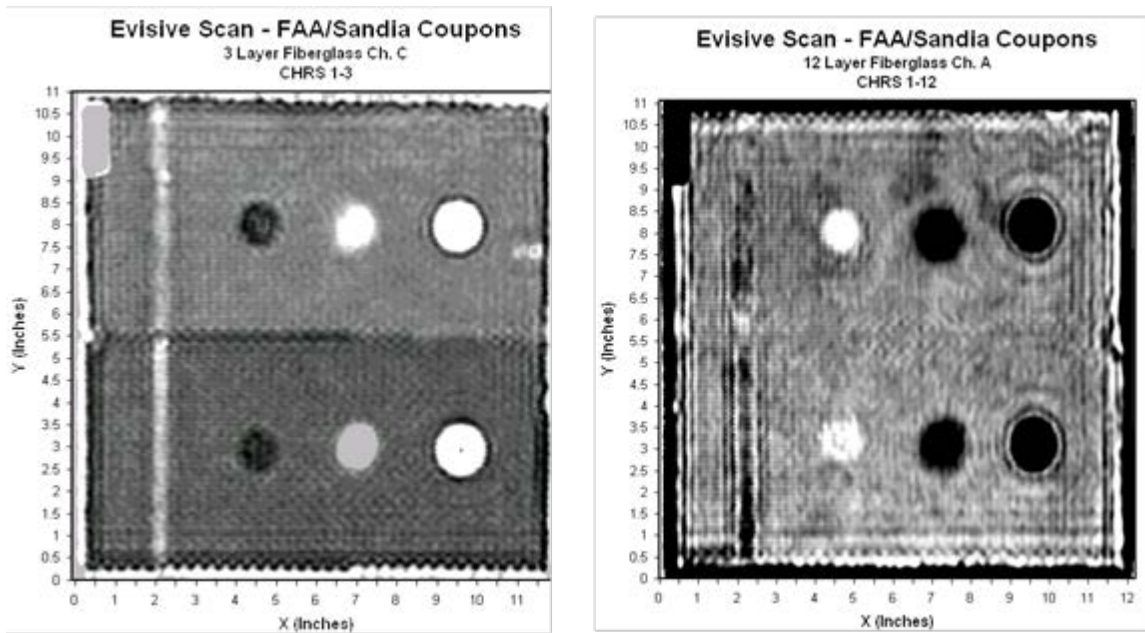


Figure 72. Sample MW inspection results for 3-ply and 12-ply fiberglass panels with delamination, disbands, potted core, and core splice

The ability of MWs to penetrate dielectric materials makes MW inspections an NDT technique suitable for interrogating structures made of composites. Additionally, the sensitivity of MWs to the presence of dissimilar layers in composite materials allows for accurate thickness measurement and variation detection. The quality of the experimental images captured with these systems has demonstrated the potential of the technique for material NDT purposes. Basically, these systems use an antenna (i.e., a horn antenna used in the first experiments or open-ended rectangular waveguide used in recent years) to illuminate the composite with electromagnetic (EM) waves and then to monitor the reflected waves. The EM waves penetrate deep into the

dielectric material where they interact with its interior and reflect back to the antenna. For this particular application, the EM wavelength goes from 1–100 mm. The properties of the reflected wave convey information about the composite. The imaging mechanism is based on the idea that MWs are very sensitive to discontinuities in the material space and the presence of water (the water reflects specularly with the wavelength of MWs).

The MW NDT techniques may be conducted on a contact or noncontact basis. In addition, these techniques are conducted from only one side of the sample (reflection techniques). Furthermore, when compared with UT techniques, MW NDT approaches require no coupling material (e.g., glass or water) and do not suffer from signal attenuation; the MWs have good propagation in the air. The MW techniques are able to detect voids, delaminations, and porosity variation in a variety of materials, as well as impact damage and water infiltration, all problems that affect the composite materials; they also provide the possibility of process control during the manufacturing of composites so that the final product may not require any scrutiny but rather only occasional testing once under some loading. Finally, MW NDT techniques do not require a high level of expertise from an operator and can be conducted in real time with simple, portable hardware. The main limitation of the MW method is that it is limited to nonconductive materials; it has been successfully applied to fiberglass composite structures, but cannot be used to inspect carbon graphite composites.

3.6 SHEAROGRAPHY

Shearography is a wide-area interferometric imaging technique that is capable of detecting micron-sized displacements in the surface of a structure. Shearography equipment, shown in figure 73, monitors the surface of a structure for any changes in the surface strain field. Stressing the material in the appropriate way ensures that the subsurface anomalies are manifested on the surface of the structure. Shearography is implemented by comparing two interference patterns on a detector plane, typically before and after an object motion. If the motion and subsequent out-of-plane deformations cause changes in the optical path, then the speckle patterns differ. These images can be compared by subtraction or other algorithms to obtain an image of the object with fringe patterns superimposed. These fringe patterns can then be used to identify the presence, size, and depth of flaws in a structure.



Figure 73. The LTI-5200 portable shearography system with camera on a test specimen

A typical shearography system uses a charge-coupled device (CCD) camera with a shearing lens, which is completely integrated into a compact measurement head, to view laser light reflected from the surface under inspection. The object under test is illuminated with laser light and images from the object at different states of loading are taken. The loading of the surface is created by different excitation methods such as vacuum, thermal, vibration, or mechanical load, which induces some deformation of the outer surface. Such deformations are locally altered by the presence of subsurface defects (e.g., disbonding or delaminations in composites). A comparison of the different images captured before and after loading allows a deformation gradient to be calculated. This deformation gradient can be a sensitive measure for identifying local defects. Overlapping sheared images are produced in the interferometric process. Two overlapped portions of the sheared images combine and interfere to produce a speckle pattern. When an applied stress deforms the specimen, the speckle pattern is slightly modified. A comparison of the two speckle patterns (i.e., stressed and unstressed) produces a fringe pattern which depicts the relative displacement of the area being inspected. Figure 74 shows the basic principles of shearography.

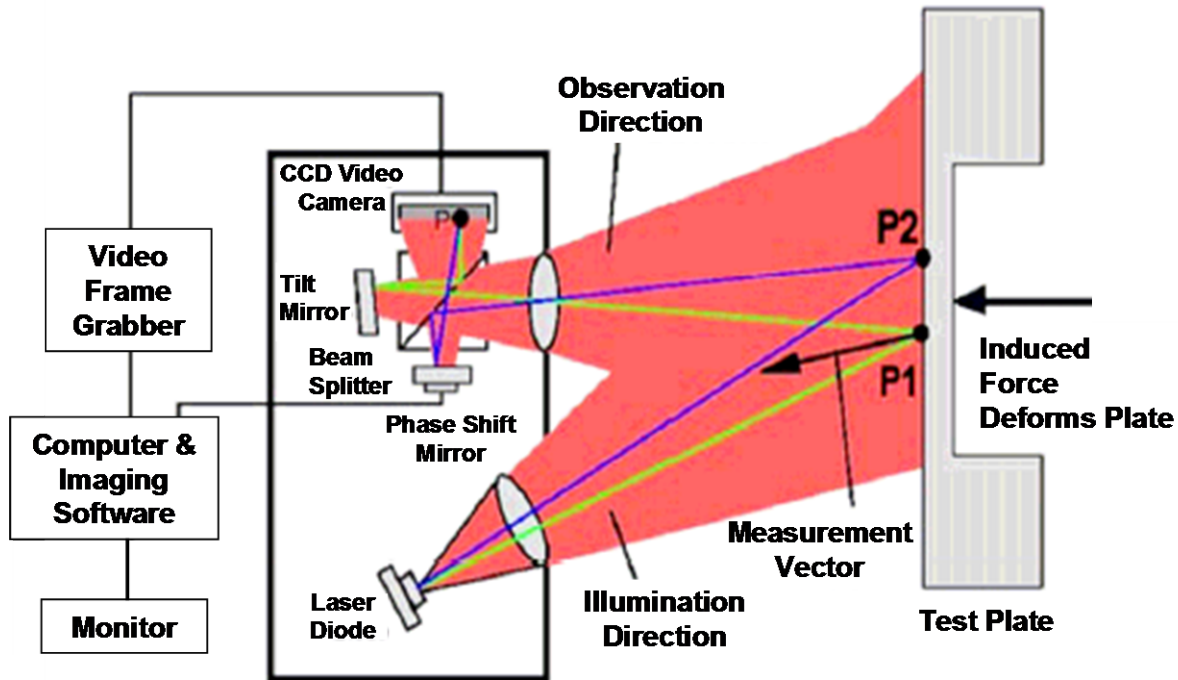


Figure 74. Basic principles of shearography

Shearography inspections can detect anomalies like disbonds, delaminations, voids, separation of structural components, wrinkles, kissing disbonds, impact damage, internal corrosion, crushed core, changes in sections, and core splices [16]. With the use of the CCD camera technique, no photograph laboratory is required. This makes it possible to use shearography for real-time NDT of structures. Laser shearography views only the surface and does not penetrate into the material. As a result, subsurface defects must affect the surface strain field to be detectable.

3.6.1 Laser Technology, Inc. LTI-5200 System

The Laser Technology, Inc.(LTI) LTI-5200 is designed for large-area inspections of bonded metallic or composite structures. Inspection rates of 14 m² per hour and the capability to inspect face sheet, core bond lines (near and far side), core splice joints, and bonded repairs makes this system well-suited for composite applications. The LTI-5200 is a compact, portable vacuum shearography system designed for large-area inspection of aerospace, marine, and rail composite and cored sandwich structures and components. The LTI-5200 vacuum attaches in any orientation. An increasing vacuum level allows imaging and measurement of subsurface defects. Figure 75 shows the LTI-5200 inspecting a composite honeycomb aircraft rudder assembly. Figure 76 shows a schematic of this setup in which detection of both near-side and far-side honeycomb disbonds are possible. Figures 77–79 show samples of shearography images that identify flaws in composite honeycomb panels, whereas figure 80 shows shearography images of a damaged, solid laminate composite structure.

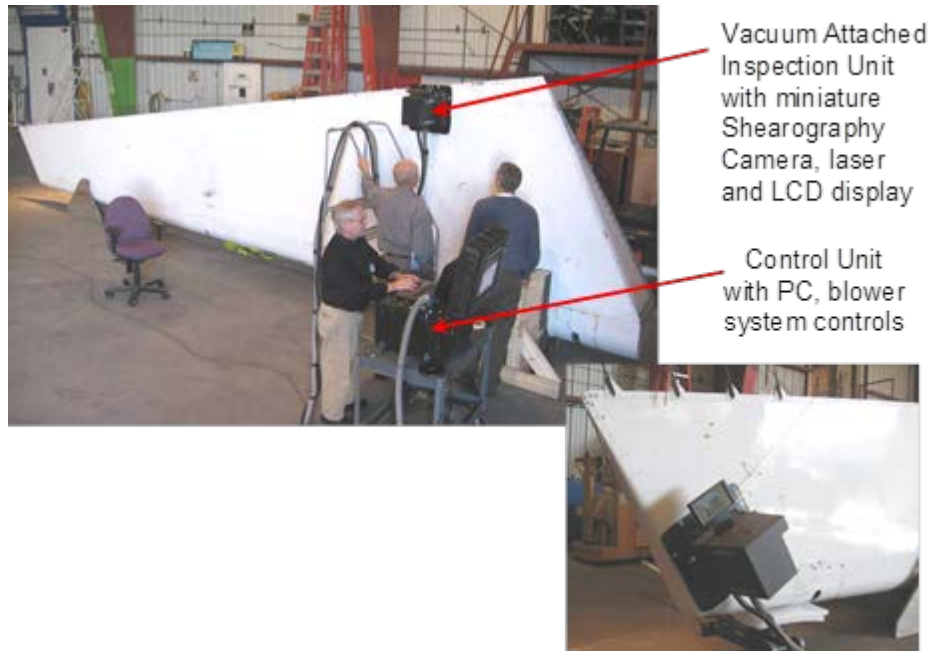


Figure 75. Composite rudder inspection using LTI-5200 portable vacuum shearography system

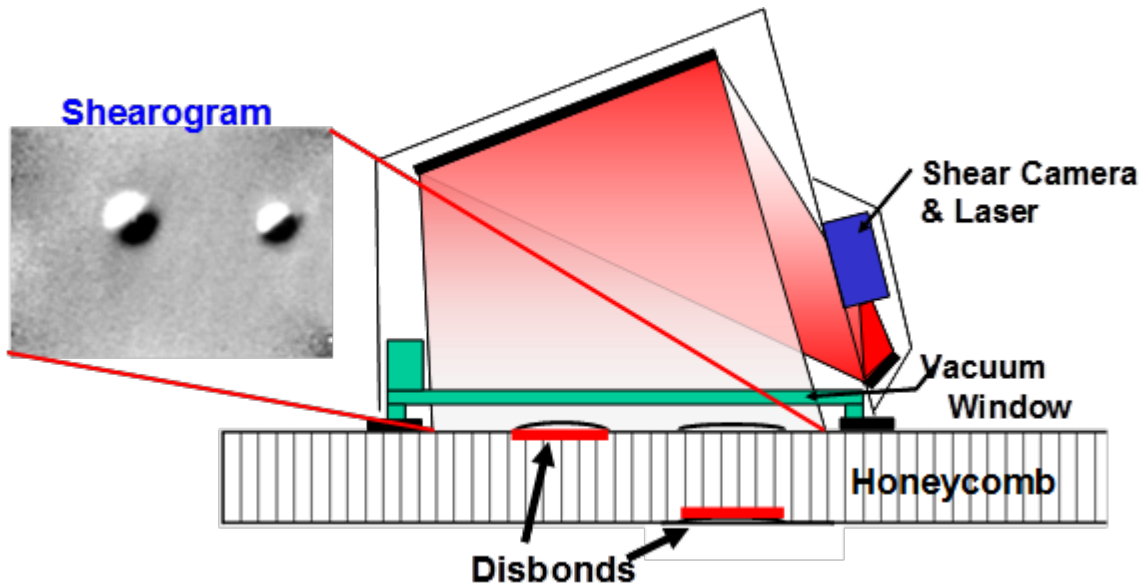


Figure 76. Schematic of shearography inspection for near-side and far-side disbond detection

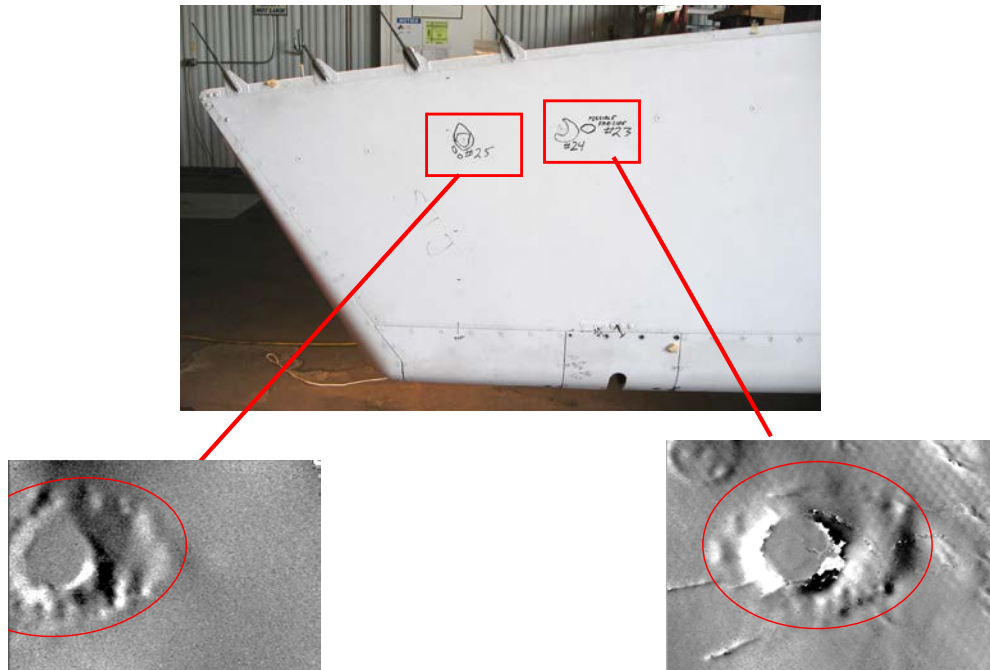
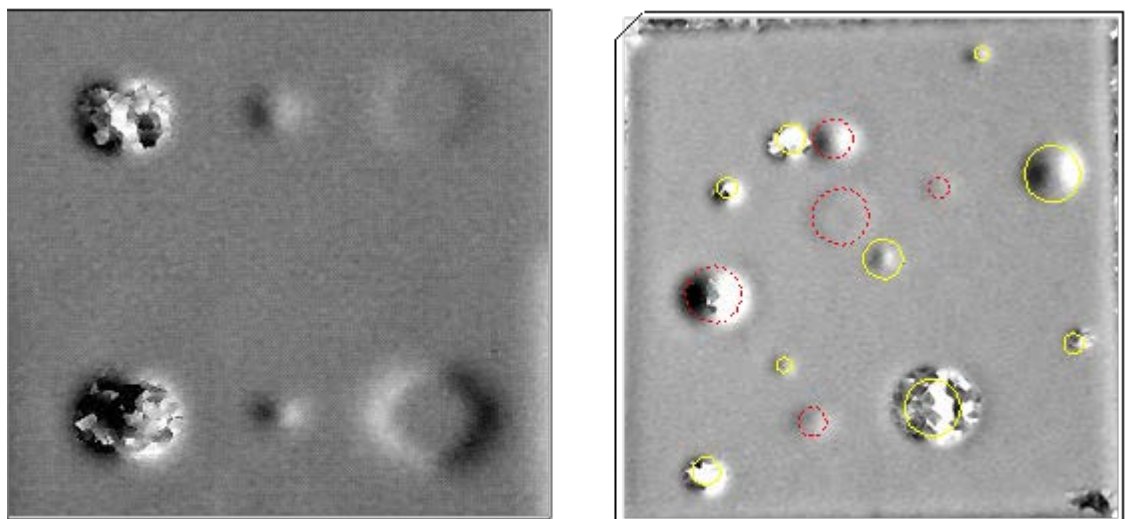


Figure 77. Near-side and far-side disbonds in an A310 composite rudder detected by the LTI-5200 shearography system



**Yellow = Hits (all)
Red Dashed = Backside Detections**

(a)

(b)

Figure 78. Close-up view of LTI-5200 shearography images showing (a) flaws in a composite honeycomb structure and (b) a sample shearography result for a 6-ply fiberglass panel showing near-side and far-side flaw imaging

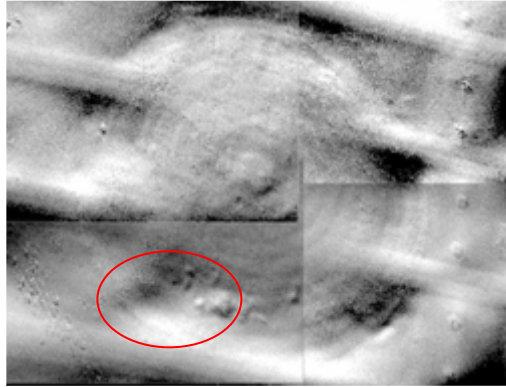


Figure 79. An LTI-5200 shearographic inspection image of a scarfed repair to a honeycomb structure with anomaly indications in the repair plies

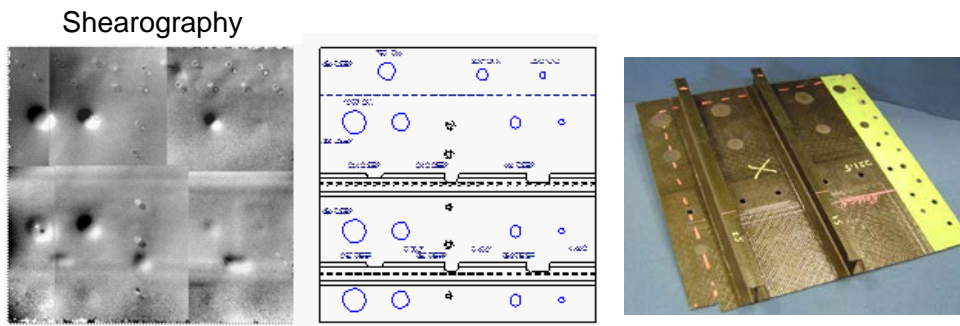


Figure 80. Shearography image produced from inspection of composite laminate panel (0.11" thick skin; the flaw profile is shown in the middle drawing)

3.6.2 Dantec Dynamics Q-810 Laser Shearography System

The Dantec Dynamics Q-810 Laser Shearography System, shown in figure 81, is oriented toward use on composite materials over large surface areas. It can detect defects such as delaminations, disbonds, kissing bonds, wrinkling, impact damage, and crushed core with no surface preparation. The turnkey optical systems are noncontact and full-field and work on such materials as carbon fiber, glass fiber, laminates, honeycomb, foam, metal, and glare. The integrated systems are optimized for large surface area inspections (e.g., on aircraft fuselages, wings, control surfaces, ship hulls, wind turbine blades, and rocket components).



Figure 81. The Q-810 laser shearography system

The full-field inspection rate of the Q-810 Laser Shearography System is approximately 300 mm x 200 mm every 10 seconds. With adaptive seals, the Q-810 can be used on flat surfaces and highly curved surfaces. The system operates independently of the local environmental conditions and can be used for production or in-field inspections. The interferometric technique measures microscopic surface deformations caused by internal flaws when a small load is applied to the object. This can be completed using thermal, pressure, vibration, or mechanical excitation. The results are displayed live as the material responds to the excitation. Further image processing is also available for export and reporting. Figure 82 shows a sample shearography image produced by the Q-810 system inspecting a composite laminate that contains wrinkles.

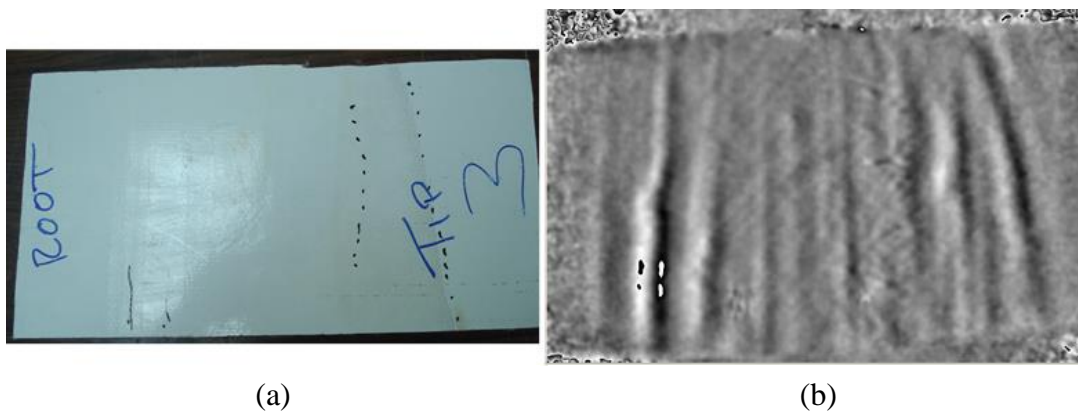


Figure 82. The (a) test specimen and (b) Q-810 shearography image of wrinkles in a composite laminate

3.7 PULSED THERMOGRAPHY

Thermography is an NDI method that uses thermal gradients to analyze the physical characteristics of a structure (e.g., internal defects). In thermography, a thermal gradient is converted into a visible image by using a thermally sensitive detector such as an IR camera [17 and 18]. Flash thermography relies on the heat absorption characteristics of the structure to indicate the presence of defects. In thermographic NDI, part of the IR band of the EM spectrum is used to map the surface temperature of an inspected item. The temperature distribution on a structure can be measured optically by the radiation that it produces at IR wavelengths. Many defects affect the thermal properties of materials (e.g., corrosion, disbonds, cracks, impact damage, panel thinning, and fluid ingress into composite or honeycomb materials). In general, a source of energy is used to create a temperature difference between the specimen and the surrounding environment. Variations in the structure or material properties result in variations in heat flow and surface temperature which are recorded by the IR camera. Figure 83 shows a schematic of a thermographic inspection system and highlights the physics of flaw detection.

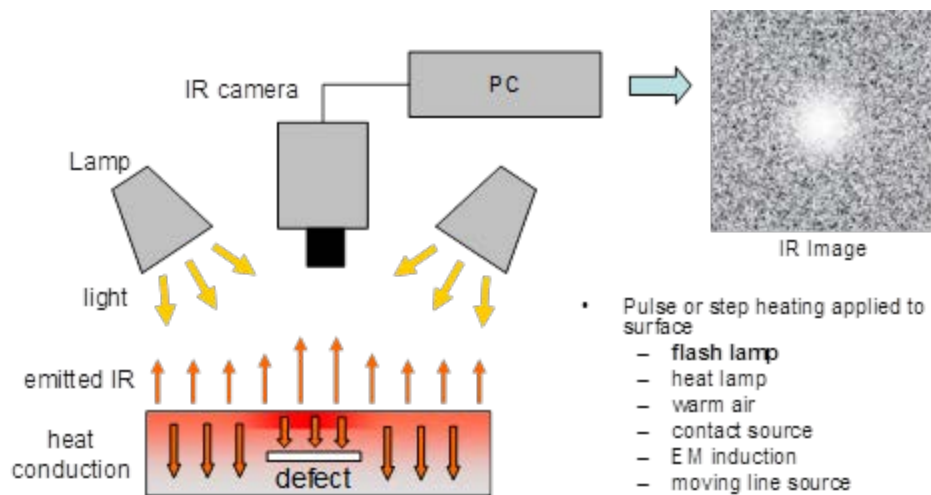


Figure 83. Principle of active pulsed thermography

Thermographic inspection is accomplished using high-power flash lamps or other heat sources, an IR video camera, and image processing hardware and software, all of which are controlled by a PC. A suitable application of external heat sources allows for the detection of common aircraft defects by an appropriate IR survey. The heat source, such as flash lamps, is used to raise the surface temperature of the structure. The subsequent heat transfer into the material is affected by any defects that may be present. The resulting temperature distribution is then recorded by the IR camera and displayed on the computer monitor. As the heat diffuses through the structure, the surface temperature is monitored for a period of time by the IR camera. In practice, the computer actually obtains several images at progressively later times after each flash. Areas that appear hotter than normal may indicate the presence of a delamination or disbond beneath the surface that is preventing heat diffusion into deeper layers. By using a computer to analyze and manipulate the IR data, subtle variations can be enhanced in the image. Typical computer enhancements include analysis of the first and second derivatives of the heat versus time signatures at each point in the time sequence to produce images showing rates of change.

Through the use of temperature versus time images produced by the thermography system, it is possible to determine the depths of disbonds, delaminations, and other flaws in a structure. Typical gantry-based and handheld thermographic inspection systems are shown in figure 84.

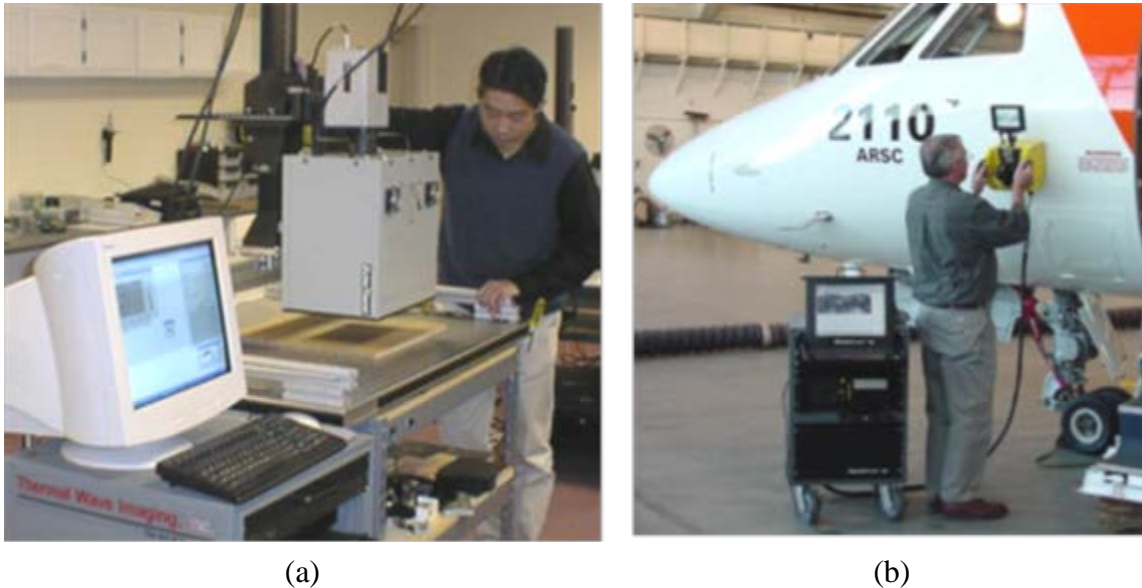


Figure 84. Laboratory (a) Thermal Wave Imaging system inspecting composite flow detection panels and (b) portable field system inspecting an aircraft fuselage

Thermographic inspection procedures on aircraft parts can be used to detect certain local changes in materials that occur in homogenous parts. These may typically be considered (but not exclusively) voids; inclusions; disbonds; fluid ingress or contamination; foreign objects; and damaged or broken structural assemblies. Thermographic inspection can be carried out on almost every type of material used in the construction of an aircraft. The means of excitation, the detection method, and the inspection parameters can be varied depending on the material to be inspected and the flaws to be detected.

The advantages of the thermography inspection method include:

- Can be performed without physical contact with the surface
- Single images can include relatively large areas (1–2 ft²), allowing for rapid inspections of large surface areas
- 2D images of the inspected surface help the operator visualize the location and extent of any defect

The primary disadvantages of thermography are:

- It is often necessary to apply a high-emissivity coating during inspections to obtain an acceptable image; steps have been taken to minimize the labor time associated with this task
- Damage to layers deep within a structure is more difficult to detect than damage in surface layers because the larger mass of material tends to dissipate the applied heat energy

After presenting the thermography principles and equipment, it is worthwhile to discuss some specifics on the critical component: the IR camera. An IR camera is a noncontact device that detects IR energy (i.e., heat) and converts it into an electronic signal, which is then processed to produce a thermal image on a video monitor and perform temperature calculations. Heat detected by an IR camera can be precisely quantified or measured to monitor thermal performance and to identify and evaluate the relative severity of heat-related problems. Recent innovations, such as detector technology, the incorporation of built-in visual imaging, automatic functionality, and IR software development, deliver more cost-effective thermal analysis solutions. A brief comparison of some IR cameras used for thermographic inspection systems is provided in figure 85.

			
	<u>A40</u>	<u>Merlin Mid</u>	<u>Phoenix</u>
Detector Material:	Vanadium Oxide (VOx)	Indium Antimonide (InSb)	Indium Antimonide (InSb)
Detector Cooling:	Uncooled Microbolometer	Integral Stirling or LN2	Integral Stirling or LN2
Spectral Range:	7.5-13 micron	3-5 micron	3-5 micron
Thermal Sensitivity:	0.08° C	0.025 °C	0.025 °C
Focal Plane Array:	320 x 240	320 x 256	640 x 512
Frame Rate:	60 Hz	60 Hz	30 Hz
Weight:	3.1 lbs	9 lbs	Camera: 7 lbs & RTIE: 6 lbs
Size:	8.2" x 4.3" x 3.6"	9.8" x 5.5" x 5.0"	Camera: 7.5" x 4.4" x 5.2"

Figure 85. Comparison of IR cameras for thermography inspection

3.7.1 Thermal Wave Imaging's EchoTherm Thermography Inspection System

In the SLE, a turnkey thermography inspection system, the thermal wave imager, was used to assess the merits of thermography to detect flaws in composite honeycomb construction. Figure 86 shows a photograph of this inspection device and example applications on aircraft. The Thermal Wave Imaging (TWI) ThermoScope and EchoTherm NDI systems are designed for in-service applications and are integrated hardware and software systems for analyzing and

measuring physical properties of materials using pulsed thermography. The system includes TWI's thermographic signal reconstruction processing technique, which increases spatial and temporal resolution of a thermogram sequence.



Figure 86. The TWI system equipment and inspection of an aircraft

Figures 87 and 88 show sample results from thermographic inspections on bonded tear straps and composite honeycomb structures, respectively. Figure 87 shows how a disbond between an aircraft skin and the substructure tear strap affects the thermographic image by changing the heat transfer in that local region. Similarly, the IR image in figure 88 shows the various flaws that were engineered into the honeycomb panel. Figures 89 and 90 contain additional IR images of various flaws in composite honeycomb and composite laminate structures. One of the limitations of thermography is the depth of penetration of the inspection. For composite laminates, the inspection depth limit is approximately 0.2". Only flaws that manifest themselves as variations in the surface temperature of the structure can be readily imaged by the IR camera. Novel heating methods are currently being used to infuse higher levels of heat energy into the structure and improve the detection of deeper flaws.

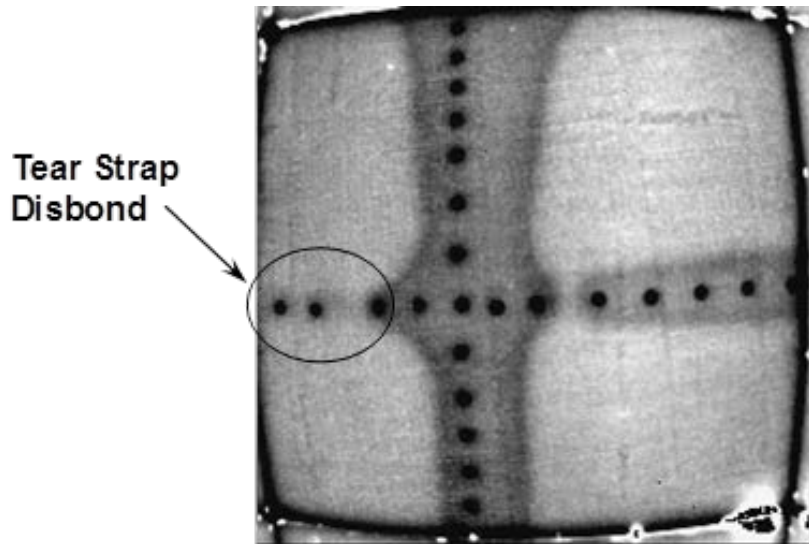
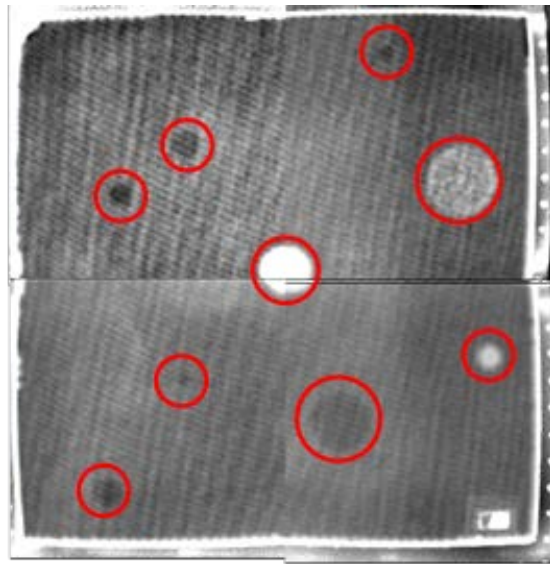


Figure 87. Sample thermography image showing a disbond in an aluminum fuselage-tear strap structure



(a)



(b)

Figure 88. A (a) Flir A40 uncooled camera inspecting the honeycomb test panels and a (b) sample IR image from a fiberglass panel

Pulsed Thermography

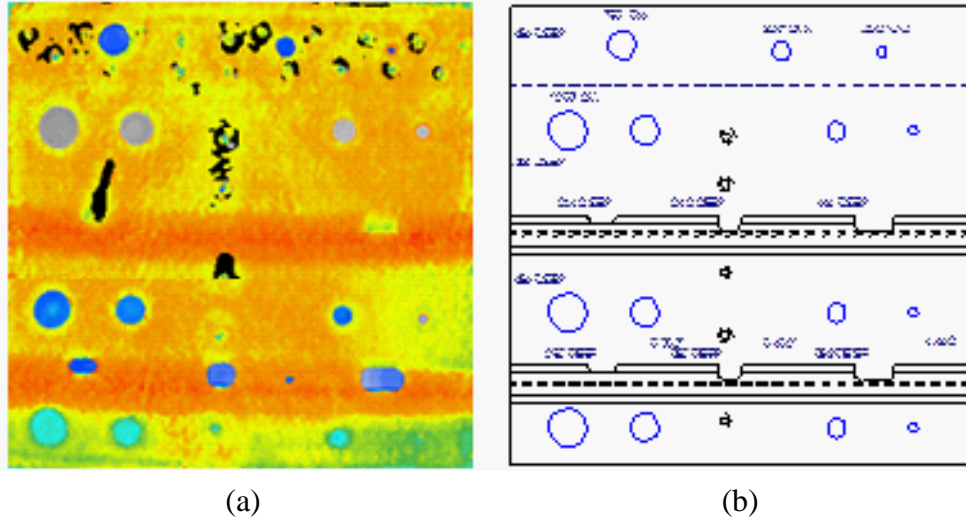
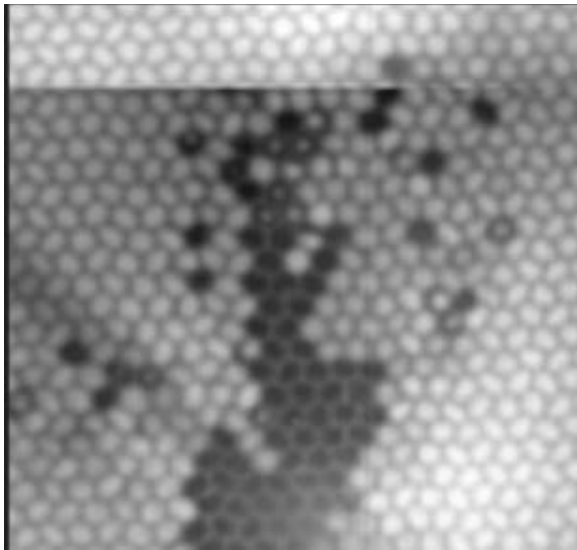
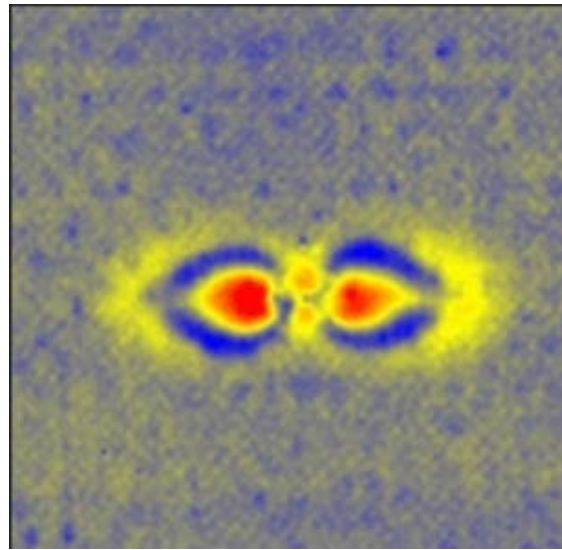


Figure 89. A (a) thermography image produced from inspection of composite laminate panel with flaw profile and (b) a drawing of the flaw profile



Water Ingress in a Composite Honeycomb Structure



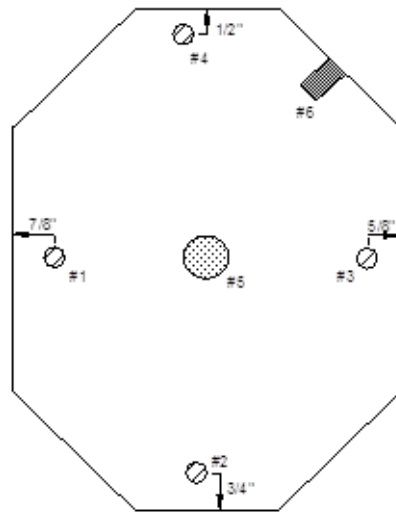
Impact Damage in a Solid Laminate Composite Structure

Figure 90. Sample thermography images showing damage in composite structures

The TWI system was applied to a bonded, composite doubler repair which was installed on a DC-9 fuselage section in Sandia Labs' AANC hangar. Figure 91 shows a schematic of the 10-ply doubler highlighting the size, shape, and location of the embedded flaws. The resultant sequence of images produced by a TWI inspection is also contained in figure 91. The features seen at early times are defects closest to the outside surface of the patch (note appearance of flaws #1 and #2 in the first few frames). The disbonds, located at the base of the doubler, and the deeper

delaminations appear in the later frames corresponding to their delayed effect on the thermal field. All six embedded flaws were identified in the TWI images and flaws smaller than 0.5" in diameter could be detected.

Boron/Epoxy Doubler on the DC-8 Test Bed (AFT section)
 10 Ply Lay-Up with Engineered Flaws
 8" H X 6" W with Ply Orientations of [0,+45,-45,90,0]



○ Delaminations between adjacent plies; teflon insert = 3/8" diameter
 ■ Disbonds between doubler and aluminum skin; pull tab = 3/8" w X 1/2" h
 ● Disbond between doubler and aluminum skin; teflon insert = 1" diameter

Flaw No.	Located Between Plies
1	8 & 9
2	6 & 7
3	3 & 4
4	2 & 3

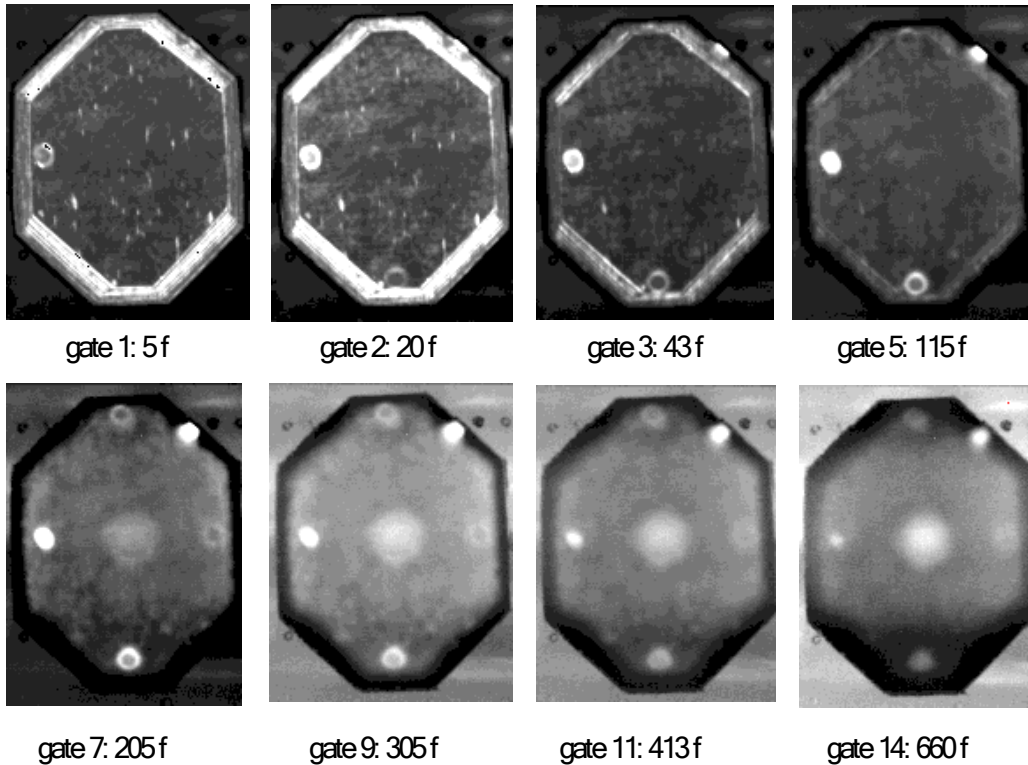


Figure 91. Sequence of thermal wave images from DC-9 composite doubler inspection (frame time [f] = 1/60 of a second)

3.8 LINE SCANNING THERMOGRAPHY

Line Scanning Thermography (LST) is a noncontact inspection method based in dynamic thermography. The LST technique provides a quick and efficient methodology to scan wide areas rapidly; the technique has been used for the inspection of composite propellers, sandwich panels, motor case tubes, and wind turbine blades, among other applications. Figure 92 shows examples of composite structures scanned using the LST technique.

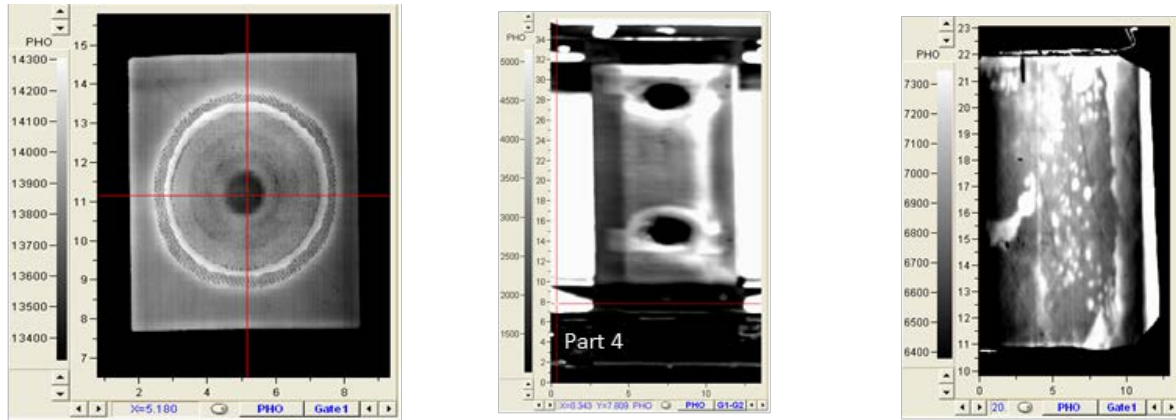


Image of a scarf composite repair in a sandwich composite panel.

Impact damage detection in a composite laminate structure .

Voids inside the adhesive strip presented as hot spots.

Figure 92. Examples of thermal images generated after scanning a composite structure using the LST technique

After heat deposition in a dynamic thermography technique, internal flaws in the material show up by variations in both the surface temperature distribution and the transient surface temperature decay rate. The LST is a dynamic thermography technique patented by the National Aeronautics and Space Administration (NASA) [19 and 20]. This technique deposits heat along a thin line which is swept from edge to edge of the surface under inspection. An IR camera moves in tandem with the heat source at a set speed and captures the thermal profile of the sample after the heat deposition takes place. A diagram of the basic setup is shown in figure 93. The camera's field of view is restricted to an area of the sample surrounding the heat application region. The image on the left of figure 93 shows a side view of the heat source, IR camera, and surface being studied. The image on the right shows the LST thermal image generated by stacking a selected pixel line captured in every frame. During the scan, the temperature of the region swept by the heat source increases, whereas the surface temperature of the region in front of the heat application remains constant. In LST, the scanning speed and heat intensity should be optimized to match the heat diffusion in the inspected material. A thin material with good thermal conductivity will require a fast scanning speed and significant heat deposition. Conversely, a thick material or material with lower thermal conductivity will require a slower scan with reduced heat deposition intensity.

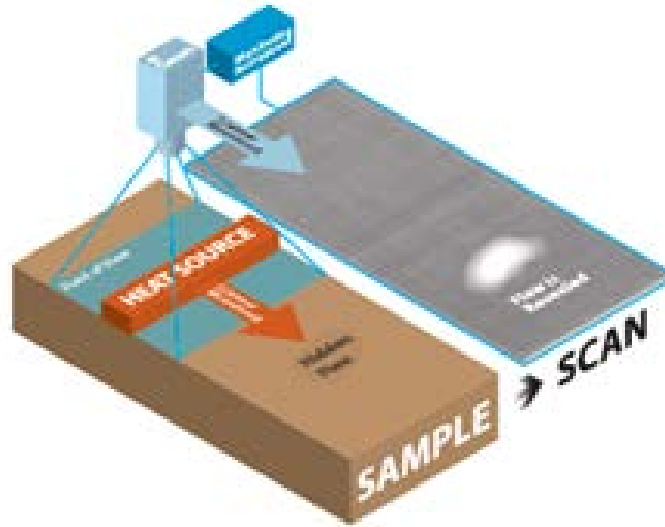


Figure 93. Setup of LST in which IR camera and heat source move in tandem over the surface to be inspected

The LST technique produces a series of images of the entire scanned area. Each image in the series shows the surface temperature distribution at a given time after heat deposition. The images are generated by defining an observation window or a given pixel line from all frames acquired from the camera during the scan. The final image or image of the entire area scanned is formed by stacking the selected pixel line from all the frames captured during the scan. When using images with a sensor resolution of 240 x 320 pixels, a maximum of 240 images of the entire area can be constructed. The time elapsed between consecutive pixel lines depends on the scanning speed and the camera frame rate. Figure 94 shows an example of the images that can be generated using the LST technique following heat deposition. The images show the same scale and were generated using different observation windows. Each image in the series shows the surface temperature distribution of the whole area scanned at a given time after heat deposition; the time is defined by the distance between the heat application, observation gate, and speed at which the scan is set. The LST thermal image is generated by stacking the selected observation line from all frames recorded during the scan. The panel on the right in figure 94 shows a collection of LST thermal images generated from different observation gates. The images show the same scale and represent how the surface temperature drops after heat deposition.

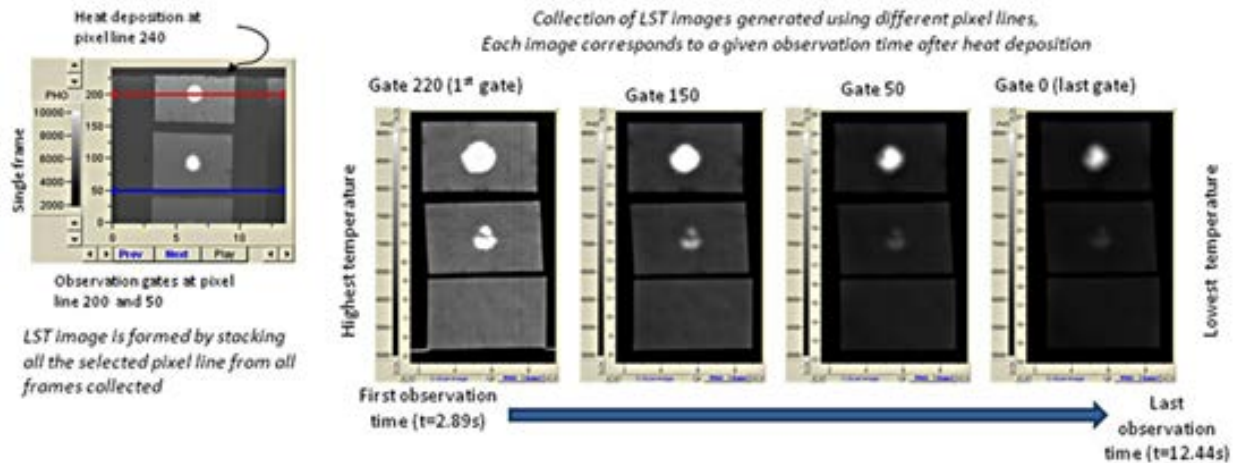


Figure 94. Panel showing the observation gate selection with respect to the heat deposition location

The observation of a defect using LST requires proper optimization of the scanning parameters (i.e., scan velocity and heat deposition intensity), which determine the section of the cooling curve that will be observed. The amount of heat deposited over the surface should be sufficient to produce a thermal gradient between the defect and the sound area. In particular, when scanning thin materials displaying good thermal conductivities, the scanning speed should be set higher than the speed used on materials that have lower thermal diffusivities. Scanning at high speeds allows for the observation of earlier times after heat deposition, whereas scanning at lower speeds allows for images corresponding to latter observation times.

3.8.1 MISTRAS Line Scan Thermography Inspection System

Figures 95 and 96 show the MISTRAS Line Scan Thermography scanner used for scanning composites. The LST technique requires that the camera move in sync with the lamp used for depositing the heat over the surface of interest. The movement is controlled using a motor. These components have been organized in different ways depending on the structure to be scanned and the size of the area of interest. MISTRAS has fabricated three different systems for inspecting different structures. The first is a gantry-type system capable of performing vertical scans of up to 1.5 m long and 40.64 cm wide. The system uses a cooled IR camera working in the mid-wave IR range (3–5 micrometers). The lamp used in the system corresponds with a quartz lamp 40.6 cm long. The second LST system is a small area scanner that has a 30.5 cm x 81.2 cm scan area and uses suction cups to attach to the surface of interest. It uses a microbolometer working in the 8–12 micrometer range. The third MISTRAS LST system is a motorized crawler designed to scan flat areas. This scanner uses a 4–6 cm wide field of view and can cover scan lengths of up to 12 m in a single scan. It can hold a cooled camera or a microbolometer. The crawler can be easily modified to scan composite structures of different thickness (e.g., fiberglass wind turbine blades) for which it is necessary to wait a significant amount of time for observation after the heat deposition. The modification is achieved by adding a train which increases the separation between the observation area and the heat deposition location.



Figure 95. MISTRAS Line Scan Thermography System crawler used on composites



Figure 96. MISTRAS Line Scan Thermography System small area scanner

Figure 97 shows some sample inspection results from the MISTRAS Line Scan Thermography system applied to a 32-ply (0.23" thick skin) solid laminate composite panel with a 58-ply (0.192" thick) upper stringer and 50-ply (0.125" thick) lower stringer. Most of the flaws are detected in the LST image, with the deeper flaws presenting the biggest challenge to LST detection.

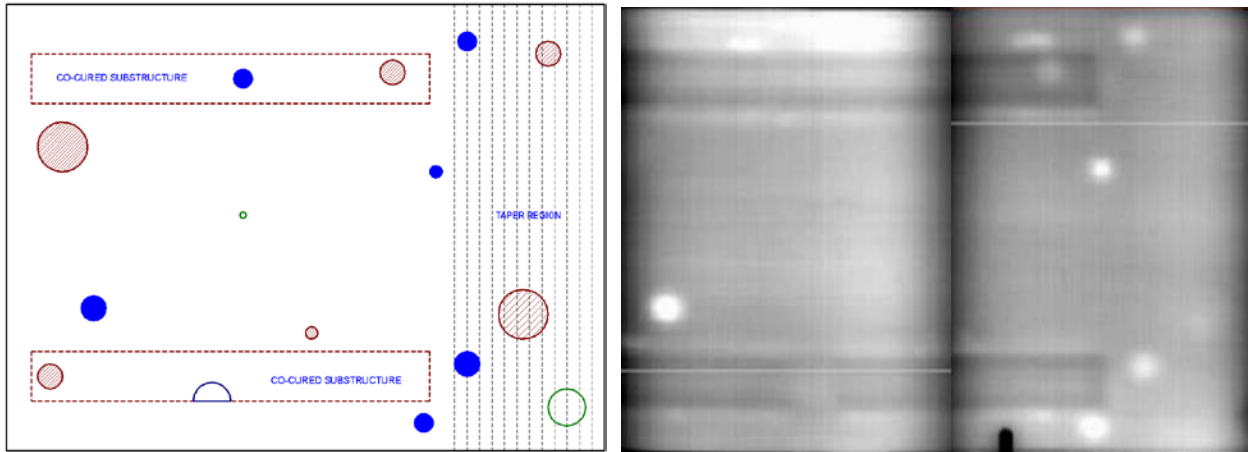


Figure 97. Results produced by the MISTRAS Line Scan Thermography System on a 32-ply panel with substructure elements

3.9 LOCK-IN THERMOGRAPHY

The principle of lock-in thermography is based on the application of a periodic input energy wave (i.e., thermal emitter, UT, MW, eddy current, flash lamp) to the surface of the object being inspected and an examination of the resulting local temperatures on the surface of the object [21]. The wave generated by the input energy is absorbed and the phase angle is shifted when the wave penetrates the object's surface. When the input wave reaches internal areas of the object where a delamination or inclusion is present, the thermophysical properties are not homogeneous in relation to the surrounding material and the input wave is partially reflected. The reflected portion of the wave interferes with the incoming input wave at the surface of the object and causes an interference pattern in the local surface temperature. In turn, the local surface temperature oscillates at the same frequency as the thermal wave. The internal structure of the object can then be derived by evaluating the phase shift of the local surface temperatures in relation to the input energy wave. However, the ability to derive internal thermophysical inconsistencies within the object requires that the input energy source be used at an optimal frequency. The optimal frequency is dependent on both the thermophysical characteristics of the object and its thickness. A schematic of the typical equipment setup for lock-in thermography is shown in figure 98. The dynamic stimulus can be applied from a wide variety of sources when using lock-in thermography. For composite inspection, this includes halogen lamps, UT, and mechanical stimulation.

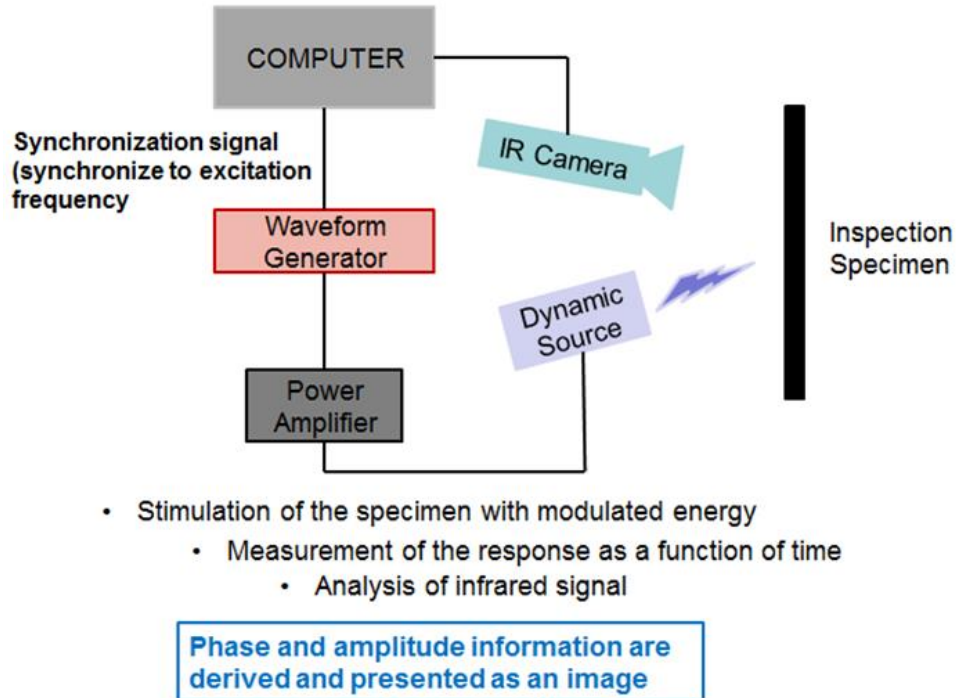


Figure 98. Equipment setup used for typical lock-in thermography inspection

For lock-in thermography, the recorded temperature information gathered by the IR camera is transformed into the frequency domain. The measured temporal evolution in each pixel of the temperature is Fourier-transformed for all images of the recorded sequence. Phase and amplitude information are derived and presented as an image [21].

Advantages of the lock-in thermography method include:

- Summation results in noise filtering, which enhances the contrast in inspection results
- Depth range for phase information is twice that of pulse thermography mode
- Lock-in allows detection of thermal waves with a sensitivity of 100–1000 times greater than the best thermal camera—down to the μ -Kelvin range
- The phase image is insensitive to external effects such as sunlight, reflections depending on surface finish, dirt, and emissivity differences—problems common to conventional thermography
- The phase information is insensitive to uneven distribution of the applied heat
- Large areas can be examined within a few minutes and from a distance through noncontact measurement
- A less costly, uncooled IR camera is normally sufficient
- Affordable heat sources are widely available (e.g., halogen lamps, the most common excitation source for lock-in thermography)
- Visualization of deep defects is possible

3.9.1 MoviTHERM Lock-In Thermography System

Figure 99 shows the MoviTHERM lock-in thermography equipment featuring a FLIR SR2 SC7650 camera with a Hedler 2500-watt lamp. Lock-in thermography can be used to detect damage such as delamination, inclusions, and impact in composite structures. Figure 100 shows inspection results from a 32-ply (0.23" thick skin) solid laminate composite panel with a 58-ply (0.192" thick) upper stringer and 50-ply (0.125" thick) lower stringer. The engineered flaw profile is also shown on the left for comparison. An important excitation source used in lock-in thermography is UT. Typical settings for this method are 100 W at 20 KHz, with a 200 millisecond burst frequency for synchronization. A disadvantage of the UT technique is that it can be destructive and care is required during excitation of the part. A powerful tool for laboratory and factory measurements is mechanical excitation for heat generation through the thermoelastic effect. Applications of this technique include measurement of fatigue limits, imaging of stress patterns, crack propagation studies, and imaging of vibration patterns.



Figure 99. MoviTHERM lock-in thermography with halogen heat lamp being used as the excitation source

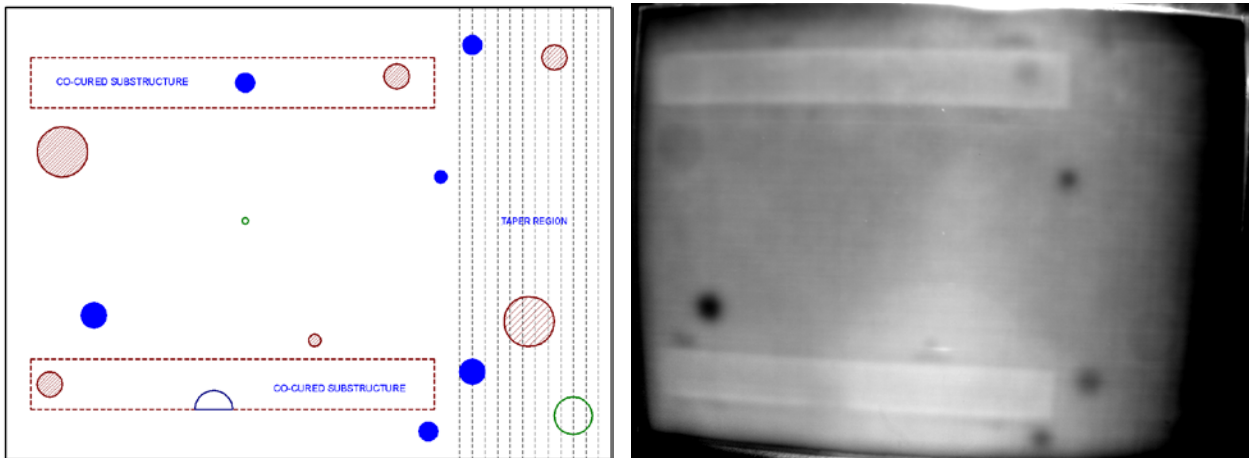


Figure 100. Results produced by lock-in thermography on a 32-ply panel with substructure elements

4. COMPOSITE SLE DESIGN

The FAA requested that the AANC conduct this experiment to make an overall assessment of flaw detection in composite laminate aircraft structures. The composite SLE includes a set of 15 composite laminate test specimens (see figure 101) that contain engineered flaws (e.g., disbonds,

interply delaminations, and impact damage). Five NDI feedback specimens were also produced. These feedback specimens contained all of the same construction and flaw types as those found in the blind POD test specimens. The flaw profiles in the NDI feedback specimens were provided to each inspector to allow them to become comfortable with the inspection demands before moving on to the blind POD specimens. Figure 1, shown at the beginning of this report, depicts the inspection surfaces on the set of painted specimens, whereas figure 101 shows the back side and unpainted surfaces of the same specimen set. The Sandia researchers traveled to airlines and third-party maintenance depots to acquire flaw detection data provided by qualified aviation inspectors. The experiment required approximately 2–3 days of each inspector’s time. In general, inspectors were asked to locate and size hidden flaws in the test specimens. The test program was intended to evaluate the technical capability of the inspector, the inspection procedures, and the equipment (NDI method). The inspections emphasized flaw detection methods applicable to solid laminate structures from 12–64 plies thick.



Figure 101. Subset of the 15 solid laminate test specimens and five NDI feedback specimens

The primary goals of this experiment were to:

- provide additional information on laminate inspections for the “Composite Repair NDT/NDI Handbook” (ARP 5089)/other AANC/FAA/CACRC composite inspection NDI training initiatives.
- optimize composite laminate inspection procedures.
- determine in-service flaw detection capabilities of conventional NDI methods.
- measure the potential for flaw detection improvements through the application of advanced NDI methods and equipment.
- compare results from handheld devices with results from scanning systems (focus on A-scan vs. C-scan and human factor issues in large-area coverage).

The latter two goals were achieved through the extension of this study to NDI equipment/method developers and the application of advanced NDI techniques to this experiment. Results from this testing will quantify the degree of improvements possible through the integration of more advanced NDI techniques and improved procedures. This report includes the results from the application of advanced inspection methods. A previous report presents the results from the conventional NDI testing [22].

This experiment used a series of solid laminate composite specimens with statistically relevant flaw profiles to evaluate flaw detection using PE-UT and other NDI methods. These tests were conducted using NDI equipment the inspectors had experience using for this type of inspection. The experiment focused on understanding the factors influencing the performance of NDI methods (e.g., device and inspector) when applied to the inspection of solid laminate composites. Some portions of the testing were blind POD studies, whereas others determined S/N ratios from which flaw detection could be inferred. The experiment results evaluated inspection performance attributes including accuracy and sensitivity, (e.g., flaw hits, misses, false calls, flaw sizing) and usability features (e.g., versatility, portability, complexity, inspection time).

The primary factors affecting NDI included in this study were composite materials, flaw profiles, geometry of structure, thickness of structure, presence of substructure elements, ply drop-off (taper), presence of bond lines, presence of fasteners, sealed joints, skin over honeycomb substructure, and inspection environment conditions. This phase of the study utilized airline personnel to study PE-UT inspections with a POD experiment in the field to formulate improvements in this critical inspection method.

4.1 EXPERIMENT DESIGN GUIDELINES

The experiment design criteria were as follows:

- Conventional and advanced inspection techniques are being assessed.
- Carbon plies were used for all parts (e.g., carbon pre-preg, uniaxial tape). Some pre-cured carbon stringers were secondarily bonded and some stringers were co-cured.
- Use multiple stringers and create bays that have 2D ply taper.
- Cure specimens as per normal manufacturer temperature-time cure profile. Laminates are cured at 85 psi. Secondary bonds are produced at vacuum bag pressure only.
- Purpose of the honeycomb portion of specimens is to ascertain difficulties in recognizing the back wall echo in the presence of resin pools around the honeycomb edges.
- Inspection surface will be a painted, production tool surface as per normal part manufacture.
- General OEM laminate inspection procedures are provided as guidance for inspectors.
- Specimen drawings, similar to those found in OEM manuals, are provided to inspectors to aid in interpretation of PE-UT signals.
- Test specimen designs include the variables that were deemed to be the most important because they have the greatest effect on NDI [22].
- Include approximately 200 flaws with sufficient unflawed regions to allow for assessment of false calls.
- For the most part, maintain a minimum of 2" separation between flaws to eliminate signal cross-talk; include a few flaw pairs that are closely clustered to study the ability to define boundaries of flaws.
- For the most part, maintain a minimum of 0.50" distance from flaws to edge of panels; include a few instances of flaws close to edge to study flaw detection near a natural edge.
- The final test specimen matrix is shown in Table 1 and includes the different design variables integrated into each specimen. The specimen set consists of three bullnose (BN) specimens (BN1, BN2, and BN3), four complex taper (CT) specimens (CT1-A, CT1-B, CT2-A, and CT2-B), and eight simple taper (ST) specimens (ST1U-A, ST1L-A, ST2U-A, ST2L-A, ST32-1, ST32-2, ST32-3, and ST32-4)—for a total of 15 POD specimens

Table 1. Test specimen matrix with design variables for solid composite laminate flaw detection experiment

Engineered Specimens (Design Variables)					
Test Specimen	Design Variable 1	Design Variable 2	Design Variable 3	Design Variable 4	Design Variable 5
BN1	12 plies over Honeycomb	24 plies over substructure	24 plies over radius	38-ply spar	N/A
BN2	12 plies over Honeycomb	24 plies over substructure	24 plies over radius	38-ply spar	N/A
BN3	12 plies over Honeycomb	24 plies over substructure	24 plies over radius	38-ply spar	N/A
CT1-A & CT1-B	12 plies	20 plies	12- to 20-ply taper (.50" step)	12- to 20-ply taper (.25" step)	N/A
CT2-A & CT2-B	12 plies	20 plies	12- to 20-ply taper (.50" step)	12- to 20-ply taper (.25" step)	N/A
ST 1 Upper (ST1U-A)	12 plies	20 plies	12- to 20-ply taper (.50" step)	12 plies w/substructure	20 plies w/substructure
ST 1 Lower (ST1L-A)	12 plies	20 plies	12- to 20-ply taper (.50" step)	12 plies w/substructure	20 plies w/substructure
ST 2 Upper (ST2U-A)	12 plies	20 plies	12- to 20-ply taper (.50" step)	12 plies w/substructure	20 plies w/substructure
ST 2 Lower (ST2L-A)	12 plies	20 plies	12- to 20-ply taper (.50" step)	12 plies w/substructure	20 plies w/substructure
ST New 32 (ST32-1–ST32-4)	32 plies	20- to 32-ply taper (.50" step)	32 plies w/substructure	N/A	N/A

Figure 102 shows the POD study breakdown in results in which the overall goal is to determine POD level for composite laminate structures in general. This is an all-inclusive POD result determined from all of the inspection results from a specific inspection technique (e.g., PE-UT). The next POD levels are results from the 12–20 ply laminates and the 20–32 ply laminates for a specific inspection method. This will also produce individual POD results for each inspector, which can then be used in a comparison to look at the variance within a specific inspection method.

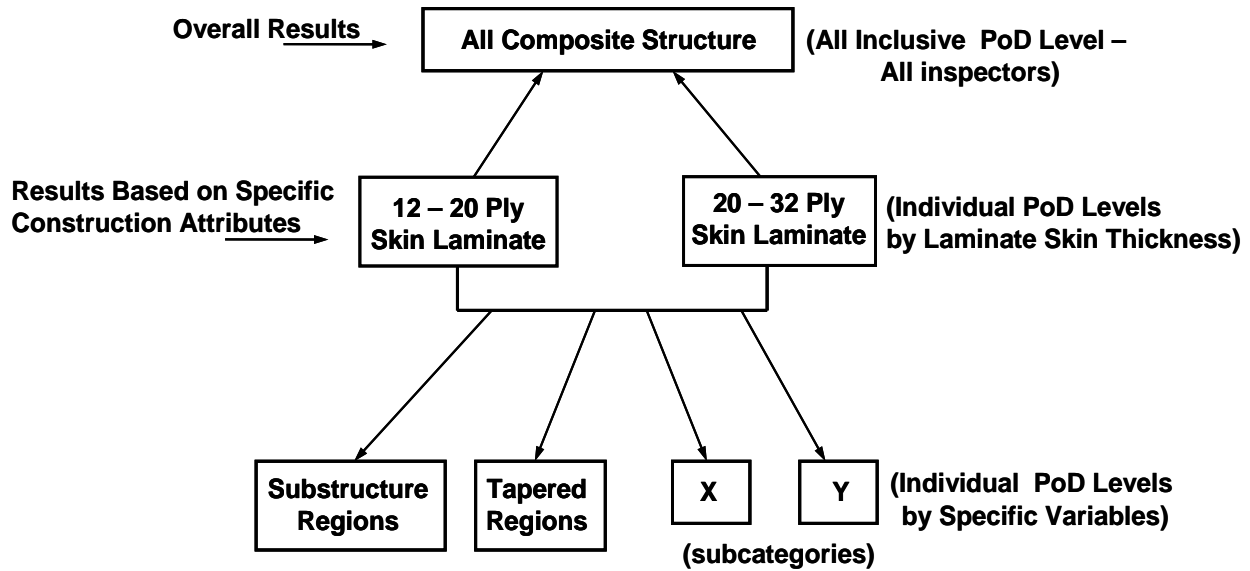


Figure 102. The POD study breakdown to produce separate POD values related to specific inspection variables

Note that the specimens have several discrete laminate thicknesses, substructures, and taper regions. Other isolated POD information to be derived from this study includes flaw detection performance in selected areas such as substructure regions or tapered areas. These results can then be compared to inspection results from other categories (e.g., constant thickness regions) to pinpoint the greatest challenges associated with composite NDI.

All of the important variables are represented but cannot be individually uncoupled. As a result, it was desirable to distribute the construction variables (thickness, taper, honeycomb, fastened regions, secondarily bonded regions, geometry) and flaws (size, depth) to represent the distribution and impediments found in aircraft structure. A summary of the primary experiment design considerations follows:

- The overall SLE can be broken down into two separate experiments. There is a thin laminate skin experiment with skins ranging from 12–20 plies (0.078”–0.130” thick) and total thickness extending to 62 plies (0.406”) when substructure is considered. There is also a thick laminate skin experiment with 32-ply skins (0.21” thick) and total thickness extending to 58 plies (0.377”) when substructure is considered.
- Surface area and number of flaws (i.e., number of specimens) versus time for inspector to complete the tests using handheld probes. The goal was to produce experiments that could be completed in 2–3 days for the 12–20 ply thin laminate skin experiment (11 specimens) and in 1–2 days for the 20–32 ply thick laminate skin experiment (four specimens).
- Disbonds were included between the laminate skin and substructure elements and delaminations were placed in both the laminate skin and the substructure (stringers). Some premanufactured stringers were used; flat bottom holes were the only means of

simulating delamination flaws in those stringers. Inserts were used for adding delamination flaws for specimens in which the substructure was co-cured with the skin.

- Boeing provided laminate inspection procedures for the B777 and Airbus provided laminate inspection procedures for the A300. Both procedures were placed in the experiment protocols for inspector use.

4.2 SPECIMEN DESIGN AND EXPERIMENT IMPLEMENTATION APPROACH

To implement a realistic experiment, it was necessary to design representative specimens that included a full spectrum of variables found on composite aircraft structures. This included the different construction scenarios such as various ply thicknesses, different substructure thicknesses, bonding methods for substructure (co-cured and secondarily bonded), and geometry issues (taper/ply drop-offs) that can make inspections difficult. Another important factor in the specimen design was to determine the most prevalent flaw types found on this type of structure and to develop methods to engineer representative flaws. This included determining the various flaw sizes required for the statistical analysis.

Though the size of the flaw or damage that must be detected is affected by many parameters (e.g., structure type, location on aircraft, and stress and fatigue levels), the general goal for composite inspections is to detect flaws that are 1" in diameter or larger. Many of the NDI reference standards in OEM NDT manuals use 1" diameter flaws to guide equipment setup. In addition, the CACRC-ITG members generally concede that 1" flaw detection provides a good center point for this SLE. Therefore, the flaw sizes in the SLE design were established with 1" diameter at the center. Larger and smaller flaws were included so that POD values smaller than 1" (as small as 0.25") and POD values larger than 1" (as large as 2") could be ascertained.

Specimen and flaw types used in the SLE experiment included:

- Interply delaminations – “Tight” and “loose” delaminations in which Grafoil inserts simulated tight interply contact (i.e., kissing delaminations) and pillow inserts simulated loose interply contact (i.e., thin slide of entrapped air)
- Flat bottom hole – Larger delaminations that simulate the presence of air gaps
- Pillow insert disbonds at substructure interfaces simulating tight contact but no adhesive strength (i.e., kissing disbonds)
- Pull tab disbonds simulating the presence of a variable air gap between the laminate and bonded substructure
- Subsurface impact damage with no surface demarcations. This was simulated with tapered flat bottom holes with stair-step sides. Figure 103 compares normal impact damage morphology with the simulated version

- Flaw Sizing – Normal procedures and standards focus on flaw detection for 1" diameter flaws and larger. However, this study also assessed performance for flaws as small as 0.25" in diameter. Inspectors were told to use any "positive indications to find flaws as small as 0.25" in diameter." The flaw sizes used in this study were 0.25", 0.5", 0.75", 1", 1.5" and 2" in diameter
- Flaw Depth – Close-to-front and close-to-back surfaces are hardest to detect flaws. Some flaws along the midline are included. Locate the flaws in constant thickness and in transition, tapered regions.
- Laminate Type – Carbon graphite, uniaxial tape
- Laminate Thickness – Panels have 12- (~.078"), 20- (~.130"), 24- (~.156"), and 32- (~.229") ply laminate skins, which include both constant thickness and tapered regions. Ply steps in taper areas are 0.25" step per ply (12–20 ply specimens) and 0.5" step per ply (12–20 and 20–32 ply specimens). The substructure elements included in the test specimens had thicknesses of 0.075", 0.125", 0.192", 0.225", and 0.250"
- Test Specimen Size – Some specimens were large enough to highlight a need for scanners. Some specimens were small and complex enough to make scanning difficult or unnecessary (see appendix D "Summary of SLE Test Specimens")
- Test Specimen Geometry – Included flat surfaces, angled surfaces, and curved surfaces. Specimens had complex geometry (CG) on the inside (e.g., substructure, taper, fasteners, etc.) and smooth surfaces on the outside

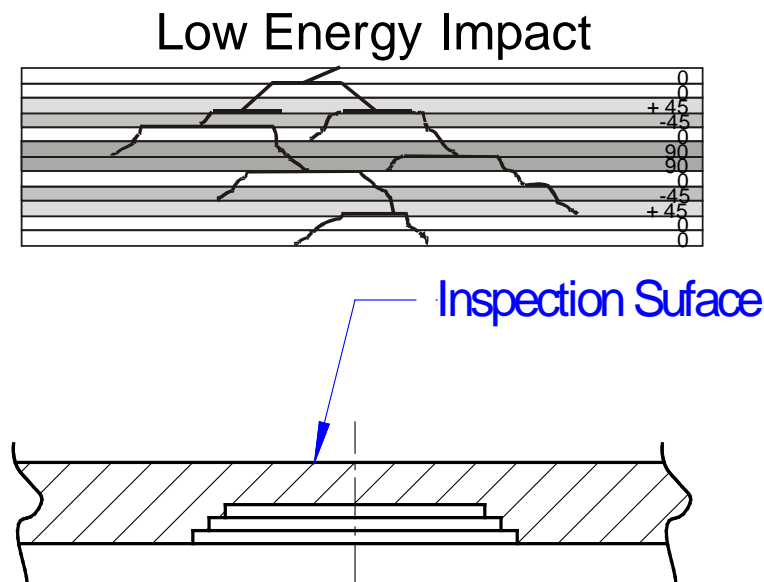


Figure 103. Simulated impact damage (laminates cross-section)

The application of NDI was as follows:

- NDI Feedback Specimens, with known flaw profiles, were inspected first to allow the inspectors to become comfortable with the inspection demands of the experiment.
- The PE-UT inspection technique was applied in a blind mode to the set of POD specimens to study hits, misses, false calls, and flaw sizing. Experimenter information packets and face-to-face briefings were provided to produce some procedural guidance and ensure uniformity of results.
- The experiment investigated the full range of human factor issues including inspection coverage methods and effects of the inspection environment.
- Test specimen characterization was conducted with knowledge of flaw locations to determine quantitative S/N ratios. The ability to achieve successful flaw detection was then inferred by studying S/N levels at various threshold levels.
- A valid cumulative POD curve for an inspection device requires results from a minimum of 10 inspectors using that device or inspection method. Two NDI categories were considered in the SLE: conventional (results provided in this report) and advanced NDI (results to be provided in a separate, forthcoming report). It should be noted that to break down some of the important inspection variables (e.g., flaw detection in the presence of CG), more than 10 inspectors were required for a single inspection device.
- For the most part, the inspectors used their own NDI equipment. Experiment monitors allowed access to acceptable inspection devices for testing (i.e., equipment which met Boeing and Airbus specifications), and the inspectors made the final choice based on availability and familiarity with that equipment. Some testing with nonstandard devices was conducted (e.g., Ramp Damage Check Experiment [RDCE]) to form a basis of comparison with results obtained using conventional PE-UT devices.
- Equipment and experiment familiarization was achieved through the use of NDI feedback specimens or solid laminate training specimens. The feedback specimens were representative of the test specimens that were tested in blind mode. Figures 104–109 contain engineering drawings and sample photographs of the set of five NDI feedback specimens. These specimens, along with the flaw location drawings, were sent out in advance of the experiment to allow the inspectors to learn about NDI equipment responses. Experiment monitors also provide one-on-one briefings (see appendices A and B) to aid the proper deployment of the equipment prior to beginning the blind flaw detection tests.
- An “SLE Experimenter Information Packet” (appendix A) and “SLE Experimenter Briefing Packet” (appendix B) were provided to every participant. Face-to-face airline briefing sessions were completed at each site prior to beginning the NDI tests. To ensure maximum uniformity in information provided to participants, all team members who

were experiment monitors attended one of the airline briefing sessions provided by the AANC.

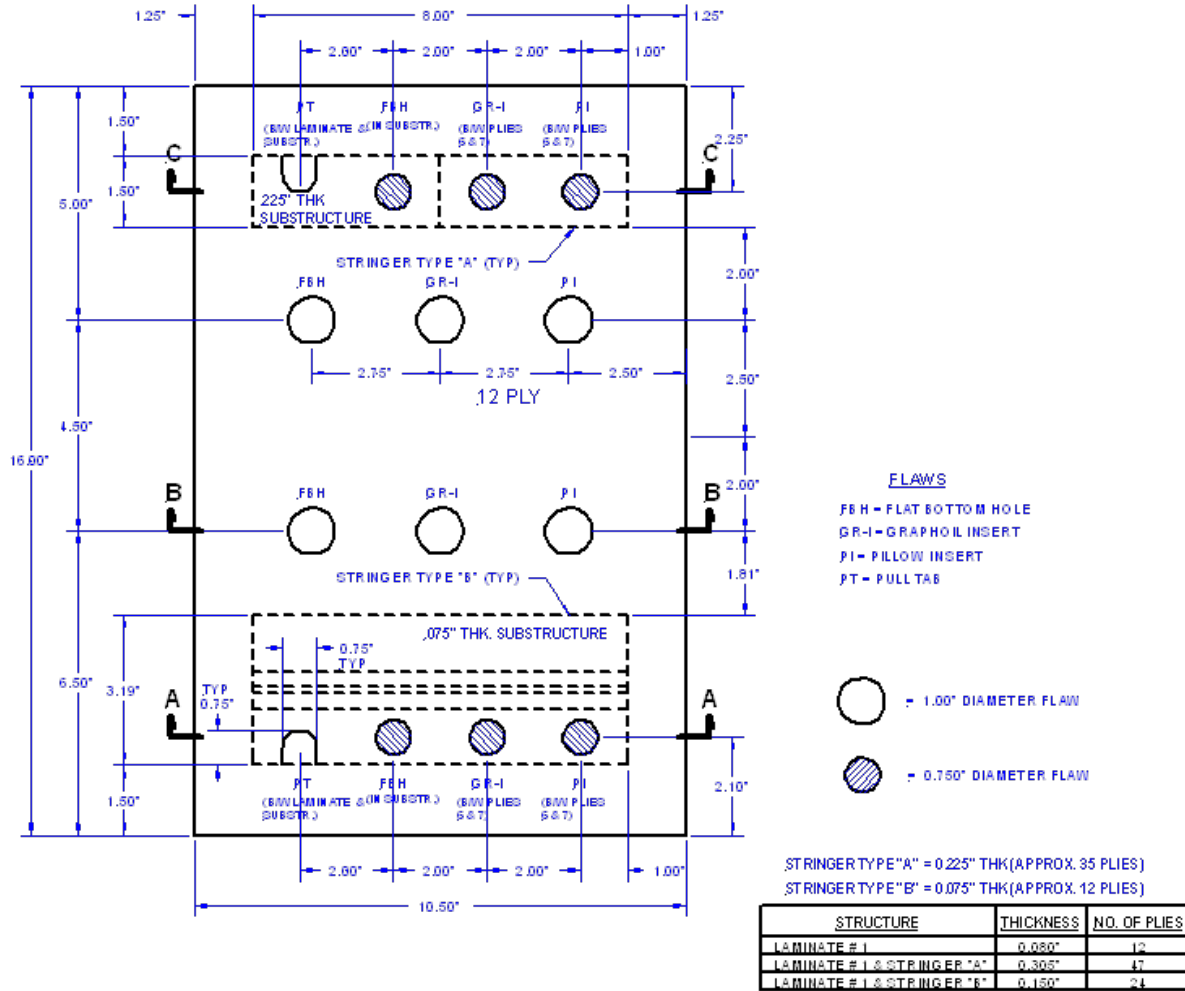


Figure 104. Final design of the 12-ply training/feedback specimen

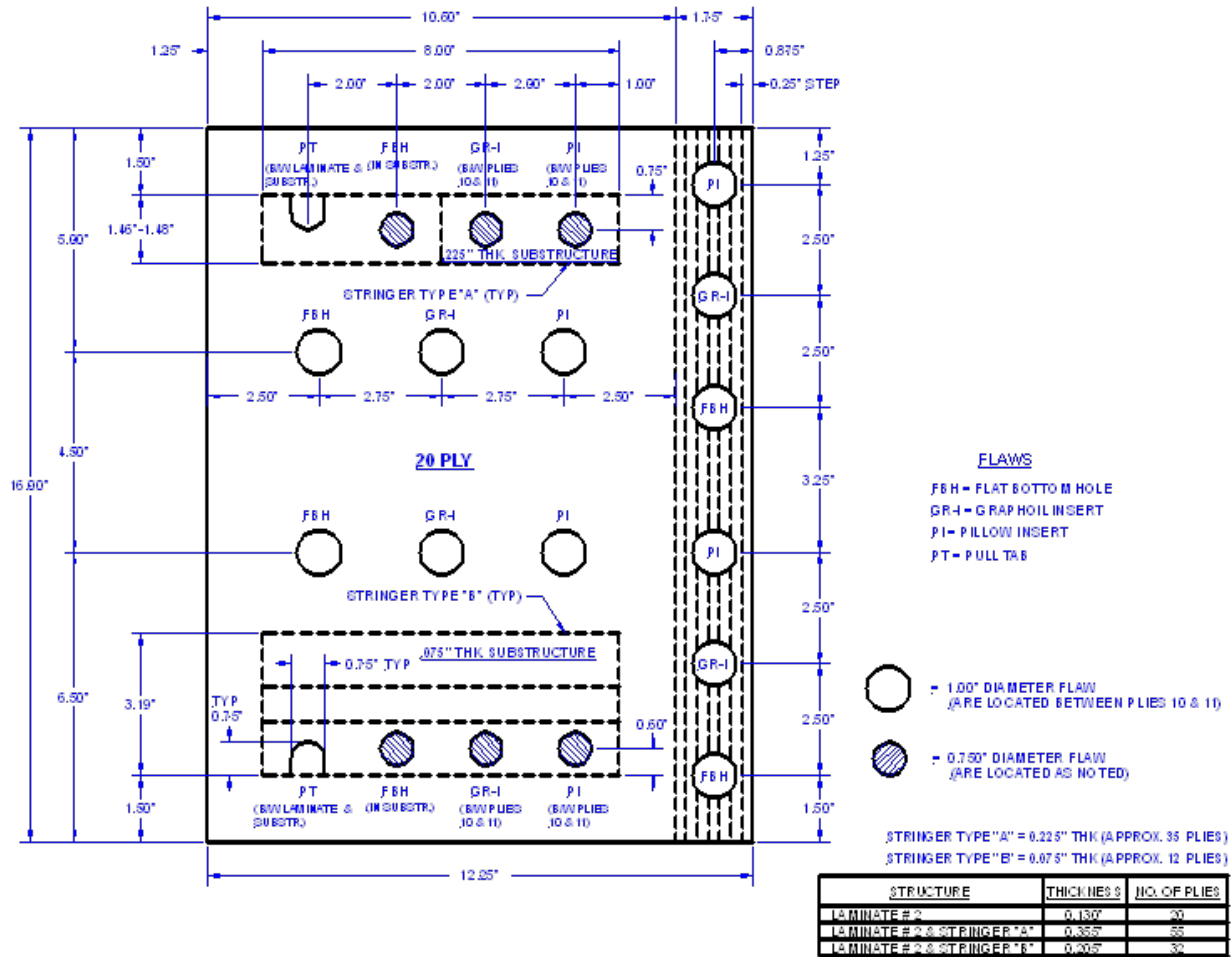


Figure 105. Final design of the 20-ply training/feedback specimen with taper

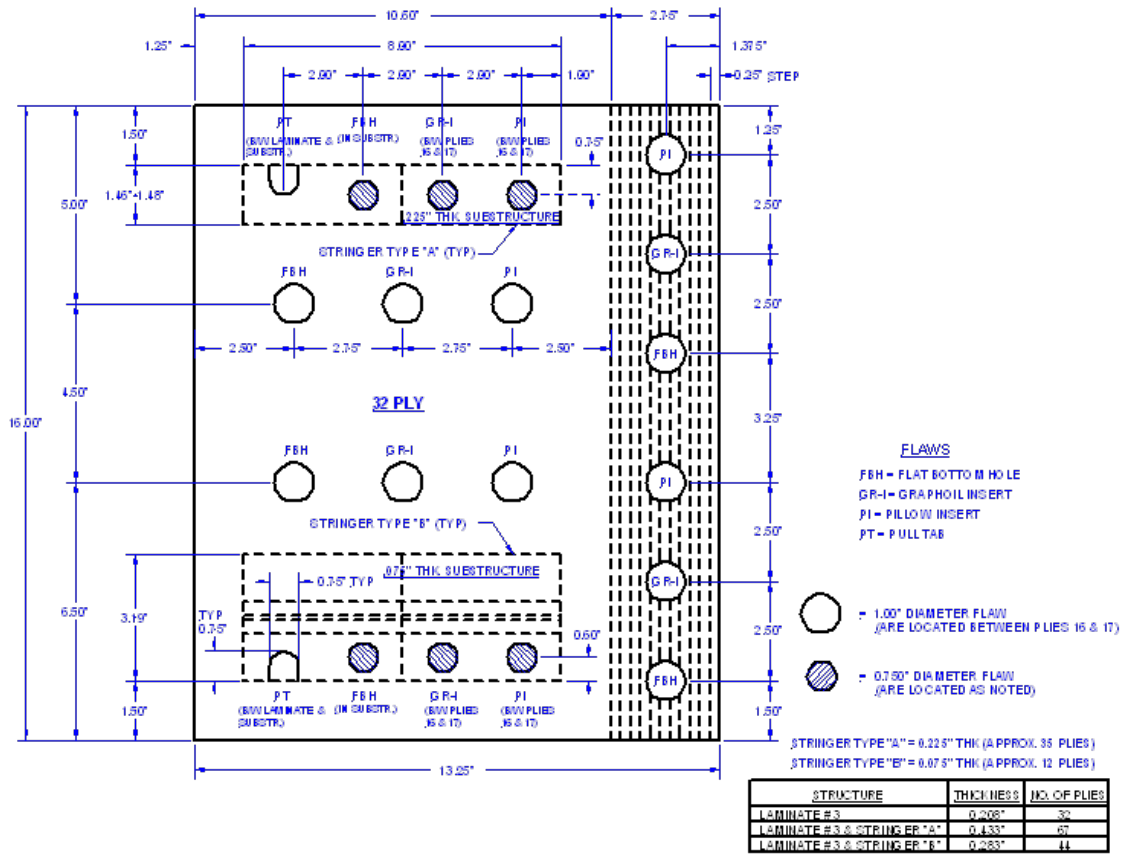


Figure 106. Final design of the 32-ply training/feedback specimen with taper

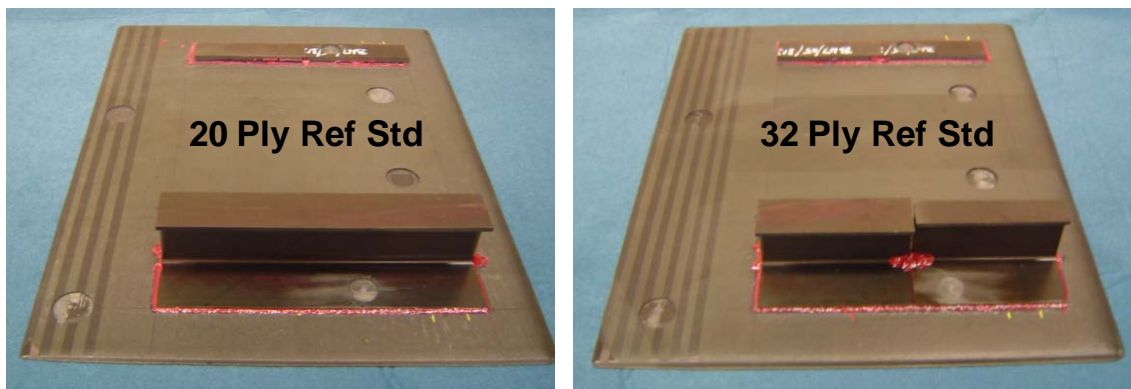


Figure 107. The 20- and 32-ply NDI feedback specimens (backside view) used by inspectors prior to starting the blind POD inspections

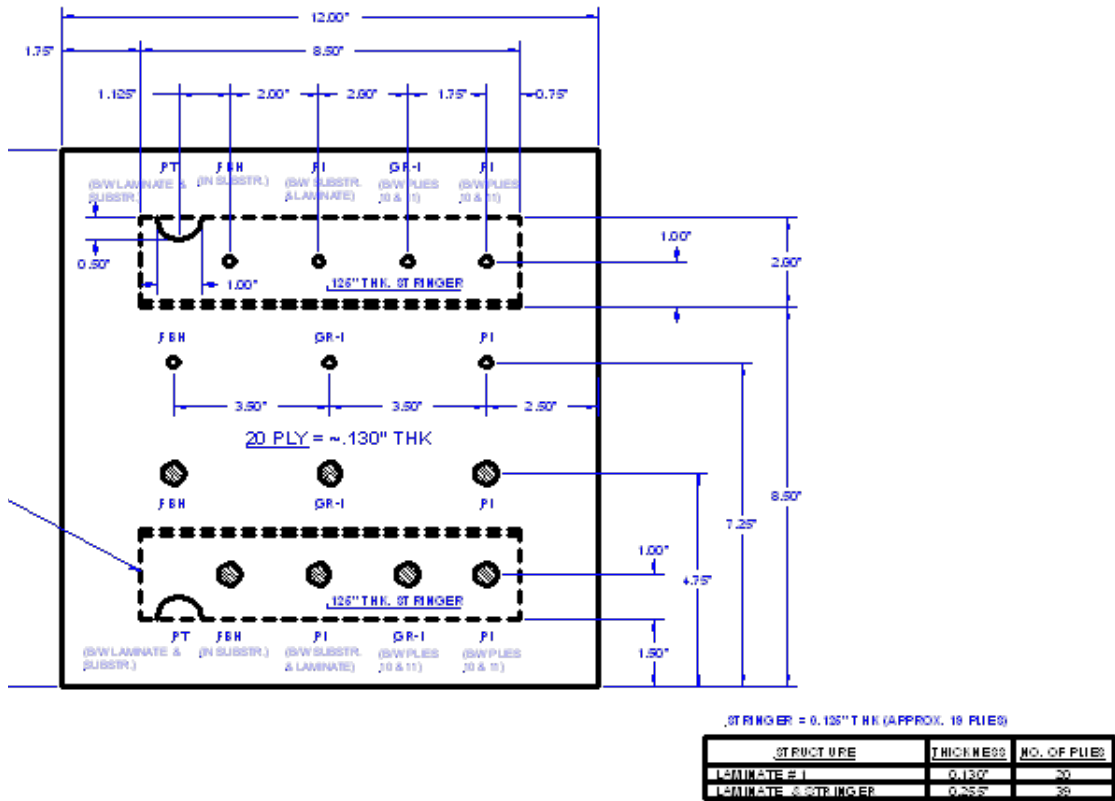


Figure 108. Final design of the second 20-ply training/feedback specimen without taper and different substructure and smaller flaws

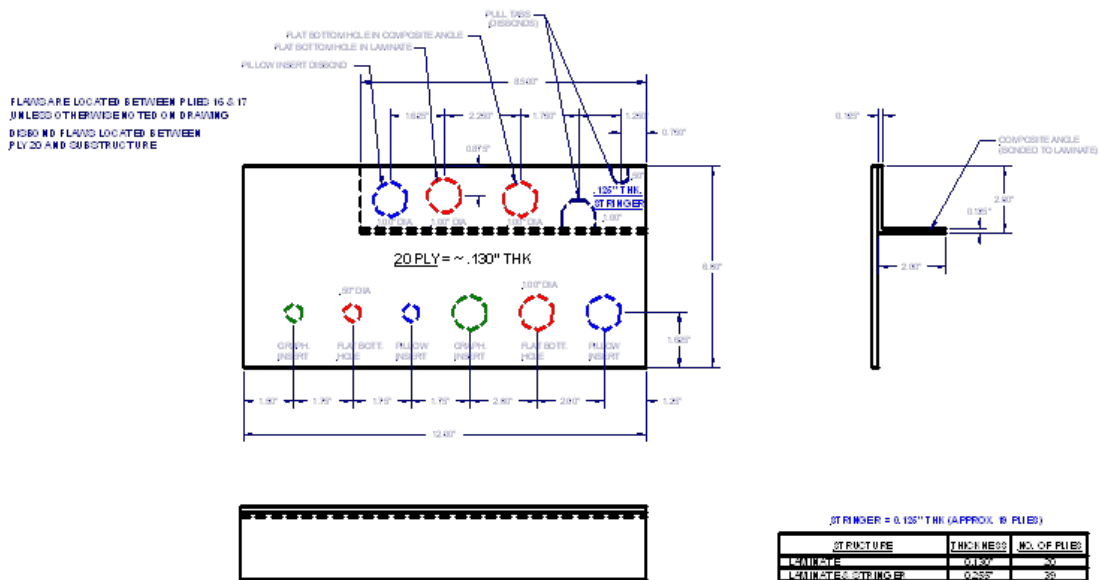


Figure 109. Final design of the third 20-ply training/feedback specimen

The following is information about the test specimen designs:

- Proper flaw spacing and sufficient area for assessing false calls produced a need for 15 test specimens broken down into four CT specimens, four 12–20 ply simple taper specimens, four 32-ply simple taper specimens, and three BN specimens. There are a total of 11 specimens in the thin laminate experiment and 4 specimens in the thick laminate experiment.
- The following is information about the engineered solid laminate test specimens (see table 1):
 - BN specimens – inspection area = 5.5 ft² each; total of 16.5 ft²
 - CT specimens – inspection area = 1.3 ft² each; total of 5.2 ft²
 - Simple taper specimens (12–20 plies) – inspection area = 3.1 ft² each; total of 12.4 ft²
 - Total inspection area for the 12–20 ply thin laminate experiment = 34.1 ft²
 - Simple taper specimens (20–32 plies) = 3.0 ft² each; total of 12.0 ft²
 - Total inspection area for the 20–32 ply thick laminate experiment = 12.0 ft²
- Figure 110 shows the two types of ply tapers and how they were integrated with the substructure elements. The specimens contained both simple (i.e., one directional) tapers and complex (i.e., two directional) tapers.

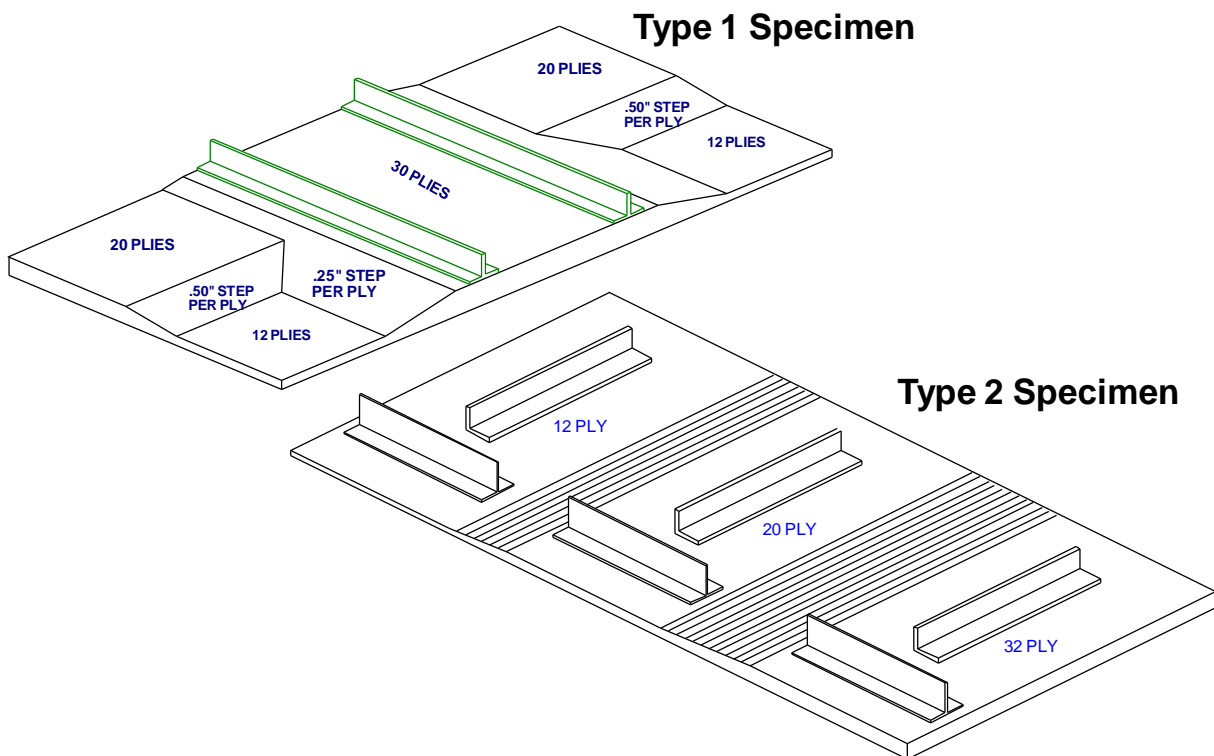


Figure 110. Solid composite laminate specimens with substructure and single (type 1) or dual (type 2) ply tapers on the back side

- Figure 111 shows the BN specimen design. It includes honeycomb regions in the top and bottom skins to study the inspection impediment of honeycomb under thick laminates. Flaws were placed in the transition region where the laminate splits around the honeycomb. The rounded section in the front was produced separately and fastened into place. The aft spar is a pre-fabricated C-section and is sealed and fastened. Flaws were placed in the fastened and sealed regions of the spar attachment joint. This specimen is approximately 5.5 ft². There are three specimens of this design for a total inspection area of 16.5 ft².

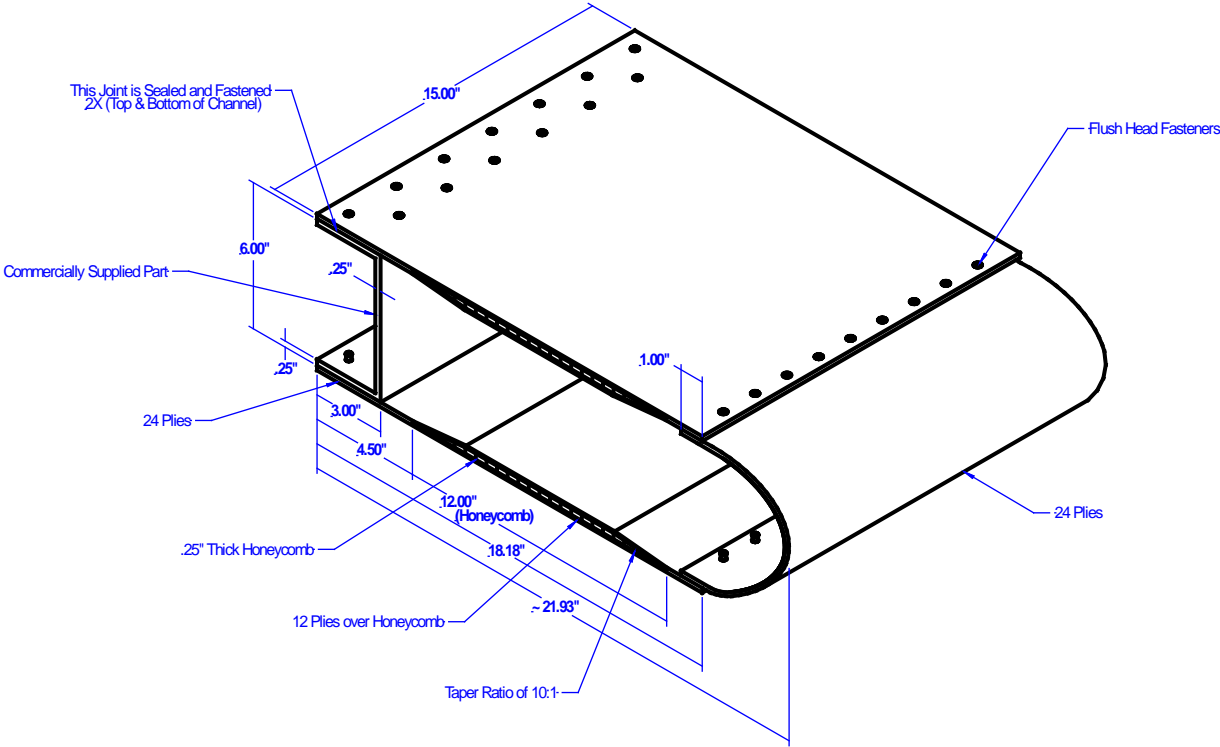


Figure 111. The BN test specimen drawing

- Figures 112–116 show the designs for the thin and thick laminate with taper specimen types. Figures 112 and 113 highlight the complex, double taper inspection challenge that is included in this study. Figures 114 and 115 show the simple taper designs that provide more surface area of constant thickness and substructure stinger/rib regions that contain secondary bonds.

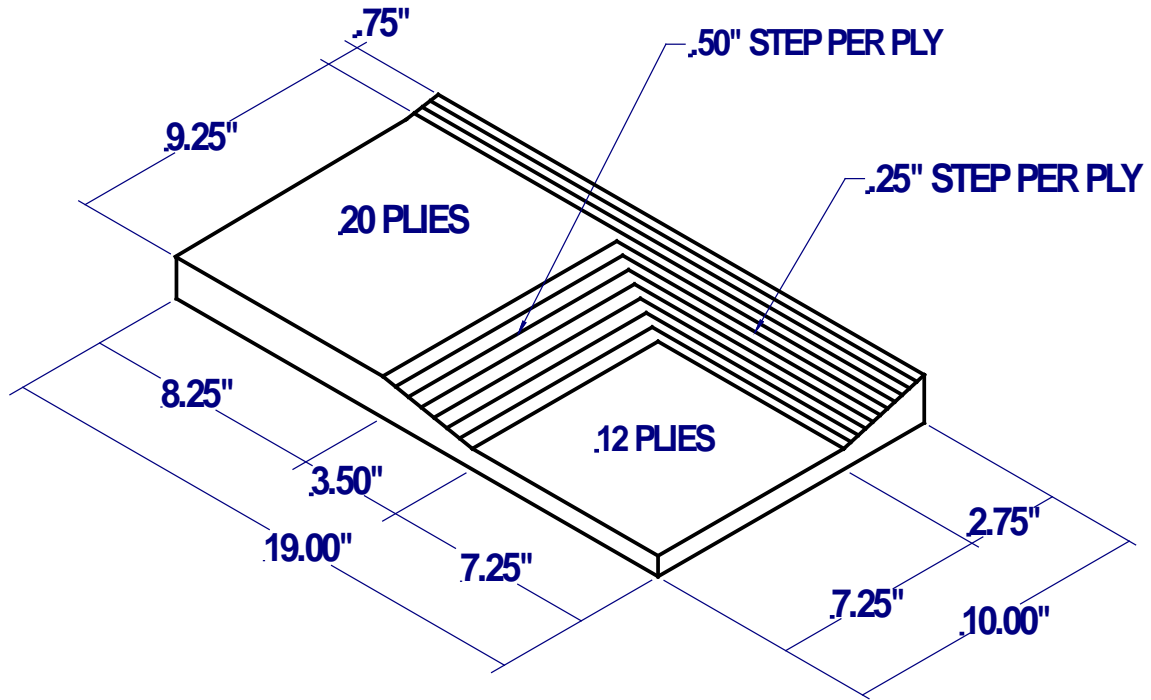


Figure 112. The CT "A" test specimen drawing

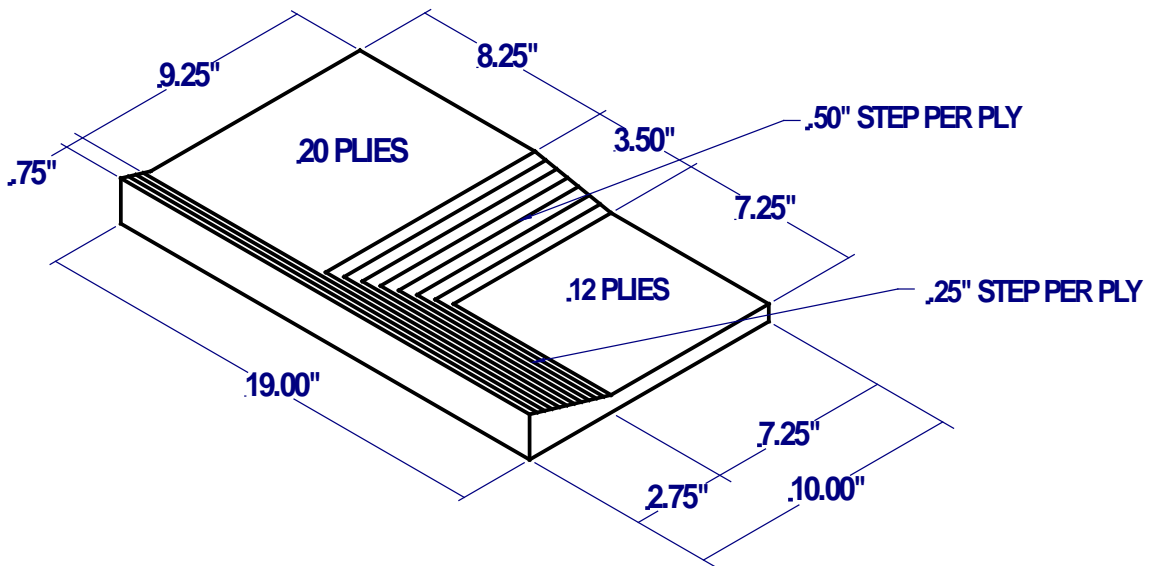


Figure 113. The CT "B" test specimen drawing

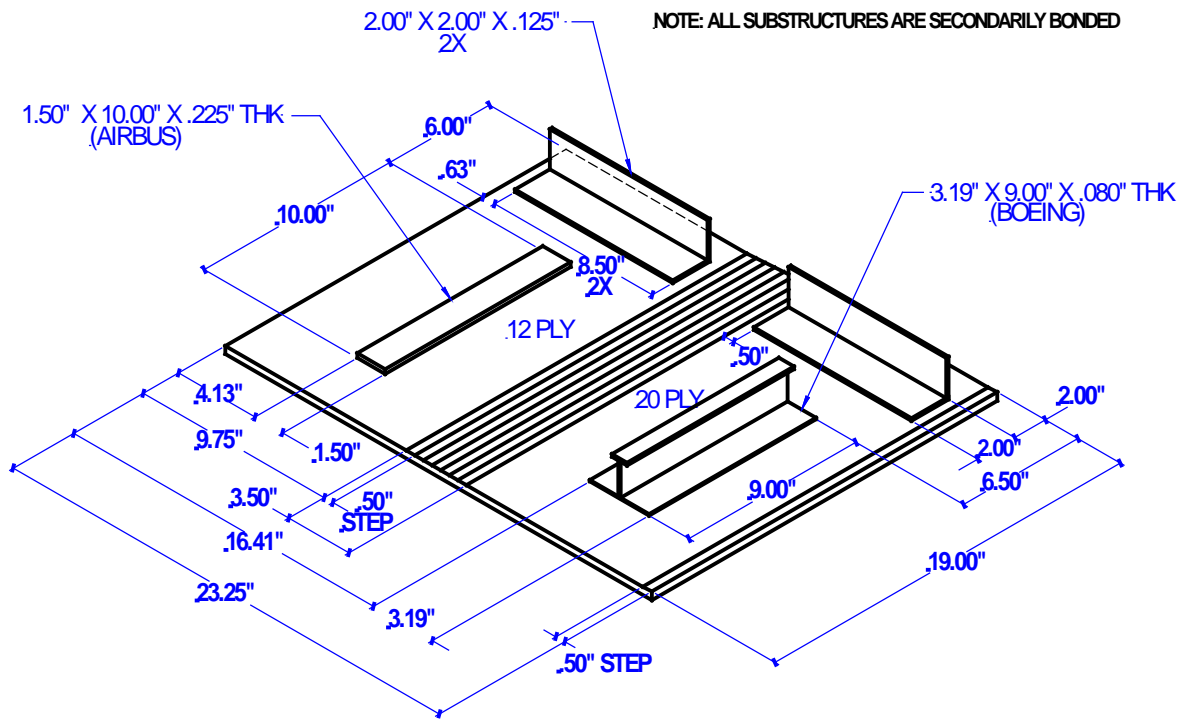


Figure 114. Simple taper upper test specimen drawing (12–20 plies)

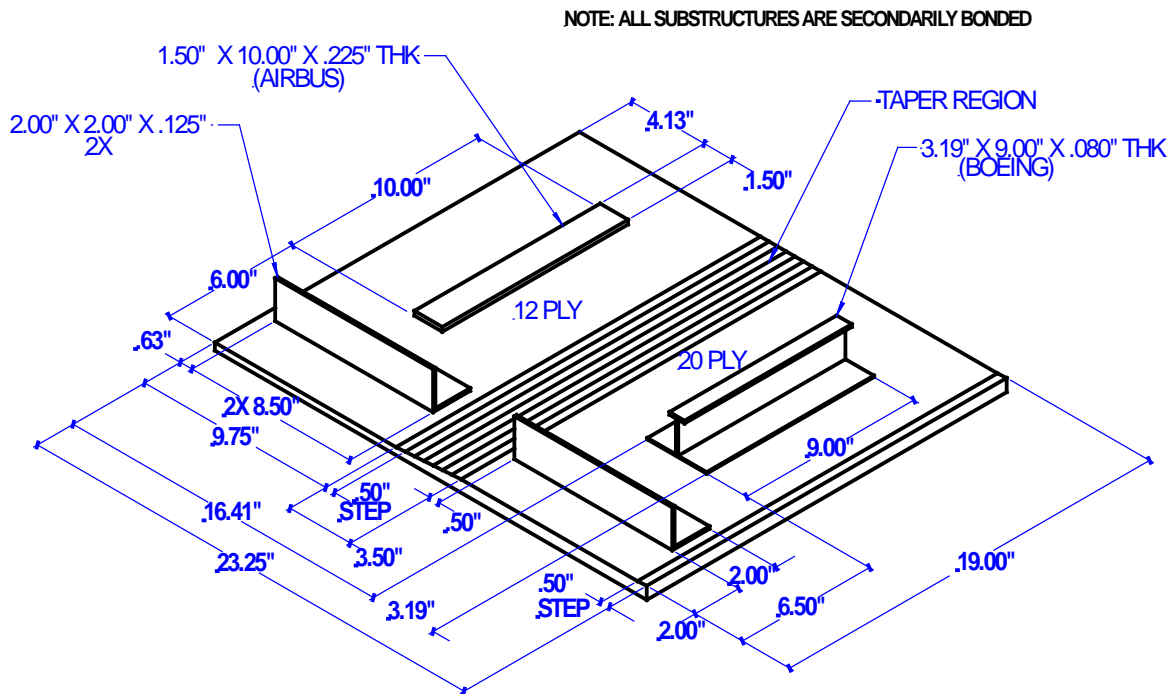


Figure 115. Simple taper lower test specimen drawing (12–20 plies)

specimen set. Table 4 shows the combined area calculations for the 12–20 ply and 20–32 ply specimen sets. Note that the inspection areas for both the CG and constant thickness regions are almost equal.

Table 2. Thin 12–20 ply total inspection area

Thin (12–20 ply) – Total Area = 34.1 ft ²				
Panel Type	(ft ²)	# Panels	Total (ft ²)	Geometry
BN	5.6	3	16.8	Combined
	4.663	3	13.989	CG
	0.937	3	2.811	Constant Thickness
CT	1.319	4	5.276	Combined
	0.424	4	1.696	CG
	0.895	4	3.58	Constant Thickness
STU/STL	3.002	4	12.008	Combined
	0.977	4	3.908	CG
	2.025	4	8.1	Constant Thickness

Table 3. Thick 20–32 ply total inspection area

Thick (20–32 ply) – Total Area = 12 ft ²				
Panel Type	(ft ²)	# Panels	Total (ft ²)	Geometry
STE32s	3	4	12	Combined
	1.194	4	4.776	CG
	1.806	4	7.224	Constant Thickness

Table 4. Combined 12–20 ply and 20–32 ply total inspection area

Combined (12–20 ply) & (20–32 ply) Total Area = 46.1 ft ²		
Geometry	Total (ft ²)	% Area
CG	24.4	53%
Constant Thickness	21.7	47%
Total	46.1	100%

4.3 FLAW MANUFACTURE OPTIONS

A key aspect of the production of the test specimens was determining the methods to engineer realistic flaws. To evaluate several different methods for engineering flaws into a composite laminate, a number of thick composite laminate trial specimens were produced with different laminate thicknesses and ply taper regions. Figure 117 shows one example of the trial specimens; it contains a matrix of six possible ways to produce delaminations. Flaws of different sizes were

placed at different depths. Subsequent inspections produced S/N data (PE-UT and low frequency bond test) and attenuation data. The goal was to determine methods for producing both “loose” delaminations (i.e., high attenuation and S/N values) and “tight” delaminations (i.e., relatively low S/N values and attenuation levels in the range of the 12 dB accept–reject threshold). Test results showed that the 4-ply pillow inserts produced more gross flaws, whereas the Grafoil inserts better simulated the tighter flaws. As a result, the experiment includes both flaw scenarios. Figure 118 shows a C-scan image produced by PE-UT inspections and the S/N values associated with each flaw type and size. The goal was to only use flaws that produced an S/N level of 3 or greater. The pull tab and flat bottom hole flaw engineering methods were also adopted into this experiment.

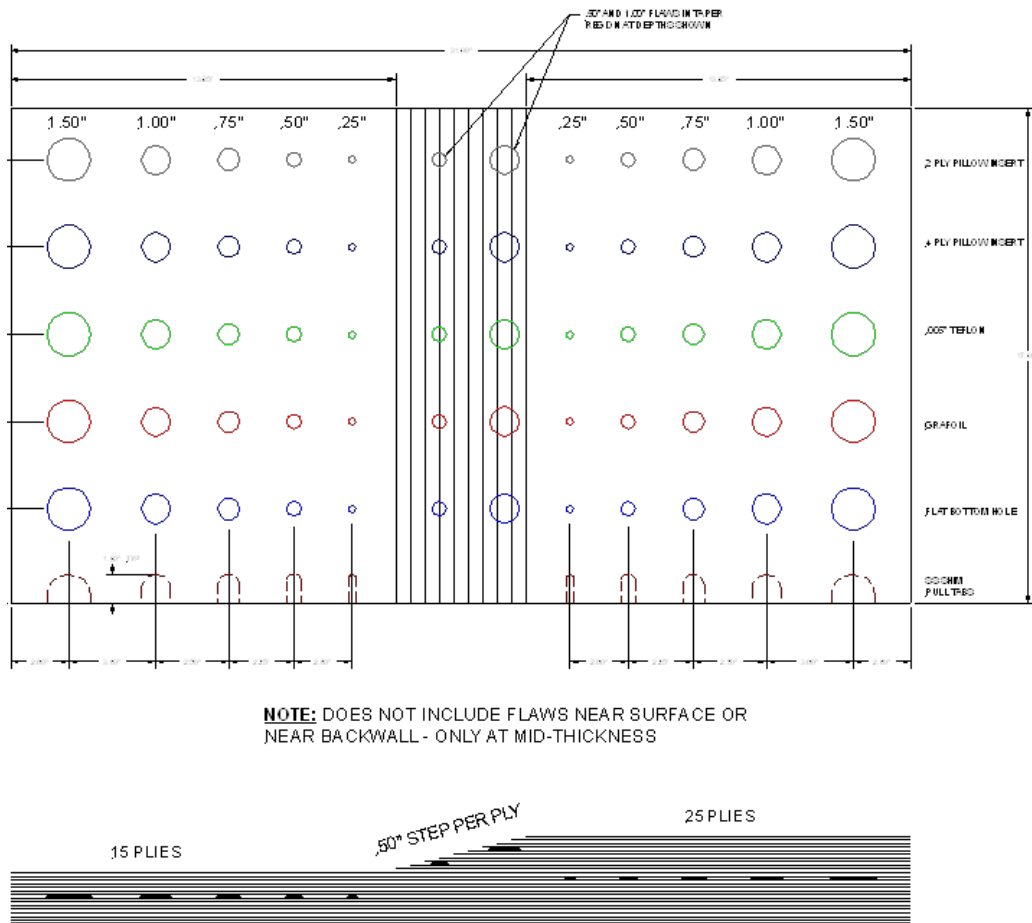


Figure 117. Trial S/N solid laminate specimen for preliminary testing of methods for producing engineered flaws

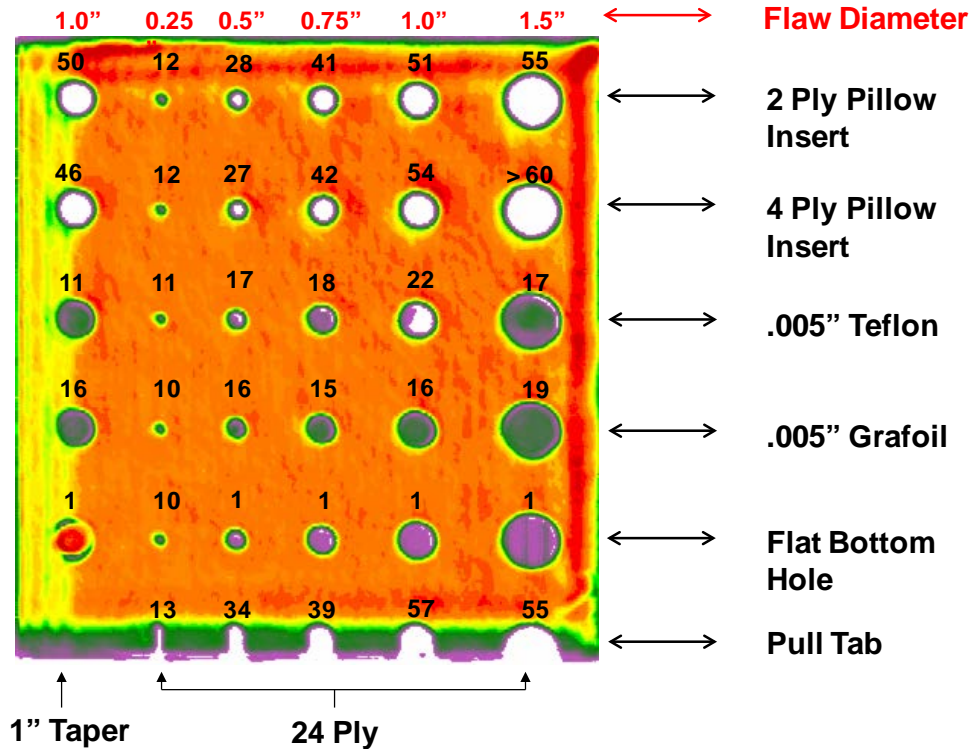


Figure 118. A UT scan of trial solid laminate specimen showing attenuation levels to establish viability of flaw engineering methods

Figures 119 and 120 show some of the test specimens being fabricated. Figure 119 shows the Mylar templates that were used to ensure the proper placement of the flaws in each of the specimens, whereas figure 120 shows the vacuum bagging/autoclave production process, some of the ply taper regions, secondary bonding of some substructure elements, and some of the post-production flaws that were added to the back side of the test specimens.



Figure 119. Solid composite laminate flaw detection experiment – test specimen fabrication

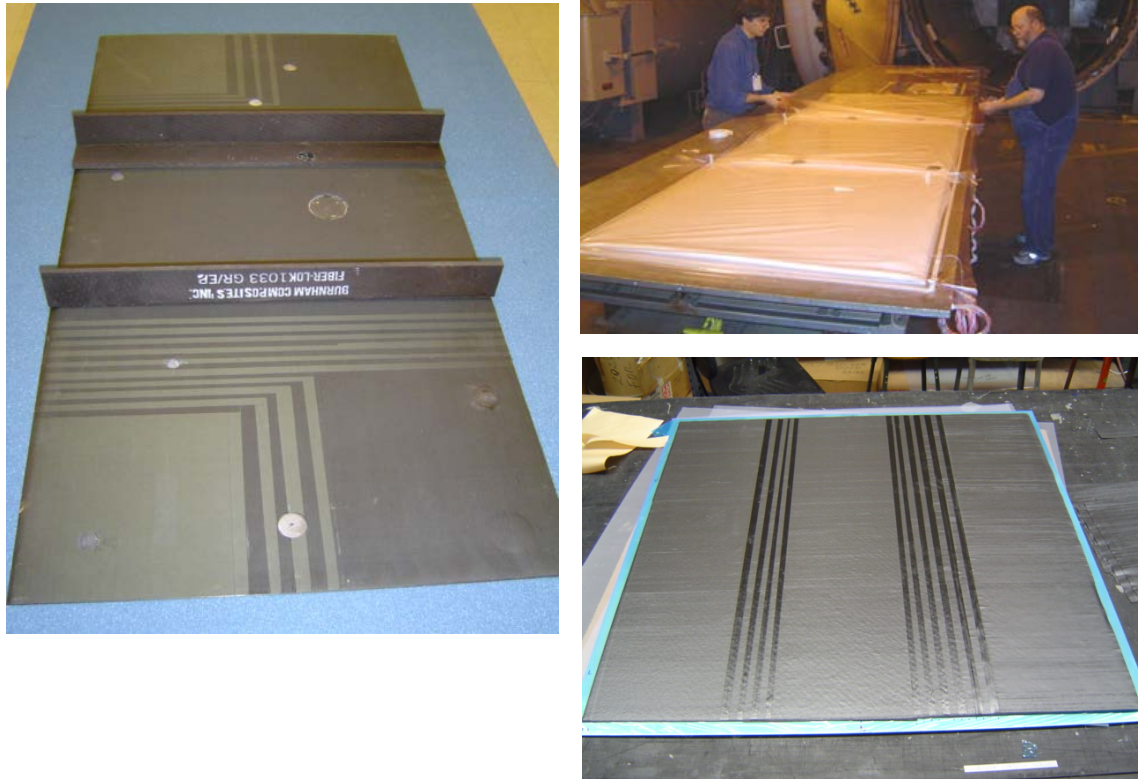


Figure 120. Layup of composite laminates with simple taper and CT, and bonding of substructure elements

4.3.1 Flaw Characterization

To make a quantitative assessment of the viability of each engineered flaw in the SLE test specimens, the S/N ratio of each defect versus the surrounding good structure was determined. The S/N ratio was calculated using the amplitudes of the A-scan signals in the test specimens. The noise level was determined by examining the output variation corresponding to inspections along adjacent sections of good structure. This was compared to the signal obtained during inspections of the flawed areas.

BS = base signal; peak signal at unflawed area

NS = noise signal; (max-min)/2 over range of unflawed area in each quadrant

FS = flaw signal; peak signal at each flaw site

$$S/N = \frac{FS - BS}{NS} \quad (1)$$

In general, an S/N ratio of at least 3 is desired to infer the presence of a flaw. Therefore, all flaws in the SLE database were checked to ensure that their S/N ratio was 3 or larger. Testing using

this scheme did not require calibration on a “median” or “neutral” reference standard. The key measurement for each case was the difference between unflawed areas of the test panel and the defect area. The S/N ratio can be calculated based on the flaw signal decrease in the back wall signal or the flaw signal presence (i.e., amplitude) of a new intermediate signal between the front and back wall, which also indicates an anomaly. Table 5 shows some sample results from the series of S/N calculations for BN and CT specimens. If the drop in the back wall signal was used as the flaw signal basis for the calculations, the S/N values ranged from 29–89. If the new intermediate peak is used as the flaw signal basis for the calculations, the S/N values ranged from 8–69. In both calculations, all flaws are considered viable for this study because they provide sufficient signal variation to be readily detectable.

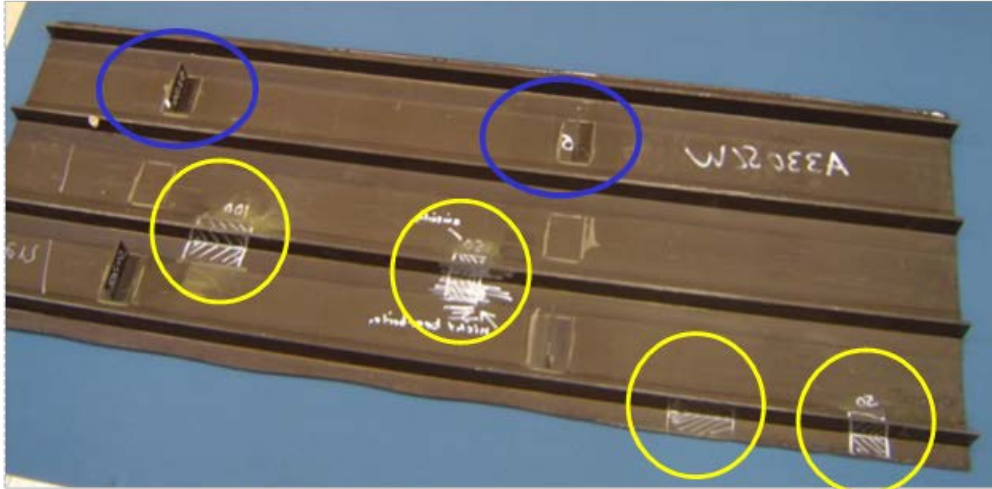
Table 5. Sample S/N calculations for flaws in the BN and CT test specimens

PE-UT Amplitude Measurements								
Flaw No.	Panel Location	Laminate Thickness	Flaw Identification (Type/Size, Loc.)	Viability of Flaws – Attenuation	Backwall Response (% FSH)	S/N Ratio (Backwall signal)	Flaw Response (% FSH)	S/N Ratio (Flaw signal)
1	BN1	12–24	4PL-PI, 0.50", b/t 4&5	17.6	21.1	87.1	80	44
3	BN1	12–24	GR-I, 1.0", b/t 4&5	23.3	11.0	93.4	120	69
5	BN1	12	4PL-PI, 1.0", b/t 4&5	18.7	18.7	88.6	120	69
6	BN1	12–24	GR-I, 0.75", b/t 4&5	22.7	12.1	31.4	120	22
8	BN1	12–24	4PL-PI, 1.5", b/t 8&9	21.4	14.1	31.0	125	8
10	BN1	12	GR-I, 1.0", b/t 6&7	19.5	17.6	30.3	120	22
68	CT1	12–32 T	4PL-PI, 0.25", b/t 16&17	23.4	6.3	32.3	31	10
69	CT1	20–32 T	GR-I, 2.0", b/t 16&17	21.6	7.8	31.7	101	36
70	CT1	12–32 T	GR-I, 0.75", b/t 22&23	26.0	4.7	32.9	117	42
71	CT1	12–32 T	4PL-PI, 1.5", b/t 16&17	23.0	6.6	32.2	117	42
72	CT1	20–32 T	GR-I, 0.75", b/t 16&17	20.7	8.6	31.4	109	39
75	CT1	12	4PL-PI, 0.25", b/t 6&7	20.6	11.7	29.1	78	17

4.4 EXPERIMENT TIMING

Based on the AANC’s experience with the similar composite honeycomb flaw detection experiment, it was assumed that inspectors could not provide more than 3–3 1/2 days of their time to complete the set of inspections. This experiment’s planned inspections for all 15 test specimens were expected to be more time-consuming than the inspections in the composite honeycomb flaw detection experiment; therefore, it was important to determine the amount of surface area that an airline inspector could realistically cover in a 3-day test. Trial experiments were conducted with the simulated vertical stabilizer specimen shown in figure 121. This allowed for a quantitative assessment of the possible surface area that could be inspected in a 3-day span. To acquire some timing data, an A330 vertical stabilizer test specimen with engineered flaws was sent to United Airlines. Inspection results from two inspectors at United Airlines showed that almost all the flaws were detected. The two inspections took 2 hours and 35 minutes and 3 1/2 hours, respectively, for the 10 ft² panel. This timing data indicated an expected

coverage of 2.9–3.9 ft²/hr using handheld PE-UT methods. Overall, these results indicated that a 3–3 1/2 day experiment (i.e., 18–22 hours of inspection time) could cover approximately 60 ft² of inspection area. This experiment contains a total of 46 ft² (34.1 ft² thin laminate and 12.0 ft² thick laminate) of inspection area. For comparison, inspection results from several different NDI methods are shown in figure 122. Note that the PA-UT scanner, MAUS resonance scans, and handheld PE-UT inspections all produced similar flaw detection.



Simulated Vertical Stabilizer with Stringers, Rib Sections and Engineered Flaws

Four stringer-to-skin disbonds (yellow)

Two rib to-skin-partial disbonds (blue)

Figure 121. Vertical stabilizer large composite laminate test specimen used to obtain preliminary timing information for handheld PE-UT inspections

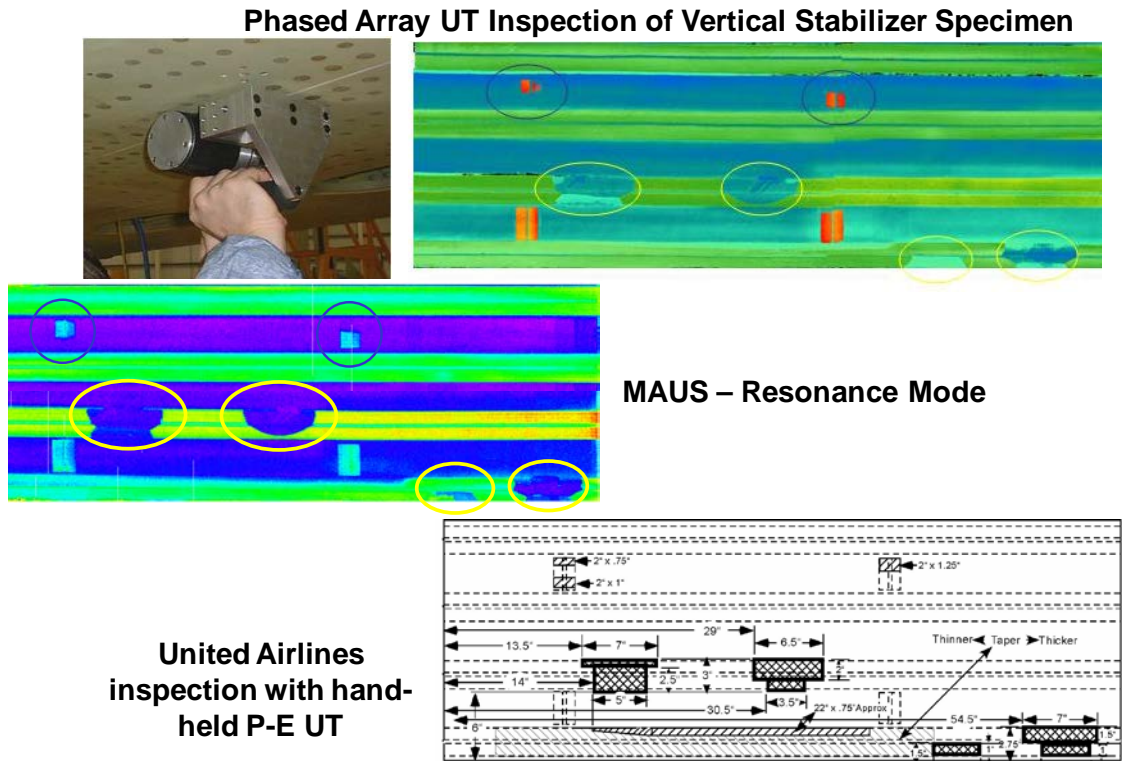


Figure 122. Inspection results showing detection of all stabilizer flaws by PA-UT, resonance scans, and handheld PE-UT

4.5 THE RDCE

Several OEMs and airlines requested that the AANC adapt the SLE to conduct a blind evaluation of the viability of the GE Bondtracer (BT) and Olympus Ramp Damage Checker (RDC) devices. As a result, a customized POD experiment was produced from the SLE called the RDCE. The purpose of the RDCE is to assess new UT-based “Go”/“No Go” equipment that OEMs plan to allow airlines to deploy at airports and other nonscheduled maintenance depots using non-NDI personnel (e.g., airframe and power plant mechanics [A&Ps], also known as aircraft maintenance mechanics). These “Go”/“No Go” devices are described in section 3. The equipment can be deployed whenever visual clues or other events that warrant closer scrutiny of a composite laminate structure occur. Ground personnel, with appropriate training on such equipment, will set up the equipment in accordance with OEM-supplied procedures and then make an assessment of the region in question. It is important to note that such “Go”/“No Go” UT equipment is intended to be used to assess local indications or regions only. They are not intended for wide-area inspections that cover areas of several square feet. Therefore, equipment operators must be directed to very distinct locations. This was a key consideration in the design of the RDCE.

The following were elements and considerations of the RDCE design:

- Selected locations and shapes were identified on the SLE specimens so that personnel participating in the RDCE knew:
 - exactly which regions to check.
 - which region to use for equipment calibration prior to inspection.
- Selected locations, while a subset of the SLE, included all types of flaws and construction scenarios, including substructure elements
- Selected locations averaged 8.62 in.² (0.06 ft²) in area over 140 locations for a total inspection area of 8.38 ft². The area was divided into 53% of the locations having flaws and 47% of the locations having no flaws. The inspection area to flaw ratio was greater than 20:1; for every 1 in.² of flaw area there were more than 20 in.² of unflawed area in the overall RDCE
- Flaw sizes are the same as those deployed in the SLE – 0.25", 0.5", 0.75", 1", 1.5", and 2"
- Eighty flaws were included in the RDCE design
- The RDCE was designed to allow for calculating PODs based on each individual participant's results
- The GE BT and Olympus RDC devices were deployed by an equal number of participants
- Both NDI inspectors and non-NDI personnel (all A&P qualified) were tested to determine if any difference in performance was observed

The following is an explanation of the RDCE implementation:

- The NDI feedback specimens, equipment setup procedures, and overview training (see appendix E) were provided to all inspectors participating in the RDCE. Experiment participants were allowed to work with the NDI feedback specimens to increase their proficiency in either the BT or RDC devices before proceeding to the blind POD experiment
- Each blank experiment panel (see figure 123) from the SLE was prepared for the focused inspections that were specifically selected for the RDCE
- An inspection region was consistently marked on each composite test specimen using a series of templates. Inspection locations and calibration locations were marked on each specimen by the experiment monitors using the RDCE design templates shown in figure 124. The template was placed on each specimen and the inspection regions on each panel

were then clearly marked using this template. Each section was marked using a vis-à-vis white board marker that can be erased without leaving any residue markings on the panel. In addition, the proper calibration regions were also provided so that the equipment was calibrated on an unflawed location of matching thickness

- Panels marked with inspection locations were provided to each RDCE participant
- Specialized drawings, as shown in figure 125, were provided to each participant for guidance. The drawings showed the inspection regions to be covered along with the panel design (e.g., laminate thicknesses; substructure regions and thicknesses; taper regions) so that the inspectors were aware of the composite ply arrangement in each region
- Inspectors made their flaw indications directly on the test panel, as shown in figure 126. Grading templates were then placed on top of the inspector's flaw calls to determine flaw hits, misses, false calls, and ability to correctly size each detected flaw



Figure 123. Test panel from the SLE

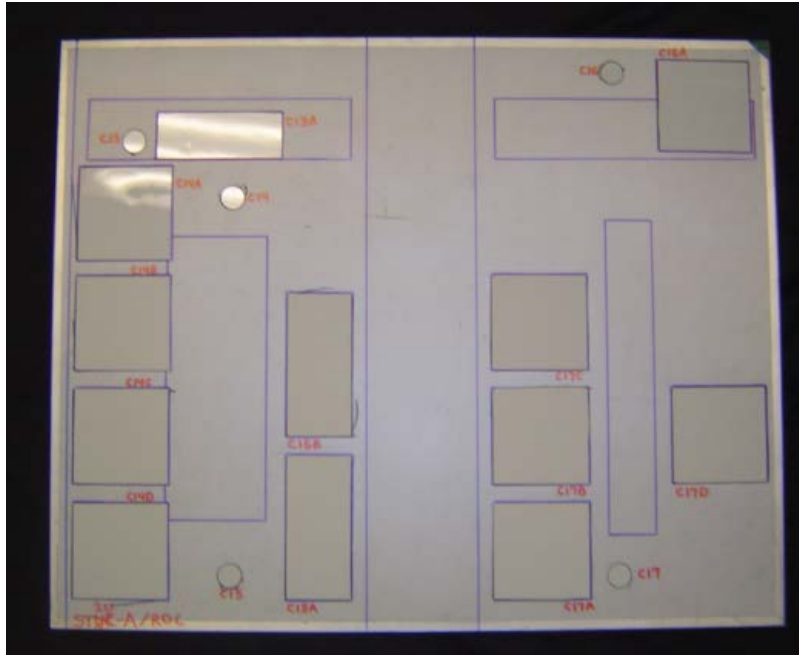


Figure 124. Use of template to mark the series of small inspection regions and the appropriate calibration point for the BT or RDC equipment

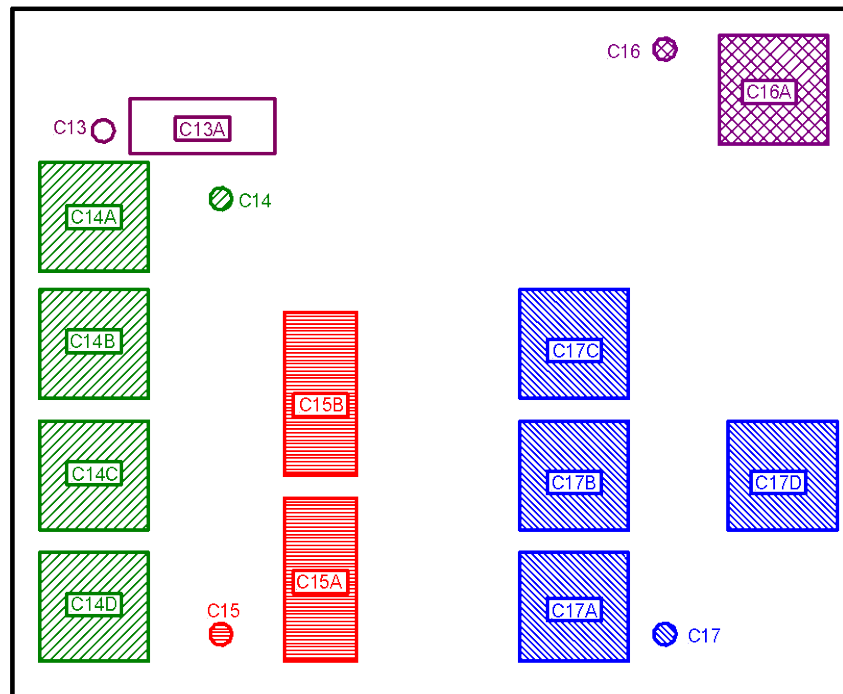


Figure 125. Drawings provided to inspectors that show the inspection regions to be covered, appropriate calibration points (note color coding), and panel design features

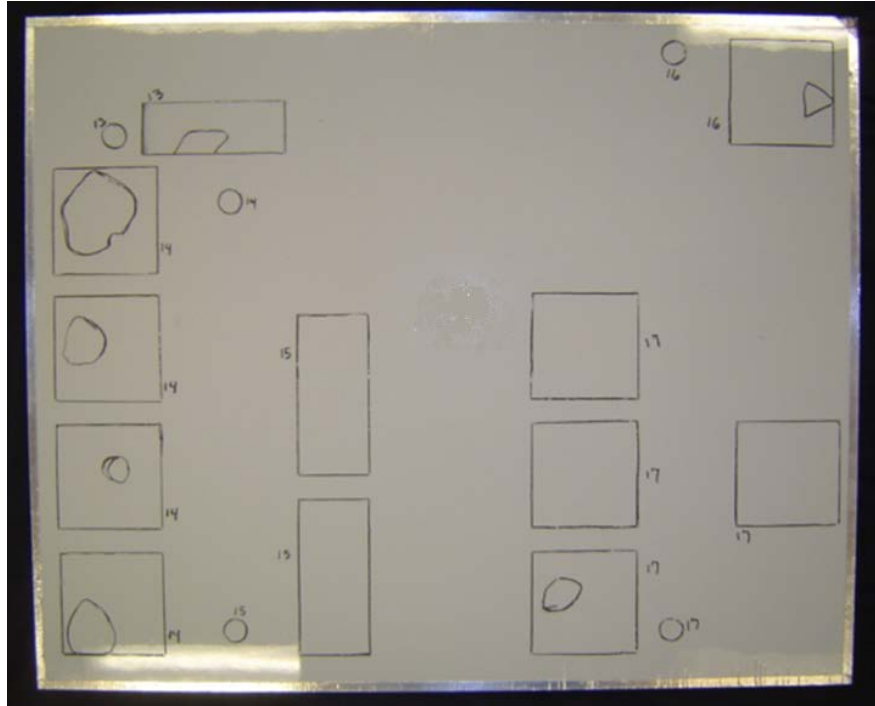


Figure 126. Test panel showing an inspector's flaw markings within the directed inspection regions

5. COMPOSITE LAMINATE FLAW DETECTION EXPERIMENT IMPLEMENTATION

Experiment protocols were written to guide every aspect of the SLE implementation. The experiment protocols ensured that the information provided to all experiment participants was consistent and comprehensive; all participants received similar guidance and inspection aids. In addition, the experiment protocols provided step-by-step guidance to the experiment monitors so that all data and observations associated with the SLE were acquired in a consistent manner. A thorough experiment briefing package was sent out in advance of every airline visit. The experiment briefing package (see appendix A) was provided to experiment participants at least one week in advance of the SLE blind testing. The set of NDI feedback specimens, with flaw locations clearly marked, was also sent out in advance so that experiment participants could conduct PE-UT inspections to familiarize themselves with the composite structure and flaw detection requirements.

The first day of each experiment started with the experimenter briefing (see appendix B). Figure 127 shows one of the briefings being provided to inspectors. This briefing explains the purpose of the experiment and the process the inspectors will use to indicate their flaw findings. The briefing was used at each facility to ensure a consistent presentation on the experiment goals and a thorough explanation of how the experiment will proceed. It also allowed the inspectors to ask questions. At this time, the inspectors were introduced to the inspection transducers, UT devices, and aids (e.g., delay lines) that they could optionally use. Inspectors could also decide to deploy their own PE-UT equipment and transducers. Composite laminate inspection procedures were provided to the AANC by Boeing and Airbus for use in the SLE. These sample composite

laminated NDI procedures were presented to the inspectors for their use. During the course of the NDI tests, the experiment monitors logged various observations and the exact flaw calls provided by the inspectors. Appendix C contains the “Experiment Monitor Data Acquisition Sheets” that were used to guide the data logging.



Figure 127. Experiment instructions being provided to supplement the written experimenter briefing and information packet

Once the briefing was completed, each blind inspection process was preceded by inspections on appropriate NDI feedback specimens supplied by the experiment monitors. The inspector was provided with information on the manufactured flaws present in the NDI feedback specimens and was allowed to use the specimens for check-out and setup of their inspection equipment. The NDI feedback specimens have similar construction to the blind test specimens and include similar flaws. Therefore, the specimens were also used to allow inspectors to become familiar with the inspection device and learn about a specific piece of equipment’s response to various composite structures and flaws within those structures. Figures 104–109 show the flaw profiles of all the NDI feedback specimens.

Additional UT transducers were also provided by the experiment monitors so the inspectors could experiment with different frequencies, probe diameters, and types (i.e., contact or delay). Once the inspectors were comfortable with their setup on the NDI feedback specimens,

experiment monitors distributed the blind specimens to them for inspection. Inspectors were asked only to locate and properly size the flaws they found by marking directly on the specimens using standard grease pencils. This data was then recorded and graded to determine their POD level, number of false calls, and inspectors' accuracy in sizing the flaws. Other secondary data was collected such as inspection time on each panel, inspector experience, NDI training level, inspection frequency, probe type, and equipment used for inspection. The typical setup for the experiment deployment is shown in figures 128–130, in which each inspector has a workstation to set up their equipment and test specimens.



Figure 128. Typical experiment setup with separate inspector workstations



Figure 129. Inspector completing inspection using specimen drawing for reference of structural details



Figure 130. Inspector completing inspection and marking flaw detection on the test specimen

The participants included over 70 inspectors from 18 aircraft maintenance facilities, including 14 different airlines and two MROs. All of the maintenance facility inspectors used handheld PE-UT inspection devices. The maintenance facilities included: All Nippon Airways, American Airlines, Cathay Pacific Airlines, China Airlines, Continental Airlines (pre-merger with United Airlines), Delta Air Lines (two facilities), Federal Express (two facilities), Goodrich Aerospace, Japan Airlines, Northwest Airlines (pre-merger with Delta Air Lines), Singapore Airlines, Taikoo Aircraft, Thai Airways, United Airlines, and US Airways. The participating companies are shown in figure 131. In addition, the SLE was completed using a wide array of advanced NDI methods (see figure 132). The advanced NDI methods evaluated with the SLE include: PA-UT (Olympus OmniScan, Toshiba Matrixeye, GE Phasor with RotoArray wheel probe), linear array UT (Boeing MAUS FlawInspecta, Sonatest rolling WheelProbe with OmniScan, and RapidScan 2), LUS (iPhoton), digital acoustic video (Imperium AcoustoCam), shearography (Dantec Dynamics, LTI), flash thermography (TWI), line thermography (MISTRAS), transient thermography (MoviTHERM), lock-in thermography (MoviTHERM), UT video (DolphiTech DolphiCam), and MW (Evisive). A previously released Department of Transportation (DOT) report describes the POD results from the conventional PE-UT method, whereas this report focuses on the advanced NDI methods that can potentially be applied to inspect composite laminate structures. Comparisons between results from advanced NDI and the conventional PE-UT method are also presented in this report.



Figure 131. Airline participants in the SLE



Figure 132. Advanced NDI methods that participated in the SLE

6. RESULTS FROM COMPOSITE LAMINATE FLAW DETECTION EXPERIMENT

Each inspection technique used in this blind flaw detection experiment was evaluated using the following performance attributes:

- Accuracy and sensitivity
- Data analysis capabilities
- Versatility
- Portability
- Complexity
- Human factors
- Inspection time

The most important of these parameters are the quantitative metrics because they are objective standards that can be numerically counted or quantified. Accuracy is the ability to detect flaws reliably and correctly in composite structures and repairs without false calls. Sensitivity is the extent to which the inspection system responds to flaws as a function of size, type, and location in the structure (e.g., proximity to edges, taper regions, and underlying or adjacent structural elements).

The graphs in this section show the detailed results for all aspects of the SLE, including the POD curves for each NDI method applied to the SLE. Results from conventional PE-UT inspections carried out by airlines inspectors are summarized first in section 6.1. Next, the individual results from each advanced inspection method are presented. Finally, comparisons are made between the various methods and between conventional and advanced NDI results.

The results listed in section 6.1 provide a comprehensive baseline of how the aviation industry currently performs in the detection of flaws in composite laminate aircraft components. Once these industry baseline results were obtained, the emphasis shifted to quantifying the degree of inspection improvement that could be obtained through the application of alternative and more advanced NDI methods (i.e., equipment and techniques). The same experiment was deployed with a wide array of advanced NDI methods, and the results from those tests are presented in this section.

Table 6 lists the set of advanced NDI methods that were used on the SLE. Note that some of the experiments included only a subset of the total number of test specimens. Some POD tests were only performed on the 12–20 ply specimen set, whereas other tests were only performed on the 20–32 ply specimen set. Some tests covered the entire SLE (i.e., all specimens). Because of limited time on the part of some of the participants listed in table 6, some evaluations were conducted using only the NDI feedback specimens for which the flaw profiles were known by the inspectors. All of these categories are clearly delineated in table 6. The specimen sets which were deployed with each method are also summarized in table 7.

Table 6. List of advanced inspection methods applied to the solid composite laminate POD experiment and the type of specimens inspected by each method

20–32 Ply – Solid Laminate Experiment – Advanced NDI Participants				
Inspection Company	Probe Frequency	Number of Elements	Inspection Method	Inspection Device
Olympus NDT	5 MHz	64	PA-UT	OmniScan MX2
Toshiba	3.5 MHz	32	PA-UT	Matrixeye
All Nippon	3.5 MHz	32	PA-UT	Matrixeye
GEIT	5 MHz	64	PA-UT	GE RotaArray, Phasor XS
NDT Solutions	5 MHz	64	Linear Array UT	FlawInspecta (MAUS)
Sandia Labs	5 MHz	64	Linear Array UT	Sonatest WheelProbe, OmniScan MX1
iPhoton	500 KHz–20 MHz	N/A	LUS	iPlus III
Imperium	500 KHz–7.5 MHz	1	Digital Acoustic Video	AcoustoCam
TWI	N/A	N/A	Flash Thermography	Ecotherm
MISTRAS	N/A	N/A	Line Thermography	THELIS-P Scanner
MoviTHERM	N/A	N/A	Lock-in Thermography	FLIR Camera SR2 SC7650
Dantec	N/A	N/A	Shearography	Q-800
LTI	N/A	N/A	Shearography	LTI-5100 HD
Evisive	N/A	N/A	Microwave	Evisive Scan
12–20 Ply – Solid Laminate Experiment – Advanced NDI Participants				
Inspection Company	Probe Frequency	Number of Elements	Inspection Method	Inspection Device
Olympus NDT	5 MHz	64	PA-UT	OmniScan MX2
Toshiba	3.5 MHz	32	PA-UT	Matrixeye
NDT Solutions	5 MHz	64	Linear Array UT	FlawInspecta (MAUS)
iPhoton	500 KHz–20 MHz	N/A	LUS	iPlus III
Imperium	500 KHz–7.5 MHz	1	Digital Acoustic Video	AcoustoCam
TWI	N/A	N/A	Flash Thermography	Ecotherm
MISTRAS	N/A	N/A	Line Thermography	THELIS-P Scanner
MoviTHERM	N/A	N/A	Lock-in Thermography	FLIR Camera SR2 SC7650
Dantec	N/A	N/A	Shearography	Q-800
Evisive	N/A	N/A	Microwave	Evisive Scan
NDI Feedback Panels Only – Solid Laminate Experiment – Advanced NDI Participants				
Inspection Company	Probe Frequency	Number of Elements	Inspection Method	Inspection Device
DolphiTech	2 MHz–6 MHz	16,000	UT Video	DolphiCam
RCON NDT	5 MHz	64	Linear Array UT	Sonatest WheelProbe, RapidScan 2

Table 7. Summary of test specimen coverage by participants in SLE

Participant	12–20 Ply (Thin Laminate) POD Experiment	12–32 Ply (Thick Laminate) POD Experiment	Overall Solid Laminate Experiment (Both 12–20 & 20–32)	NDI Feedback Specimen Only
All Nippon		x		
Dantec	x	x	x	
DolphiTech				x
Evisive	x	x	x	
GEIT		x		
Imperium	x	x	x	
iPhoton	x	x	x	
LTI		x		
MISTRAS	x	x	x	
MoviTHERM	x	x	x	
NDT Solutions	x	x	x	
Olympus NDT	x	x	x	
RCON NDT				x
Sandia Labs		x		
Toshiba	x	x	x	
TWI	x	x	x	

6.1 SUMMARY OF MAIN INSPECTION RESULTS FROM CONVENTIONAL UT INSPECTIONS

Roach et al. contains the comprehensive set of results from the SLE applied to conventional PE-UT inspections as deployed by airline inspectors in the field [4]. A summary of those results is provided here to form a basis of comparison with the advanced NDI methods.

The POD curves for each inspector and the resulting cumulative POD curve for both the thin (12–20 ply) laminate experiment and thick (20–32 ply) laminate experiment are calculated in [4]. The curves show the variation within the group of inspectors that completed each experiment. In the thin laminate experiment, the best performing inspector produced a $POD_{[90/95]} = 0.53''$ diameter flaw, the worst inspector produced a $POD_{[90/95]} = >3.00''$ diameter flaw, and the overall cumulative result was a $POD_{[90/95]} = 1.29''$ diameter flaw. For the thick laminate experiment, the best performing inspector produced a $POD_{[90/95]} = 0.54''$ diameter flaw, the worst inspector produced a $POD_{[90/95]} = >3.00''$ diameter flaw, and the cumulative result was a $POD_{[90/95]} = 0.82''$ diameter flaw.

Tabulated results in Roach et al. also show the percentage of flaws detected for each flaw size in the different inspection categories of constant thickness geometry, CG, and for all flaws [4]. Constant thickness geometry is defined as the inspection regions where the number of plies

remains constant. The CG regions are defined as those areas containing tapered skins (i.e., changing thickness), substructure, curved portions, fasteners, and laminate bonded to honeycomb. The constant thickness geometry comprised 53% of the total 46.1 ft² of inspection area, whereas the CG comprised 47% of the total 46.1 ft² in the total solid laminate experiment. The tables also show the inspector's ability to properly size each flaw they detected. For example, of all the flaws the inspectors found in the constant thickness category, 21% were correctly sized (100% coverage). Additional tables show the false calls for each inspector completing the thin and thick laminate experiments and an average false call rate broken down into the different geometry categories and sizes.

Overall, the POD results were consistent with a few outliers, which is common for human performance assessment experiments. To represent the range of construction found on aircraft, the substructure on the thick laminate was co-cured and the substructure on the thin laminate was secondarily bonded. The secondarily bonded structure can be more difficult to inspect. The thickness of the substructure can also be a major factor in flaw detection. A large number of variables were studied and isolated to determine their impact on POD values. Overall, the false call rates were low.

6.1.1 Summary Inspection Results for the 12–20 Ply Thin Laminate Experiment

Figure 133 shows the spread of all the individual inspector $POD_{[90]}$ curves (dashed lines) compared to the cumulative $POD_{[90]}$ curve (solid line) for all 27 inspectors. These results were produced by considering all flaws in constant thickness and CG regions. The spread shows 15 inspectors with a $POD_{[90]}$ value less than the cumulative $POD_{[90]} = 1.20$ " diameter flaw ($POD_{[90/95]} = 1.29$ ") and 12 inspectors with a $POD_{[90]}$ value higher than the cumulative $POD_{[90]}$ value. The variation within the experiment ranges from a $POD_{[90]} = 0.53$ " diameter flaw for the best performing inspector to a $POD_{[90]} = 2.17$ " diameter flaw for the worst performing inspector. The standard deviation for the inspector $POD_{[90]}$ data set is 0.417" diameter flaw. Figure 134 compares the maximum likelihood estimate ($POD_{[90]}$) to the POD curve that is calculated when a 90% flaw detection is combined with a 95% confidence bound ($POD_{[90/95]}$). This solid line in figure 134 provides the performance curve that the industry normally uses to measure the performance of NDI methods as deployed by representative inspectors. For these experiments, POD values were calculated using a pass/fail analysis with a log normal model. Figure 134 shows that the cumulative $POD_{[90/95]}$ for all flaws in the thin laminate experiment (i.e., 12–20 ply skins plus substructure elements) was $POD_{[90/95]} = 1.29$ " diameter flaw.

The use of performance brackets to assess POD is shown in figure 135. Performance brackets were used to place inspectors into groups and then calculate the resulting $POD_{[90/95]}$ for each performance bracket. These performance brackets utilized the inspectors that fell into the 30, 70, and 90 percentile categories. The inspectors that fell into the 30 percentile group (eight inspectors, each having a $POD_{[90]}$ less than 1.0") produced a 39% improvement to $POD_{[90/95]} = 0.79$ " diameter flaw value compared to the overall cumulative $POD_{[90/95]} = 1.29$ " diameter flaw. The 50 percentile group (19 inspectors, each having a $POD_{[90]}$ less than 1.35") produced an 18% improvement with a $POD_{[90/95]} = 1.06$ " diameter flaw. The 90 percentile group (24 inspectors, each having a $POD_{[90]}$ less than 1.7") shows only an 8% improvement with a $POD_{[90/95]} = 1.19$ " diameter flaw. These performance brackets might be useful to airlines and MROs that can judge where their inspectors fall within the brackets and the resulting

performance they will obtain from their inspectors. The results in figure 135 also reveal the degree of inspection improvements that are possible if inspectors can shift their performance from the higher (worse) performance brackets to the lower (better) performance brackets. This shift in performance can be brought about by improved or more extensive composite inspection training or through a number of other measures that are described in detail in [4].

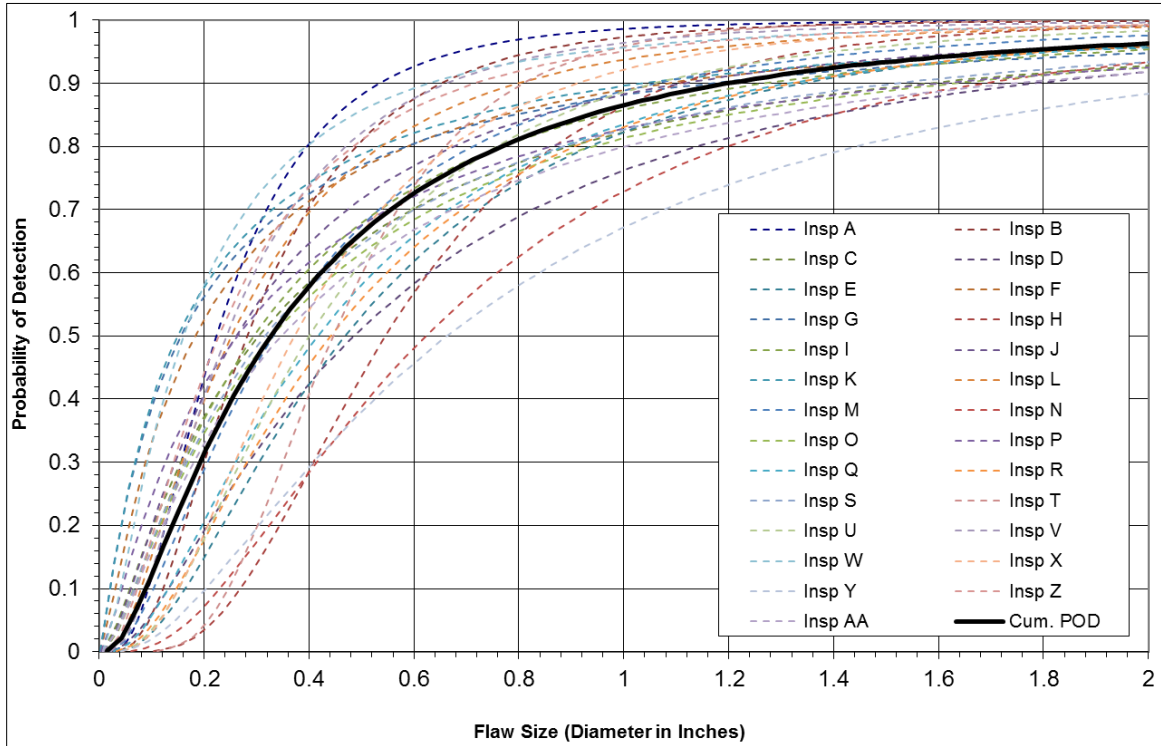


Figure 133. Individual and cumulative POD curve comparison for the 12–20 ply specimen set for all flaws in constant thickness and CG regions for all inspectors (27) (PE-UT method)

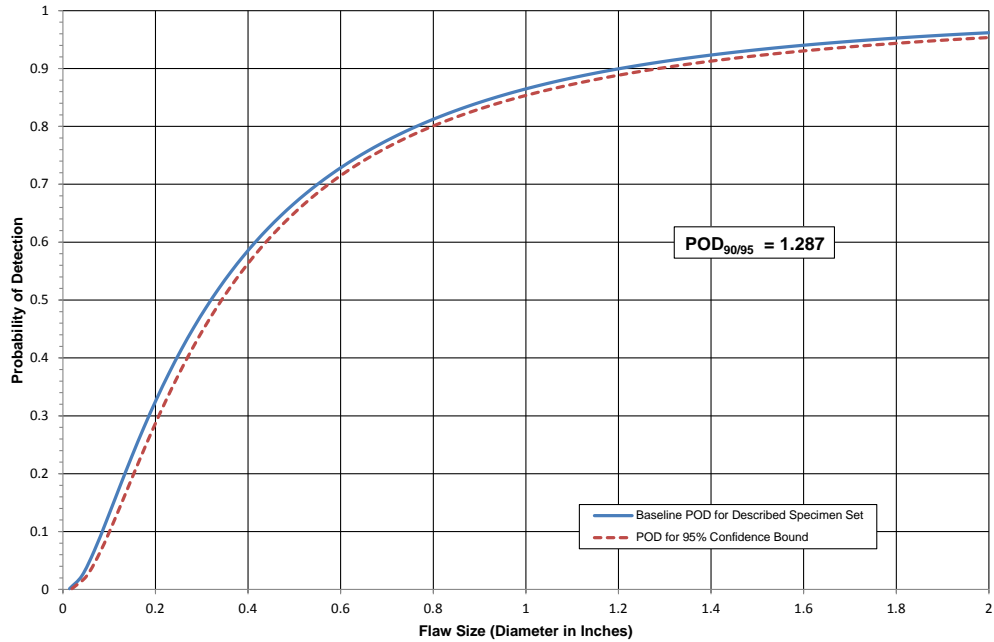


Figure 134. Cumulative POD curve for the 12–20 ply specimen set for all flaws in constant thickness and CG regions for all inspectors (27) (PE-UT method)

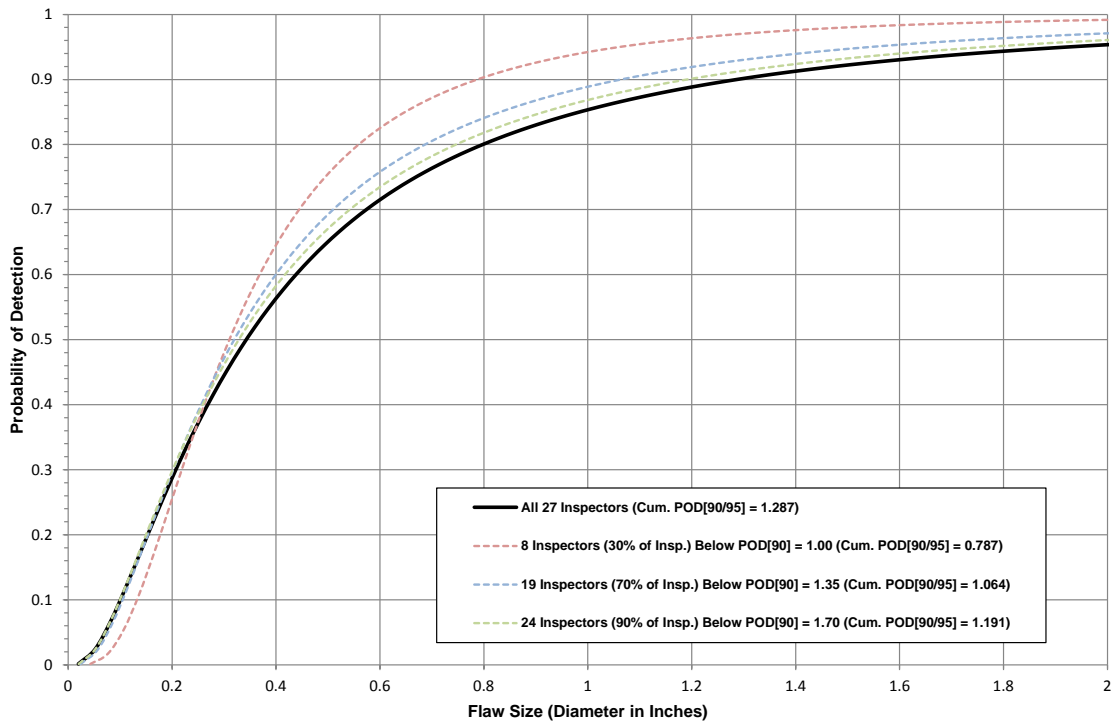


Figure 135. Cumulative POD curve comparison of the performance brackets for the 12–20 ply specimen set for all flaws in constant thickness and CG regions (PE-UT method)

The overall POD values were analyzed further to study the flaw detection performance within specific composite construction regions in the test specimen set. Figure 136 shows the POD curve representing inspectors' performance in the constant thickness regions only. The constant thickness regions are defined as regions that have no taper and no substructure; they maintain a constant laminate thickness. The $POD_{[90/95]} = 0.80''$ for constant thickness geometry regions indicates a better performance compared to the overall cumulative $POD_{[90/95]} = 1.29''$, when the CG regions are also included in the calculation. This result clearly shows the inspection challenge associated with the CG regions. A complementary set of results were determined using the inspection results from only the CG construction scenarios. Figure 137 shows the POD curve representing inspectors' performance in the CG regions only. The CG regions are defined as regions containing a taper, substructure (secondarily bonded), curved portion, fasteners, or laminate over honeycomb. The $POD_{[90/95]} = 1.493''$ for the CG regions is a poorer performance than the cumulative $POD_{[90/95]} = 1.29''$, when the constant thickness regions are also included in the calculation. This shows that the CG regions are a major factor in driving up the overall cumulative 12–20 ply POD value. Only 25% of the flaws in the fastener regions were detected and only 51% of the flaws were detected in the substructure regions. Consider the fact that 43% of all the flaws in the CG data set are in the substructure and fastener regions and it can be seen how poor performance in these two construction areas will greatly affect the overall flaw detection performance in the CG set. The substructure and fastener regions pinpoint the largest contributing factor in the CG POD value, as well as the overall cumulative POD value. Improved flaw detection in these areas, through the use of better inspection techniques and possibly specialized training, could significantly reduce the overall cumulative POD value.

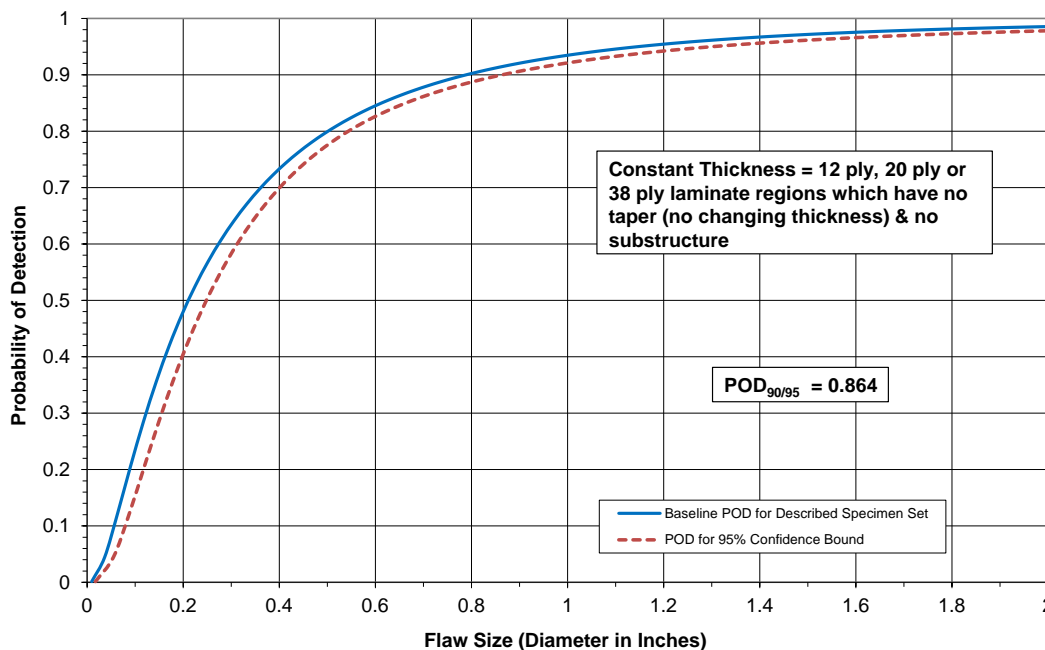


Figure 136. Cumulative POD curve for the 12–20 ply specimen set for flaws in the constant thickness region only (all inspectors; PE-UT method)

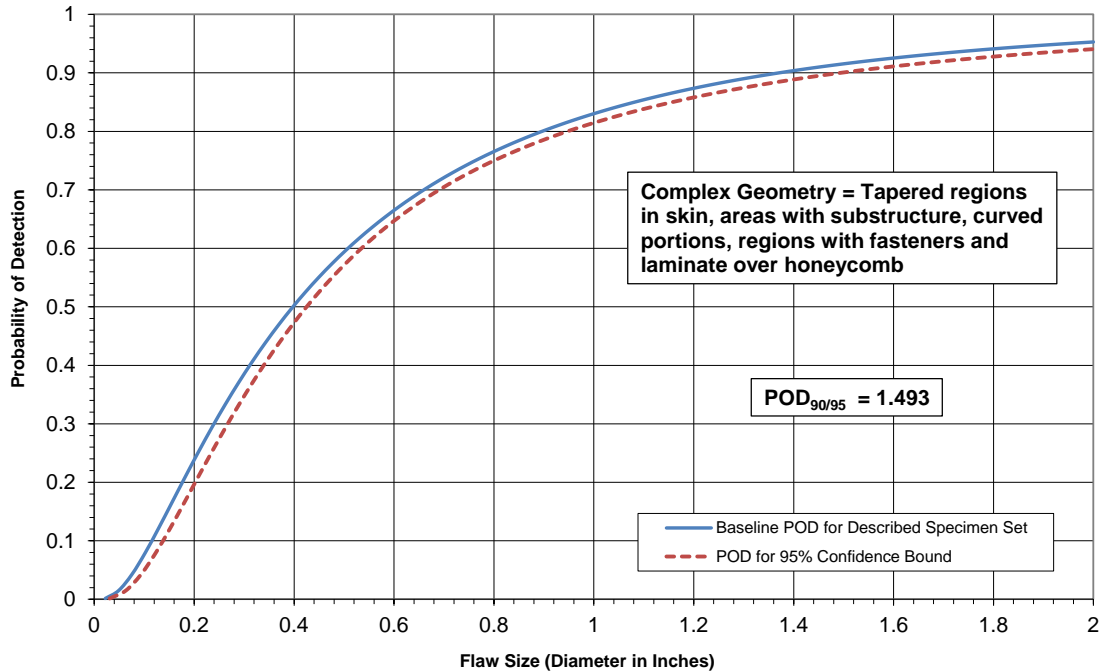


Figure 137. Cumulative POD curve for the 12–20 ply specimen set for flaws in the CG regions only (all inspectors; PE-UT method)

The experiment monitors recorded the various methods that inspectors used to ensure inspection area coverage. Monitor notes determined if 100% surface coverage was achieved. Some inspectors covered the inspection area with their UT transducers using a pure freehand approach (i.e., no guides or markings on the panels). Some inspectors divided the inspection surface into quadrants to reduce freehand coverage errors. Some inspectors used a series of tick marks, often placed at 0.5" or 1" intervals, to divide the inspection surface into a number of rows and columns. Some inspectors used flexible straight edges to guide their transducer movement. The different surface coverage techniques that were observed fall into four categories. The POD results produced by each of these inspection coverage methods were calculated separately and are shown in figure 138 along with the corresponding $POD_{[90/95]}$ values. The method that produced the lowest (best) POD level was when inspectors (seven in total) made tick marks for spacing and used a straight edge on all panels throughout the experiment. This produced a $POD_{[90/95]} = 1.055''$ which is an 18% improvement compared to the overall cumulative 12–20 ply $POD_{[90/95]}$ value of 1.29". The poorest performing coverage method was when inspectors (five in total) used the freehand method on all panels throughout the experiment. This produced a $POD_{[90/95]} = 2.390''$, which is an 86% decrease in performance compared to the cumulative 12–20 ply $POD_{[90/95]}$ value.

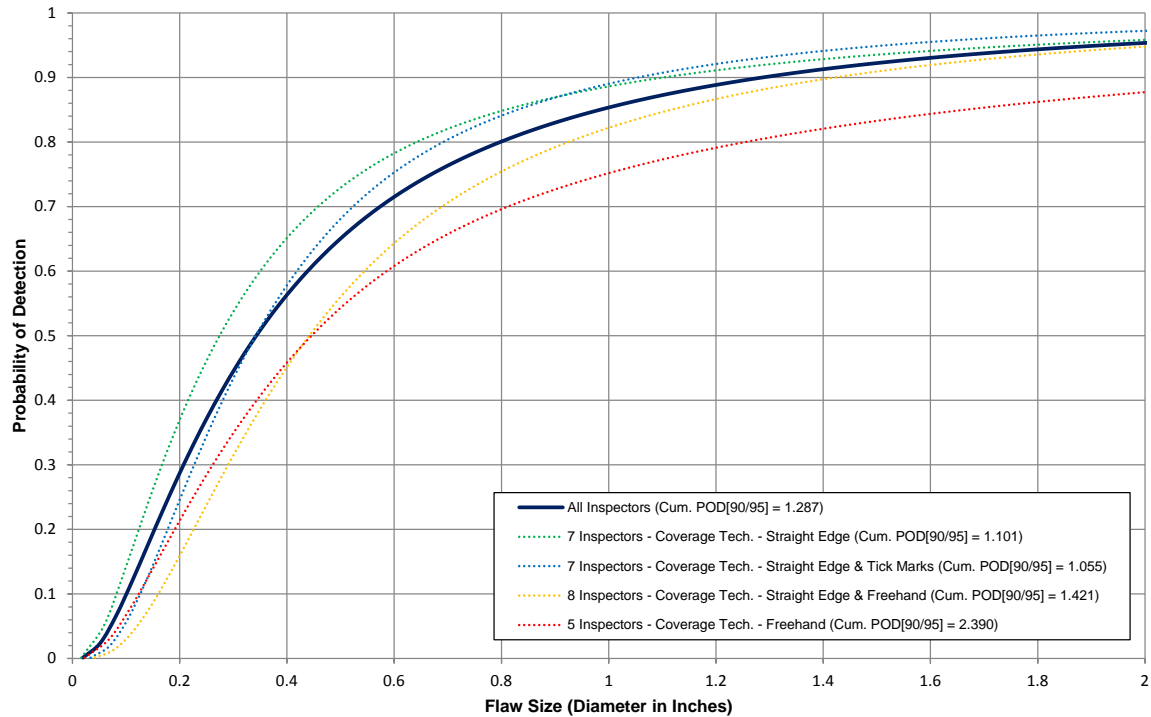


Figure 138. Cumulative POD curve comparison of different surface coverage techniques for the 12–20 ply specimen set for all flaws in constant thickness and CG regions (all inspectors (27); PE-UT method)

Table 8 summarizes the number of false calls made by each inspector. This table shows the number of false calls made by each inspector for the 12–20 ply specimen set and lists the sizing category that incorporates each false call. The average number of false calls made was 4.4 false calls per inspector (34 ft² inspection area), with an average of one false call per 7.73 ft² of inspection area. Note that the majority of false calls were made in the CG regions. Table 9 shows the false call data when false calls of less than 0.25 in.² (i.e., very small items) were removed from the calculations. Table 9 also shows the resulting average number of false calls were reduced to 2.4 false calls per inspector (34 ft² inspection area) with an average of one false call per 14.17 ft² of inspection area. Therefore, the overall false call rate was determined to be very low.

Table 8. Inspection false call table for the 12–20 ply specimen set (all inspectors; pulse echo method)

Inspection False Calls for 12–20 Ply Specimen Set – All Inspectors – PE-UT																													
Configuration/Sizing (in. ²)	Insp. A	Insp. B	Insp. C	Insp. D	Insp. E	Insp. F	Insp. G	Insp. H	Insp. I	Insp. J	Insp. K	Insp. L	Insp. M	Insp. N	Insp. O	Insp. P	Insp. Q	Insp. R	Insp. S	Insp. T	Insp. U	Insp. V	Insp. W	Insp. X	Insp. Y	Insp. Z	Insp. AA	Total	Avg.
Constant Thickness																													
0–.25	1	1	0	0	0	0	0	0	0	0	0	0	0	0	0	0	4	0	1	0	0	0	1	0	0	0	0	8	0.3
.26–.75	0	0	0	0	0	0	0	0	0	1	0	0	0	0	0	0	0	0	0	0	0	0	0	0	0	0	0	1	0.0
.76–1.25	0	0	0	0	0	0	0	0	0	0	0	0	0	0	0	0	0	0	0	0	0	0	0	1	0	0	0	1	0.0
1.26–2.00	0	0	0	0	0	0	0	0	0	0	0	0	0	0	0	0	0	0	0	0	0	0	0	0	0	0	0	0	0.0
>2.00	0	0	0	0	0	0	0	0	0	0	0	0	0	1	0	0	0	0	0	0	0	0	0	0	0	0	0	1	0.0
Constant Thickness Total	1	1	0	0	0	0	0	0	0	1	0	0	0	1	0	4	0	1	0	0	0	1	1	0	0	0	0	11	0.4
CG																													
0–.25	3	9	0	0	1	1	0	0	1	2	6	0	0	1	2	3	7	2	1	0	0	0	1	4	4	0	0	48	1.8
.26–.75	3	1	0	1	0	0	0	0	1	3	0	0	0	5	1	0	2	3	5	3	0	0	2	0	1	0	0	31	1.1
.76–1.25	0	1	0	1	0	0	2	0	0	0	0	0	0	5	3	0	0	0	1	0	0	0	0	1	1	0	0	15	0.6
1.26–2.00	1	1	0	0	0	0	1	0	0	1	0	0	0	1	0	0	0	1	0	0	0	0	0	0	0	0	0	6	0.2
>2.00	0	0	0	0	0	2	3	0	0	0	0	0	0	1	3	0	0	0	0	0	0	0	0	0	0	0	0	9	0.3
CG Total	7	12	0	2	1	3	6	0	2	6	6	0	0	13	9	3	9	6	7	3	0	0	3	5	6	0	0	109	4.0
Total (All Flaws)	8	13	0	2	1	3	6	0	2	7	6	0	0	13	10	3	13	6	8	3	0	0	4	6	6	0	0	33	4.4
1 False Call on Average Per 7.73 ft ² of Inspection Area																													

Table 9. Inspection false call table with false calls that are below 0.25 in² in size removed for the 12–20 ply specimen set (all inspectors; pulse echo method)

Inspection False Calls for 12–20 Ply Specimen Set – All Inspectors – PE-UT (False Calls that are below 0.25 in ² in size have been removed)																														
Configuration/Sizing (in. ²)	Insp. A	Insp. B	Insp. C	Insp. D	Insp. E	Insp. F	Insp. G	Insp. H	Insp. I	Insp. J	Insp. K	Insp. L	Insp. M	Insp. N	Insp. O	Insp. P	Insp. Q	Insp. R	Insp. S	Insp. T	Insp. U	Insp. V	Insp. W	Insp. X	Insp. Y	Insp. Z	Insp. AA	Total	Avg.	
Constant Thickness																														
.26–.75	0	0	0	0	0	0	0	0	0	1	0	0	0	0	0	0	0	0	0	0	0	0	0	0	0	0	0	0	1	0.0
.76–1.25	0	0	0	0	0	0	0	0	0	0	0	0	0	0	0	0	0	0	0	0	0	0	0	0	1	0	0	0	1	0.0
1.26–2.00	0	0	0	0	0	0	0	0	0	0	0	0	0	0	0	0	0	0	0	0	0	0	0	0	0	0	0	0	0	0.0
>2.00	0	0	0	0	0	0	0	0	0	0	0	0	0	0	1	0	0	0	0	0	0	0	0	0	0	0	0	0	1	0.0
Constant Thickness Total	0	0	0	0	0	0	0	0	0	1	0	0	0	0	1	0	0	0	0	0	0	0	0	0	1	0	0	0	3	0.1
CG																														
.26–.75	3	1	0	1	0	0	0	0	1	3	0	0	0	5	1	0	2	3	5	3	0	0	2	0	1	0	0	31	1.1	
.76–1.25	0	1	0	1	0	0	2	0	0	0	0	0	0	5	3	0	0	0	1	0	0	0	0	1	1	0	0	15	0.6	
1.26–2.00	1	1	0	0	0	0	1	0	0	1	0	0	0	1	0	0	0	1	0	0	0	0	0	0	0	0	0	6	0.2	
>2.00	0	0	0	0	0	2	3	0	0	0	0	0	0	1	3	0	0	0	0	0	0	0	0	0	0	0	0	9	0.3	
CG Total	4	3	0	2	0	2	6	0	1	4	0	0	0	12	7	0	2	4	6	3	0	0	2	1	2	0	0	61	2.3	
Total (All Flaws)	4	3	0	2	0	2	6	0	1	5	0	0	0	12	8	0	2	4	6	3	0	0	2	2	2	0	0	17	2.4	
1 False Call on Average Per 14.17 ft ² of Inspection Area																														

Another critical element of the inspection process is the length of time it takes an inspector to scan a defined area. Table 10 shows the time it took each inspector to scan each panel and their total inspection time. The average total inspection time for the 12–20 ply specimen set was just under 15 hours, which produced an average inspection coverage rate of 2.27 ft²/hr. The lowest (i.e., quickest) total inspection time was just under 10 hours, with an average inspection coverage rate of 3.48 ft²/hr. The highest (i.e., slowest) total inspection time was just under 22 hours, with an average inspection coverage rate of 1.55 ft²/hr.

Table 10. Experiment timing summary table for the 12–20 ply specimen set (all inspectors; PE-UT method)

Experiment Timing Summary 12–20 Ply Specimen Set – All Inspectors – PE-UT												
	Specimen CT1-A	Specimen CT1-B	Specimen CT2-A	Specimen CT2-B	Specimen ST1U-A	Specimen ST1L-A	Specimen ST2U-A	Specimen ST2L-A	Specimen BN1	Specimen BN2	Specimen BN3	Total Insp. Time (hr:min)
Inspector A	1:15	0:44	0:35	1:03	1:09	1:53	1:03	1:39	4:13	2:23	3:14	19:11
Inspector B	0:37	0:29	0:44	0:54	2:49	1:14	1:29	0:56	2:59	3:26	3:14	18:51
Inspector C	0:38	0:43	0:54	0:54	1:07	1:02	1:09	0:53	1:58	2:29	2:37	14:24
Inspector D	1:21	0:44	0:26	1:09	1:37	1:58	1:57	1:56	2:37	2:19	1:53	17:57
Inspector E	1:04	1:10	0:57	1:11	1:03	0:23	2:16	1:06	3:02	0:59	1:11	14:22
Inspector F	0:50	1:20	1:15	1:05	3:05	1:40	2:20	1:50	2:40	1:35	1:50	19:30
Inspector G	1:20	0:51	0:54	1:20	1:41	1:25	1:09	1:12	3:35	1:51	2:14	17:32
Inspector H	0:41	0:30	0:36	0:25	1:54	0:59	0:55	1:17	1:27	2:06	1:21	12:11
Inspector I	0:50	0:34	0:35	0:45	0:54	1:06	1:34	1:11	2:45	1:12	2:06	13:32
Inspector J	1:01	0:52	0:58	0:50	2:05	1:39	1:41	1:51	2:52	2:07	2:08	18:04
Inspector K	1:11	1:12	0:42	1:02	2:36	2:05	2:10	3:04	3:13	2:22	2:22	21:59
Inspector L	1:18	0:41	0:41	0:55	2:33	1:28	1:21	1:29	1:28	1:52	1:36	15:22
Inspector M	0:36	0:24	0:26	0:31	1:08	1:12	1:35	1:38	2:05	1:53	1:39	13:07
Inspector N	1:13	1:00	0:45	0:34	1:47	1:21	1:45	1:17	1:44	1:41	2:34	15:41
Inspector O	0:40	1:05	0:35	0:38	0:57	1:34	1:02	2:15	1:32	1:54	1:30	13:42
Inspector P	0:31	0:22	0:36	0:36	1:45	0:46	0:59	1:04	1:50	1:45	2:16	12:30
Inspector Q	0:58	0:40	1:07	0:43	1:08	1:14	0:50	1:16	1:32	2:13	1:50	13:31
Inspector R	1:30	1:28	1:14	0:51	1:40	1:22	1:31	1:24	1:09	1:34	2:05	15:48
Inspector S	0:31	0:23	0:16	0:22	0:42	0:38	0:42	1:14	1:18	1:33	2:07	9:46
Inspector T	0:47	0:31	0:33	0:21	1:15	0:59	1:13	0:54	1:43	1:21	0:54	10:31
Inspector U	0:52	0:34	0:34	0:35	1:13	0:55	1:35	1:23	1:22	1:38	1:20	12:01
Inspector V	0:29	0:26	0:31	0:28	1:05	1:01	1:07	1:04	2:47	1:33	1:49	12:20
Inspector W	0:44	0:46	0:39	0:36	0:43	1:00	0:52	0:47	3:08	2:31	3:56	15:42
Inspector X	0:38	0:30	0:31	0:35	1:46	1:42	2:10	1:48	2:30	1:37	2:00	15:47
Inspector Y	0:34	0:26	0:21	0:44	1:00	1:19	1:13	1:29	1:09	1:24	2:21	12:00
Inspector Z	1:22	0:25	0:48	0:34	1:19	1:17	3:34	1:35	1:31	1:13	1:31	15:09
Inspector AA	0:49	0:52	0:54	0:52	1:19	1:01	0:53	1:19	2:09	1:22	1:43	13:13
Average Inspection Time (hr:min)	0:54	0:43	0:42	0:45	1:31	1:16	1:29	1:26	2:14	1:50	2:03	14:57
Average Inspection Coverage Rate = 2.27 ft ² /hr												

Inspector flaw calls were also graded to evaluate the accuracy of each inspector’s flaw sizing. The overall test results identified hits (i.e., calls with any amount of overlap between the call and the actual flaw location), misses (i.e., no call for an area of a known flaw), false calls (i.e., call with no overlap of a flaw), and sizing performance (i.e., the degree of overlap between experimenter calls and actual flaw areas). Table 11 summarizes the results for the overall flaw detection percentage and the associated accuracy in determining flaw size for the 12–20 ply thin laminate experiment specimen set. This table includes combined data for all inspectors and all flaws in both the constant thickness and CG regions. Note that for the 12–20 ply specimen set, 76% of all flaws were detected (2766 of 3645 flaws). The flaw sizing performance shows that 38% of the detected flaws were sized properly (5 category for 100% coverage). Twenty-four percent of the flaws were sized in the 76%–99% coverage category and 16% of the flaws were sized in the 51%–75% coverage category. Therefore, 78% of the detected flaws were sized with 51%–100% accuracy. Table 11 also shows a breakdown of percent detection based on flaw size. For example, 100% of the 2" flaws were detected, meaning all 27 inspectors found every 2" flaw in the 12–20 ply specimen set. Of the smaller flaws, only 47% of the 0.25" flaws were detected.

Table 11. Tabulated results showing overall flaw detection percentage and accuracy in determining flaw size for the 12–20 ply specimen set for all flaws in constant thickness and CG regions (all inspectors; PE-UT method)

Overall Flaw Detection Percentage & Accuracy in Determining Flaw Size 12–20 Ply Specimen Set – All Inspectors – All Flaws (Constant Thickness & CG)							
Accuracy in Sizing the Flaws That Were Detected (2766 Total Flaws Detected)						Flaw Detection Percentage (3645 Total Flaws)	
Flaw Size	5 (100%)	4 (76%–99%)	3 (51%–75%)	2 (25%–50%)	1 (< 25%)	Flaw Size	Percent Detected
0.25	57%	9%	7%	10%	16%	0.25	47%
0.50	40%	16%	12%	18%	15%	0.50	63%
0.75	42%	23%	16%	14%	5%	0.75	78%
1.00	35%	26%	19%	13%	6%	1.00	87%
1.50	29%	33%	23%	10%	6%	1.50	95%
2.00	40%	46%	11%	1%	2%	2.00	100%
Overall Sizing Performance	38%	24%	16%	13%	8%	Overall Flaw Detection	76%

6.1.2 Summary of Inspection Results for the 20–32 Ply Thick Laminate Experiment

Figure 139 shows the spread of all the individual inspector $POD_{[90]}$ curves (dashed lines) compared to the cumulative $POD_{[90]}$ curve (solid line) for all 30 inspectors who participated in the 20–32 ply thick laminate experiment. These results were produced by considering all flaws in constant thickness and CG regions. The spread shows 19 inspectors with a $POD_{[90]}$ value less than the overall cumulative $POD_{[90]} = 0.77$ " diameter flaw ($POD_{[90/95]} = 0.82$ ") and 11 inspectors with a $POD_{[90]}$ value higher than the overall cumulative $POD_{[90]}$ value. The variation within the experiment ranges from a $POD_{[90]} = 0.20$ " diameter flaw for the best performing inspector to a $POD_{[90]} = 1.70$ " diameter flaw for the worst performing inspector. The standard deviation for the

inspector $POD_{[90]}$ data set was 0.420". Figure 140 compares the maximum likelihood estimate ($POD_{[90]}$) to the POD curve that is calculated when a 90% flaw detection is combined with a 95% confidence bound ($POD_{[90/95]}$). This solid line in figure 140 provides the performance curve that the industry normally uses to measure the performance of NDI methods as deployed by representative inspectors. Figure 140 shows that the overall cumulative $POD_{[90/95]}$ for all flaws in the thick laminate experiment (i.e., 20–32 ply skins plus substructure elements) was $POD_{[90/95]} = 0.82$ " diameter flaw. When compared to the 12–20 ply thin laminate experiment, the $POD_{[90/95]}$ value for the 20–32 ply thick laminate experiment was better (i.e., lower). This is mainly due to the construction method used for this set of test panels, which involved a co-cured substructure bond line that is less attenuative and includes less "noise" in the signals than the secondarily bonded substructure (i.e., film adhesive bonding) that was used in most of the thin laminate experiment test specimens. Furthermore, the test specimens for the thick laminate experiment did not contain curvature, fasteners, sealed joints, or skin over honeycomb substructure. This eliminated some of the deployment, human factor, and signal interpretation challenges that were present in the thin laminate experiment. Finally, it should be noted that the 20–32 ply specimen set included 12 ft² of inspection area, whereas the 12–20 ply specimen set included 34 ft² of inspection area. Therefore, inspector fatigue was less of an issue in the thick laminate experiment.

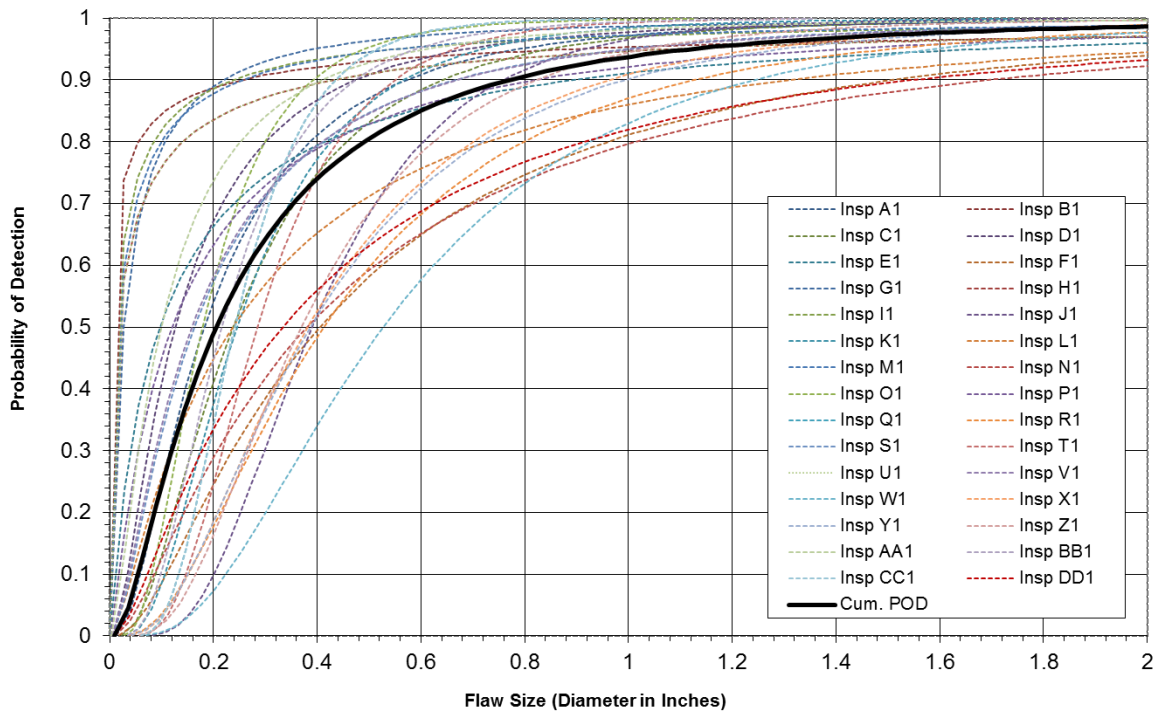


Figure 139. Individual and cumulative POD curve comparison for the 20–32 ply specimen set for all flaws in constant thickness and CG regions (all inspectors; PE-UT method)

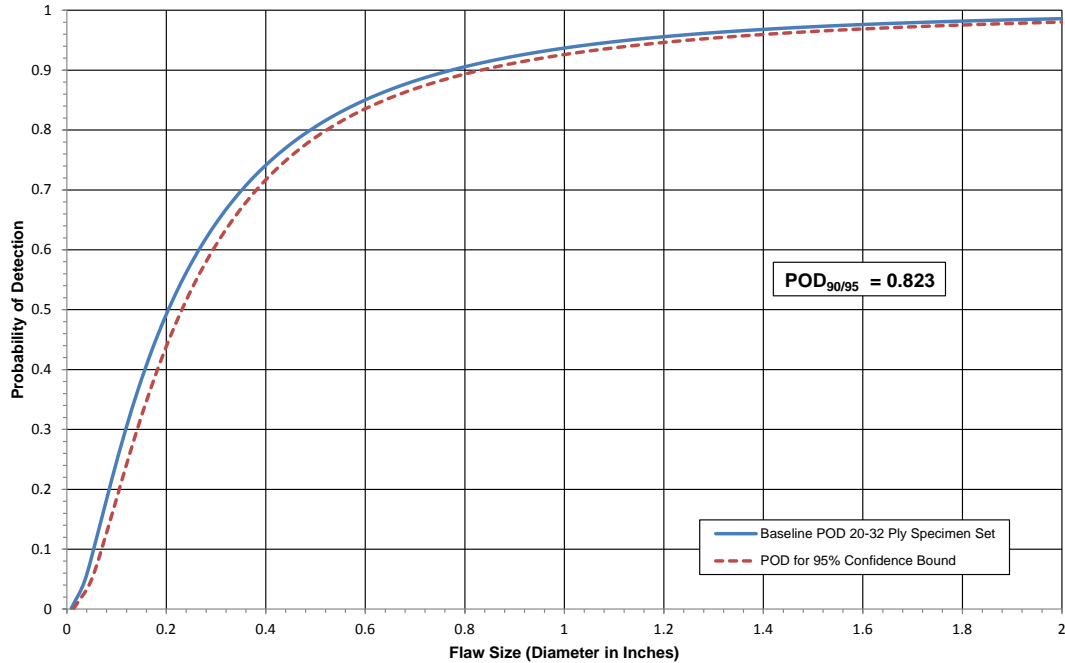


Figure 140. Cumulative POD curve for the 20–32 ply specimen set for all flaws in constant thickness and CG regions (all inspectors (30); PE-UT method)

The use of other performance brackets to assess POD is shown in figure 141. Performance brackets were used to place inspectors into groups and then calculate the resulting $POD_{[90/95]}$ for each performance bracket. These performance brackets utilized the inspectors that fell into the 40, 60, and 80 percentile categories. The inspectors that fell into the 40 percentile group (12 inspectors, each having a $POD_{[90]}$ less than 0.55") produced a 42% improvement to $POD_{[90/95]} = 0.48$ " diameter flaw value compared to the overall cumulative $POD_{[90/95]} = 0.82$ " diameter flaw. The 60 percentile group (18 inspectors, each having a $POD_{[90]}$ less than 0.75") produced a 34% improvement with a $POD_{[90/95]} = 0.54$ " diameter flaw. The 80 percentile group (24 inspectors, each having a $POD_{[90]}$ less than 1.00") showed a 20% improvement, with a $POD_{[90/95]} = 0.66$ " diameter flaw. These performance brackets might be useful to airlines and MROs that can judge where their inspectors fall within the brackets and the resulting performance they will obtain from their inspectors. The results in figure 141 also reveal the degree of inspection improvements that are possible if inspectors can shift their performance from the higher (i.e., worse) performance brackets to the lower (i.e., better) performance brackets. This shift in performance can be brought about by improved or more extensive composite inspection training or through a number of other measures that are described in detail in [4].

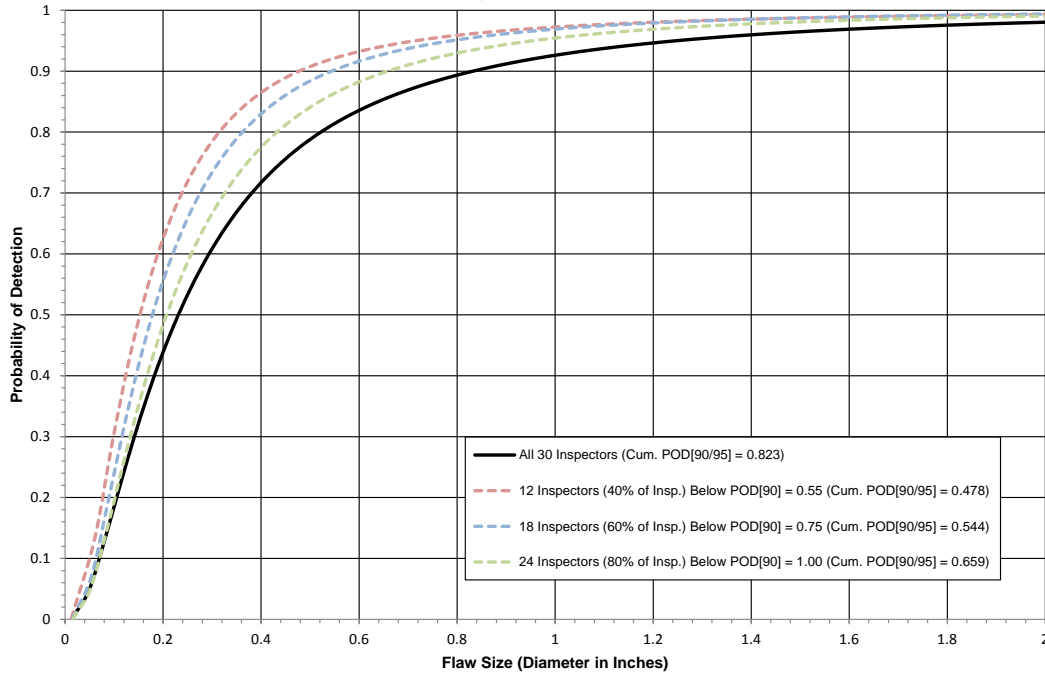


Figure 141. Cumulative POD curve performance brackets for the 20–32 ply specimen set for all flaws in constant thickness and CG regions (PE-UT method)

The overall POD values were analyzed further to study the flaw detection performance within specific composite construction regions in the test specimen set. Figure 142 shows the POD curve representing inspectors' performance in the constant thickness regions, representing only 32-ply constant thickness. The constant thickness regions for this specimen set are defined as regions that have no taper and no substructure such that they maintain a constant laminate thickness. The $POD_{[90/95]} = 0.74$ " for constant thickness geometry regions indicates a better performance compared to the overall $POD_{[90/95]} = 0.82$ ", when the CG regions are also included in the calculation. A complementary set of results was determined using the inspection results from only the CG construction scenarios. Figure 143 shows the POD curve representing inspectors' performance in the CG regions only. The CG regions for this specimen set are defined as regions containing a taper or substructure (no curved portions, fasteners, or laminate over honeycomb are included in this specimen set). The $POD_{[90/95]} = 0.93$ " for the CG regions is a slightly poorer performance than the overall $POD_{[90/95]} = 0.82$ ", when the constant thickness regions are also included in the calculation. This shows that the CG regions are a factor in driving up the overall cumulative 20–32 ply POD value.

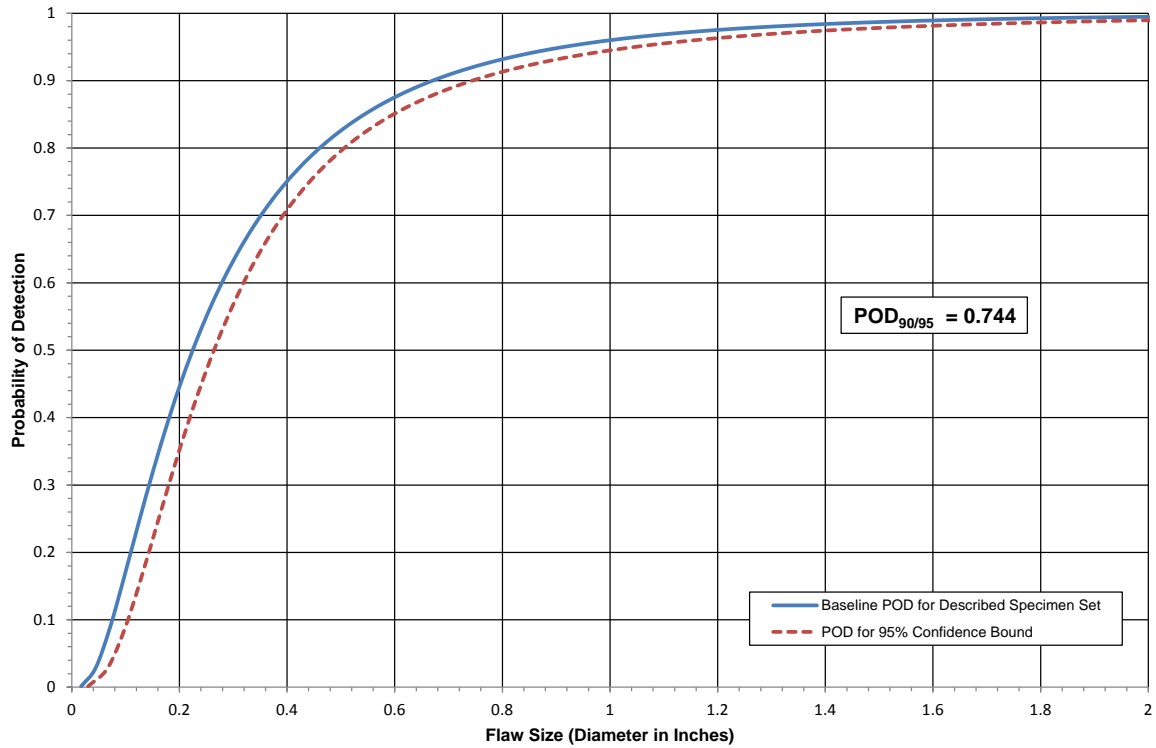


Figure 142. Cumulative POD curve for the 20–32 ply specimen set for flaws in the constant thickness regions only (32-ply; all inspectors; PE-UT method)

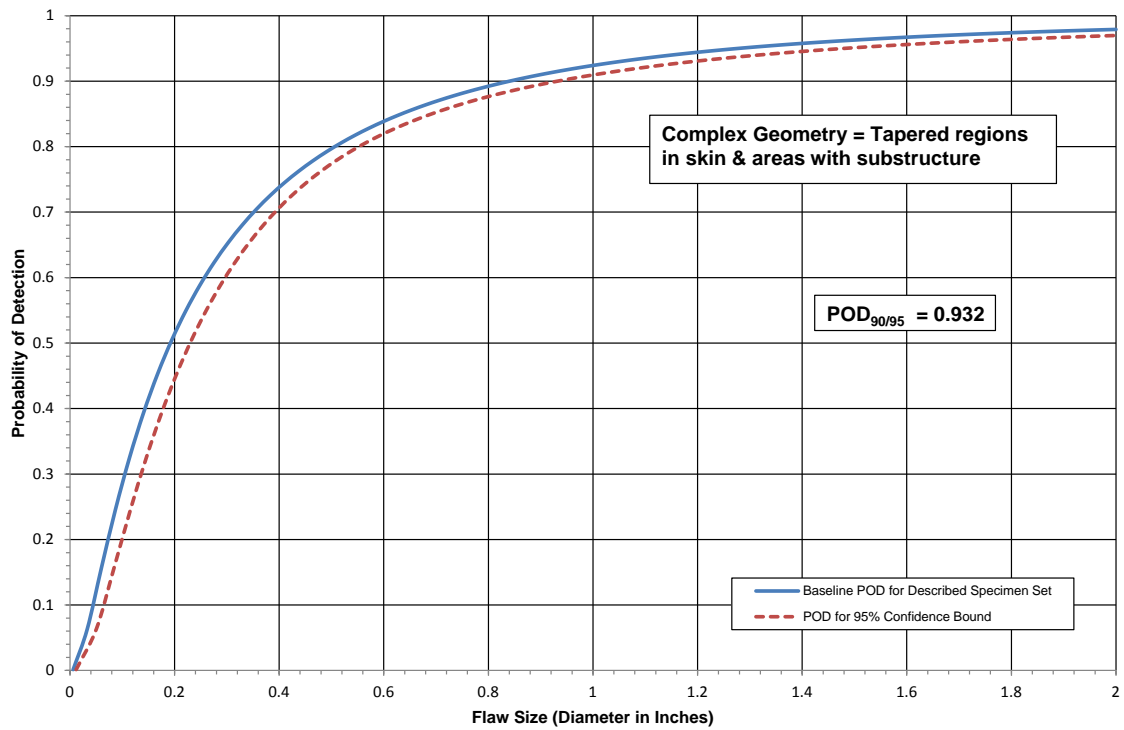


Figure 143. Cumulative POD curve for the 20–32 ply specimen set for flaws in the CG regions only (all inspectors; PE-UT method)

The experiment monitors also recorded the various methods that inspectors used to ensure inspection area coverage for the 20–32 ply thick laminate experiment. Some inspectors covered the inspection area with their UT transducers using a pure freehand approach (i.e., no guides or markings on the panels). Some inspectors divided the inspection surface into quadrants to reduce freehand coverage errors. Some inspectors used a series of tick marks, often placed at 0.5" or 1" intervals, to divide the inspection surface into a number of rows and columns. Some inspectors used flexible straight edges to guide their transducer movement. The different surface coverage techniques that were observed fall into four categories. The POD results produced by each of these inspection coverage methods were calculated separately and are shown in figure 144 along with the corresponding $POD_{[90/95]}$ values. The method that produced the lowest (i.e., best) POD level was when inspectors used a straight edge on all panels throughout the experiment (11 inspectors), achieving a $POD_{[90/95]} = 0.62$ " diameter flaw. This produced a 26% improvement compared to the overall cumulative 20–32 ply $POD_{[90/95]}$ value of 0.83". The poorest performing coverage method was when inspectors used the freehand method on all panels throughout the experiment (eight inspectors). This produced a $POD_{[90/95]} = 1.35$ ", which is a 62% decrease in performance compared to the overall cumulative 20–32 ply $POD_{[90/95]}$ value.

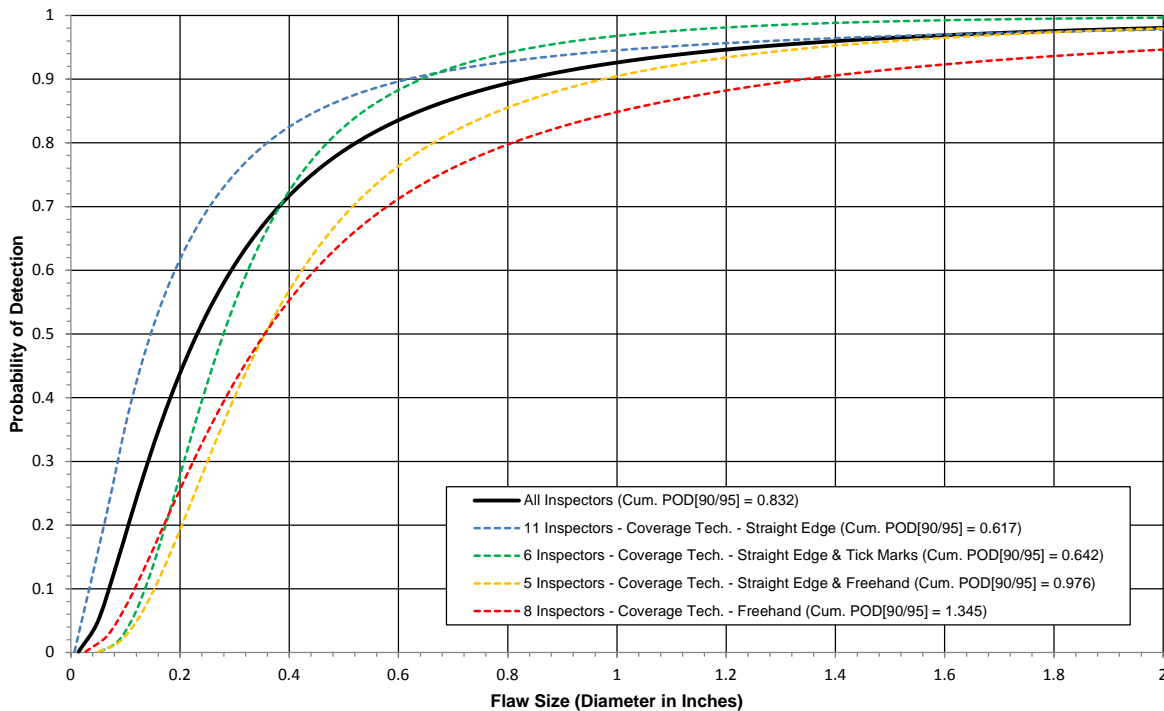


Figure 144. Cumulative POD curve comparison of different surface coverage techniques for the 20–32 ply specimen set for all flaws in constant thickness and CG regions (all inspectors (30); PE-UT method)

Table 12 shows the number of false calls made by each inspector for the 20–32 ply specimen set and lists the sizing category that incorporates each false call. The average number of false calls made was determined to be 1.1 false calls per inspector (12 ft² inspection area), with an average of one false call per 10.91 ft² of inspection area. Note that the majority of false calls were made in the CG regions. Table 13 shows the false call data when false calls of less than 0.25 in.²

(i.e., very small items) were removed from the calculations. This table shows that the resulting average number of false calls are reduced to 0.3 false calls per inspector (12 ft² inspection area), with an average of one false call per 40 ft² of inspection area. Therefore, the overall false call rate was determined to be very low.

Table 12. Inspection false call table for the 20–32 ply specimen set (all inspectors; pulse echo method)

Inspection False Calls for 20–32 Ply Specimen Set – All Inspectors – PE-UT																																
Configuration/Sizing (in. ²)	Insp. A1	Insp. B1	Insp. C1	Insp. D1	Insp. E1	Insp. F1	Insp. G1	Insp. H1	Insp. I1	Insp. J1	Insp. K1	Insp. L1	Insp. M1	Insp. N1	Insp. O1	Insp. P1	Insp. Q1	Insp. R1	Insp. S1	Insp. T1	Insp. U1	Insp. V1	Insp. W1	Insp. X1	Insp. Y1	Insp. Z1	Insp. AA1	Insp. BB1	Insp. CC1	Insp. DD1	Total	Avg.
Constant Thickness																																
0–.25	2	0	0	0	1	1	0	0	1	0	0	0	0	0	1	0	0	0	1	0	1	0	1	9	0	0	0	0	0	1	19	0.6
.26–.75	0	0	0	0	1	0	0	0	0	0	0	0	0	0	0	0	0	0	2	0	0	0	0	0	0	0	1	0	0	4	0.1	
.76–1.25	0	0	0	0	0	0	0	0	0	0	0	0	0	0	0	2	0	0	0	0	0	0	0	0	0	0	0	0	0	2	0.1	
1.26–2.00	0	0	0	0	0	0	0	0	0	0	0	0	0	0	0	0	0	0	0	0	0	0	0	0	0	0	0	0	0	0	0	
>2.00	0	0	0	0	0	0	0	0	0	0	0	0	0	0	0	0	0	0	0	0	0	0	0	0	0	0	0	0	0	0		
Constant Thickness Total	2	0	0	0	2	1	0	0	1	0	0	0	0	0	1	2	0	0	3	0	1	0	1	9	0	0	1	0	1	25	0.8	
CG																																
0–.25	0	0	0	0	0	0	0	0	0	0	0	0	0	0	0	0	0	0	1	0	0	0	0	2	2	0	0	0	0	5	0.2	
.26–.75	0	0	0	0	0	0	0	0	0	0	0	0	0	0	0	0	0	0	1	0	0	0	0	1	0	0	0	0	0	2	0.1	
.76–1.25	0	0	0	0	0	0	0	0	0	0	0	0	0	0	0	0	0	0	0	0	0	0	0	0	0	0	0	0	0	0	0	
1.26–2.00	0	0	0	0	0	0	0	0	0	0	0	0	0	0	0	0	0	0	0	0	0	0	0	0	0	0	0	0	0	0		
>2.00	0	0	0	0	0	0	0	0	0	0	0	0	0	0	0	0	0	0	1	0	0	0	0	0	0	0	0	0	0	1	0.0	
CG Total	0	0	0	0	0	0	0	0	0	0	0	0	0	0	0	0	0	0	3	0	0	0	0	3	2	0	0	0	0	8	0.3	
Total (All Flaws)	2	0	0	0	2	1	0	0	1	0	0	0	0	0	1	2	0	0	6	0	1	0	1	12	2	0	1	0	1	33	1.1	
1 False Call on Average Per 10.91 ft ² of Inspection Area																																

Table 13. Inspection false call table with false calls that are below 0.25 in.² in size removed for the 20–32 ply specimen set (all inspectors; pulse echo method)

Inspection False Calls for 20–32 Ply Specimen Set – All Inspectors – PE-UT (false calls that are below 0.25 in. ² in size have been removed)																																
Configuration/Sizing (in. ²)	Insp. A1	Insp. B1	Insp. C1	Insp. D1	Insp. E1	Insp. F1	Insp. G1	Insp. H1	Insp. I1	Insp. J1	Insp. K1	Insp. L1	Insp. M1	Insp. N1	Insp. O1	Insp. P1	Insp. Q1	Insp. R1	Insp. S1	Insp. T1	Insp. U1	Insp. V1	Insp. W1	Insp. X1	Insp. Y1	Insp. Z1	Insp. AA1	Insp. BB1	Insp. CC1	Insp. DD1	Total	Avg.
Constant Thickness																																
.26–.75	0	0	0	0	1	0	0	0	0	0	0	0	0	0	0	0	0	0	2	0	0	0	0	0	0	0	1	0	0	0	4	0.1
.76–1.25	0	0	0	0	0	0	0	0	0	0	0	0	0	0	2	0	0	0	0	0	0	0	0	0	0	0	0	0	0	0	2	0.1
1.26–2.00	0	0	0	0	0	0	0	0	0	0	0	0	0	0	0	0	0	0	0	0	0	0	0	0	0	0	0	0	0	0	0	0.0
>2.00	0	0	0	0	0	0	0	0	0	0	0	0	0	0	0	0	0	0	0	0	0	0	0	0	0	0	0	0	0	0	0	0.0
Constant Thickness Total	0	0	0	0	1	0	0	0	0	0	0	0	0	0	2	0	0	2	0	0	0	0	0	0	0	0	1	0	0	6	0.2	
CG																																
.26–.75	0	0	0	0	0	0	0	0	0	0	0	0	0	0	0	0	0	1	0	0	0	0	1	0	0	0	0	0	0	2	0.1	
.76–1.25	0	0	0	0	0	0	0	0	0	0	0	0	0	0	0	0	0	0	0	0	0	0	0	0	0	0	0	0	0	0	0	0.0
1.26–2.00	0	0	0	0	0	0	0	0	0	0	0	0	0	0	0	0	0	0	0	0	0	0	0	0	0	0	0	0	0	0	0	0.0
>2.00	0	0	0	0	0	0	0	0	0	0	0	0	0	0	0	0	1	0	0	0	0	0	0	0	0	0	0	0	0	1	0.0	
CG Total	0	0	0	0	0	0	0	0	0	0	0	0	0	0	0	0	2	0	0	0	0	1	0	0	0	0	0	0	3	0.1		
Total (All Flaws)	0	0	0	0	1	0	0	0	0	0	0	0	0	0	2	0	0	4	0	0	0	0	1	0	0	1	0	0	9	0.3		
1 False Call on Average Per 40 ft ² of Inspection Area																																

Another critical element of the inspection process is the length of time it takes an inspector to scan a defined area. Table 14 shows the time it took each inspector to scan each panel and their total inspection time. The average total inspection time for the 20–32 ply specimen set was just over 6.25 hours, which produced an average inspection coverage rate of 1.91 ft²/hr. The lowest (i.e., quickest) total inspection time was just over two hours, with an average inspection coverage rate of 5.76 ft²/hr. The highest (i.e., slowest) total inspection time was just over 9.75 hours, with an average inspection coverage rate of 1.22 ft²/hr.

Table 14. Experiment timing summary table for the 20–32 ply specimen set (all inspectors; PE-UT method)

Experiment Timing Summary 20–32 Ply Specimen Set All Inspectors – PE-UT					
Inspector	Specimen ST32-1	Specimen ST32-2	Specimen ST32-3	Specimen ST32-4	Total Insp. Time (hr:min)
A1	1:01	1:08	1:05	1:02	4:16
B1	1:13	1:35	1:53	2:32	7:13
C1	1:28	1:51	1:03	1:20	5:42
D1	2:26	2:44	2:41	1:57	9:48
E1	1:56	1:59	2:54	1:44	8:33
F1	1:31	2:18	0:50	1:11	5:50
G1	1:35	1:43	2:30	2:10	7:58
H1	1:30	2:09	2:29	2:33	8:41
I1	0:43	1:30	1:55	0:51	4:59
J1	1:43	1:18	2:31	1:32	7:04
K1	1:02	1:08	0:53	2:10	5:13
L1	2:31	1:53	2:41	1:51	8:56
M1	1:17	3:36	2:42	2:04	9:39
N1	1:54	1:09	1:57	1:42	6:42
O1	2:02	2:17	2:50	1:57	9:06
P1	0:23	0:18	0:55	0:29	2:05
Q1	0:56	3:13	1:52	1:21	7:22
R1	1:51	1:19	1:03	1:01	5:14
S1	0:51	0:39	1:37	0:58	4:05
T1	1:17	0:53	1:12	1:31	4:53
U1	1:46	1:18	1:26	2:05	6:35
V1	0:39	1:43	1:10	1:18	4:50
W1	0:47	1:19	0:32	0:28	3:06
X1	1:21	0:34	2:26	0:49	5:10
Y1	0:39	0:35	0:55	0:42	2:51
Z1	1:11	1:44	3:08	1:28	7:31
AA1	1:03	1:21	1:48	1:40	5:52
BB1	1:39	1:45	1:19	1:32	6:15
CC1	0:53	1:51	1:50	1:15	5:49
DD1	1:33	2:05	1:33	1:40	6:51
Average Inspection Time (hr:min)	1:21	1:37	1:47	1:29	6:16
Average Inspection Coverage Rate = 1.91 ft ² /hr					

Inspector flaw calls were also graded to evaluate the accuracy of each inspector’s flaw sizing. The overall test results identified hits (i.e., calls with any amount of overlap between the call and

the actual flaw location), misses (i.e., no call for an area of a known flaw), false calls (i.e., calls with no overlap of a flaw), and sizing performance (i.e., the degree of overlap between experimenter calls and actual flaw areas). Table 15 summarizes the results for the overall flaw detection percentage and the associated accuracy in determining flaw size for the 20–32 ply thick laminate experiment specimen set. Table 15 includes combined data for all inspectors and all flaws in both the constant thickness and CG regions. Note that for the 20–32 ply specimen set, 85% of all flaws were detected (1709 of 2010 flaws). The flaw sizing performance shows that 31% of the detected flaws were sized properly (5 category for 100% coverage). Twenty-seven percent of the flaws were sized in the 76%–99% coverage category and 18% of the flaws were sized in the 51%–75% coverage category. Therefore, 76% of the detected flaws were sized with 51%–100% accuracy. Table 15 also shows a breakdown of percent detection based on flaw size. For example, 99% of the 2" flaws were detected. In this case, that represents 29 of the 30 inspectors who found every 2" flaw in the 20–32 ply specimen set (i.e., only one 2" flaw was missed by an inspector). Of the smaller flaws, 56% of the 0.25" flaws were detected.

Table 15. Tabulated results showing overall flaw detection percentage and accuracy in determining flaw size for the 20–32 ply specimen set for all flaws in constant thickness and CG regions (all inspectors; PE-UT method)

Overall Flaw Detection Percentage & Accuracy in Determining Flaw Size 20–32 Ply Specimen Set – All Inspectors – All Flaws (Constant Thickness & CG)							
Accuracy in Sizing the Flaws That Were Detected (1709 Total Flaws Detected)						Flaw Detection Percentage (2010 Total Flaws)	
Flaw Size	5 (100%)	4 (76%–99%)	3 (51%–75%)	2 (25%–50%)	1 (< 25%)	Flaw Size	Percent Detected
0.25	47%	11%	6%	7%	28%	0.25	56%
0.50	31%	21%	16%	16%	16%	0.50	84%
0.75	26%	28%	20%	20%	6%	0.75	89%
1.00	30%	30%	20%	15%	5%	1.00	91%
1.50	25%	34%	26%	11%	5%	1.50	99%
2.00	32%	45%	18%	3%	2%	2.00	99%
Overall Sizing Performance	31%	27%	18%	14%	10%	Overall Flaw Detection	85%

6.1.3 Summary of Inspection Results for the Overall Combined Solid Laminate Inspection Experiment—Combined 12–20 Ply Thin Laminate Experiment and 20–32 Ply Thick Laminate Experiment

Figure 145 shows the POD curve representing the performance of all 57 inspectors for the cumulative, combined 12–20 and 20–32 ply specimen sets. The overall POD for solid laminate composite structures is $POD_{[90/95]} = 1.13''$ diameter flaw ($POD_{[90]} = 1.07''$). This represents a POD value that is consistent with the desired OEM minimum detectable flaw size, as discussed in section 4. The cumulative POD curve comparison for the 12–20 ply thin laminate experiment ($POD_{[90/95]} = 1.29''$), the 20–32 ply thick laminate experiment ($POD_{[90/95]} = 0.82''$), and the

overall, combined specimen sets ($POD_{[90/95]} = 1.13''$) is shown in figure 146. The POD values were also analyzed for the combined specimen sets within the breakdown of specific composite construction regions. Figure 147 shows the cumulative POD curve for the combined 12–20 and 20–32 ply specimen sets for all flaws in the constant thickness regions only. The overall POD for constant thickness regions in solid laminate composite structures is $POD_{[90/95]} = 0.80''$ diameter flaw. This represents a value calculated from inspection data for all flaws in the 12-ply, 20-ply, 32-ply, and 38-ply (spar component) constant thickness regions. Figure 147 also compares the constant thickness region POD curves for the 12–20 ply thin laminate experiment, 20–32 ply thick laminate experiment, and the overall, combined specimen sets. All of the $POD_{[90/95]}$ values are quite similar and in the range of 0.75"–0.85" diameter flaw. Figure 148 shows the resulting cumulative POD curve for the combined 12–20 and 20–32 ply specimen sets for all flaws in the CG regions. The overall POD for CG regions in solid laminate composite structures is $POD_{[90/95]} = 1.34''$ diameter flaw. This represents a value calculated from inspection data for all flaws in regions containing a ply taper, substructure (co-cured and secondarily bonded), curved portions, fasteners, or laminate over honeycomb. Figure 148 also compares the CG region POD curves for the 12–20 ply thin laminate experiment, 20–32 ply thick laminate experiment, and the overall, combined specimen sets. In this case, the $POD_{[90/95]}$ values ranged from 0.93"–1.49" diameter flaw.

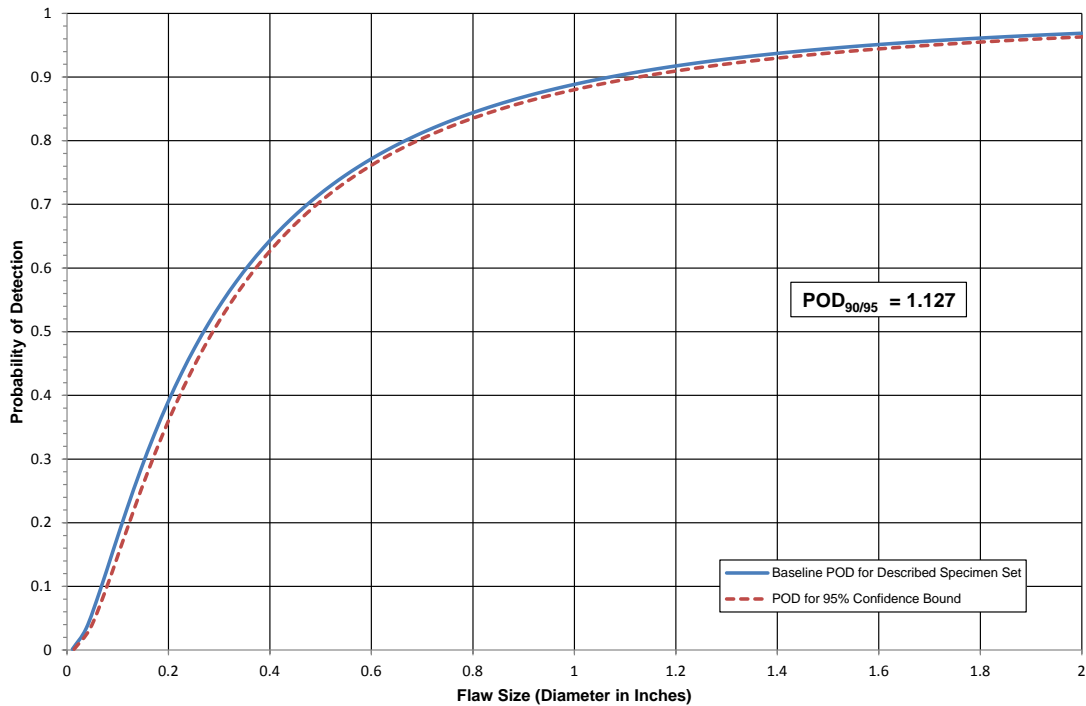


Figure 145. Cumulative POD curve for the 12–20 and 20–32 ply combined specimen sets for all flaws in constant thickness and CG regions (all inspectors [57]; PE-UT method)

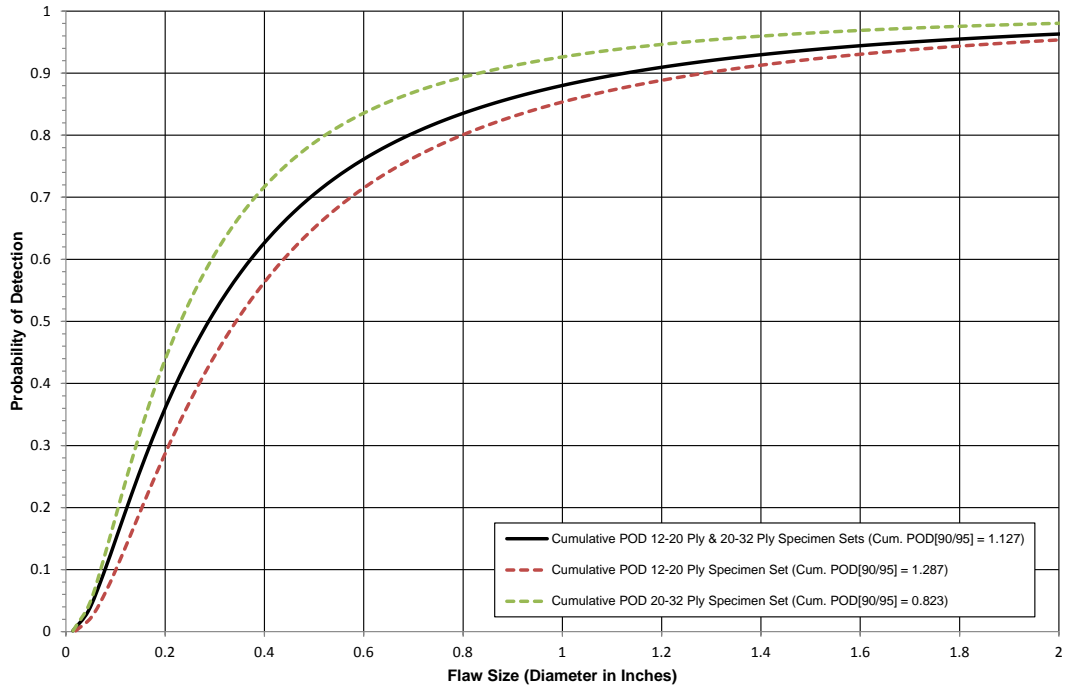


Figure 146. Cumulative POD curve comparison for the 12–20 and 20–32 ply specimen sets for all flaws in constant thickness and CG regions (all inspectors [57]; PE-UT method)

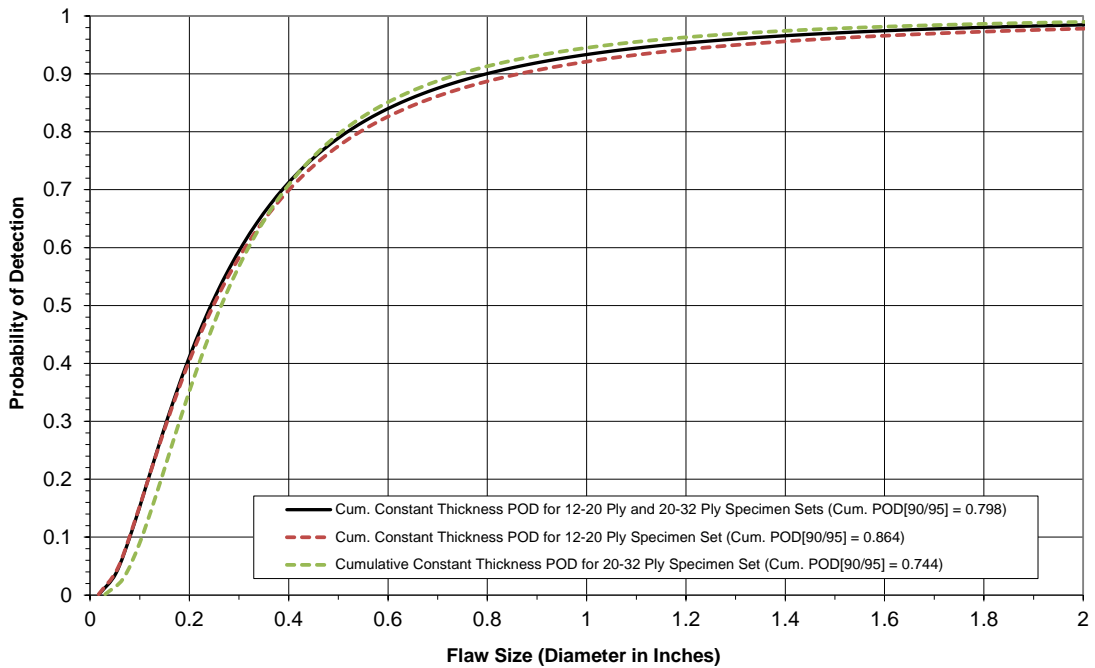


Figure 147. Cumulative POD curve comparison for the 12–20 and 20–32 ply specimen sets for all flaws in constant thickness regions only (all inspectors [57]; PE-UT method)

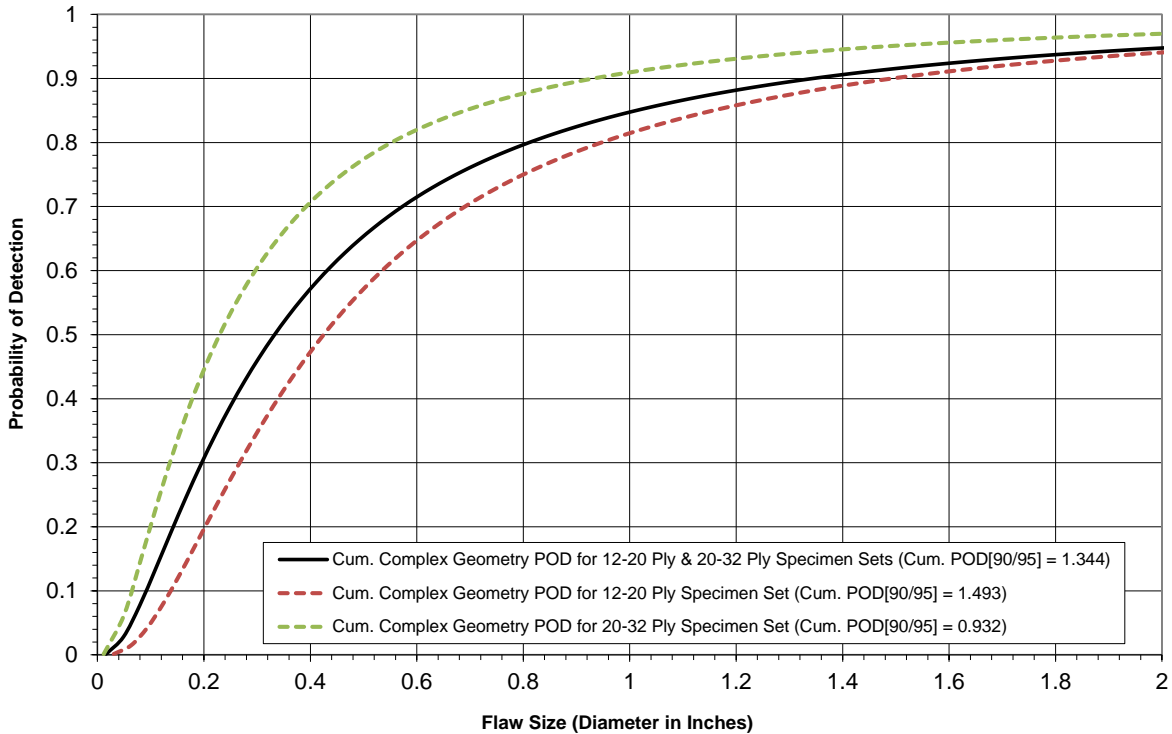


Figure 148. Cumulative POD curve comparison for the 12–20 and 20–32 ply specimen sets for all flaws in CG regions only (all inspectors [57]; PE-UT method)

The experiment monitors also recorded the various methods that inspectors used to ensure inspection area coverage for the composite laminate POD experiment. Some inspectors covered the inspection area with their UT transducers using a pure freehand approach (i.e., no guides or markings on the panels). Some inspectors divided the inspection surface into quadrants to reduce freehand coverage errors. Some inspectors used a series of tick marks, often placed at 0.5" or 1" intervals, to divide the inspection surface into a number of rows and columns. Some inspectors used flexible straight edges to guide their transducer movement. The different surface coverage techniques that were observed fall into four categories. The POD results produced by each of these inspection coverage methods were calculated separately and compared to quantify the benefits of deploying specific inspection coverage methods. These results are plotted in figure 149 along with the corresponding $POD_{[90/95]}$ values. The method that produced the lowest (i.e., best) combined POD level was when inspectors (18 in total) used a straight edge on all panels throughout both experiments. This produced a $POD_{[90/95]} = 0.89$ " diameter flaw, which is a 21% improvement compared to the cumulative combined 12–20 ply and 20–32 ply $POD_{[90/95]}$ value of 1.13" diameter flaw. The poorest performing coverage method was when inspectors (13 in total) used the freehand method on all panels throughout both experiments. This produced a $POD_{[90/95]} = 1.75$ ", which is a 55% decrease in performance compared to the overall cumulative combined 12–20 ply and 20–32 ply $POD_{[90/95]}$ value. The summary of all $POD_{[90/95]}$ values for the overall SLE (combined 12–20 ply and 20–32 ply specimen sets) is presented in table 16.

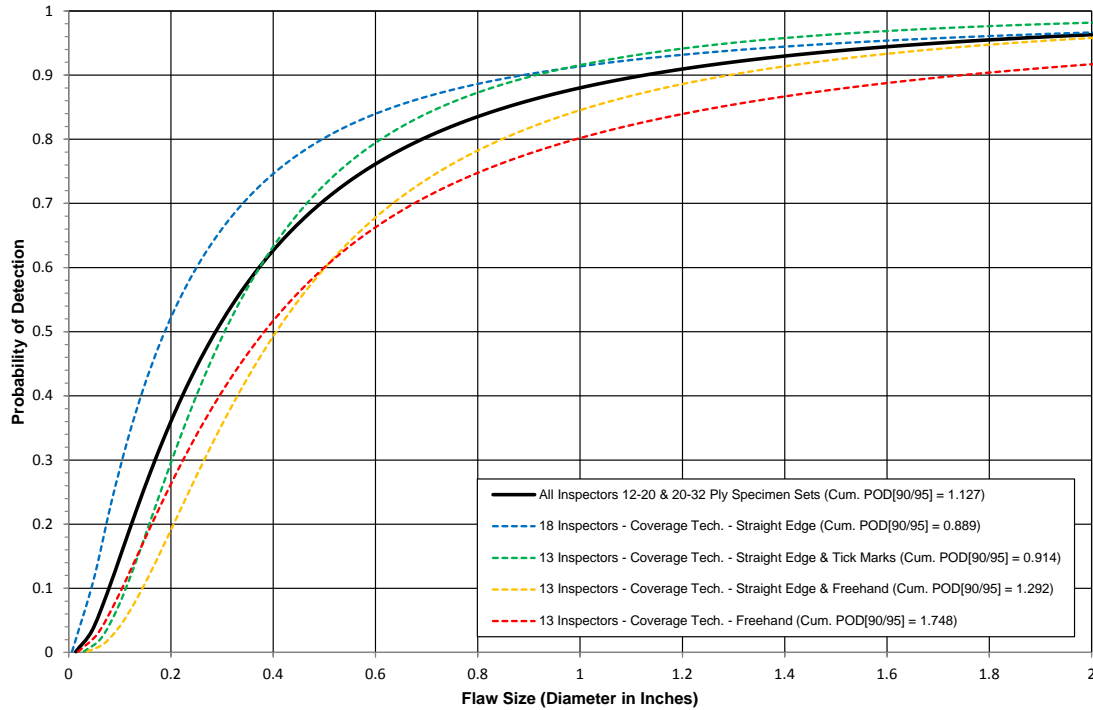


Figure 149. Cumulative POD curve comparison of different surface coverage techniques for the 12–20 and 20–32 ply specimen sets for all flaws in constant thickness and CG regions (all inspectors [57] PE-UT method)

Table 16. Cumulative POD results table for the 12–20 and 20–32 ply combined specimen sets

Cumulative POD Results Table 12–20 Ply & 20–32 Ply Specimen Sets	
Condition	POD _{90/95}
All Flaws – All Regions – All 57 Inspectors	1.127
All Flaws – All Regions – 49 Inspectors, 2 High & 2 Low Removed From Each Set	1.096
Only Flaws in Constant Thickness – All 57 Inspectors	0.798
Only Flaws in CG Regions – All 57 Inspectors	1.344
Only Flaws in Tapered Regions – All 57 Inspectors	0.779
All Flaws – All Regions – 18 Inspectors – Coverage Technique – Straight Edge	0.889
All Flaws – All Regions – 13 Inspectors – Coverage Technique – Straight Edge & Tick Marks	0.914
All Flaws – All Regions – 13 Inspectors – Coverage Technique – Straight Edge & Freehand	1.292
All Flaws – All Regions – 13 Inspectors – Coverage Technique - Freehand	1.748

6.1.4 Summary of Inspection Results for the RDCE

The SLE was used to evaluate two similar devices that are being considered for use in local, focused inspections: the Olympus RDC and GE BT devices. The following POD curves compare the performance of individual participants, which included both inspectors and A&P mechanics, for the deployment of the RDC and BT devices in the SLE. The SLE was customized, as described in section 4, to accommodate the evaluation of the RDC and BT devices. For the inspection approach that accompanies the use of either the RDC or BT device, specific, small regions were designated as focused inspection regions. These devices are not intended for wide-area inspections. Therefore, specific regions on each test specimen—some containing flaws and some containing only pristine, undamaged structure—were identified with surface markers and the experiment was completed using only the subset of inspection regions. In total, there were 140 separate inspection regions for a combined inspection area of 8.4 ft² (average of 0.06 ft² per individual region). This customized presentation of the SLE is referred to as the RDCE. All of the specimens (both thin and thick laminate) were used in the RDCE; the results provided in this section are overall results for the entire range of specimen thicknesses. Prior to conducting the RDCE, each inspector was provided with a brief training package on the RDC and BT devices. The inspectors were also allowed to get comfortable with the inspection devices through the use of the feedback specimens.

Figure 150 shows the spread of all individual inspector $POD_{[90]}$ curves (dashed lines) compared to the cumulative $POD_{[90]}$ curve (solid line) for all 20 participants in the RDCE. The participants included 10 A&P mechanics, 9 NDI inspectors, and 1 student intern (representing an untrained person). These results were produced by considering all flaws in the RDCE, including those in the constant thickness and CG regions. The spread shows 11 participants, with a $POD_{[90]}$ value less than the cumulative $POD_{[90]} = 0.75$ " diameter flaw and 9 participants with a $POD_{[90]}$ value higher than the cumulative $POD_{[90]}$ value. Overall, the result from the RDCE for all participants combined was $POD_{[90/95]} = 0.78$ " diameter flaw. The variation of results ranged from a $POD_{[90]} = 0.44$ " diameter flaw for the best performing participant to a $POD_{[90]} = 1.38$ " diameter flaw for the worst performing participant. The POD values were analyzed further to compare the flaw detection performance between the participant groups. Figure 151 compares the $POD_{[90/95]}$ cumulative curves for all inspectors and for all A&P mechanics. Both participant groups performed well, with the nine inspectors producing a cumulative $POD_{[90/95]} = 0.77$ " diameter flaw and the 10 A&P mechanics producing a cumulative $POD_{[90/95]} = 0.84$ " diameter flaw. The difference between the two POD values was less than 10%. The summary of all $POD_{[90/95]}$ values for the RDCE is presented in table 17.

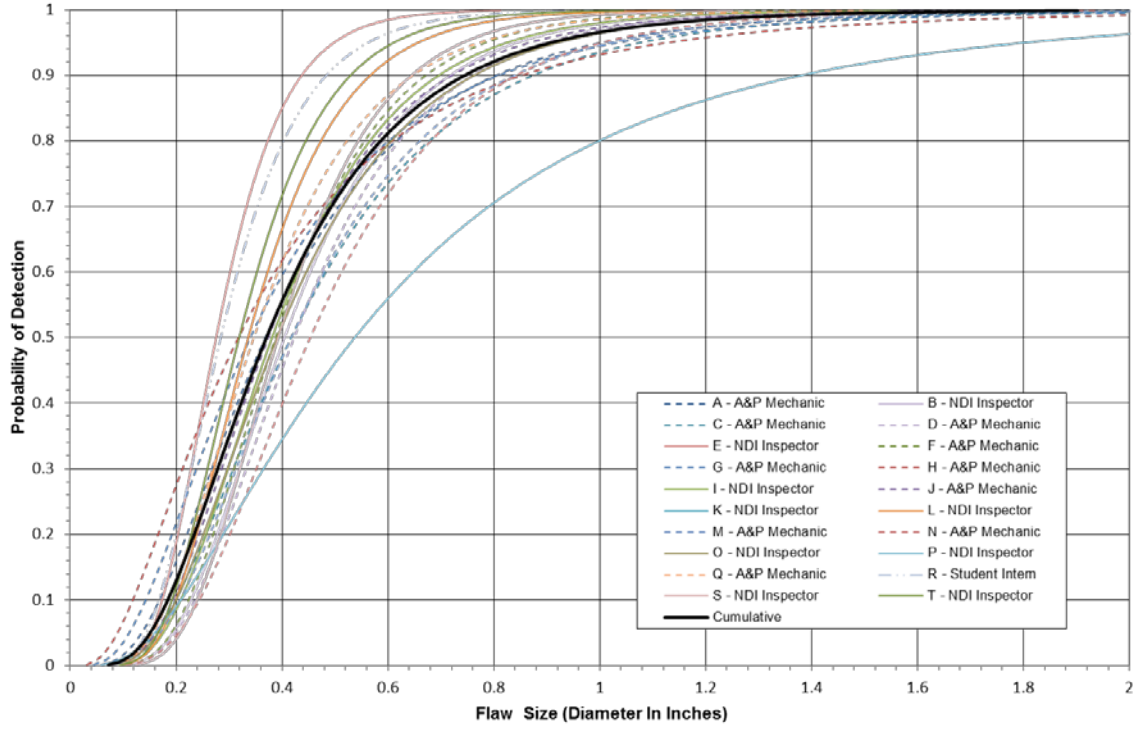


Figure 150. Individual and cumulative POD curve comparison for the RDCE specimen set for all flaws

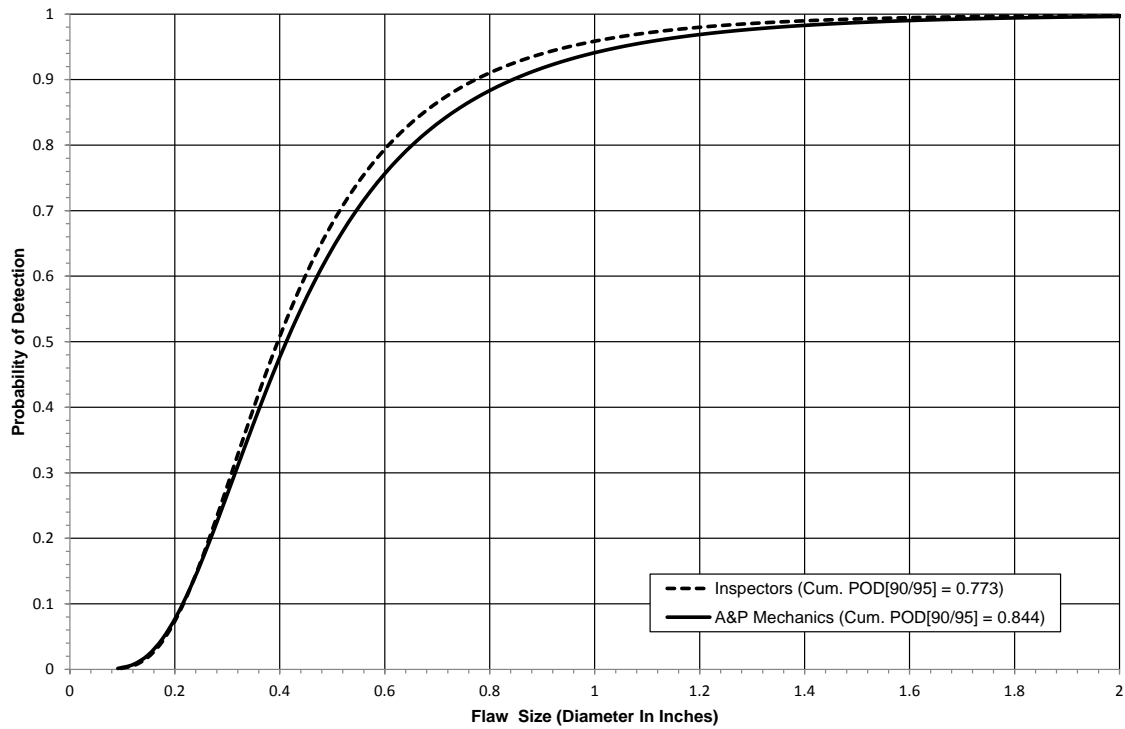


Figure 151. Cumulative POD curve comparison of all NDI inspectors and A&P mechanics for all flaws for the RDCE specimen set

Table 17. Cumulative POD results table for the RDCE specimen set

Cumulative POD Results Table – RDCE Specimen Sets	
Condition	POD _{90/95}
All Flaws – All Participants (Inspectors & A&P Mechanics, 1 Intern)	0.782
All Flaws – All NDI Inspectors (9)	0.773
All Flaws – NDI Inspectors (8) With Worst Performing Inspector Removed	0.681
All Flaws – All A&P Mechanics (10)	0.844

A false call is defined as an inspector flaw indication in an area where no flaw actually exists. However, there are manufacturing flaws that are not associated with the POD study (e.g., porosity). If an inspector made a call that correlated to an area of unintentionally high porosity, it was ignored and not deemed to be, nor designated as, a false call. Table 18 shows the number of false calls made by each participant for the RDCE specimen set and lists the sizing category that incorporates each false call. The average number of false calls made was 0.6 false calls per inspector (8.38 ft² inspection area), with an average of one false call per 13.97 ft² of inspection area. Therefore, the overall false call rate was determined to be very low.

Table 18. Inspection false call table for the RDCE specimen set (all participants; GE BT and Olympus NDT 35RDC)

Inspection False Calls for RDCE Specimen Set – All Participants – GE BT & Olympus NDT 35RDC																						
Configuration/Sizing (in. ²)	A&P A	Insp. B	A&P C	A&P D	Insp. E	A&P F	A&P G	A&P H	Insp. I	A&P J	Insp. K	Insp. L	A&P M	A&P N	Insp. O	Insp. P	A&P Q	Intern R	Insp. S	Insp. T	Total	Avg.
RDCE Specimen Set																						
0-.25	0	0	0	0	0	1	1	0	0	0	0	0	1	0	0	0	0	0	0	0	3	0.2
.26-.75	0	0	0	1	1	0	1	0	0	1	0	0	0	0	1	0	1	0	0	0	6	0.3
.76-1.25	0	0	0	2	0	0	0	0	0	0	0	0	0	0	0	0	0	0	0	0	2	0.1
1.26-2.00	0	0	0	0	0	0	0	0	0	0	0	0	0	0	0	0	0	0	0	0	0	0.0
>2.00	0	0	0	0	0	0	0	0	0	0	0	0	0	0	1	0	0	0	0	0	1	0.1
Total (All Flaws)	0	0	0	3	1	1	2	0	0	1	0	0	1	0	2	0	1	0	0	0	12	0.6
1 False Call on Average Per 13.97 ft ² of Inspection Area																						

Participant flaw calls were also graded to evaluate the accuracy of each participant’s flaw sizing. The overall test results identified hits (i.e., calls with any amount of overlap between the call and the actual flaw location), misses (i.e., no call for an area of a known flaw), false calls (i.e., call with no overlap of a flaw), and sizing performance (i.e., the degree of overlap between experimenter calls and actual flaw areas). Table 19 summarizes the results for the overall flaw detection percentage and the associated accuracy in determining the flaw size for the RDCE specimen set. The table includes combined data for all participants and all flaws. Note that for the RDCE specimen set, 81% of all flaws were detected (1294 of 1600 flaws). The flaw sizing performance shows that 13% of the detected flaws were sized properly (5 category for 100% coverage). Thirty-two percent of the flaws were sized in the 76%–99% coverage category and 30% of the flaws were sized in the 51%–75% coverage category. Therefore, 75% of the detected flaws were sized with 51%–100% accuracy. Table 19 also shows a breakdown of percent detection based on flaw size. For example, 98% of the 2" flaws were detected. Of the smaller flaws, only 23% of the 0.25" flaws were detected.

Table 19. Tabulated results showing overall flaw detection percentage and accuracy in determining flaw size for the RDCE specimen set for all flaws (all participants; GE BT and Olympus NDT 35RDC)

Overall Flaw Detection Percentage & Accuracy in Determining Flaw Size RDCE – All Flaws – All Participants							
Accuracy in Sizing the Flaws That Were Detected (1294 Total Flaws Detected)						Flaw Detection Percentage (1600 Total Flaws)	
Flaw Size	5 (100%)	4 (76%–99%)	3 (51%–75%)	2 (25%–50%)	1 (< 25%)	Flaw Size	Percent Detected
0.25	31%	22%	7%	7%	33%	0.25	23%
0.50	18%	19%	24%	24%	15%	0.50	68%
0.75	17%	26%	28%	22%	7%	0.75	95%
1.00	8%	37%	31%	19%	4%	1.00	97%
1.50	7%	36%	45%	11%	1%	1.50	98%
2.00	12%	59%	27%	3%	0%	2.00	98%
Overall Sizing Performance	13%	32%	30%	18%	7%	Overall Flaw Detection	81%

6.2 INSPECTION PERFORMANCE RESULTS FOR PHASED ARRAY AND LINEAR ARRAY UTs

6.2.1 Results for the Test Specimens Inspected by Olympus OmniScan

Figures 152–154 show the OmniScan device with a PA-UT probe and the deployment of the equipment on the various SLE test specimens. Inspections were completed with the Olympus OmniScan PA-UT inspection device connected to a 3.5 MHz, 64 element array probe. The transducer was deployed in a 26.2 mm delay line Aqualene wedge as shown in figure 152. Sample C-scan images produced from the OmniScan PA-UT inspection of the SLE test specimens are shown in figures 155–157. Both amplitude and time-of-flight images were used to detect the hidden flaws and various gates were also used to detect the range of flaws at different

depths within the specimens. Note the substructure flaws imaged in the C-scans generated by gates set for deeper flaw detection.



Figure 152. OmniScan PA-UT device and 64 element probe

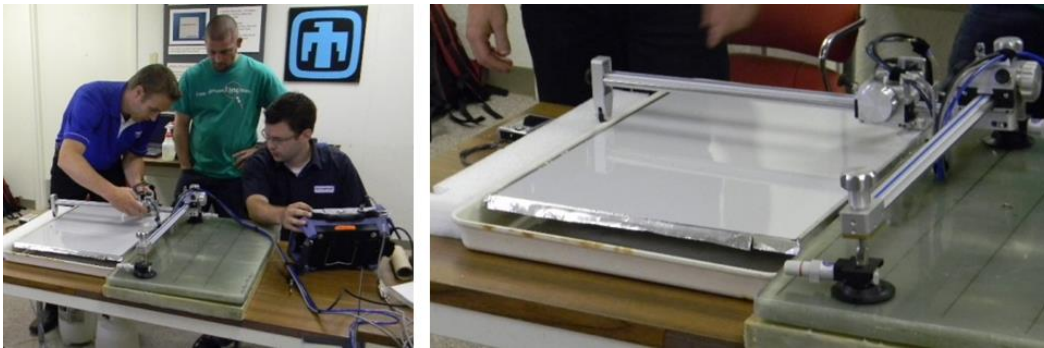


Figure 153. Deployment of OmniScan PA-UT system on solid laminate POD experiment



Figure 154. Use of different PA-UT array probes and encoders to inspect various test specimen geometries

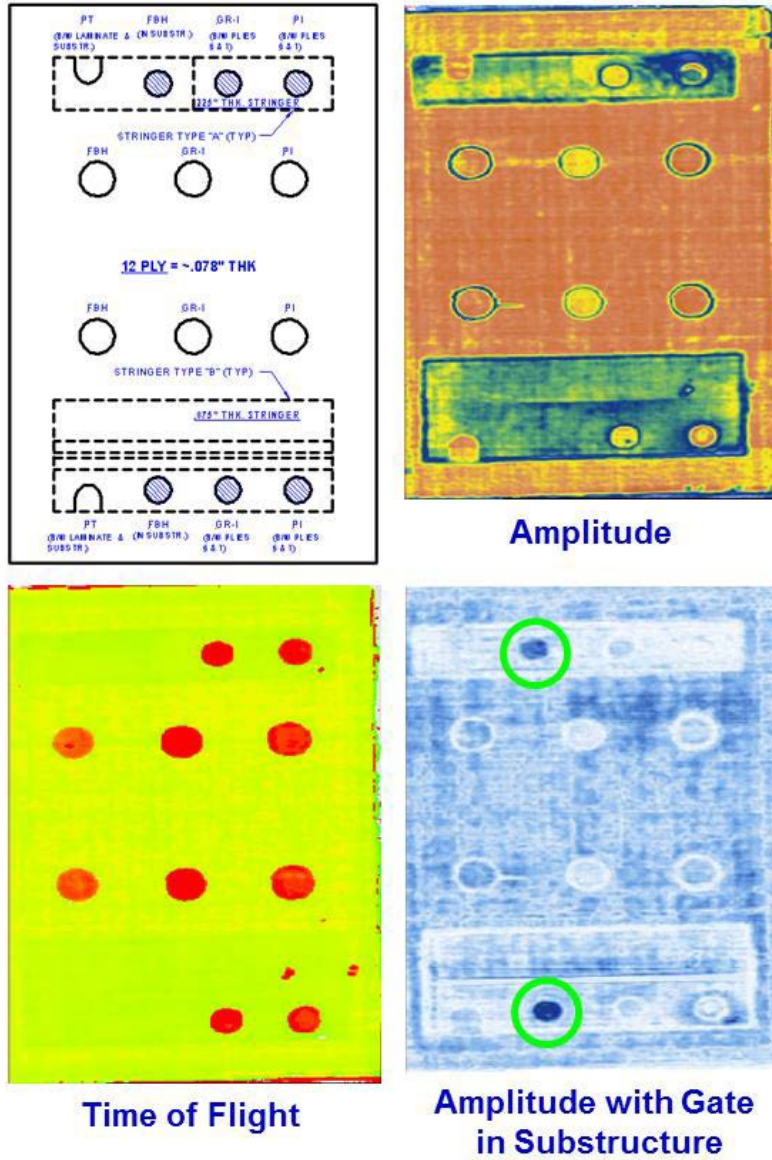


Figure 155. C-scan images produced by OmniScan PA-UT system inspection of SLE 12-ply reference panel

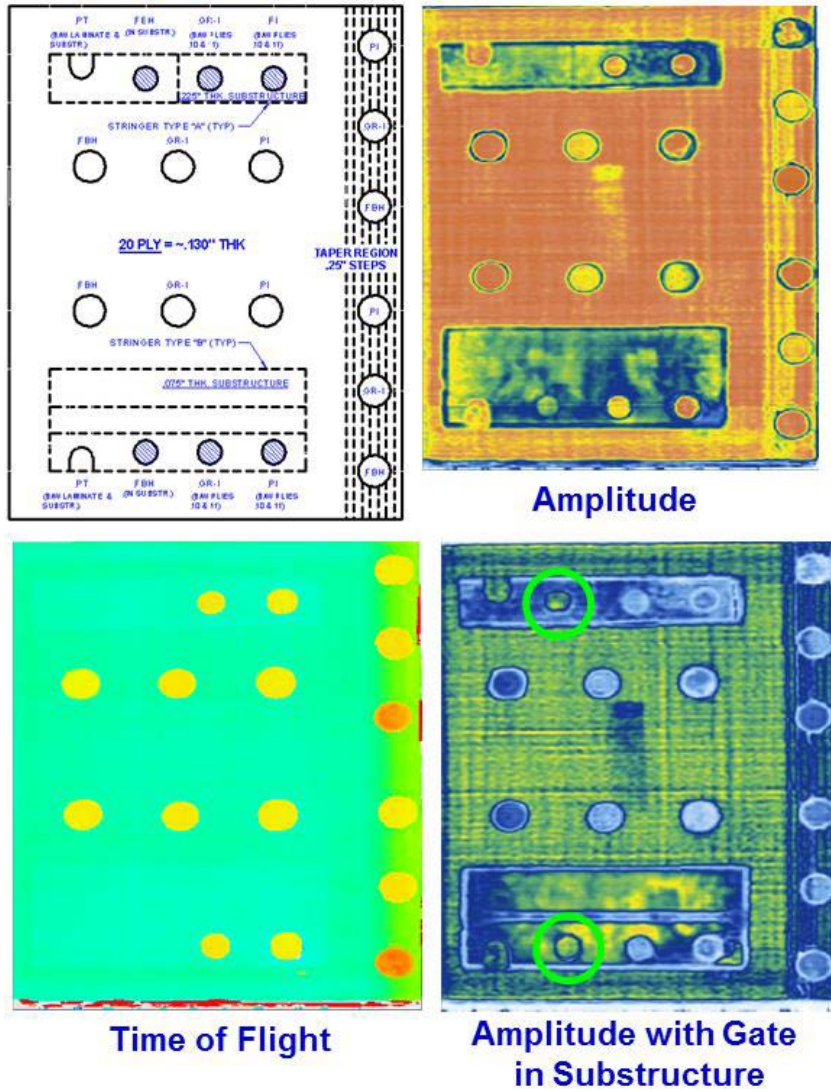


Figure 156. C-scan images produced by OmniScan PA-UT system inspection of SLE 20-ply reference panel

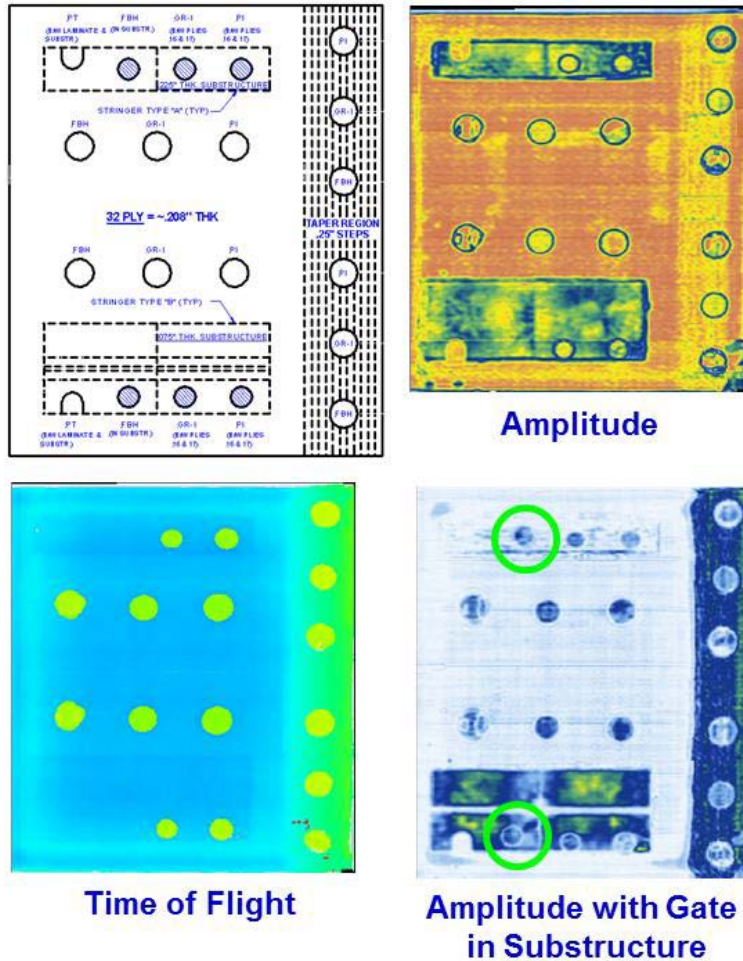


Figure 157. C-scan images produced by OmniScan PA-UT system inspection of SLE 32-ply reference panel

Figure 158 contains the cumulative POD curve when combining all flaw detection results for both the thin (12–20 ply) laminate experiment and thick (20–32 ply) laminate experiment. The OmniScan PA-UT system produced an overall $POD_{[90/95]} = 0.716''$. This is a 36% improvement over the overall result from the conventional PE-UT tests ($POD_{[90/95]} = 1.125''$) that evaluated the performance of airline inspectors (see section 6.1). The breakdown of results revealed performance for the thin laminate experiment of $POD_{[90/95]} = 0.862''$ and performance for the thick laminate experiment of $POD_{[90/95]} < 0.25''$ (i.e., 100% flaw detection, so minimum flaw size of 0.25" is upper bound for POD). Tables 20 and 21 delineate the flaw detection percentages for each of the specimen design attributes (i.e., constant thickness, CG, substructures regions, taper regions, curved surfaces, and honeycomb regions). These tables also show that there were no false calls for the entire experiment.

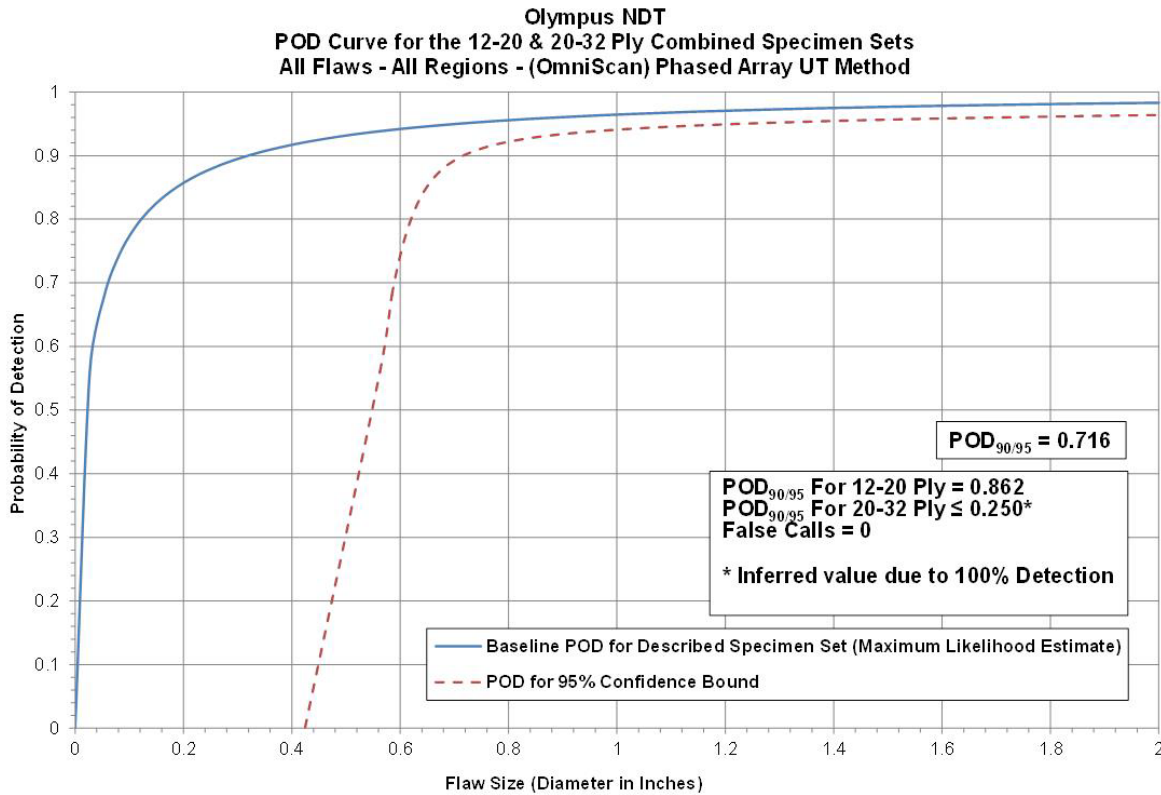


Figure 158. The POD results for OmniScan PA-UT system flaw detection in solid laminate composite structure

Table 20. Flaw detection performance for OmniScan PA-UT system separated into thin laminate and thick laminate results

Results – Olympus NDT, (OmniScan) PA-UT Method							
12–20 Ply (Thin Laminate Experiment)				20–32 Ply (Thick Laminate Experiment)			
POD _{90/95} Value	Percent Flaw Detection			POD _{90/95} Value	Percent Flaw Detection		
All Flaws Constant Thickness & CG Regions (dia. in inches)	All Flaws Constant Thickness & CG Regions	All Flaws Constant Thickness Regions Only	All Flaws CG Regions Only	All Flaws Constant Thickness & CG Regions (dia. in inches)	All Flaws Constant Thickness & CG Regions	All Flaws Constant Thickness Regions Only	All Flaws CG Regions Only
0.862	92%	100%	87%	100%*	100%	100%	100%
False Calls = 0				False Calls = 0			
*Inferred POD _{90/95} value is ≤0.25" diameter flaw (100% flaw detection, POD value cannot be determined)							

Table 21. Flaw detection performance for OmniScan PA-UT system for the overall solid laminate POD experiment

12–20 and 20–32 Ply Combined Results – Olympus NDT, (OmniScan) PA-UT Method									
POD _{90/95} Values			Percent Flaw Detection						
All Flaws Constant Thickness & CG Regions (dia. in inches)	All Flaws Constant Thickness Regions Only (dia. in inches)	All Flaws CG Regions Only (dia. in inches)	All Flaws Constant Thickness & CG Regions	All Flaws Constant Thickness Regions Only	All Flaws CG Regions Only	All Flaws Substructure Regions Only	All Flaws Taper Regions Only	All Flaws Laminate Over Honeycomb Regions Only	All Flaws Curved Surface Regions Only
0.716	100%*	0.905	95%	100%	92%	81%	100%	100%	100%
*Inferred POD _{90/95} value is ≤ 0.25 " diameter flaw (100% flaw detection, POD value cannot be determined)								False Calls = 0	

Inspector flaw calls were also graded to evaluate the accuracy of the OmniScan PA-UT method for flaw sizing. The overall test results identified hits (i.e., calls with any amount of overlap between the call and the actual flaw location), misses (i.e., no call for an area of a known flaw), false calls (i.e., call with no overlap of a flaw), and sizing performance (i.e., the degree of overlap between experimenter calls and actual flaw areas). Tables 22–27 summarize the results for flaw sizing and percent detection based on flaw size for the thin laminate and thick laminate experiments, along with a breakdown of those performance attributes in the constant thickness and CG regions. Note that for the 12–20 ply specimen set, 92% of all flaws were detected (124 of 135 flaws; see table 24). This is an improvement over the conventional PE-UT results, in which 76% of all flaws were detected. The flaw sizing performance shows that 81% of the detected flaws were sized properly (5 category for 100% coverage) versus 38% calculated for the conventional PE-UT method. Fifteen percent of the flaws were sized in the 76%–99% coverage category. Therefore, 96% of the detected flaws were sized with 76%–100% accuracy. When using conventional PE-UT, only 64% of the detected flaws were sized with 76%–100% accuracy. Table 24 shows a breakdown of percent detection based on flaw size. For example, 100% of the 2" flaws were detected. Of the smaller flaws, 79% of the 0.25" flaws were detected (versus 47% detection of the 0.25" flaws using conventional PE-UT).

Table 22. Tabulated results showing overall flaw detection percentage and accuracy in determining flaw size for the 12–20 ply specimen set for all flaws in constant thickness regions (OmniScan PA-UT system)

Olympus NDT – (OmniScan) PA-UT Flaw Detection Percentage & Accuracy in Determining Flaw Size 12–20 Ply Specimen Set – All Constant Thickness Flaws							
Accuracy in Sizing the Flaws That Were Detected						Flaw Detection Percentage	
Flaw Size	5 (100%)	4 (76%–99%)	3 (51%–75%)	2 (25%–50%)	1 (< 25%)	Flaw Size	Percent Detected
0.25	10%	0%	0%	0%	0%	0.25	100%
0.50	73%	0%	27%	0%	0%	0.50	100%
0.75	60%	40%	0%	0%	0%	0.75	100%
1.00	75%	25%	0%	0%	0%	1.00	100%
1.50	57%	43%	0%	0%	0%	1.50	100%
2.00	100%	0%	0%	0%	0%	2.00	100%
Overall Sizing Performance	73%	21%	6%	0%	0%	Overall Flaw Detection	100%

Table 23. Tabulated results showing overall flaw detection percentage and accuracy in determining flaw size for the 12–20 ply specimen set for all flaws in CG regions (OmniScan PA-UT system)

Olympus NDT – (OmniScan) PA-UT Flaw Detection Percentage & Accuracy in Determining Flaw Size 12–20 Ply Specimen Set – All CG Flaws							
Accuracy in Sizing the Flaws That Were Detected						Flaw Detection Percentage	
Flaw Size	5 (100%)	4 (76%–99%)	3 (51%–75%)	2 (25%–50%)	1 (< 25%)	Flaw Size	Percent Detected
0.25	100%	0%	0%	0%	0%	0.25	63%
0.50	86%	9%	5%	0%	0%	0.50	92%
0.75	89%	11%	0%	0%	0%	0.75	82%
1.00	90%	10%	0%	0%	0%	1.00	91%
1.50	67%	33%	0%	0%	0%	1.50	100%
2.00	100%	0%	0%	0%	0%	2.00	100%
Overall Sizing Performance	87%	12%	1%	0%	0%	Overall Flaw Detection	87%

Table 24. Tabulated results showing overall flaw detection percentage and accuracy in determining flaw size for the 12–20 ply specimen set for all flaws in constant thickness and CG regions (OmniScan PA-UT system)

Olympus NDT – (OmniScan) PA-UT Flaw Detection Percentage & Accuracy in Determining Flaw Size 12–20 Ply Specimen Set – All Flaws (Constant Thickness & CG)							
Accuracy in Sizing the Flaws That Were Detected						Flaw Detection Percentage	
Flaw Size	5 (100%)	4 (76%–99%)	3 (51%–75%)	2 (25%–50%)	1 (< 25%)	Flaw Size	Percent Detected
0.25	100%	0%	0%	0%	0%	0.25	79%
0.50	82%	6%	12%	0%	0%	0.50	94%
0.75	79%	21%	0%	0%	0%	0.75	88%
1.00	85%	15%	0%	0%	0%	1.00	94%
1.50	63%	38%	0%	0%	0%	1.50	100%
2.00	100%	0%	0%	0%	0%	2.00	100%
Overall Sizing Performance	81%	15%	3%	0%	0%	Overall Flaw Detection	92%

Table 25. Tabulated results showing overall flaw detection percentage and accuracy in determining flaw size for the 20–32 ply specimen set for all flaws in constant thickness regions (OmniScan PA-UT system)

Olympus NDT – (OmniScan) PA-UT Flaw Detection Percentage & Accuracy in Determining Flaw Size 20–32 Ply Specimen Set – All Constant Thickness Flaws							
Accuracy in Sizing the Flaws That Were Detected						Flaw Detection Percentage	
Flaw Size	5 (100%)	4 (76%–99%)	3 (51%–75%)	2 (25%–50%)	1 (< 25%)	Flaw Size	Percent Detected
0.25	100%	0%	0%	0%	0%	0.25	100%
0.50	100%	0%	0%	0%	0%	0.50	100%
0.75	100%	0%	0%	0%	0%	0.75	100%
1.00	100%	0%	0%	0%	0%	1.00	100%
1.50	100%	0%	0%	0%	0%	1.50	100%
2.00	100%	0%	0%	0%	0%	2.00	100%
Overall Sizing Performance	100%	0%	0%	0%	0%	Overall Flaw Detection	100%

Table 26. Tabulated results showing overall flaw detection percentage and accuracy in determining flaw size for the 20–32 ply specimen set for all flaws in CG regions (OmniScan PA-UT system)

Olympus NDT – (OmniScan) PA-UT Flaw Detection Percentage & Accuracy in Determining Flaw Size 20–32 Ply Specimen Set – All CG Flaws							
Accuracy in Sizing the Flaws That Were Detected						Flaw Detection Percentage	
Flaw Size	5 (100%)	4 (76%–99%)	3 (51%–75%)	2 (25%–50%)	1 (< 25%)	Flaw Size	Percent Detected
0.25	100%	0%	0%	0%	0%	0.25	100%
0.50	100%	0%	0%	0%	0%	0.50	100%
0.75	88%	13%	0%	0%	0%	0.75	100%
1.00	100%	0%	0%	0%	0%	1.00	100%
1.50	83%	17%	0%	0%	0%	1.50	100%
2.00	100%	0%	0%	0%	0%	2.00	100%
Overall Sizing Performance	95%	5%	0%	0%	0%	Overall Flaw Detection	100%

Table 27. Tabulated results showing overall flaw detection percentage and accuracy in determining flaw size for the 20–32 ply specimen set for all flaws in constant thickness and CG regions (OmniScan PA-UT system)

Olympus NDT – (OmniScan) PA-UT Flaw Detection Percentage & Accuracy in Determining Flaw Size 20–32 Ply Specimen Set – All Flaws (Constant Thickness & CG)							
Accuracy in Sizing the Flaws That Were Detected						Flaw Detection Percentage	
Flaw Size	5 (100%)	4 (76%–99%)	3 (51%–75%)	2 (25%–50%)	1 (< 25%)	Flaw Size	Percent Detected
0.25	100%	0%	0%	0%	0%	0.25	100%
0.50	100%	0%	0%	0%	0%	0.50	100%
0.75	93%	7%	0%	0%	0%	0.75	100%
1.00	100%	0%	0%	0%	0%	1.00	100%
1.50	86%	14%	0%	0%	0%	1.50	100%
2.00	100%	0%	0%	0%	0%	2.00	100%
Overall Sizing Performance	97%	3%	0%	0%	0%	Overall Flaw Detection	100%

Table 27 summarizes the results for the overall flaw detection percentage and the associated accuracy in determining flaw size for the 20–32 ply thick laminate experiment specimen set. For the 20–32 ply specimen set, 100% of all flaws were detected (67 of 67 flaws). This is an improvement over the conventional PE-UT results, in which 85% of all flaws were detected. The flaw sizing performance shows that 97% of the detected flaws were sized properly (5 category for 100% coverage) versus 31% calculated for the conventional PE-UT method. Three percent of

the flaws were sized in the 76%–99% coverage category. Therefore, 100% of the detected flaws were sized with 76%–100% accuracy. When using conventional PE-UT, only 58% of the detected flaws were sized with 76%–100% accuracy. Table 28 shows a breakdown of percent detection based on flaw size. For example, 100% of the 2" flaws were detected. Of the smaller flaws, 100% of the 0.25" flaws were detected (versus 56% detection of the 0.25" flaws using conventional PE-UT).

6.2.2 Results for the Test Specimens Inspected by Toshiba Matrixeye

Figures 159–161 show the Matrixeye device with a PA-UT probe and the deployment of the equipment on the various SLE test specimens. Inspections were completed with the Toshiba Matrixeye PA-UT inspection device connected to a 2.5 MHz, 64-element array probe. Sample C-scan images produced from the OmniScan PA-UT inspection of the SLE test specimens are shown in figures 162–164. Both amplitude and time-of-flight images were used to detect the hidden flaws, and various gates were used to detect the range of flaws at different depths within the specimens. Note the substructure flaws imaged in the C-scans generated by gates set for deeper flaw detection.



Figure 159. Matrixeye PA-UT device and 64 element probe

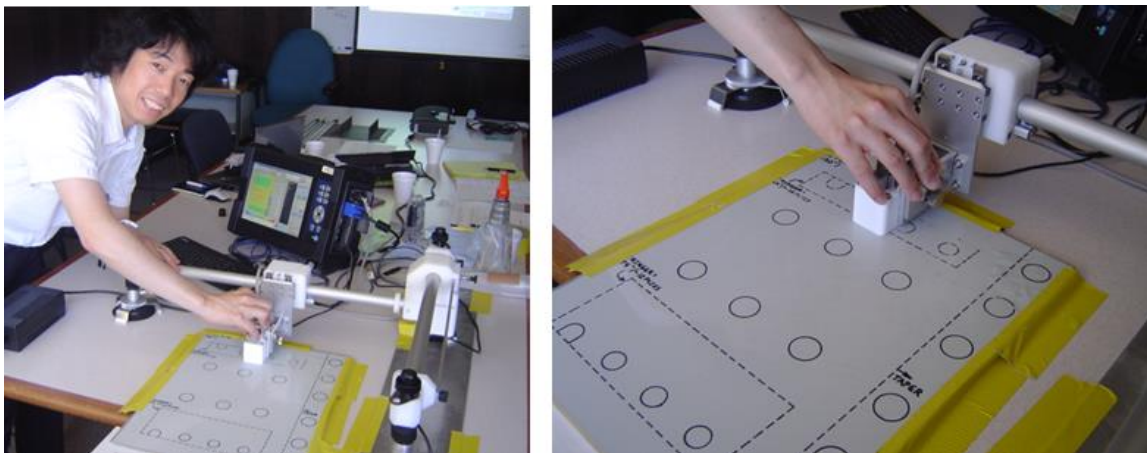


Figure 160. Deployment of the Matrixeye PA-UT system on solid laminate POD experiment



Figure 161. Use of different PA-UT array probes and encoders to inspect various test specimen geometries

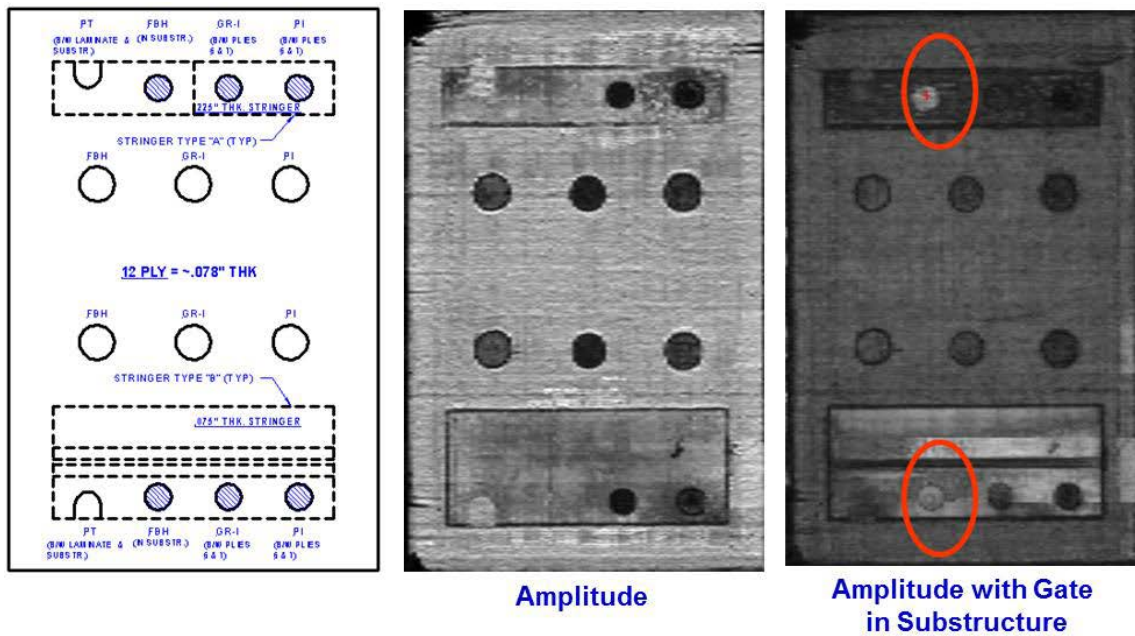


Figure 162. C-scan images produced by Matrixeye PA-UT system inspection of SLE 12-ply reference panel

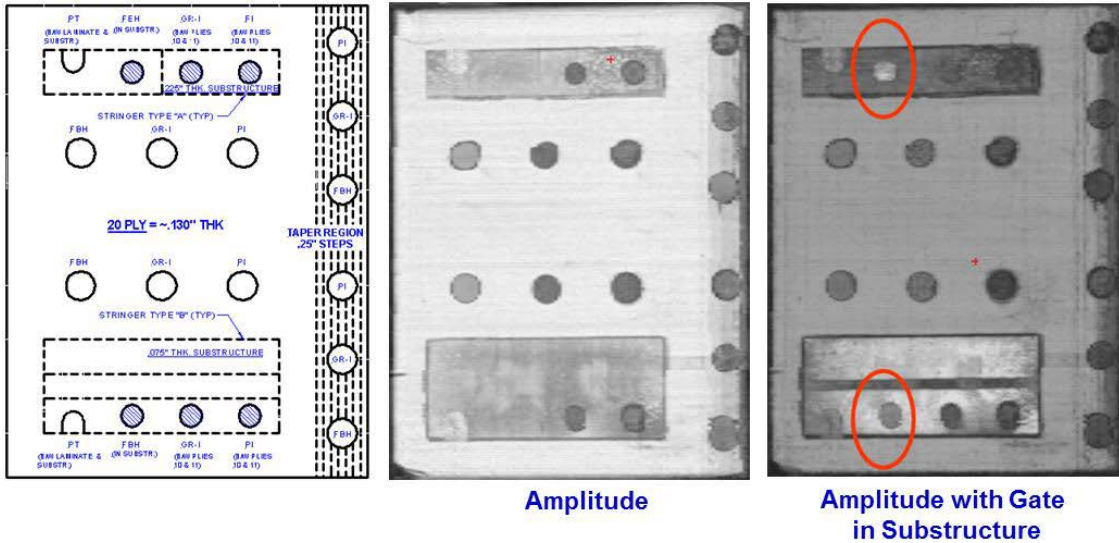


Figure 163. C-scan images produced by Matrixeye PA-UT system inspection of SLE 20-ply reference panel

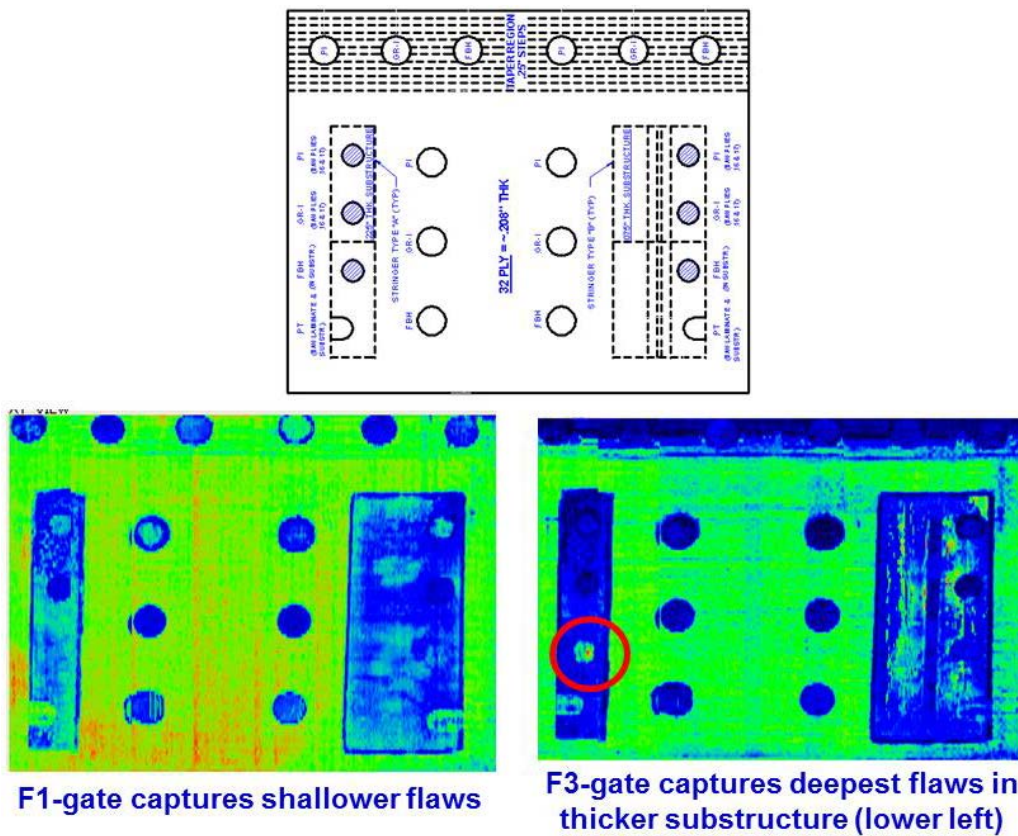


Figure 164. C-scan images produced by Matrixeye PA-UT system inspection of SLE 32-ply reference panel

Figure 165 contains the cumulative POD curve when combining all flaw detection results for both the thin (12–20 ply) laminate experiment and thick (20–32 ply) laminate experiment. The

Matrixeye PA-UT system produced an overall $POD_{[90/95]} = 0.689$ ". This is a 39% improvement over the overall result from the conventional PE-UT tests ($POD_{[90/95]} = 1.125$ "") that evaluated the performance of airline inspectors (see section 6.1). The breakdown of results revealed performance for the thin laminate experiment of $POD_{[90/95]} = 0.818$ " and performance for the thick laminate experiment of $POD_{[90/95]} = 0.606$ ". Tables 28 and 29 delineate the flaw detection percentages for each of the specimen design attributes (i.e., constant thickness, CG, substructures regions, taper regions, curved surfaces, and honeycomb regions). These tables also show that there were no false calls for the entire experiment.

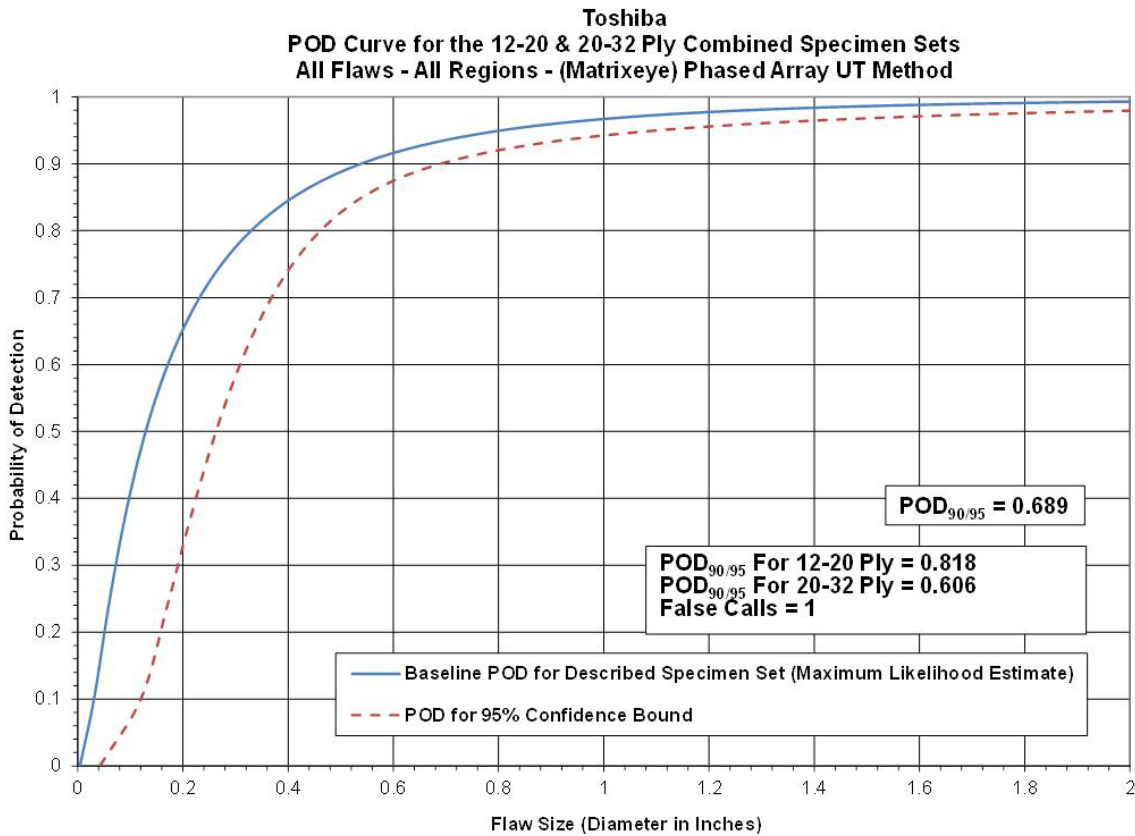


Figure 165. The POD results for Matrixeye PA-UT system flaw detection in solid laminate composite structure

Table 28. Flaw detection performance for Matrixeye PA-UT system separated into thin laminate and thick laminate results

Results – Toshiba, (Matrixeye) PA-UT Method							
12–20 Ply (Thin Laminate Experiment)				20–32 Ply (Thick Laminate Experiment)			
POD _{90/95} Value	Percent Flaw Detection			POD _{90/95} Value	Percent Flaw Detection		
All Flaws Constant Thickness & CG Regions (dia. in inches)	All Flaws Constant Thickness & CG Regions	All Flaws Constant Thickness Regions Only	All Flaws CG Regions Only	All Flaws Constant Thickness & CG Regions (dia. in inches)	All Flaws Constant Thickness & CG Regions	All Flaws Constant Thickness Regions Only	All Flaws CG Regions Only
0.818	89%	96%	85%	0.606	97%	100%	95%
False Calls = 1				False Calls = 0			

Table 29. Flaw detection performance for Matrixeye PA-UT system for the overall SLE

Results – Toshiba, (Matrixeye) PA-UT Method							
12–20 Ply (Thin Laminate Experiment)				20–32 Ply (Thick Laminate Experiment)			
POD _{90/95} Value	Percent Flaw Detection			POD _{90/95} Value	Percent Flaw Detection		
All Flaws Constant Thickness & CG Regions (dia. in inches)	All Flaws Constant Thickness & CG Regions	All Flaws Constant Thickness Regions Only	All Flaws CG Regions Only	All Flaws Constant Thickness & CG Regions (dia. in inches)	All Flaws Constant Thickness & CG Regions	All Flaws Constant Thickness Regions Only	All Flaws CG Regions Only
0.818	89%	96%	85%	0.606	97%	100%	95%
False Calls = 1				False Calls = 0			

Inspector flaw calls were also graded to evaluate the accuracy of the Matrixeye PA-UT method for flaw sizing. The overall test results identified hits (i.e., calls with any amount of overlap between the call and the actual flaw location), misses (i.e., no call for an area of a known flaw), false calls (i.e., call with no overlap of a flaw), and sizing performance (i.e., the degree of overlap between experimenter calls and actual flaw areas). Tables 30–35 summarize the results for flaw sizing and percent detection based on flaw size for the thin laminate and thick laminate experiments, along with a breakdown of those performance attributes in the constant thickness and CG regions. Note that for the 12–20 ply specimen set, 89% of all flaws were detected (120 of 135 flaws; see table 32). This is an improvement over the conventional PE-UT results, in which 76% of all flaws were detected. The flaw sizing performance shows that 97% of the detected flaws were sized properly (5 category for 100% coverage) versus 38% calculated for the conventional PE-UT method. When using conventional PE-UT, only 64% of the detected flaws were sized with 76%–100% accuracy. Table 32 also shows a breakdown of percent detection based on flaw size. For example, 100% of the 2" flaws were detected. Of the smaller flaws, 64% of the 0.25" flaws were detected (versus 47% detection of the 0.25" flaws using conventional PE-UT).

Table 30. Tabulated results showing overall flaw detection percentage and accuracy in determining flaw size for the 12–20 ply specimen set for all flaws in constant thickness regions (Matrixeye PA-UT system)

Toshiba – (Matrixeye) PA-UT Flaw Detection Percentage & Accuracy in Determining Flaw Size 12–20 Ply Specimen Set – All Constant Thickness Flaws							
Accuracy in Sizing the Flaws That Were Detected						Flaw Detection Percentage	
Flaw Size	5 (100%)	4 (76%–99%)	3 (51%–75%)	2 (25%–50%)	1 (< 25%)	Flaw Size	Percent Detected
0.25	100%	0%	0%	0%	0%	0.25	67%
0.50	91%	0%	0%	9%	0%	0.50	100%
0.75	80%	0%	0%	20%	0%	0.75	100%
1.00	92%	0%	0%	8%	0%	1.00	100%
1.50	100%	0%	0%	0%	0%	1.50	100%
2.00	100%	0%	0%	0%	0%	2.00	100%
Overall Sizing Performance	91%	0%	0%	9%	0%	Overall Flaw Detection	96%

Table 31. Tabulated results showing overall flaw detection percentage and accuracy in determining flaw size for the 12–20 ply specimen set for all flaws in CG regions (Matrixeye PA-UT system)

Toshiba – (Matrixeye) PA-UT Flaw Detection Percentage & Accuracy in Determining Flaw Size 12–20 Ply Specimen Set – All CG Flaws							
Accuracy in Sizing the Flaws That Were Detected						Flaw Detection Percentage	
Flaw Size	5 (100%)	4 (76%–99%)	3 (51%–75%)	2 (25%–50%)	1 (< 25%)	Flaw Size	Percent Detected
0.25	100%	0%	0%	0%	0%	0.25	63%
0.50	100%	0%	0%	0%	0%	0.50	75%
0.75	100%	0%	0%	0%	0%	0.75	86%
1.00	100%	0%	0%	0%	0%	1.00	96%
1.50	100%	0%	0%	0%	0%	1.50	100%
2.00	100%	0%	0%	0%	0%	2.00	100%
Overall Sizing Performance	100%	0%	0%	0%	0%	Overall Flaw Detection	85%

Table 32. Tabulated results showing overall flaw detection percentage and accuracy in determining flaw size for the 12–20 ply specimen set for all flaws in constant thickness and CG regions (Matrixeye PA-UT system)

Toshiba – (Matrixeye) PA-UT Flaw Detection Percentage & Accuracy in Determining Flaw Size 12–20 Ply Specimen Set – All Flaws (Constant Thickness &CG)							
Accuracy in Sizing the Flaws That Were Detected						Flaw Detection Percentage	
Flaw Size	5 (100%)	4 (76%–99%)	3 (51%–75%)	2 (25%–50%)	1 (< 25%)	Flaw Size	Percent Detected
0.25	100%	0%	0%	0%	0%	0.25	64%
0.50	97%	0%	0%	3%	0%	0.50	83%
0.75	93%	0%	0%	7%	0%	0.75	91%
1.00	97%	0%	0%	3%	0%	1.00	97%
1.50	100%	0%	0%	0%	0%	1.50	100%
2.00	100%	0%	0%	0%	0%	2.00	100%
Overall Sizing Performance	97%	0%	0%	3%	0%	Overall Flaw Detection	89%

Table 33. Tabulated results showing overall flaw detection percentage and accuracy in determining flaw size for the 20–32 ply specimen set for all flaws in constant thickness regions (Matrixeye PA-UT system)

Toshiba – (Matrixeye) PA-UT Flaw Detection Percentage & Accuracy in Determining Flaw Size 20–32 Ply Specimen Set – All Constant Thickness Flaws							
Accuracy in Sizing the Flaws That Were Detected						Flaw Detection Percentage	
Flaw Size	5 (100%)	4 (76%–99%)	3 (51%–75%)	2 (25%–50%)	1 (< 25%)	Flaw Size	Percent Detected
0.25	100%	0%	0%	0%	0%	0.25	100%
0.50	100%	0%	0%	0%	0%	0.50	100%
0.75	100%	0%	0%	0%	0%	0.75	100%
1.00	100%	0%	0%	0%	0%	1.00	100%
1.50	100%	0%	0%	0%	0%	1.50	100%
2.00	100%	0%	0%	0%	0%	2.00	100%
Overall Sizing Performance	100%	0%	0%	0%	0%	Overall Flaw Detection	100%

Table 34. Tabulated results showing overall flaw detection percentage and accuracy in determining flaw size for the 20–32 ply specimen set for all flaws in CG regions (Matrixeye PA-UT system)

Toshiba – (Matrixeye) PA-UT Flaw Detection Percentage & Accuracy in Determining Flaw Size 20–32 Ply Specimen Set – All CG Flaws							
Accuracy in Sizing the Flaws That Were Detected						Flaw Detection Percentage	
Flaw Size	5 (100%)	4 (76%–99%)	3 (51%–75%)	2 (25%–50%)	1 (< 25%)	Flaw Size	Percent Detected
0.25	100%	0%	0%	0%	0%	0.25	86%
0.50	100%	0%	0%	0%	0%	0.50	100%
0.75	100%	0%	0%	0%	0%	0.75	88%
1.00	100%	0%	0%	0%	0%	1.00	100%
1.50	100%	0%	0%	0%	0%	1.50	100%
2.00	100%	0%	0%	0%	0%	2.00	100%
Overall Sizing Performance	100%	0%	0%	0%	0%	Overall Flaw Detection	95%

Table 35. Tabulated results showing overall flaw detection percentage and accuracy in determining flaw size for the 20–32 ply specimen set for all flaws in constant thickness and CG regions (Matrixeye PA-UT system)

Toshiba – (Matrixeye) PA-UT Flaw Detection Percentage & Accuracy in Determining Flaw Size 20–32 Ply Specimen Set – All Flaws (Constant Thickness & CG)							
Accuracy in Sizing the Flaws That Were Detected						Flaw Detection Percentage	
Flaw Size	5 (100%)	4 (76%–99%)	3 (51%–75%)	2 (25%–50%)	1 (< 25%)	Flaw Size	Percent Detected
0.25	100%	0%	0%	0%	0%	0.25	91%
0.50	100%	0%	0%	0%	0%	0.50	100%
0.75	100%	0%	0%	0%	0%	0.75	93%
1.00	100%	0%	0%	0%	0%	1.00	100%
1.50	100%	0%	0%	0%	0%	1.50	100%
2.00	100%	0%	0%	0%	0%	2.00	100%
Overall Sizing Performance	100%	0%	0%	0%	0%	Overall Flaw Detection	97%

Table 35 summarizes the results for the overall flaw detection percentage and the associated accuracy in determining flaw size for the 20–32 ply specimen set (thick laminate experiment). For the 20–32 ply specimen set, 97% of all flaws were detected (65 of 67 flaws). This is an improvement over the conventional PE-UT results, in which 85% of all flaws were detected. The flaw sizing performance shows that 100% of the detected flaws were sized properly (5 category

for 100% coverage) versus 31% calculated for the conventional PE-UT method. Therefore, 100% of the detected flaws were sized with 76%–100% accuracy. When using conventional PE-UT, only 58% of the detected flaws were sized with 76%–100% accuracy. Table 35 also shows a breakdown of percent detection based on flaw size. For example, 100% of the 2" flaws were detected. Of the smaller flaws, 91% of the 0.25" flaws were detected (versus 56% detection of the 0.25" flaws using conventional PE-UT).

6.2.3 Results for the Test Specimens Inspected by Boeing MAUS V with FlawInspecta

Figures 166–168 show the MAUS FlawInspecta device with a linear array UT probe and the deployment of the equipment on the various SLE test specimens. Inspections were completed with the Boeing MAUS V with a FlawInspecta linear array UT inspection device connected to a 5 MHz, 64-element linear array probe with a total pitch of 3.2". The inspections were performed with the FlawInspecta upgrade for the Boeing MAUS V, which does not support phased array inspection. The Diagnostic Sonar FlawInspecta standalone system supports phased array inspections; however, this inspection system was not used during this experiment. The transducer was deployed in a water-filled delay line shoe, as shown in figure 166. Sample C-scan images produced from the MAUS FlawInspecta linear array UT inspection of the SLE test specimens are shown in figure 169. Both amplitude and time-of-flight images were used to detect the hidden flaws and various gates were used to detect the range of flaws at different depths within the specimens. Note the substructure flaws imaged in the C-scans generated by gates set for deeper flaw detection.



Figure 166. The MAUS FlawInspecta linear array UT device and 64 element probe

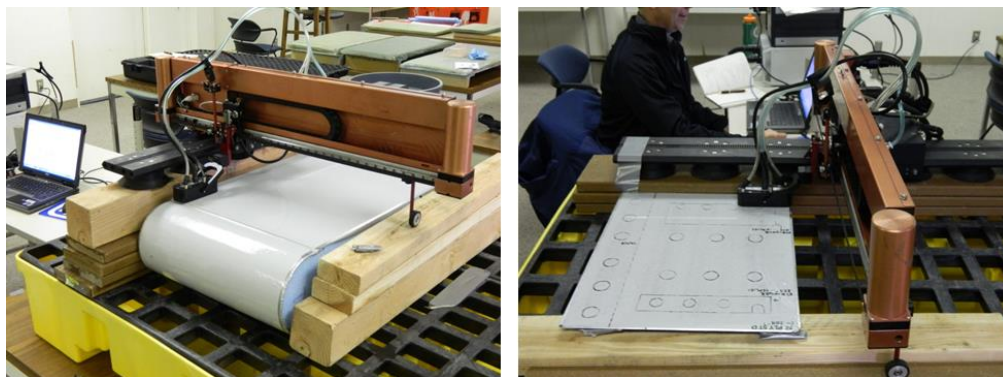


Figure 167. Deployment of the MAUS FlawInspecta linear array UT system on SLE



Figure 168. Use of different linear array probes and encoders to inspect various test specimen geometries

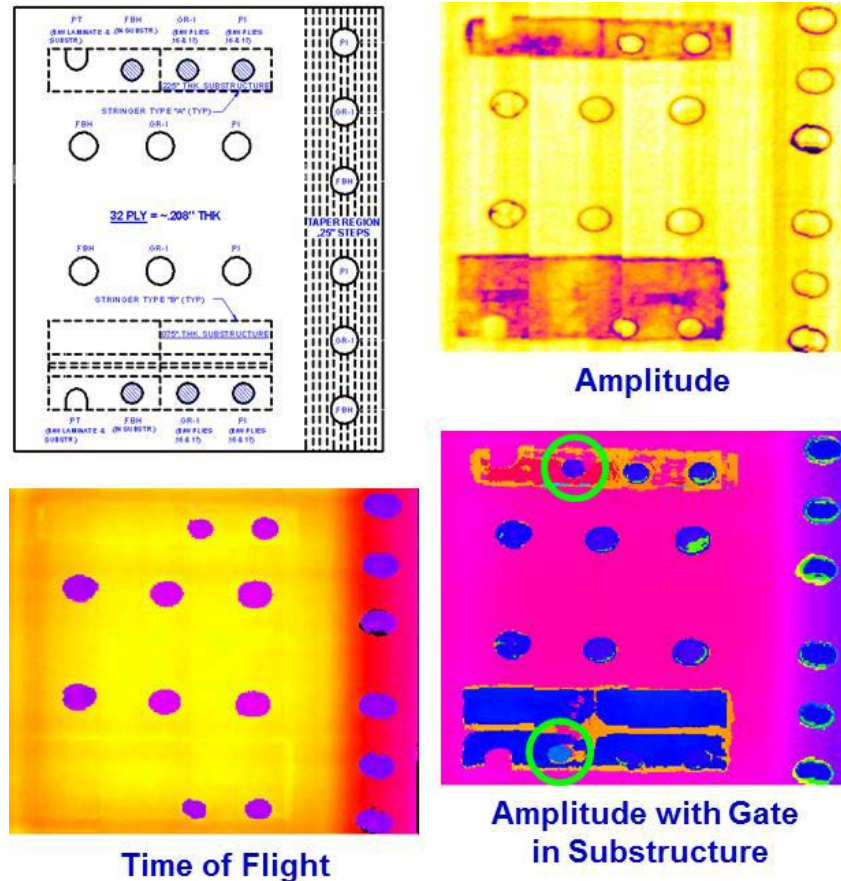


Figure 169. C-scan images produced by the MAUS FlawInspecta linear array UT system inspection of SLE 32-ply reference panel

Figure 170 contains the cumulative POD curve when combining all flaw detection results for both the thin (12–20 ply) laminate experiment and thick (20–32 ply) laminate experiment. The MAUS FlawInspecta linear array UT system produced an overall $POD_{[90/95]} = 0.884''$. This is a 21% improvement over the overall result from the conventional PE-UT tests ($POD_{[90/95]} = 1.125''$) that evaluated the performance of airline inspectors (see section 6.1). The breakdown of results revealed performance for the thin laminate experiment of $POD_{[90/95]} = 1.393''$ and performance for the thick laminate experiment of $POD_{[90/95]} < 0.25''$ (i.e., 100% flaw detection so minimum flaw size of 0.25" is upper bound for POD). Tables 36 and 37 delineate the flaw detection percentages for each of the specimen design attributes (i.e., constant thickness, CG, substructures regions, taper regions, curved surfaces, and honeycomb regions). These tables also show that there were no false calls for the entire experiment.

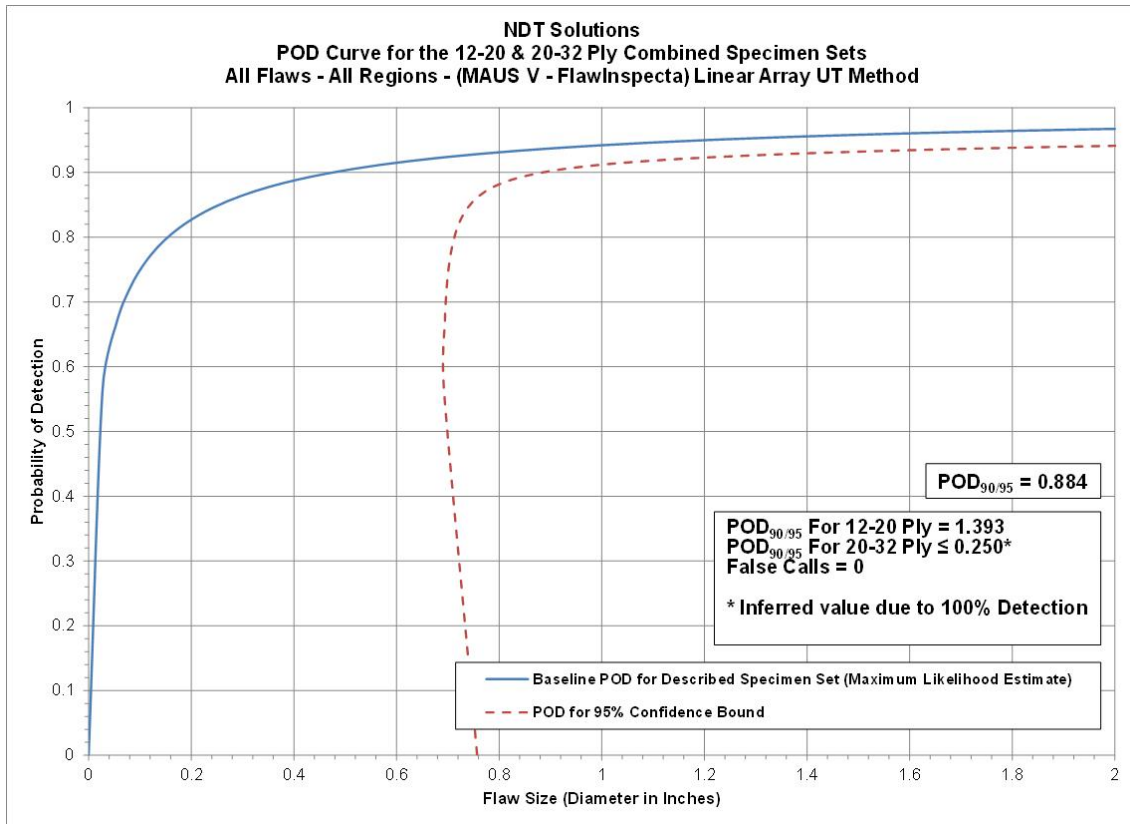


Figure 170. The POD results for MAUS FlawInspecta linear array UT system flaw detection in solid laminate composite structure

Table 36. Flaw detection performance for MAUS FlawInspecta linear array UT system separated into thin laminate and thick laminate results

Results – NDT Solutions, (MAUS V – FlawInspecta) Linear Array UT Method							
12–20 Ply (Thin Laminate Experiment)				20–32 Ply (Thick Laminate Experiment)			
POD _{90/95} Value	Percent Flaw Detection			POD _{90/95} Value	Percent Flaw Detection		
All Flaws Constant Thickness & CG Regions (dia. in inches)	All Flaws Constant Thickness & CG Regions	All Flaws Constant Thickness Regions Only	All Flaws CG Regions Only	All Flaws Constant Thickness & CG Regions (dia. in inches)	All Flaws Constant Thickness & CG Regions	All Flaws Constant Thickness Regions Only	All Flaws CG Regions Only
1.139	88%	92%	86%	100%*	100%	100%	100%
False Calls = 0				False Calls = 0			
*Inferred POD _{90/95} value is ≤ 0.25" diameter flaw (100% flaw detection, POD value cannot be determined)							

Table 37. Flaw detection performance for MAUS FlawInspecta linear array UT system for the overall SLE

12–20 and 20–32 Ply Combined Results – NDT Solutions, (MAUS V – FlawInspecta) Linear Array UT Method									
POD _{90/95} Values			Percent Flaw Detection						
All Flaws Constant Thickness & CG Regions (dia. in inches)	All Flaws Constant Thickness Regions Only (dia. in inches)	All Flaws CG Regions Only (dia. in inches)	All Flaws Constant Thickness & CG Regions	All Flaws Constant Thickness Regions Only	All Flaws CG Regions Only	All Flaws Substructure Regions Only	All Flaws Taper Regions Only	All Flaws Laminate Over Honeycomb Regions Only	All Flaws Curved Surface Regions Only
0.884	0.775	1.120	92%	94%	91%	79%	100%	100%	100%
								False Calls = 0	

Inspector flaw calls were also graded to evaluate the accuracy of the MAUS FlawInspecta linear array UT method for flaw sizing. The overall test results identified hits (i.e., calls with any amount of overlap between the call and the actual flaw location), misses (i.e., no call for an area of a known flaw), false calls (i.e., call with no overlap of a flaw), and sizing performance (the degree of overlap between experimenter calls and actual flaw areas). Tables 38–43 summarize the results for flaw sizing and percent detection based on flaw size for the thin laminate and thick laminate experiments, along with a breakdown of those performance attributes in the constant thickness and CG regions. Note that for the 12–20 ply specimen set, 88% of all flaws were detected (119 of 135 flaws; see table 40).. This is an improvement over the conventional PE-UT results, in which 76% of all flaws were detected. The flaw sizing performance shows that 82% of the detected flaws were sized properly (5 category for 100% coverage) versus 38% calculated for the conventional PE-UT method. Thirteen percent of the flaws were sized in the 76%–99% coverage category. Therefore, 95% of the detected flaws were sized with 76%–100% accuracy. When using conventional PE-UT, only 64% of the detected flaws were sized with 76%–100% accuracy. Table 40 also shows a breakdown of percent detection based on flaw size. For example, 100% of the 2" flaws were detected. Of the smaller flaws, 79% of the 0.25" flaws were detected (versus 47% detection of the 0.25" flaws using conventional PE-UT).

Table 38. Tabulated results showing overall flaw detection percentage and accuracy in determining flaw size for the 12–20 ply specimen set for all flaws in constant thickness regions (MAUS FlawInspecta linear array UT system)

NDT Solutions – (MAUS V – FlawInspecta) Linear Array UT Flaw Detection Percentage & Accuracy in Determining Flaw Size 12–20 Ply Specimen Set – All Constant Thickness Flaws							
Accuracy in Sizing the Flaws That Were Detected						Flaw Detection Percentage	
Flaw Size	5 (100%)	4 (76%–99%)	3 (51%–75%)	2 (25%–50%)	1 (< 25%)	Flaw Size	Percent Detected
0.25	100%	0%	0%	0%	0%	0.25	83%
0.50	60%	30%	10%	0%	0%	0.50	91%
0.75	75%	13%	13%	0%	0%	0.75	80%
1.00	67%	25%	8%	0%	0%	1.00	100%
1.50	57%	43%	0%	0%	0%	1.50	100%
2.00	100%	0%	0%	0%	0%	2.00	100%
Overall Sizing Performance	70%	23%	7%	0%	0%	Overall Flaw Detection	92%

Table 39. Tabulated results showing overall flaw detection percentage and accuracy in determining flaw size for the 12–20 ply specimen set for all flaws in CG regions (MAUS FlawInspecta linear array UT system)

NDT Solutions – (MAUS V – FlawInspecta) Linear Array UT Flaw Detection Percentage & Accuracy in Determining Flaw Size 12–20 Ply Specimen Set – All CG Flaws							
Accuracy in Sizing the Flaws That Were Detected						Flaw Detection Percentage	
Flaw Size	5 (100%)	4 (76%–99%)	3 (51%–75%)	2 (25%–50%)	1 (< 25%)	Flaw Size	Percent Detected
0.25	100%	0%	0%	0%	0%	0.25	75%
0.50	81%	14%	5%	0%	0%	0.50	88%
0.75	94%	6%	0%	0%	0%	0.75	82%
1.00	95%	0%	5%	0%	0%	1.00	87%
1.50	78%	22%	0%	0%	0%	1.50	100%
2.00	100%	0%	0%	0%	0%	2.00	100%
Overall Sizing Performance	89%	8%	3%	0%	0%	Overall Flaw Detection	86%

Table 40. Tabulated results showing overall flaw detection percentage and accuracy in determining flaw size for the 12–20 ply specimen set for all flaws in constant thickness and CG regions (MAUS FlawInspecta linear array UT system)

NDT Solutions – (MAUS V – FlawInspecta) Linear Array UT Flaw Detection Percentage & Accuracy in Determining Flaw Size 12–20 Ply Specimen Set – All Flaws (Constant Thickness & CG)							
Accuracy in Sizing the Flaws That Were Detected						Flaw Detection Percentage	
Flaw Size	5 (100%)	4 (76%–99%)	3 (51%–75%)	2 (25%–50%)	1 (< 25%)	Flaw Size	Percent Detected
0.25	100%	0%	0%	0%	0%	0.25	79%
0.50	74%	19%	6%	0%	0%	0.50	89%
0.75	88%	8%	4%	0%	0%	0.75	81%
1.00	84%	9%	6%	0%	0%	1.00	91%
1.50	69%	31%	0%	0%	0%	1.50	100%
2.00	100%	0%	0%	0%	0%	2.00	100%
Overall Sizing Performance	82%	13%	4%	0%	0%	Overall Flaw Detection	88%

Table 41. Tabulated Results Showing Overall Flaw Detection Percentage and Accuracy in Determining Flaw Size for the 20–32 Ply Specimen Set for All Flaws in Constant Thickness Regions (MAUS FlawInspecta Linear Array UT System)

NDT Solutions – (MAUS V – FlawInspecta) Linear Array UT Flaw Detection Percentage & Accuracy in Determining Flaw Size 20–32 Ply Specimen Set – All Constant Thickness Flaws							
Accuracy in Sizing the Flaws That Were Detected						Flaw Detection Percentage	
Flaw Size	5 (100%)	4 (76%–99%)	3 (51%–75%)	2 (25%–50%)	1 (< 25%)	Flaw Size	Percent Detected
0.25	100%	0%	0%	0%	0%	0.25	100%
0.50	100%	0%	0%	0%	0%	0.50	100%
0.75	100%	0%	0%	0%	0%	0.75	100%
1.00	100%	0%	0%	0%	0%	1.00	100%
1.50	0%	100%	0%	0%	0%	1.50	100%
2.00	100%	0%	0%	0%	0%	2.00	100%
Overall Sizing Performance	96%	4%	0%	0%	0%	Overall Flaw Detection	100%

Table 42. Tabulated results showing overall flaw detection percentage and accuracy in determining flaw size for the 20–32 ply specimen set for all flaws in CG regions (MAUS FlawInspecta linear array UT system)

NDT Solutions – (MAUS V – FlawInspecta) Linear Array UT Flaw Detection Percentage & Accuracy in Determining Flaw Size 20–32 Ply Specimen Set – All CG Flaws							
Accuracy in Sizing the Flaws That Were Detected						Flaw Detection Percentage	
Flaw Size	5 (100%)	4 (76%–99%)	3 (51%–75%)	2 (25%–50%)	1 (< 25%)	Flaw Size	Percent Detected
0.25	86%	14%	0%	0%	0%	0.25	100%
0.50	100%	0%	0%	0%	0%	0.50	100%
0.75	100%	0%	0%	0%	0%	0.75	100%
1.00	100%	0%	0%	0%	0%	1.00	100%
1.50	83%	17%	0%	0%	0%	1.50	100%
2.00	100%	0%	0%	0%	0%	2.00	100%
Overall Sizing Performance	95%	5%	0%	0%	0%	Overall Flaw Detection	100%

Table 43. Tabulated results showing overall flaw detection percentage and accuracy in determining flaw size for the 20–32 ply specimen set for all flaws in constant thickness and CG regions (MAUS FlawInspecta linear array UT system)

NDT Solutions – (MAUS V – FlawInspecta) Linear Array UT Flaw Detection Percentage & Accuracy in Determining Flaw Size 20–32 Ply Specimen Set – All Flaws (Constant Thickness & CG)							
Accuracy in Sizing the Flaws That Were Detected						Flaw Detection Percentage	
Flaw Size	5 (100%)	4 (76%–99%)	3 (51%–75%)	2 (25%–50%)	1 (< 25%)	Flaw Size	Percent Detected
0.25	91%	9%	0%	0%	0%	0.25	100%
0.50	100%	0%	0%	0%	0%	0.50	100%
0.75	100%	0%	0%	0%	0%	0.75	100%
1.00	100%	0%	0%	0%	0%	1.00	100%
1.50	71%	29%	0%	0%	0%	1.50	100%
2.00	100%	0%	0%	0%	0%	2.00	100%
Overall Sizing Performance	96%	4%	0%	0%	0%	Overall Flaw Detection	100%

Table 43 summarizes the results for the overall flaw detection percentage and the associated accuracy in determining flaw size for the 20–32 ply specimen set (thick laminate experiment). For the 20–32 ply specimen set, 100% of all flaws were detected (67 of 67 flaws). This is an improvement over the conventional PE-UT results, in which 85% of all flaws were detected. The flaw sizing performance shows that 96% of the detected flaws were sized properly (5 category

for 100% coverage) versus 31% calculated for the conventional PE-UT method. Four percent of the flaws were sized in the 76%–99% coverage category. Therefore, 100% of the detected flaws were sized with 76%–100% accuracy. When using conventional PE-UT, only 58% of the detected flaws were sized with 76%–100% accuracy. Table 43 also shows a breakdown of percent detection based on flaw size. For example, 100% of the 2" flaws and 100% of the 0.25" flaws were detected (versus 56% detection of the 0.25" flaws using conventional PE-UT).

6.2.4 Results for the Test Specimens Inspected by the GE RotoArray

Figures 171 and 172 show the Phasor XS and RotoArray device with a PA-UT probe and the deployment of the equipment on the various SLE test specimens. Inspections were completed with the GE 5 MHz, 64-element phased array probe. Figure 171 shows how the PA-UT transducer was deployed inside a rolling wheel arrangement. The rolling wheel included an encoder system to provide linear motion associated with each rolling scan and a water filled tube that provided a delay line between the transducer and the inspection surface. A sample C-scan image produced by the Phasor XS/RotoArray UT inspection of the SLE test specimens is shown in figure 173. The GE RotoArray was tested using the Phasor XS just prior to the RotoArray becoming commercially available. GE can now cable the RotoArray to work with an Olympus OmniScan unit, but this combination was not tested during this experiment.



Figure 171. The GE Phasor XS with RotoArray PA-UT device



Figure 172. Deployment of the GE Phasor XS with RotoArray PA-UT system on SLE

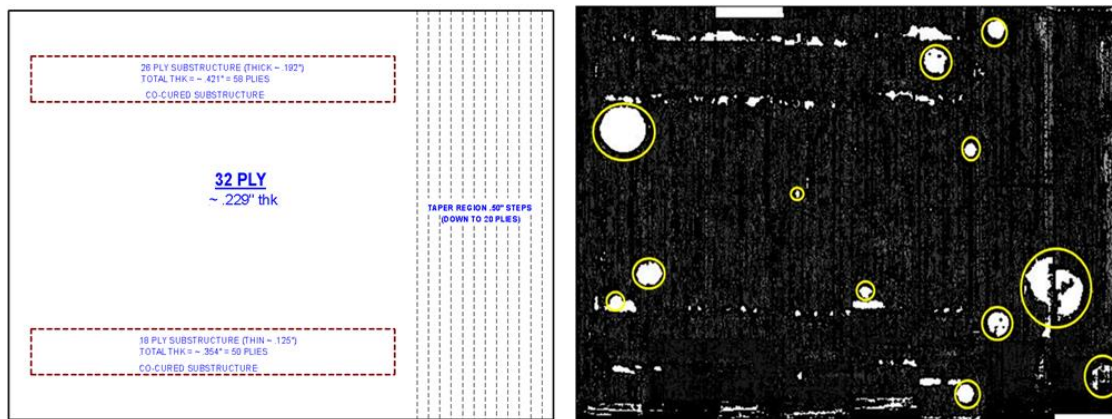


Figure 173. C-scan images produced by Phasor XS with RotoArray PA-UT system inspection of SLE 32-ply reference panel

Figure 174 contains the POD flaw detection curve for the thick (20–32 ply) laminate experiment. The RotoArray device was not applied to the thin laminate experiment; all results presented here are for the thick laminate experiment only. The RotoArray PA-UT system produced a thick laminate $POD_{[90/95]} > 3.0''$. This represents a drop in performance of 265% versus the thick laminate results from the conventional PE-UT tests ($POD_{[90/95]} = 0.823''$) that evaluated the performance of airline inspectors (see section 6.1). Table 44 delineates the flaw detection percentages for each of the specimen design attributes (i.e., constant thickness, CG, substructures regions, and taper regions). Note that the RotoArray did well in detecting flaws in the constant thickness regions (92% detection) of the test specimens, but struggled in the regions of CG (47% detection). This table also shows that there were no false calls for the entire experiment.

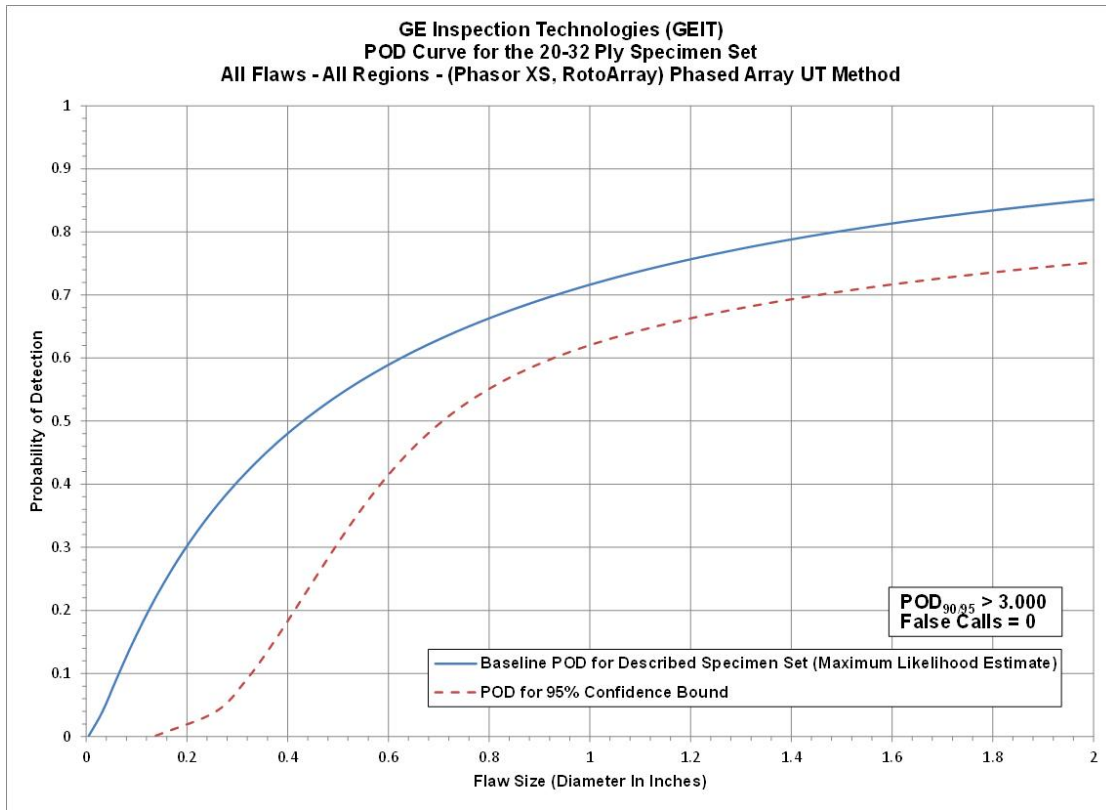


Figure 174. The POD results for the RotoArray PA-UT system flaw detection in solid laminate composite structure (20–32 ply specimen set)

Table 44. Flaw detection performance for the RotoArray PA-UT system separated into thick laminate results

Results – GE Inspection Technologies, (Phasor XS, RotoArray) PA-UT Method			
20–32 Ply (Thick Laminate Experiment)			
POD _{90/95} Value	Percent Flaw Detection		
All Flaws Constant Thickness & CG Regions (dia. in inches)	All Flaws Constant Thickness & CG Regions	All Flaws Constant Thickness Regions Only	All Flaws CG Regions Only
> 3.000	63%	92%	47%
False Calls = 0			

Inspector flaw calls were also graded to evaluate the accuracy of the RotoArray device for flaw sizing. The overall test results identified hits (i.e., calls with any amount of overlap between the call and the actual flaw location), misses (i.e., no call for an area of a known flaw), false calls (i.e., call with no overlap of a flaw), and sizing performance (i.e., the degree of overlap between experimenter calls and actual flaw areas). Tables 45–47 summarize the results for flaw sizing and percent detection based on flaw size for the thick laminate experiment, along with a

breakdown of those performance attributes in the constant thickness and CG regions. Table 47 summarizes the results for the overall flaw detection percentage and the associated accuracy in determining flaw size for the 20–32 ply thick laminate experiment specimen set. For the 20–32 ply specimen set, 63% of all flaws were detected (42 of 67 flaws). This represents a drop in performance versus the conventional PE-UT results, in which 85% of all flaws were detected. The flaw sizing performance shows that 83% of the detected flaws were sized properly (5 category for 100% coverage) versus 31% calculated for the conventional PE-UT method. Seven percent of the flaws were sized in the 76%–99% coverage category. Therefore, 90% of the detected flaws were sized with 76%–100% accuracy. When using conventional PE-UT, only 58% of the detected flaws were sized with 76%–100% accuracy. Table 47 also shows a breakdown of percent detection based on flaw size. For example, 100% of the 2" flaws were detected. Of the smaller flaws, only 36% of the 0.25" flaws were detected (a performance decrease versus 56% detection of the 0.25" flaws using conventional PE-UT).

Table 45. Tabulated results showing overall flaw detection percentage and accuracy in determining flaw size for the 20–32 ply specimen set for all flaws in constant thickness regions (RotoArray PA-UT system)

GE Inspection Technologies – (Phasor XS, RotoArray) PA-UT Flaw Detection Percentage & Accuracy in Determining Flaw Size 20–32 Ply Specimen Set – All Constant Thickness Flaws							
Accuracy in Sizing the Flaws That Were Detected						Flaw Detection Percentage	
Flaw Size	5 (100%)	4 (76%–99%)	3 (51%–75%)	2 (25%–50%)	1 (< 25%)	Flaw Size	Percent Detected
0.25	100%	0%	0%	0%	0%	0.25	50%
0.50	100%	0%	0%	0%	0%	0.50	100%
0.75	100%	0%	0%	0%	0%	0.75	100%
1.00	100%	0%	0%	0%	0%	1.00	100%
1.50	100%	0%	0%	0%	0%	1.50	100%
2.00	0%	67%	0%	33%	0%	2.00	100%
Overall Sizing Performance	86%	9%	0%	5%	0%	Overall Flaw Detection	92%

Table 46. Tabulated results showing overall flaw detection percentage and accuracy in determining flaw size for the 20–32 ply specimen set for all flaws in CG regions (RotoArray PA-UT system)

GE Inspection Technologies – (Phasor XS, RotoArray) PA-UT Flaw Detection Percentage & Accuracy in Determining Flaw Size 20–32 Ply Specimen Set – All CG Flaws							
Accuracy in Sizing the Flaws That Were Detected						Flaw Detection Percentage	
Flaw Size	5 (100%)	4 (76%–99%)	3 (51%–75%)	2 (25%–50%)	1 (< 25%)	Flaw Size	Percent Detected
0.25	100%	0%	0%	0%	0%	0.25	29%
0.50	75%	0%	0%	25%	0%	0.50	44%
0.75	100%	0%	0%	0%	0%	0.75	38%
1.00	100%	0%	0%	0%	0%	1.00	36%
1.50	60%	0%	0%	40%	0%	1.50	83%
2.00	50%	50%	0%	0%	0%	2.00	100%
Overall Sizing Performance	80%	5%	0%	15%	0%	Overall Flaw Detection	47%

Table 47. Tabulated results showing overall flaw detection percentage and accuracy in determining flaw size for the 20–32 ply specimen set for all flaws in constant thickness and CG regions (RotoArray PA-UT system)

GE Inspection Technologies – (Phasor XS, RotoArray) PA-UT Flaw Detection Percentage & Accuracy in Determining Flaw Size 20–32 Ply Specimen Set – All Flaws (Constant Thickness & CG)							
Accuracy in Sizing the Flaws That Were Detected						Flaw Detection Percentage	
Flaw Size	5 (100%)	4 (76%–99%)	3 (51%–75%)	2 (25%–50%)	1 (< 25%)	Flaw Size	Percent Detected
0.25	100%	0%	0%	0%	0%	0.25	36%
0.50	88%	0%	0%	13%	0%	0.50	62%
0.75	100%	0%	0%	0%	0%	0.75	64%
1.00	100%	0%	0%	0%	0%	1.00	59%
1.50	67%	0%	0%	33%	0%	1.50	86%
2.00	20%	60%	0%	20%	0%	2.00	100%
Overall Sizing Performance	83%	7%	0%	10%	0%	Overall Flaw Detection	63%

6.2.5 Results for the Test Specimens Inspected by Sonatest Linear Array WheelProbe

Figure 175 shows the Sonatest RapidScan 2 system that includes the control and data acquisition hardware along with the Sonatest Array WheelProbe (i.e., linear array UT WheelProbe). Figure 176 shows the Sonatest Array WheelProbe connected to the Olympus OmniScan device and the deployment of this equipment on the various SLE test specimens. Figure 175 shows how the

linear array UT transducer was deployed inside a 50 mm diameter rolling wheel arrangement. The rolling wheel included an encoder system to provide linear motion associated with each rolling scan and a water filled tube that provided a delay line between the transducer and the inspection surface. Coupling between the Array WheelProbe and the inspection surface was produced by a thin film of water or a water-UT couplant mixture that was sprayed on the surface. Inspections for the POD experiment were completed with the Sonatest 5 MHz, 64-element Array WheelProbe connected to the OmniScan readout unit. The Sonatest RapidScan 2 UT inspection system, pictured in figure 175, was only applied to the SLE feedback specimens. As a result, there are no POD levels or flaw detection percentages available for RapidScan 2 comparisons with the other advanced NDI methods.



Figure 175. Sonatest RapidScan 2 and linear Array WheelProbe



Figure 176. Deployment of Sonatest UT linear array probe with OmniScan unit on the SLE

A sample C-scan image produced from the RapidScan 2 and rolling wheel array is shown in figure 177. Sample C-scan images produced from the inspection of the SLE test specimens by the Sonatest Array WheelProbe connected to the OmniScan unit are shown in figure 178. Both amplitude and time-of-flight images were used to detect the hidden flaws; various gates were used to detect the range of flaws at different depths within the specimens. Note the substructure flaws imaged in the C-scans generated by gates set for deeper flaw detection.

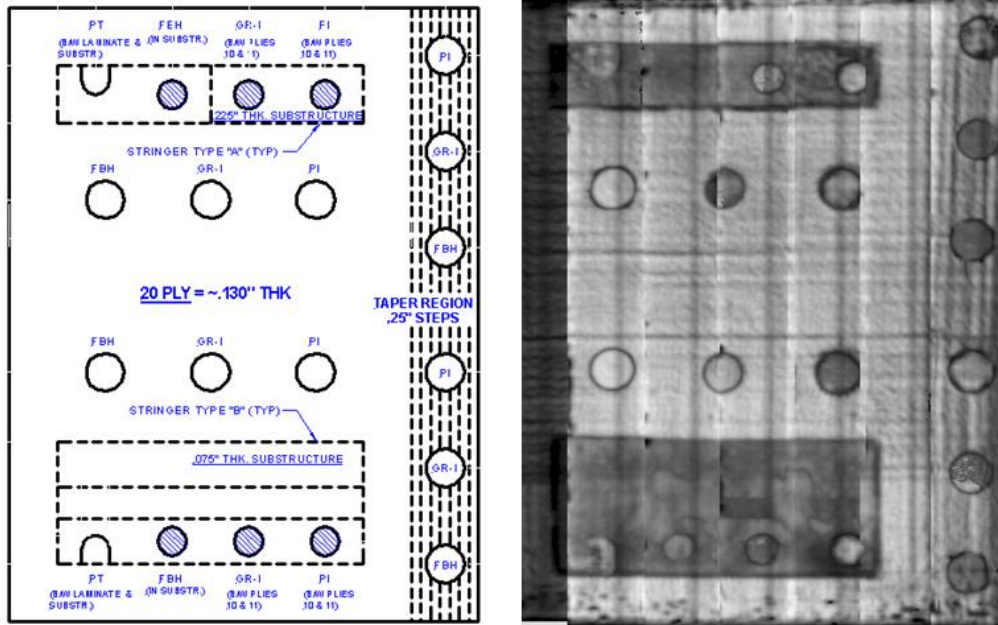


Figure 177. C-scan images produced by RapidScan 2 linear array UT system inspection of SLE 20-ply reference panel

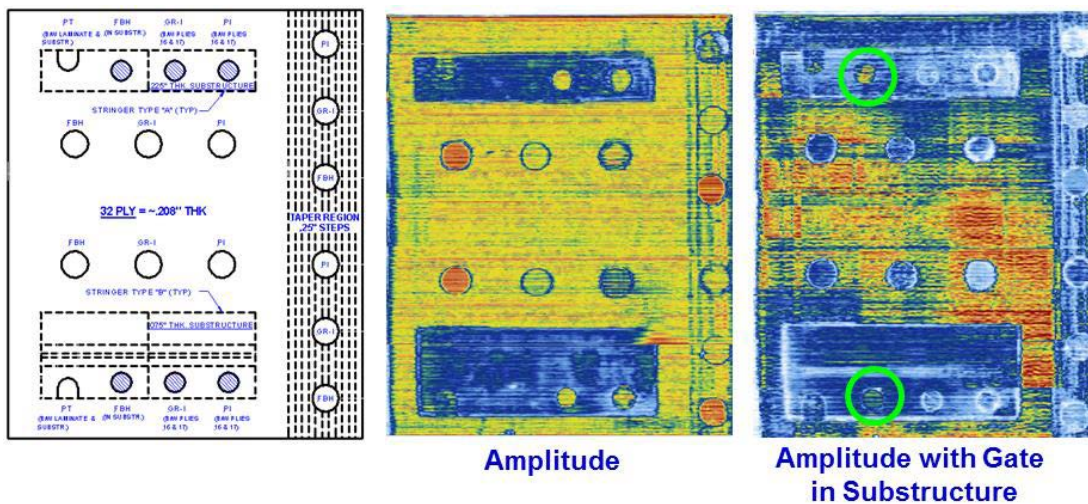


Figure 178. C-scan images produced by the inspection of the SLE 32-ply reference panel using the Sonatest linear Array WheelProbe connected to the OmniScan device

The Sonatest Array WheelProbe was not applied to the thin laminate experiment, so all results presented here are for the thick laminate experiment only. A POD flaw detection curve for the Array WheelProbe/OmniScan applied to the thick (20–32 ply) laminate experiment could not be produced because the Sonatest Array WheelProbe method detected all flaws in every test specimen. Therefore, the Sonatest Array WheelProbe UT system with OmniScan readout produced a thick laminate $POD_{[90/95]} < 0.25''$ (i.e., 100% flaw detection so minimum flaw size of 0.25'' is upper bound for POD). This is an over 70% improvement versus the thick laminate results from the conventional PE-UT tests ($POD_{[90/95]} = 0.823''$) that evaluated the performance

of airline inspectors (see section 6.1). Table 48 delineates the flaw detection percentages for each of the specimen design attributes (i.e., constant thickness, CG, substructures regions, and taper regions). Note that the Sonatest Array WheelProbe did well in detecting flaws in both the constant thickness regions (100% detection) of the test specimens and in the regions of CG (100% detection). Table 48 also shows that there were no false calls for the entire experiment.

Table 48. Flaw detection performance for Sonatest linear Array WheelProbe separated into thick laminate results

Results – Sandia National Labs, (OmniScan, Sonatest WheelProbe) Linear Array UT Method			
20–32 Ply (Thick Laminate Experiment)			
POD _{90/95} Value	Percent Flaw Detection		
All Flaws Constant Thickness & CG Regions (dia. in inches)	All Flaws Constant Thickness & CG Regions	All Flaws Constant Thickness Regions Only	All Flaws CG Regions Only
100%*	100%	100%	100%
False Calls = 0			
*Inferred POD _{90/95} value is ≤ 0.25 " diameter flaw (100% flaw detection, POD value cannot be determined)			

Inspector flaw calls were also graded to evaluate the accuracy of the Sonatest Array WheelProbe UT method for flaw sizing. The overall test results identified hits (i.e., calls with any amount of overlap between the call and the actual flaw location), misses (i.e., no call for an area of a known flaw), false calls (i.e., call with no overlap of a flaw), and sizing performance (i.e., the degree of overlap between experimenter calls and actual flaw areas. Tables 49–51 summarize the results for flaw sizing and percent detection based on flaw size for the thick laminate experiment, along with a breakdown of those performance attributes in the constant thickness and CG regions.

Table 49. Tabulated results showing overall flaw detection percentage and accuracy in determining flaw size for the 20–32 ply specimen set for all flaws in constant thickness regions (Sonatest linear Array WheelProbe)

Sandia National Labs – (OmniScan, Sonatest WheelProbe) Linear Array UT Flaw Detection Percentage & Accuracy in Determining Flaw Size 20–32 Ply Specimen Set – All Constant Thickness Flaws							
Accuracy in Sizing the Flaws That Were Detected						Flaw Detection Percentage	
Flaw Size	5 (100%)	4 (76%–99%)	3 (51%–75%)	2 (25%–50%)	1 (< 25%)	Flaw Size	Percent Detected
0.25	100%	0%	0%	0%	0%	0.25	100%
0.50	100%	0%	0%	0%	0%	0.50	100%
0.75	100%	0%	0%	0%	0%	0.75	100%
1.00	100%	0%	0%	0%	0%	1.00	100%
1.50	100%	0%	0%	0%	0%	1.50	100%
2.00	100%	0%	0%	0%	0%	2.00	100%
Overall Sizing Performance	100%	0%	0%	0%	0%	Overall Flaw Detection	100%

Table 50. Tabulated results showing overall flaw detection percentage and accuracy in determining flaw size for the 20–32 ply specimen set for all flaws in CG regions (Sonatest linear Array WheelProbe)

Sandia National Labs – (OmniScan, Sonatest WheelProbe) Linear Array UT Flaw Detection Percentage & Accuracy in Determining Flaw Size 20–32 Ply Specimen Set – All CG Flaws							
Accuracy in Sizing the Flaws That Were Detected						Flaw Detection Percentage	
Flaw Size	5 (100%)	4 (76%–99%)	3 (51%–75%)	2 (25%–50%)	1 (< 25%)	Flaw Size	Percent Detected
0.25	100%	0%	0%	0%	0%	0.25	100%
0.50	100%	0%	0%	0%	0%	0.50	100%
0.75	100%	0%	0%	0%	0%	0.75	100%
1.00	100%	0%	0%	0%	0%	1.00	100%
1.50	100%	0%	0%	0%	0%	1.50	100%
2.00	100%	0%	0%	0%	0%	2.00	100%
Overall Sizing Performance	100%	0%	0%	0%	0%	Overall Flaw Detection	100%

Table 51. Tabulated results showing overall flaw detection percentage and accuracy in determining flaw size for the 20–32 ply specimen set for all flaws in constant thickness and CG regions (Sonatest linear Array WheelProbe)

Sandia National Labs – (OmniScan, Sonatest WheelProbe) Linear Array UT Flaw Detection Percentage & Accuracy in Determining Flaw Size 20–32 Ply Specimen Set – All Flaws (Constant Thickness & CG)							
Accuracy in Sizing the Flaws That Were Detected						Flaw Detection Percentage	
Flaw Size	5 (100%)	4 (76%–99%)	3 (51%–75%)	2 (25%–50%)	1 (< 25%)	Flaw Size	Percent Detected
0.25	100%	0%	0%	0%	0%	0.25	100%
0.50	100%	0%	0%	0%	0%	0.50	100%
0.75	100%	0%	0%	0%	0%	0.75	100%
1.00	100%	0%	0%	0%	0%	1.00	100%
1.50	100%	0%	0%	0%	0%	1.50	100%
2.00	100%	0%	0%	0%	0%	2.00	100%
Overall Sizing Performance	100%	0%	0%	0%	0%	Overall Flaw Detection	100%

Table 51 summarizes the results for the overall flaw detection percentage and the associated accuracy in determining flaw size for the 20–32 ply specimen set (thick laminate experiment). For the 20–32 ply specimen set, 100% of all flaws were detected (67 of 67 flaws). This is an improvement over the conventional PE-UT results, in which 85% of all flaws were detected. The flaw sizing performance shows that 100% of the detected flaws were sized properly (5 category for 100% coverage) versus 31% calculated for the conventional PE-UT method. When using conventional PE-UT, only 58% of the detected flaws were sized with 76%–100% accuracy. Table 51 also shows a breakdown of percent detection based on flaw size. For example, 100% of the 2" flaws were detected and 100% of the 0.25" flaws were detected (versus 56% detection of the 0.25" flaws using conventional PE-UT).

6.3 INSPECTION PERFORMANCE RESULTS FOR LUS

6.3.1 Results for Test Specimens Inspected by iPhoton iPLUS LUS System

Figures 179–181 show the iPLUS LUS System device and the deployment of the equipment on the various SLE test specimens. Inspections were completed with the iPhoton iPLUS LUS inspection device connected to a transducer that could operate in the 0.5 MHz–20 MHz range. An articulating robot system was used to move and align the LUS head around the test specimens. The setup for each flat panel only took a few minutes for the first panel of each type. The inspector placed the panel on the floor and used the laser to create a rectangular pattern around the panel to determine the scan area prior to the first scan. One of the unique features of the iPhoton system is that you can teach the system to inspect complex parts for use on subsequent similar inspections. Figure 181 shows how the inspector set up a BN specimen by teaching the system to make five different scans: one for the top, one for the bottom, and three for the BN itself. This took about an hour to program; however, once this movement pattern was properly programmed, it only took two minutes to actually scan each BN specimen.



Figure 179. The iPhoton LUS gantry-based inspection system



Figure 180. Deployment of the iPhoton LUS system on SLE

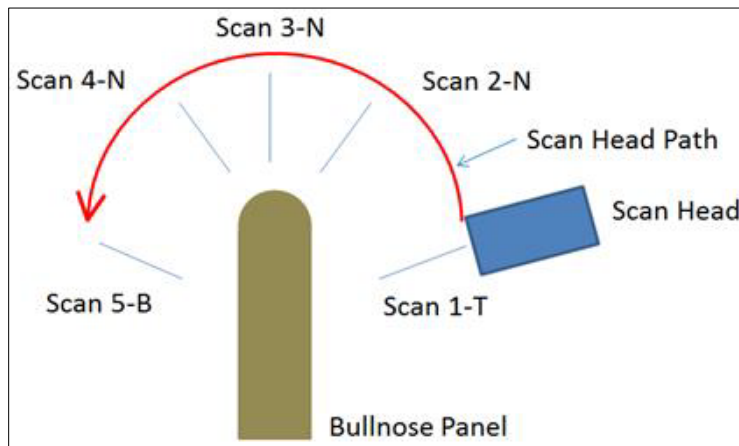


Figure 181. Use of scan pattern teaching to automate the scans of parts with the iPLUS LUS robot

Sample C-scan images produced from the iPLUS LUS inspection of the SLE test specimens are shown in figure 182. Both amplitude and time-of-flight images were used to detect the hidden flaws; various gates were used to detect the range of flaws at different depths within the specimens. Note the substructure flaws imaged in the C-scans generated by gates set for deeper flaw detection. The slicer C-scan shown in figure 182 is a flaw detection tool in the iPLUS software that consists of producing a C-scan image from the amplitudes of all A-scans at a particular point in time. This allows for very specific data to be highlighted such that damage at specific depths can be identified.

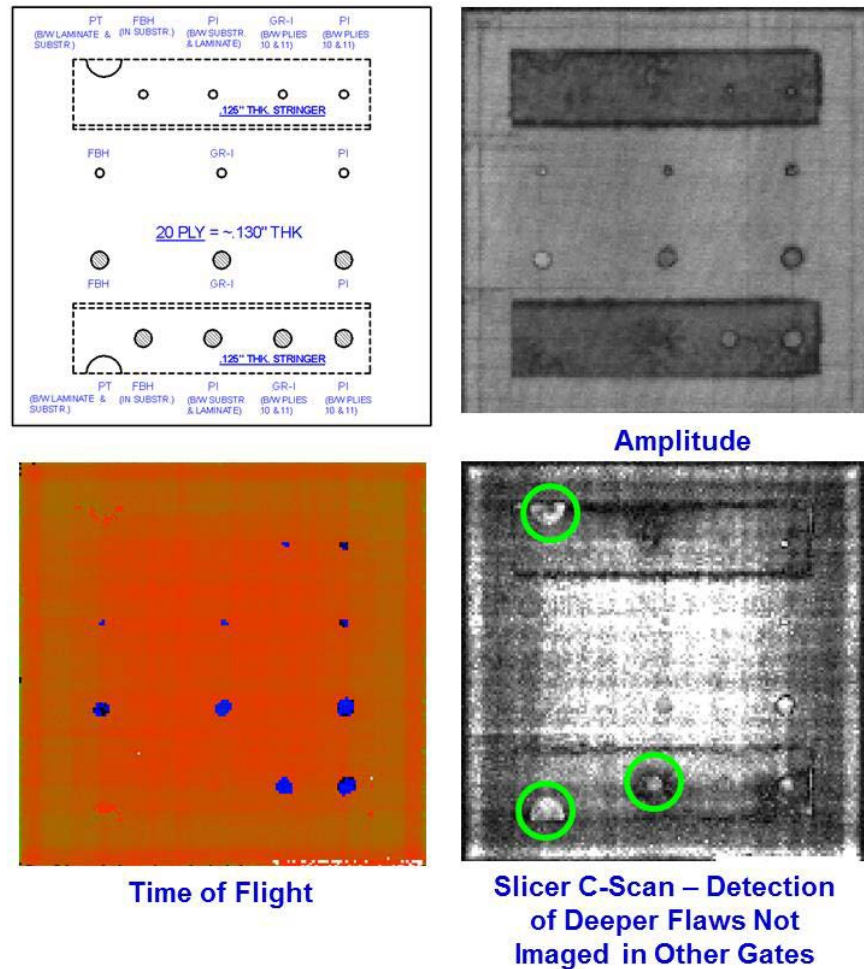


Figure 182. C-scan images produced by iPLUS LUS inspection of SLE 20-ply reference panel

Figure 183 contains the cumulative POD curve when combining all flaw detection results for both the thin (12–20 ply) laminate experiment and thick (20–32 ply) laminate experiment. The iPLUS LUS system produced an overall $POD_{[90/95]} = 0.851''$. This is a 24% improvement over the overall result from the conventional PE-UT tests ($POD_{[90/95]} = 1.125''$) that evaluated the performance of airline inspectors (see section 6.1). The breakdown of results revealed performance for the thin laminate experiment of $POD_{[90/95]} = 1.204''$ and performance for the thick laminate experiment of $POD_{[90/95]} < 0.25''$ (i.e., 100% flaw detection so minimum flaw size

of 0.25" is the upper bound for POD). Tables 52 and 53 delineate the flaw detection percentages for each of the specimen design attributes (i.e., constant thickness, CG, substructures regions, taper regions, curved surfaces, and honeycomb regions). These tables also show that there were no false calls for the entire experiment.

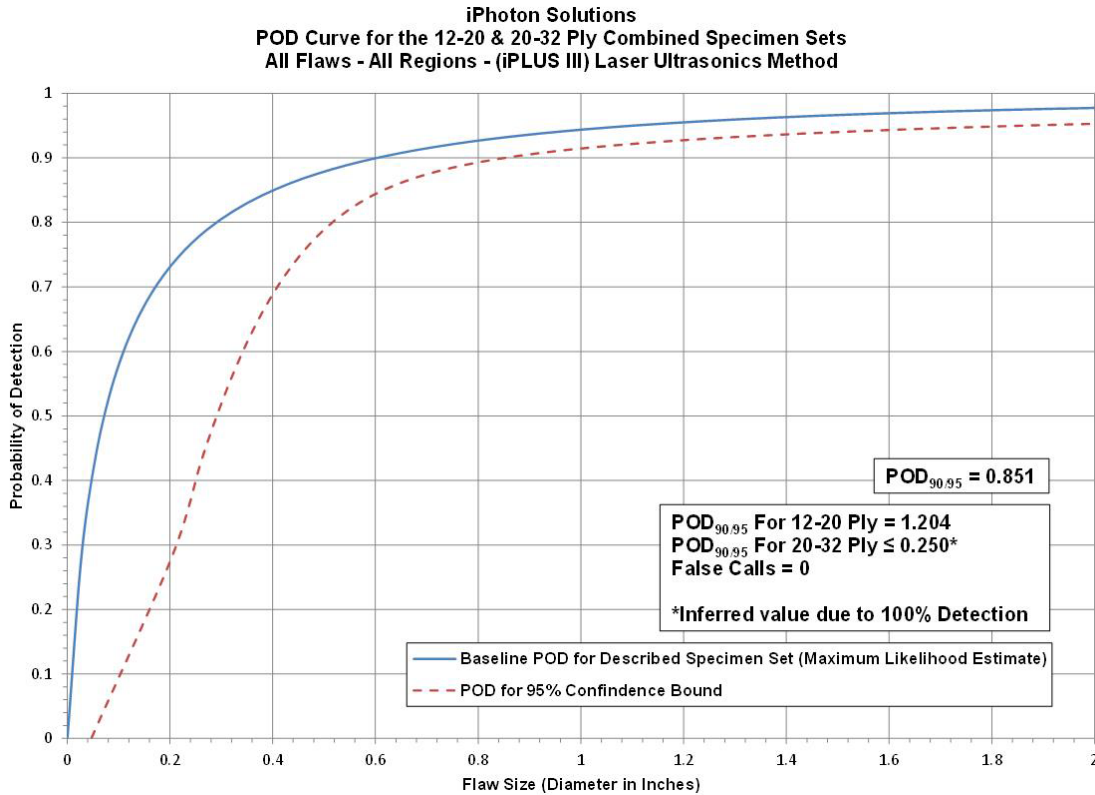


Figure 183. The POD results for the iPLUS LUS system flaw detection in solid laminate composite structure

Table 52. Flaw detection performance for the iPLUS LUS system separated into thin laminate and thick laminate results

Results – iPhoton Solutions, (iPLUS III) LUS Method							
12–20 Ply (Thin Laminate Experiment)				20–32 Ply (Thick Laminate Experiment)			
POD _{90/95} Value	Percent Flaw Detection			POD _{90/95} Value	Percent Flaw Detection		
All Flaws Constant Thickness & CG Regions (dia. in inches)	All Flaws Constant Thickness & CG Regions	All Flaws Constant Thickness Regions Only	All Flaws CG Regions Only	All Flaws Constant Thickness & CG Regions (dia. in inches)	All Flaws Constant Thickness & CG Regions	All Flaws Constant Thickness Regions Only	All Flaws CG Regions Only
1.204	86%	100%	78%	100%*	100%	100%	100%
False Calls = 0				False Calls = 0			
*Inferred POD _{90/95} value is ≤ 0.25" diameter flaw (100% flaw detection, POD value cannot be determined)							

Table 53. Flaw detection performance for the iPLUS LUS system for the overall SLE

12–20 and 20–32 Ply Combined Results – iPhoton Solutions, (iPLUS III) LUS Method									
POD _{90/95} Values			Percent Flaw Detection						
All Flaws Constant Thickness & CG Regions (dia. in inches)	All Flaws Constant Thickness Regions Only (dia. in inches)	All Flaws CG Regions Only (dia. in inches)	All Flaws Constant Thickness & CG Regions	All Flaws Constant Thickness Regions Only	All Flaws CG Regions Only	All Flaws Substructure Regions Only	All Flaws Taper Regions Only	All Flaws Laminate Over Honeycomb Regions Only	All Flaws Curved Surface Regions Only
0.851	100%*	1.311	91%	100%	85%	67%	100%	100%	100%
*Inferred POD _{90/95} value is ≤ 0.25" diameter flaw (100% flaw detection, POD value cannot be determined)								False Calls = 0	

Inspector flaw calls were also graded to evaluate the accuracy of the iPLUS LUS method for flaw sizing. The overall test results identified hits (i.e., calls with any amount of overlap between the call and the actual flaw location), misses (i.e., no call for an area of a known flaw), false calls (i.e., call with no overlap of a flaw), and sizing performance (i.e., the degree of overlap between experimenter calls and actual flaw areas). Tables 54–59 summarize the results for flaw sizing and percent detection based on flaw size for the thin laminate and thick laminate experiments, along with a breakdown of those performance attributes in the constant thickness and CG regions.

Table 54. Tabulated results showing overall flaw detection percentage and accuracy in determining flaw size for the 12–20 ply specimen set for all flaws in constant thickness regions (iPLUS LUS system)

iPhoton Solutions – (iPLUS III) LUS Method Flaw Detection Percentage & Accuracy in Determining Flaw Size 12–20 Ply Specimen Set – All Constant Thickness Flaws							
Accuracy in Sizing the Flaws That Were Detected						Flaw Detection Percentage	
Flaw Size	5 (100%)	4 (76%–99%)	3 (51%–75%)	2 (25%–50%)	1 (< 25%)	Flaw Size	Percent Detected
0.25	100%	0%	0%	0%	0%	0.25	100%
0.50	91%	9%	0%	0%	0%	0.50	100%
0.75	100%	0%	0%	0%	0%	0.75	100%
1.00	92%	8%	0%	0%	0%	1.00	100%
1.50	100%	0%	0%	0%	0%	1.50	100%
2.00	100%	0%	0%	0%	0%	2.00	100%
Overall Sizing Performance	96%	4%	0%	0%	0%	Overall Flaw Detection	100%

Table 55. Tabulated results showing overall flaw detection percentage and accuracy in determining flaw size for the 12–20 ply specimen set for all flaws in CG regions (iPLUS LUS system)

iPhoton Solutions – (iPLUS III) LUS Method Flaw Detection Percentage & Accuracy in Determining Flaw Size 12–20 Ply Specimen Set – All CG Flaws							
Accuracy in Sizing the Flaws That Were Detected						Flaw Detection Percentage	
Flaw Size	5 (100%)	4 (76%–99%)	3 (51%–75%)	2 (25%–50%)	1 (< 25%)	Flaw Size	Percent Detected
0.25	100%	0%	0%	0%	0%	0.25	50%
0.50	94%	6%	0%	0%	0%	0.50	71%
0.75	100%	0%	0%	0%	0%	0.75	73%
1.00	95%	5%	0%	0%	0%	1.00	91%
1.50	100%	0%	0%	0%	0%	1.50	100%
2.00	100%	0%	0%	0%	0%	2.00	100%
Overall Sizing Performance	97%	3%	0%	0%	0%	Overall Flaw Detection	78%

Table 56. Tabulated results showing overall flaw detection percentage and accuracy in determining flaw size for the 12–20 ply specimen set for all flaws in constant thickness and CG regions (iPLUS LUS system)

iPhoton Solutions – (iPLUS III) LUS Method Flaw Detection Percentage & Accuracy in Determining Flaw Size 12–20 Ply Specimen Set – All Flaws (Constant Thickness & CG)							
Accuracy in Sizing the Flaws That Were Detected						Flaw Detection Percentage	
Flaw Size	5 (100%)	4 (76%–99%)	3 (51%–75%)	2 (25%–50%)	1 (< 25%)	Flaw Size	Percent Detected
0.25	100%	0%	0%	0%	0%	0.25	71%
0.50	93%	7%	0%	0%	0%	0.50	80%
0.75	100%	0%	0%	0%	0%	0.75	81%
1.00	94%	6%	0%	0%	0%	1.00	94%
1.50	100%	0%	0%	0%	0%	1.50	100%
2.00	100%	0%	0%	0%	0%	2.00	100%
Overall Sizing Performance	97%	3%	0%	0%	0%	Overall Flaw Detection	86%

Table 57. Tabulated results showing overall flaw detection percentage and accuracy in determining flaw size for the 20–32 ply specimen set for all flaws in constant thickness regions (iPLUS LUS system)

iPhoton Solutions – (iPLUS III) LUS Method Flaw Detection Percentage & Accuracy in Determining Flaw Size 20–32 Ply Specimen Set – All Constant Thickness Flaws							
Accuracy in Sizing the Flaws That Were Detected						Flaw Detection Percentage	
Flaw Size	5 (100%)	4 (76%–99%)	3 (51%–75%)	2 (25%–50%)	1 (< 25%)	Flaw Size	Percent Detected
0.25	100%	0%	0%	0%	0%	0.25	100%
0.50	100%	0%	0%	0%	0%	0.50	100%
0.75	83%	17%	0%	0%	0%	0.75	100%
1.00	83%	17%	0%	0%	0%	1.00	100%
1.50	100%	0%	0%	0%	0%	1.50	100%
2.00	100%	0%	0%	0%	0%	2.00	100%
Overall Sizing Performance	92%	8%	0%	0%	0%	Overall Flaw Detection	100%

Table 58. Tabulated results showing overall flaw detection percentage and accuracy in determining flaw size for the 20–32 ply specimen set for all flaws in CG regions (iPLUS LUS system)

iPhoton Solutions – (iPLUS III) LUS Method Flaw Detection Percentage & Accuracy in Determining Flaw Size 20–32 Ply Specimen Set – All CG Flaws							
Accuracy in Sizing the Flaws That Were Detected						Flaw Detection Percentage	
Flaw Size	5 (100%)	4 (76%–99%)	3 (51%–75%)	2 (25%–50%)	1 (< 25%)	Flaw Size	Percent Detected
0.25	100%	0%	0%	0%	0%	0.25	100%
0.50	100%	0%	0%	0%	0%	0.50	100%
0.75	100%	0%	0%	0%	0%	0.75	100%
1.00	82%	18%	0%	0%	0%	1.00	100%
1.50	100%	0%	0%	0%	0%	1.50	100%
2.00	100%	0%	0%	0%	0%	2.00	100%
Overall Sizing Performance	95%	5%	0%	0%	0%	Overall Flaw Detection	100%

Table 59. Tabulated results showing overall flaw detection percentage and accuracy in determining flaw size for the 20–32 ply specimen set for all flaws in constant thickness and CG regions (iPLUS LUS system)

iPhoton Solutions – (iPLUS III) LUS Method Flaw Detection Percentage & Accuracy in Determining Flaw Size 20–32 Ply Specimen Set – All Flaws (Constant Thickness & CG)							
Accuracy in Sizing the Flaws That Were Detected						Flaw Detection Percentage	
Flaw Size	5 (100%)	4 (76%–99%)	3 (51%–75%)	2 (25%–50%)	1 (< 25%)	Flaw Size	Percent Detected
0.25	100%	0%	0%	0%	0%	0.25	100%
0.50	100%	0%	0%	0%	0%	0.50	100%
0.75	93%	7%	0%	0%	0%	0.75	100%
1.00	82%	18%	0%	0%	0%	1.00	100%
1.50	100%	0%	0%	0%	0%	1.50	100%
2.00	100%	0%	0%	0%	0%	2.00	100%
Overall Sizing Performance	94%	6%	0%	0%	0%	Overall Flaw Detection	100%

Note that for the 12–20 ply specimen set, 86% of all flaws were detected (116 of 135 flaws; see table 56). This is an improvement over the conventional PE-UT results, in which 76% of all flaws were detected. The flaw sizing performance shows that 97% of the detected flaws were sized properly (5 category for 100% coverage) versus 38% calculated for the conventional PE-UT method. Three percent of the flaws were sized in the 76%–99% coverage category. Therefore, 100% of the detected flaws were sized with 76%–100% accuracy. When using conventional PE-UT, only 64% of the detected flaws were sized with 76%–100% accuracy. Table 56 also shows a breakdown of percent detection based on flaw size. For example, 100% of the 2" flaws were detected. Of the smaller flaws, 71% of the 0.25" flaws were detected (versus 47% detection of the 0.25" flaws using conventional PE-UT).

Table 59 summarizes the results for the overall flaw detection percentage and the associated accuracy in determining flaw size for the 20–32 ply specimen set (thick laminate experiment). For the 20–32 ply specimen set, 100% of all flaws were detected (67 of 67 flaws). This is an improvement over the conventional PE-UT results in which 85% of all flaws were detected. The flaw sizing performance shows that 94% of the detected flaws were sized properly (5 category for 100% coverage) versus 31% calculated for the conventional PE-UT method. Six percent of the flaws were sized in the 76%–99% coverage category. Therefore, 100% of the detected flaws were sized with 76%–100% accuracy. When using conventional PE-UT, only 58% of the detected flaws were sized with 76%–100% accuracy. Table 59 also shows a breakdown of percent detection based on flaw size. For example, 100% of the 2" flaws were detected. Of the smaller flaws, 100% of the 0.25" flaws were detected (versus 56% detection of the 0.25" flaws using conventional PE-UT).

The final POD curves in figure 184 highlight the human factor issues associated with any inspection that still involves human interpretation of data. This second, improved POD curve

was generated by results obtained when the inspector revisited the same iPLUS data, but spent additional time to study potential flaws in the images. The iPLUS system possesses full waveform data capture capabilities, which facilitated the ease of a second data review of both A-scan and C-scan data. When the data was analyzed a second time, it was observed that the POD value improved by 25% to an overall $POD_{[90/95]} = 0.641$ ". This new POD level is a 43% improvement over the overall result from the conventional PE-UT tests ($POD_{[90/95]} = 1.125$ ". This indicates that flaw detection, together with potentially reducing false calls, can be improved through the use of a second, follow-on inspector to aid in data interpretation.

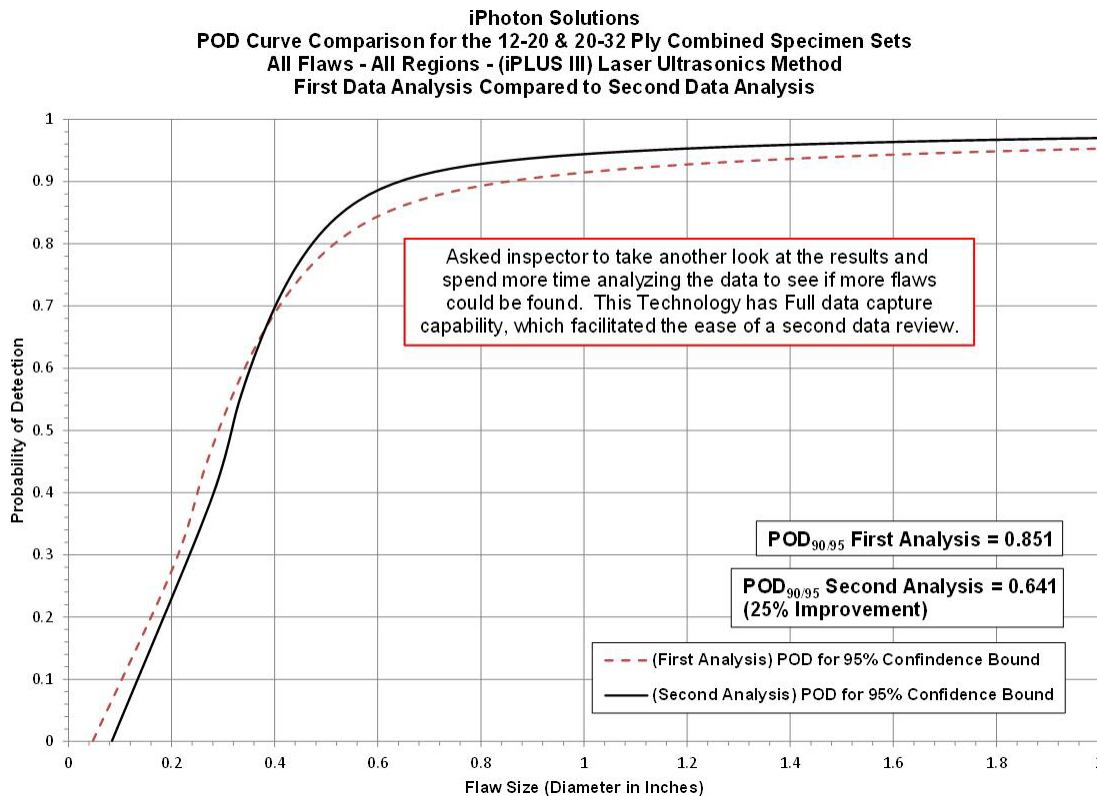


Figure 184. The POD improvements stemming from a second analysis of iPLUS LUS data

6.4 INSPECTION PERFORMANCE RESULTS FOR VIDEO-BASED UTs

6.4.1 Results for the Test Specimens Inspected by Imperium AcoustoCam

Figures 185–187 show the AcoustoCam device and the deployment of the equipment on the various SLE test specimens. Figure 187 reveals an issue associated with device accessibility within the spar cap channel region of the BN specimens. The size of the AcoustoCam imaging camera did not allow for full coverage of the inspection surface in this region. Inspections were completed with the Imperium AcoustoCam video-based (Digital Acoustic Video) UT inspection system, for which the single element transducer could operate in the 500 KHz–7.5 MHz range. The video setup possessed a resolution of 120 x 120 pixels (14,400 pixels per image). Sample UT images and A-scan data produced from the AcoustoCam video-based UT inspection of the SLE test specimens are shown in figure 188. Amplitude images and A-scan data were used to

detect the hidden flaws; various gates were used to detect the range of flaws at different depths within the specimens.



Figure 185. Imperium AcoustoCam video-based UT device



Figure 186. Deployment of the AcoustoCam video-based UT system on solid laminate POD experiment



Figure 187. Photographs showing some restriction in AcoustoCam movement within the confined spaces present on BN specimens (spar cap channel region)

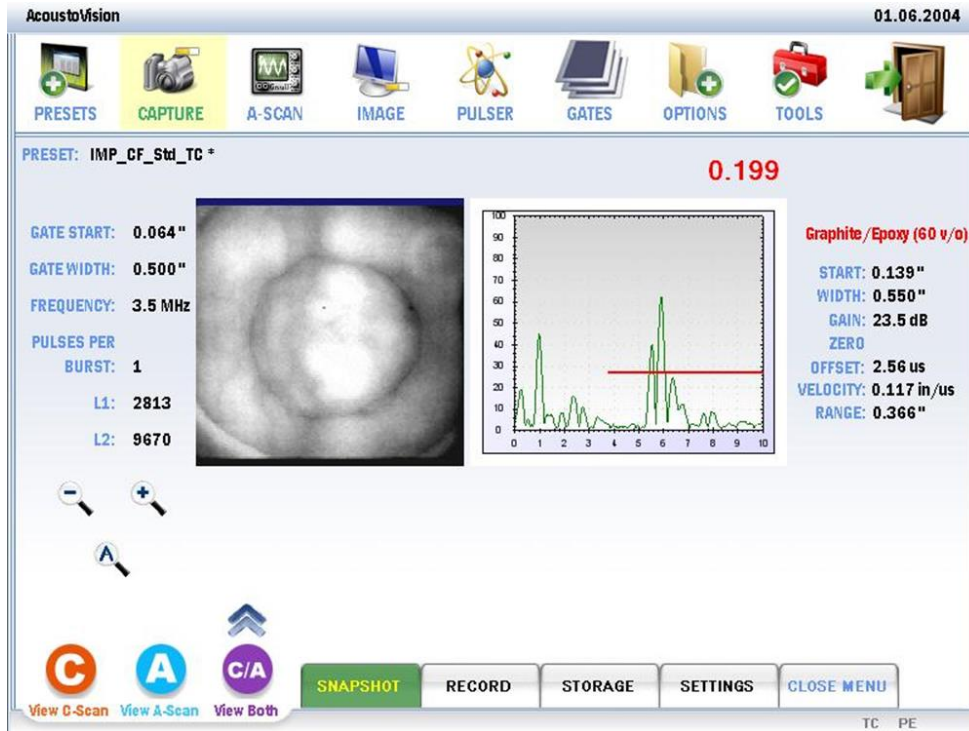


Figure 188. Typical UT image and A-scan display produced by AcoustoCam showing an individual flaw (small images can be placed into a full 2D C-scan using FirstMap software)

Figures 189 and 190 contain sample C-scan images produced by the AcoustoCam system. The new AcoustoCam FirstMap software takes a series of individual small images (see figure 188) and connects them in the proper order to generate real-time images of large inspection areas that are easier to read, more precise, and offer a greater level of detail. The built-in encoder and FirstMap software were not available at the time of the experiment.

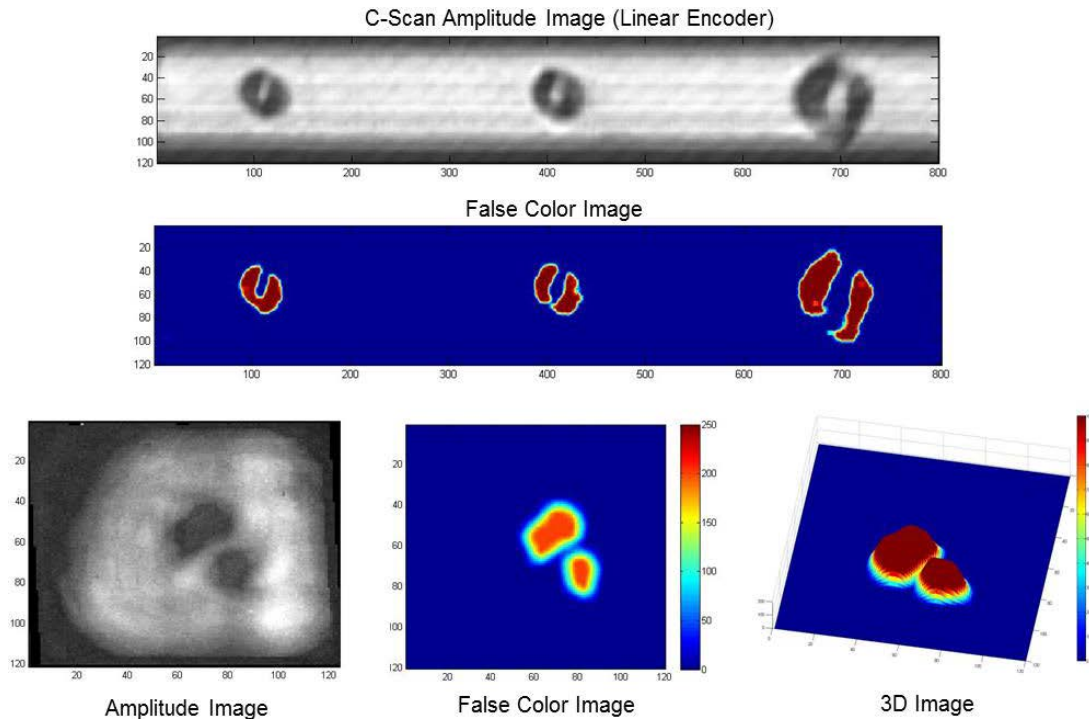


Figure 189. Image display options in AcoustoCam UT system

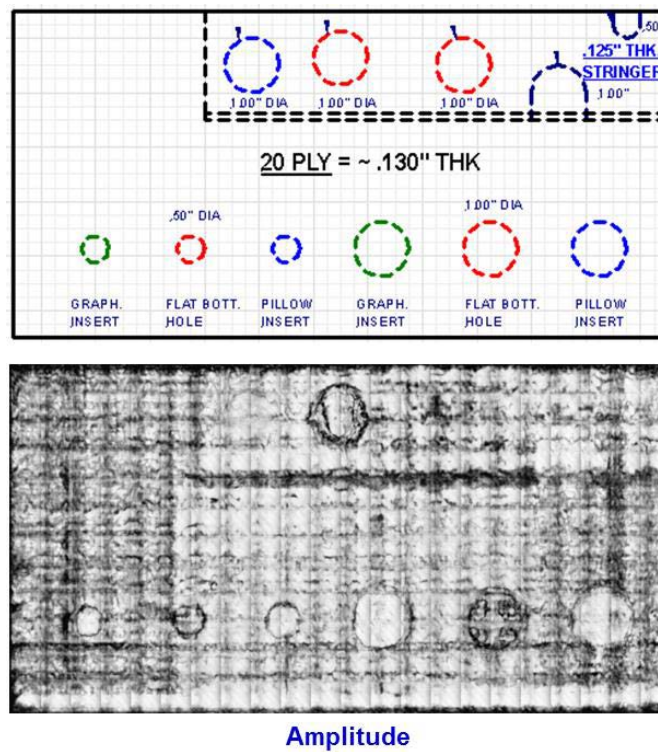


Figure 190. C-scan images produced by AcoustoCam video-based UT system inspection of SLE 20-ply reference panel (a series of individual images are placed into full 2D C-scan using FirstMap software)

Figure 191 contains the cumulative POD curve, combining all flaw detection results for both the thin (12–20 ply) laminate experiment and thick (20–32 ply) laminate experiment. The AcoustoCam video-based UT inspection system produced an overall $POD_{[90/95]} = 1.118''$. This is a 1% improvement over the overall result from the conventional PE-UT tests ($POD_{[90/95]} = 1.125''$) that evaluated the performance of airline inspectors (see section 6.1). The breakdown of results revealed performance for the thin laminate experiment of $POD_{[90/95]} = 1.422''$ and performance for the thick laminate experiment of $POD_{[90/95]} < 0.25''$ (i.e., 100% flaw detection; minimum flaw size of 0.25'' is upper bound for POD). Tables 60 and 61 delineate the flaw detection percentages for each of the specimen design attributes (i.e., constant thickness, CG, substructures regions, taper regions, curved surfaces and honeycomb regions). Tables 60 and 61 also show that there were no false calls for the entire experiment.

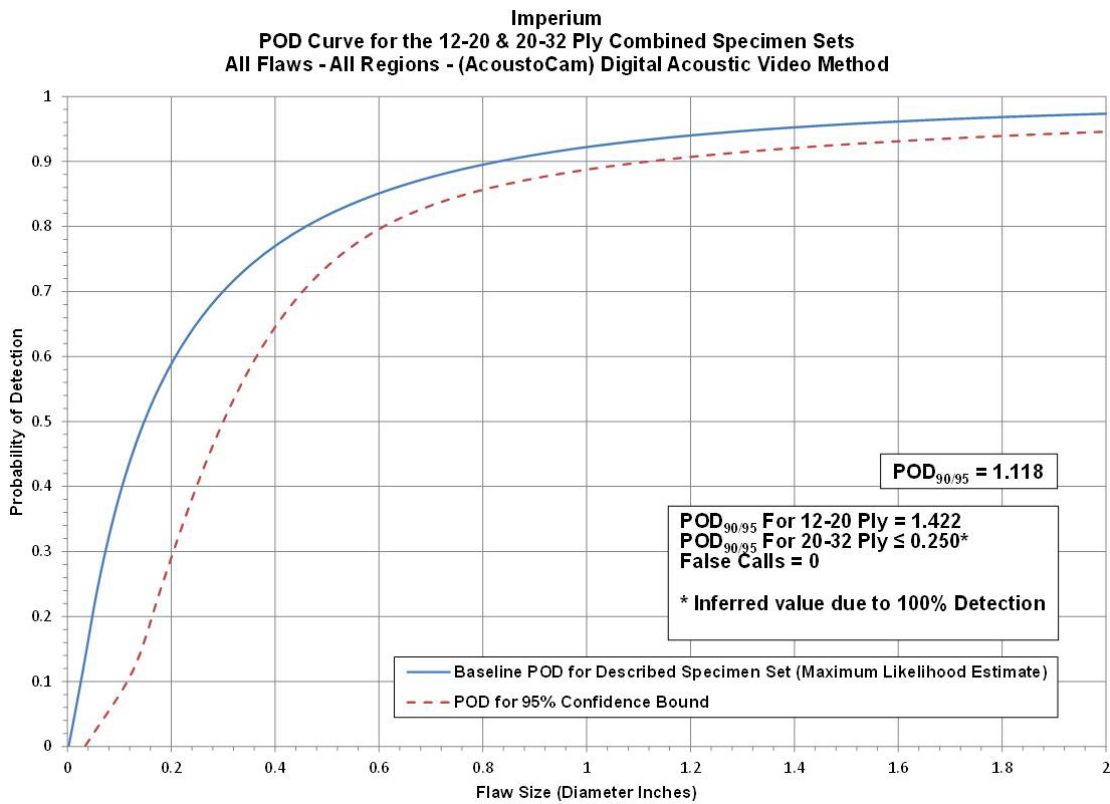


Figure 191. The POD results for AcoustoCam video-based UT system flaw detection in solid laminate composite structure

Table 60. Flaw detection performance for AcoustoCam video-based UT system separated into thin laminate and thick laminate results

Results – Imperium, (AcoustoCam) Digital Acoustic Video Method							
12–20 Ply (Thin Laminate Experiment)				20–32 Ply (Thick Laminate Experiment)			
POD _{90/95} Value	Percent Flaw Detection			POD _{90/95} Value	Percent Flaw Detection		
All Flaws Constant Thickness & CG Regions (dia. in inches)	All Flaws Constant Thickness & CG Regions	All Flaws Constant Thickness Regions Only	All Flaws CG Regions Only	All Flaws Constant Thickness & CG Regions (dia. in inches)	All Flaws Constant Thickness & CG Regions	All Flaws Constant Thickness Regions Only	All Flaws CG Regions Only
1.422	79%	90%	74%	100%*	100%	100%	100%
False Calls = 0				False Calls = 0			
*Inferred POD _{90/95} value is ≤ 0.25 " diameter flaw (100% flaw detection, POD value cannot be determined)							

Table 61. Flaw detection performance for AcoustoCam video-based UT system for the overall SLE

12–20 and 20–32 Ply Combined Results – Imperium, (AcoustoCam) Digital Acoustic Video Method									
POD _{90/95} Values			Percent Flaw Detection						
All Flaws Constant Thickness & CG Regions (dia. in inches)	All Flaws Constant Thickness Regions Only (dia. in inches)	All Flaws CG Regions Only (dia. in inches)	All Flaws Constant Thickness & CG Regions	All Flaws Constant Thickness Regions Only	All Flaws CG Regions Only	All Flaws Substructure Regions Only	All Flaws Taper Regions Only	All Flaws Laminate Over Honeycomb Regions Only	All Flaws Curved Surface Regions Only
1.118	97%	1.376	86%	93%	82%	64%	100%	96%	89%
								False Calls = 0	

Inspector flaw calls were also graded to evaluate the accuracy of the AcoustoCam video-based UT method for flaw sizing. The overall test results identified hits (i.e., calls with any amount of overlap between the call and the actual flaw location), misses (i.e., no call for an area of a known flaw), false calls (i.e., call with no overlap of a flaw), and sizing performance (i.e., the degree of overlap between experimenter calls and actual flaw areas). Tables 62–67 summarize the results for flaw sizing and percent detection based on flaw size for the thin laminate and thick laminate experiments, along with a breakdown of those performance attributes in the constant thickness and CG regions. Note that for the 12–20 ply specimen set, 79% of all flaws were detected (107 of 135 flaws; see table 64). This is a slight improvement over the conventional PE-UT results, in which 76% of all flaws were detected. The flaw sizing performance shows that 74% of the detected flaws were sized properly (5 category for 100% coverage) versus 38% calculated for the conventional PE-UT method. Twelve percent of the flaws were sized in the 76%–99% coverage category. Therefore, 86% of the detected flaws were sized with 76%–100% accuracy. When using conventional PE-UT, only 64% of the detected flaws were sized with 76%–100% accuracy. Table 64 shows a breakdown of percent detection based on flaw size. For example, 100% of the 2" flaws were detected. Of the smaller flaws, 50% of the 0.25" flaws were detected (versus 47% detection of the 0.25" flaws using conventional PE-UT).

Table 62. Tabulated results showing overall flaw detection percentage and accuracy in determining flaw size for the 12–20 ply specimen set for all flaws in constant thickness regions (AcoustoCam video-based UT system)

Imperium – (AcoustoCam) Digital Acoustic Video Flaw Detection Percentage & Accuracy in Determining Flaw Size 12–20 Ply Specimen Set – All Constant Thickness Flaws							
Accuracy in Sizing the Flaws That Were Detected						Flaw Detection Percentage	
Flaw Size	5 (100%)	4 (76%–99%)	3 (51%–75%)	2 (25%–50%)	1 (< 25%)	Flaw Size	Percent Detected
0.25	75%	0%	0%	0%	25%	0.25	67%
0.50	64%	0%	18%	18%	0%	0.50	100%
0.75	75%	13%	13%	0%	0%	0.75	80%
1.00	91%	0%	9%	0%	0%	1.00	92%
1.50	71%	29%	0%	0%	0%	1.50	100%
2.00	100%	0%	0%	0%	0%	2.00	100%
Overall Sizing Performance	77%	7%	9%	5%	2%	Overall Flaw Detection	90%

Table 63. Tabulated results showing overall flaw detection percentage and accuracy in determining flaw size for the 12–20 ply specimen set for all flaws in CG regions (AcoustoCam video-based UT system)

Imperium – (AcoustoCam) Digital Acoustic Video Flaw Detection Percentage & Accuracy in Determining Flaw Size 12–20 Ply Specimen Set – All CG Flaws							
Accuracy in Sizing the Flaws That Were Detected						Flaw Detection Percentage	
Flaw Size	5 (100%)	4 (76%–99%)	3 (51%–75%)	2 (25%–50%)	1 (< 25%)	Flaw Size	Percent Detected
0.25	67%	0%	0%	33%	0%	0.25	38%
0.50	77%	8%	8%	0%	8%	0.50	54%
0.75	74%	21%	5%	0%	0%	0.75	86%
1.00	79%	16%	0%	0%	5%	1.00	83%
1.50	56%	11%	22%	0%	11%	1.50	100%
2.00	0%	100%	0%	0%	0%	2.00	100%
Overall Sizing Performance	72%	16%	6%	2%	5%	Overall Flaw Detection	74%

Table 64. Tabulated results showing overall flaw detection percentage and accuracy in determining flaw size for the 12–20 ply specimen set for all flaws in constant thickness and CG regions (AcoustoCam video-based UT system)

Imperium – (AcoustoCam) Digital Acoustic Video Flaw Detection Percentage & Accuracy in Determining Flaw Size 12–20 Ply Specimen Set – All Flaws (Constant Thickness & CG)							
Accuracy in Sizing the Flaws That Were Detected						Flaw Detection Percentage	
Flaw Size	5 (100%)	4 (76%–99%)	3 (51%–75%)	2 (25%–50%)	1 (< 25%)	Flaw Size	Percent Detected
0.25	71%	0%	0%	14%	14%	0.25	50%
0.50	71%	4%	13%	8%	4%	0.50	69%
0.75	74%	19%	7%	0%	0%	0.75	84%
1.00	83%	10%	3%	0%	3%	1.00	86%
1.50	63%	19%	13%	0%	6%	1.50	100%
2.00	67%	33%	0%	0%	0%	2.00	100%
Overall Sizing Performance	74%	12%	7%	3%	4%	Overall Flaw Detection	79%

Table 65. Tabulated results showing overall flaw detection percentage and accuracy in determining flaw size for the 20–32 ply specimen set for all flaws in constant thickness regions (AcoustoCam video-based UT system)

Imperium – (AcoustoCam) Digital Acoustic Video Flaw Detection Percentage & Accuracy in Determining Flaw Size 20–32 Ply Specimen Set – All Constant Thickness Flaws							
Accuracy in Sizing the Flaws That Were Detected						Flaw Detection Percentage	
Flaw Size	5 (100%)	4 (76%–99%)	3 (51%–75%)	2 (25%–50%)	1 (< 25%)	Flaw Size	Percent Detected
0.25	25%	0%	0%	25%	50%	0.25	100%
0.50	50%	25%	25%	0%	0%	0.50	100%
0.75	50%	17%	33%	0%	0%	0.75	100%
1.00	67%	33%	0%	0%	0%	1.00	100%
1.50	0%	0%	100%	0%	0%	1.50	100%
2.00	67%	33%	0%	0%	0%	2.00	100%
Overall Sizing Performance	50%	21%	17%	4%	8%	Overall Flaw Detection	100%

Table 66. Tabulated results showing overall flaw detection percentage and accuracy in determining flaw size for the 20–32 ply specimen set for all flaws in CG regions (AcoustoCam video-based UT system)

Imperium – (AcoustoCam) Digital Acoustic Video Flaw Detection Percentage & Accuracy in Determining Flaw Size 20–32 Ply Specimen Set – All CG Flaws							
Accuracy in Sizing the Flaws That Were Detected						Flaw Detection Percentage	
Flaw Size	5 (100%)	4 (76%–99%)	3 (51%–75%)	2 (25%–50%)	1 (< 25%)	Flaw Size	Percent Detected
0.25	57%	29%	0%	0%	14%	0.25	100%
0.50	56%	22%	0%	11%	11%	0.50	100%
0.75	50%	25%	25%	0%	0%	0.75	100%
1.00	36%	36%	27%	0%	0%	1.00	100%
1.50	50%	50%	0%	0%	0%	1.50	100%
2.00	100%	0%	0%	0%	0%	2.00	100%
Overall Sizing Performance	51%	30%	12%	2%	5%	Overall Flaw Detection	100%

Table 67. Tabulated results showing overall flaw detection percentage and accuracy in determining flaw size for the 20–32 ply specimen set for all flaws in constant thickness and CG regions (AcoustoCam video-based UT system)

Imperium – (AcoustoCam) Digital Acoustic Video Flaw Detection Percentage & Accuracy in Determining Flaw Size 20–32 Ply Specimen Set – All CG Flaws							
Accuracy in Sizing the Flaws That Were Detected						Flaw Detection Percentage	
Flaw Size	5 (100%)	4 (76%–99%)	3 (51%–75%)	2 (25%–50%)	1 (< 25%)	Flaw Size	Percent Detected
0.25	45%	18%	0%	9%	27%	0.25	100%
0.50	54%	23%	8%	8%	8%	0.50	100%
0.75	50%	21%	29%	0%	0%	0.75	100%
1.00	47%	35%	18%	0%	0%	1.00	100%
1.50	43%	43%	14%	0%	0%	1.50	100%
2.00	80%	20%	0%	0%	0%	2.00	100%
Overall Sizing Performance	51%	27%	13%	3%	6%	Overall Flaw Detection	100%

Table 67 summarizes the results for the overall flaw detection percentage and the associated accuracy in determining flaw size for the 20–32 ply specimen set (thick laminate experiment). For the 20–32 ply specimen set, 100% of all flaws were detected (67 of 67 flaws). This is an improvement over the conventional PE-UT results, in which 85% of all flaws were detected. The flaw sizing performance shows that 51% of the detected flaws were sized properly (5 category

for 100% coverage) versus 31% calculated for the conventional PE-UT method. Twenty-seven percent of the flaws were sized in the 76%–99% coverage category. Therefore, 78% of the detected flaws were sized with 76%–100% accuracy. When using conventional PE-UT, only 58% of the detected flaws were sized with 76%–100% accuracy. Table 67 also shows a breakdown of percent detection based on flaw size. For example, 100% of the 2" flaws and 100% of the 0.25" flaws were detected (versus 56% detection of the 0.25" flaws using conventional PE-UT).

6.4.2 Results for the Test Specimens Inspected by DolphiTech DolphiCam

Figures 192 and 193 show the DolphiTech DolphiCam device and deployment of the equipment on various composite test specimens. Inspections were completed with the DolphiCam video-based UT inspection system, which contains a 16,000 element UT transducer, ranging from 2–6 MHz. Sample UT images—A-scan and B-scan data produced from the DolphiCam video-based UT inspection of various test specimens—are shown in figures 194–197. C-scans produced from different types of composite laminate damage are shown in these figures. Amplitude, time-of-flight, and B-scan images are used to detect the hidden flaws; various gates were also used to detect the range of flaws at different depths within the specimens. Figure 197 shows a series of individual damage images that have been arranged to produce an overall 2D map of an SLE feedback test panel. The DolphiCam now has software to automate this placement of individual images into an overall C-scan; however, this software was not available for testing when DolphiTech participated in this SLE.

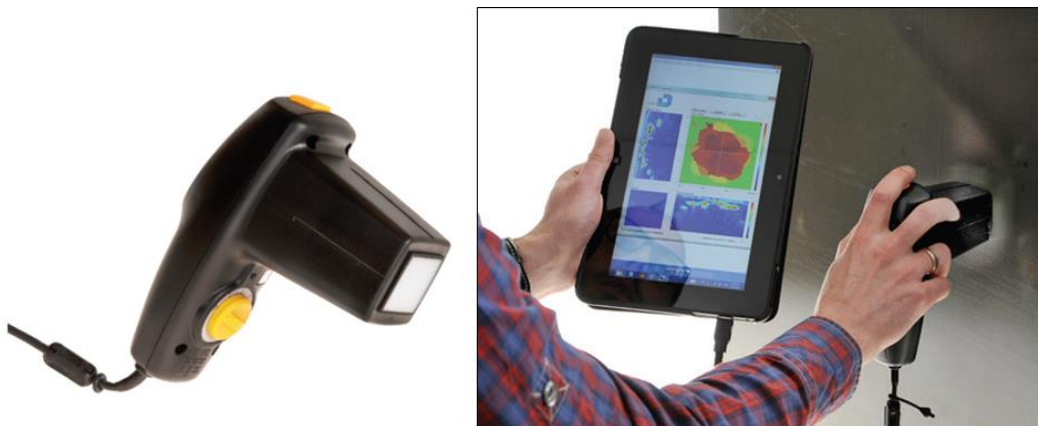


Figure 192. DolphiTech DolphiCam video-based UT device

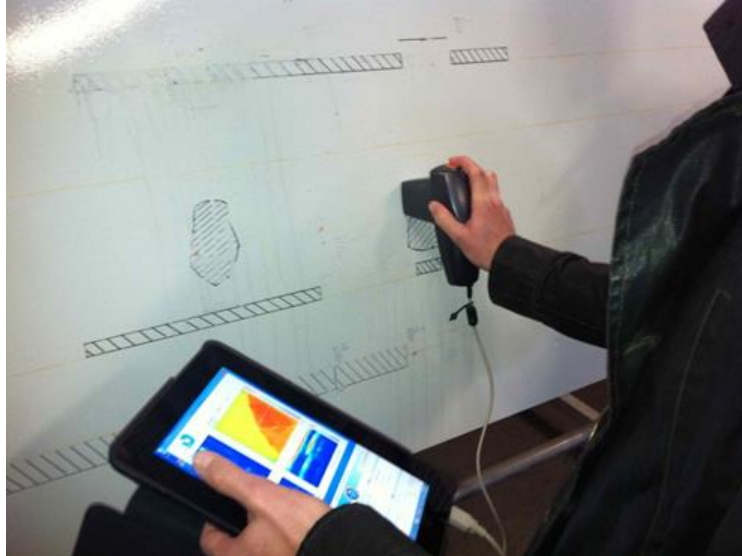


Figure 193. Deployment of DolphiCam video-based UT system on full-scale composite panel (image of impact damage on screen)

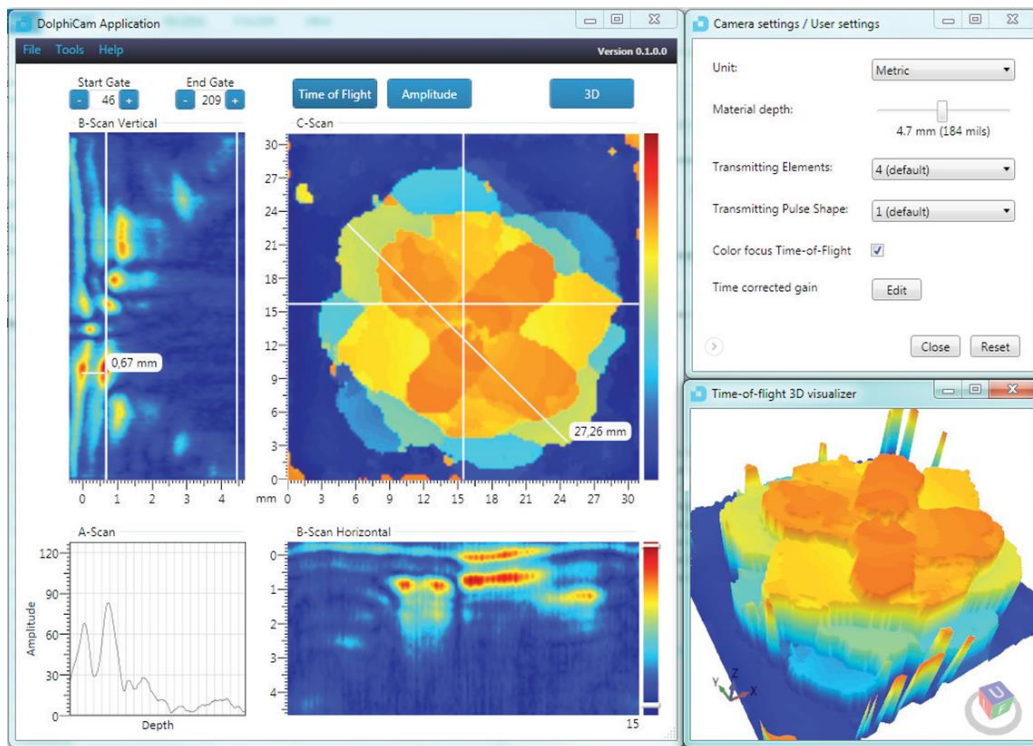


Figure 194. Typical UT image and A-scan display produced by DolphiCam showing an individual flaw

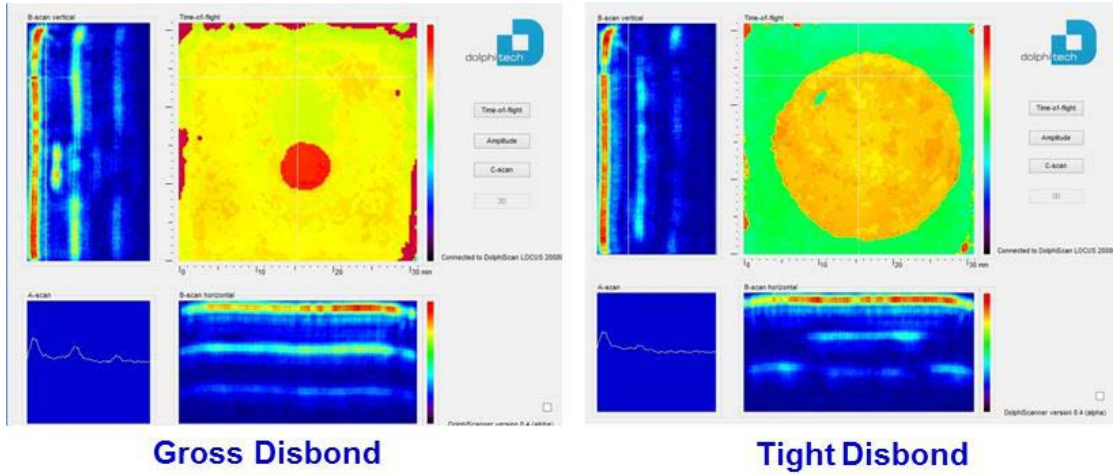


Figure 195. Image displays produced by DolphiCam UT system for different flaw types

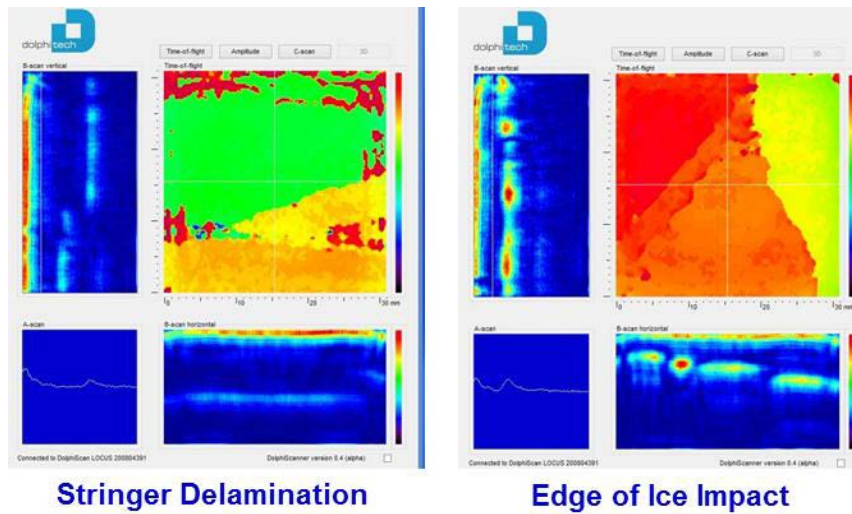


Figure 196. Image displays produced by DolphiCam UT system for delamination and impact damage

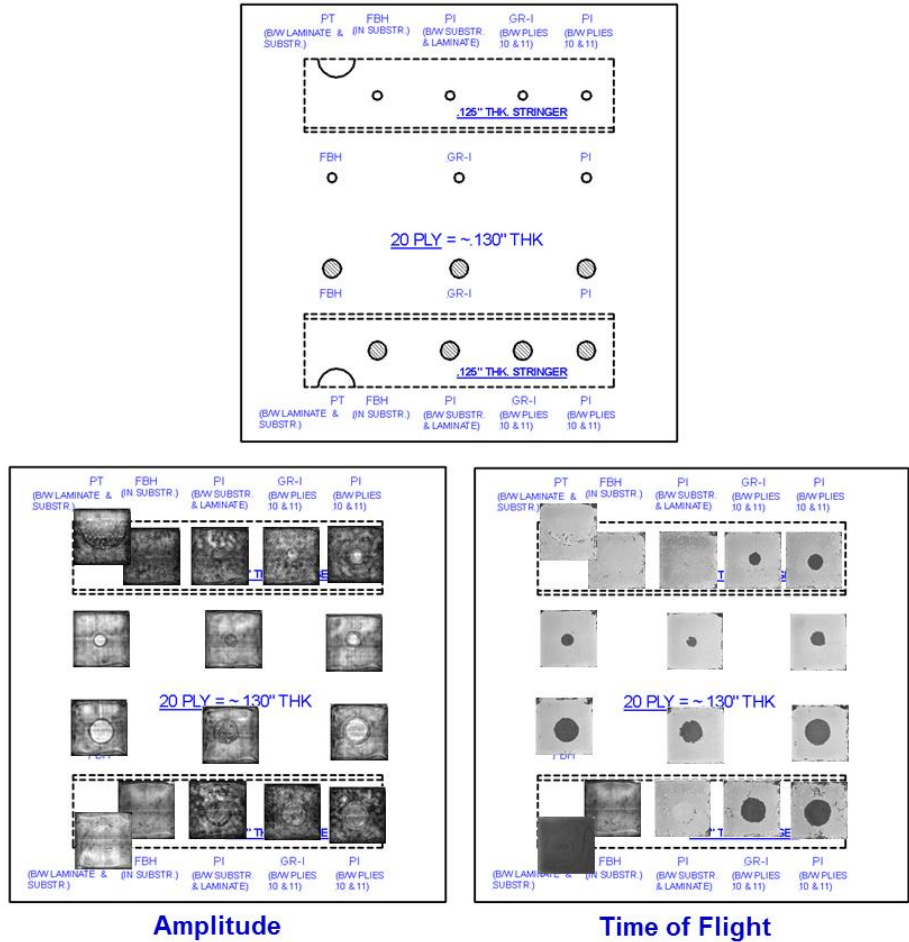


Figure 197. Flaw images produced by DolphiCam video-based UT system inspection of SLE 20-ply reference panel

The DolphiCam video-based UT inspection system was only applied to the SLE feedback specimens and some of the AANC composite impact panels. As a result, there are no POD levels or flaw detection percentages available for comparison with the other advanced NDI methods.

6.5 INSPECTION PERFORMANCE RESULTS FOR MW

6.5.1 Results for the Test Specimens Inspected by Evisive MW

Figures 198 and 199 show the Evisive MW device and the deployment of the equipment on the various SLE test specimens. Inspections were completed with the Evisive MW inspection device connected to a 24 GHz probe. Sample A-scan and C-scan data produced from the Evisive MW inspection of the SLE test specimens are shown in figure 200. As discussed in section 3, the MW inspection method requires specific material properties to be successful in generating the signals needed for identifying damage in a component. The carbon fiber composite material did not have the acceptable dielectric properties needed for the propagation of the Evisive scan waves. Therefore, no productive scans could be obtained from the MW inspection method. Figure 200 shows the lack of detail in the MW scan, which eliminated the possibility of differentiating the

flaws from the unflawed regions. As a result, there are no POD levels or flaw detection percentages available for comparison with the other advanced NDI methods.

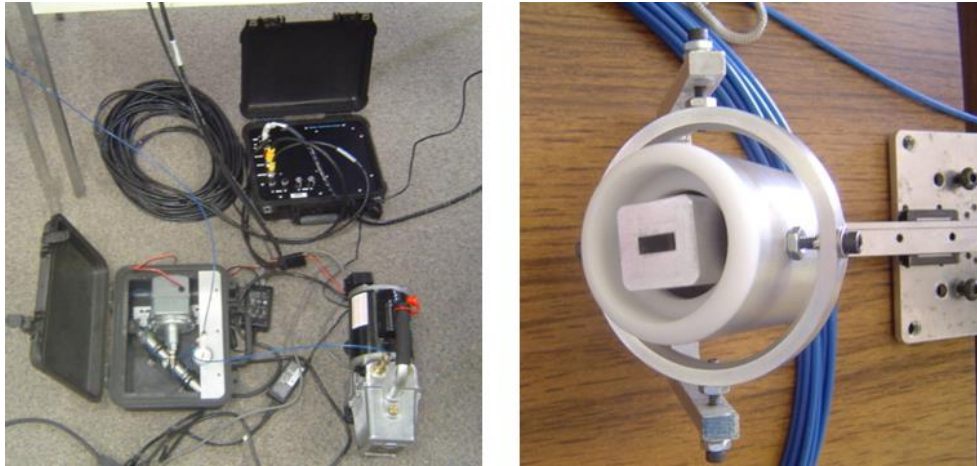


Figure 198. Evisive MW device

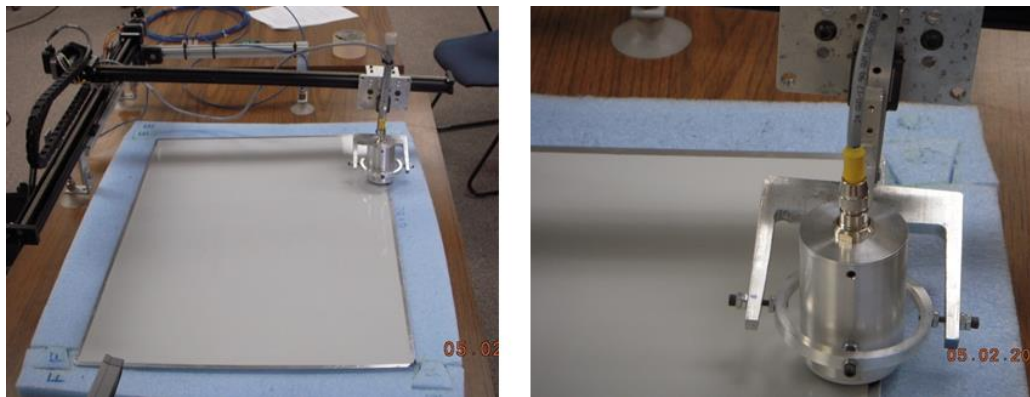


Figure 199. Deployment of Evisive MW system on SLE

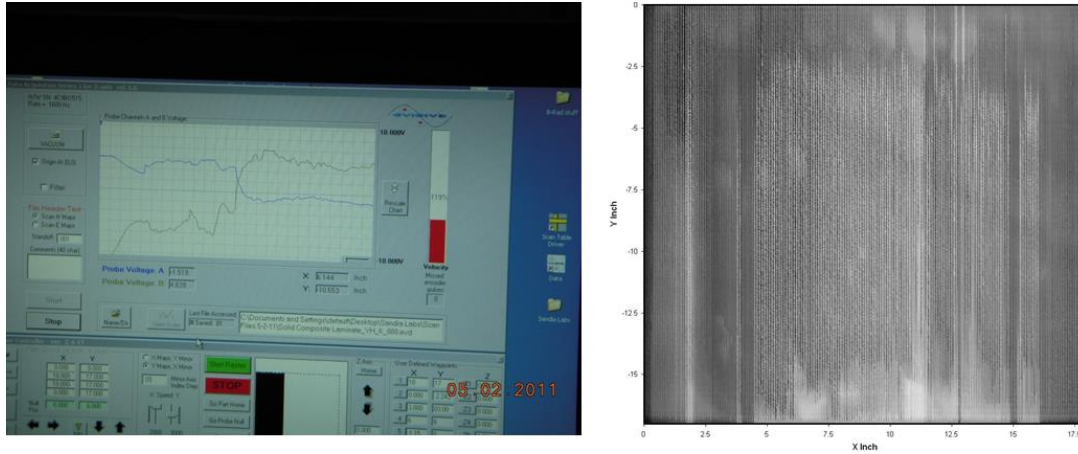


Figure 200. Typical A-scan display image produced by Evisive MW system in SLE

6.6 INSPECTION PERFORMANCE RESULTS FOR SHEAROGRAPHY

6.6.1 Results for the Test Specimens Inspected by LTI Shearography

Figure 201 shows the LTI Shearography System (5100 HD) and the deployment of the equipment on the various SLE test specimens. Inspections were completed with the 5100 HD shearography inspection device that included a LTI-5100 HD camera, TES-200 Thermal Excitation System, and a 150 mW green laser. Sample shearography images produced from the 5100 HD shearography inspection of the SLE test specimens are shown in figures 202 and 203. Changes in surface deformation, and associated shading of the images, were used to detect the hidden flaws. Substructure flaws must manifest themselves as changes (anomalies) in out-of-plane deformation on the surface of the part to be detected by shearography. As a result, thick and stiff structures are a challenge for the shearography inspection method. Small flaws, especially those embedded deep within a structure, are difficult to image as their presence has less of an effect on surface deformations.



Figure 201. Deployment of LTI Shearography System (5100 HD) on SLE

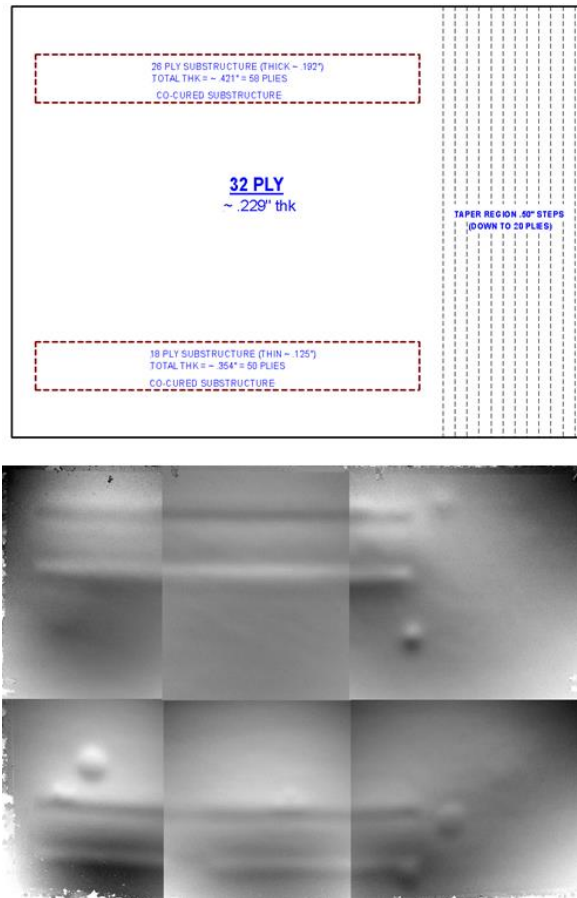
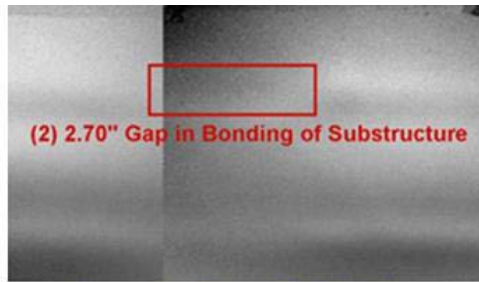
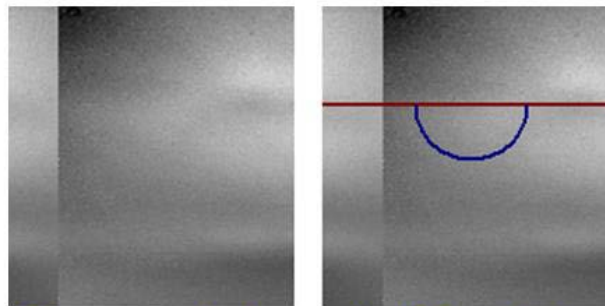


Figure 202. Shearography images produced by LTI Shearography System inspection of SLE 32-ply laminate test panel



Sample Flaw Called by Shearography System



Shearography Image (left) Containing Undetected Flaw (indicated on right)

Figure 203. Shearography images produced by LTI Shearography System showing flaw detection and missed flaws

Figure 204 contains the POD flaw detection curve for the thick (20–32 ply) laminate experiment. The 5100 HD shearography device was not applied to the thin laminate experiment; all results are for the thick laminate experiment only. The 5100 HD shearography system produced a thick laminate $POD_{[90/95]} > 3.0''$. This represents a 265% drop in performance versus the thick laminate results from the conventional PE-UT tests ($POD_{[90/95]} = 0.823''$) that evaluated the performance of airline inspectors (see section 6.1). Table 68 delineates the flaw detection percentages for each of the specimen design attributes (i.e., constant thickness, CG, substructures regions, and taper regions). Note that the 5100 HD shearography performed slightly better detecting flaws in the constant thickness regions (42% detection) of the test specimens than in the CG regions (33% detection), although both were worse performance numbers than those produced by conventional PE-UT. No flaws in the substructure were detected, although many (5 out of 6) of the disbonds (pull-tabs) at the 32-ply level were detected. No flat bottom hole disbonds, graphoil insert disbonds, or pillow insert disbonds were detected. This table also shows that there were no false calls for the entire experiment.

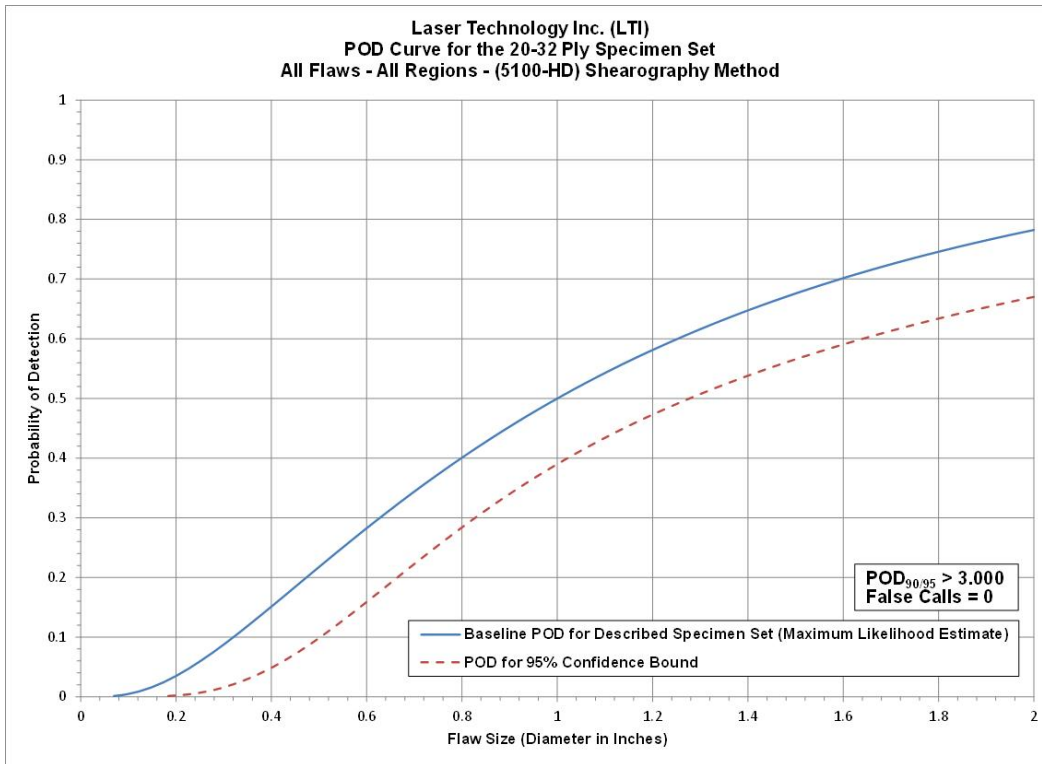


Figure 204. The POD results for LTI shearography system flaw detection in solid laminate composite structure (20–32 ply specimen set)

Table 68. Flaw detection performance for LTI shearography system separated into thick laminate results

Results – Laser Technology Inc. (LTI) – (5100 HD) Shearography Method			
20–32 Ply (Thick Laminate Experiment)			
POD _{90/95} Value	Percent Flaw Detection		
All Flaws Constant Thickness & CG Regions (dia. in inches)	All Flaws Constant Thickness & CG Regions	All Flaws Constant Thickness Regions Only	All Flaws CG Regions Only
> 3.000	36%	42%	33%
False Calls = 0			

Inspector flaw calls were also graded to evaluate the accuracy of the 5100 HD shearography method for flaw sizing. The overall test results identified hits (i.e., calls with any amount of overlap between the call and the actual flaw location), misses (i.e., no call for an area of a known flaw), false calls (i.e., call with no overlap of a flaw), and sizing performance (i.e., the degree of overlap between experimenter calls and actual flaw areas). Tables 69–71 summarize the results for flaw sizing and percent detection based on flaw size for the thick laminate experiment, along with a breakdown of those performance attributes in the constant thickness and CG regions.

Table 69. Tabulated results showing overall flaw detection percentage and accuracy in determining flaw size for the 20–32 ply specimen set for all flaws in constant thickness regions (LTI shearography system)

Laser Technology Inc. (LTI) – (5100 HD) Shearography Flaw Detection Percentage & Accuracy in Determining Flaw Size 20–32 Ply Specimen Set – All Constant Thickness Flaws							
Accuracy in Sizing the Flaws That Were Detected						Flaw Detection Percentage	
Flaw Size	5 (100%)	4 (76%–99%)	3 (51%–75%)	2 (25%–50%)	1 (< 25%)	Flaw Size	Percent Detected
0.25	0%	0%	0%	0%	0%	0.25	0%
0.50	50%	0%	50%	0%	0%	0.50	50%
0.75	100%	0%	0%	0%	0%	0.75	50%
1.00	67%	33%	0%	0%	0%	1.00	50%
1.50	0%	0%	0%	0%	0%	1.50	0%
2.00	50%	0%	0%	0%	50%	2.00	67%
Overall Sizing Performance	70%	10%	10%	0%	10%	Overall Flaw Detection	42%

Table 70. Tabulated results showing overall flaw detection percentage and accuracy in determining flaw size for the 20–32 ply specimen set for all flaws in CG regions (LTI shearography system)

Laser Technology Inc. (LTI) – (5100 HD) Shearography Flaw Detection Percentage & Accuracy in Determining Flaw Size 20–32 Ply Specimen Set – All CG Flaws							
Accuracy in Sizing the Flaws That Were Detected						Flaw Detection Percentage	
Flaw Size	5 (100%)	4 (76%–99%)	3 (51%–75%)	2 (25%–50%)	1 (< 25%)	Flaw Size	Percent Detected
0.25	0%	0%	0%	0%	0%	0.25	0%
0.50	100%	0%	0%	0%	0%	0.50	22%
0.75	25%	25%	25%	0%	25%	0.75	50%
1.00	100%	0%	0%	0%	0%	1.00	36%
1.50	25%	50%	25%	0%	0%	1.50	67%
2.00	0%	0%	0%	0%	0%	2.00	0%
Overall Sizing Performance	57%	21%	14%	0%	7%	Overall Flaw Detection	33%

Table 71. Tabulated results showing overall flaw detection percentage and accuracy in determining flaw size for the 20–32 ply specimen set for all flaws in constant thickness and CG regions (LTI shearography system)

Laser Technology Inc. (LTI) – (5100 HD) Shearography Flaw Detection Percentage & Accuracy in Determining Flaw Size 20–32 Ply Specimen Set – All Flaws (Constant Thickness & CG)							
Accuracy in Sizing the Flaws That Were Detected						Flaw Detection Percentage	
Flaw Size	5 (100%)	4 (76%–99%)	3 (51%–75%)	2 (25%–50%)	1 (< 25%)	Flaw Size	Percent Detected
0.25	0%	0%	0%	0%	0%	0.25	0%
0.50	75%	0%	25%	0%	0%	0.50	31%
0.75	57%	14%	14%	0%	14%	0.75	50%
1.00	86%	14%	0%	0%	0%	1.00	41%
1.50	25%	50%	25%	0%	0%	1.50	57%
2.00	50%	0%	0%	0%	50%	2.00	40%
Overall Sizing Performance	63%	17%	13%	0%	8%	Overall Flaw Detection	36%

Table 71 summarizes the results for the overall flaw detection percentage and the associated accuracy in determining flaw size for the 20–32 ply specimen set (thick laminate experiment). For the 20–32 ply specimen set, 36% of all flaws were detected (24 of 67 flaws). This represents a drop in performance versus the conventional PE-UT results, in which 85% of all flaws were detected. The flaw sizing performance shows that 63% of the detected flaws were sized properly (5 category for 100% coverage) versus 31% calculated for the conventional PE-UT method. Seventeen percent of the flaws were sized in the 76%–99% coverage category. Therefore, 80% of the detected flaws were sized with 76%–100% accuracy. When using conventional PE-UT, only 58% of the detected flaws were sized with 76%–100% accuracy. Table 71 shows a breakdown of percent detection based on flaw size. For example, 40% of the 2" flaws were detected. Of the smaller flaws, 0% of the 0.25" flaws were detected (a performance decrease versus 56% detection of the 0.25" flaws using conventional PE-UT).

6.6.2 Results for the Test Specimens Inspected by Dantec Dynamics Shearography

Figures 205–207 show the Dantec Dynamics Q-800 shearography device and the deployment of the equipment on the various SLE test specimens. Inspections were completed with the Q-800 shearography system consisting of a miniaturized shearography sensor with integrated high-resolution CCD and variable computer-controlled shear optics. Illumination was provided by an integrated diode laser array and the entire system was controlled from a laptop PC using the Istra 4D software platform. This shearography system can be used to detect defects such as delaminations, disbonds, kissing bonds, wrinkling, and impact damage. The interferometric technique measures microscopic surface deformations caused by internal flaws when a small load is applied to the object. This can be completed using thermal, pressure, vibration, or mechanical excitation. The results are displayed live as the material responds to the excitation and can then be interpreted by the operator. The Q-810 device was used with vacuum loading for

some of the test specimens (see figure 206), whereas other inspections used thermal loading (i.e., heat gun) and the Q-800 shearography device to induce the deformations needed for flaw detection (see figure 207). Sample shearography images produced from the Dantec Dynamics shearography inspection of the SLE test specimens are shown in figure 208.

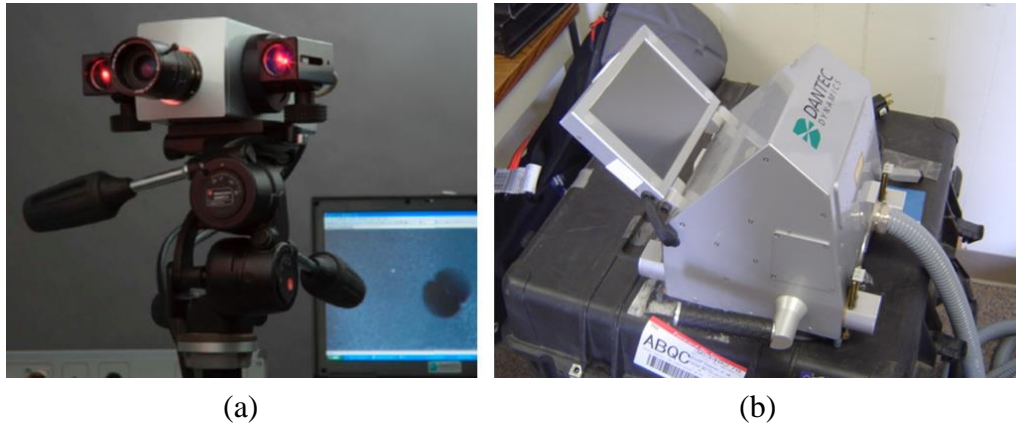


Figure 205. Dantec Dynamics shearography devices: the (a) Q800 and (b) Q810



Figure 206. Deployment of the Dantec Dynamics Q800 shearography systems on SLE

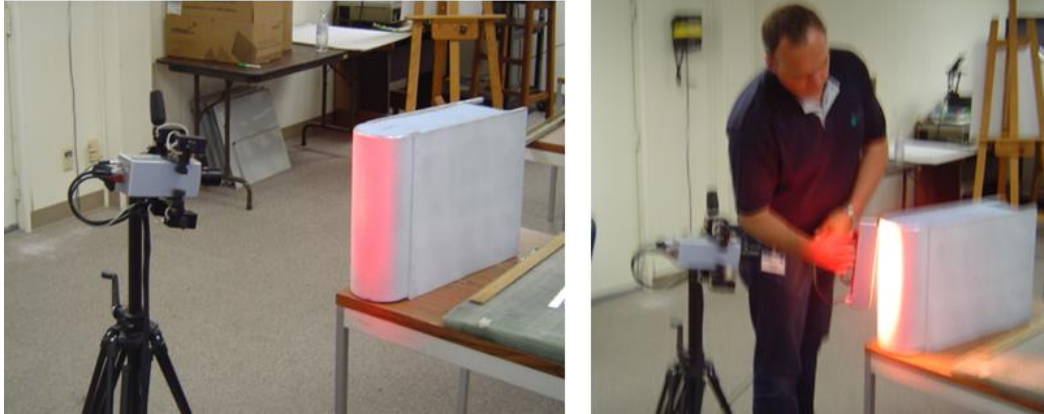


Figure 207. Deployment of the Dantec Dynamics Q810 shearography systems on SLE

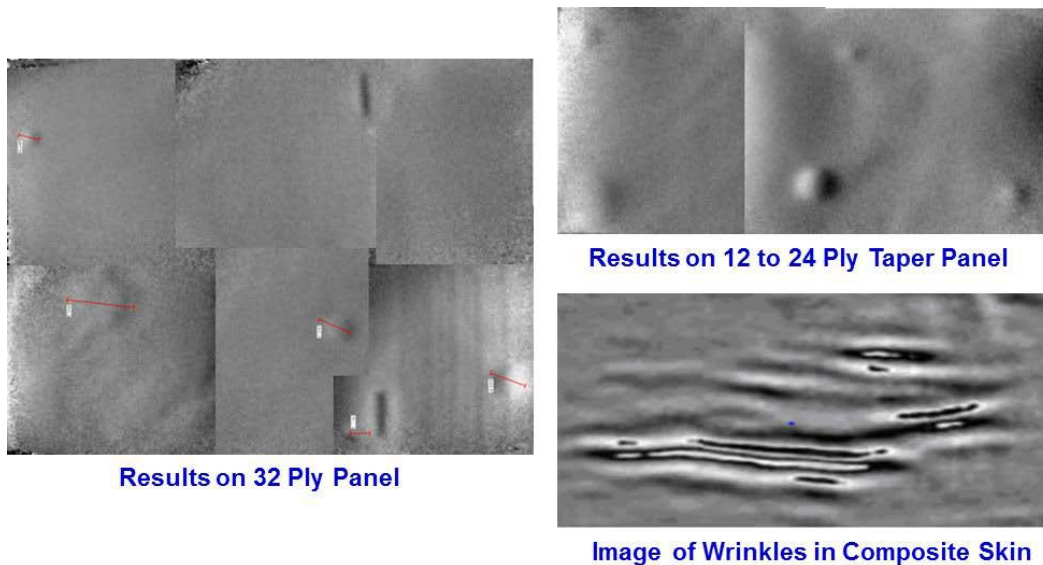


Figure 208. Shearography images produced by Dantec Dynamics shearography inspection of composite test specimens

Figure 209 contains the cumulative POD curve when combining all flaw detection results for both the thin (12–20 ply) laminate experiment and thick (20–32 ply) laminate experiment. The Dantec Dynamics Q-800 and Q-810 shearography systems produced an overall $POD_{[90/95]} > 3.0''$. This represents a drop in performance of 167% versus the overall result from the conventional PE-UT tests ($POD_{[90/95]} = 1.125''$) that evaluated the performance of airline inspectors (see section 6.1). The breakdown of results revealed performance for the thin laminate experiment of $POD_{[90/95]} > 3.0''$ and performance for the thick laminate experiment of $POD_{[90/95]} > 3.0''$. Both performance levels were well below those observed using conventional PE-UT methods. Tables 72 and 73 delineate the flaw detection percentages for each of the specimen design attributes (i.e., constant thickness, CG, substructures regions, taper regions, curved surfaces, and honeycomb regions). Tables 72 and 73 also show that there was 1 false call for the entire experiment.

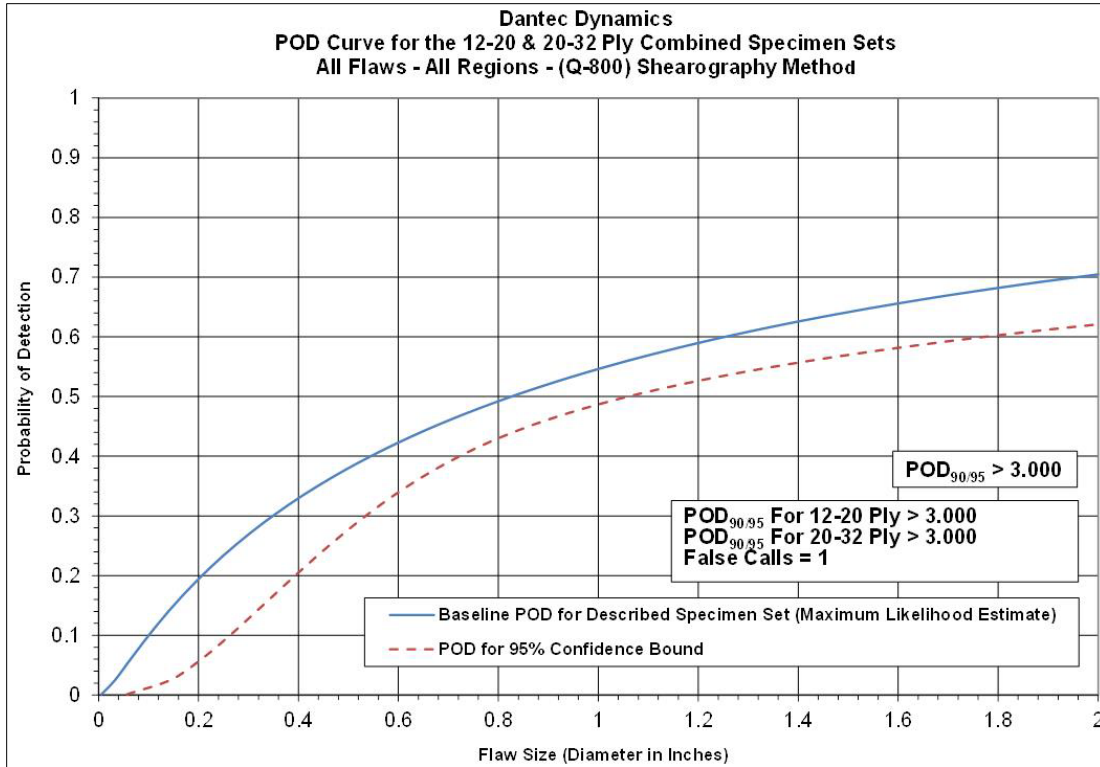


Figure 209. The POD results for Dantec Dynamics shearography system flaw detection in solid laminate composite structure

Table 72. Flaw detection performance for Dantec Dynamics shearography system separated into thin laminate and thick laminate results

Results – Dantec Dynamics, (Q-800) Shearography Method							
12–20 Ply (Thin Laminate Experiment)				20–32 Ply (Thick Laminate Experiment)			
POD _{90/95} Value	Percent Flaw Detection			POD _{90/95} Value	Percent Flaw Detection		
All Flaws Constant Thickness & CG Regions (dia. in inches)	All Flaws Constant Thickness & CG Regions	All Flaws Constant Thickness Regions Only	All Flaws CG Regions Only	All Flaws Constant Thickness & CG Regions (dia. in inches)	All Flaws Constant Thickness & CG Regions	All Flaws Constant Thickness Regions Only	All Flaws CG Regions Only
>3.000	53%	67%	46%	>3.000	34%	54%	23%
False Calls = 1				False Calls = 0			

Table 73. Flaw detection performance for Dantec Dynamics shearography system for the overall SLE

12–20 and 20–32 Ply Combined Results – Dantec Dynamics, (Q-800) Shearography Method									
POD _{90/95} Values			Percent Flaw Detection						
All Flaws Constant Thickness & CG Regions (dia. in inches)	All Flaws Constant Thickness Regions Only (dia. in inches)	All Flaws CG Regions Only (dia. in inches)	All Flaws Constant Thickness & CG Regions	All Flaws Constant Thickness Regions Only	All Flaws CG Regions Only	All Flaws Substructure Regions Only	All Flaws Taper Regions Only	All Flaws Laminate Over Honeycomb Regions Only	All Flaws Curved Surface Regions Only
> 3	> 3	> 3	47%	63%	38%	28%	43%	48%	67%
								False Calls = 1	

Tables 74–79 summarize the results for flaw sizing and percent detection based on flaw size for the thin laminate and thick laminate experiments. Note that for the 12–20 ply specimen set, 53% of all flaws were detected (72 of 135 flaws; see table 76). This is a performance decrease versus the conventional PE-UT results, in which 76% of all flaws were detected. Table 76 also shows a breakdown of percent detection based on flaw size. For example, 100% of the 2" flaws were detected. Of the smaller flaws, only 14% of the 0.25" flaws were detected (versus 47% detection of the 0.25" flaws using conventional PE-UT). For the 20–32 ply specimen set, 34% of all flaws were detected (23 of 67 flaws; see table 79). This is a performance decrease versus the conventional PE-UT results, in which 85% of all flaws were detected. Table 79 also shows a breakdown of percent detection based on flaw size. For example, 60% of the 2" flaws were detected. Of the smaller flaws, only 9% of the 0.25" flaws were detected (versus 56% detection of the 0.25" flaws using conventional PE-UT). It was not possible to evaluate the flaw sizing performance of the Dantec Dynamics Q-800 and Q-810 shearography system because flaw sizing was not provided by the experiment participants.

Table 74. Tabulated results showing overall flaw detection percentage and accuracy in determining flaw size for the 12–20 ply specimen set for all flaws in constant thickness regions (Dantec Dynamics shearography system)

Dantec Dynamics – (Q-800) Shearography Flaw Detection Percentage & Accuracy in Determining Flaw Size 12–20 Ply Specimen Set – All Constant Thickness Flaws							
Accuracy in Sizing the Flaws That Were Detected						Flaw Detection Percentage	
Flaw Size	5 (100%)	4 (76%–99%)	3 (51%–75%)	2 (25%–50%)	1 (< 25%)	Flaw Size	Percent Detected
0.25	Flaw sizing not provided					0.25	33%
0.50						0.50	64%
0.75						0.75	60%
1.00						1.00	75%
1.50						1.50	86%
2.00						2.00	100%
Overall Sizing Performance						N/A	N/A

Table 75. Tabulated results showing overall flaw detection percentage and accuracy in determining flaw size for the 12–20 ply specimen set for all flaws in CG regions (Dantec Dynamics shearography system)

Dantec Dynamics – (Q-800) Shearography Flaw Detection Percentage & Accuracy in Determining Flaw Size 12–20 Ply Specimen Set – All CG Flaws							
Accuracy in Sizing the Flaws That Were Detected						Flaw Detection Percentage	
Flaw Size	5 (100%)	4 (76%–99%)	3 (51%–75%)	2 (25%–50%)	1 (< 25%)	Flaw Size	Percent Detected
0.25	Flaw sizing not provided					0.25	0%
0.50						0.50	46%
0.75						0.75	55%
1.00						1.00	48%
1.50						1.50	56%
2.00						2.00	100%
Overall Sizing Performance						N/A	N/A

Table 76. Tabulated results showing overall flaw detection percentage and accuracy in determining flaw size for the 12–20 ply specimen set for all flaws in constant thickness and CG regions (Dantec Dynamics shearography system)

Dantec Dynamics – (Q-800) Shearography Flaw Detection Percentage & Accuracy in Determining Flaw Size 12–20 Ply Specimen Set – All Flaws (Constant Thickness & CG)							
Accuracy in Sizing the Flaws That Were Detected						Flaw Detection Percentage	
Flaw Size	5 (100%)	4 (76%–99%)	3 (51%–75%)	2 (25%–50%)	1 (< 25%)	Flaw Size	Percent Detected
0.25	Flaw sizing not provided					0.25	14%
0.50						0.50	51%
0.75						0.75	56%
1.00						1.00	57%
1.50						1.50	69%
2.00						2.00	100%
Overall Sizing Performance						N/A	N/A

Table 77. Tabulated results showing overall flaw detection percentage and accuracy in determining flaw size for the 20–32 ply specimen set for all flaws in constant thickness regions (Dantec Dynamics shearography system)

Dantec Dynamics – (Q-800) Shearography Flaw Detection Percentage & Accuracy in Determining Flaw Size 20–32 Ply Specimen Set – All Constant Thickness Flaws							
Accuracy in Sizing the Flaws That Were Detected						Flaw Detection Percentage	
Flaw Size	5 (100%)	4 (76%–99%)	3 (51%–75%)	2 (25%–50%)	1 (< 25%)	Flaw Size	Percent Detected
0.25	Flaw sizing not provided					0.25	25%
0.50						0.50	75%
0.75						0.75	50%
1.00						1.00	67%
1.50						1.50	0%
2.00						2.00	67%
Overall Sizing Performance						N/A	N/A

Table 78. Tabulated results showing overall flaw detection percentage and accuracy in determining flaw size for the 20–32 ply specimen set for all flaws in CG regions (Dantec Dynamics shearography system)

Dantec Dynamics – (Q-800) Shearography Flaw Detection Percentage & Accuracy in Determining Flaw Size 20–32 Ply Specimen Set – All CG Flaws							
Accuracy in Sizing the Flaws That Were Detected						Flaw Detection Percentage	
Flaw Size	5 (100%)	4 (76%–99%)	3 (51%–75%)	2 (25%–50%)	1 (< 25%)	Flaw Size	Percent Detected
0.25	Flaw sizing not provided					0.25	0%
0.50						0.50	22%
0.75						0.75	13%
1.00						1.00	45%
1.50						1.50	17%
2.00						2.00	50%
Overall Sizing Performance						N/A	N/A

Table 79. Tabulated results showing overall flaw detection percentage and accuracy in determining flaw size for the 20–32 ply specimen set for all flaws in constant thickness and CG regions (Dantec Dynamics shearography system)

Dantec Dynamics – (Q-800) Shearography Flaw Detection Percentage & Accuracy in Determining Flaw Size 20–32 Ply Specimen Set – All Flaws (Constant Thickness & CG)							
Accuracy in Sizing the Flaws That Were Detected						Flaw Detection Percentage	
Flaw Size	5 (100%)	4 (76%–99%)	3 (51%–75%)	2 (25%–50%)	1 (< 25%)	Flaw Size	Percent Detected
0.25	Flaw sizing not provided					0.25	9%
0.50						0.50	38%
0.75						0.75	29%
1.00						1.00	53%
1.50						1.50	14%
2.00						2.00	60%
Overall Sizing Performance						N/A	N/A

6.7 INSPECTION PERFORMANCE RESULTS FOR PULSED THERMOGRAPHY

6.7.1 Results for the Test Specimens Inspected by TWI Pulsed IR

Figures 210 and 211 show the TWI’s EcoTherm IR device and the deployment of the equipment on the various SLE test specimens. Inspections were completed using the TWI EcoTherm

thermography system that included a Phoenix Midway-Indigo camera (60 Hz in the 3–5 mm range). Mosaic and Voyager IR software was used for data analysis and to accommodate inspections of thick laminate structures. For the thermography system to detect a flaw, the flaw size-to-depth ratio had to be at least 1 or greater. Coverage area for a single shot is roughly 12" x 10" and multiple shots with some overlap coverage were used to ensure complete coverage of test specimens.

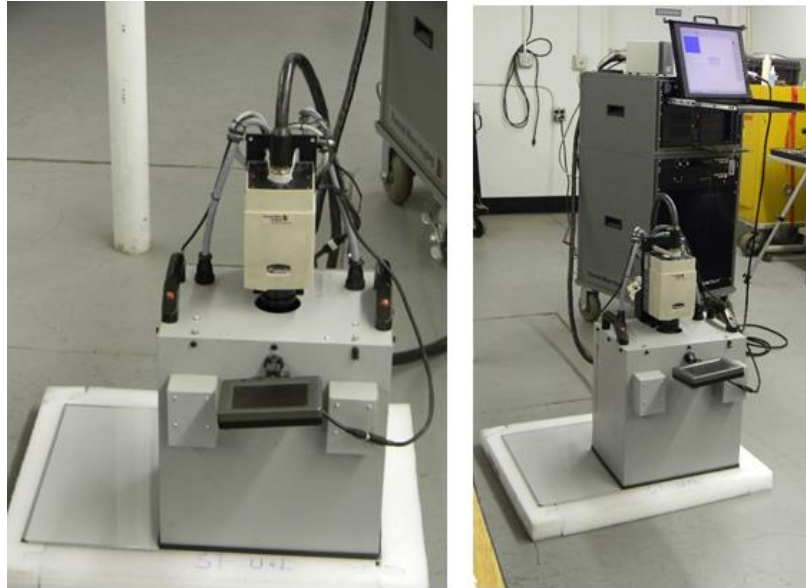


Figure 210. The TWI EchoTherm flash thermography system

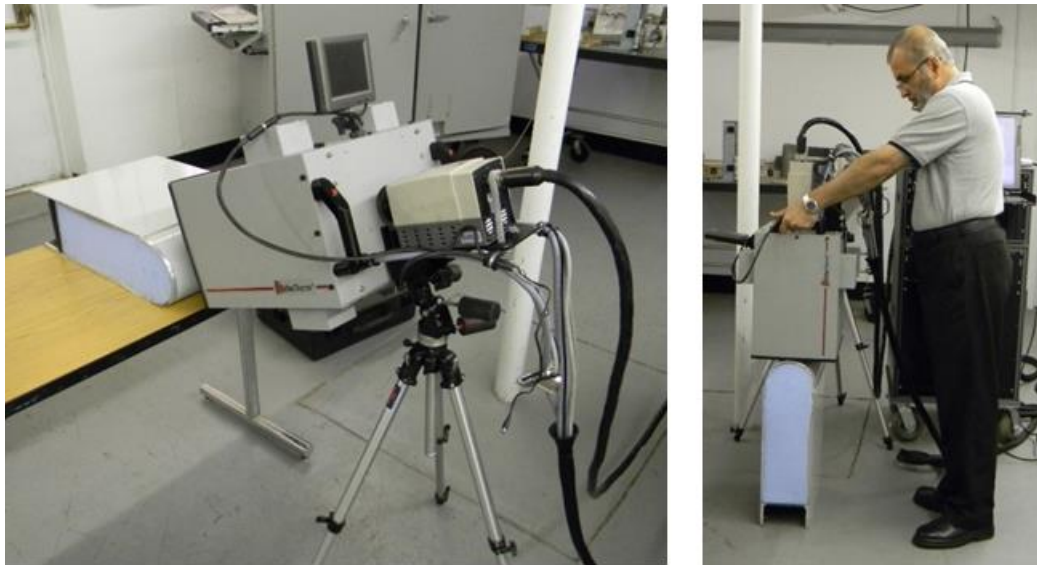


Figure 211. Deployment of the EchoTherm flash thermography system on SLE

A sample thermography image produced from the EcoTherm IR inspection of the SLE test specimens is shown in figure 212. Both flash and extended pulse thermography were applied to

the thick 32-ply laminates to detect the deeper flaws. Still images captured at various times and movies of the IR signature of the part over time were both used to detect the range of flaws at different depths within the specimens. The IR images showing the substructure flaws correspond well to the thermography images generated later in time than those showing the near-surface flaws. The Mosaic software was used to connect all images into a single image corresponding to each test specimen. Figure 212 shows how four different IR shots can be joined together to form a single view of an entire test specimen.

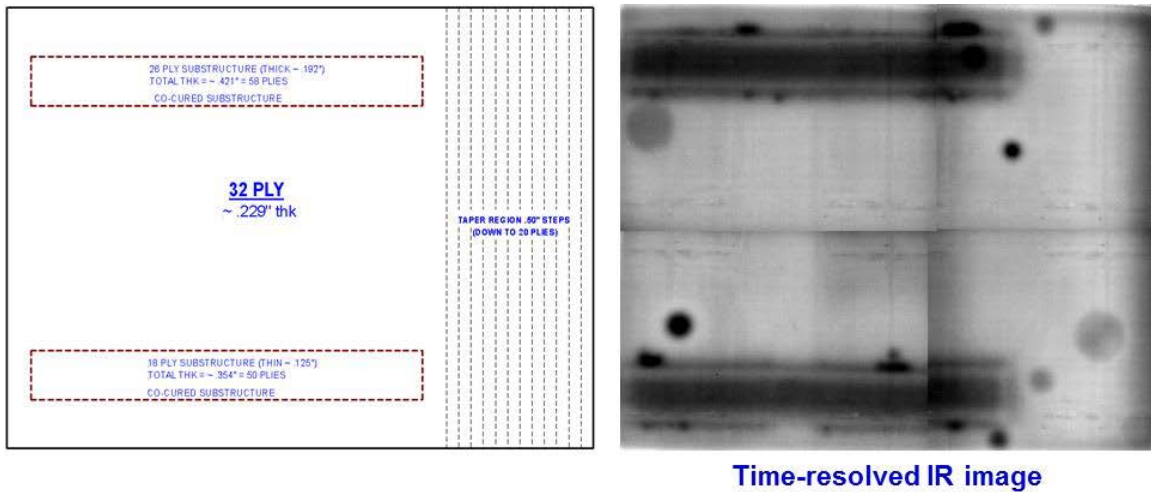


Figure 212. An IR image produced by EchoTherm flash thermography system inspection of SLE 32-ply test specimen

Figure 213 contains the cumulative POD curve when combining all flaw detection results for both the thin (12–20 ply) laminate experiment and thick (20–32 ply) laminate experiment. The EcoTherm thermography system produced an overall $POD_{[90/95]} = 2.299''$. This represents a drop in performance of 104% versus the overall result from the conventional PE-UT tests ($POD_{[90/95]} = 1.125''$) that evaluated the performance of airline inspectors (see section 6.1). The breakdown of results revealed performance for the thin laminate experiment of $POD_{[90/95]} = 1.225''$ and performance for the thick laminate experiment of $POD_{[90/95]} > 3.0''$. The results in the thinner laminates are much better than the flaw detection observed in the thicker laminates, indicating that depth of penetration is a critical factor in the successful application of thermography inspection methods. Tables 80 and 81 delineate the flaw detection percentages for each of the specimen design attributes (i.e., constant thickness, CG, substructures regions, taper regions, curved surfaces, and honeycomb regions). These tables also show that there were no false calls for the entire experiment.

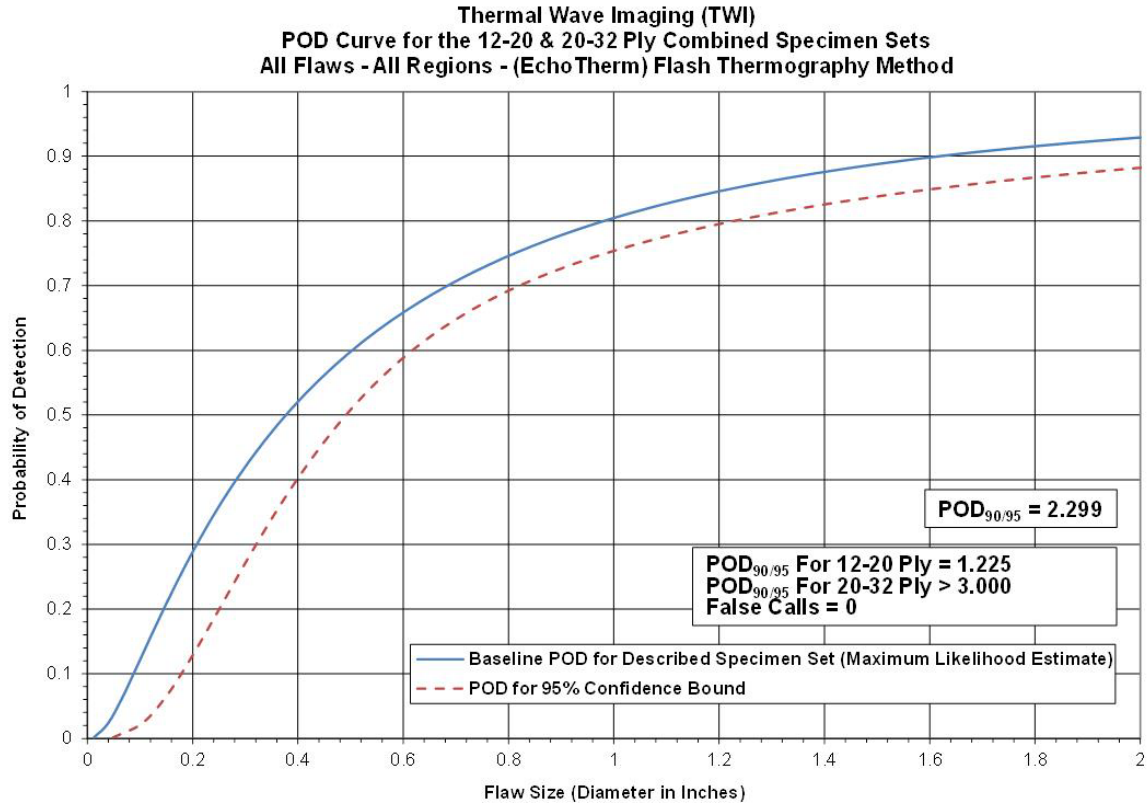


Figure 213. The POD results for EchoTherm flash thermography system flaw detection in solid laminate composite structure

Table 80. Flaw detection performance for EchoTherm flash thermography system separated into thin laminate and thick laminate results

Results – TWI, (EchoTherm) Flash Thermography Method							
12–20 Ply (Thin Laminate Experiment)				20–32 Ply (Thick Laminate Experiment)			
POD _{90/95} Value	Percent Flaw Detection			POD _{90/95} Value	Percent Flaw Detection		
All Flaws Constant Thickness & CG Regions (dia. in inches)	All Flaws Constant Thickness & CG Regions	All Flaws Constant Thickness Regions Only	All Flaws CG Regions Only	All Flaws Constant Thickness & CG Regions (dia. in inches)	All Flaws Constant Thickness & CG Regions	All Flaws Constant Thickness Regions Only	All Flaws CG Regions Only
1.225	76%	90%	69%	>3.000	55%	58%	53%
False Calls = 0				False Calls = 0			

Table 81. Flaw detection performance for EchoTherm flash thermography system for the overall SLE

12–20 and 20–32 Ply Combined Results – TWI, (EchoTherm) Flash Thermography Method									
POD _{90/95} Values			Percent Flaw Detection						
All Flaws Constant Thickness & CG Regions (dia. in inches)	All Flaws Constant Thickness Regions Only (dia. in inches)	All Flaws CG Regions Only (dia. in inches)	All Flaws Constant Thickness & CG Regions	All Flaws Constant Thickness Regions Only	All Flaws CG Regions Only	All Flaws Substructure Regions Only	All Flaws Taper Regions Only	All Flaws Laminate Over Honeycomb Regions Only	All Flaws Curved Surface Regions Only
2.299	2.685	2.406	70%	79%	65%	41%	75%	96%	89%
									False Calls = 0

Inspector flaw calls were also graded to evaluate the accuracy of the EcoTherm thermography method for flaw sizing. The overall test results identified hits (i.e., calls with any amount of overlap between the call and the actual flaw location), misses (i.e., no call for an area of a known flaw), false calls (i.e., call with no overlap of a flaw), and sizing performance (i.e., the degree of overlap between experimenter calls and actual flaw areas). Tables 82–87 summarize the results for flaw sizing and percent detection based on flaw size for the thin laminate and thick laminate experiments and provide a breakdown of those performance attributes in the constant thickness and CG regions. Note that for the 12–20 ply specimen set, 76% of all flaws were detected (103 of 135 flaws; see table 84). This is similar to the conventional PE-UT results in which 76% of all flaws were detected. The flaw sizing performance shows that 94% of the detected flaws were sized properly (5 category for 100% coverage) versus 38% calculated for the conventional PE-UT method. Three percent of the flaws were sized in the 76%–99% coverage category. Therefore, 97% of the detected flaws were sized with 76%–100% accuracy. When using conventional PE-UT, only 64% of the detected flaws were sized with 76%–100% accuracy. Table 84 shows a breakdown of percent detection based on flaw size. For example, 100% of the 2" flaws were detected. Of the smaller flaws, only 36% of the 0.25" flaws were detected (versus 47% detection of the 0.25" flaws using conventional PE-UT).

Table 82. Tabulated results showing overall flaw detection percentage and accuracy in determining flaw size for the 12–20 ply specimen set for all flaws in constant thickness regions (EchoTherm flash thermography system)

TWI, (EchoTherm) Flash Thermography Flaw Detection Percentage & Accuracy in Determining Flaw Size 12–20 Ply Specimen Set – All Constant Thickness Flaws							
Accuracy in Sizing the Flaws That Were Detected						Flaw Detection Percentage	
Flaw Size	5 (100%)	4 (76%–99%)	3 (51%–75%)	2 (25%–50%)	1 (< 25%)	Flaw Size	Percent Detected
0.25	100%	0%	0%	0%	0%	0.25	67%
0.50	89%	0%	0%	11%	0%	0.50	82%
0.75	89%	11%	0%	0%	0%	0.75	90%
1.00	100%	0%	0%	0%	0%	1.00	100%
1.50	100%	0%	0%	0%	0%	1.50	100%
2.00	50%	50%	0%	0%	0%	2.00	100%
Overall Sizing Performance	93%	5%	0%	2%	0%	Overall Flaw Detection	90%

Table 83. Tabulated results showing overall flaw detection percentage and accuracy in determining flaw size for the 12–20 ply specimen set for all flaws in CG regions (EchoTherm flash thermography system)

TWI, (EchoTherm) Flash Thermography Flaw Detection Percentage & Accuracy in Determining Flaw Size 12–20 Ply Specimen Set – All CG Flaws							
Accuracy in Sizing the Flaws That Were Detected						Flaw Detection Percentage	
Flaw Size	5 (100%)	4 (76%–99%)	3 (51%–75%)	2 (25%–50%)	1 (< 25%)	Flaw Size	Percent Detected
0.25	100%	0%	0%	0%	0%	0.25	13%
0.50	92%	8%	0%	0%	0%	0.50	54%
0.75	100%	0%	0%	0%	0%	0.75	73%
1.00	100%	0%	0%	0%	0%	1.00	87%
1.50	78%	0%	11%	11%	0%	1.50	100%
2.00	100%	0%	0%	0%	0%	2.00	100%
Overall Sizing Performance	95%	2%	2%	2%	0%	Overall Flaw Detection	69%

Table 84. Tabulated results showing overall flaw detection percentage and accuracy in determining flaw size for the 12–20 ply specimen set for all flaws in constant thickness and CG regions (EchoTherm flash thermography system)

TWI, (EchoTherm) Flash Thermography Flaw Detection Percentage & Accuracy in Determining Flaw Size 12–20 Ply Specimen Set – All Flaws (Constant Thickness & CG)							
Accuracy in Sizing the Flaws That Were Detected						Flaw Detection Percentage	
Flaw Size	5 (100%)	4 (76%–99%)	3 (51%–75%)	2 (25%–50%)	1 (< 25%)	Flaw Size	Percent Detected
0.25	100%	0%	0%	0%	0%	0.25	36%
0.50	91%	5%	0%	5%	0%	0.50	63%
0.75	96%	4%	0%	0%	0%	0.75	78%
1.00	100%	0%	0%	0%	0%	1.00	91%
1.50	88%	0%	6%	6%	0%	1.50	100%
2.00	67%	33%	0%	0%	0%	2.00	100%
Overall Sizing Performance	94%	3%	1%	2%	0%	Overall Flaw Detection	76%

Table 85. Tabulated results showing overall flaw detection percentage and accuracy in determining flaw size for the 20–32 ply specimen set for all flaws in constant thickness regions (EchoTherm flash thermography system)

TWI, (EchoTherm) Flash Thermography Flaw Detection Percentage & Accuracy in Determining Flaw Size 20–32 Ply Specimen Set – All Constant Thickness Flaws							
Accuracy in Sizing the Flaws That Were Detected						Flaw Detection Percentage	
Flaw Size	5 (100%)	4 (76%–99%)	3 (51%–75%)	2 (25%–50%)	1 (< 25%)	Flaw Size	Percent Detected
0.25	100%	0%	0%	0%	0%	0.25	25%
0.50	100%	0%	0%	0%	0%	0.50	50%
0.75	100%	0%	0%	0%	0%	0.75	67%
1.00	100%	0%	0%	0%	0%	1.00	83%
1.50	0%	0%	0%	0%	0%	1.50	0%
2.00	100%	0%	0%	0%	0%	2.00	67%
Overall Sizing Performance	100%	0%	0%	0%	0%	Overall Flaw Detection	58%

Table 86. Tabulated results showing overall flaw detection percentage and accuracy in determining flaw size for the 20–32 ply specimen set for all flaws in CG regions (EchoTherm flash thermography system)

TWI, (EchoTherm) Flash Thermography Flaw Detection Percentage & Accuracy in Determining Flaw Size 20–32 Ply Specimen Set – All CG Flaws							
Accuracy in Sizing the Flaws That Were Detected						Flaw Detection Percentage	
Flaw Size	5 (100%)	4 (76%–99%)	3 (51%–75%)	2 (25%–50%)	1 (< 25%)	Flaw Size	Percent Detected
0.25	100%	0%	0%	0%	0%	0.25	29%
0.50	100%	0%	0%	0%	0%	0.50	44%
0.75	80%	0%	20%	0%	0%	0.75	63%
1.00	100%	0%	0%	0%	0%	1.00	55%
1.50	100%	0%	0%	0%	0%	1.50	83%
2.00	100%	0%	0%	0%	0%	2.00	50%
Overall Sizing Performance	96%	0%	4%	0%	0%	Overall Flaw Detection	53%

Table 87. Tabulated results showing overall flaw detection percentage and accuracy in determining flaw size for the 20–32 ply specimen set for all flaws in constant thickness and CG regions (EchoTherm flash thermography system)

TWI, (EchoTherm) Flash Thermography Flaw Detection Percentage & Accuracy in Determining Flaw Size 20–32 Ply Specimen Set – All Flaws (Constant Thickness & CG)							
Accuracy in Sizing the Flaws That Were Detected						Flaw Detection Percentage	
Flaw Size	5 (100%)	4 (76%–99%)	3 (51%–75%)	2 (25%–50%)	1 (< 25%)	Flaw Size	Percent Detected
0.25	100%	0%	0%	0%	0%	0.25	27%
0.50	100%	0%	0%	0%	0%	0.50	46%
0.75	89%	0%	11%	0%	0%	0.75	64%
1.00	100%	0%	0%	0%	0%	1.00	65%
1.50	100%	0%	0%	0%	0%	1.50	71%
2.00	100%	0%	0%	0%	0%	2.00	60%
Overall Sizing Performance	97%	0%	3%	0%	0%	Overall Flaw Detection	55%

Table 87 summarizes the results for the overall flaw detection percentage and the associated accuracy in determining flaw size for the 20–32 ply specimen set (thick laminate experiment). For the 20–32 ply specimen set, 55% of all flaws were detected (37 of 67 flaws). This represents a drop in performance versus the conventional PE-UT results in which 85% of all flaws were detected. The flaw sizing performance shows that 97% of the detected flaws were sized properly

(5 category for 100% coverage) versus 31% calculated for the conventional PE-UT method. Table 87 shows a breakdown of percent detection based on flaw size. For example, 50% of the 2" flaws were detected. Of the smaller flaws, only 29% of the 0.25" flaws were detected (versus 56% detection of the 0.25" flaws using conventional PE-UT).

6.8 INSPECTION PERFORMANCE RESULTS FOR LST

6.8.1 Results for the Test Specimens Inspected by MISTRAS LST

Figures 214–216 show the MISTRAS THELIS-P LST device and the deployment of this equipment on the various SLE test specimens. Inspections were completed with the THELIS-P LST inspection device, which incorporated an Indium Antimony IR camera and a rolling heat source that produced temperature gradients in the specimen in advance of the IR camera. A sample thermography image produced from the THELIS-P LST inspection of the SLE test specimens is shown in figure 217. Still images captured at various times and movies of the IR signature of the part over time were both used to detect the range of flaws at different depths within the specimens. The IR images showing the substructure flaws correspond to the thermography images generated later in time than those showing the near-surface flaws.



Figure 214. MISTRAS LST THELIS-P device



Figure 215. Deployment of the MISTRAS LST system on SLE

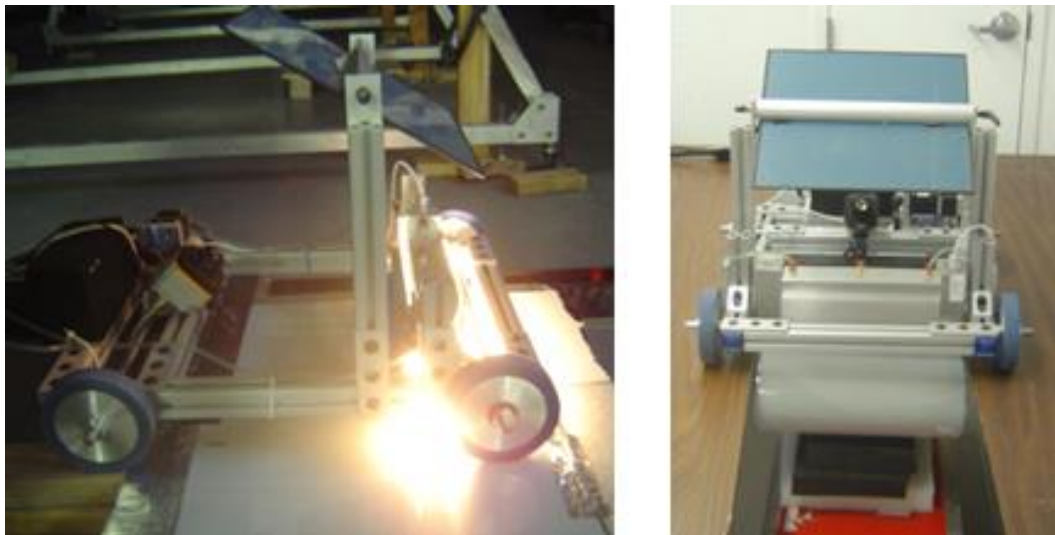


Figure 216. MISTRAS LST – use of heat lamps to provide thermal gradient to test specimens and rolling encoder to provide position data for IR image correlation

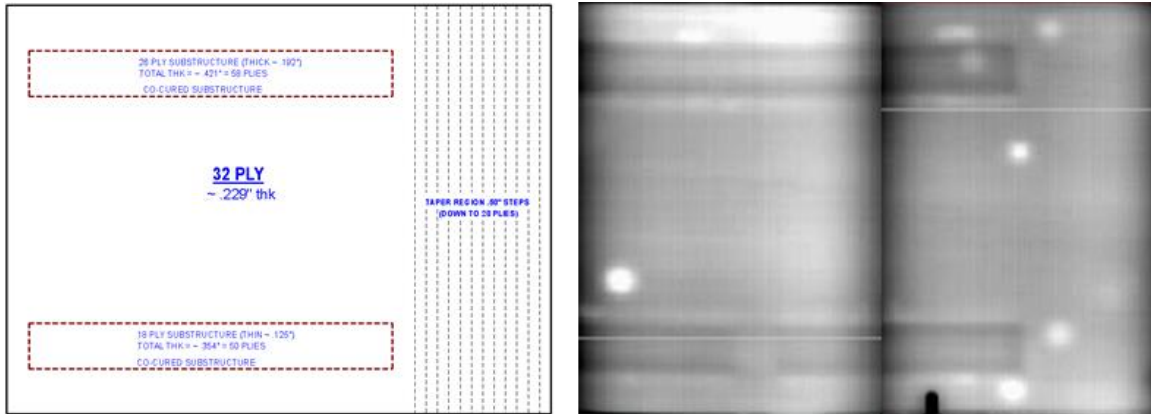


Figure 217. An IR image produced by THELIS-P LST system inspection of SLE 32-ply test specimen

Figure 218 contains the cumulative POD curve when combining all flaw detection results for both the thin (12–20 ply) laminate experiment and thick (20–32 ply) laminate experiment. The THELIS-P LST system produced an overall $POD_{[90/95]} > 3.0''$. This represents a drop in performance of 167% versus the overall result from the conventional PE-UT tests ($POD_{[90/95]} = 1.125''$) that evaluated the performance of airline inspectors (see section 6.1). The breakdown of results revealed performance for the thin laminate experiment of $POD_{[90/95]} > 3.0''$ and performance for the thick laminate experiment of $POD_{[90/95]} > 3.0''$. Tables 88 and 89 delineate the flaw detection percentages for each of the specimen design attributes (i.e., constant thickness, CG, substructures regions, taper regions, curved surfaces, and honeycomb regions). Tables 88 and 89 also show that there were no false calls for the entire experiment.

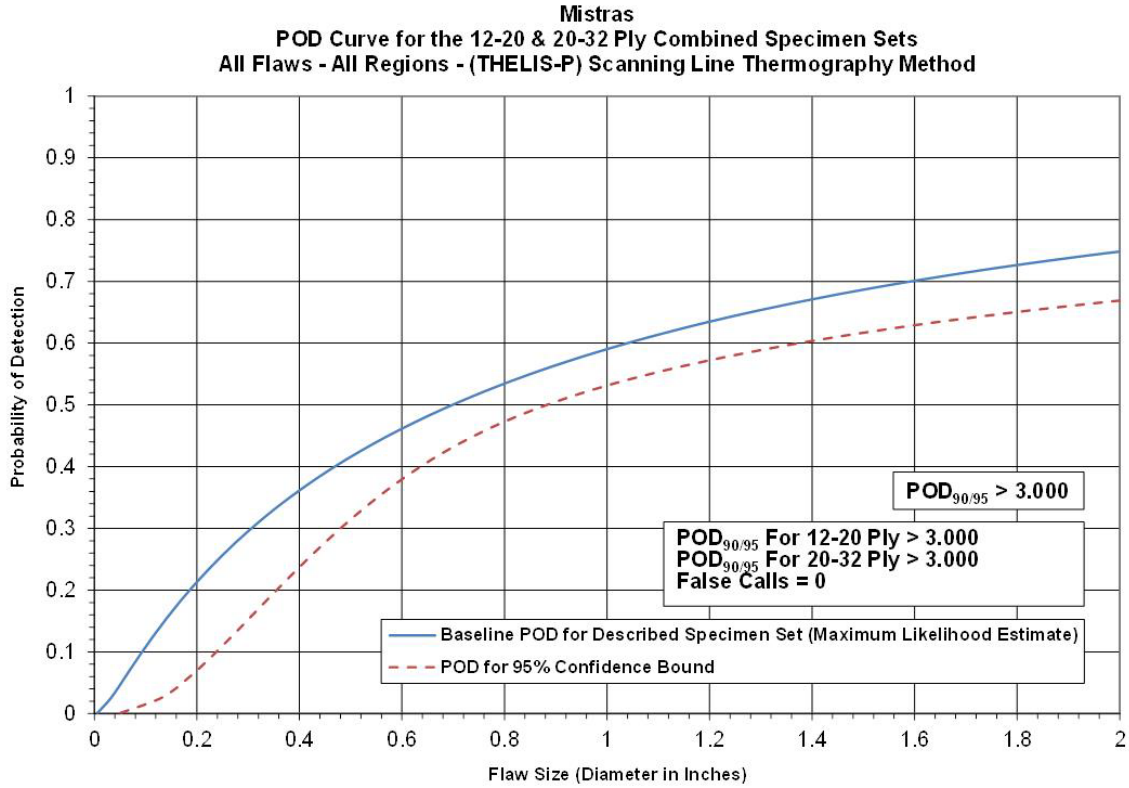


Figure 218. The POD results for THELIS-P LST system flaw detection in solid laminate composite structure

Table 88. Flaw detection performance for THELIS-P LST system separated into thin laminate and thick laminate results

Results – MISTRAS, (THELIS-P) LST Method							
12–20 Ply (Thin Laminate Experiment)				20–32 Ply (Thick Laminate Experiment)			
POD _{90/95} Value	Percent Flaw Detection			POD _{90/95} Value	Percent Flaw Detection		
All Flaws Constant Thickness & CG Regions (dia. in inches)	All Flaws Constant Thickness & CG Regions	All Flaws Constant Thickness Regions Only	All Flaws CG Regions Only	All Flaws Constant Thickness & CG Regions (dia. in inches)	All Flaws Constant Thickness & CG Regions	All Flaws Constant Thickness Regions Only	All Flaws CG Regions Only
>3.000	54%	60%	51%	>3.000	45%	42%	47%
False Calls = 0				False Calls = 0			

Table 89. Flaw detection performance for THELIS-P LST system for the overall SLE

12–20 and 20–32 Ply Combined Results – MISTRAS, (THELIS-P) LST Method									
POD _{90/95} Values			Percent Flaw Detection						
All Flaws Constant Thickness & CG Regions (dia. in inches)	All Flaws Constant Thickness Regions Only (dia. in inches)	All Flaws CG Regions Only (dia. in inches)	All Flaws Constant Thickness & CG Regions	All Flaws Constant Thickness Regions Only	All Flaws CG Regions Only	All Flaws Substructure Regions Only	All Flaws Taper Regions Only	All Flaws Laminate Over Honeycomb Regions Only	All Flaws Curved Surface Regions Only
> 3	> 3	> 3	51%	54%	49%	40%	53%	74%	33%
									False Calls = 0

Inspector flaw calls were also graded to evaluate the accuracy of the THELIS-P LST method for flaw sizing. The overall test results identified hits (i.e., calls with any amount of overlap between the call and the actual flaw location), misses (i.e., no call for an area of a known flaw), false calls (i.e., call with no overlap of a flaw), and sizing performance (i.e., the degree of overlap between experimenter calls and actual flaw areas). Tables 90–95 summarize the results for flaw sizing and percent detection based on flaw size for the thin laminate and thick laminate experiments and provide a breakdown of those performance attributes in the constant thickness and CG regions. Note that for the 12–20 ply specimen set, 54% of all flaws were detected (73 of 135 flaws; see table 92). This is a drop in performance compared to the conventional PE-UT results, in which 76% of all flaws were detected. Table 92 shows a breakdown of percent detection based on flaw size. For example, 67% of the 2" flaws were detected. Of the smaller flaws, only 14% of the 0.25" flaws were detected (versus 47% detection of the 0.25" flaws using conventional PE-UT). It was not possible to evaluate the flaw sizing performance of the THELIS-P LST system because flaw sizing was not provided by the experiment participants.

Table 90. Tabulated results showing overall flaw detection percentage and accuracy in determining flaw size for the 12–20 ply specimen set for all flaws in constant thickness regions (THELIS-P LST system)

MISTRAS, (THELIS-P) LST Flaw Detection Percentage & Accuracy in Determining Flaw Size 12–20 Ply Specimen Set – All Constant Thickness Flaws							
Accuracy in Sizing the Flaws That Were Detected						Flaw Detection Percentage	
Flaw Size	5 (100%)	4 (76%–99%)	3 (51%–75%)	2 (25%–50%)	1 (< 25%)	Flaw Size	Percent Detected
0.25	Flaw sizing not provided					0.25	33%
0.50						0.50	64%
0.75						0.75	60%
1.00						1.00	67%
1.50						1.50	71%
2.00						2.00	50%
Overall Sizing Performance						N/A	N/A

Table 91. Tabulated results showing overall flaw detection percentage and accuracy in determining flaw size for the 12–20 ply specimen set for all flaws in CG regions (THELIS-P LST system)

MISTRAS, (THELIS-P) LST Flaw Detection Percentage & Accuracy in Determining Flaw Size 12–20 Ply Specimen Set – All CG Flaws							
Accuracy in Sizing the Flaws That Were Detected						Flaw Detection Percentage	
Flaw Size	5 (100%)	4 (76%–99%)	3 (51%–75%)	2 (25%–50%)	1 (< 25%)	Flaw Size	Percent Detected
0.25	Flaw sizing not provided					0.25	0%
0.50						0.50	33%
0.75						0.75	55%
1.00						1.00	74%
1.50						1.50	67%
2.00						2.00	100%
Overall Sizing Performance						N/A	N/A

Table 92. Tabulated results showing overall flaw detection percentage and accuracy in determining flaw size for the 12–20 ply specimen set for all flaws in constant thickness and CG regions (THELIS-P LST system)

MISTRAS, (THELIS-P) LST Flaw Detection Percentage & Accuracy in Determining Flaw Size 12–20 Ply Specimen Set – All Flaws (Constant Thickness & CG)							
Accuracy in Sizing the Flaws That Were Detected						Flaw Detection Percentage	
Flaw Size	5 (100%)	4 (76%–99%)	3 (51%–75%)	2 (25%–50%)	1 (< 25%)	Flaw Size	Percent Detected
0.25	Flaw sizing not provided					0.25	14%
0.50						0.50	43%
0.75						0.75	56%
1.00						1.00	71%
1.50						1.50	69%
2.00						2.00	67%
Overall Sizing Performance						N/A	N/A

Table 93. Tabulated results showing overall flaw detection percentage and accuracy in determining flaw size for the 20–32 ply specimen set for all flaws in constant thickness regions (THELIS-P LST system)

MISTRAS, (THELIS-P) Line Scanning Thermography Flaw Detection Percentage & Accuracy in Determining Flaw Size 20–32 Ply Specimen Set – All Constant Thickness Flaws							
Accuracy in Sizing the Flaws That Were Detected						Flaw Detection Percentage	
Flaw Size	5 (100%)	4 (76%–99%)	3 (51%–75%)	2 (25%–50%)	1 (< 25%)	Flaw Size	Percent Detected
0.25	Flaw sizing not provided					0.25	25%
0.50						0.50	25%
0.75						0.75	67%
1.00						1.00	50%
1.50						1.50	0%
2.00						2.00	33%
Overall Sizing Performance						N/A	N/A

Table 94. Tabulated results showing overall flaw detection percentage and accuracy in determining flaw size for the 20–32 ply specimen set for all flaws in CG regions (THELIS-P LST system)

MISTRAS, (THELIS-P) LST Flaw Detection Percentage & Accuracy in Determining Flaw Size 20–32 Ply Specimen Set – All CG							
Accuracy in Sizing the Flaws That Were Detected						Flaw Detection Percentage	
Flaw Size	5 (100%)	4 (76%–99%)	3 (51%–75%)	2 (25%–50%)	1 (< 25%)	Flaw Size	Percent Detected
0.25	Flaw sizing not provided					0.25	14%
0.50						0.50	56%
0.75						0.75	50%
1.00						1.00	55%
1.50						1.50	50%
2.00						2.00	50%
Overall Sizing Performance						N/A	N/A

Table 95. Tabulated results showing overall flaw detection percentage and accuracy in determining flaw size for the 20–32 ply specimen set for all flaws in constant thickness and CG regions (THELIS-P LST system)

MISTRAS, (THELIS-P) LST Flaw Detection Percentage & Accuracy in Determining Flaw Size 20–32 Ply Specimen Set – All Flaws (Constant Thickness & CG)							
Accuracy in Sizing the Flaws That Were Detected						Flaw Detection Percentage	
Flaw Size	5 (100%)	4 (76%–99%)	3 (51%–75%)	2 (25%–50%)	1 (< 25%)	Flaw Size	Percent Detected
0.25	Flaw sizing not provided					0.25	18%
0.50						0.50	46%
0.75						0.75	57%
1.00						1.00	53%
1.50						1.50	43%
2.00						2.00	40%
Overall Sizing Performance						N/A	N/A

Table 95 summarizes the results for the overall flaw detection percentage and associated accuracy in determining flaw size for the 20–32 ply specimen set (thick laminate experiment). For the 20–32 ply specimen set, 45% of all flaws were detected (30 of 67 flaws). This is a drop in performance compared to the conventional PE-UT results, in which 85% of all flaws were detected. Table 95 shows a breakdown of percent detection based on flaw size. For example, 40% of the 2" flaws were detected. Of the smaller flaws, only 18% of the 0.25" flaws were

detected (versus 56% detection of the 0.25" flaws using conventional PE-UT). It was not possible to evaluate the flaw sizing performance of the THELIS-P LST system because flaw sizing was not provided by the experiment participants.

6.9 INSPECTION PERFORMANCE RESULTS FOR LOCK-IN THERMOGRAPHY

6.9.1 Results for the Test Specimens Inspected by MoviTHERM Lock-In Thermography

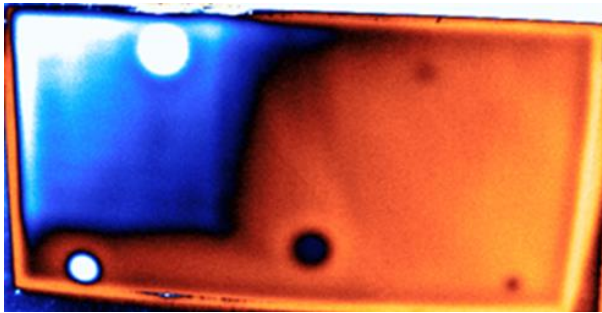
Figures 219 and 220 show the MoviTHERM lock-in thermography device and deployment of this equipment on the various SLE test specimens. Inspections were completed with the lock-in thermography inspection device, which incorporated a FLIR SR2 SC7650 camera and a Hedler 2500 watt lamp. Figure 220 shows the use of lighting to produce thermal gradients in the test specimens so that the IR camera can detect changes in heat transfer associated with flaws in the part. A sample thermography image produced from the lock-in thermography inspection of the SLE test specimens is shown in figure 221. Still images captured at various times and movies of the IR signature of the part over time were both used to detect the range of flaws at different depths within the specimens. The IR images showing the substructure flaws correspond to the thermography images generated later in time than those showing the near-surface flaws.



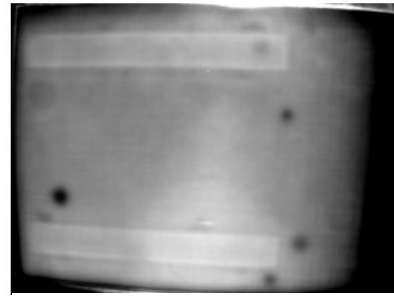
Figure 219. The MoviTHERM lock-in thermography device



Figure 220. Deployment of the MoviTHERM lock-in thermography system on SLE



(a)



(b)

Figure 221. Thermography images produced by MoviTHERM lock-in thermography system inspection of (a) SLE 12–24 ply and (b) 32-ply test specimens

Figure 222 contains the cumulative POD curve when combining all flaw detection results for both the thin (12–20 ply) laminate experiment and thick (20–32 ply) laminate experiment. The MoviTHERM lock-in thermography system produced an overall $POD_{[90/95]} > 3.0''$. This represents a drop in performance of 167% versus the overall result from the conventional PE-UT tests ($POD_{[90/95]} = 1.125''$) that evaluated the performance of airline inspectors (see section 6.1). The breakdown of results revealed performance for the thin laminate experiment of $POD_{[90/95]} > 3.0''$ and performance for the thick laminate experiment of $POD_{[90/95]} > 3.0''$. Tables 96 and 97 delineate the flaw detection percentages for each of the specimen design attributes (i.e., constant thickness, CG, substructures regions, taper regions, curved surfaces, and honeycomb regions). Tables 96 and 97 also show that there were 26 false calls for the entire experiment.

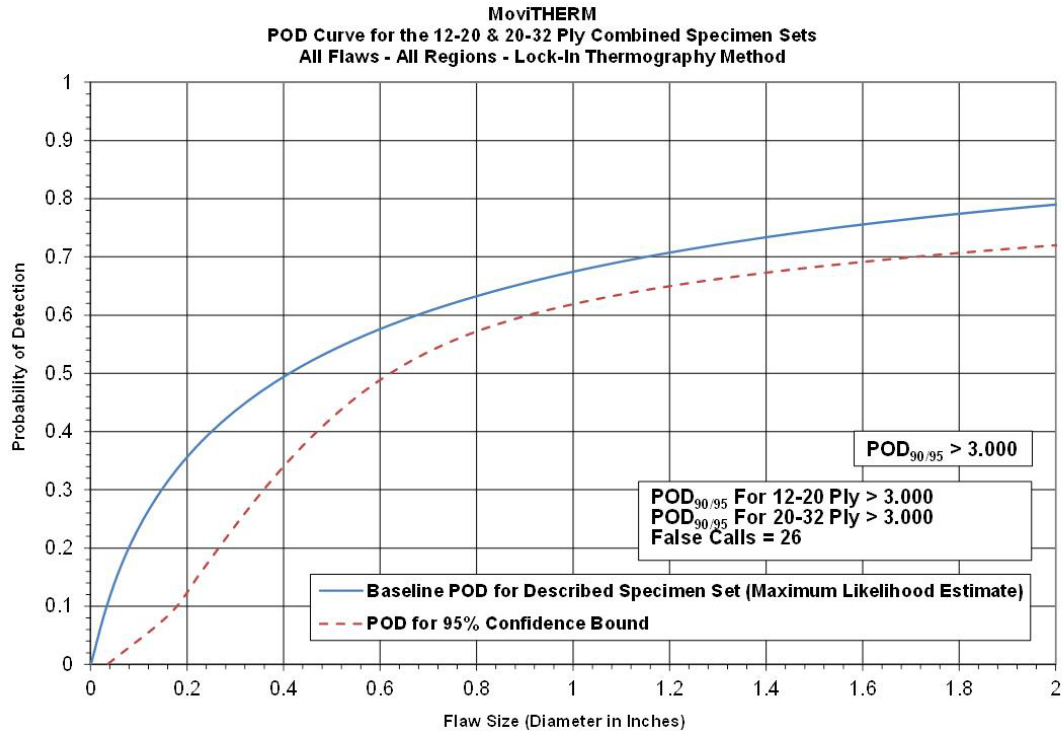


Figure 222. The POD results for MoviTHERM lock-in thermography system (flaw detection in solid laminate composite structure)

Table 96. Flaw detection performance for MoviTHERM lock-in thermography system separated into thin laminate and thick laminate results

Results – MoviTHERM, Lock-In Thermography Method							
12–20 Ply (Thin Laminate Experiment)				20–32 Ply (Thick Laminate Experiment)			
POD _{90/95} Value	Percent Flaw Detection			POD _{90/95} Value	Percent Flaw Detection		
All Flaws Constant Thickness & CG Regions (dia. in inches)	All Flaws Constant Thickness & CG Regions	All Flaws Constant Thickness Regions Only	All Flaws CG Regions Only	All Flaws Constant Thickness & CG Regions (dia. in inches)	All Flaws Constant Thickness & CG Regions	All Flaws Constant Thickness Regions Only	All Flaws CG Regions Only
>3.000	67%	77%	62%	>3.000	48%	63%	40%
False Calls = 22				False Calls = 4			

Table 97. Flaw detection performance for MoviTHERM lock-in thermography system for the overall SLE

12–20 and 20–32 Ply Combined Results – MoviTHERM, Lock-In Thermography Method									
POD _{90/95} Values			Percent Flaw Detection						
All Flaws Constant Thickness & CG Regions (dia. in inches)	All Flaws Constant Thickness Regions Only (dia. in inches)	All Flaws CG Regions Only (dia. in inches)	All Flaws Constant Thickness & CG Regions	All Flaws Constant Thickness Regions Only	All Flaws CG Regions Only	All Flaws Substructure Regions Only	All Flaws Taper Regions Only	All Flaws Laminate Over Honeycomb Regions Only	All Flaws Curved Surface Regions Only
> 3	> 3	> 3	61%	72%	55%	40%	60%	78%	67%
									False Calls = 26

Inspector flaw calls were also graded to evaluate the accuracy of the MoviTHERM lock-in thermography method for flaw sizing. The overall test results identified hits (i.e., calls with any amount of overlap between the call and the actual flaw location), misses (i.e., no call for an area of a known flaw), false calls (i.e., call with no overlap of a flaw), and sizing performance (i.e., the degree of overlap between experimenter calls and actual flaw areas). Tables 98–103 summarize the results for flaw sizing and percent detection based on flaw size for the thin laminate and thick laminate experiments and provide a breakdown of these same performance attributes in the constant thickness and CG regions. Note that for the 12–20 ply specimen set, 67% of all flaws were detected (90 of 135 flaws; see table 100). This is a drop in performance compared to the conventional PE-UT results, in which 76% of all flaws were detected. Table 100 shows a breakdown of percent detection based on flaw size. For example, 100% of the 2" flaws were detected. Of the smaller flaws, 50% of the 0.25" flaws were detected (versus 47% detection of the 0.25" flaws using conventional PE-UT). It was not possible to evaluate the flaw sizing performance of the MoviTHERM lock-in thermography system because flaw sizing was not provided by the experiment participants.

Table 98. Tabulated results showing overall flaw detection percentage and accuracy in determining flaw size for the 12–20 ply specimen set for all flaws in constant thickness regions (MoviTHERM lock-in thermography system)

MoviTHERM, Lock-In Thermography Flaw Detection Percentage & Accuracy in Determining Flaw Size 12–20 Ply Specimen Set – All Constant Thickness Flaws							
Accuracy in Sizing the Flaws That Were Detected						Flaw Detection Percentage	
Flaw Size	5 (100%)	4 (76%–99%)	3 (51%–75%)	2 (25%–50%)	1 (< 25%)	Flaw Size	Percent Detected
0.25	Flaw sizing not provided					0.25	67%
0.50						0.50	55%
0.75						0.75	80%
1.00						1.00	100%
1.50						1.50	71%
2.00						2.00	100%
Overall Sizing Performance						N/A	N/A

Table 99. Tabulated results showing overall flaw detection percentage and accuracy in determining flaw size for the 12–20 ply specimen set for all flaws in CG regions (MoviTHERM lock-in thermography system)

MoviTHERM, Lock-In Thermography Flaw Detection Percentage & Accuracy in Determining Flaw Size 12–20 Ply Specimen Set – All CG Flaws							
Accuracy in Sizing the Flaws That Were Detected						Flaw Detection Percentage	
Flaw Size	5 (100%)	4 (76%–99%)	3 (51%–75%)	2 (25%–50%)	1 (< 25%)	Flaw Size	Percent Detected
0.25	Flaw sizing not provided					0.25	38%
0.50						0.50	54%
0.75						0.75	59%
1.00						1.00	78%
1.50						1.50	67%
2.00						2.00	100%
Overall Sizing Performance						N/A	N/A

Table 100. Tabulated results showing overall flaw detection percentage and accuracy in determining flaw size for the 12–20 ply specimen set for all flaws in constant thickness and CG regions (MoviTHERM lock-in thermography system)

MoviTHERM, Lock-In Thermography Flaw Detection Percentage & Accuracy in Determining Flaw Size 12–20 Ply Specimen Set – All Flaws (Constant Thickness & CG)							
Accuracy in Sizing the Flaws That Were Detected						Flaw Detection Percentage	
Flaw Size	5 (100%)	4 (76%–99%)	3 (51%–75%)	2 (25%–50%)	1 (< 25%)	Flaw Size	Percent Detected
0.25	Flaw sizing not provided					0.25	50%
0.50						0.50	54%
0.75						0.75	66%
1.00						1.00	86%
1.50						1.50	69%
2.00						2.00	100%
Overall Sizing Performance						N/A	N/A

Table 101. Tabulated results showing overall flaw detection percentage and accuracy in determining flaw size for the 20–32 ply specimen set for all flaws in constant thickness regions (MoviTHERM lock-in thermography system)

MoviTHERM, Lock-In Thermography Flaw Detection Percentage & Accuracy in Determining Flaw Size 20–32 Ply Specimen Set – All Constant Thickness Flaws							
Accuracy in Sizing the Flaws That Were Detected						Flaw Detection Percentage	
Flaw Size	5 (100%)	4 (76%–99%)	3 (51%–75%)	2 (25%–50%)	1 (< 25%)	Flaw Size	Percent Detected
0.25	Flaw sizing not provided					0.25	50%
0.50						0.50	50%
0.75						0.75	67%
1.00						1.00	83%
1.50						1.50	0%
2.00						2.00	67%
Overall Sizing Performance						N/A	N/A

Table 102. Tabulated results showing overall flaw detection percentage and accuracy in determining flaw size for the 20–32 ply specimen set for all flaws in CG regions (MoviTHERM lock-in thermography system)

MoviTHERM, Lock-In Thermography Flaw Detection Percentage & Accuracy in Determining Flaw Size 20–32 Ply Specimen Set – All CG Flaws							
Accuracy in Sizing the Flaws That Were Detected						Flaw Detection Percentage	
Flaw Size	5 (100%)	4 (76%–99%)	3 (51%–75%)	2 (25%–50%)	1 (< 25%)	Flaw Size	Percent Detected
0.25	Flaw sizing not provided					0.25	14%
0.50						0.50	33%
0.75						0.75	50%
1.00						1.00	36%
1.50						1.50	67%
2.00						2.00	50%
Overall Sizing Performance						N/A	N/A

Table 103. Tabulated results showing overall flaw detection percentage and accuracy in determining flaw size for the 20–32 ply specimen set for all flaws in constant thickness and CG regions (MoviTHERM lock-in thermography system)

MoviTHERM, Lock-In Thermography Flaw Detection Percentage & Accuracy in Determining Flaw Size 20–32 Ply Specimen Set – All Flaws (Constant Thickness & CG)							
Accuracy in Sizing the Flaws That Were Detected						Flaw Detection Percentage	
Flaw Size	5 (100%)	4 (76%–99%)	3 (51%–75%)	2 (25%–50%)	1 (< 25%)	Flaw Size	Percent Detected
0.25	Flaw sizing not provided					0.25	27%
0.50						0.50	38%
0.75						0.75	57%
1.00						1.00	53%
1.50						1.50	57%
2.00						2.00	60%
Overall Sizing Performance						N/A	N/A

Table 103 summarizes the results for the overall flaw detection percentage and associated accuracy in determining flaw size for the 20–32 ply specimen set (thick laminate experiment). For the 20–32 ply specimen set, 48% of all flaws were detected (32 of 67 flaws). This is a drop in performance compared to the conventional PE-UT results, in which 85% of all flaws were detected. Table 103 also shows a breakdown of percent detection based on flaw size. For

example, 60% of the 2" flaws were detected. Of the smaller flaws, only 27% of the 0.25" flaws were detected (versus 56% detection of the 0.25" flaws using conventional PE-UT). It was not possible to evaluate the flaw sizing performance of the MoviTHERM lock-in thermography system because flaw sizing was not provided by the experiment participants.

6.10 COMPARISON OF ADVANCED NDI METHODS

Figure 223 provides an overall $POD_{[90]}$ comparison of all advanced NDI methods evaluated in this study that completed both the thin (12–20 ply) and thick (20–32 ply) laminate experiments (complete SLE set of specimens), along with the baseline of the aviation industry that was produced from airline inspectors using conventional, hand-deployed, single-element PE-UT inspections. Some of the advanced NDI methods performed better than conventional PE-UT, whereas some methods performed worse. It was revealed that some advanced NDI methods are not well-suited for composite laminate inspections or thick laminate inspections. In addition, it should be noted that the array of advanced NDI methods that were evaluated in this study were in various levels of technology readiness. Therefore, improvements in both equipment and deployment may improve the performance of many of the advanced NDI methods. Simple feedback from this experiment provided NDI developers with critical information that can lead to equipment improvements.

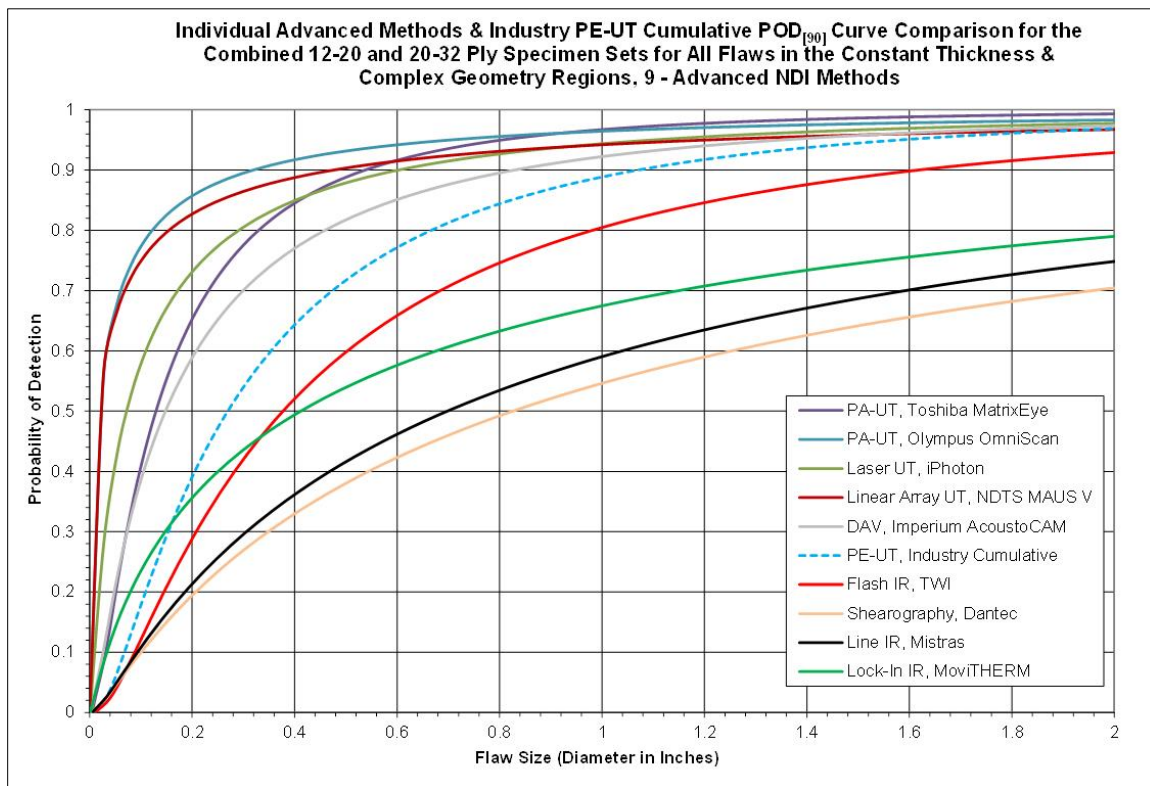


Figure 223. The POD results comparing performance of all advanced NDI methods (flaw detection in solid laminate composite structure)

Overall, the PA-UT, linear array UT, and the LUS methods all outperformed the industry baseline results, producing $POD_{[90/95]}$ levels that were 24%–39% better than those produced with the conventional PE-UT method. The use of C-scan images that accompanied all PA-UT equipment is a key factor in this improvement. The C-scan images provide much better data with which to identify flaws and ensured 100% area coverage. Human factor issues regarding temporary inattentiveness to the A-scan signals, a significant concern with the hand-deployed PE-UT method, are not present when wide-area C-scan methods are used. Similarly, the imaging capability of acoustography methods resulted in overall POD levels that were slightly better than those produced with the conventional PE-UT method. Therefore, proper inspection area coverage and use of color-coded images are two of the key ingredients in the improved performance observed with array UT, LUS, and acoustography.

Because of time limitations, not all of the advanced NDI methods were able to complete the entire SLE. Some methods completed only the thin laminate or thick laminate portions of the entire experiment. Tables 104 and 105 summarize the advanced NDI results for the thin laminate experiment (12–20 ply skins). The POD levels listed on table 104 indicate that the PA-UT, linear array UT, LUS, and acoustography results are similar to or better than the industry baseline results obtained from conventional PE-UT. In addition, pulsed (i.e., flash) thermography produced results in the thin laminate experiment that are slightly better than those produced with the conventional PE-UT method. It has been noted that depth of penetration is an issue for thermographic inspections; however, the thin laminate experiment uses specimens that are within the inspection capability of thermography. Therefore, pulsed (i.e., flash) IR is an option for inspecting thin laminate composite structures. Line thermography, lock-in thermography, shearography, and MW inspection methods did not produce acceptable performance levels. Table 105 presents the side-by-side data in the form of percent of flaws detected. The top performers listed above—PA-UT, linear array UT, LUS, acoustography, and pulsed IR—primarily have detection levels in the 80%–100% levels over all constant thickness and CG regions, with the exception of flaw detection percentages in the more challenging substructure regions.

Table 104. Comparison of POD flaw detection performance for all advanced NDI methods separated into thin laminate results (breakout by constant thickness regions, CG regions, and all flaws)

12–20 Ply Results Comparison (Thin Laminate Experiment)	POD _{90/95} Values		
	All Flaws Constant Thickness & CG Regions (dia. in inches)	All Flaws Constant Thickness Regions Only (dia. in inches)	All Flaws Complex Geometry Regions Only (dia. in inches)
Olympus NDT, PA-UT	0.862	100%*	1.292
Toshiba, PA-UT	0.818	0.606	1.094
NDT Solutions (NDTS), Linear Array UT	1.393	1.097	1.348
iPhoton, LUS	1.204	100%	1.627
Imperium, Digital Acoustic Video	1.422	1.290	1.541
TWI, Flash Thermography	1.225	0.889	1.360
MISTRAS, Line Thermography	>3	>3	2.841
MoviTHERM, Lock-In Thermography	>3	>3	>3
Dantec, Shearography	>3	>3	>3
Evisive, Microwave	No Data – Carbon material does not have acceptable dielectric properties for the propagation of Evisive scan waves		
*Inferred POD _{90/95} value is ≤ 0.25 " diameter flaw (100% flaw detection, POD value cannot be determined)			

Table 105. Comparison of percent flaw detection performance for all advanced NDI methods separated into thin laminate results (breakout by constant thickness regions, CG regions and all flaws)

12–20 Ply Results Comparison (Thin Laminate Experiment)	Percent Flaw Detection						
	All Flaws Constant Thickness & CG Regions	All Flaws Constant Thickness Regions Only	All Flaws Complex Geometry Regions Only	All Flaws Substructure Regions Only	All Flaws Taper Regions Only	All Flaws Laminate Over Honeycomb Regions Only	All Flaws Curved Surface Regions Only
Olympus NDT, PA-UT	92%	100%	87%	71%	100%	100%	100%
Toshiba, PA-UT	89%	96%	85%	66%	100%	100%	100%
NDT Solutions (NDTS), Linear Array UT	88%	92%	86%	68%	100%	100%	100%
iPhoton, LUS	86%	100%	78%	50%	100%	100%	100%
Imperium, Digital Acoustic Video	79%	90%	74%	45%	100%	96%	89%
TWI, Flash Thermography	76%	90%	69%	42%	88%	96%	89%
MISTRAS, Line Thermography	54%	60%	51%	37%	59%	74%	33%
MoviTHERM, Lock-In Thermography	67%	77%	62%	50%	65%	78%	67%
Dantec, Shearography	53%	67%	46%	34%	59%	48%	67%
Evisive, Microwave	No Data – Carbon material does not have acceptable dielectric properties for the propagation of Evisive scan waves						

Tables 106 and 107 summarize the advanced NDI results for the thick laminate experiment (20–32 ply skins). Note that there are not enough flaws in the individual constant thickness and CG categories to produce POD curves for these attributes alone. Therefore, it is only possible to produce the overall POD for the thick laminate experiment. The other categories are listed as N/A. Once again, the POD levels listed on table 106 show that the PA-UT, linear array UT, LUS, and acoustography results are similar to or better than the industry baseline results obtained from conventional PE-UT. However, pulsed thermography produced results in the thick laminate experiment that are worse than those produced with the conventional PE-UT method. In this case, the depth of penetration produced a significant inspection impediment such that the thick laminate experiment specimens were no longer within the inspection capability of thermography. Therefore, pulsed IR is not an option for inspecting thick laminate composite structures. Line thermography, lock-in thermography, shearography, and MW inspection methods did not produce acceptable performance levels. Table 107 presents the side-by-side data in the form of percent of flaws detected. The top performers listed above—PA-UT, LUS, acoustography, and pulsed IR—primarily have detection levels in the 90%–100% levels over all constant thickness and CG regions.

Table 106. Comparison of POD flaw detection performance for all advanced NDI methods separated into thick laminate results (breakout by constant thickness regions, CG regions, and all flaws)

20–32 Ply Results Comparison (Thick Laminate Experiment)	POD _{90/95} Values		
	All Flaws Constant Thickness & CG Regions (dia. in inches)	All Flaws Constant Thickness Regions Only (dia. in inches)	All Flaws Complex Geometry Regions Only (dia. in inches)
Olympus NDT, PA-UT	100%*	N/A	N/A
Toshiba, PA-UT	0.606	N/A	N/A
All Nippon, PA-UT	0.524	N/A	N/A
GEIT, PA-UT	>3	N/A	N/A
NDT Solutions (NDTS), Linear Array UT	100%*	N/A	N/A
Sandia, Linear Array UT	100%*	N/A	N/A
iPhoton, LUS	100%*	N/A	N/A
Imperium, Digital Acoustic Video	100%*	N/A	N/A
TWI, Flash Thermography	>3	N/A	N/A
MISTRAS, Line Thermography	>3	N/A	N/A
MoviTHERM, Lock-In Thermography	>3	N/A	N/A
Dantec, Shearography	>3	N/A	N/A
LTI, Shearography	>3	N/A	N/A
Evisive, Microwave	No Data – Carbon material does not have acceptable dielectric properties for the propagation of Evisive scan waves		
*Inferred POD _{90/95} value is ≤ 0.25 " diameter flaw (100% flaw detection, POD value cannot be determined)			
N/A-Not enough data to calculate POD for the described specimen set.			

Table 107. Comparison of percent flaw detection performance for all advanced NDI methods separated into thick laminate results (breakout by constant thickness regions, CG regions, and all flaws)

20–32 Ply Results Comparison (Thick Laminate Experiment)	Percent Flaw Detection				
	All Flaws Constant Thickness & CG Regions	All Flaws Constant Thickness Regions Only	All Flaws Complex Geometry Regions Only	All Flaws Substructure Regions Only	All Flaws Taper Regions Only
Olympus NDT, PA-UT	100%	100%	100%	100%	100%
Toshiba, PA-UT	97%	100%	95%	90%	100%
All Nippon, PA-UT	97%	100%	95%	90%	100%
GEIT, PA-UT	63%	92%	47%	10%	78%
NDT Solutions (NDTS), Linear Array UT	100%	100%	100%	100%	100%
Sandia, Linear Array UT	100%	100%	100%	100%	100%
iPhoton, LUS	100%	100%	100%	100%	100%
Imperium, Digital Acoustic Video	100%	100%	100%	100%	100%
TWI, Flash Thermography	55%	58%	53%	40%	65%
MISTRAS, Line Thermography	45%	42%	47%	45%	48%
MoviTHERM, Lock-In Thermography	48%	63%	40%	20%	57%
Dantec, Shearography	34%	54%	23%	15%	30%
LTI, Shearography	36%	42%	33%	25%	39%
Evisive, Microwave	No Data – Carbon material does not have acceptable dielectric properties for the propagation of Evisive scan waves				

Figure 224 highlights one of the only deployment obstacles that were identified in this study. The BN test specimens contained a spar channel region with a U-shaped geometry. This provided a tight inspection region such that it was not possible to deploy large scanning systems or large interrogation probes. The photographs in figure 224 show how the acoustography camera, PA-UT probes, and thermography units have limited-to-no mobility within this spar region. Even if the PA-UT probe was removed from its X-Y scanner and attached to a smaller linear encoder device, the resultant footprint limits its ability to inspect the entire area. Therefore, there are some limitations on the regions that these advanced NDI systems can inspect, mostly pertaining to areas with small access ports or tight geometry changes. In these cases, it may be necessary to deploy the smaller, manually-deployed single-element PE-UT inspections.



Imperium



NDT Solutions



Mistras

Figure 224. Images showing accessibility challenge associated with inspection of spar channel; channel results removed for additional POD analysis (see tables 108 and 109)

Tables 108 and 109 summarize the advanced NDI results for the entire SLE (thin laminate experiment and thick laminate experiment combined). The $POD_{[90/95]}$ values listed in the first column (i.e., all flaws, all specimens) correspond to the $POD_{[90]}$ plots presented in figure 223. These two tables also include the breakdown for $POD_{[90/95]}$ levels by test specimen attribute (i.e., constant thickness, CG) and the percent flaw detection broken down into each of the test specimen features (i.e., constant thickness, presence of substructures, taper regions, curved surfaces, and honeycomb region). Tables 108 and 109 also summarize the effect of removing the channel flaws and recalculating the $POD_{[90/95]}$ values. A 10% improvement was observed for two of the participants for all flaws in constant thickness and CG (channel flaws only removed).

Table 108. Comparison of POD and flaw detection values for all advanced NDI methods including adjustments in POD calculations to show effects of various inspection impediments (category set A)

	POD _{90/95} Values			Percent Flaw Detection	
	All Flaws Constant Thickness & CG Regions	All Flaws Constant Thickness Regions Only	All Flaws Complex Geometry Regions Only	All Flaws Constant Thickness & CG Regions	All Flaws Constant Thickness Regions Only
12–20 and 20–32 Ply Combined Results					
Olympus NDT, PA-UT	0.716	100%*	0.905	95%	100%
NDT Solutions (NDTS, Linear Array UT	0.884	0.775	1.120	92%	94%
NDT Solutions (NDTS), Channel Removed (See Note 2)	0.797	0.567	1.120	N/A	N/A
Toshiba, PA-UT	0.689	0.516	0.926	92%	97%
iPhoton, LUS	0.851	100%*	1.311	91%	100%
iPhoton, Regraded (See Note 1)	0.641	100%*	0.859	94%	100%
Imperium, Digital Acoustic Video	1.118	0.968	1.376	86%	93%
Imperium, Channel Removed (See Note 2)	0.973	0.567	1.376	N/A	N/A
TWI, Flash Thermography	2.299	2.685	2.406	70%	79%
TWI, Example (See Note 3)	2.005	1.618	2.406	N/A	N/A
MISTRAS, Line Thermography	> 3	> 3	> 3	51%	54%
MISTRAS, Channel Removed (See Note 2)	> 3	> 3	> 3	N/A	N/A
MoviTHERM, Lock-In Thermography	> 3	> 3	> 3	61%	72%
Dantec, Shearography	> 3	> 3	> 3	47%	63%
Evisive, Microwave	No Data – Carbon material does not have acceptable dielectric properties for the propagation of Evisive scan waves				
*Inferred POD _{90/95} value is ≤ 0.25 " diameter flaw (100% flaw detection, POD value cannot be determined)					
Note 1-Asked inspector to take another look at the results and spend more time to see if more flaws could be found. Technology has full data capture capability, which facilitated the ease of a second data review.					
Note 2-Channel data removed. Deployment issues due to size of device or scanning equipment used.					
Note 3-Changed 2" diameter miss to hit for "All Flaw Constant Thickness & CG Regions" and for "All Flaws Constant Thickness Regions Only" to show effect of missing a large flaw.					

Table 109. Comparison of POD and flaw detection values for all advanced NDI methods including adjustments in POD calculations to show effects of various inspection impediments (category set B)

	Percent Flaw Detection Continued				
	All Flaws Complex Geometry Regions Only	All Flaws Substructure Regions Only	All Flaws Taper Regions Only	All Flaws Laminate Over Honeycomb Regions Only	All Flaws Curved Surface Regions Only
12–20 and 20–32 Ply Combined Results					
Olympus NDT, PA-UT	92%	81%	100%	100%	100%
NDT Solutions (NDTS, Linear Array UT	91%	79%	100%	100%	100%
NDT Solutions (NDTS), Channel Removed (See Note 2)	N/A	N/A	N/A	N/A	N/A
Toshiba, PA-UT	88%	74%	100%	100%	100%
iPhoton, LUS	85%	67%	100%	100%	100%
iPhoton, Regraded (See Note 1)	91%	79%	100%	100%	100%
Imperium, Digital Acoustic Video	82%	64%	100%	96%	89%
Imperium, Channel Removed (See Note 2)	N/A	N/A	N/A	N/A	N/A
TWI, Flash Thermography	65%	41%	75%	96%	89%
TWI, Example (See Note 3)	N/A	N/A	N/A	N/A	N/A
MISTRAS, Line Thermography	49%	40%	53%	74%	33%
MISTRAS, Channel Removed (See Note 2)	N/A	N/A	N/A	N/A	N/A
MoviTHERM, Lock-In Thermography	55%	40%	60%	78%	67%
Dantec, Shearography	38%	28%	43%	48%	67%
Evisive, Microwave	No Data – Carbon material does not have acceptable dielectric properties for the propagation of Evisive scan waves				
Note 1-Inferred POD _{90/95} value is ≤ 0.25 " diameter flaw (100% flaw detection, POD value cannot be determined)					
Note 2-Asked inspector to take another look at the results and spend more time to see if more flaws could be found. Technology has full data capture capability, which facilitated the ease of a second data review.					
Note 3-Channel data removed. Deployment issues due to size of device or scanning equipment used.					
Note 4-Changed 2" diameter miss to hit for "All Flaw Constant Thickness & CG Regions" and for "All Flaws Constant Thickness Regions Only" to show effect of missing a large flaw.					

All of these results provide similar conclusions as those described above. The PA-UT, linear array UT, LUS, and acoustography NDI methods produce flaw detection levels that are similar to or better than the industry baseline results obtained from conventional PE-UT. Pulsed thermography produced overall results that show promise but are slightly worse than those produced with the conventional PE-UT method. It was shown that pulsed IR is an option for inspecting thin laminate composite structures. Line thermography, lock-in thermography, shearography, and MW inspection methods did not produce acceptable performance levels. The top performers—PA-UT, linear array UT, LUS, and acoustography—primarily have detection levels in the 90%–100% levels over all constant thickness and CG regions, with the exception of flaw detection percentages in the more challenging substructure regions. For flaws in the substructure region, the more successful advanced NDI methods produced flaw detection rates in the 70%–80% level. This can be compared with the results obtained from conventional PE-UT,

in which the set of airline inspectors produced flaw detection rates of 63% for flaws in the substructures.

Tables 110 and 111 summarize the inspection rates obtained from each of the advanced NDI methods. Recall that the manually deployed, single-element PE-UT method produced an overall coverage rate of 2 ft² per hour. In addition, it was determined that this is the optimum inspection rate because faster inspection rates would not produce much improvement in performance. However, the advanced NDI methods all possessed much faster inspection rates. The best performing PA-UT and linear array UT methods ranged in inspections rates from 3–40 ft² per hour. The acoustography methods were in the 5–8 ft² per hour range, whereas the LUS method produced inspection rates of 30–40 ft² per hour. The conclusion is that the advanced NDI methods that performed better than the conventional PE-UT method—PA-UT, linear array UT, LUS, and acoustography—also provide much better inspection rates while producing lower false call rates. The advantage of wide-area inspections, through larger field of views or the use of surface scanning hardware, is evident in tables 110 and 111.

Table 110. Comparison of inspection times and area coverage rate for all advanced NDI methods (thin laminate 12–20 ply specimen set)

Experiment Timing Summary 12–20 Ply Specimen Set – Advanced Methods (Inspection Times Only)													
NDI Method	Specimen											Total Inspection Time (hr:min)	Inspection Coverage Rate (ft ² /hr)
	CT1-A	CT1-B	CT2-A	CT2-B	ST1U-A	ST1L-A	ST2U-A	ST2L-A	BN1	BN2	BN3		
Dantec (Shearography)	0:15	0:11	0:25	0:15	1:05	0:52	1:30	0:47	1:14	0:59	1:08	8:41	3.93
Imperium (Digital Acoustic Video)	0:05	0:08	0:09	0:09	0:35	0:29	0:19	0:35	0:45	0:30	0:34	4:18	7.93
iPhoton (LUS)	0:03	0:03	0:02	0:02	0:03	0:04	0:06	0:04	0:15	0:16	0:15	1:13	28.03
MISTRAS (Line Thermography)	0:04	0:03	0:05	0:04	0:08	0:10	0:08	0:08	0:23	0:23	0:16	1:52	18.27
MoviTHERM (Lock-In Therm.)	0:24	0:13	0:26	0:52	0:57	0:50	0:32	1:34	4:32	2:30	1:25	14:15	2.39
NDT Solutions (Linear Array UT)	0:01	0:01	0:02	0:01	0:06	0:04	0:05	0:08	0:19	0:24	0:22	1:33	22.00
Olympus NDT (PA-UT)	0:04	0:12	0:05	0:04	0:33	0:15	0:11	0:12	1:20	1:25	2:26	6:47	5.03
Toshiba (PA-UT)	0:19	0:19	0:13	0:21	0:28	0:40	0:34	0:40	1:41	1:58	1:22	8:35	3.97
TWI (Flash Thermography)	0:12	0:05	0:05	0:09	0:14	0:09	0:21	0:17	0:47	0:53	1:01	4:13	8.09

Table 111. Comparison of inspection times and area coverage rate for all advanced NDI methods (thick laminate 20–32 ply specimen set)

Experiment Timing Summary 20–32 Ply Specimen Set Advanced Methods (Inspection Times Only)						
NDI Method	Specimen				Total Inspection Time (hr:min)	Inspection Coverage Rate (ft ² /hr)
	ST32-1	ST32-2	ST32-3	ST32-4		
All Nippon (PA-UT)	1:15	2:25	1:11	1:01	5:52	2.05
Dantec (Shearography)	1:00	0:39	0:23	0:34	2:36	4.62
GEIT (RotoArray)	1:16	1:18	1:09	0:59	4:42	2.55
Imperium (Digital Acoustic Video)	0:24	0:27	0:29	0:59	2:19	5.18
iPhoton (LUS)	0:06	0:04	0:04	0:04	0:18	40.00
LTI (Shearography)	0:58	1:02	0:39	0:49	3:28	3.46
MISTRAS (Line Thermography)	0:12	0:21	0:11	0:12	0:56	12.86
MoviTHERM (Lock-In Therm.)	0:22	0:13	0:14	0:15	1:04	11.25
NDT Solutions (Linear Array UT)	0:08	0:03	0:04	0:03	0:18	40.00
Olympus NDT (PA-UT)	0:12	0:11	0:32	0:23	1:18	9.23
Sandia Labs (Wheel Probe)	0:46	0:36	0:38	1:40	3:40	3.27
Toshiba (PA-UT)	0:40	0:36	0:34	0:37	2:27	4.90
TWI (Flash Thermography)	0:21	0:24	0:24	0:18	1:27	8.28

The final analysis of the advanced NDI results assessed the maturity of each inspection technique based on the observations from the SLE. Standard technology readiness levels (TRLs)—which are similar across the Department of Energy, the DOT, NASA, and the Department of Defense—were used to place each inspection method into an appropriate TRL category. Table 112 describes each of the TRLs ranging from basic concepts (TRL 2) to fully functional and tested/marketed technology (TRL 9). Table 113 shows that most of the NDI methods were considered to be in the latter or final stages of development and ready for utilization. It was observed that some of the devices could benefit from customization to address the unique demands of composite laminate inspections. Such customization and additional exposure to composite inspections should improve the performance of the advanced NDI methods. However, it is clear that some of the methods are simply not well-suited for inspection of composite laminate structures (i.e., composite skins with substructure elements). Table 112 provides some insight into the personnel deploying each inspection system. Because the data presented here stems from a single application of each inspection system—as opposed to the conventional PE-UT evaluation, which is an industry baseline produced from 57 airline inspectors—the expertise and experience of the person(s) conducting the experiment plays a large role in the results. Therefore, an inspector proficiency rating was applied to each experiment participant, which was determined by the experiment participant and the AANC experiment observers. Some of these ratings indicate that the results could be improved with a more experienced user. Other ratings show that even inexperienced users can produce good results with certain equipment (e.g., Sonatest RapidScan linear array UT).

Table 112. Descriptions of TRLs

TRLs for the Department of Energy	
TRL	Description
TRL 1.	Scientific research begins translation to applied R&D – Lowest level of technology readiness. Scientific research begins to be translated into applied research and development. Examples might include paper studies of a technology’s basic properties.
TRL 2.	Invention begins – Once basic principles are observed, practical applications can be invented. Applications are speculative and there may be no proof or detailed analysis to support the assumptions. Examples are limited to analytic studies.
TRL 3.	Active R&D is initiated – Active research and development is initiated. This includes analytical studies and laboratory studies to physically validate analytical predictions of separate elements of the technology. Examples include components that are not yet integrated or representative.
TRL 4.	Basic technological components are integrated – Basic technological components are integrated to establish that the pieces will work together.
TRL 5.	Fidelity of breadboard technology improves significantly – The basic technological components are integrated with reasonably realistic supporting elements so it can be tested in a simulated environment. Examples include “high fidelity” laboratory integration of components.
TRL 6.	Model/prototype is tested in relevant environment – Representative model or prototype system, which is well beyond that of TRL 5, is tested in a relevant environment. Represents a major step up in a technology’s demonstrated readiness. Examples include testing a prototype in a high-fidelity laboratory environment or in a simulated operational environment.
TRL 7.	Prototype near or at planned operational system – Represents a major step up from TRL 6, requiring demonstration of an actual system prototype in an operational environment.
TRL 8.	Technology is proven to work – Actual technology completed and qualified through test and demonstration.
TRL 9.	Actual application of technology is in its final form – Technology proven through successful operations.

Table 113. The TRL ratings for the advanced NDI methods as pertains to maturity for aircraft inspections in a maintenance hangar environment

TRL						
Company	Method	Device Manufacturer	Inspection Device	TRL at Time of		IPR* at Time of
				Experiment	Report	Experiment
All Nippon	PA-UT	Toshiba	Matrixeye	9	9	2
Sandia Labs	Linear Array UT	Sonatest	Wheel Probe w/ Omniscan MX1	9	9	0
Dantec	Shearography	Dantec	Q-800	9	9	4
Evisive, Inc.	Microwave	Evisive	Evisive Scan	N/A	N/A	N/A
GEIT	PA-UT	GE	RotoArray w/ Phasor XS	7	9	1
Imperium	Digital Acoustic Video	Imperium	AcoustoCam	7	9	4
iPhoton	LUS	iPhoton	iPLUS	9	9	4
LTI	Shearography	LTI	LTI-5100 HD	9	9	4
MISTRAS	Line Thermography	MISTRAS	THELIS-P Scanner	6	7	2
MoviTHERM	Lock-In Thermography	MoviTHERM	FLIR Camera, SR2 SC7650	9	9	4
NDT Solutions	Linear Array UT	Boeing	FlawInspecta – MAUS V	9	9	4
Olympus NDT	PA-UT	Olympus	Olympus OmniScan MX2	9	9	4
Toshiba	PA-UT	Toshiba	Matrixeye	9	9	4
TWI	Flash Thermography	TWI	Ecotherm	9	9	4
DolphiTech	UT Video	Sonatest	DolphiCam	6	9	4
RCON NDT	Linear Array UT	Sonatest	Wheel Prove w/ RapidScan 2	9	9	4

*Inspector Proficiency Rating (IPR) (at the time of the experiment)	
0	Never used the device prior to experiment
1	Used the device a couple of times
2	Very familiar with the device
3	Used the device for many years
4	Expert user of the device

One of the inspection devices, the Toshiba Matrixeye PA-UT system, was also deployed by an airline inspector. This exercise allowed for the evaluation of the performance of inexperienced airline inspectors deploying advanced NDI. The airline inspector was a level III UT inspector; he had experience in the inspection of composite laminate structures. Figure 225 shows the deployment of the Matrixeye device by the airline inspector. This inspector completed the thick laminate experiment so that it was possible to compare the consistency of results between the deployments of the Matrixeye by two different agencies: Toshiba and All Nippon Airways inspectors.



Figure 225. Deployment of Matrixeye PA-UT system by All Nippon Airways on SLE

Figure 226 contains the POD flaw detection curve for the thick (20–32 ply) laminate experiment. The Matrixeye PA-UT system, deployed by an airline inspector, produced a thick laminate $POD_{[90/95]} = 0.524''$. This is a 36% improvement over the thick laminate results from the conventional PE-UT tests ($POD_{[90/95]} = 0.823''$) that evaluated the performance of airline inspectors (see section 6.1). It is also slightly better than the results produced by Toshiba personnel deploying the Matrixeye device ($POD_{[90/95]} = 0.606''$). Table 114 delineates the flaw detection percentages for each of the specimen design attributes (i.e., constant thickness, CG, substructure regions, and taper regions). The flaw detection percentages produced by the airline inspector were the same as those produced by Toshiba personnel. This table also shows that there was 1 false call for the entire experiment.

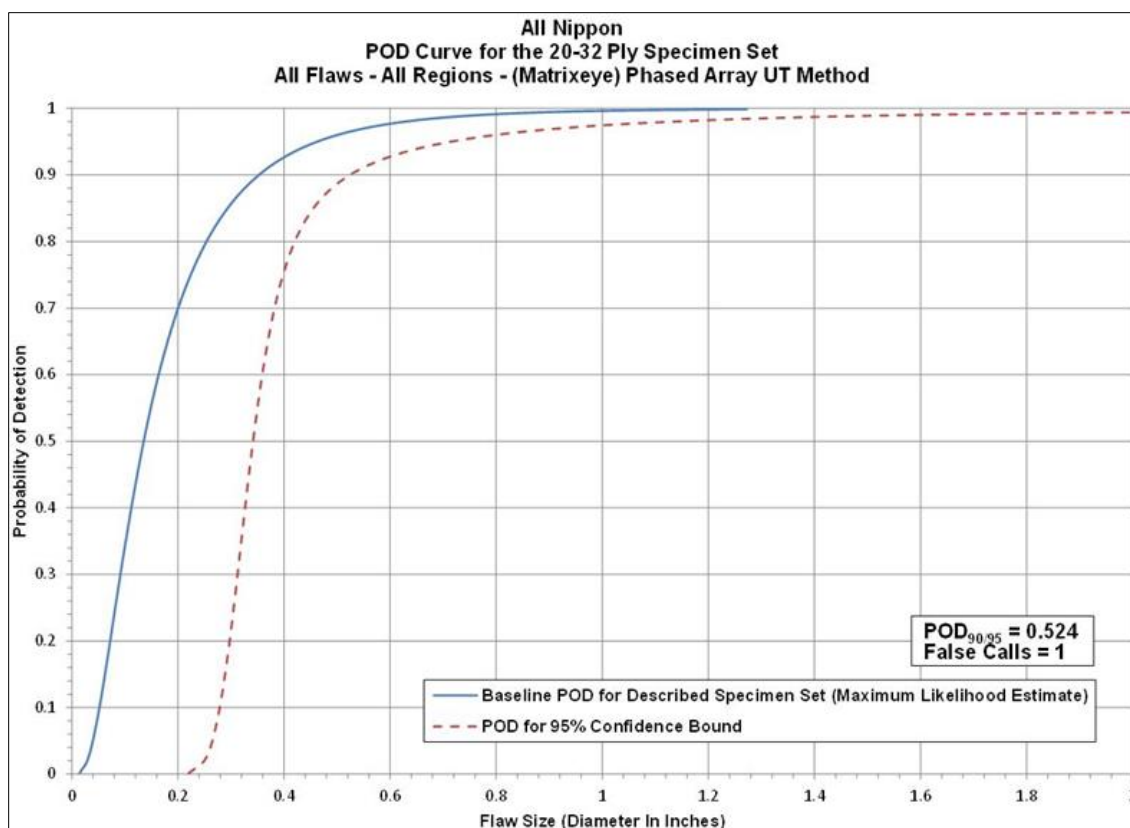


Figure 226. The POD results for Matrixeye PA-UT system (All Nippon Airways deployment; flaw detection in solid laminate composite structure)

Table 114. Flaw detection performance for Matrixeye PA-UT system (All Nippon Airways deployment) separated into thick laminate results

Results – All Nippon – (Matrixeye) PA-UT			
20–32 Ply (Thick Laminate Experiment)			
POD _{90/95} Value	Percent Flaw Detection		
All Flaws Constant Thickness & CG Regions (dia. in inches)	All Flaws Constant Thickness & CG Regions	All Flaws Constant Thickness Regions Only	All Flaws CG Regions Only
0.524	97%	100%	95%
False Calls = 1			

Inspector flaw calls were also graded to evaluate the accuracy of the Matrixeye PA-UT method for flaw sizing. The overall test results identified hits (i.e., calls with any amount of overlap between the call and the actual flaw location), misses (i.e., no call for an area of a known flaw), false calls (i.e., call with no overlap of a flaw), and sizing performances (i.e., the degree of overlap between experimenter calls and actual flaw areas). Tables 115–117 summarize the

results for flaw sizing and percent detection based on flaw size for the thick laminate experiment and provide a breakdown of those performance attributes in the constant thickness and CG regions. Table 117 summarizes the results for the overall flaw detection percentage and the associated accuracy in determining flaw size for the 20–32 ply specimen set (thick laminate experiment). For the 20–32 ply specimen set, 97% of all flaws were detected (65 of 67 flaws). This is an improvement over the conventional PE-UT results, in which 85% of all flaws were detected. It is also the same flaw detection level that was produced by Toshiba personnel deploying the Matrixeye device. The flaw sizing performance shows that 100% of the detected flaws were sized properly (5 category for 100% coverage) versus 31% calculated for the conventional PE-UT method. Table 117 shows a breakdown of percent detection based on flaw size. For example, 100% of the 2" flaws were detected. Of the smaller flaws, 82% of the 0.25" flaws were detected (versus 56% detection of the 0.25" flaws using conventional PE-UT). These results indicate that the Matrixeye PA-UT device can be successfully deployed by airline inspectors to improve flaw detection beyond the current industry baseline.

Table 115. Tabulated results showing overall flaw detection percentage and accuracy in determining flaw size for the 20–32 ply specimen set for all flaws in constant thickness regions (Matrixeye PA-UT system; All Nippon Airways deployment)

All Nippon – (Matrixeye) PA-UT Flaw Detection Percentage & Accuracy in Determining Flaw Size 20–32 Ply Specimen Set – All Constant Thickness Flaws							
Accuracy in Sizing the Flaws That Were Detected						Flaw Detection Percentage	
Flaw Size	5 (100%)	4 (76%–99%)	3 (51%–75%)	2 (25%–50%)	1 (< 25%)	Flaw Size	Percent Detected
0.25	100%	0%	0%	0%	0%	0.25	100%
0.50	100%	0%	0%	0%	0%	0.50	100%
0.75	100%	0%	0%	0%	0%	0.75	100%
1.00	100%	0%	0%	0%	0%	1.00	100%
1.50	100%	0%	0%	0%	0%	1.50	100%
2.00	100%	0%	0%	0%	0%	2.00	100%
Overall Sizing Performance	100%	0%	0%	0%	0%	Overall Flaw Detection	100%

Table 116. Tabulated results showing overall flaw detection percentage and accuracy in determining flaw size for the 20–32 ply specimen set for all flaws in CG regions (Matrixeye PA-UT system; All Nippon Airways deployment)

All Nippon – (Matrixeye) PA-UT Flaw Detection Percentage & Accuracy in Determining Flaw Size 20–32 Ply Specimen Set – All CG Flaws							
Accuracy in Sizing the Flaws That Were Detected						Flaw Detection Percentage	
Flaw Size	5 (100%)	4 (76%–99%)	3 (51%–75%)	2 (25%–50%)	1 (< 25%)	Flaw Size	Percent Detected
0.25	100%	0%	0%	0%	0%	0.25	71%
0.50	100%	0%	0%	0%	0%	0.50	100%
0.75	100%	0%	0%	0%	0%	0.75	100%
1.00	100%	0%	0%	0%	0%	1.00	100%
1.50	100%	0%	0%	0%	0%	1.50	100%
2.00	100%	0%	0%	0%	0%	2.00	100%
Overall Sizing Performance	100%	0%	0%	0%	0%	Overall Flaw Detection	95%

Table 117. Tabulated results showing overall flaw detection percentage and accuracy in determining flaw size for the 20–32 ply specimen set for all flaws in constant thickness and CG regions (Matrixeye PA-UT system; All Nippon Airways deployment)

All Nippon – (Matrixeye) PA-UT Flaw Detection Percentage & Accuracy in Determining Flaw Size 20–32 Ply Specimen Set – All Flaws (Constant Thickness & CG)							
Accuracy in Sizing the Flaws That Were Detected						Flaw Detection Percentage	
Flaw Size	5 (100%)	4 (76%–99%)	3 (51%–75%)	2 (25%–50%)	1 (< 25%)	Flaw Size	Percent Detected
0.25	100%	0%	0%	0%	0%	0.25	82%
0.50	100%	0%	0%	0%	0%	0.50	100%
0.75	100%	0%	0%	0%	0%	0.75	100%
1.00	100%	0%	0%	0%	0%	1.00	100%
1.50	100%	0%	0%	0%	0%	1.50	100%
2.00	100%	0%	0%	0%	0%	2.00	100%
Overall Sizing Performance	100%	0%	0%	0%	0%	Overall Flaw Detection	97%

7. CONCLUSIONS AND RECOMMENDATIONS

7.1 OVERVIEW THOUGHTS ON NONDESTRUCTIVE INSPECTION FOR SOLID LAMINATE COMPOSITE STRUCTURES

This section provides overview thoughts on nondestructive inspection for solid laminate composite structures:

- This program assessed current industry capabilities by quantifying flaw detection performance in composite laminate structures.
- Engineering and economic benefits of composites will continue to expand its use.
- Damage tolerance and durability is good, but parts will sustain damage.
- Maintenance and training issues are being addressed at airlines and maintenance and repair organizations to accommodate the transition to increased inspection of composite structures.
- This experiment provided overall probability of detection (POD) values for inspecting composite laminate structures so that the aviation industry can:
 - better understand what type of damage detection is possible for specific inspection scenarios.
 - adjust inspection procedures to optimize performance.
 - determine the level of flaw detection improvements that are possible through the application of more sophisticated and advanced nondestructive inspection (NDI).
 - smartly enhance inspector preparation and training to generate the performance improvements possible through optimized NDI deployment, sufficient knowledge of the inspection idiosyncrasies, and increased exposure to realistic, composite inspection demands.
- The solid laminate flaw detection experiment (SLE) study showed that lower POD values are obtained in constant thickness regions and higher POD values for more complex regions.
- Overall, the results from the solid laminate experiment established a capability baseline for current NDI techniques and quantified improvements stemming from advanced NDI.
- The field testing approach to this experiment provided insights into procedural and implementation issues.

- Though the size of the flaw (i.e., damage) that must be detected is affected by many parameters (e.g., structure type, location on aircraft, stress, and fatigue levels), the general goal for composite inspections is to detect flaws that are 1" in diameter or larger. Many of the NDI reference standards in original equipment manufacturer (OEM) nondestructive testing manuals use 1" diameter flaws to guide equipment setup. In addition, the Commercial Aircraft Composite Repair Committee Inspection Task Group members generally concede that 1" flaw detection provides a good center point for this SLE. Therefore, the flaw sizes in the SLE design were established with a 1" diameter at the center. Larger and smaller flaws were included such that POD values smaller than 1" (as small as 0.25") and POD values larger than 1" (as large as 2") could be ascertained.
- The NDI growth areas are focusing on features for large-area, rapid scanning; improved data presentation; enhanced sensitivity; defect characterization; automated analysis; and advanced sensors/probes.
- The viability of certain NDI methods, selected to meet specific application demands, and the quantification of performance must be continually pursued. Toward that end, this composite laminate flaw detection experiment is available for continued testing. All future testing will have the results from this pulse-echo ultrasonic (PE-UT) and advanced NDI assessment to serve as the basis of comparison and help quantify NDI improvements.

7.2 RESULTS FROM CONVENTIONAL PE-UT POD TESTS

The following is a summary from a related study that addressed the use of airline inspectors to quantify the performance of the conventional PE-UT method [23]:

- Overall Inspector Performance – The overall results for the composite laminate flaw detection experiment, which includes all areas and all skin and substructure flaws, are as follows:
 - Thin 12–20 ply skins $POD_{[90/95]} = 1.29''$ diameter (60%–90% of flaws were detected depending on the inspector)
 - Thick 20–32 ply skins $POD_{[90/95]} = 0.82''$ diameter (70%–95% of flaws were detected depending on the inspector)
 - Overall (combined 12–20 & 20–32 ply skins) $POD_{[90/95]} = 1.13''$ diameter

These results indicate that a flaw of approximately 1.125" diameter could be reliably detected (within the industry standard of 90% POD, with a 95% confidence) by an inspector using manually deployed, PE-UT equipment to inspect a composite structure in the 10–32 ply skin thickness range (plus substructures, which make the total lay-up a maximum of 64 plies).

- Performance Brackets – To determine the difference between outstanding, good, and average inspectors, the flaw detection data was adjusted to eliminate individual inspectors whose performance dropped below a specific level. The POD analyses were then completed on the remaining set of inspection data to calculate the resulting overall POD levels corresponding to inspector categories. The results from this analytical approach are as follows:
 - 12–20 ply skins $POD_{[90/95]} = 1.29''$ diameter (all inspectors)
 - 12–20 ply skins $POD_{[90/95]} = 1.19''$ diameter (top 90 percentile) - average
 - 12–20 ply skins $POD_{[90/95]} = 1.06''$ diameter (top 70 percentile) - good
 - 12–20 ply skins $POD_{[90/95]} = 0.79''$ diameter (top 30 percentile) - outstanding
 - 20–32 ply skins $POD_{[90/95]} = 0.82''$ diameter (all inspectors)
 - 20–32 ply skins $POD_{[90/95]} = 0.70''$ diameter (top 80 percentile) - average
 - 20–32 ply skins $POD_{[90/95]} = 0.54''$ diameter (top 60 percentile) - good
 - 20–32 ply skins $POD_{[90/95]} = 0.48''$ diameter (top 40 percentile) - outstanding

Inspectors in the upper bracket performed approximately 40% better than the overall results produced by all inspectors combined. The purpose of this exercise was to demonstrate the clear improvements that are possible if inspectors are able to improve their skills to reach the next performance level. Methods that an airline might use to transition their inspectors toward the “outstanding” bracket include enhanced/increased training, apprenticeships, exposure to representative inspections, enhanced procedures, reiteration of proper procedures, and inspector teaming or other oversight.

- False Calls – Overall, false calls were not considered a problem. The false call rates were as follows:
 - 12–20 ply = One false call per 7.7 ft^2
 - 12–20 ply (using only false calls that were larger than $0.25''$ diameter) = One false call per 14 ft^2
 - 20–32 ply = One false call per 10.9 ft^2
 - 20–32 ply (using only false calls that were larger than $0.25''$ diameter) = One false call per 40 ft^2
 - Overall (combined 12–20 & 20–32 ply) = One false call per 8.4 ft^2
 - Overall (combined 12–20 & 20–32 ply and using only false calls that were larger than $0.25''$ diameter) = One false call per 17 ft^2
- Flaw Sizing – Inspectors were asked to provide the size and shape of the flaws that they detected. Once the inspectors found a flaw, their ability to size the flaw using their UT equipment was very consistent. Approximately 60% of the flaws were sized between

75%-100% of their actual size, whereas approximately 80% were sized at 50%-100% of their actual size.

- Inspection Challenges: Flaw Detection in Substructure Regions – The most challenging flaws to detect were those in the presence of substructure elements, either in the bond line or in the substructure itself (e.g., stringer, frame). The complexity of the PE-UT waveform increases drastically in the areas of substructure elements. In addition, the added signal penetration requirement and associated porosity increase coupled with reflections from dissimilar materials (resin or bond lines versus composite laminates) create lower amplitude signals. This decreases the signal-to-noise (S/N) ratios such that flaw signals are more difficult to discern. Furthermore, intermediate signals, stemming from internal inclusions, disbonds, and delaminations, are more difficult to clearly identify amid an extensive set of internal reflection peaks and signal harmonics. The reduction in performance when inspecting complex geometry (CG) regions is summarized in the following results:
 - 12–20 ply skins $POD_{[90/95]} = 1.29''$ diameter (all regions)
 - 12–20 ply skins $POD_{[90/95]} = 0.86''$ diameter (constant thickness regions)
 - 12–20 ply skins $POD_{[90/95]} = 1.49''$ diameter (all CG regions)
 - 20–32 ply skins $POD_{[90/95]} = 0.82''$ diameter (all regions)
 - 20–32 ply skins $POD_{[90/95]} = 0.74''$ diameter (constant thickness regions)
 - 20–32 ply skins $POD_{[90/95]} = 0.93''$ diameter (all CG regions)
 - Overall (12–20 & 20–32 ply skins) $POD_{[90/95]} = 1.13''$ diameter (all regions)
 - Overall (12–20 & 20–32 ply skins) $POD_{[90/95]} = 0.80''$ diameter (constant thickness regions)
 - Overall (12–20 & 20–32 ply skins) $POD_{[90/95]} = 1.34''$ diameter (all CG regions)

For the 12–20 ply skin specimen set, only 51% of the flaws in the regions with substructure elements were detected. This includes flaws in the surface skin and flaws in the substructure elements or bond line beneath the surface skin. Only 65% of the flaws greater than 0.75" diameter were detected, whereas 30% of the flaws less than 0.75" diameter were detected. For all specimens combined in the overall composite laminate flaw detection experiment (12–20 and 20–32 ply skin specimens), the inspection performance declined in the CG regions. It was determined that the inspection performance in all substructure regions was 19% worse than the overall $POD_{[90/95]}$ and was 68% worse than the $POD_{[90/95]}$ value obtained in the constant thickness region (0.80" in constant thickness versus 1.34" in the substructure regions). Additional experience and

use of representative NDI reference standards could help improve the detection levels in substructure regions.

- Inspection Challenges: Confounding Effects of Signal Harmonics – Figure 227 shows how signal harmonics can appear in the range of interest when harmonics from thinner surface laminates fold into the same time frame as the actual signals of interest generated from the back wall of a substructure element. In these cases, it may be critical to use the appearance of new intermediate signals to infer the presence of damage. Substantial changes in the expected shape of the back wall signals could also indicate the presence of intermediate damage, where such changes may not be below the normal accept-reject threshold.

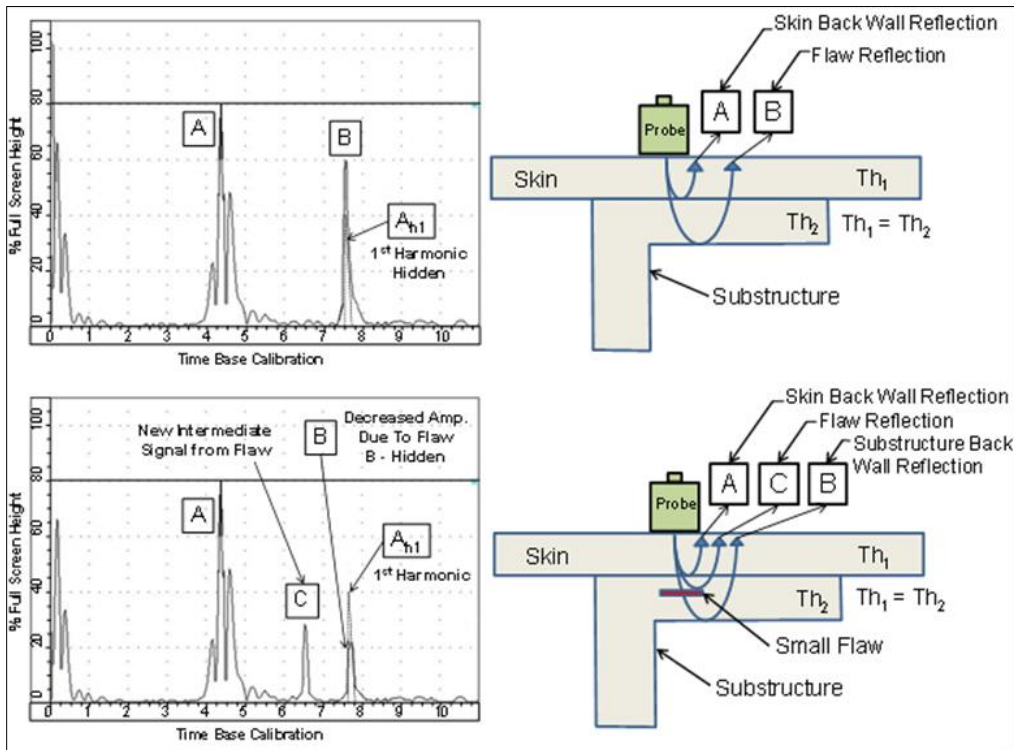


Figure 227. Inspection impediment in which signal harmonics occur in the same time frame as the signals of interest

- Human Factors Issue: Effect of Inspection Rate on POD – The average inspection rates for the SLE experiment were as follows:
 - 12–20 ply average coverage rate = 2.3 ft²/hour (max rate = 3.5 ft²/hour; min rate = 1.5 ft²/hour)
 - 20–32 ply average coverage rate = 1.9 ft²/hour (max rate = 4.2 ft²/hour; min rate = 1.2 ft²/hour)

It was noted that there was an approximate 10% improvement in POD levels when comparing inspection rates of 2 ft²/hour or less with those above 2 ft²/hour. Therefore, inspection rates faster than 2 ft²/hour are not recommended. Previous studies by the Airworthiness Assurance NDI Validation Center revealed that there are diminishing improvements to be obtained by slowing the inspection rate to very small numbers. Therefore, rates below 1.5 ft²/hour are not expected to yield better results except in cases in which structural complexities warrant slower inspection rates to properly understand the resulting UT signals.

- Proper Execution of Procedures: Use of Aids to Ensure Proper Coverage – The inspection procedures discuss proper coverage of the inspection area and even suggest the use of grids or other methods to ensure that the UT transducer is moved over the entire surface area. In addition, conformable straight edges and rulers were provided to the inspectors for their use. Some inspectors completed their work using simple freehand (i.e., unguided) motion over the entire surface area of each specimen. Some inspectors divided the test specimens into quadrants while still moving the transducer in a freehand motion so that they could better monitor their coverage and transducer movement. Some inspectors used straight edges to guide their transducer movement, and some of that group of inspectors added tick marks to ensure that they moved their straight edge in 0.5" increments along the test specimens. Finally, some inspectors used straight edges in some regions and a freehand motion in other regions (the percentage of each was not logged, but this combined practice was noted). The inspection results showed a significant improvement in POD for inspectors that used straight edges. The following POD values compare inspectors who used freehand transducer deployment with inspectors who used straight edges with tick marks:
 - 12–20 ply freehand $POD_{[90/95]} = 2.39''$ diameter
 - 12–20 ply straight edge with tick marks $POD_{[90/95]} = 1.06''$ diameter
 - 20–32 ply freehand $POD_{[90/95]} = 1.35''$ diameter
 - 20–32 ply straight edge with tick marks $POD_{[90/95]} = 0.64''$ diameter
 - Overall (combined 12–20 & 20–32 Ply) freehand $POD_{[90/95]} = 1.75''$ diameter
 - Overall (combined 12–20 & 20–32 Ply) straight edge with tick marks $POD_{[90/95]} = 0.91''$ diameter

Therefore, the inspection performance decreases by a factor of 100%–125% when the inspectors attempt to cover the entire inspection area using a freehand method.

7.3 RESULTS FROM POD TESTS USING ADVANCED NDI METHODS

This section provides a discussion of the results from POD tests using advanced NDI methods:

- Overall, it was determined that there are advanced NDI methods that can be used to improve on the flaw detection performance that was obtained from conventional PE-UT used by airline inspectors (aviation industry baseline). The advanced NDI methods (i.e., equipment plus deployment approach) that were evaluated in this experiment covered a wide range of technology readiness levels (TRLs); it is important to view the performance of each NDI method in light of the TRL level. Subsequent advances in the NDI device may improve performance in the future.
- Some of the advanced NDI methods were better suited for composite laminate inspections than others. Structural features such as material type, thickness, and geometry affect some NDI methods more than others, rendering some NDI methods unusable for composite laminate inspections or limiting their application to some subset of the spectrum of composite laminate designs represented in this flaw detection experiment. Therefore, in addition to identifying current limitations on the applications of the advanced NDI methods tested, this experiment also highlighted some development needs that may help guide system redesigns to improve these advanced NDI methods for composite inspections.
- All of the NDI methods evaluated in this experiment produced some form of a 2D image. These images either covered relatively large areas compared to single-element PE-UT or the smaller images could be tiled together to produce a wide-area coverage method. It has been demonstrated that the use of color-coded or gray-scale images with wide-area coverage that accommodates comparisons with adjacent areas is extremely helpful in both identifying flaws and reducing false calls. It may be useful to conduct composite laminate inspections using the scanning methods evaluated here and then complete flaw confirmation inspections on questionable regions using conventional PE-UT, where focused A-scan signals can complement the C-scans. Another advantage of the advanced NDI systems is that they have the ability to store the images for future use. This allows for additional image interpretation from other inspectors and an ability to track questionable regions to determine if subtle shadings remain unchanged over time, or if they evolve into something that is clearly damage in the part.
- The following is a summary of the $POD_{[90/95]}$ performance values for the advanced methods that participated in the complete solid laminate experiment (i.e., combined thin [12–20 ply] laminate experiment and thick [20–32 ply] laminate experiment). These results are compared to the cumulative industry baseline result produced by conventional PE-UT ($POD_{[90/95]} = 1.125''$):
 - OmniScan phased array ultrasonics (PA-UT) produced an overall $POD_{[90/95]} = 0.716''$; 36% performance improvement
 - Matrixeye PA-UT produced an overall $POD_{[90/95]} = 0.689''$; 39% performance improvement
 - Mobile Automated Scanner (MAUS) V FlawInspecta linear array UT produced an overall $POD_{[90/95]} = 0.884''$; 21% performance improvement

- iPhoton laser-ultrasonics (LUS) concept (iPLUS) produced an overall $POD_{[90/95]} = 0.851''$; 24% performance improvement
 - AcoustoCam digital acoustic video produced an overall $POD_{[90/95]} = 1.118''$; 1% performance improvement
 - EcoTherm pulsed thermography produced an overall $POD_{[90/95]} = 2.299''$; 104% drop in performance
 - Q-800 shearography produced an overall $POD_{[90/95]} > 3.0''$; 167% drop in performance
 - THELIS-P Line Scanning Thermography (LST) produced an overall $POD_{[90/95]} > 3.0''$; 167% drop in performance
 - MoviTHERM lock-in thermography produced an overall $POD_{[90/95]} > 3.0''$; 167% drop in performance
- The following is a summary of the $POD_{[90/95]}$ performance values for the advanced methods that completed the thin (12–20 ply) laminate experiment. These results are compared to the cumulative industry baseline result produced by conventional PE-UT ($POD_{[90/95]} = 1.287''$):
 - OmniScan PA-UT produced a $POD_{[90/95]} = 0.862''$; 33% performance improvement
 - Matrixeye PA-UT produced a $POD_{[90/95]} = 0.818''$; 36% performance improvement
 - MAUS V FlawInspecta linear array UT produced a $POD_{[90/95]} = 1.393''$; 8.2% drop in performance
 - iPLUS LUS produced a $POD_{[90/95]} = 1.204''$; 6.4% performance improvement
 - AcoustoCam digital acoustic video produced a $POD_{[90/95]} = 1.422''$; 10.5% drop in performance
 - EcoTherm pulsed thermography produced a $POD_{[90/95]} = 2.299''$; 4.8% performance improvement
 - Q-800 shearography produced a $POD_{[90/95]} > 3.0''$; 133% drop in performance
 - THELIS-P LST produced a $POD_{[90/95]} > 3.0''$; 133% drop in performance

- MoviTHERM lock-in thermography produced a $POD_{[90/95]} > 3.0''$; 133% drop in performance
- The following is a summary of the $POD_{[90/95]}$ performance values for the advanced methods that completed the thick (20–32 ply) laminate experiment. These results are compared to the cumulative industry baseline result produced by conventional PE-UT ($POD_{[90/95]} = 0.823''$):
 - OmniScan PA-UT produced a $POD_{[90/95]} < 0.25''$; 70% performance improvement
 - Matrixeye PA-UT produced a $POD_{[90/95]} = 0.606''$; 26% performance improvement
 - MAUS V FlawInspecta linear array UT produced a $POD_{[90/95]} < 0.25''$; 70% performance improvement
 - Sonatest Array WheelProbe with Omniscan produced a $POD_{[90/95]} < 0.25''$; 70% performance improvement
 - RotoArray with Phasor XS produced a $POD_{[90/95]} > 3.0''$; 264% drop in performance
 - iPLUS LUS produced a $POD_{[90/95]} < 0.25''$; 70% performance improvement
 - AcoustoCam digital acoustic video produced a $POD_{[90/95]} < 0.25''$; 70% performance improvement
 - EcoTherm pulsed thermography produced a $POD_{[90/95]} > 3.0''$; 264% drop in performance
 - Q-800 shearography produced a $POD_{[90/95]} > 3.0''$; 264% drop in performance
 - LTI-5200 shearography produced a $POD_{[90/95]} > 3.0''$; 264% drop in performance
 - THELIS-P LST produced a $POD_{[90/95]} > 3.0''$; 264% drop in performance
 - MoviTHERM lock-in thermography produced a $POD_{[90/95]} > 3.0''$; 264% drop in performance
- False calls were not considered to be an issue. False call rates for the top performers were less than those observed with the hand-deployed, single-element PE-UT inspection method. Similarly, the ability to accurately determine the size of each detected flaw was improved significantly through the use of the advanced NDI methods. The challenging detection of flaws in the presence of substructure elements, either in the bond line or in the substructure itself (e.g., stringer, frame), was also improved when deploying the higher performing advanced NDI systems discussed in this report.

- From the fieldable methods tested in this experiment, it was shown that most of the PA-UT methods and some of the linear array UT methods exceeded the capabilities of conventional PE-UT. A clear improvement was shown in the overall $POD_{[90/95]}$ results ranging from 20% to nearly 40%. Note that LUS performed very well but the system is not portable, so it is not considered fieldable at this time. Advantages of using PA-UT or linear array UT systems over conventional PE-UT include the following:
 - Improved flaw detection percentages
 - Improved flaw detection of smaller flaws
 - Improved detection of substructure flaws
 - Improved sizing performance
 - Faster scan speeds (coverage)
 - Fewer false calls – C-scan superior imaging compared to an A-scan is a major factor influencing an inspector’s ability to detect and interpret a flaw, which reduces the number of false calls
- The top performers—PA-UT, linear array UT, LUS, and acoustography—primarily have detection levels in the 90%–100% levels over all constant thickness and CG regions, with the exception of flaw detection percentages in the more challenging substructure regions. For flaws in the substructure region, the more successful advanced NDI methods produced flaw detection rates in the 70%–80% level. This can be compared with the results obtained from conventional PE-UT, in which the set of airline inspectors produced flaw detection rates of 63% for flaws in the substructures.
- There are some deployment issues with many of the advanced NDI methods when it comes to inspecting highly curved surfaces (i.e., bullnose) and tight spaces (i.e., channels). Many of the inspection methods studied were limited in their ability to detect flaws in these regions using their normal setup, whereas some inspectors switched to different handheld encoders to attempt flaw detection. The use of scanning systems hinders the ability to inspect these regions without using a different setup. Scanning systems work well on large areas that are not highly curved, such as a fuselage or wing section. Therefore, the size of the probes or interrogating heads in many of the advanced NDI systems evaluated in this study limited the regions that these systems can inspect to mostly areas with small access ports or tight geometry changes. In these cases, it may be necessary to use the smaller, manually deployed, single-element PE-UT inspections.
- This experiment revealed that human factor issues still exist when using the more automated scanning inspection approach. A second, improved POD curve was generated by results obtained when the inspector revisited the same iPLUS data but spent additional time to study potential flaws in the images. The iPLUS system possesses full waveform

data capture capabilities, which facilitated the ease of a second data review of both A-scan and C-scan data. When the data was analyzed a second time, it was observed that the POD value improved by 25% to an overall $POD_{[90/95]} = 0.641''$. This new POD level is a 43% improvement over the overall result from the conventional PE-UT tests ($POD_{[90/95]} = 1.125''$). This indicates that flaw detection, and potentially reductions in false calls, can be improved through the use of a second, follow-on inspector to aid in data interpretation.

- The depth of penetration required to conduct successful inspections in solid laminate structures is a major impediment to many of the advanced NDI methods. This is especially evident when looking at the results from line thermography, lock-in thermography, and shearography inspections. External excitation, such as those deployed with these methods, and the resultant need to observe changes in surface conditions stemming from subsurface anomalies, make it difficult for these methods to detect deeply embedded flaws. Note, for example, the performance of pulsed thermography in the thin laminate experiment. It is slightly better than the performance produced by the conventional PE-UT method. These thin laminate test specimens are within the depth of penetration sensitivity for pulsed thermography. Therefore, flash (i.e., pulsed) infrared is an option for inspecting thin laminate composite structures. Contrast these results with those produced by pulsed thermography in the thick laminate experiment, in which the interrogation must be completed on much thicker laminates. In this case, the POD results are much worse than those obtained from the conventional PE-UT method. Similarly, shearography performs well for wide-area imaging to detect near surface flaws. Substructure flaws must manifest themselves as changes (i.e., anomalies) in out-of-plane deformation on the surface of the part to be detected by shearography. As a result, thick and stiff structures are a challenge for the shearography inspection method. Small flaws, especially those embedded deep within a structure, are difficult to image as their presence has less of an effect on surface deformations. It should also be noted that a companion POD experiment for flaw detection in honeycomb composites—in which the skin thickness ranged from 3–12 plies—revealed that both thermography and shearography inspections produce outstanding results for honeycomb structures. The POD levels produced by thermography and shearography were much better than those produced by conventional honeycomb inspection methods [24].
- The advantage of scanning PE-UT (the phased and linear array UT methods studied in this experiment) is the addition of C-scan imaging to complement the A-scan signals used in conventional, single element PE-UT. The advantages of the scanning UT methods are:
 - C-scan area views provide the inspector with easier-to-use and more reliable data with which to recognize flaw patterns and eliminate the human factor concerns related to continuously observing and detecting subtle changes in A-scan signals
 - Scanning approach ensures full coverage of the inspection region and allows for more rapid inspections of large surface areas

- Multiple gate settings can be used simultaneously to optimize flaw detection at different depths within complex structures
- An additional advantage related to the PA-UT method is that it can carefully control the generation of UT signals and data acquisition from select elements in the array to produce customized focusing of the array to improve the sensitivity of the inspection. Electronic focusing allows for optimizing the beam shape and size at the expected defect location, therefore further optimizing the POD. The ability to focus at multiple depths also improves flaw sizing of critical defects in volumetric inspections. Focusing can significantly improve the S/N ratio in challenging applications, and electronic scanning across many groups of elements allows for C-scan images to be produced very rapidly.
- Phased array and linear array wheel probes have the same advantages as traditional array scanning systems but offer the ability to scan surface structures without scanner setup time. Another advantage is that wheel probes maintain better contact with the inspection surface and virtually eliminate probe wobble. As mentioned above, one drawback of rolling wheel probes is that their size can create deployment challenges and make it difficult for inspection to be undertaken in tight spaces.
- The General Electric RotoArray was tested using the Phasor XS controller device prior to the RotoArray being commercially available. The newness of the hardware, coupled with the inexperience associated with its use, contributed to the performance that was lower than other PA-UT and linear array UT methods. Testing using a new commercially available RotoArray might produce improved results.
- Key advantages of LUS are:
 - the ability to scan quickly in a noncontact mode, all the way to the edge of a part.
 - the ability to launch a through-thickness longitudinal wave even when the laser beam impinges on the surface at an angle.
 - very large-area rapid scanning at high sensitivity.
 - the ability to scan complex geometries.

Disadvantages of LUS include:

- the lack of system portability.
- sensitivity to surface coatings (variations in coatings can affect the strength of the UT signal).
- maximum sensitivity requires tuning for each structure type.

- significant system expertise/training is needed to ensure alignment to produce uniform signal.
- safety concerns necessitating personnel exclusion zones.
- the potential for the laser to damage the part surface if not used with caution.
- cost, as some articulated robotic systems can run \$2 million or more.
- The potential advantages of acoustography include:
 - Accommodates full-field area inspection as opposed to point-by-point inspection
 - Provides near real-time, rapid screening of components
 - Possesses high lateral resolution in which UT is converted into visual images by minute molecules
 - Simplicity provided by visual image, which is intuitive and easy to interpret compared with electronic signals
 - Automated approach can accommodate use by lower-skilled operators
 - System is hand portable with no need for mechanical scanning equipment
 - System is easy to set up

The inability to inspect in tight spaces and limited large-area imaging are some of the disadvantages of acoustography.

- The advantages of the thermography inspection method include:
 - Thermography can be performed without physical contact with the surface
 - Single images can include relatively large areas (1–2 ft²), allowing for rapid inspections of large surface areas
 - 2D images of the inspected surface helps the operator visualize the location and extent of any defect

The primary disadvantages of thermography are:

- It is often necessary to apply a high-emissivity coating during inspections to obtain an acceptable image; steps have been taken to minimize the labor time associated with this task

- Damage to layers deep within a structure is more difficult to detect than damage in surface layers because the larger mass of material tends to dissipate the applied heat energy
- An advantage of shearography is that through judicious selection of the surface loading method, it can detect some types of flaws, such as wrinkles, localized weak bonds, and kissing disbonds, that may be transparent to most other inspection methods. The major limitation of shearography is that it cannot be applied to thick laminates because deeply embedded flaws in laminate are difficult to detect with shearography. Therefore, it is well-suited for thinner-skinned honeycomb structures.
- Advantages associated with microwave (MW) techniques include:
 - They can be conducted on a contact or no-contact basis
 - Only need to inspect from one side of a structure
 - No coupling is required
 - They do not require a high level of expertise from the operator

The main disadvantage of MW techniques is that they are limited to nonconductive materials. It has been successfully applied to fiberglass composite structures but cannot be used to inspect carbon graphite composites. Therefore, the MW inspection method did not produce acceptable performance levels during this experiment.

- Overall, this solid laminate experiment was able to quantify the flaw detection performance of a wide array of advanced NDI methods that are candidates for inspecting solid laminate composite structures. Sensitivity, deployment, data presentation, and human factor aspects have been highlighted here so that users can draw their own conclusions with respect to which NDI system provides the best approach for their unique needs.

7.4 SUMMARY OF KEY POINTS AND BEST NDI PRACTICES

This section provides a summary of the key points and best NDI practices that were identified in this study:

- Overall, the results from this study provide input and recommendations to the Federal Aviation Administration regarding guidance (e.g., advisory circular) that can enhance the composite inspection process. This study is driven by a goal to improve aircraft safety. Airlines and OEMs can use these results to guide NDI deployment and training, define what flaws/damage can be reliably found by inspectors, and reduce the human factor issues to produce improved NDI performance in the field.
- For an inspector deploying handheld PE-UT inspection methods, the overall POD_[90/95] level for solid laminate composite structures occurs when the flaw, or damage, is approximately 1.0" in diameter. Flaw detection in skins has a lower (i.e., better)

POD_[90/95] whereas flaw detection in substructure elements has a higher (i.e., worse) POD_[90/95].

- For an inspector deploying handheld PE-UT inspection methods, the inspection performance in all substructure regions was 19% worse than the overall POD_[90/95] and 68% worse than the POD_[90/95] value obtained in the constant thickness region (POD_[90/95] = 0.80" in constant thickness versus 1.34" in the substructure regions).
- It was determined that there are advanced NDI methods that can be used to improve on the flaw detection performance that was obtained from conventional PE-UT used by airline inspectors (aviation industry baseline). For an inspector using the higher-performing advanced inspection methods (i.e., all methods with POD levels better than conventional PE-UT), the overall POD_[90/95] level for solid laminate composite structures occurs when the flaw (i.e., damage) is approximately 0.8" in diameter, with the best performance of POD_[90/95] = 0.64" and the lowest performance of POD_[90/95] = 1.118" (compared with POD_[90/95] = 1.13" for hand-deployed PE-UT).
- Flaw detection percentages were improved through the use of the higher-performing advanced inspection methods (i.e., all methods with POD levels better than conventional PE-UT). The top performers—PA-UT, linear array UT, LUS, and acoustography—primarily had detection levels in the 90%–100% levels over all constant thickness and CG regions, with the exception of flaw detection percentages in the more challenging substructure regions. The comparison between the performance of these methods and the conventional PE-UT results is as follows:
 - Flaw detection percentage for overall experiment (all flaws) – advanced NDI methods = 92%; conventional PE-UT = 79%
 - Flaw detection percentage in constant thickness regions – advanced NDI methods = 97%; conventional PE-UT = 86%
 - Flaw detection percentage in the CG regions (i.e., substructure, taper, curved surfaces) – advanced NDI methods = 88%; conventional PE-UT = 75%
 - Flaw detection percentage in the most challenging substructure regions – advanced NDI methods = 74%; conventional PE-UT = 63%.
- When inspecting composites with substructure elements, additional signal penetration requirements coupled with a more extensive set of complex reflections results in a clear reduction in NDI performance in the region of the substructure elements. Additional NDI training and use of more representative NDI reference standards is recommended to improve flaw detection in the presence of substructure elements.
- False call rates for composite laminate inspections using PE-UT methods were extremely low, with one false call occurring per 8.5 ft² of inspection area, or one false call per 17 ft² of inspection area if only false calls greater than 0.25 ft² in area are considered. False call

rates for the high-performing advanced NDI methods were less than those observed with conventional PE-UT.

- Successful efforts to transition inspectors from “average” to “good” or “outstanding” performance levels will have a significant effect on $POD_{[90/95]}$ levels. Possible measures to achieve this include increased training, apprenticeships, exposure to representative inspections, enhanced procedures, inspector teaming, and awareness training on inspection obstacles.
- Signal harmonics and composite construction scenarios that result in a complex set of signal reflections were determined to be the major contributors in reducing NDI performance, whereas laminate thickness, tapered ply regions, and curved (or non-flat) surfaces were not significant factors on the NDI results.
- From a human factors perspective, the inspection of large areas can reduce NDI performance. The recommendation is that any wide-area inspections be divided into a number of smaller regions to allow for the necessary inspection focus. The use of two-man teams is another recommendation for NDI improvement, and this was supported by the analysis from this experiment.
- All of the advanced NDI methods evaluated in this experiment produced some form of a 2D image. The use of color-coded or gray-scale images with wide-area coverage that accommodates comparisons with adjacent areas is extremely helpful in both identifying flaws and reducing false calls. The advantage of scanning PE-UT (the phased and linear array UT methods studied in this experiment) is the addition of C-scan imaging to complement the A-scan signals used in conventional, single-element PE-UT.
- The advanced NDI methods (i.e., equipment plus deployment approach) that were evaluated in this experiment covered a wide range of TRLs; it is important to view the performance of each NDI method in light of the TRL level. Subsequent advances in the NDI devices may improve performance in the future.
- With respect to both POD and the generation of false calls, it was determined that the optimum inspection rate is approximately 2 ft² per hour. Furthermore, the SLE tests revealed that aircraft inspectors currently conduct their inspections with a coverage rate of approximately 2 ft² per hour.
- The use of inspection coverage aids, such as straight edges/tick marks, is highly recommended. It was determined that inspectors who used such aids performed significantly better than inspectors who did not.
- This experiment revealed that human factor issues still exist when using the more automated scanning inspection approaches of the advanced NDI methods. A second, improved POD curve was generated by results obtained when the inspector revisited the same data. This indicates that flaw detection, and potentially reductions in false calls, can

be improved further through the use of a second, follow-on inspector to aid in data interpretation.

- The Ramp Damage Check Experiment revealed the ability of untrained personnel to receive basic training and properly deploy the “Go”/“No Go” NDI equipment if they use sufficient attention to detail. The key is that the user must properly set up the equipment for the subsequent inspections to be effective.
- Limitations in the application of the “Go”/“No Go” devices were identified, and user guidance with respect to equipment deployment in various composite constructions was developed. Equipment users must understand the exact layout of the composite structure (i.e., surface, subsurface, and taper regions) to complete an accurate calibration and to understand the resulting indications from the equipment.
- The inspection devices that operate in a “Go”/“No Go” mode, such as the ramp damage check and the Bondtracer devices, cannot be easily deployed in taper regions or other regions with rapidly changing configurations.
- The use of an audible alarm on the “Go”/“No Go” devices and/or the addition of an alarm light to the handheld probes are highly recommended. This would prevent the operator from having to look at the device to read the display at all times. It would also eliminate tedious eye motion and the concern over proper equipment orientation relative to the user.
- In general, the lack of routine exposure to composite inspections makes it difficult for inspectors to maintain the necessary level of expertise. It is recommended that OEMs, or some other aviation agency, design a set of composite specimens—much like the NDI feedback specimens used in this experiment—for insertion into aircraft NDI shops. Added exposure to available flaw specimens is viewed as a way to keep the inspectors ready, well-trained, and current on composite inspections.
- Overall, this solid laminate experiment was able to quantify the flaw detection performance of a wide array of advanced NDI methods that are candidates for inspection of solid laminate composite structures. Sensitivity, deployment, data presentation, and human factor aspects have been highlighted here so that users can draw their own conclusions with respect to which NDI system provides the best approach for their unique needs.

8. REFERENCES

1. Roach, D.P., Dorrell, L.R., Kollgaard, J., Dreher, T., “Improving Aircraft Composite Inspections Using Optimized Reference Standards,” *SAE Airframe Maintenance and Repair Conference*, SAE Technical Paper 98AEMR-34, November 1998.

2. Roach, D., Rackow, K., "Composite Honeycomb NDI Reference Standards," SAE Aerospace Recommended Practice ARP5606, in conjunction with CACRC Inspection Task Group, March 2001.
3. Roach, D., Rackow, K., "Solid Composite Laminate NDI Reference Standards," SAE Aerospace Recommended Practice ARP5606, in conjunction with CACRC Inspection Task Group, March 2001.
4. Roach, D., Rice, T., Rackow, K., "A Quantitative Assessment of Conventional NDI Techniques for Detecting Flaws in Composite Laminate Aircraft Structures," FAA Report DOT/FAA/TC-15/6
5. Baker, A.A., "Fatigue Studies Related to Certification of Composite Crack Patching for Primary Metallic Aircraft Structure," *FAA-NASA Symposium on Continued Airworthiness of Aircraft Structures*, FAA Report DOT/FAA/AR-97/2, I, July 1997.
6. Fredell, R.S., "Damage Tolerant Repair Techniques for Pressurized Aircraft Fuselages," "PhD Dissertation, Delft University, 1994.
7. Rice, R., Francini, R., Rahman, S., et. al, "Effects of Repair on Structural Integrity," FAA Report DOT/FAA/CT-93/79, December 1993.
8. Jones, R., Chiu, C., Paul, J., "Designing for Damage Tolerant Bonded Joints," *Composite Structures*, Vol. 25, 1993.
9. Chiu, W.K., Rees, D., Chalkley, P., Jones, R., "Designing for Damage Tolerant Repairs," ARL Aircraft Structures Report 450, August 1992.
10. Roach, D.P., Moore, D., and Walkington, P., "Nondestructive Inspection of Bonded Composite Doublers for Aircraft," *Proceedings of SPIE Conference on Nondestructive Evaluation of Aging Aircraft*, December 1996.
11. Roach, D., Beattie, A., Dahlke, L., et. al, "Emerging Nondestructive Inspection Methods for Aging Aircraft," Department of Energy SAND Report 92-2732, March 1994; FAA Report DOT/FAA/CT-94/11, October 1994.
12. Palmer, D.D., Wood, N.O., "Development of MAUS Enhancements for Large Area Wing Inspections," *Air Force Structural Integrity Conference*, December 1999.
13. Calder, C.A., Wilcox, W.W., "Noncontact Material Testing Using Laser Energy Deposition and Interferometry," *Materials Evaluation*, Vol. 38, No. 1, 1980, pp. 86-91.
14. Fiedler, C.J., Ducharme, T., Kwan, J., "The Laser-Ultrasonic Inspection System (LUIS) at The Sacramento Air Logistics Center," *Review of Progress in QNDE*, Thompson, D.O. and Chimenti D.E., eds., Plenum Press, New York, Volume 16, 1997, pp. 515-522.

15. Dubois, M., Drake, T., Osterkamp, M., “Low-Cost Ultrasonic Inspection of Composites for Aerospace Applications with LaserUT™ Technologies,” *Journal of JSNDI*, Volume 57, Number 1, pp. 11-18, (2008).
16. Mayer, T. Scherling, D., Sun, J., “Shearography Testing on Aerospace CFRP Components,” *Journal of Inspection Physics*, June 2002.
17. Thomas, R., Favro, L., Han, X., Zhong, O., “Thermal Methods Used in Composite Inspection,” *Comprehensive Composite Materials*, Volume 5, Pergamon/Elsevier Science, Oxford, 2000.
18. Favro, L., Han, X., Thomas, R., “Quantitative Thermal-wave Measurement of Defects in Composite Aircraft Structures,” *44th International SAMPE Symposium and Exhibition*, 1999.
19. Cramer, K.E., Winfree, W.P., Reid, D., Johnson, J., “Thermographic Detection and Quantitative Characterization of Corrosion by Application of Thermal Line Source,” *SPIE Conference on Nondestructive Evaluation of Utilities and Pipelines III*, 1999, pp. 277–768.
20. Cramer, K.E., Winfree, W.P., “Method and Apparatus for the Portable Identification of Material Thickness and Defects Using Spatially Controlled Heat Application,” U.S. Patent 6000844, 1999.
21. Tarin, M., Rotolante, R., “NDT in Composite Materials with Flash, Transient, and Lock-in Thermography,” *FLIR Technical Series, Application Note for Research & Science*, 2011.
22. Roach, D., Rackow, K., “Development and Utilization of Composite Honeycomb and Solid Reference Standards for Aircraft Applications,” Department of Energy SAND Report SAND2003-2112, June 2004.
23. Roach, D., Rice, T., “A Quantitative Assessment of Conventional NDI Techniques for Detecting Flaws in Composite Laminate Aircraft Structures,” FAA Report DOT/FAA/AR-26/14, July 2014.
24. Roach, D., “An Inspector Calls – The Search for Hidden Flaws in Composite Honeycomb Structures,” *Journal of Aerospace Testing International*, February 2004.

APPENDIX A—COMPOSITE LAMINATE FLAW DETECTION EXPERIMENT:
EXPERIMENTER INFORMATION PACKET

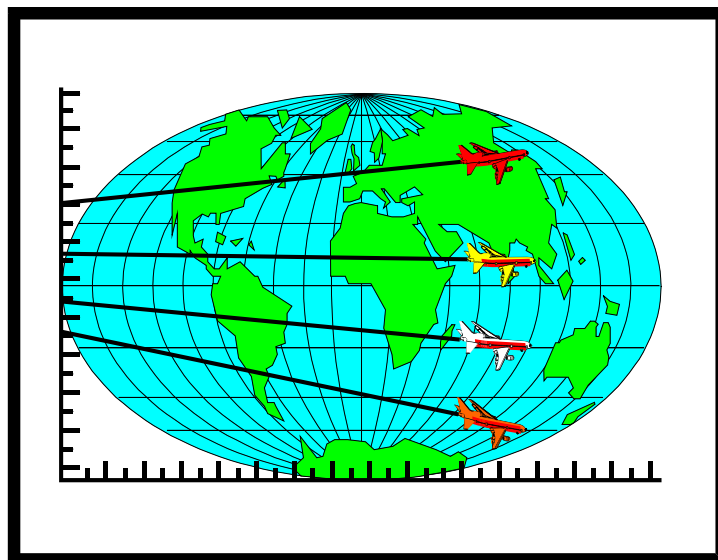
The following was sent to host coordinators prior to experiment deployment:



**Sandia
National
Laboratories**

Detection of Hidden Flaws in Aircraft Solid Laminate Composite Structure

EXPERIMENTER INFORMATION PACKET



**Experiment Coordinators: D. Roach (505)844-6078
T. Rice (505)844-7738**

**FAA Airworthiness Assurance Center
Infrastructure Assurance and NDI Department
Sandia National Labs**

Experimenter Briefing and Information

Introduction

The Sandia National Labs' FAA Airworthiness Assurance NDI Validation Center (AANC), under contract to the Federal Aviation Administration's William J. Hughes Technical Center, is conducting an experiment to assess flaw detection in composite laminate aircraft structures. The Composite Laminate Flaw Detection Experiment, including a set of 15 composite laminate test specimens containing engineered flaws, will travel to airlines, third party maintenance depots, aircraft manufacturers, and NDI developer labs to acquire flaw detection data. The experiment will require approximately 2 to 4 days of each inspector's time. In general, inspectors will be asked to locate and size hidden flaws in the test specimens. After a sufficient number of inspectors have completed the experiment (using standard pulse-echo UT), industry-wide performance curves will be established that determine: 1) how well current inspection techniques (PE-UT) are able to reliably find flaws in composite laminate structure, and 2) the degree of improvements possible through the integration of more advanced NDI techniques and procedures. The inspections will emphasize flaw detection methods applicable to solid laminate structures ranging from 12 plies to 64 plies thick. The results will be published as industry-wide performance measures and all links to specific aircraft maintenance depots will be permanently removed.

Inspectors will gain experience and feedback on the implementation of your inspections on representative aircraft structure. No individual inspector's names will be linked to any experiment results. Similarly, no organization's name will be linked to any group of experiment results. However, results will be made available to potential users and they will be able to compare the results of competing inspection techniques and systems.

The inspectors will receive feedback on how they performed in the experiment. This will come in the form of tabulated results indicating the number of flaws correctly detected, the number of flaws missed, the number of false calls made, and the ability of the inspector to accurately size the flaws they detected. We can also provide feedback on the type of flaws that were detected and missed so that the inspector will learn what types of flaws they have trouble detecting. It is important to note that the feedback to the inspectors is kept confidential. In the final aggregate results, we ensure that the participants are always kept anonymous so that there is no way to correlate any results to a specific person or airline.

Background

The inspection category for evaluation in this experiment is the inspection for representative disbonds, interply delaminations, and "simulated" impact flaws in solid laminate composite structures. The test articles are modeled after the general range of construction scenarios found on commercial aircraft. The test program is intended to evaluate the technical capability of the inspection procedures, process and the equipment (i.e. NDI technique). Evaluation of inspector specific or environment specific factors associated with performing this inspection are not the primary objective of this experiment. However, notice will be taken by the experiment monitor if such factors seem to influence results or if unplanned events occur which could impact the results of the inspection. Specific notice will be taken if issues such as deployment or maneuverability adversely affect the outcome of the inspection.

For this experiment a set of test specimens containing engineered flaws have been manufactured. The inspections will be conducted on a series of panels and Bullnose specimens of different sizes. These panels will be placed on a foam frame to support the entire perimeter of the panel and the Bullnose specimens will be placed on a flat surface to produce uniform boundary conditions across all experimenters. You will be asked to inspect each test specimen and provide any information you can about the presence of applicable flaws. If you determine that flaws are present, you should then provide size and shape information about each detected flaw. The results should be marked directly on the test specimen using only markers provided by the experiment monitors. *Inspectors should use any positive indications to find flaws as small as 1/4" in diameter.* Experimenters should work at a pace that is comfortable for them. Although monitors will note start and stop times for your inspection, time to inspect is a secondary variable of the experiment. Inspectors should take whatever time is necessary to ensure that any and all flaws in the test specimens are found.

1. TEST SPECIMENS AND THE FLAW DETECTION EXPERIMENT

Engineered Specimens - Engineered specimens have been manufactured that mimic the inspection applications of interest and include realistic flaws found in those structures. Specific information on the construction of the test panels follows. Experimenters will be told the configuration of each panel they inspect and be provided with drawings for reference.

- **Laminate Type** - carbon graphite
- **Laminate Thickness** - Panels have 12 (~.078"), 20 (~.130"), 24 (~.156") and 32 (~.229") plies.
- **Paint** - All panels are painted as per current aircraft specifications.
- **Substructure Thicknesses** - .075", .125", .192", .225", and .250"
- **Tapered Area Ranges** - 12-20 (.50" step), 20-32 (.50" step), 12-20 (.25" step)
- **Specimen Deployment** - During testing, panels will be placed on a flat surface to support the entire footprint.
- **Flaw Detection** - Inspectors should use any positive indications to find flaws as small as 1/4" in diameter.
- **Inspection Device** - For the most part, the inspector will utilize their own NDI equipment. We will provide acceptable inspection devices (UT probes) to be used for this testing (meet Boeing/Airbus specs) and the inspectors will make the final choice based on availability and familiarity with that equipment. Some testing with non-standard devices may also be conducted in order to form a basis of comparison with results obtained using the recommended pulse echo UT devices.
- There are two separate experiments. There is a Thin Laminate Skin experiment with skins ranging from 12-20 plies (0.078" to 0.130" thick) and total thickness extending to 62 plies (0.406") when substructure is considered. There is also Thick Laminate Skin experiment with 32 ply skins (0.21" thick) and total thickness extending to 58 plies (0.377") when substructure is considered.

Equipment Calibration and Familiarization - Each blind inspection process will be preceded by inspections on appropriate training/feedback specimens supplied by the experiment monitors.

The inspector will be given information on the manufactured flaws present in the training/feedback specimens and will be allowed to use them for check-out of their inspection equipment. The training/feedback specimens will have similar construction as the blind test specimens and include similar flaws. Thus, they also can be used to allow inspectors to become familiar with an inspection device and learn about a specific equipment's response for various solid laminate composite structures and flaws within those structures. Figures A-1 thru A-5 show the flaw profiles of all the training/feedback specimens.

Figure A-6 is a drawing of various cross-sectional views of the 12 ply training/feedback specimen showing how the pillow inserts & Graphoil inserts are used to simulate interply delaminations, flat bottom holes are used to simulate the presence of an air gap, and pull tabs are used to simulate the presence of an air gap between the laminate and the bonded substructure. The training/feedback specimens will be used as a training tool prior to starting the experiment and will also be used by inspectors during the course of the experiment to set up their equipment.

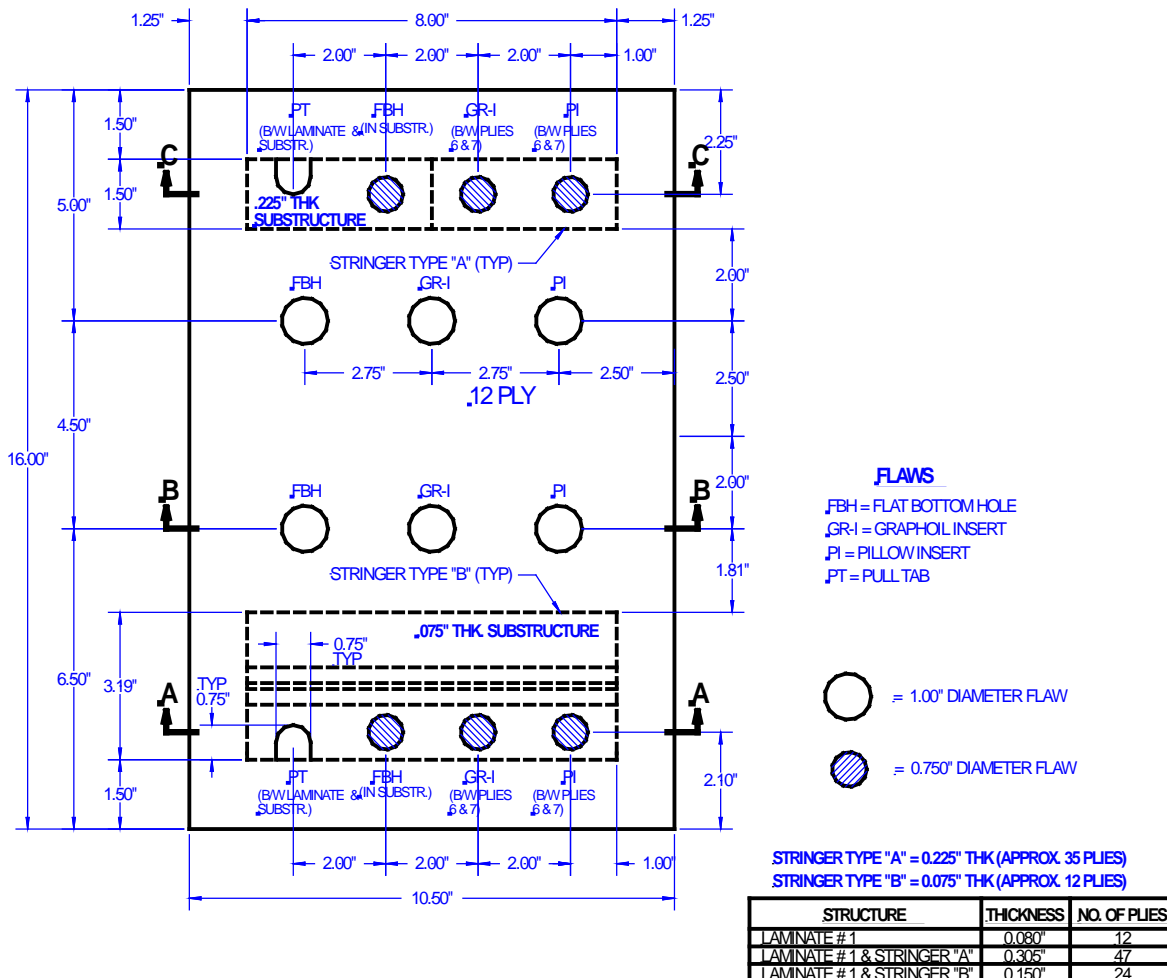


Figure A-1. Final design of 12 ply training/feedback specimen

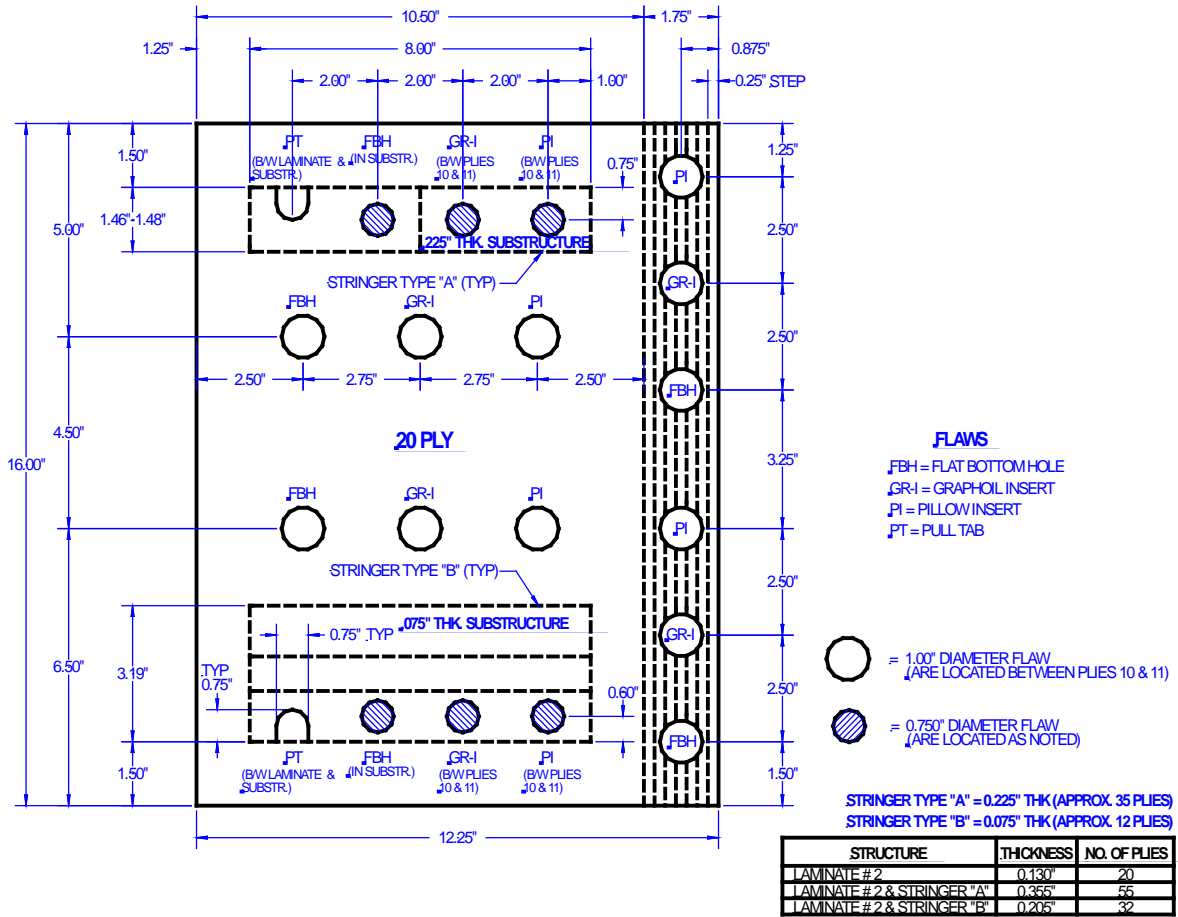


Figure A-2. Final design of first 20 ply training/feedback specimen with taper

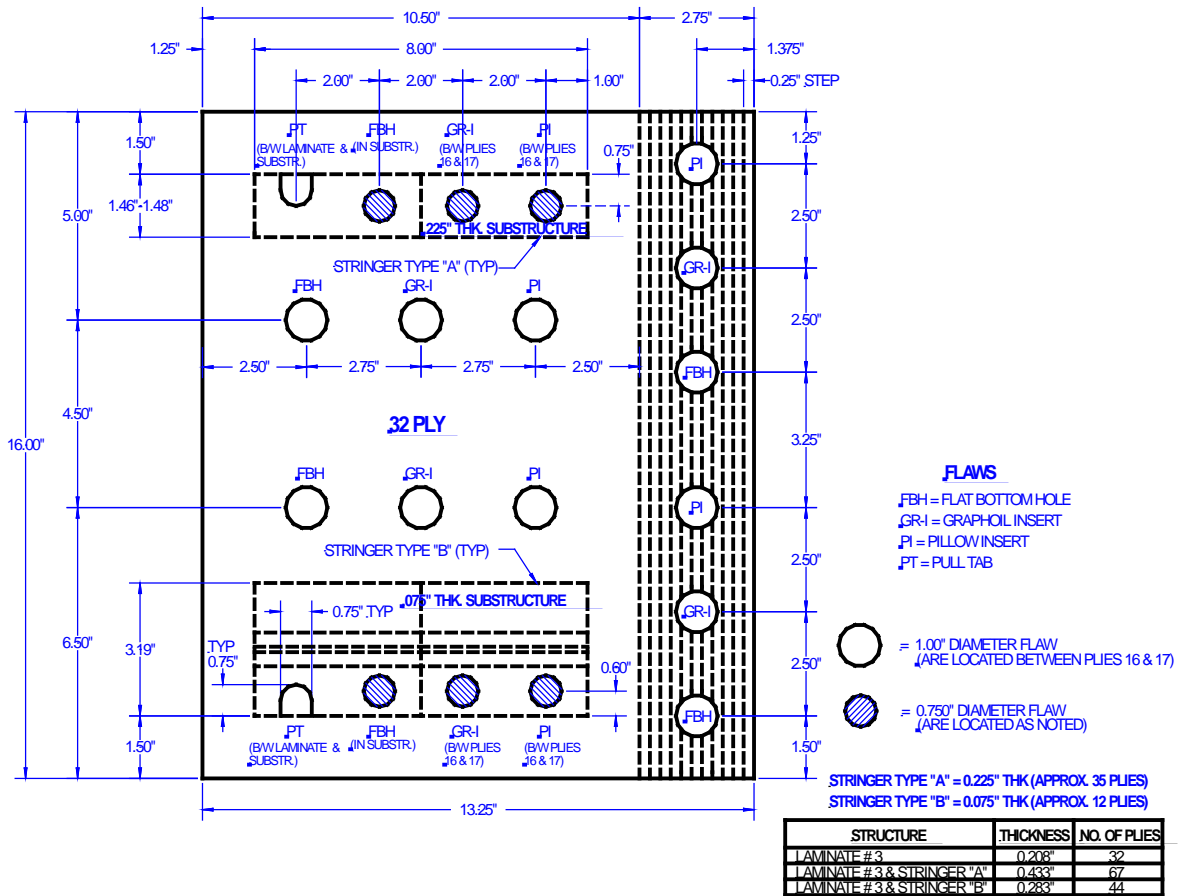


Figure A-3. Final design of 32 ply training/feedback specimen with taper

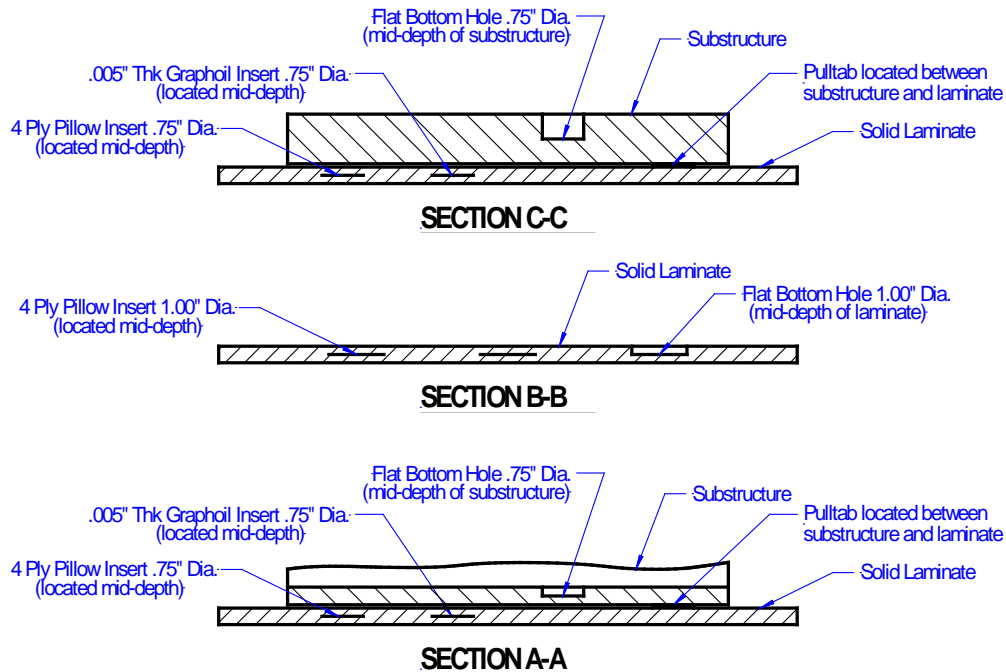


Figure A-6. Cross section views of 12 ply training/feedback specimen showing the locations of the different flaws

2. PERFORMANCE METRICS

Multiple performance attributes will be discussed in the final report for this experiment. These are given in the table below and are briefly discussed following the table. Quantitative metrics (standards applied to events that can be numerically counted or quantified) will be applied when appropriate but many of the performance attributes will be discussed using qualitative metrics (standards that rely on human judgments of performance). Where practical, qualitative assessments will be based on predetermined criteria to ensure grading consistency. The intent is to provide useful summaries of the major factors that would influence the user communities' perception of the viability of the technique or specific equipment. Because different users may have different priorities, we will not rank or prioritize the various measures.

Quantitative Metrics - objective standards applied to events that can be numerically counted or quantified.

Qualitative Metrics - subjective standards that rely on human judgments of performance; where practical, qualitative assessments will be based on predetermined criteria to ensure grading consistency.

STRUCTURED EXPERIMENT EVALUATION CRITERIA	
1.	<u>Accuracy and Sensitivity</u>
2.	Data Analysis Capabilities
3.	Versatility
4.	Portability
5.	Complexity
6.	Human Factors
7.	Inspection Time

1. Accuracy and Sensitivity

Accuracy is the ability to **detect** flaws reliably and correctly in composite structures and repairs without overcalling (false calls). Sensitivity is the extent to which the inspection system responds to flaws as a function of size, type, and location (e.g., proximity to repair edges, underlying or adjacent structural elements) in the structure.

Test results will be graded to evaluate the accuracy of quantitative measurements and to assess qualitative measurement parameters. The test results will identify hits (calls with any amount of overlap between the call and the solution), misses (no call for an area of a known flaw), false calls (call with no overlap of a flaw), degree of overlap between experimenter calls and actual flaw areas, and accuracy of quantitative call.

2. Data Analysis Capabilities

Data analysis capabilities define how well the inspection system and process can correctly characterize flaws. Analysis capabilities include, but are not limited to, the ability to identify the flaw size (e.g., lateral extent), flaw location, and flaw type (i.e., distinguish between disbonds and delaminations). Quantitative aspects of the data analysis capabilities are provided by evaluating the accuracy and sensitivity as discussed above. Also, the repeatability, reliability, degree of automation, data storage and retrieval capabilities and constraints, and subjective interpretation requirements are considered when assessing the data analysis capabilities.

3. Versatility

Versatility is the capability of the inspection system to be easily adapted for application to varying inspection tasks and conditions (e.g., varying surface conditions, specimen orientations and accessibility). Versatility is primarily assessed using qualitative metrics, such as calibration and equipment reconfiguration requirements to address differing inspection applications. Furthermore, variations in system performance due to changes in the surface condition (e.g., paint variations, front and/or back surface contaminants, surface scratches or dents), and specimen configuration (e.g., accessibility and orientation).

4. Portability

Portability is the capability of the inspection system to be easily moved and used in standard aircraft inspection applications. Portability is assessed using qualitative metrics such as the inspection system's size, weight, apparent ease of use in each evaluated inspection application, and inspection restrictions (i.e., limitations created by power requirements, tethering or remote control issues, safety, or other factors that may restrict equipment usage). Equipment storage and shipment requirements will also be considered when evaluating the system portability.

5. Complexity

Complexity is the intricacy of the tasks required to perform the inspections and data analysis. The inspection system should be suitable for use by qualified airline NDI personnel. Also, the inspection process should be efficient, repeatable, and reliable. Complexity is assessed using qualitative metrics, such as: the number of people required to perform the inspection; the number and difficulty of the range of tasks required for the inspection (including setup, calibration, system reconfiguration for changing inspection requirements, data acquisition, and data analysis); the number of simultaneous tasks required; tasks requiring unusual manipulative skills (as compared to traditional inspection needs) or which place the inspector in awkward positions that may be uncomfortable; and tasks that require advanced interpretative skills (including calibration, data acquisition, and data analysis - both qualitative and quantitative).

6. Human Factors

For purposes of this evaluation, human factors include procedures or equipment (hardware or software) related inspection elements that may act as a source of human error. Environmental factors such as temperature, noise, and lighting level will not be considered. The Human Factors criterion is assessed subjectively considering: man-machine interface issues (e.g., data presentation clarity and ease of interpretation, presentation speed, layout and usability of knobs and dials, opportunities for operational or interpretative errors, glare effects, safety to the inspector and others in the surrounding area, etc.); written procedure usability (e.g., clarity, correctness, correlation to tasks actually performed); inspector education, training (initial and recurring) and experience requirements; objective versus subjective calibration, inspection, and analysis processes.

7. Inspection Time

Inspection time is assessed quantitatively. Setup, clean up, inspection, and analysis time will be measured. This includes re-calibration and equipment reconfiguration time to move to differing inspection applications.

3. Experimenter Flaw Calls and Data Logging

The purpose of this experiment is to determine the capability of various inspection methods to detect and measure flaws in solid laminate composite aircraft structure. The Composite Laminate Flaw Detection Experiment will travel to airlines, third party maintenance depots, aircraft manufacturers, and NDI developer labs to acquire flaw detection data.

For this experiment a set of test specimens containing engineered flaws has been manufactured. The inspections will be conducted on a series of panels and Bullnose specimens of various sizes. These panels will be placed on a foam frame to support the entire perimeter and the Bullnose specimens will be placed on a flat surface to produce uniform boundary conditions across all experimenters. You will be asked to inspect each test specimen and provide any information you can about the presence of applicable flaws. If you determine that flaws are present, you should then provide size and shape information about each detected flaw. If possible, the results can be marked directly on the test specimen using only the markers provided by the experiment monitors.

If instructed by the experiment monitors, inspection results can also be marked on a full-scale sheet of tracing paper. Registration points/lines should be used on the tracing paper to assure location accuracy of the flaws. Also, test specimen numbers should be logged onto each log sheet. Note: if providing C-scan or other signal data as final results, you should identify flawed area and size (x and y dimension if at all possible on the scan image). Figure A-7 shows a sample set of flaw marks on one of the solid laminate test specimens. This study would like to assess performance for flaws as small as 1/4" in diameter. Inspectors should use any positive indications to find flaws as small as 1/4" in diameter. It is not necessary to track small anomalies, such as porosity, that are less than 1/4" in length.

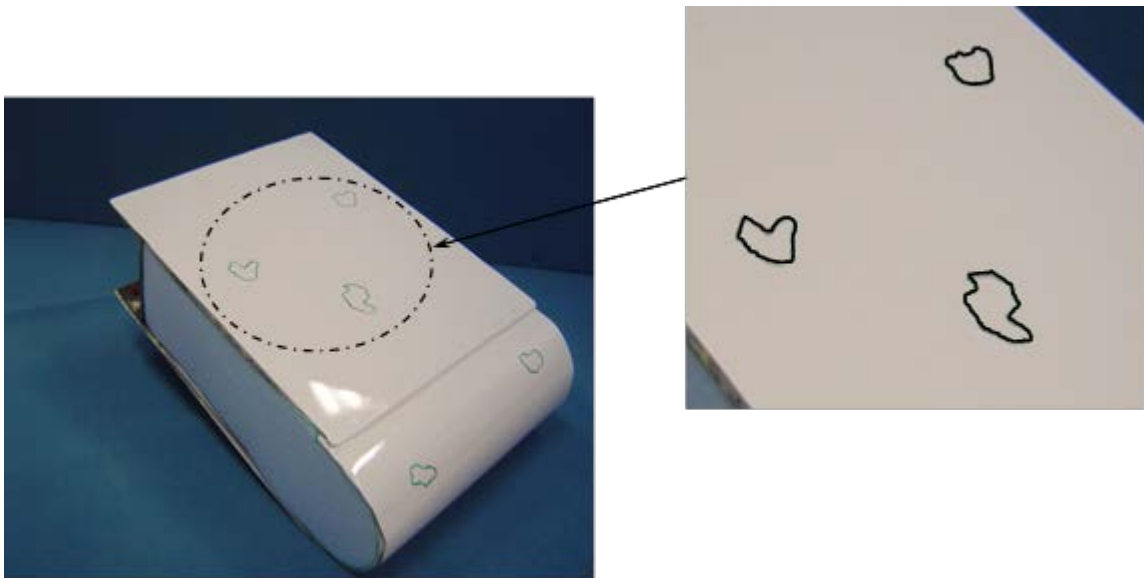


Figure A-7. Sample set of inspector's flaw marks on a solid laminate test specimen

Typical Signals & Flaw Calls

Figures A-8 through A-11 show a series of representative ultrasonic signals that may be produced during a pulse-echo UT inspection of a solid laminate structure. Figure A-8 shows signals that might be expected from an inspection on a co-cured laminate (skin and substructure cured at the same time) as the transducer engages flaws at various depths in the structure. Figure A-9 shows a similar set of signals stemming from an inspection on a secondarily-bonded laminate (skin and substructure cured separately and bonded in another process). Note that the secondary bond creates a bond line signal that will appear in time before the back wall signal.

Figures A-10 and A-11 show two different signals corresponding to flaws in the laminate. In Figure A-10, the back wall signal disappears, or is reduced drastically, while a new intermediate signal between the front and back wall appears. In Figure A-11, the back wall signal is reduced significantly (approximately 30%) while a new, substantial, intermediate signal appears between the front and back wall. Normally, one would use a drop in the back wall signal below 20% Full Screen Height (FSH) as an indication of a flaw. However, due to the nature of this study and the desire to detect flaws as small as 0.25" there may be instances where the back wall signal drops significantly (perhaps 50% FSH) but not below the 20% FSH threshold. This may be due to the fact that the UT transducer has a larger footprint than the 0.25" flaw. Thus, the transducer is actually covering an area that is both flawed (center region with disruption of UT signal) and unflawed (outer region with no disruption in UT signal). However, as shown in Figure A-11, there will also be a large intermediate signal (in the 80% FSH range) that appears between the front and back wall. When this is accompanied by a non-uniform or unusual reduction in the back wall signal, it could indicate the presence of a small delamination. A schematic of the signal travel through the flawed and unflawed regions beneath the transducer is shown in Figure A-12. UT waves at points (A) and (C) are unaffected by the presence of the small delamination flaw but the UT waves at point (C) interact with the delamination. These waves around point (C) cause the back wall signal to be reduced and also create an intermediate signal between the front and back wall. Inspectors should utilize the small flaws in the feedback panels in order to understand the type of signals associated with these flaws. This will be helpful in interpreting the flaw signals in this experiment.

Specimen Deployment

During the inspections, the various panels will be placed on a foam frame to support the entire perimeter and the Bullnose specimens will be placed on a flat surface to produce uniform boundary conditions across all experimenters. The test specimens should not be turned over at any time. The foam frame, supplied, should be assembled as per Figure A-13 to support the panels properly. The order of inspections will be set forth by the experiment monitors. The inspection order may be varied, but once started on a specific panel the inspector will be expected to complete that panel before moving onto another. The test specimens and the training/feedback specimens are painted.

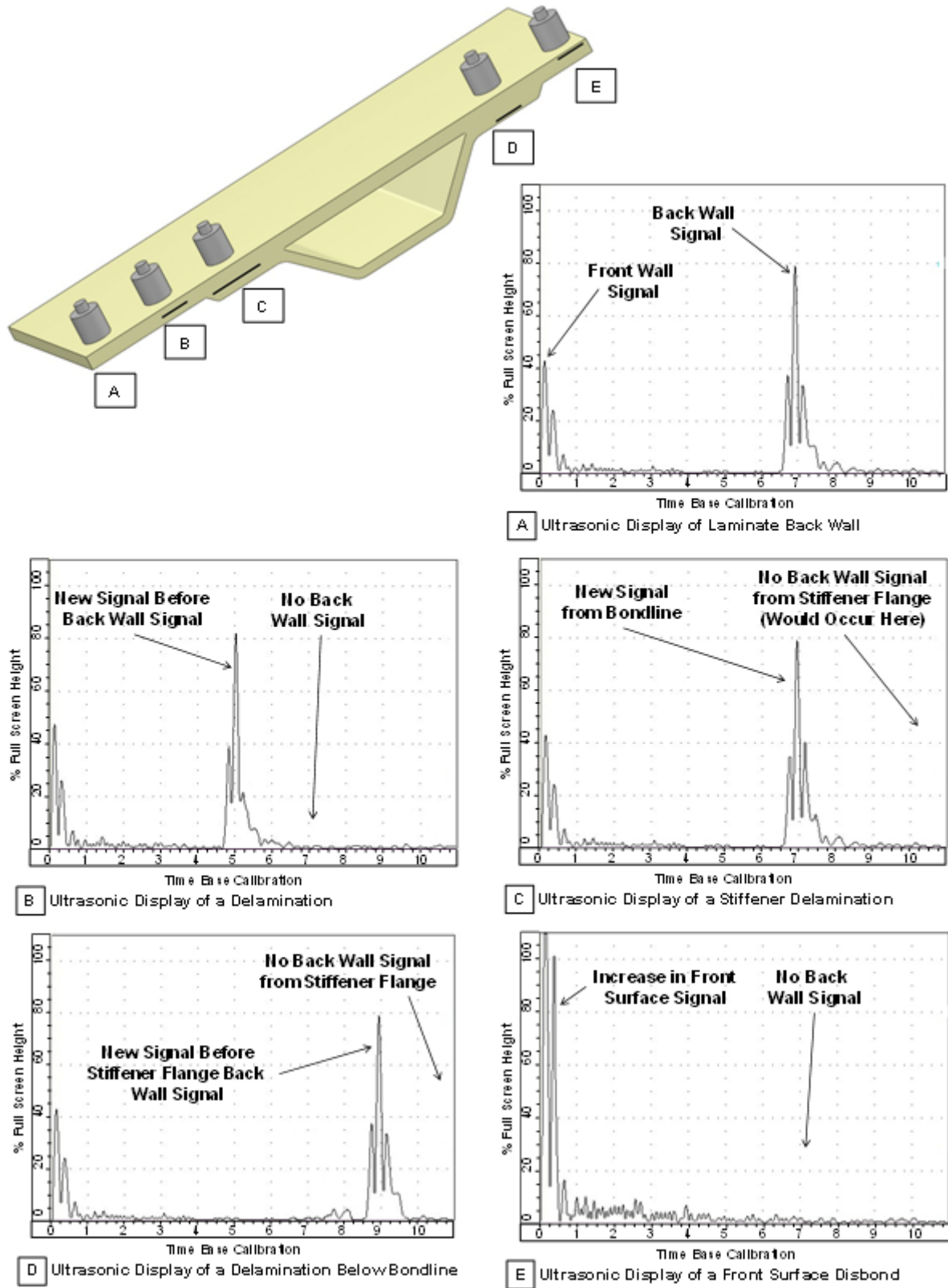


Figure A-8. Delamination indications at different structure thicknesses for co-cured substructures

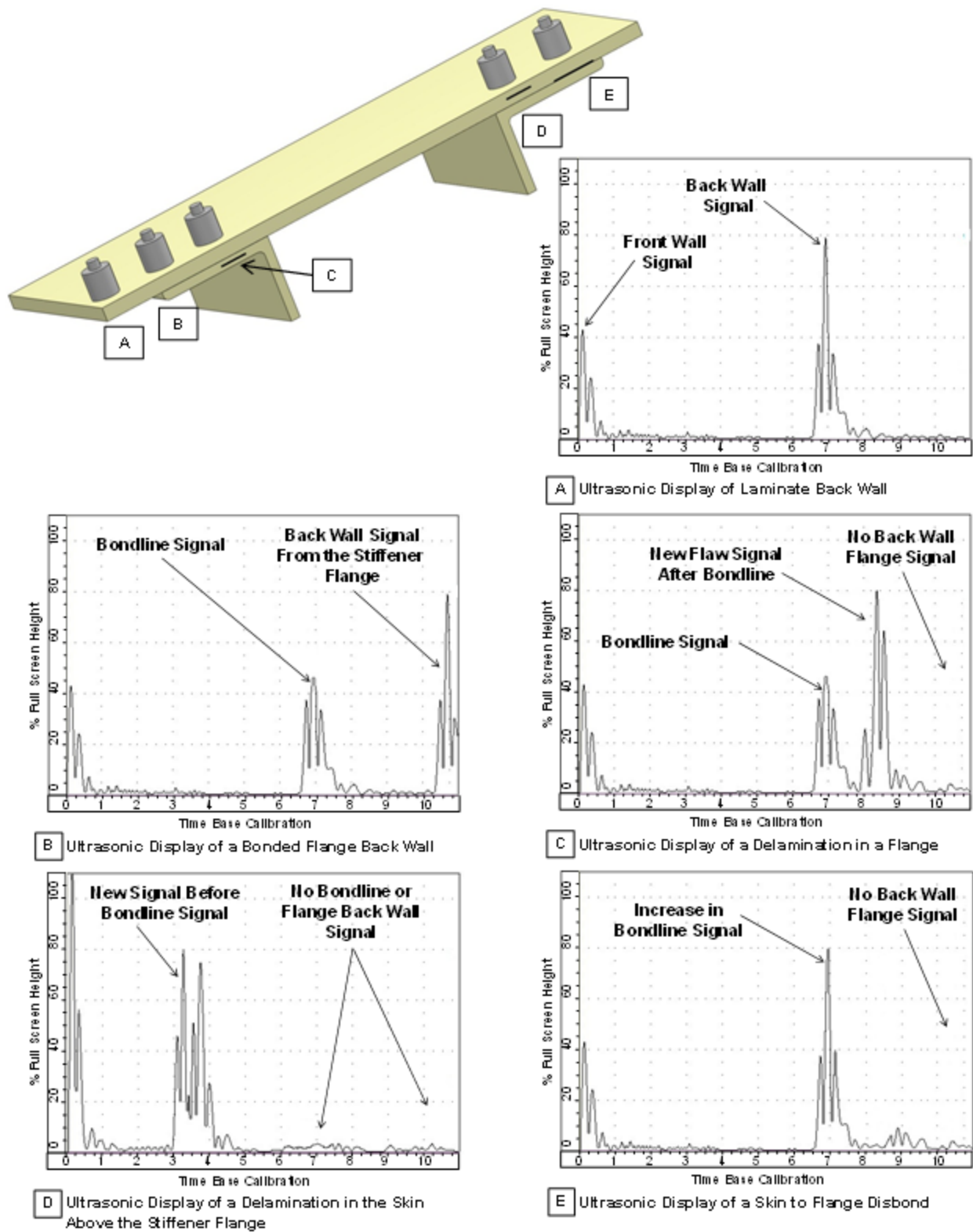


Figure A-9. Delamination indications at different structure thicknesses for secondarily bonded substructures

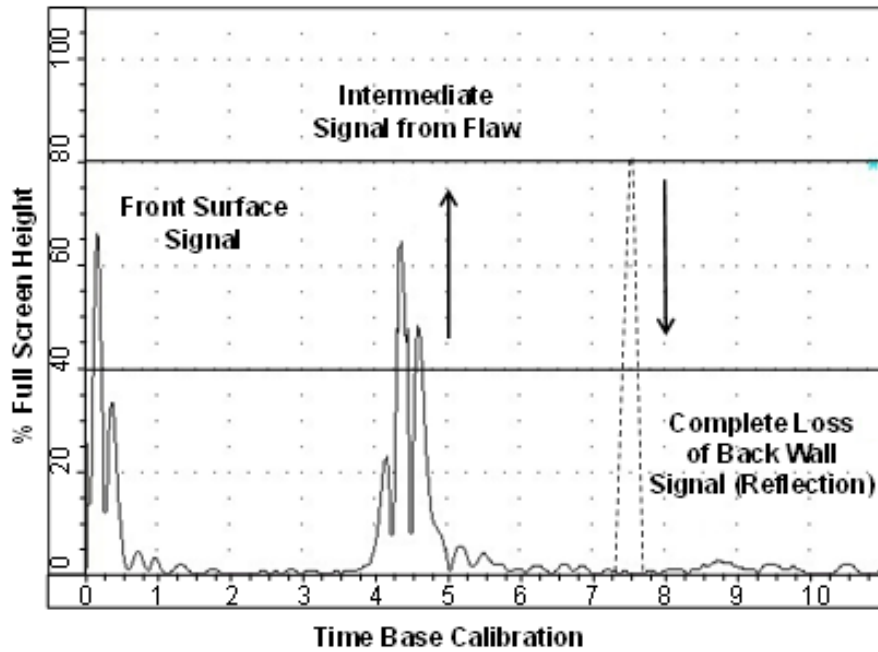


Figure A-10. Intermediate peak and reduction of back wall signal indicating a flaw

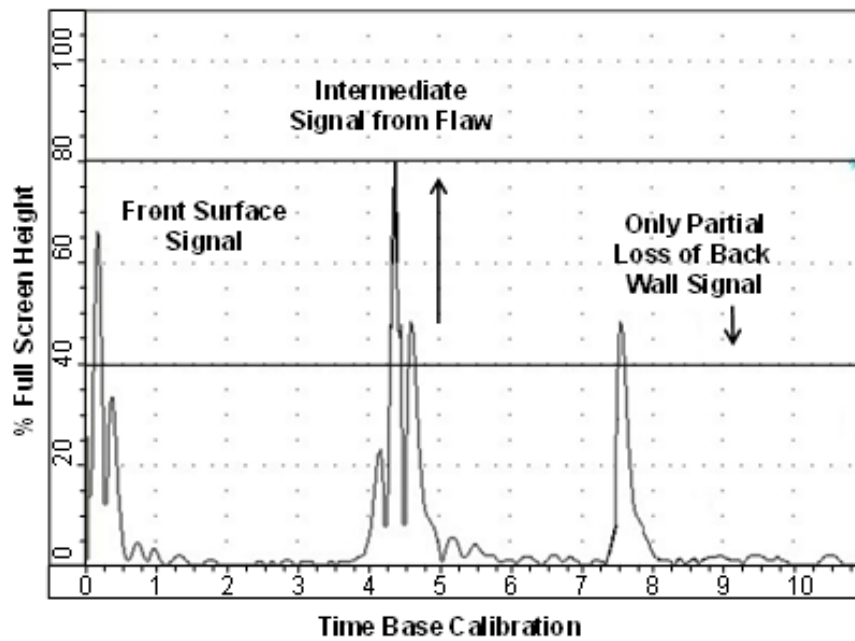


Figure A-11. Intermediate peak with only a partial reduction in back wall signal that may indicate a small flaw

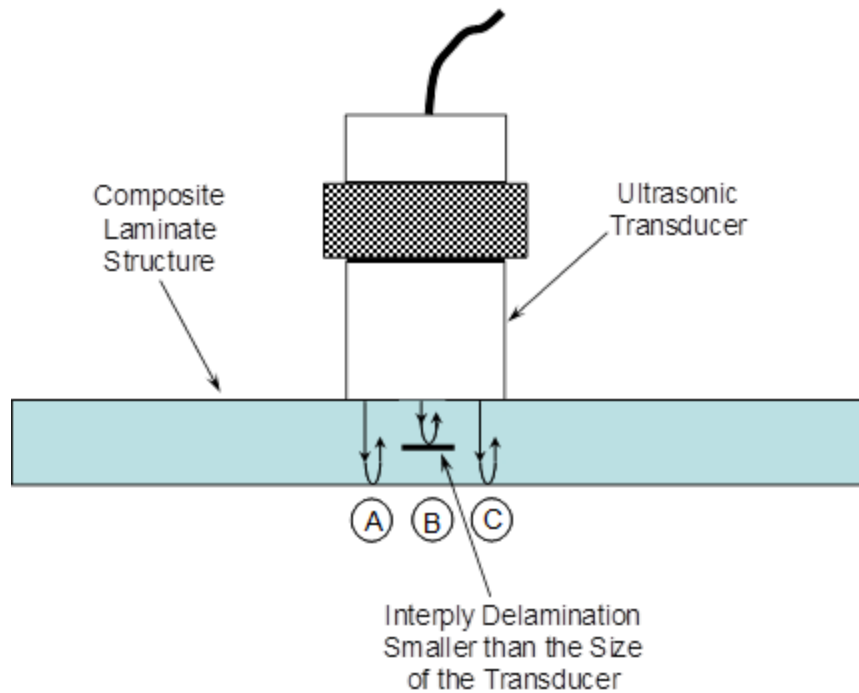


Figure A-12. Schematic showing reflection of pulse-echo UT signals when the flaw is smaller than the diameter of the UT probe

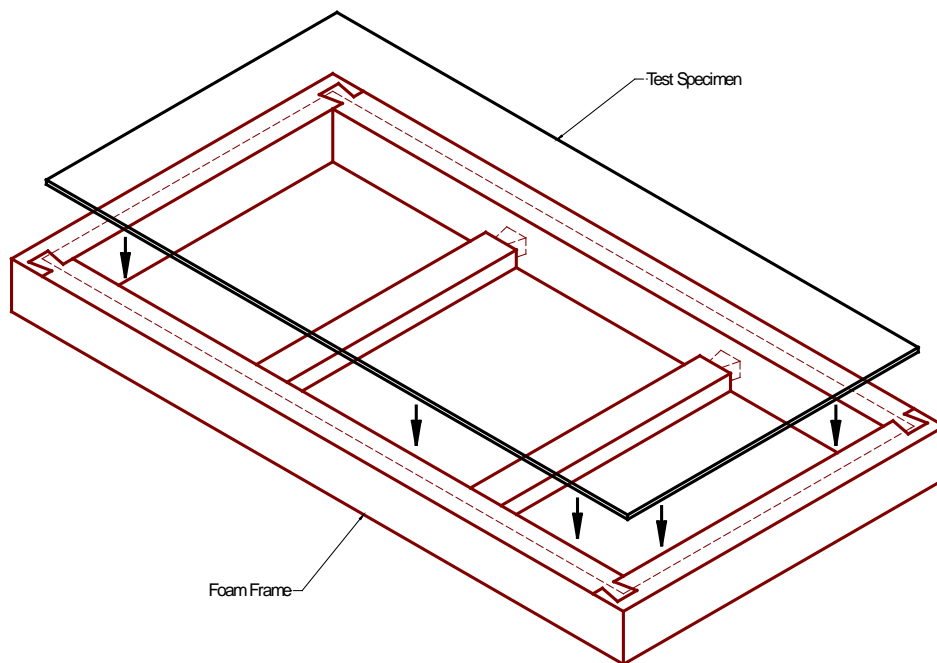


Figure A-13. During inspections, place each panel such that it is supported around its perimeter by a foam frame. This will provide uniform boundary conditions.

Additional guidance for inspectors performing this experiment are as follows:

- Experimenters should work at a pace that is comfortable for them. Although monitors will note start and stop times for your inspection, time to inspect is a secondary variable of the experiment.
- Applicable procedures from OEM manuals will be provided as a reference tool. Inspectors should use their own judgment as to how to perform the inspection (i.e. a strict procedure will not be enforced).
- Inspection coverage should be 100% of the panel with the exception of a small .50" band around the perimeter of the panels where edge effects may create problems.
- The Solid Laminate Training/Feedback Specimens, or equivalent, should be used to set up the equipment. Minor equipment adjustments stemming from in-situ calibration on the parts being inspected are allowed.
- Inspectors should draw the entire size/shape of the flaw (i.e. delineate the edges).
- Training/feedback specimens should be used as an aid to determine where to make flaw call edges. This is based on the diameter of the probe and how much of the probe needs to be over the flaw in order to react/detect.
- Inspectors do not need to determine the type of flaw just the location, size, and shape of the suspected anomaly.
- Inspectors should ignore any visual clues (surface anomalies in the paint or small surface marks) and to avoid using these as flaw detection aids. Such anomalies may be intentionally planted to add complexity to the inspection. Inspectors should only make a call on those flaws that are highlighted by their inspection device.

Test results will be graded to evaluate the accuracy of quantitative measurements and to assess qualitative measurement parameters. The test results will identify hits (calls with any amount of overlap between the call and the solution), misses (no call for an area of a known flaw), false calls (call with no overlap of a flaw), and the degree of overlap between experimenter calls and actual flaw areas. Figure A-14 is a grading parameter drawing that shows how the hits-misses-false calls results will be graded. Percentage of flaw covered will be another variable of primary interest. Error in lateral extent of flaw and maximum linear extent of overcall are variables of secondary concern and are not currently being considered as part of the grading plan.

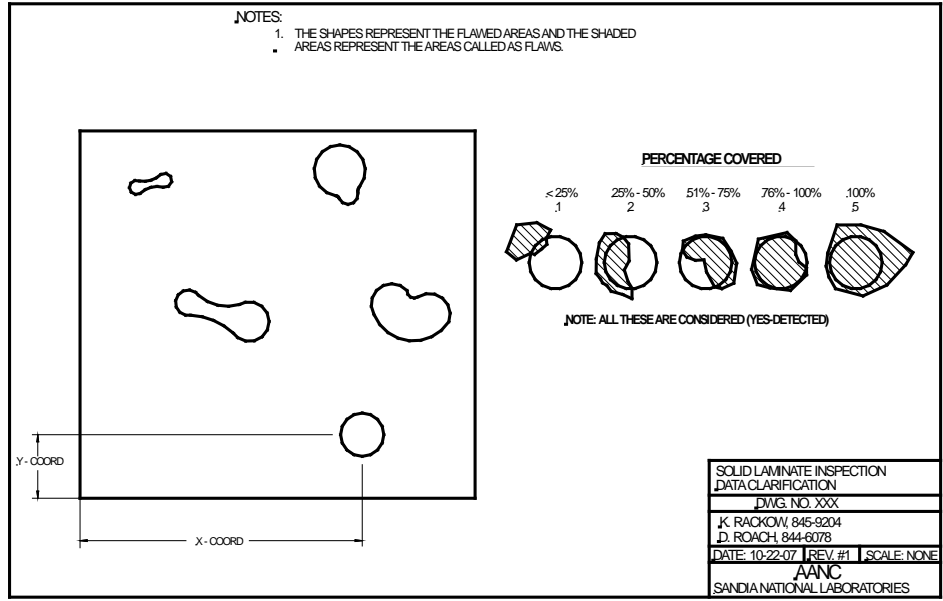


Figure A-14. Schematic showing the sizing categories comparing experimenter flaw calls with actual flaw information

4. Sample NDI Procedures for Pulse Echo Ultrasonic Inspection of Solid Laminate Composite Structures

Boeing and Airbus inspection procedures for solid laminate structures are provided as reference during the experiment. The procedures are for general deployment of NDT equipment that is relevant to this flaw detection experiment. The NDI procedures are included here as general information to aid inspectors in preparing for the flaw detection experiment. It is not expected that these procedures are sufficient to train an inexperienced inspector. Rather, they provide additional background and guidance to inspectors who are already familiar with the equipment and have experience in performing this type of solid laminate composite inspection. The Solid Laminate NDI Feedback Specimens provided with this experiment can be used in lieu of, or in addition to, the NDI standards described in the Boeing and Airbus inspection procedures.

APPENDIX B—COMPOSITE LAMINATE FLAW DETECTION EXPERIMENT:
EXPERIMENT BRIEFING

The following presentation was provided to inspectors prior to starting the experiment:

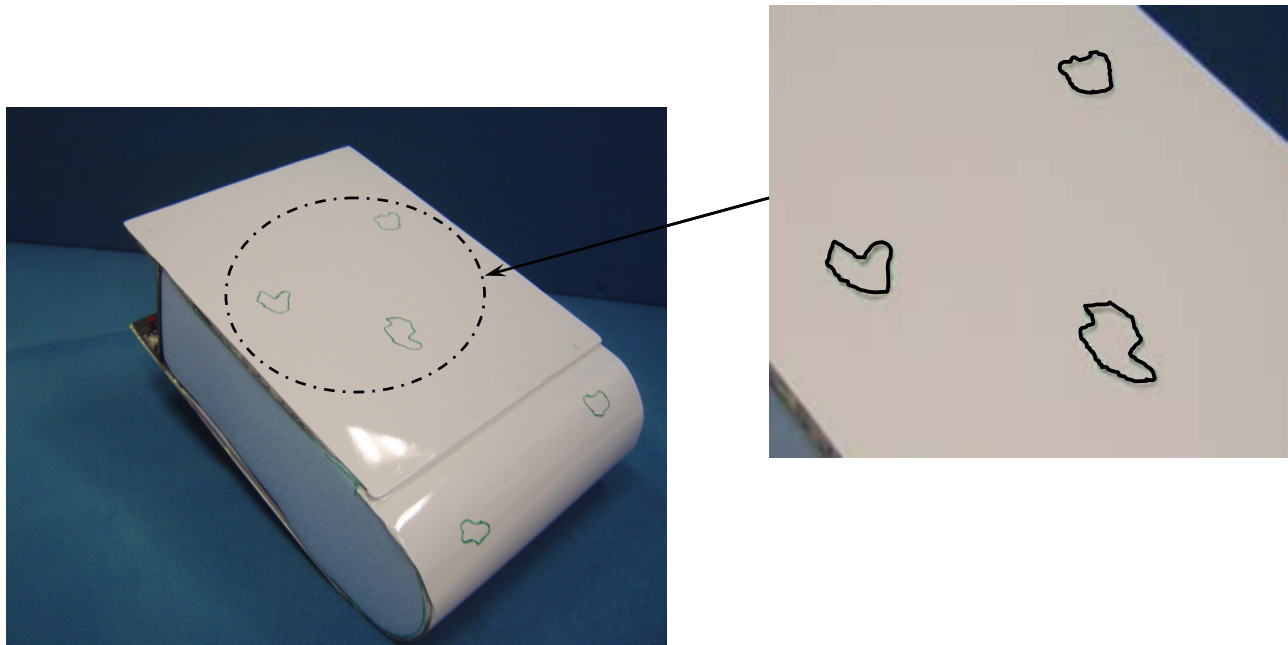
Composite Laminate Flaw Detection Experiment

Experiment Briefing

- The purpose of this experiment is to determine the capability of various inspection methods to detect and measure flaws in composite solid laminate aircraft structure. The Composite Laminate Flaw Detection Experiment will travel to many airlines and third party maintenance depots but it is not an evaluation of individual inspectors or particular companies.
- This effort will also identify the factors influencing composite inspections so that improved methods & procedures can be developed.
- You will be inspecting for representative disbonds, interply delaminations, and impact flaws in solid laminate composite structures. The test articles are modeled after the general range of construction scenarios found on commercial aircraft.
- Inspections will be conducted on a series of test panels and structures. The flat panels will be placed on a foam frame and the Bullnose specimens will be placed on a flat surface to produce uniform boundary conditions across all experimenters. You will be asked to inspect each test specimen and provide any information you can about the presence of flaws. If you determine that flaws are present, you should then provide size and shape information about each detected flaw. The results should be marked directly on the test specimen with the provided marking device.
- At no time should the inspector look at the underside of the blind test specimens. All references to test specimen structural configuration should be done by reviewing drawings provided for each specimen type. Note: two drawings will be provided for each specimen type. The first one will show the structural configuration of the panel in the orientation it is being inspected (painted side up with dark triangle marked in upper right-hand corner). The second drawing is an Isometric of the panel if the bottom side of the panel was turned up (just to show structural details that are on underside).
- When you have completed your inspection of the panel do not remove the panel from the inspection frame. Call on your experiment monitor to remove the test panel and provide the next panel.
- We will be recording the equipment make and model, probe information, and various settings that are used during the inspections, so if at any time you change probes, frequency or other pertinent settings during your inspections please call it to our attention so that we can record them.

- There are spray bottles available if you would like to mix the couplant with water to dilute it and then spray on the test specimens for coupling purposes.
- There are two separate experiments. There is a Thin Laminate Skin experiment [1] with skins ranging from 12-20 plies (0.078" to 0.130" thick) and total thickness extending to 62 plies (0.406") when substructure is considered. There is also Thick Laminate Skin experiment [2] with 32 ply skins (0.21" thick) and total thickness extending to 58 plies (0.377") when substructure is considered.
- Inspectors can complete the Thin Laminate Skin experiment in 3 days. There are 11 specimens in this experiment. Inspectors can complete the Thick Laminate Skin experiment in 1 to 2 days. There are 4 specimens in this experiment.
- Experimenters should work at a pace that is comfortable for them; time to inspect is a secondary variable of the experiment. Inspectors should take whatever time is necessary to assure that any and all flaws in the test specimens are found.
- Test Specimens
 - **Material Type** - carbon graphite
 - **Laminate Thicknesses** - Panels have 12 (~.078"), 20 (~.130"), 24 (~.156"), and 32 (~.229") plies.
 - **Substructure Thicknesses** – .075", .125", .192", .225", and .250"
 - **Tapered Area Ranges** – 12-20 (.50" step), 20-32 (.50" step), and 12-20 (.25" step)
 - **Paint** - All panels are painted as per current aircraft specifications.
 - **Flaw Detection** - Inspectors should use any positive indications to find flaws as small as 1/4" in diameter.
 - **Inspection Device** – You may use any inspection device that you would normally use to inspect composite laminate structures.
- Each blind inspection process should be preceded by inspections on appropriate solid laminate training/feedback specimens supplied by the experiment monitors. You will be given information on the manufactured flaws present in the training/feedback specimens. The training/feedback specimens have the same construction as the blind test specimens and include similar flaws.
- Inspectors may need or choose to use alternate probes due to: a) variation and extremes in thickness, and b) our desire to find flaws as small as 1/4" diameter. The training/feedback specimens allow inspectors to try probes of various sizes and frequencies so that they can optimize their equipment before performing the blind inspections.
- The figure below shows a sample set of flaw marks on one of the solid laminate composite test specimens. This study would like to assess performance for flaws as small as 1/4" in diameter. Inspectors should use any positive indications to find flaws as small as 1/4" in diameter. It is not necessary to track small anomalies, such as porosity, that are less than 1/4" in length.

- Experimenters should try various transducers on the feedback panels (known flaw profiles) provided in this experiment to determine the best transducer to use for each laminate thickness. Existing Boeing and Airbus procedures reference the use of UT transducers in the range of 1-10 MHz (1, 2.25, 5, 10 MHz are all listed). The transducer diameters are listed as 0.5” and 0.25” dia. The required flaw detection listed in the Boeing procedures is 5/64” dia. Both the Boeing and Airbus procedures are contained in the “Experimenters Information Packet.”
- An inspector will complete all specimens (11) for the 12-20 ply experiment or 4 specimens for the 20-32 ply experiment and will be asked to finish all of a specific specimen design (i.e. Bullnose, Complex Taper) before moving on to the next specimen type.



- Additional guidance for inspectors performing this experiment are as follows:
 - Experimenters should work at a pace that is comfortable for them. Although monitors will note start and stop times for your inspection, time to inspect is a secondary variable of the experiment.
 - Applicable procedures from OEM manuals will be provided as a reference tool. Inspectors should use their own judgment as to how to perform the inspection (i.e. a strict procedure will not be enforced).
 - Inspection coverage should be 100% of the panel with the exception of a small .50" band around the perimeter of the panels where edge effects may create problems.
 - The Solid Laminate Training/Feedback Specimens provided should be used to set up the equipment. Minor equipment adjustments stemming from in-situ calibration on the parts being inspected are allowed.
 - Inspectors should draw the entire size/shape of the flaw (i.e. delineate the edges).
 - Inspectors do not need to determine the type of flaw just the location, size, and shape of the suspected anomaly.

- Inspectors should ignore any visual clues (surface anomalies in the paint or small surface marks) and to avoid using these as flaw detection aids. Such anomalies may be intentionally planted to add complexity to the inspection. Inspectors should only make a call on those flaws that are indicated by their inspection device.
- Training/Feedback Specimens should be used as an aid to determine where to make flaw call edges. This is based on the diameter of the probe and how much of the probe needs to be over the flaw in order to react/detect.
- Go through the series of A-scan signals in Experimenter Information Packet to clarify flaw calls.
- Test results will identify hits (calls with any amount of overlap between the call and the solution), misses (no call for an area of a known flaw), false calls (call with no overlap of a flaw), and the degree of overlap between experimenter calls and actual flaw areas.
- You will be provided with feedback to indicate how you performed - percentage of flaws found, how well you sized the flaws, and number of false calls made. Inspectors will gain experience and feedback on the implementation of your inspections on representative aircraft structure. No individual inspector's names will be linked to any experiment results. Similarly, no organization's name will be linked to any group of experiment results. However, results of all participants will be combined and potential users will be able to compare the results of competing inspection techniques and systems.
- We can also provide feedback on the type of flaws that were detected and missed so that the inspector will learn what types of flaws they have trouble detecting. It is important to note that the feedback to the inspectors is kept confidential. In the final aggregate results, we ensure that the participants are always kept anonymous so that there is no way to correlate any results to a specific person or airline.
- A series of Boeing and Airbus inspection procedures, relevant to this flaw detection experiment, are included in your "Experimenter Information Packet." Use them as you see fit. They provide information on equipment setup and scan patterns for typical solid laminate inspections.

**APPENDIX C—COMPOSITE SOLID LAMINATE FLAW DETECTION EXPERIMENT:
EXPERIMENT MONITOR DATA ACQUISITION SHEETS**

SOLID LAMINATE INSPECTION TIMING RESULTS AND PANEL DISTRIBUTION (12-20 PLY)														
Panel Description	Panel Inspection Order (random)	Start Time 1	Stop Time 1	Elapsed Time 1	Start Time 2	Stop Time 2	Elapsed Time 2	Start Time 3	Stop Time 3	Elapsed Time 3	Start Time 4	Stop Time 4	Elapsed Time 4	Total Elapsed Time
Complex Taper 1-A														
Complex Taper 1-B														
Complex Taper 2-A														
Complex Taper 2-B														
Simple Taper 1-A Upper														
Simple Taper 1-A Lower														
Simple Taper 2-A Upper														
Simple Taper 2-A Lower														
Bullnose 1														
Bullnose 2														
Bullnose 3														
Total														

Inspector Name: _____ Date: _____
 Company: _____
 Inspection Method: _____

Note: Multiple start and stop times for a single test specimen are provided in case the inspector needs to take a break(s) before completing inspection of a single specimen.

Figure C-1. Solid laminate inspection timing results and panel distribution (12-20 ply)

SOLID LAMINATE INSPECTION TIMING RESULTS AND PANEL DISTRIBUTION (20-32 PLY)														
Panel Description	Panel Inspection Order (random)	Start Time 1	Stop Time 1	Elapsed Time 1	Start Time 2	Stop Time 2	Elapsed Time 2	Start Time 3	Stop Time 3	Elapsed Time 3	Start Time 4	Stop Time 4	Elapsed Time 4	Total Elapsed Time
New 32 - 1														
New 32 - 2														
New 32 - 3														
New 32 - 4														
Total														

Inspector Name: _____ Date: _____
 Company: _____
 Inspection Method: _____

Note: Multiple start and stop times for a single test specimen are provided in case the inspector needs to take a break(s) before completing inspection of a single specimen.

Figure C-2. Solid laminate inspection timing results and panel distribution (20-32 ply)

EQUIPMENT CALIBRATION

Name of inspector/facility: _____

Inspector Number: _____

12-20 or 20-32 ply Experiment: _____

Inspectors Experience: Overall NDI - _____ NDI of Composites - _____

Record the technique to be used : _____

Record equipment information :

Manufacturer: _____

Model: _____ Serial #: _____

Certification Date: _____

Record probe or other ancillary equipment information:

Manufacturer: _____

Reference #: _____

Record any other accessory information: _____

Ask the participant to provide specific equipment set/up or calibration settings. Examples of the type of information to be provided could include some of the following:

Gain: horizontal _____ vertical _____ meter _____

Frequency (kHz) _____

Filtering _____

Calibration Level _____

_____ Inspection threshold

Coil output impedance _____

Digitization _____

Figure C-3 (sheet 1). Experiment monitor data acquisition sheet

Equipment calibration performed: YES NO (circle one)

Record calibration standard information:

a) Solid Laminate Composite Ref. Stds. were used: YES NO (circle one)

b) Other Ref. Stds. used (if so, list) _____

c) Is calibration standard used referenced in NDT manual? YES NO (circle one)

d) How long did it take to calibrate the equipment? _____

Note any difficulties encountered during equipment calibration.

Note any innovative procedures or practices used for equipment calibration.

Figure C-3 (sheet 2). Experiment monitor data acquisition sheet

Inspection

Name of inspector/facility: _____

Device Deployed _____

Experience, background information (including experience on device deployed). _____

List NDI devices used at the facility for composite inspections: _____

Note any difficulties encountered during the inspection. _____

Note any innovative procedures or practices used during the inspection of this specimen.

INSPECTION DATA LOGGING

Figure C-4 (sheet 3). Experiment monitor data acquisition sheet

ANALYSIS

Name of inspector/facility: _____

Did the operator/inspector follow pre-set criteria for flaw identification? Yes No

If Yes, describe the criteria; If No, describe how the decision was made.

Note any difficulties encountered during the analysis of this specimen?

Note any innovative procedures or practices used for analysis?

Figure C-5 (sheet 4). Experiment monitor data acquisition sheet

APPENDIX D—COMPOSITE LAMINATE FLAW DETECTION EXPERIMENT:
SUMMARY OF TEST SPECIMENS

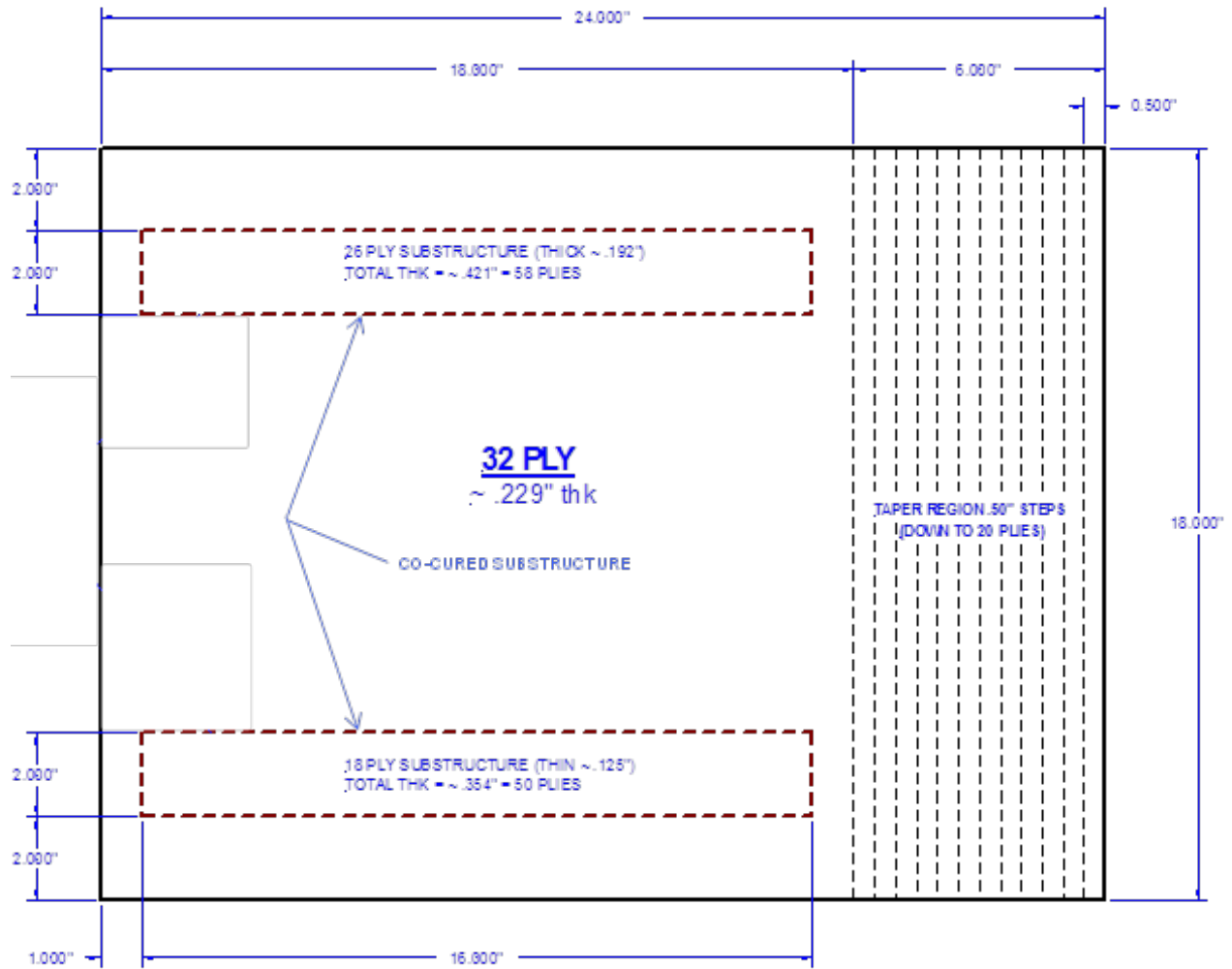


Figure D-1. Simple taper 20-32 ply specimen – 4 panels, all the same size but different flaw profiles

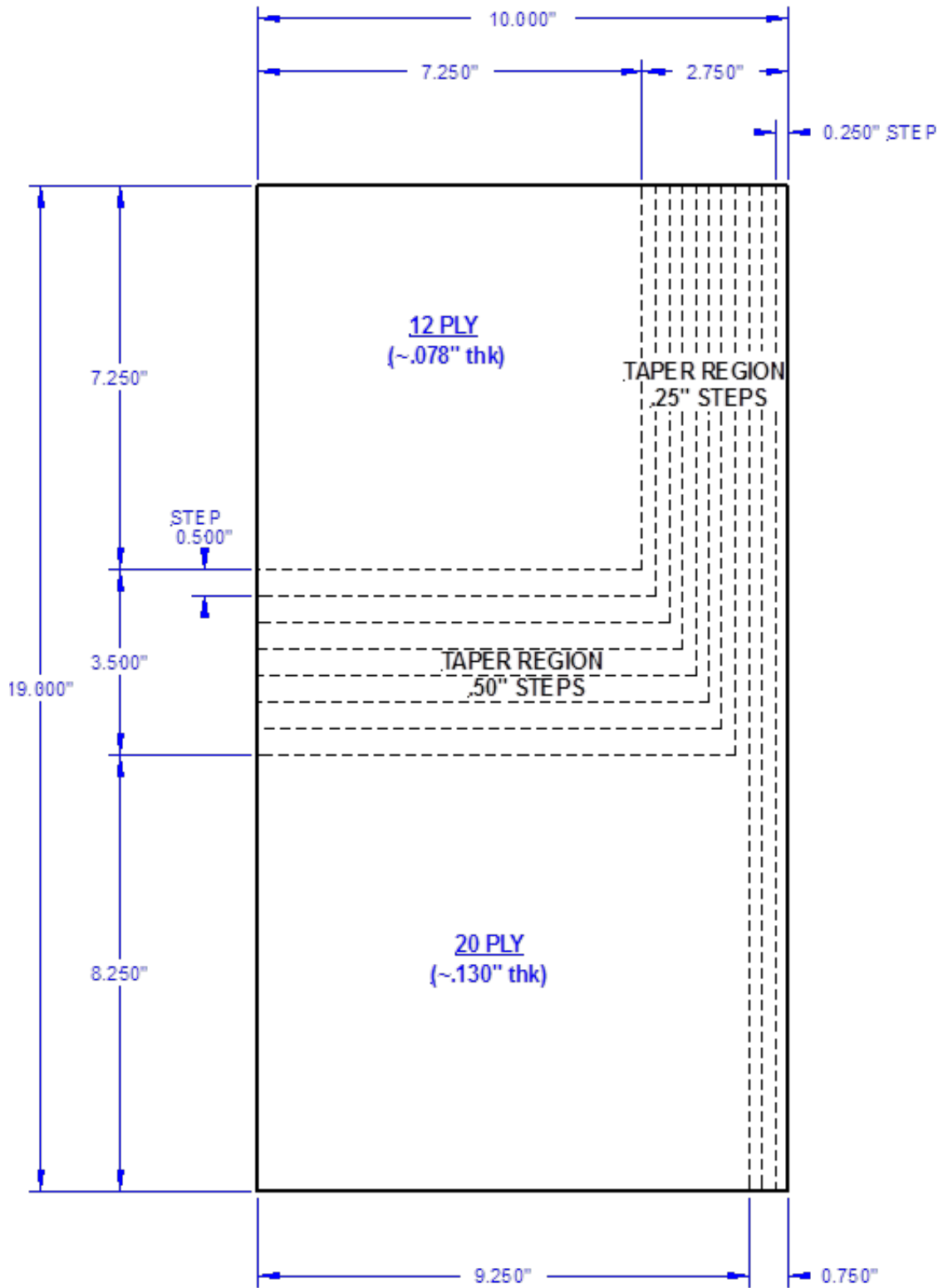


Figure D-2. Complex taper 12-20 ply specimen – 4 panels, all the same size but different flow profiles

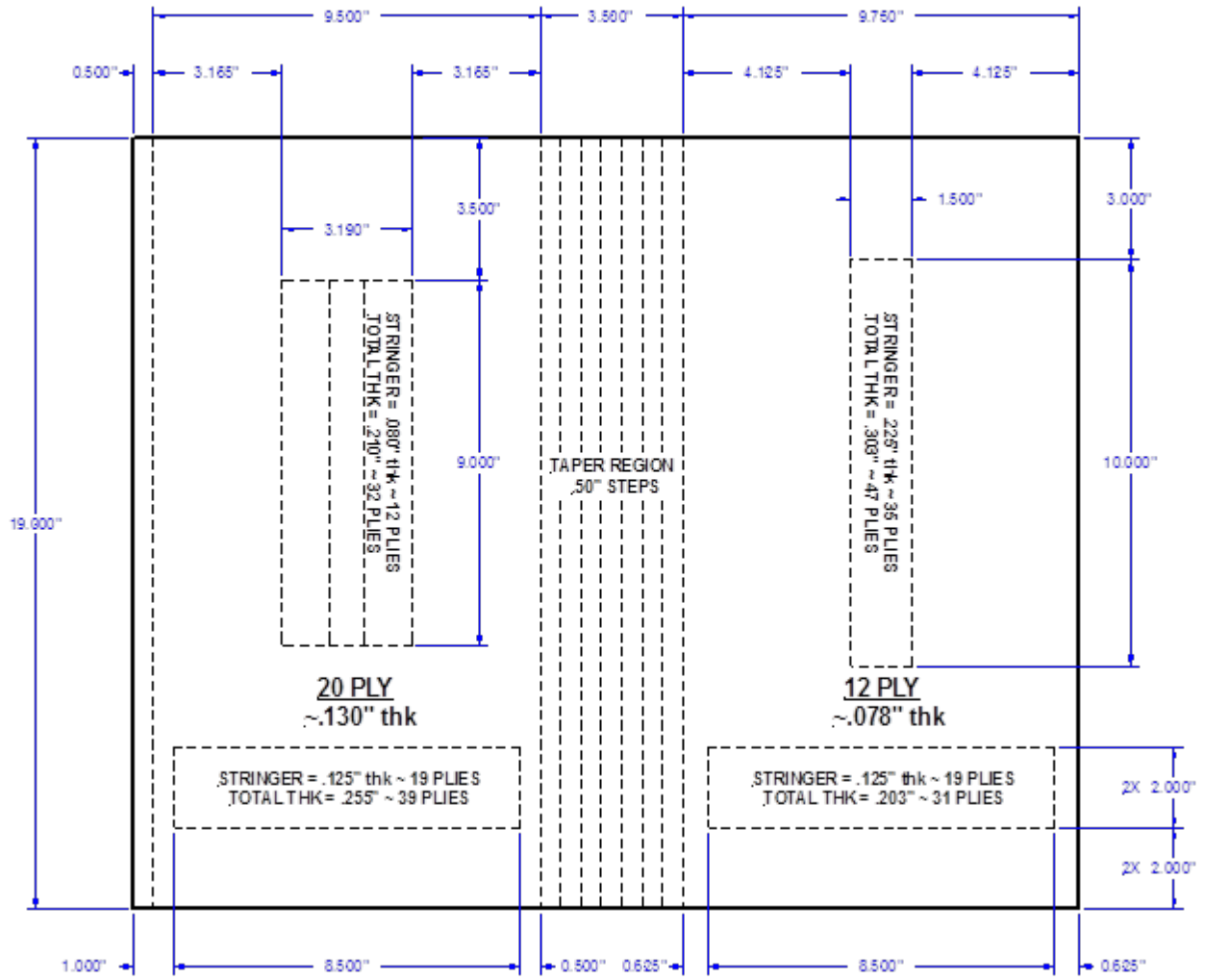


Figure D-3. Simple taper 12-20 ply specimen – 4 panels, all the same size but different flaw profiles

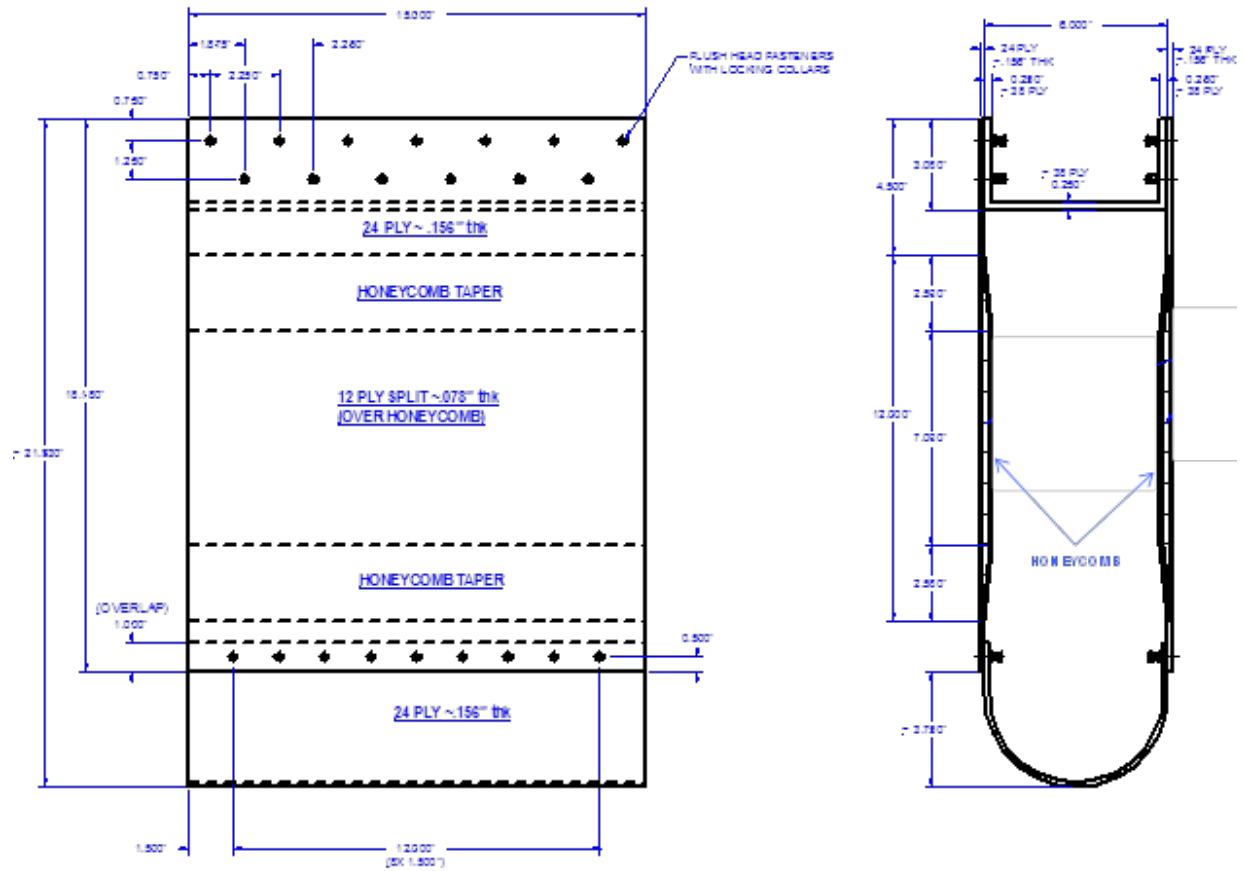


Figure D-4. Bullnose 12-20 ply specimen – 3 panels, all the same size but different flaw profiles

APPENDIX E— DISTRIBUTION LIST FOR REPORT

Frances Abrams
US Air Force
WPAFB, OH

Paul Acres
Lockheed-Martin
Ft Worth, TX

Douglas Adams
Vanderbilt University
Nashville, TN

Tasdiq Ahmed
Thermal Wave Imaging
Ferndale, MI

Aydin Akdeniz
Boeing
Seattle, WA

Dick Alberts
Digiray Corporation
Danville, CA

Nick Amabile
US Navy
Lakehurst, NJ

Jay Amos
Cessna Aircraft Co.
Wichita, KS

Shreyas Ananthan
US Department of Energy
Washington, DC

Paulo Anchieta da Silva
Embraer
São José dos Campos, Brazil

Jim Arnold
United Airlines
Houston, TX

Yoshiaki Asako
Mitsubishi
Addison, TX

Masahiro Asano
Japan Airlines
Tokyo, Japan

Cindy Ashforth
FAA
Seattle, WA

Hesham Azzam
HAHN Spring Ltd
Southampton, United Kingdom

John Bakuckas
FAA WJ Hughes Technical Center
Atlantic City Int'l Airport, NJ

Rocky Ballew
United Airlines
San Francisco, CA

Tom Barber
Delta Airlines
Minneapolis, MN

Dan Barnard
Iowa State Univ – CNDE
Ames, IA

David Barrett
US Navy
Patuxent River MD

Bob Barry
Bell Helicopter
Ft. Worth, TX

Eric Bartoletti
Southwest Airlines
Grapevine, TX

Zachary Bender
Delta Air Lines
Atlanta, GA

Rob Bergman
GE Energy
Schenectady, NY

Phil Berkley
GKN Westland Aerospace
United Kingdom

Malcolm Berner
Delta Air Lines
Atlanta, GA

Blake Bertrand
Boeing
Seattle, WA

Subra Bettadapur
US Navy
Patuxent River, MD

Anne Birt
QinetiQ
Farnborough, United Kingdom

Werner Bischoff
Lufthansa Technik AG
Hamburg, Germany

Wolfgang Bisle
Airbus
Bremen, Germany

James Bitner
Olympus NDT
Kennewick, WA

Sara Black
High Performance Composites
Denver, CO

Kay Blohowiak
Boeing
Seattle, WA

Clemens Bockenheimer
Airbus
Toulouse, France

Bryce Boe
Raytheon Aircraft Co.
Wichita, KS

John Bohler
Delta Air Lines
Atlanta, GA

Christian Boller
Fraunhofer Institute
Saarbrücken, Germany

Mike Borgman
Spirit Aviation
Wichita, KS

Richard Bossi
Boeing
Seattle, WA

Francis Boudreault-Leclerc
Olympus NDT
Québec, Canada

John Brausch
US Air Force
WPAFB, OH

Nick Brinkhoff
Cessna Aircraft Co.
Wichita, KS

Alistair Burns
Air New Zealand
Auckland, New Zealand

Rex Carlton
Delta Airlines
Minneapolis, MN

Charles Buynak
US Air Force
WPAFB, OH

Chris Carella
UTC Aerospace Systems
Vergennes, VT

Sander Carneiro
Agencia Nacional de Aviação Civil
São José dos Campos, Brazil

Christopher Chandler
Delta Airlines
Atlanta, GA

Che-Yin Chang
China Airlines
Taoyuan, Taiwan

Fu-Kuo Chang
Stanford University
Stanford, CA

Randy Chappelle
Delta Air Lines
Atlanta, GA

Carlos Chaves
Embraer
São José dos Campos, Brazil

BoChye Cher
Singapore Air
Singapore

Eric Chesmar
United Airlines
San Francisco, CA

George Clamser
Delta Airlines
Atlanta, GA

Heath Coker
Delta Airlines
Atlanta, GA

Ron Cook
American Airlines
Tulsa, OK

Jeff Cornell
Aviation Technical Services
Seattle, WA

Vicente Cortes
Airbus
Madrid, Spain

Ed Cosgro
Petroleum Helicopters, Inc.
Lafayette, LA

Richard Costantino
UTC Aerospace Systems
Chula Vista, CA

Joe Cotter
UPS
Louisville, KY

Danny Crab
Cargolux Airlines
Luxembourg

Elliott Cramer
NASA - LaRC
Hampton, VA

John Cramer
Kalitta Air
Detroit, MI

Eric Cregger
Boeing
Seattle, WA

Matt Crompton
Dantec Dynamics
Holtsville, NY

Curt Davies
FAA WJ Hughes Technical Center
Atlantic City Int'l Airport, NJ

Mark Davis
Sikorsky Aircraft
Stratford, CT

Paul Davis
Delta Airlines
Atlanta, GA

Russell Day
Kalitta Air
Detroit, MI

Mark Derriso
US Air Force
Wright-Patterson AFB, OH

Mike Derby
US Dept of Energy
Washington, DC

Matt Dill
Nordam
Tulsa, OK

Leo Dominguez
American Airlines/TAESL
Fort Worth, Texas

Fernando Dotta
Embraer
São José dos Campos, Brazil

Steve Douglas
FAA
Washington, DC

Christopher Dragan
Air Force Institute of Technology
Warsaw, Poland

Tommy Drake
iPhoton
Fort Worth, TX

Tom Dreher
Rolls Royce Engine
Indianapolis, IN

Marc Dubois
iPhoton
Fort Worth, TX

Don Duncan
US Airways
Charlotte, NC

Paul Ebert
ST Aerospace
San Antonio, TX

Tom Eischeid
General Electric
Lewistown, PA

Rebeca Elford
United States Air Force
Kirtland AFB, NM

John Ellington
FedEx
Indianapolis, IN

Robert Fabyan
Kalitta Air
Detroit, MI

Tim Fallon
US Navy
Patuxent River, MD

Bennett Feferman
Laser Technology Inc.
Norristown, PA

Luis Fernandes
TAP Portugal
Portugal

Joy Finnegan
Aviation Maintenance
Rockville, MD

Carl Fisher
FedEx
Memphis, TN

Tom Flournoy
FAA WJ Hughes Technical Center
Atlantic City Int'l Airport, NJ

Brian Flinn
University of Washington
Seattle, WA

Rafael Fávaro Foltran
Agencia Nacional de Aviação Civil
São José dos Campos, Brazil

Peter Foote
Cranfield University
Cranfield, United Kingdom

Andrew Freese
Air New Zealand
Auckland, New Zealand

Mark Freisthler
FAA
Renton, WA

Scott Fung
FAA
Renton, WA

Steve Galea
Defence Science and Technology Org
Melbourne, Australia

Yolanda de Frutos Galindo
Airbus
Madrid, Spain

Dave Galella
FAA WJ Hughes Technical Center
Atlantic City Int'l Airport, NJ

Rachel Gayle
United States Air Force
Kirtland AFB, NM

Marc Genest
National Research Council Canada
Ottawa, Canada

Gary Georgeson
Boeing
Seattle, WA

Roger Gibreal
Aviation Technical Services
Seattle, WA

Brad Gilliland
General Electric
Pleasant Hill, MO

Keith Gilmore
United Airlines
San Francisco, CA

Juan Gomez
United Airlines
Orlando, FL

Thomas Gonzales
FedEx
Los Angeles, CA

Steve Goncz
Sky West
Salt Lake City, UT

Grant Gordon
Honeywell
Phoenix, AZ

Nathalie Gouret
Airbus
Blagnac Cedex, France

John Graff
Delta Airlines
Minneapolis, MN

Dennis Granger
US Army
Redstone Arsenal, AL

Robert Grant
FAA
Ft. Worth, TX

Philip Griggs
GE Aviation
Cincinnati, OH

Courtney Guasti
US Army
Redstone Arsenal, AL

Mike Gutierrez
Federal Express
Los Angeles, CA

Fred Guzman
Delta Airlines
Minneapolis, MN

Jason Habermehl
Olympus NDT
Quebec, Canada

Bob Hager
Delta Air Lines
Minneapolis, MN

Colin Hanna
Bombardier
Belfast, United Kingdom

Tim Harris
Boeing
Ft. Lauderdale, FL

Eric Hauge
Boeing
Seattle, WA

Dale Hawkins
FAA
Washington, DC

Pekka Hayrinen
Finnair
Helsinki, Finland

Rudolf Henrich
Airbus
Bremen, Germany

Nick Heminger
Aviation Technical Services
Seattle, WA

Daniel Hebert
Transport Canada
Ottawa, Ontario, Canada

Dirk Heider
University of Delaware
Newark, DE

Scott Herbert
AAR Corp.
Indianapolis, IN

Steve Hicks
Timco
Greensboro, NC

Derek Highet
Cathay Pacific Airlines
Hong Cong, China

Keiji Hirabayashi
All Nippon Airways
Tokyo, Japan

Jim Hofer
Boeing
Huntington Beach, CA

Wolfgang Hoffman
European Aviation Safety Agency
Cologne, Germany

Ed Hohman
Bell Helicopter
Fort Worth, TX

Mike Hoke
ABARIS Training
Reno

Quincy Howard
Boeing
Seattle, WA

Scott Huddleston
US Army
Redstone Arsenal, AL

Jeong-Beom Ihn
Boeing
Seattle, WA

Takahiro Ikeda
Toshiba
Yokohama, Japan

Larry Ilcewicz
FAA
Renton, WA

Yutaka Iwahori
Japan Aerospace Exploration Agency
Tokyo, Japan

Dan Jacobson
San Diego Composites
San Diego, CA

Bill Jappe
Boeing
Huntington Beach, CA

Patrick Johnston
NASA Langley Research Center
Hampton, VA

Kevin Jones
Gulfstream Aerospace Corp.
Savannah, GA

Rusty Jones
FAA
Washington, DC

Ray Kaiser
Delta Air Lines
Minneapolis, MN

Frank Kane
United States Air Force
Kirtland AFB, NM

Hirokuza Karasawa
Toshiba
Yokohama, Japan

Kazunori Kato
Japan Airlines
Tokyo, Japan

Russell Keller
Boeing
Seattle, WA

Seth Kessler
Metis Design Corporation
Cambridge, MA

Hyonny Kim
UC San Diego
La Jolla, CA

Tim Kinsella
Falcon Jet
Little Rock, AR

James Kissel
Delta Airlines
Minneapolis, MN

Rene Klieber
SR Technics
Zurich, Switzerland

Kenneth Knopp
FAA WJ Hughes Technical Center
Atlantic City Int'l Airport, NJ

Hiroshi Kobayashi
All Nippon Airways
Tokyo, Japan

Kendall Koerner
Spirit Aerosystems
Wichita, KS

Alan Koh
Singapore Air
Singapore

Jeff Kollgaard
Boeing
Seattle, WA

Jerzy Komorowski
National Research Council Canada |
Ottawa, ON, Canada

Ajay Koshti
NASA-Johnson Space Center
Houston, TX

Mike Krehbiel
American Airlines
Tulsa, OK

Paul Kulowitch
US Navy
Patuxent River, MD

André Lamarre
Olympus NDT
Québec, Canada

Bob Lasser
Imperium
Beltsville, MD

Francois Landry
Bell Helicopter
Montreal, Canada

Dy Le
US Army
Aberdeen Proving Ground, MD

Ray Leseck
US Airways
Neville Island, PA

Arne Lewis
Boeing
Seattle, WA

Obdulia Ley
MISTRAS
Princeton, NJ

Marco Liberatoscioli
Alitalia
Rome, Italy

Glenn Light
Southwest Research Institute
San Antonio, TX

Eric Lindgren
US Air Force
WPAFB, OH

John Linn
Boeing
Seattle, WA

Jack Little
Evisive Inc.
Baton Rouge, LA

John Lundeen
US Navy
Patuxent River, MD

Robert Luiten
KLM Airlines
Amsterdam, The Netherlands

John Lundeen
US Navy
Patuxent River, MD

Doug Lutz
General Electric
Lewistown, PA

Renato Maia
Embraer
São José dos Campos, Brazil

Ben Manning
Express Jet
Houston, TX

Carol Martineau
FAA
Washington, DC

Marcias Martinez
Technical University of Delft
Delft, The Netherlands

Ryan Mather
Timco
Macon, GA

Junya Matsuda
Japan Airlines
Tokyo, Japan

Shin Matsumoto
Toshiba
Tokyo, Japan

Jim Mazza
US Air Force
WPAFB, OH

Sergio Mayer
Embraer
San Jose dos Campos, Brazil

Glae McDonald
US Airways
Charlotte, NC

Jim Mcfeat
BAe Systems
Bristol, United Kingdom

Robert Mcquire
FAA
Atlantic City, NJ

Jason Meade
United Airlines
Houston, TX

Alexander Melton
Delta Air Lines
Atlanta, GA

Thomas Mensah
Georgia Aerospace
Atlanta, GA

Steve Micich
AAR Corp.
Indianapolis, IN

Clark Miller
Southwest Airlines
Highland Village, TX

Ronald Miller
Delta Airlines
Minneapolis, MN

Scott Miller
Alaska Airlines
Seattle, WA

Eric Mitchell
American Airlines
Tulsa, OK

Yoichi Mizuma
Japan Airlines
Tokyo, Japan

Elyse Moody
Aviation Week Overhaul & Maintenance
New York, NY

Calvin Moore
US Air Force
Tinker Air Force Base, OK

Tom Moran
US Air Force
WPAFB, OH

Matt Moye
US Air Force
Tinker Air Force Base, OK

Tommy Mullis
US Air Force
Warner Robins, GA

Francois Museux
Airbus
Blagnac, France

Yosuke Nagao
Japan Aerospace Exploration Agency
Tokyo, Japan

Tamotsu Nagasaka
All Nippon Airways
Tokyo, Japan

John Newman
Laser Technology Inc.
Norristown, PA

Bill Nicol
MoviMED
Irvine, CA

Steve Nolet
TPI Composites
Warren, RI

Ronan O'Higgins,
University of Limerick,
Limerick, Republic of Ireland

Toshimichi Ogisu
Fuji Heavy Industries
Tochigi, Japan

Paul Oulton
United Airlines
San Francisco, CA

Christophe Paget
Airbus
Bristol, United Kingdom

Georgios Papageorgiou
Olympic Airways
Athens, Greece

Rob Pappas
FAA
Washington, DC

Mohd. Alamin Pardi
Malaysia Airlines
Selangor, Malaysia

Mick Patino
American Airlines
Tulsa, OK

Kieran Patton
Shannon Aerospace
County Clare, Ireland

Luiz Perin
Embraer
São José dos Campos, Brazil

Dorsey Perkins
Southwest Airlines
Grapevine, TX

Will Perry
General Electric
Lewistown, PA

Hartmut Peters
Lufthansa Technik AG
Hamburg, Germany

Keith Phillips
Airbus
Bristol, United Kingdom

Steve Phillips
Kalitta Air
Detroit, MI

Jérôme Pinsonnault
Bombardier
Montreal, Canada

David Piotrowski
Delta Air Lines
Atlanta, GA

Jan Popp
Lufthansa
Hamburg, Germany

Bill Prosser
NASA Langley Research Center
Hampton, VA

Bernd Rackers
Airbus
Bremen, Germany

Tom Reep
Zetec
Issaquah, WA

Kevin Rees
U.S. Army
Corpus Christi, TX

Jeff Register
General Electric
Minneapolis, MN

Joerg Reinersmann
General Electric
Huerth, Germany

Paul Risso
United Airlines
San Francisco, CA

Kurt Robinson
Delta Air Lines
Atlanta, GA

Ana Rodriguez
Airbus
Madrid, Spain

Raul Rojas
Delta Airlines
Atlanta, GA

Craig Rolfson
Delta Airlines
Minneapolis, MN

Ralph Rotolante
MoviTherm
Boxborough, MA

Jean Rouchon
European Aviation Safety Agency
Toulouse Cedex, France

Ricardo Rulli
Embraer
São José dos Campos, Brazil

Rick Russell
NASA
Kennedy Space Center, FL

Bob Saathoff
Cessna Aircraft Company
Wichita, KS

Patrick Safarian
FAA
Renton, WA

Lamia Salah
Wichita State Univ. - NIAR
Wichita, KS

Liming Salvino
US Navy
Singapore

Fernando Santos
NDT Expert
Toulouse, France

Luis Santos
Embraer
São José dos Campos, Brazil

Jeffery Schaff
Sikorsky Aircraft
Stratford, CT

Carlyn Schlottman
Boeing
Seal Beach, CA

George Schneider
Sikorsky Aircraft
Stratford, CT

Bob Scoble
United Airlines
San Francisco, CA

Dachar Sertpunnuak
Thai Airways International
Bangkok, Thailand

Steve Shepard
Thermal Wave Imaging
Ferndale, MI

Jimmy Shiver
UTC Aerospace Systems
Birmingham, AL

Vilmar da Silva do Valle
Embraer
San Jose dos Campos, Brazil

Walt Sippel
FAA
Renton, WA

Eskil Skoglund
DolphiTech
Raufoss, Norway

Jesse Skramstad
NDT Solutions, Inc.
New Richmond, WI

Duane Slabaugh
Delta Airlines
Atlanta, GA

Art Smith
AAR Corp.
Indianapolis, IN

Scott Smotherman
ST Aerospace Mobile
Mobile, AL

Hideki Soejima
Fuji Heavy Industries
Tochigi, Japan

David Sokol
LSP Technologies
Dublin, OH

Holger Speckmann
Airbus
Bremen, Germany

Giancarlo Spera
Alitalia
Rome, Italy

Reinhardt Spiegel
Airbus
Stade, Germany

Bob Stakenborghs
Evisive, Inc.
Baton Rouge, LA

Raymond Stolarz
JetBlue Airways
Jamaica, NY

Larry Sullivan
UTC Aerospace Systems
Chula Vista, CA

Paul Swindell
FAA WJ Hughes Technical Center
Atlantic City Int'l Airport, NJ

Ralph Sykes
Lockheed Martin
Marietta, GA

Nobuo Takeda
University of Tokyo
Tokyo, Japan

Chinnaphan Thattiyaphong
Thai Airways International
Bangkok, Thailand

Robert Thomason
ST Aerospace
San Antonio, TX

Jeffery Thompson
Boeing
Seattle, WA

Darrell Thornton
UPS
Louisville, KY

Zuhair Tibi
Jet Blue
New York, NY

Samuel Tucker
United Airlines
San Francisco, CA

Andrew Vechart
Honeywell Aerospace AT
Golden Valley, MN

Victor Vilents
PK Design
Moscow, Russia

John Vogt
Nordam
Tulsa, OK

Dennis von Seelen
Lufthansa Airlines
Hamburg, Germany

Chinh Vuong
FAA
Ft. Worth, Tx

Simon Waite
European Aviation Safety Agency
Köln, Germany

Rusty Waldrop
US Coast Guard
Elizabeth City, NC

Patrick Walter
Texas Christian University
Ft. Worth, TX

Rick Wampler
Delta Air Lines
Atlanta, GA

Thomas Walz
Dantec Dynamics
Holtsville, NY

Ben Wang
Florida State Univ
Tallahassee, FL

Ed Weinstein
FAA WJ Hughes Technical Center
Atlantic City Int'l Airport, NJ

Lorenz Wenk
Airbus
Hamburg, Germany

Clemens Westerkamp
University of Applied Sciences
Osnabrueck, Germany

Dave Westlund
FAA WJ Hughes Technical Center
Atlantic City Int'l Airport, NJ

Kyle Wetzel
Wetzel Engineering
Lawrence, KS

Al Williams
ST Aerospace Mobile
Mobile, AL

Scott Williams
Southwest Airlines
Grapevine, TX

William Winfree
NASA Langley Research Center
Hampton, VA

Buzz Wincheski
NASA Langley Research Center
Hampton, VA

Ian Won
FAA
Renton, WA

Roy Wong
Bombardier
Montreal, Quebec Canada

Nancy Wood
Boeing
St. Louis, MO

John Vogt
Nordham
Tulsa, OK

Jun Yamanaka
Japan Airlines
Tokyo, Japan

Rick Young
NASA Langley Research Center
Hampton, VA

Lei Yue
Taikoo Xiamen Aircraft Engineering
Xiamen Fujian, China

Sandia National Labs:

1522 Ciji Nelson
1522 David Moore
1522 Kevin Rolfe
1527 Colin McConnell
1833 David Calkins
1833 Michael Kelly
1833 William Miller
6121 David Minster
6121 Joshua Paquette
6122 Daniel Laird
6000 Jill Hruby
6600 Billy Marshall
6610 Jeff Danneels
6620 Roberto Mata
6620 Willy Morse
6620 Dennis Roach
6621 Michel Bode
6621 Randy Duvall
6621 Steve Heffelfinger
6621 Carl Jacques
6621 Stephen Neidigk
6621 Tom Rice
6622 Robert Baca
6623 Mark Soo Hoo
6625 Barry Boughton
6630 Brad Parks
9532 Recorded Information Management